

NASA Technical Memorandum 4738
ATCOM Technical Report 97-A-001

Unsteady Velocity Measurements Taken Behind a Model Helicopter Rotor Hub in Forward Flight

John D. Berry
Joint Research Program Office
Aeroflightdynamics Directorate
U.S. Army Aviation and Troop Command
Langley Research Center • Hampton, Virginia

Available electronically at the following URL address: <http://techreports.larc.nasa.gov/ltrs/ltrs.html>

Printed copies available from the following:

NASA Center for AeroSpace Information
800 Elkridge Landing Road
Linthicum Heights, MD 21090-2934
(301) 621-0390

National Technical Information Service (NTIS)
5285 Port Royal Road
Springfield, VA 22161-2171
(703) 487-4650

Summary

Drag caused by separated flow behind the hub of a helicopter has an adverse effect on aerodynamic performance of the aircraft. To determine the effect of separated flow on a configuration used extensively for helicopter aerodynamic investigations, an experiment was conducted using a laser velocimeter to measure velocities in the wake of a model helicopter hub operating at Mach-scaled conditions in forward flight.

Velocity measurements were taken using a laser velocimeter with components in the vertical and downstream directions. Measurements were taken at 13 stations downstream from the rotor hub. At each station, measurements were taken in both a horizontal and vertical row of locations. These measurements were analyzed for harmonic content based on the rotor period of revolution. After accounting for these periodic velocities, the remaining unsteady velocities were treated as turbulence. Turbulence intensity distributions are presented. Average turbulent intensities ranged from approximately 2 percent of free stream to over 15 percent of free stream at specific locations and azimuths. The maximum average value of turbulence was located near the rear-facing region of the fuselage.

Introduction

As helicopters demand higher forward speeds, all sources of configuration drag must be minimized. The adverse effect of aerodynamic forces, principally drag, produced in the hub region of helicopters is a significant concern. Data obtained during helicopter development show that the percentage of drag attributed only to the hub is greater than 22 percent of the entire aircraft drag for a representative configuration (ref. 1). Because the hub contributes such a significant portion of overall vehicle drag, it is important to understand and accurately predict the sources and effects of hub drag. Another adverse aerodynamic effect occurs during flight conditions when the downstream turbulent flow from the hub interacts with the empennage and tail rotor in standard helicopter configurations. This effect degrades yaw control during these flight conditions.

Modeling the helicopter configuration accurately is important for preventing significant delays during vehicle development. The complexity used in modeling the aerodynamics of helicopter fuselages varies greatly. Parameters may be determined from both powered and unpowered scale model wind tunnel tests and from analyses ranging greatly in complexity. It is important to understand that few analyses fully account for the differences in fuselage drag caused by the effect of the rotor wake on the fuselage, an effect studied during wind tun-

nel experiments (ref. 2). Currently, only experimental methods using powered rotorcraft fuselage models can give insight into the adverse effects of the hub region described in the previous paragraph.

Aerodynamic investigations were conducted to measure the velocity fields in the vicinity of a model helicopter configuration (ref. 3). The model configuration consisted of a generic rotor and fuselage representative of a wide range of realistic helicopters. Comparisons of the measured velocity field with analytical predictions were made (refs. 4 and 5) to help understand and validate rotor inflow velocity predictions. The effect of the helicopter fuselage on these inflow velocity measurements was studied (ref. 6). However, the effects of the region of acknowledged separation behind the rotor hub were not assessed.

This investigation was conducted to provide and analyze data needed to form the basis for modeling the region behind the hub. The use of a well-documented helicopter model configuration used for previous aerodynamic configuration studies adds to the value of this specific experimental data.

Symbols

Figure 1 shows the coordinate system used in this study.

b	number of blades, 4
C_T	rotor thrust coefficient, $\frac{T}{\rho \pi R^2 (\Omega R)^2}$, 0.0064 (nominal)
c	blade chord, 2.61 in.
F	Fourier transform of once-per-revolution velocity
F_u	magnitude of harmonic components of u velocity
F_w	magnitude of harmonic components of w velocity
N_u	number of points in each azimuthal bin used for computation (represented by N_u in figures)
N_w	measurement count for vertical velocity measurement (represented by N_w in figures)
PMT	photomultiplier tube
R	rotor radius, 2.82 ft
r	radial distance from hub center, ft
T	thrust, lbf
T	2D turbulence intensity, $\frac{\sqrt{1/2(u'^2 + w'^2)}}{u_\infty}$
u	velocity in x direction, ft/sec
\bar{u}	mean velocity in x direction, ft/sec

u'	velocity fluctuation in x direction, $u - \bar{u}$, ft/sec
$\overline{u'^2}$	average square of fluctuating velocity in x direction
u_∞	free stream velocity, ft/sec
w	velocity in z direction, ft/sec
\bar{w}	mean velocity in z direction, ft/sec
w'	velocity fluctuation in z direction, $w - \bar{w}$, ft/sec
$\overline{w'^2}$	average square of fluctuating velocity in z direction
w_f	velocity induced in forward flight, ft/sec
w_h	velocity induced in hover, ft/sec
x	downstream distance from hub center, ft
y	lateral distance from hub center, ft
z	vertical distance from hub center, ft
α	angle of attack of rotor tip-path-plane (positive nose up), deg
ρ	density of air, slug/ft ³
σ	standard deviation
ψ	rotor azimuth measured from downstream position positive counterclockwise (as viewed from above), deg
Ω	rotational speed of rotor shaft, 221 rad/sec (nominal)
Subscripts:	
f	forward flight quantity
h	hover quantity
u	u component or direction quantity
w	w component or direction quantity
∞	free stream quantity

Model and Apparatus

Langley 14- by 22-Foot Subsonic Tunnel

The Langley 14- by 22-Foot Subsonic Tunnel (ref. 7) is a closed-circuit single-return atmospheric wind tunnel (fig. 2). The unusual test requirements associated with vertical/short takeoff and landing (V/STOL) and rotorcraft aerodynamic research led to design and construction of this tunnel in 1970. The tunnel has a test section that can be operated in a variety of configurations—closed, slotted, partially open, and open. The closed test section is 14.5 ft high by 21.75 ft wide by 50 ft long with a maximum speed of about 338 ft/sec. The open test section configuration, which has a maximum speed capability of about 270 ft/sec, is formed by raising the ceiling

and walls to create a floor-only configuration. For this investigation the tunnel was operated in the open test section configuration, where a nominal turbulence level of 0.25 percent has been documented.

The tunnel is equipped with an on-line static data reduction system that can display computed average aerodynamic coefficients with interactions and wall interference corrections in real time. A significant facility system of this tunnel is the two-component laser velocimeter.

Laser Velocimeter

The laser velocimeter used in this investigation is designed to measure the components of velocity in the longitudinal (downstream) and vertical directions (ref. 8). This system is composed of four subsystems: optics, traversing mechanism, data acquisition, and seeding.

The optics subsystem (fig. 3) operates in backscatter mode and at a relatively high power to overcome the long focal lengths needed to scan the width of the tunnel test section. The cylindrical sample volume resulting from the beam intersection in the 10- to 20-ft focal length range of the system is less than 1 cm in length with a diameter of 0.2 mm.

The traversing mechanism subsystem includes five axes of freedom—two by direct translation of the optics bench, one by zoom focus of the sample volume across the test section, and two by tilting of the final steering mirror as the laser beams exit the optics package. The traversing mechanism system for the velocimeter has nominal downstream travel of 6 ft and vertical travel of 12 ft. This travel is ideally suited for scanning the entire flow field of rotor systems less than 6 ft in diameter.

The data acquisition subsystem used for this investigation is based on frequency domain processing of the signals from the receive optics (ref. 9). Velocity information from the frequency domain processor and azimuthal information from the model are recorded in a buffer interface that allows for later azimuthal correlation of the velocity signals.

The principle for laser velocimetry is based on analysis of the light reflected by particles that move with the flow through a specific location. The seeding system in the 14- by 22-Foot Subsonic Tunnel (ref. 3) inserts monodisperse 1.7- μ m-diameter polystyrene particles into the portion of the flow where the laser measurements are being made.

Rotor Test System

The rotor test system used for the experimental data in this report is built on a generic test system (ref. 10) developed at the 14- by 22-Foot Subsonic Tunnel. This test system, the 2-Meter Rotor Test System (2MRTS), consists of a 29-hp rotor drive system with collective and cyclic blade pitch controls, a four-blade articulated hub mounted on a six-component strain-gauge balance, and a fuselage skin mounted on a separate similar balance. These two six-component strain-gauge balances provide independent measurements of the rotor and fuselage aerodynamic loads. Figure 4(a) shows the test configuration installed in the wind tunnel with the laser velocimeter shown in the background.

The shape of the fuselage is designed to represent a wide range of helicopter fuselages without being specific to any particular one. The fuselage geometry can be described by a set of equations (refs. 6 and 11). Development of computer models is simplified by using a geometry derived from equations. Figure 4(b) shows the shape of the fuselage with example cross sections.

The rotor hub used in this study is a four-bladed articulated hub (ref. 10). The hub articulation is set at 2.0 in. from the center of rotation with coincident flap and lag hinges. The blade grip component of the hub has a maximum diameter of 1.625 in. and extends to 7.5 in. from the center of rotation. The airfoil section of the blade is fully developed at 8.5 in. from the center of rotation. The center section of the hub has a maximum height of 2.125 in. from the plane of blade articulation. The pitch rod attaches to the blade grip at a radius of 2.0 in. from the center of rotation and is attached to the swash plate at a radius of 1.4 in. with a vertical offset of approximately 4 in. Figure 4(c) shows the exposed geometry of the hub.

The rotor system tested consists of four rectangular blades with a constant NACA 0012 airfoil section. The blades have an equivalent linear twist of -8.0° from the center of rotation to the tip. The chord of 2.61 in. and radius of 33.88 in. give the system a solidity ($bc/\pi R$) of 0.098.

Test and Procedure

The velocity measurements were taken at a flight condition similar to that reported for a previous laser measurement program (ref. 12). The advance ratio was set to 0.23. A nondimensional thrust coefficient of 0.0064 was set with a tip-path angle of -3.0° relative to the free stream. The rotor tip speed was set to 624.0 ft/sec. This tip speed has proven to be benign in terms of rotor system life and is an important consider-

ation when gathering laser velocimeter measurements. The rotor cyclic controls were trimmed to eliminate once-per-revolution flapping of the rotor blades. Table 1 lists the significant flight condition parameters. The peak-to-peak deviation and standard deviation of these parameters were determined from the static data recorded at each measurement and are listed in table 1 to establish the uniformity of the flight condition from one velocity measurement to the next. Peak-to-peak deviation in this context refers to the maximum value recorded minus the minimum value recorded.

The grid of points where measurements were obtained was determined from consideration of mean rotor downwash. The center of the rotor downwash is expected to travel on a trajectory defined by the forward speed of the wind tunnel flow and the average momentum imparted to the flow by the lifting rotor. From momentum calculations (ref. 1)

$$w_f^4 - 2u_\infty w_f^3 \sin \alpha + u_\infty^2 w_f^2 - w_h^4 = 0 \quad (1)$$

where

$$w_h = \Omega R \sqrt{\frac{C_T}{2}} \quad (2)$$

Substituting the flight conditions of this investigation, the vertical component of forward velocity, w_f , is 8.61 ft/sec. This value was used to determine a uniform slope for the grid of measurement points. Since the onset flow is approximately 144 ft/sec, the vertical offset of each plane of measurements, which were spaced 2 in. apart in the downstream direction, is approximately 0.12 in. This vertical offset was used to define the center of each downstream grid. There were nominally 15 measurement locations at each downstream station, 1 at the center of the grid defined above, 4 spaced above the center, 4 on the left, 4 on the right, and nominally 2 below. The measurement locations are given in table 2 and shown in figure 5.

The unsteady flow field in the vicinity of a helicopter rotor in forward flight is expected to be periodic with blade passage. Measurements taken with the laser velocimeter are derived from the random distribution of seed particles passing through the sample volume. The resulting random interval between samples requires that a special technique be applied to the data to determine the periodic content of the velocity measurement. Since no cross-stream component of velocity was measured, the swirl induced by the rotor and seen in the lateral component of velocity was not measured.

To determine the periodic unsteady velocity from laser velocimeter samples, the correlation between the

velocity of an individual sample and the rotor azimuth must be established. Approximately 4000 samples were taken at each measurement location. The laser data buffer stores the rotor azimuth with each valid velocity measurement from the frequency domain processor. Because it is expected that the rotor will produce velocity that is periodic with blade passage, sorting the velocity measurements by the azimuth of the rotor defines the periodic content. For this analysis, 128 azimuthal ranges or “bins” of 2.8° were used for the sorting. An interactive analysis routine for validating particle velocity distributions was used to edit the measurement data prior to entry into the working velocity database. This routine allows the user to review the velocity histogram at each measurement point and eliminate invalid samples such as those resulting from reflections from the body. After editing, the average number of measurements in each azimuthal u velocity bin was 30.2; the average number for w measurements was 30.6.

Repeat measurements were taken at random intervals during this investigation. Repeat measurements were also taken at one of two measurement locations at the specified test condition after major breaks in the test process. Data resulting from these repeat measurements were used for two purposes: (1) confirmation that systems were operating properly and that the test conditions were maintained, and (2) as a check on the uncertainty of the measurement technique. When discrepancies were uncovered, the test procedure was checked to determine the source of the discrepancies. When the repeat points did not discern a problem, the data were included in the Results and Discussion section to demonstrate the general repeatability of the measurement process.

Measurement Uncertainty

Potential sources of measurement uncertainty were considered. Data from the laser velocimeter suggest several effects may contribute to measurement uncertainty and are given as follows:

Source of uncertainty	Bias, percent	Random, percent
Crossbeam angle error	± 0.81	Not applicable
Diverging fringes	Not measured	Not measured
Velocity bias	0	0
Bragg bias	0	0
Velocity gradient	Negligible	Negligible
Frequency domain processor	Not applicable	0.20
Particle lag	± 0.50	Negligible
Total error	± 1.31	0.2

The total laser velocimeter error, in percent of velocity, is estimated as

$$\text{Total} = \sqrt{\text{Bias}^2 + \text{Random}^2} = 1.33 \text{ percent}$$

This estimate presumes the actual flow accelerations are no greater than those presented in reference 12.

Analysis

The flow in the region downstream of a helicopter hub is expected to have two principal unsteady components: an oscillating component with period equal to rotor blade passage, and a turbulent or aperiodic component. The velocity measurements made during this experimental program were analyzed to separate these two unsteady components. The periodic part of the velocity was determined by the sorting of velocity measurements into azimuthal bins. The average value of velocities in these bins was assumed to represent the periodic component of the unsteady velocity at the measurement location. The turbulence at a measurement location was then calculated as the unsteady deviation of the velocity from the expected periodic value.

Turbulent intensity was computed from statistical information gathered during the laser velocimeter data reduction process. The turbulent intensity was computed as a function of azimuth by using information about data in each azimuthal bin. If the turbulence was not computed as a function of azimuth, the expected periodic variance of velocity with azimuth would influence the level of computed turbulent intensity. One of the parameters of the data reduction process is the standard deviation σ of particles in each azimuthal bin described above. The standard deviation σ is computed from

$$\sigma_u = \sqrt{\frac{\sum_{i=1}^{N_u} (u_i - \bar{u})^2}{N_u - 1}} \quad (3)$$

where N_u is the number of points in each azimuthal bin used for the computation. Since

$$\overline{u'^2} = \frac{\sum_{i=1}^{N_u} (u_i - \bar{u})^2}{N_u} \quad (4)$$

then the term $\overline{u'^2}$ is computed from the deviation as

$$\overline{u'^2} = \sigma_u^2 \left(\frac{N_u - 1}{N_u} \right) \quad (5)$$

Turbulent intensity T is defined (ref. 13) by

$$T = \frac{\sqrt{1/3(\overline{u'^2} + \overline{v'^2} + \overline{w'^2})}}{u_\infty} \quad (6)$$

For two-dimensional velocity data the intensity is redefined as

$$T = \frac{\sqrt{1/2(\overline{u'^2} + \overline{w'^2})}}{u_\infty} \quad (7)$$

From this follows the calculation of turbulent intensity T at each azimuthal bin from the statistical data computed from the velocity measurements in each bin as follows:

$$T = \frac{\sqrt{\sigma_u^2 \frac{N_u - 1}{2N_u} + \sigma_w^2 \frac{N_w - 1}{2N_w}}}{u_\infty} \quad (8)$$

The value of mean turbulence at every measurement location has been computed as the average of the turbulence from each of the azimuthal bins.

Although most azimuthal bins had sufficient number of particles for this statistical analysis, a few measurement locations had no particles. To prevent the assumption that no particles indicates no turbulence, a linear interpolation of the turbulence across the empty bins was used to prevent skewing the mean turbulent intensity values.

Results and Discussion

Figure 6 shows the distribution of mean turbulent intensity in the lateral and vertical directions at each downstream station. Figure 6 is divided to show 15 downstream stations (labeled a–o). Each downstream station in figure 6 shows two parts: the left part of the figure is the lateral distribution of mean turbulent intensity and the right part of the figure shows the vertical distribution of mean turbulent intensity.

Figure 6 shows that the level of mean turbulence is clearly greater on the side of the hub where the rotor blades are retreating relative to the oncoming flow. On the side of the hub where the blades are advancing, the average level of turbulence is less. The lateral intensity levels appear to reduce slowly as the flow progresses downstream but retain the relative distribution of strength. Much less mean turbulence is observed above the rotor ($z > 0$) than behind or below the rotor ($z < 0$). The value of mean turbulence downstream of the hub center ($z = 0$)

seems to decay at a slower rate than below the downstream center. Beyond 24 in. ($r/R = 0.73$) downstream, the average turbulence directly behind the hub center has a larger value than the turbulence values below it. The significantly lower turbulence values seen beyond $y = 5$ in. ($r/R = 0.15$) on the advancing side indicate little or no separation of the flow at the root of the blade on the advancing side at this flight condition.

Multiple measurements were taken at two specific locations. (See figs. 6(a) and 6(i).) In the location approximately 8 in. above the hub where no separation is expected (fig. 6(a)), all of the measurements correlate well. In a region of expected separation (fig. 6(i)) slightly less correlation is shown although the values are consistent. This demonstration of repeatability in estimated turbulence from the statistics of velocity measurements improves confidence in the method of obtaining turbulence values.

Figures 7–21 present details of the velocity measurements and derived turbulent intensity values for each measurement location. Each figure shows seven plots. The top two plots show the azimuthal variation of the two components of velocity. The following two plots (F_u and F_w) are the spectral amplitudes of the velocity as functions of the order number. These values are computed by performing a Fourier transform on the azimuth-dependent velocity and computing the magnitude at each order number. The order ratio represents the frequency ratio of the periodic velocity signal in multiples of rotor fundamental frequency; for example, an order ratio value of 2 indicates a 2-per-rev frequency content in the velocity. The next two plots show the number of independent measurements taken of the two velocity components at each azimuth. The final plot in each figure is the computed turbulence intensity value as a function of rotor azimuth.

From the velocity and azimuthal information, several details of the flow behind the center of the model rotor system can be seen. For example, in figures 7(a)–(e) the downstream component of velocity demonstrates an increasing level of twice per revolution. This 2-per-rev character, although unexpected, has been observed during previous tests. This characteristic is observed at downstream stations (figs. 7–10, (a)–(e)) until the measurements at 16 in. behind the hub. At 16 in. ($r/R = 0.49$) behind the hub the blade passage (four per revolution) frequency content exceeds the 2-per-rev content at locations above the hub centerline.

A possible significance of 4 per rev exceeding 2 per rev is that the magnitude of the load on the blade (four per revolution in the fixed system) becomes significant at 16 in. from the center of the hub. After 16 in.

downstream of the hub the 2-per-rev character shifts closer to the fuselage at most stations (figs. 11–21(e), (f), and (g)). There are also some measurement locations where the existence of 2-per-rev occurs without an upstream/downstream correlation, as seen in figures 12(k), 13(i), 17(h) and (i), and 18(i). Although the 2-per-rev seems to be most closely related to flow associated with the interaction of the hub flow and the fuselage, no definite explanation is currently available to completely explain its existence. A possible explanation is the existence of geometry on the hub that is 2 per rev, meaning two opposed flapping potentiometers and a rotating scissors that is mirrored about the shaft. The relative frontal areas of these geometric features are, however, relatively small.

Beginning with figure 10, the flow associated with the back-facing region on the fuselage can be seen. Scales for the downstream component of velocity at the two stations closest to the fuselage have been adjusted to show the reverse flow that occurs at the two stations closest to the fuselage. At the next station downstream, the downstream velocity is also quite low (figs. 11(f) and (g)). Figures 6(d)–(i) show average turbulence values as high as approximately 15 percent and azimuthal peaks of over 20 percent. This region of the highest measured levels of turbulence extends back to approximately 26 in. behind the hub (77 percent of radius).

Another flow feature that is seen only in the detailed velocity and azimuthal plots is the periodic content comparison between the advancing and the retreating side of the rotor hub. For example, in figure 13(h) (9 in. to the right of the hub and 20 in. downstream) the vertical component of velocity has a smooth but periodic character. By comparison, figure 13(o) (9 in. to the left of the hub but also 20 in. downstream) also shows a 4-per-revolution content in the vertical component of velocity, but it is not smooth. The turbulent intensity computed on the left (retreating) side of the rotor hub experiences a level of about 10 percent of free stream while the right (advancing) side experiences only about a 2-percent level of free stream.

Figure 14(e) includes very similar measurements taken at two different times during the flow measurements. Figure 15(g) also shows four separate sets of very similar measurements. Although the number of samples collected in each of the azimuth bins determines the quality of the statistical data derived from these measurements, the observed repeatability of measurements contributes to the subjective confidence in the method.

Close interaction between the rotor blade and the measurement location is seen in the velocity distribution

at stations between 22 in. and 36 in. ($r/R = 0.67$ to 1.09) downstream of the hub (figs. 14–21), especially at the first location above the mean downwash point (4 in. above, figs. 14–21(d) in all cases). At azimuths of 0° , 90° , 180° , and 270° the vertical component of velocity shows a sudden disruption. The character of the vertical component of velocity seen in figure 14(d) indicates a concentration of circulation or vorticity in the flow field close to the measurement location. This character is believed to come from the abrupt change in the bound circulation at the rotor blade tip as it passes by the measurement location. This is further confirmed by the complete lack of such a signature in the downstream component of velocity. This probably indicates that the circulation is aligned with the flow at the time of the measurement.

In figure 19(d) for station 32, the downstream component of velocity shows a perturbation corresponding to the vertical component event. The blades are 32.88 in. long and the effect of the end of the blade just beyond the measurement location of 32 in. now contributes to the downstream component of velocity as the blade passes the measurement location. This character confirms the general understanding of the transfer of bound circulation to trailed circulation manifest in the tip vortex. This signature is also seen in the downstream component of velocity in figure 20(d) for station 34 and figure 21(d) for station 36.

In figure 14(d) the measurement count goes to zero at three azimuthal locations. In figures 15–19 ((d) for each figure) the measurement count (N_w) for the vertical velocity measurement goes to zero at four azimuthal locations. In figures 18(d) and 19(d) both the vertical and lateral velocity measurement counts go to zero at four azimuthal locations. This lack of measurement is believed to be caused by a blade obscuring or penetrating the measurement volume and interrupting the laser velocimeter signal.

In figure 12(h) a “spike” is seen in the turbulent intensity data at approximately 304° of azimuth. Analysis of the contributing data indicates that there is a single “high” data element in the deviation of velocity in the downstream direction. In figure 12(h) the value is 22.7 fps while the neighboring data are on the order of 3 fps. Since the number of particle measurements in this azimuthal bin is 32, the reason for this spike is unknown.

Conclusions

The unsteady flow behind the hub of a helicopter configuration influences the overall flow characteristics of the helicopter. The unsteady flow behind the hub of a

research configuration was measured. This configuration has been documented by extensive laser velocimeter measurements and provides an excellent data set for analytical correlation. The measurement of the unsteady character of the flow behind the hub was taken to assist in determination of relative effects of this unsteady region.

Flow behind the hub of this characteristic helicopter configuration was measured at 13 stations downstream from the rotor hub. At each station measurements were made in both a horizontal and vertical row of locations. The downstream stations extend beyond the radius of the rotor. At each measurement point the vertical and downstream components of velocity were measured using a laser velocimeter. Approximately 4000 samples were taken at each measurement point. For each sample, the rotor azimuth was recorded. The correlation of velocity measurements with rotor azimuth allowed definition of periodic velocities at each measurement location.

The unsteady flow in the region behind the hub has been analyzed in two parts. The principal part of the unsteady flow is presumed to be caused by the periodic passage of the rotor blades. The secondary part of the unsteady flow is caused by turbulence or aperiodic flow. An unusual characteristic of the flow is the twice-per-revolution periodic characteristic found in specific regions of the flow. The turbulent flow has been characterized with a two-dimensional turbulent intensity that is independent of the periodic part of the unsteady flow.

The resulting characterization of the unsteady flow behind the rotor hub shows that the aperiodic magnitude of the flow is greater on the retreating side than the advancing side of the rotor. The periodic magnitudes are shown to be greater on the advancing side of the rotor. There is a region of the largest aperiodic flow behind the rear-facing slope of the helicopter fuselage shape. The magnitudes of the aperiodic flow can be as much as 15 percent of the free stream.

The velocity field associated with the concentration of circulation on the rotor blades is seen in the azimuth-dependent velocities at measurement locations close to the passage of the rotor blades. Some azimuthal measurements were obscured because of the passage of the blades at these locations. Measurements close to the end of the rotor blades show the influence of the abrupt change in the bound circulation at the blade tip as it passes by the measurement location.

References

1. Stepniewski, W. Z.: *Rotary-Wing Aerodynamics*. Volume I: Basic Theories of Rotor Aerodynamics (With Application to Helicopters). Dover Publ., Inc., 1984.
2. Wilson, John C.; and Mineck, Raymond E.: *Wind-Tunnel Investigation of Helicopter-Rotor Wake Effects on Three Helicopter Fuselage Models*. NASA TM X-3185, 1975.
3. Elliott, Joe W.; Althoff, Susan L.; and Sailey, Richard H.: *Inflow Measurement Made With a Laser Velocimeter on a Helicopter Model in Forward Flight*. Volume III—Rectangular Planform Blades at an Advance Ratio of 0.30. NASA TM-100543, AVSCOM TM-88-B-006, 1988.
4. Hoad, Danny R.; Althoff, Susan L.; and Elliott, Joe W.: Rotor Inflow Variability With Advance Ratio. *44th Annual Forum Proceedings*, American Helicopter Soc., 1988, pp. 57–72.
5. Charles, Bruce D.; and Hassan, Ahmed A.: A Correlation Study of Rotor Inflow in Forward Flight. *44th Annual Forum Proceedings*, American Helicopter Soc., 1988, pp. 73–85.
6. Berry, John D.; and Althoff, Susan L.: Inflow Velocity Perturbations Due to Fuselage Effects in the Presence of a Fully Interactive Wake. *46th Annual Forum Proceedings*, Volume II, American Helicopter Soc., 1990, pp. 1111–1120.
7. Gentry, Garl L., Jr.; Quinto, P. Frank; Gatlin, Gregory M.; and Applin, Zachary T.: *The Langley 14- by 22-Foot Subsonic Tunnel: Description, Flow Characteristics, and Guide for Users*. NASA TP-3008, 1990.
8. Sellers, William L.; and Elliott, Joe W.: Applications of Laser Velocimeter in the Langley 4- by 7-Meter Tunnel. *Flow Visualization and Laser Velocimetry for Wind Tunnels*, William W. Hunter, Jr., and Jerome T. Foughner, Jr., eds., NASA CP-2243, 1982, pp. 283–293.
9. Mace, W. D., Jr.; Elliott, Joe W.; Blancha, Barry; and Murphy, Jay: Comparison of Frequency Domain and Time Domain Laser Velocimeter Signal Processors. *14th International Congress on Instrumentation in Aerospace Simulation Facilities*, IEEE, 1991, pp. 103–112.
10. Phelps, Arthur E., III; and Berry, John D.: *Description of the U.S. Army Small-Scale 2-Meter Rotor Test System*. NASA TM-87762, AVSCOM-TM-86-B-4, 1987.
11. Freeman, Carl E.; and Mineck, Raymond E.: *Fuselage Surface Pressure Measurements of a Helicopter Wind-Tunnel Model With a 3.15-Meter Diameter Single Rotor*. NASA TM-80051, 1979.
12. Elliott, Joe W.; Althoff, Susan L.; and Sailey, Richard H.: *Inflow Measurement Made With a Laser Velocimeter on a Helicopter Model in Forward Flight*. Volume 2: Rectangular Planform Blades at an Advance Ratio of 0.23. NASA TM-100542, AVSCOM-TM-88-B-005, 1988.
13. Schlichting, Hermann (J. Kestin, transl.): *Boundary-Layer Theory*, Sixth ed., McGraw-Hill Book Co., Inc., 1968.

Table 1. Flight Condition Parameters

Parameter	Average	Peak to peak deviation	Standard deviation
Velocity, ft/sec	143.4	1.8	0.36
Tip path attitude, deg	-2.7	1.1	0.28
Density, Slugs/ft ³	0.002330	0.000043	0.000008
Hover tip speed, ft/sec	621.4	3.2	0.58
Advance ratio	0.230	0.003	0.0006
Collective cyclic, deg	6.4	0.2	0.05
Lateral cyclic, deg	-0.8	0.5	0.16
Longitudinal cyclic, deg	2.8	0.6	0.22
Lift, lbf	145.6	5.2	1.1
Drag, lbf	0.73	1.23	0.273
Thrust coefficient	0.0064	0.0003	0.00006
Power, hp	7.6	0.9	0.24
Rotation rate, rpm	2110.8	8.1	1.42
Unit Reynolds number, per ft	889874	29060	5673

Table 2. Measurement Locations

x, in.	y, in.	z, in.	Figure
8	0	8.518	7(a)
8	0	7.518	7(b)
8	0	5.518	7(c)
8	0	3.518	7(d)
8	0	-.482	7(e)
8	0	-4.482	7(f)
8	9	-.482	7(g)
8	8	-.482	7(h)
8	6	-.482	7(i)
8	4	-.482	7(j)
8	-4	-.482	7(k)
8	-6	-.482	7(l)
8	-8	-.482	7(m)
8	-9	-.482	7(n)
10	0	8.398	8(a)
10	0	7.398	8(b)
10	0	5.398	8(c)
10	0	3.398	8(d)
10	0	-.602	8(e)
10	0	-4.602	8(f)
10	9	-.602	8(g)
10	8	-.602	8(h)
10	6	-.602	8(i)
10	4	-.602	8(j)
10	-4	-.602	8(k)
10	-6	-.602	8(l)
10	-8	-.602	8(m)
10	-9	-.602	8(n)
12	0	8.278	9(a)
12	0	7.278	9(b)
12	0	5.278	9(c)
12	0	3.278	9(d)
12	0	-.722	9(e)
12	0	-4.722	9(f)
12	9	-.722	9(g)
12	8	-.722	9(h)
12	6	-.722	9(i)
12	4	-.722	9(j)
12	-4	-.722	9(k)
12	-6	-.722	9(l)
12	-8	-.722	9(m)
12	-9	-.722	9(n)

Table 2. Continued

x , in.	y , in.	z , in.	Figure
14	0	8.157	10(a)
14	0	7.157	10(b)
14	0	5.157	10(c)
14	0	3.157	10(d)
14	0	−.843	10(e)
14	0	−4.843	10(f)
14	0	−6.843	10(g)
14	9	−.843	10(h)
14	8	−.843	10(i)
14	6	−.843	10(j)
14	4	−.843	10(k)
14	−4	−.843	10(l)
14	−6	−.843	10(m)
14	−8	−.843	10(n)
14	−9	−.843	10(o)
16	0	8.037	11(a)
16	0	7.037	11(b)
16	0	5.037	11(c)
16	0	3.037	11(d)
16	0	−.963	11(e)
16	0	−4.963	11(f)
16	0	−6.963	11(g)
16	9	−.963	11(h)
16	8	−.963	11(i)
16	6	−.963	11(j)
16	4	−.963	11(k)
16	−4	−.963	11(l)
16	−6	−.963	11(m)
16	−8	−.963	11(n)
16	−9	−.963	11(o)
18	0	7.917	12(a)
18	0	6.917	12(b)
18	0	4.917	12(c)
18	0	2.917	12(d)
18	0	−1.083	12(e)
18	0	−5.083	12(f)
18	0	−7.083	12(g)
18	9	−1.083	12(h)
18	8	−1.083	12(i)
18	6	−1.083	12(j)
18	4	−1.083	12(k)
18	−4	−1.083	12(l)
18	−6	−1.083	12(m)
18	−8	−1.083	12(n)
18	−9	−1.083	12(o)

Table 2. Continued

x, in.	y, in.	z, in.	Figure
20	0	7.796	13(a)
20	0	6.796	13(b)
20	0	4.796	13(c)
20	0	2.796	13(d)
20	0	-1.204	13(e)
20	0	-5.204	13(f)
20	0	-7.204	13(g)
20	9	-1.204	13(h)
20	8	-1.204	13(i)
20	6	-1.204	13(j)
20	4	-1.204	13(k)
20	-4	-1.204	13(l)
20	-6	-1.204	13(m)
20	-8	-1.204	13(n)
20	-9	-1.204	13(o)
22	0	7.676	14(a)
22	0	6.676	14(b)
22	0	4.676	14(c)
22	0	2.676	14(d)
22	0	-1.324	14(e)
22	0	-5.324	14(f)
22	0	-7.324	14(g)
22	9	-1.324	14(h)
22	8	-1.324	14(i)
22	6	-1.324	14(j)
22	4	-1.324	14(k)
22	-4	-1.324	14(l)
22	-6	-1.324	14(m)
22	-8	-1.324	14(n)
22	-9	-1.324	14(o)
24	0	7.555	15(a)
24	0	6.555	15(b)
24	0	4.555	15(c)
24	0	2.555	15(d)
24	0	-1.445	15(e)
24	0	-5.445	15(f)
24	0	-7.445	15(g)
24	9	-1.445	15(h)
24	8	-1.445	15(i)
24	6	-1.445	15(j)
24	4	-1.445	15(k)
24	-4	-1.445	15(l)
24	-6	-1.445	15(m)
24	-8	-1.445	15(n)
24	-9	-1.445	15(o)

Table 2. Continued

x, in.	y, in.	z, in.	Figure
26	0	7.435	16(a)
26	0	6.435	16(b)
26	0	4.435	16(c)
26	0	2.435	16(d)
26	0	-1.565	16(e)
26	0	-5.565	16(f)
26	0	-7.565	16(g)
26	9	-1.565	16(h)
26	8	-1.565	16(i)
26	6	-1.565	16(j)
26	4	-1.565	16(k)
26	-4	-1.565	16(l)
26	-6	-1.565	16(m)
26	-8	-1.565	16(n)
26	-9	-1.565	16(o)
28	0	7.315	17(a)
28	0	6.315	17(b)
28	0	4.315	17(c)
28	0	2.315	17(d)
28	0	-1.685	17(e)
28	0	-5.685	17(f)
28	0	-7.685	17(g)
28	9	-1.685	17(h)
28	8	-1.685	17(i)
28	6	-1.685	17(j)
28	4	-1.685	17(k)
28	-4	-1.685	17(l)
28	-6	-1.685	17(m)
28	-8	-1.685	17(n)
28	-9	-1.685	17(o)
30	0	7.194	18(a)
30	0	6.194	18(b)
30	0	4.194	18(c)
30	0	2.194	18(d)
30	0	-1.806	18(e)
30	0	-5.806	18(f)
30	0	-7.806	18(g)
30	9	-1.806	18(h)
30	8	-1.806	18(i)
30	6	-1.806	18(j)
30	4	-1.806	18(k)
30	-4	-1.806	18(l)
30	-6	-1.806	18(m)
30	-8	-1.806	18(n)
30	-9	-1.806	18(o)

Table 2. Concluded

x, in.	y, in.	z, in.	Figure
32	0	7.074	19(a)
32	0	6.074	19(b)
32	0	4.074	19(c)
32	0	2.074	19(d)
32	0	-1.926	19(e)
32	0	-5.926	19(f)
32	0	-7.926	19(g)
32	9	-1.926	19(h)
32	8	-1.926	19(i)
32	6	-1.926	19(j)
32	4	-1.926	19(k)
32	-4	-1.926	19(l)
32	-6	-1.926	19(m)
32	-8	-1.926	19(n)
32	-9	-1.926	19(o)
34	0	6.953	20(a)
34	0	5.953	20(b)
34	0	3.953	20(c)
34	0	1.953	20(d)
34	0	-2.047	20(e)
34	0	-6.047	20(f)
34	0	-8.047	20(g)
34	9	-2.047	20(h)
34	8	-2.047	20(i)
34	6	-2.047	20(j)
34	4	-2.047	20(k)
34	-4	-2.047	20(l)
34	-6	-2.047	20(m)
34	-8	-2.047	20(n)
34	-9	-2.047	20(o)
36	0	6.833	21(a)
36	0	5.833	21(b)
36	0	3.833	21(c)
36	0	1.833	21(d)
36	0	-2.167	21(e)
36	0	-6.167	21(f)
36	0	-8.167	21(g)
36	9	-2.167	21(h)
36	8	-2.167	21(i)
36	6	-2.167	21(j)
36	4	-2.167	21(k)
36	-4	-2.167	21(l)
36	-6	-2.167	21(m)
36	-8	-2.167	21(n)
36	-9	-2.167	21(o)

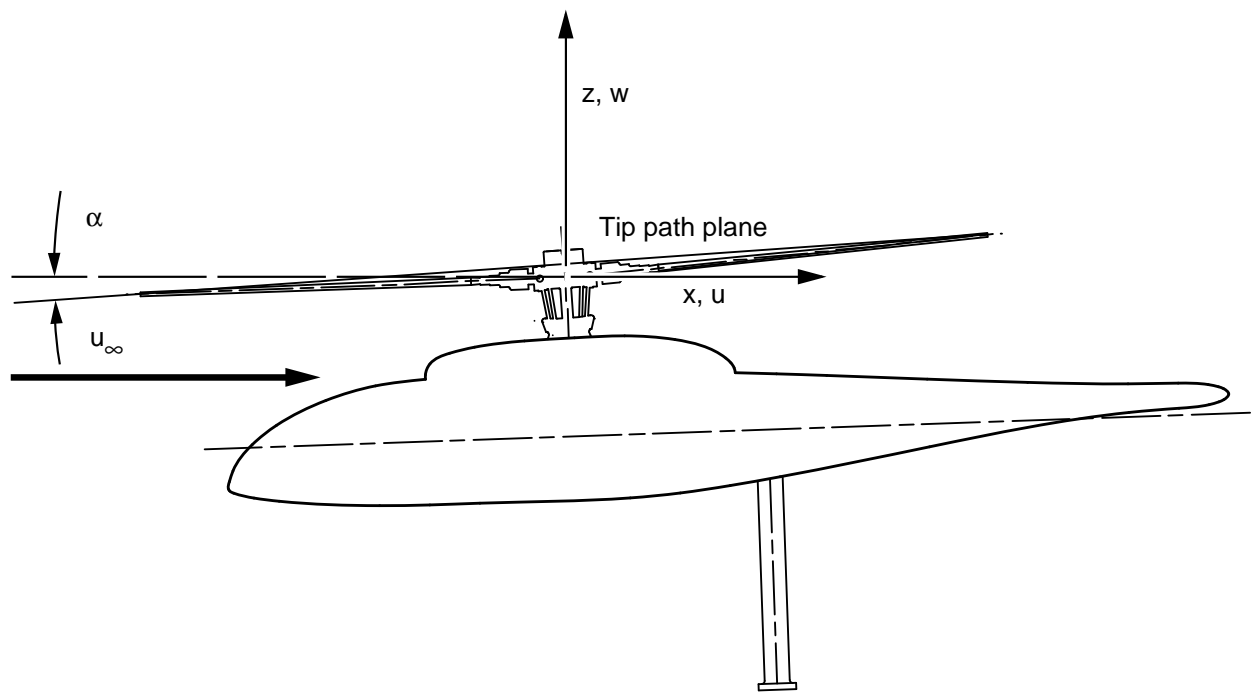


Figure 1. Reference coordinate system.



Figure 2. 14- by 22-Foot Subsonic Tunnel.

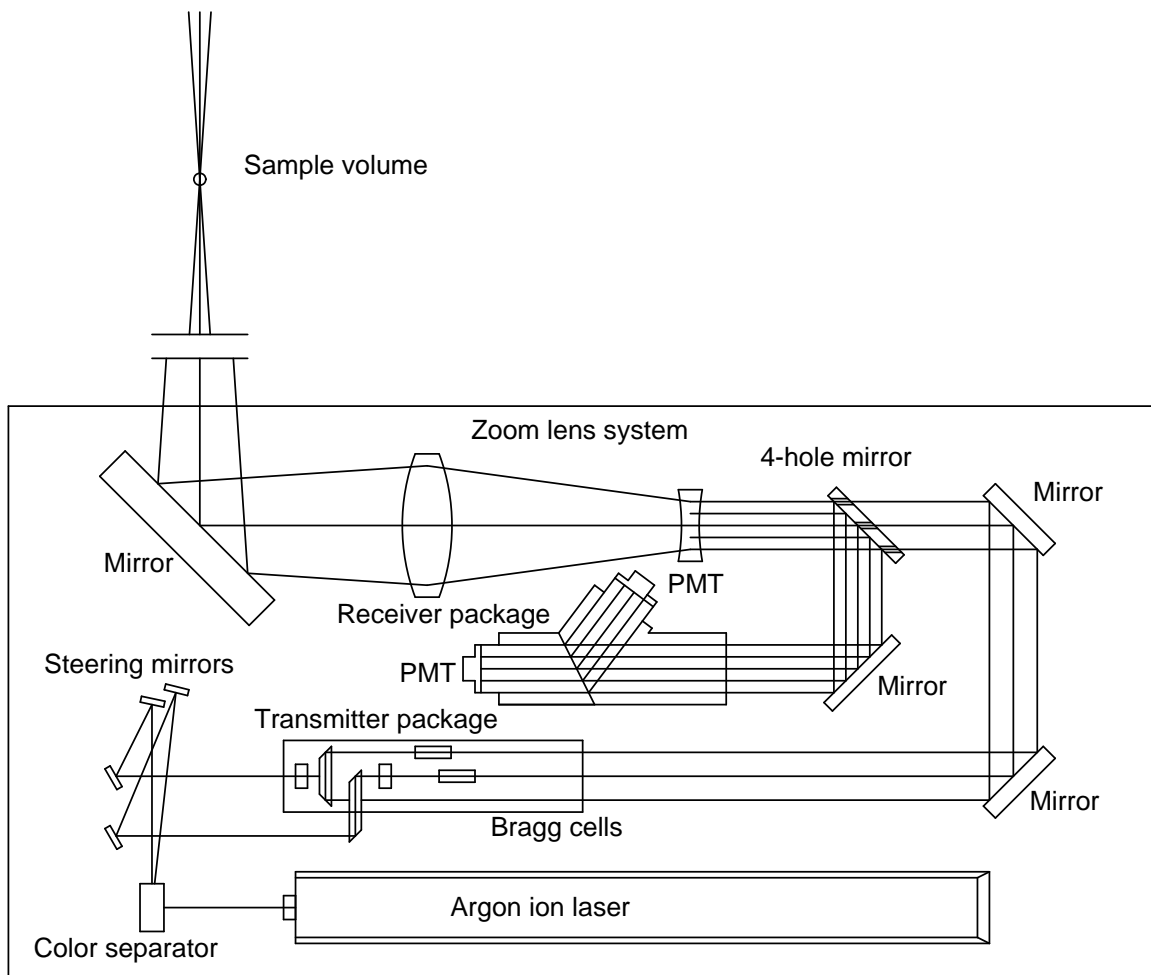
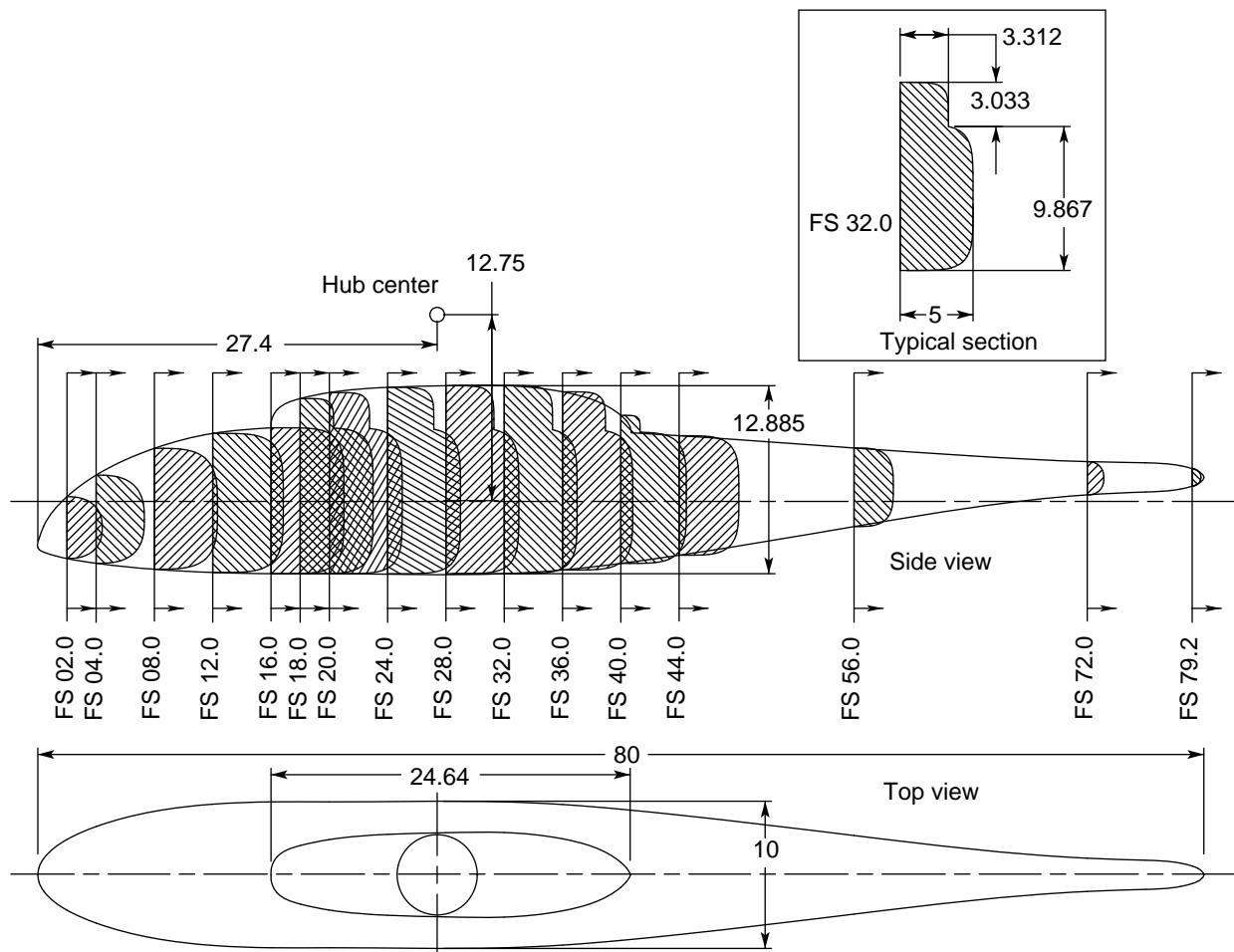


Figure 3. Schematic of laser velocimeter optic subsystem.



(a) Helicopter configuration in wind tunnel.

Figure 4. Model configuration.



(b) Fuselage geometry. Dimensions are in inches.

Figure 4. Continued.



18

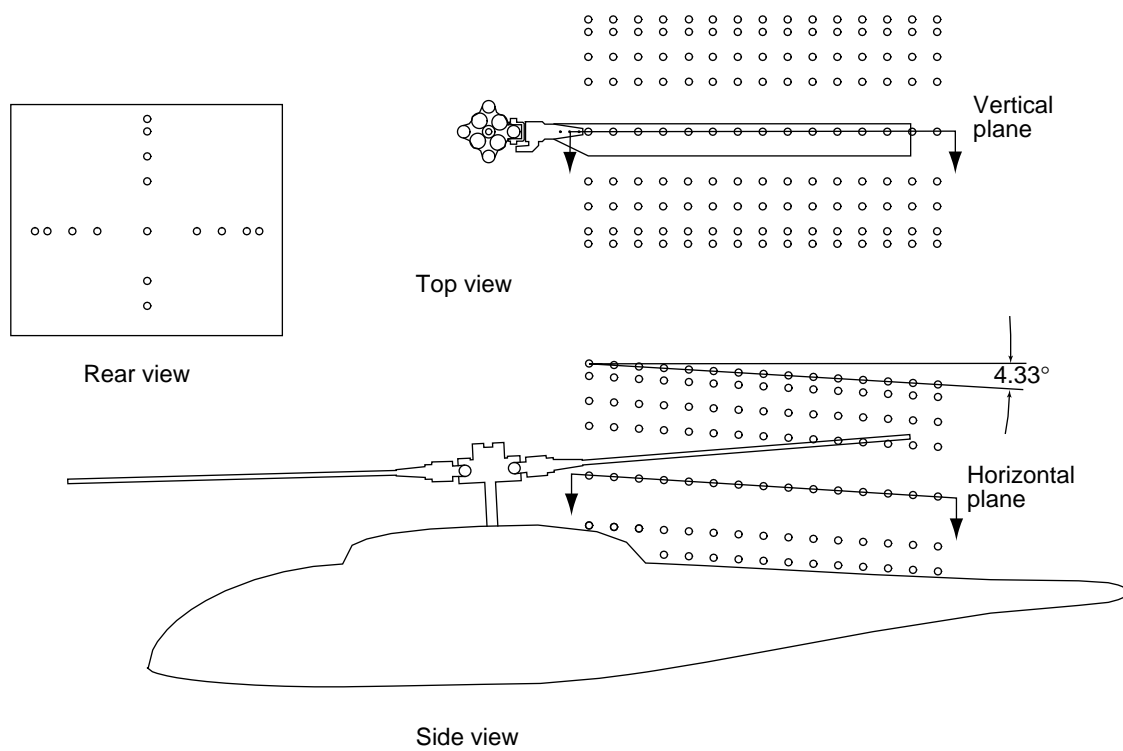
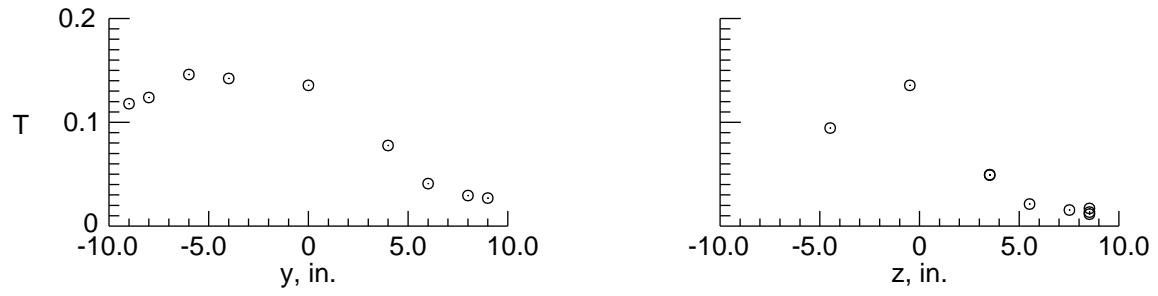
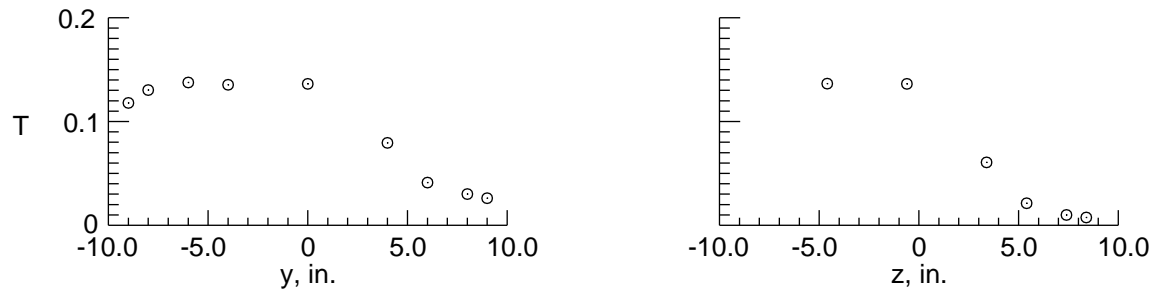


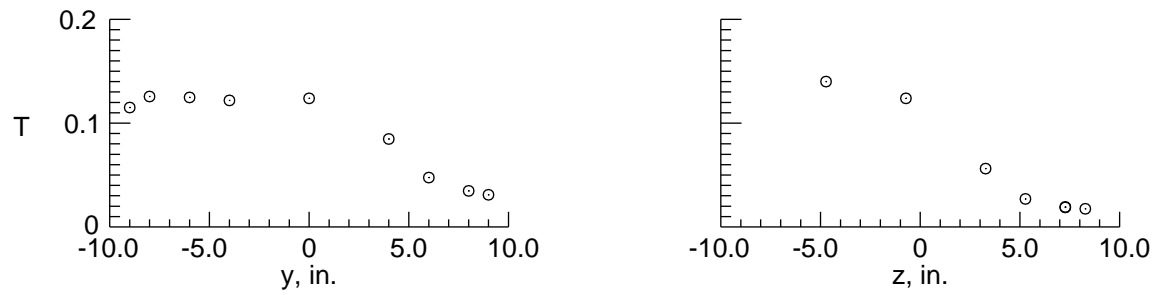
Figure 5. Velocity measurement locations.



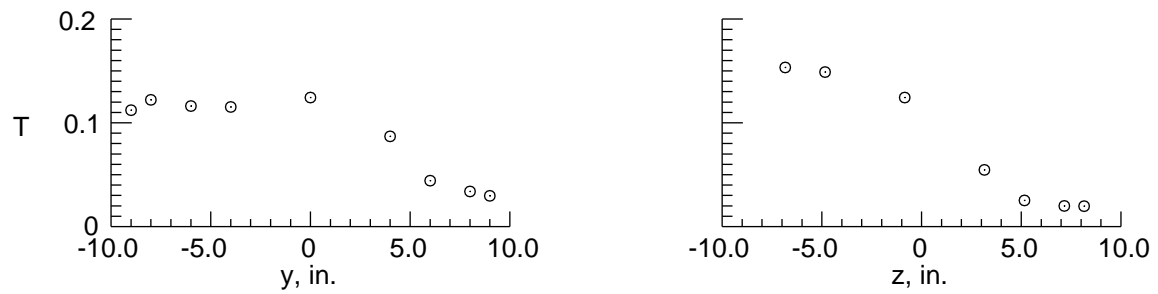
(a) $x = 8$ in.



(b) $x = 10$ in.



(c) $x = 12$ in.



(d) $x = 14$ in.

Figure 6. Distribution of mean turbulence intensity.

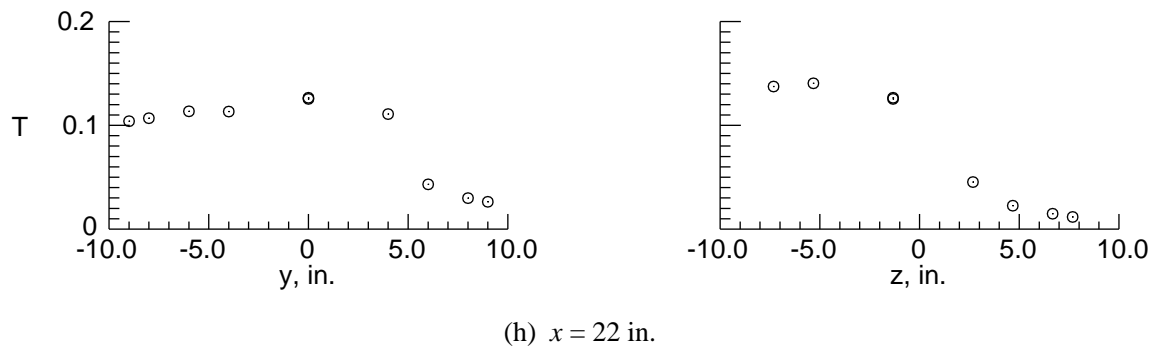
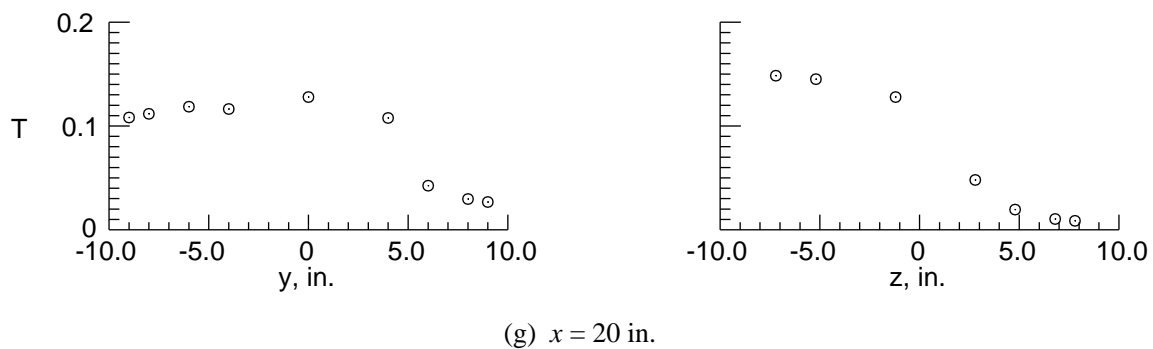
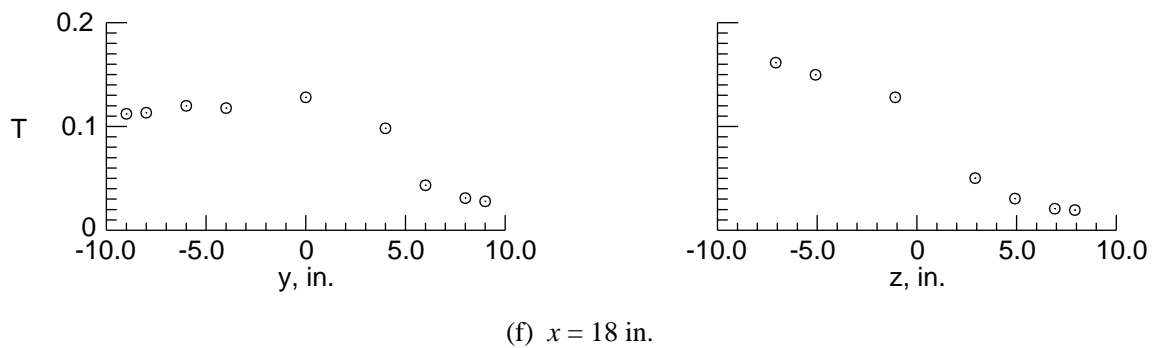
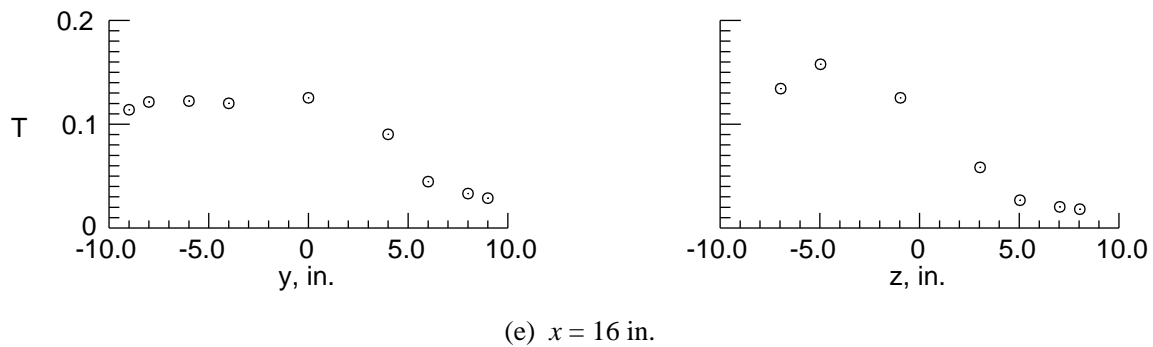


Figure 6. Continued.

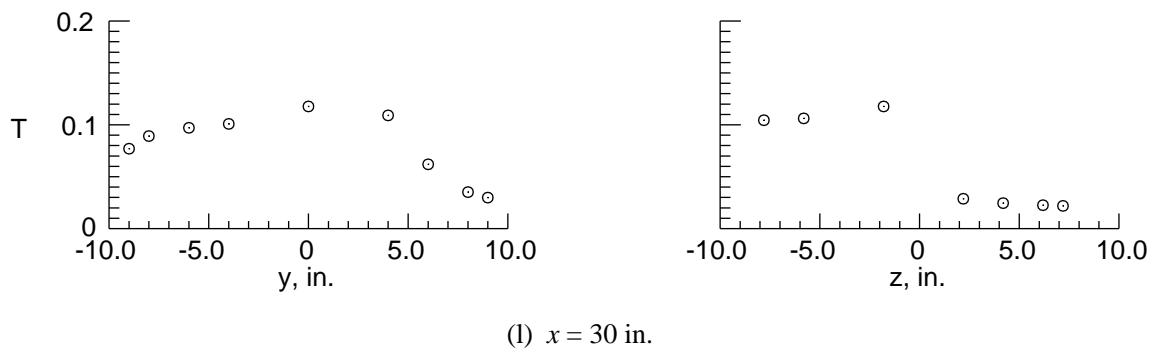
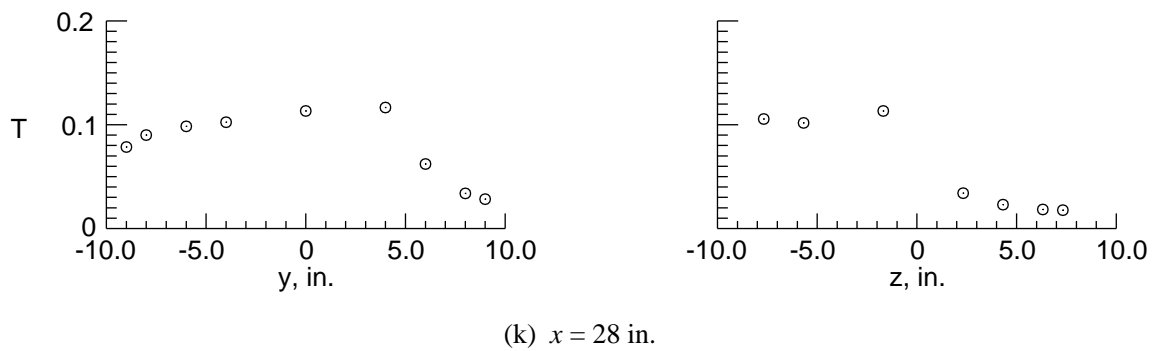
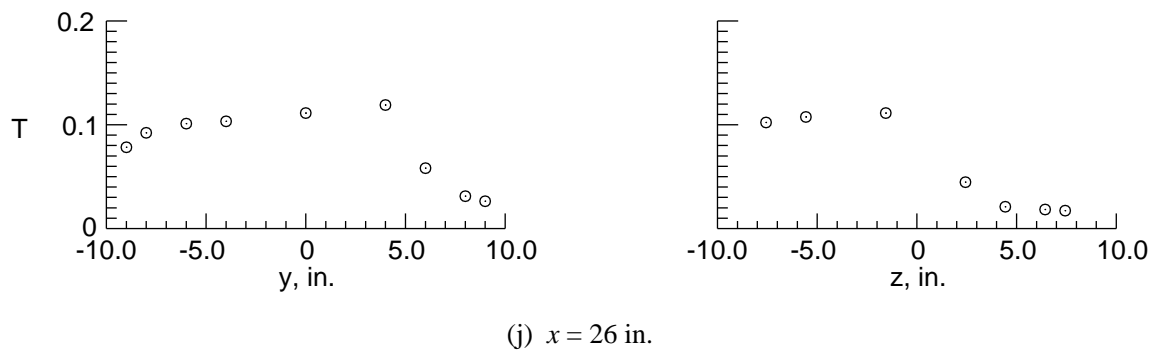
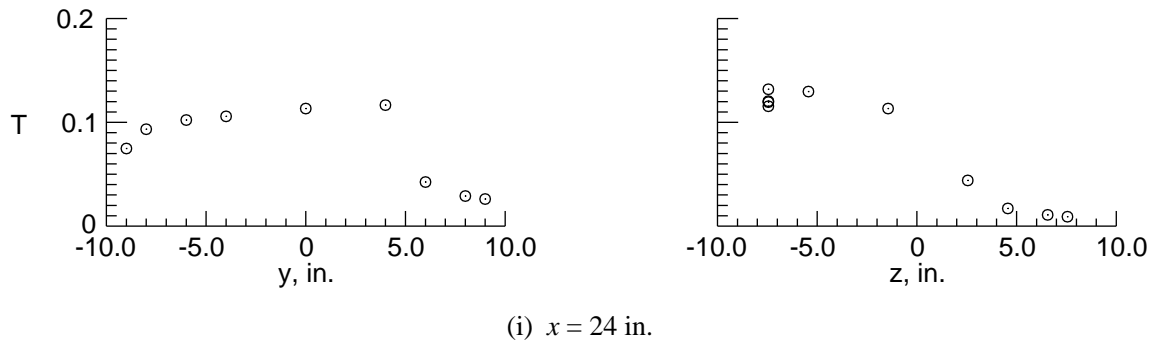
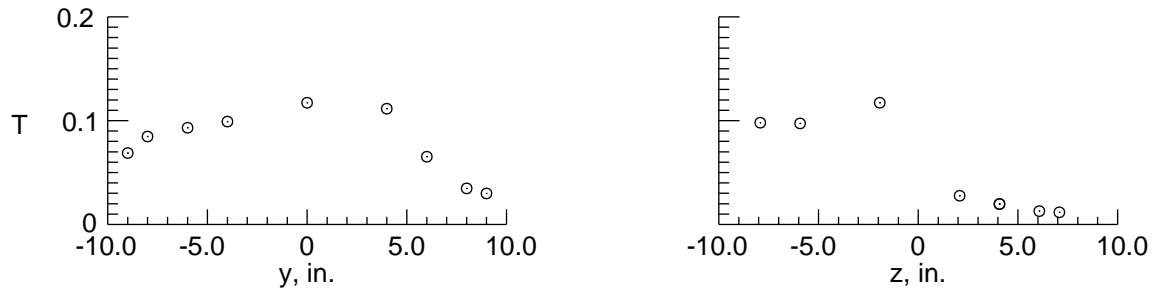
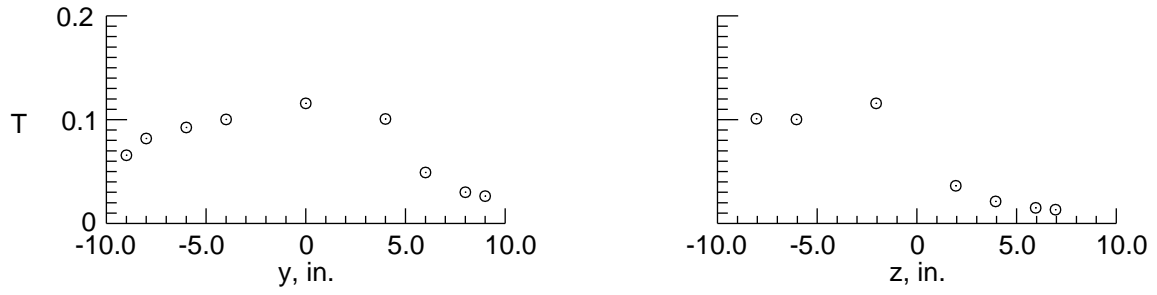


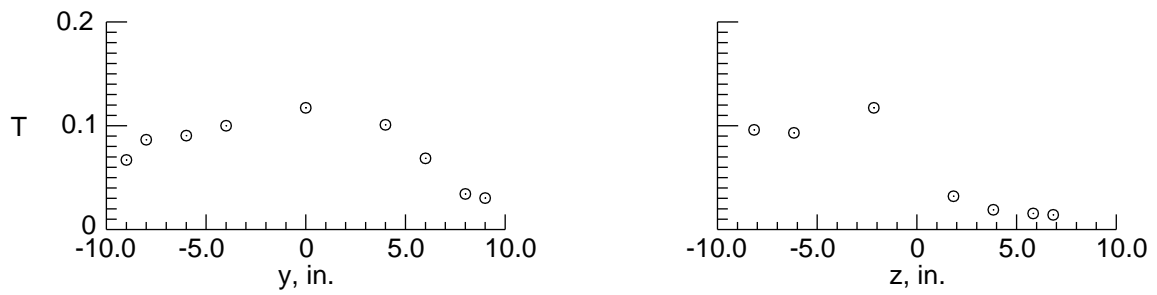
Figure 6. Continued.



(m) $x = 32$ in.

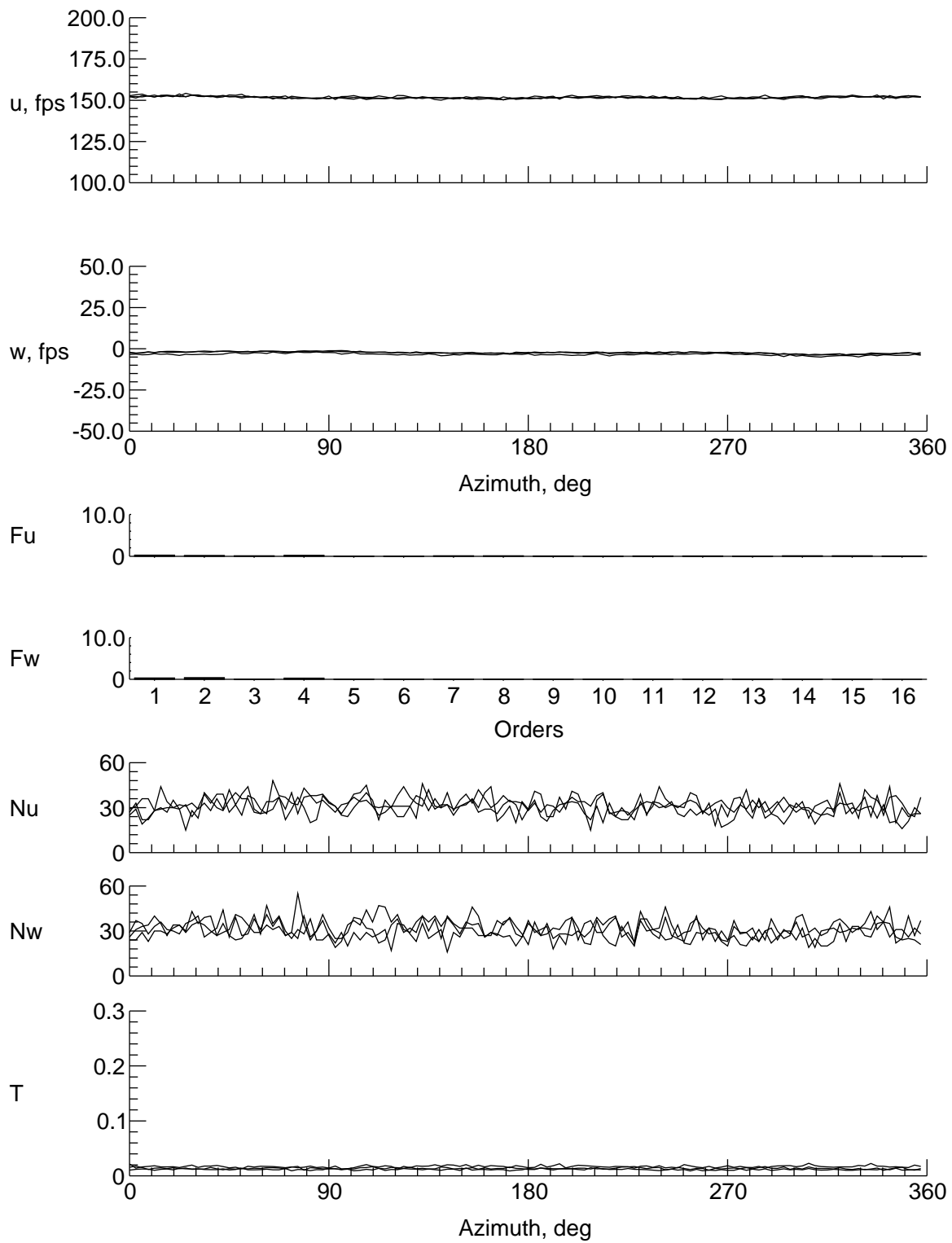


(n) $x = 34$ in.



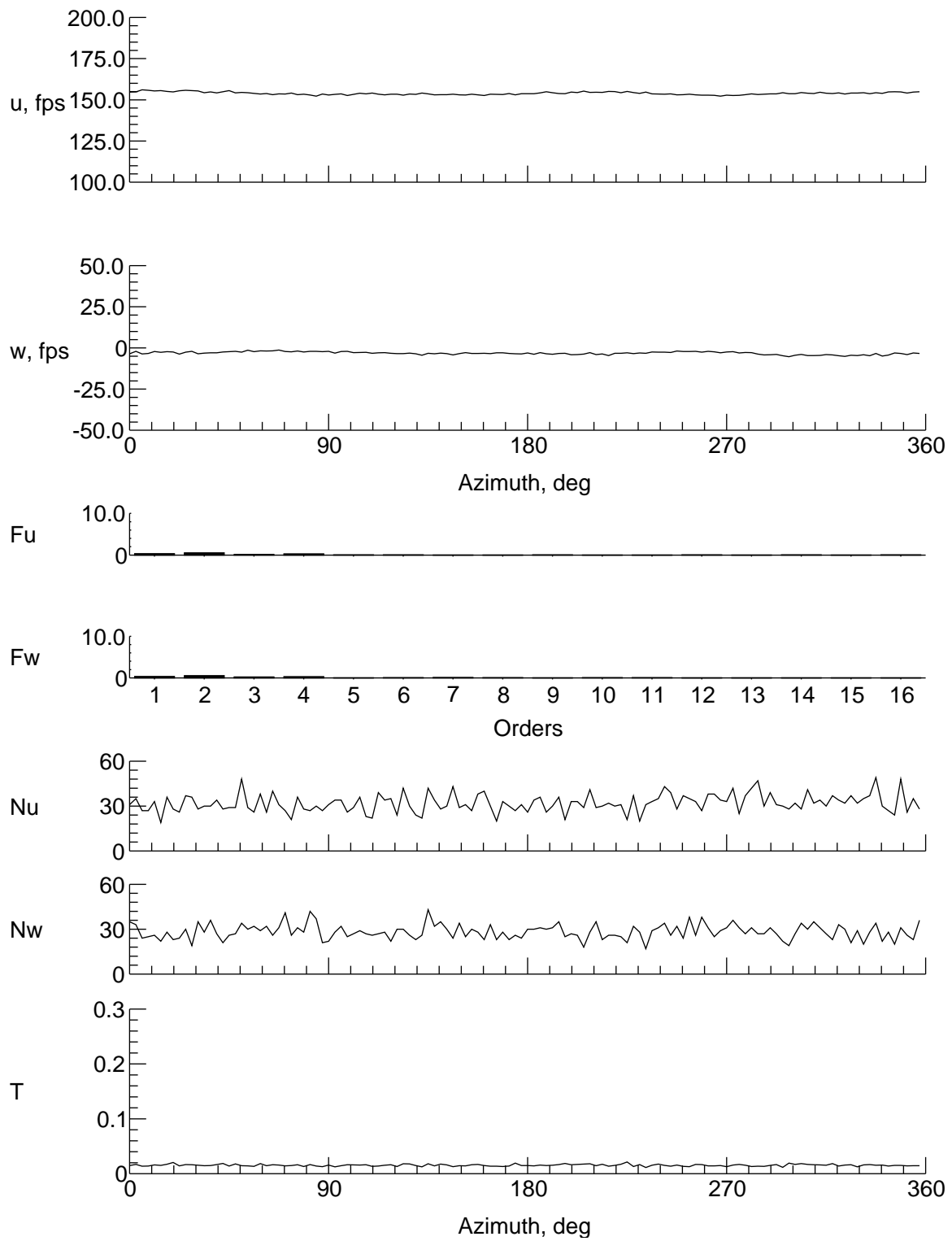
(o) $x = 32$ in.

Figure 6. Concluded.



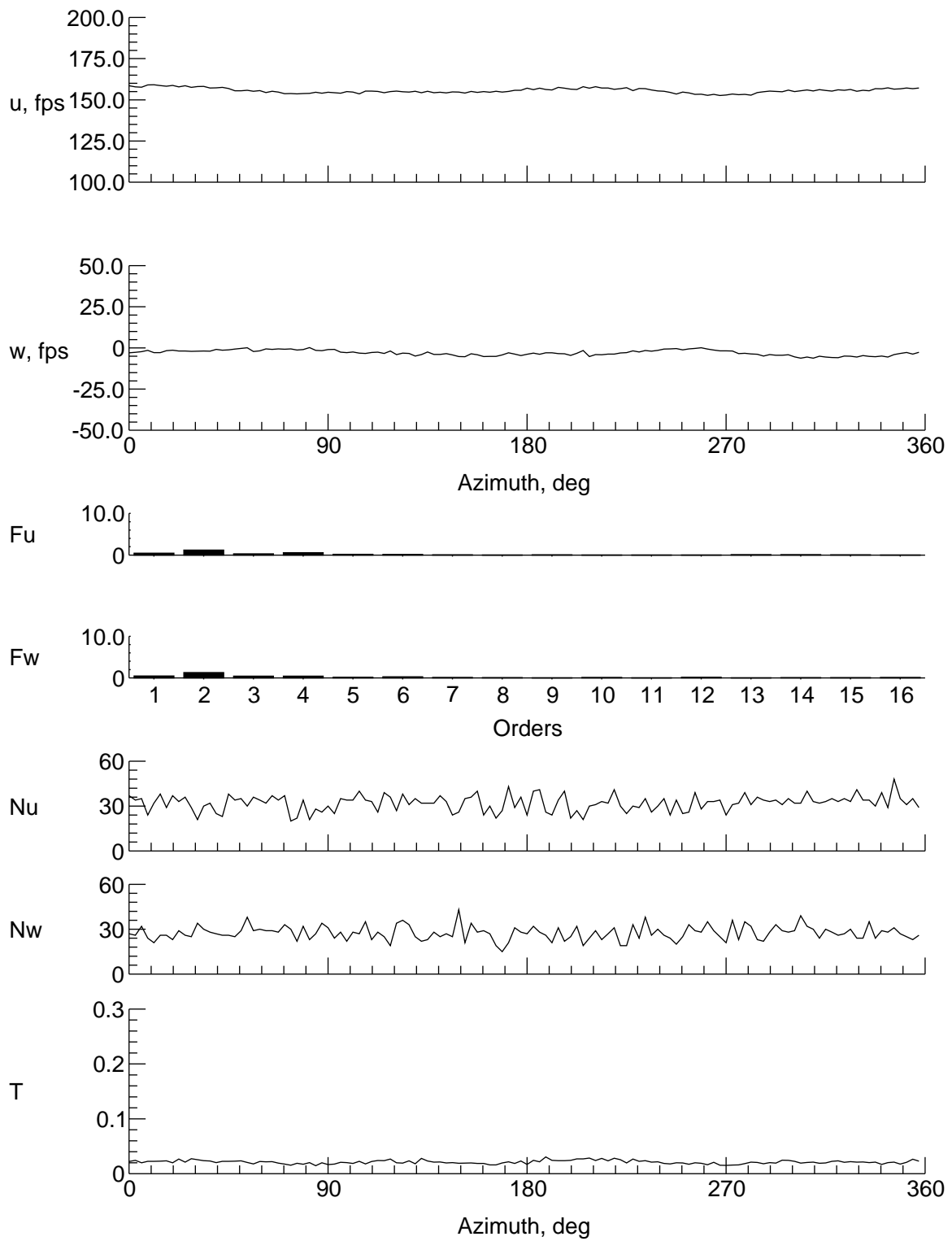
(a) $y = 0$ in., $z = 8.518$ in.

Figure 7. Velocity and turbulence at station 8 in.



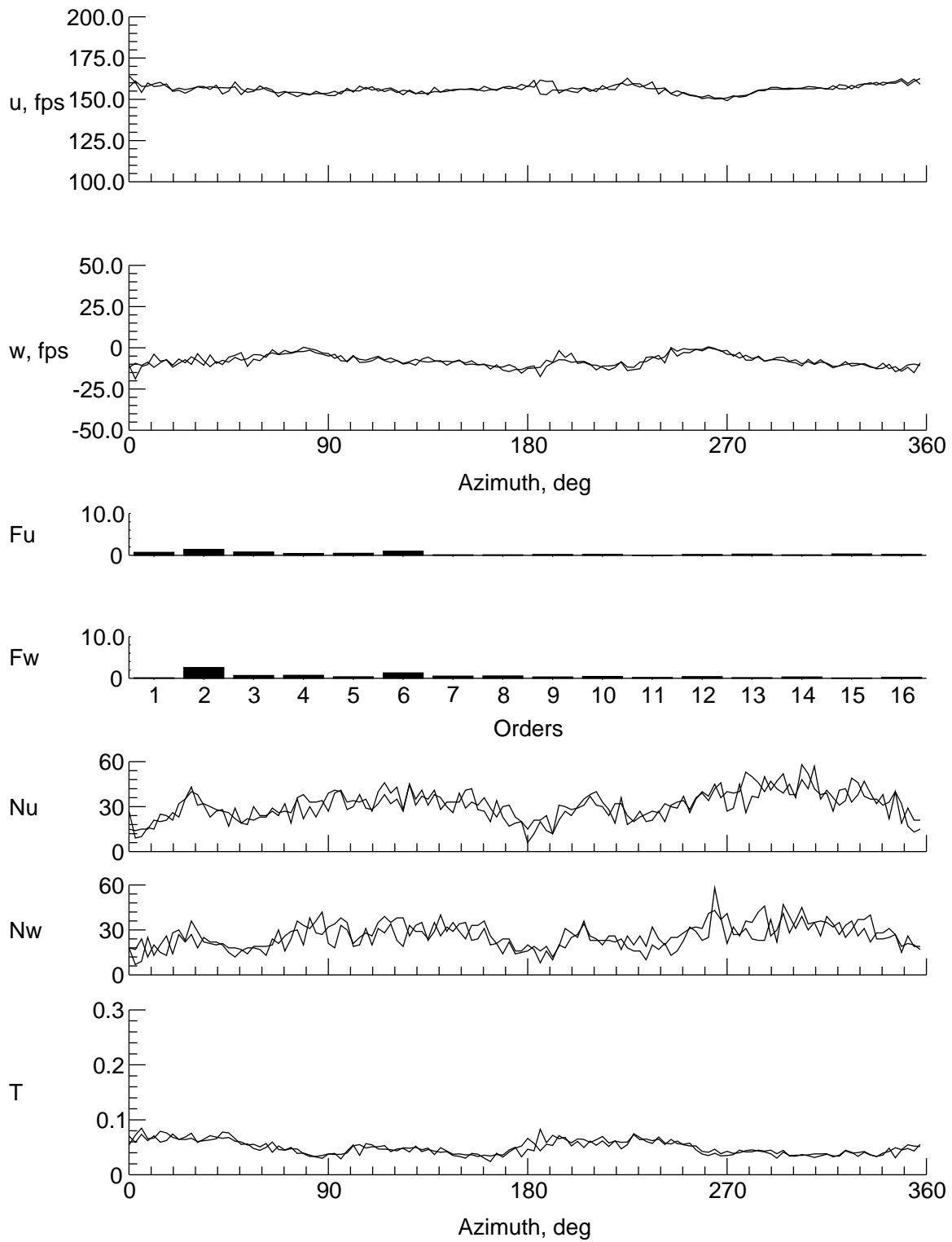
(b) $y = 0$ in., $z = 7.518$ in.

Figure 7. Continued.



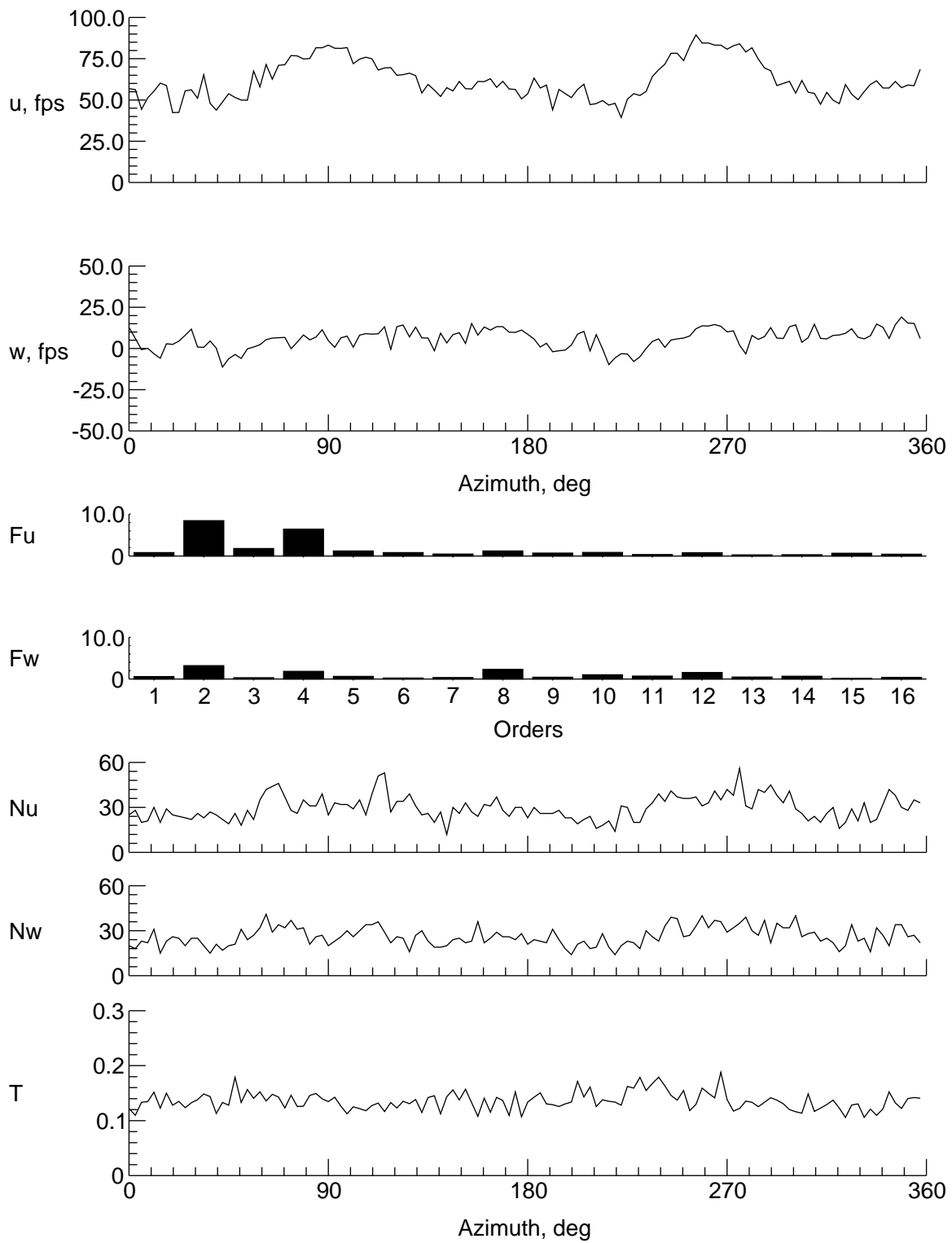
(c) $y = 0$ in., $z = 5.518$ in.

Figure 7. Continued.



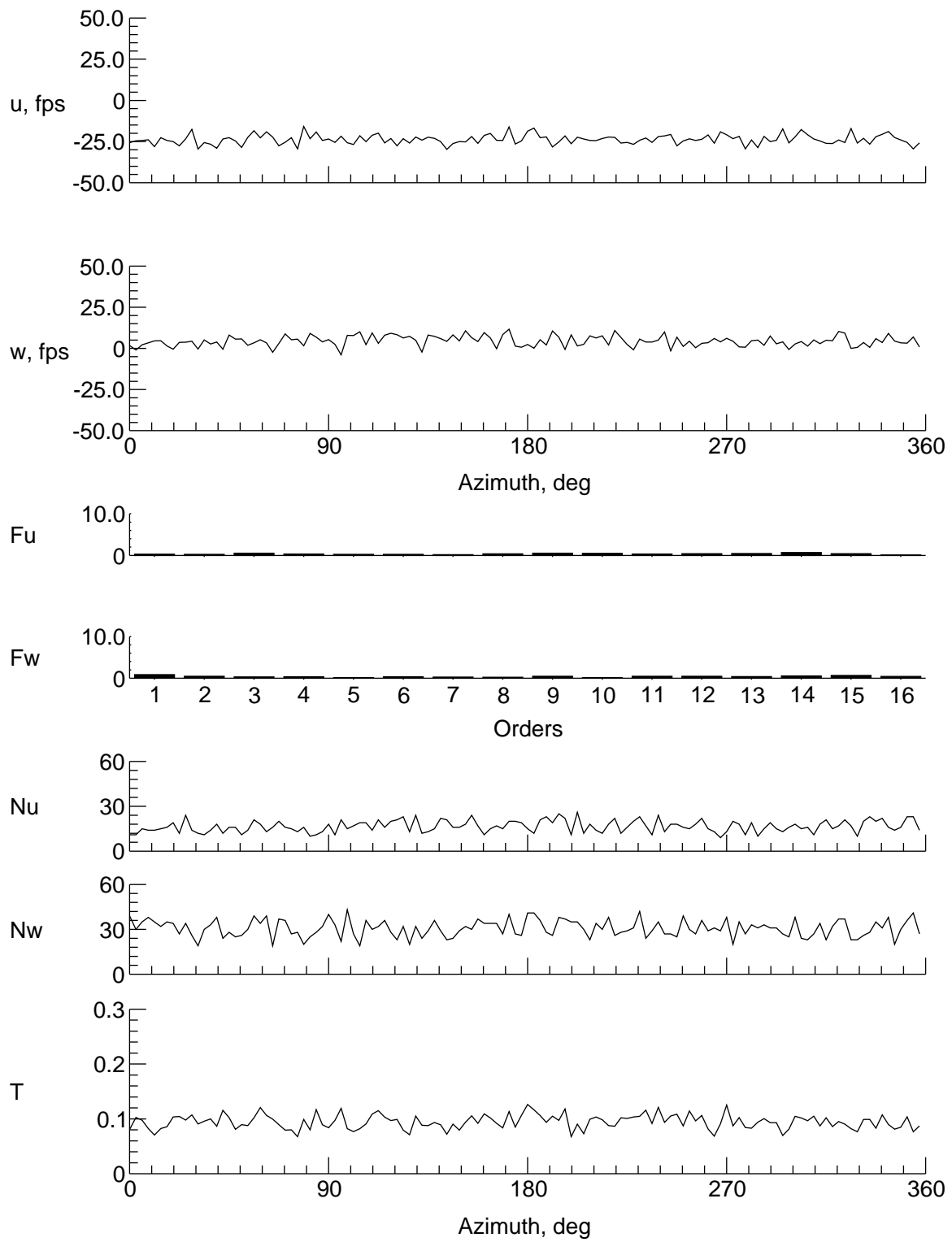
(d) $y = 0$ in., $z = 3.518$ in.

Figure 7. Continued.



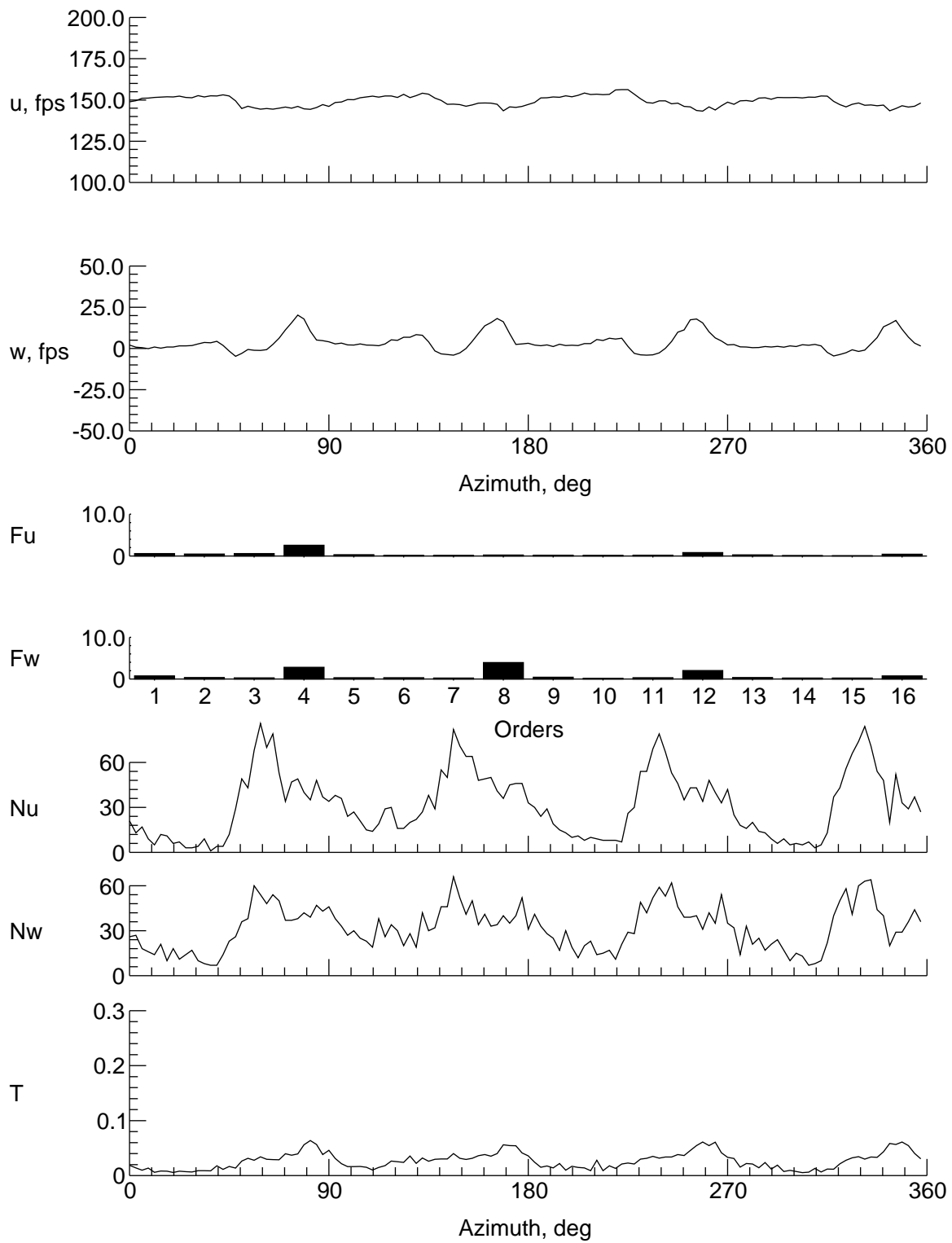
(e) $y = 0$ in., $z = -0.482$ in.

Figure 7. Continued.



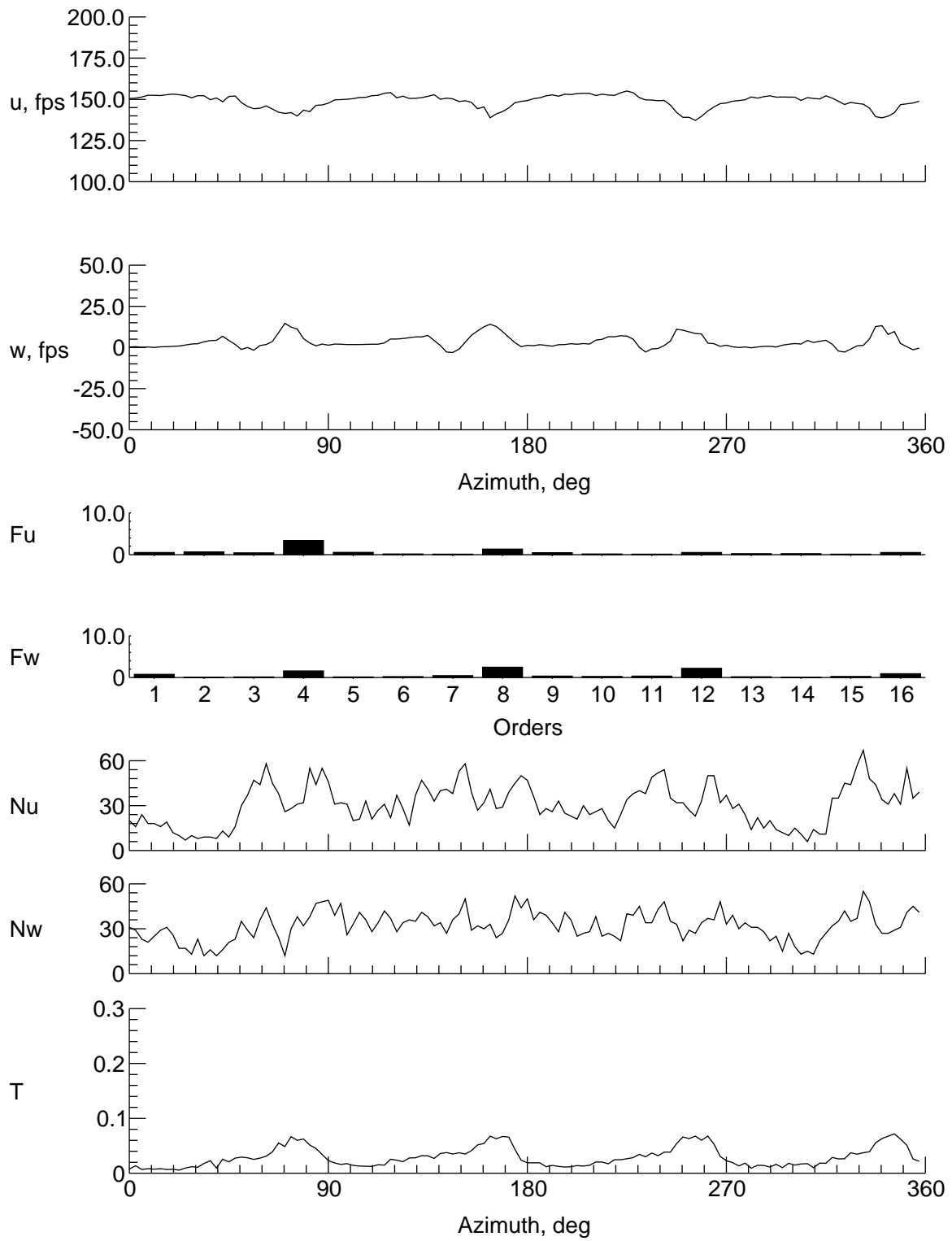
(f) $y = 0$ in., $z = -4.482$ in.

Figure 7. Continued.



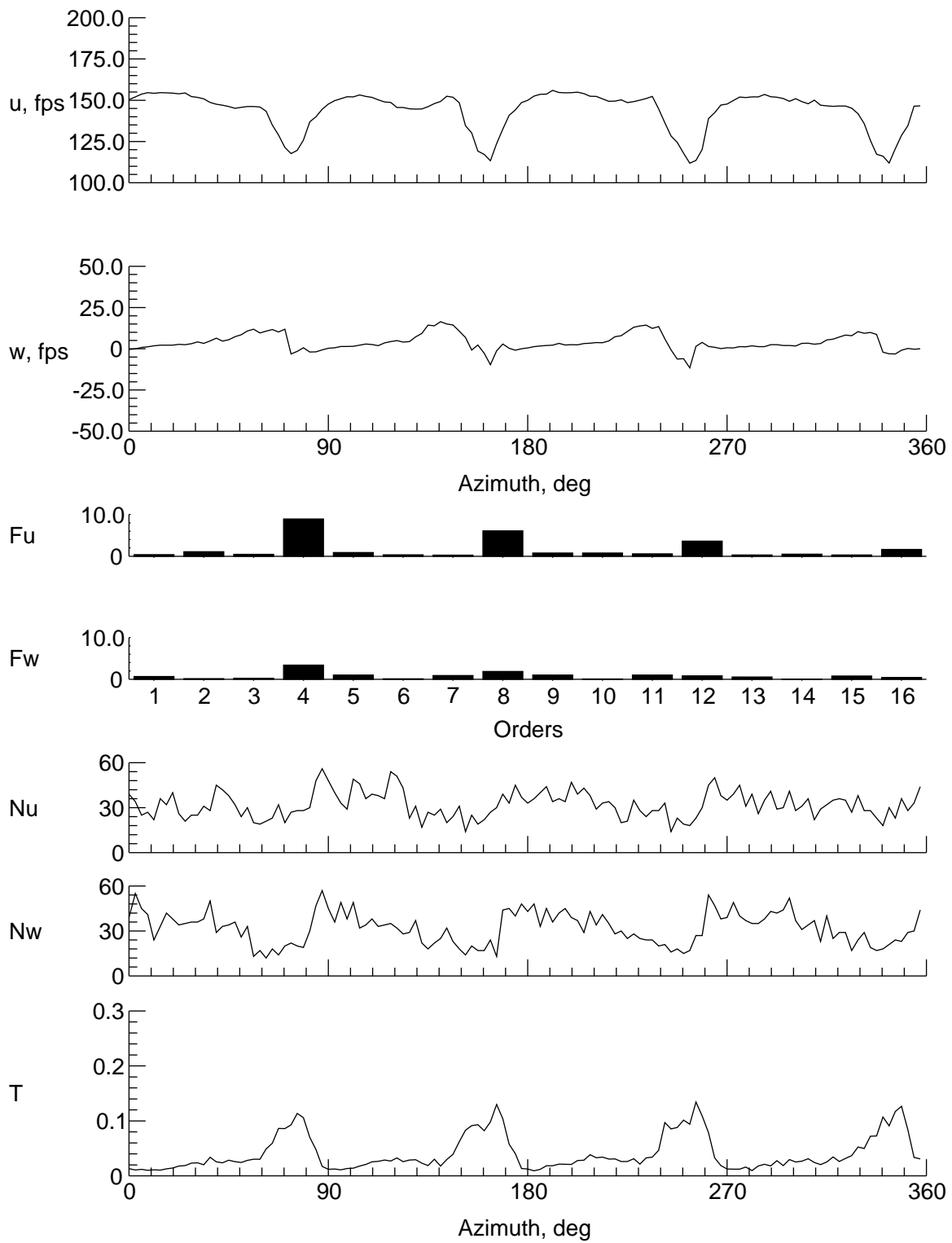
(g) $y = 9$ in., $z = -0.482$ in.

Figure 7. Continued.



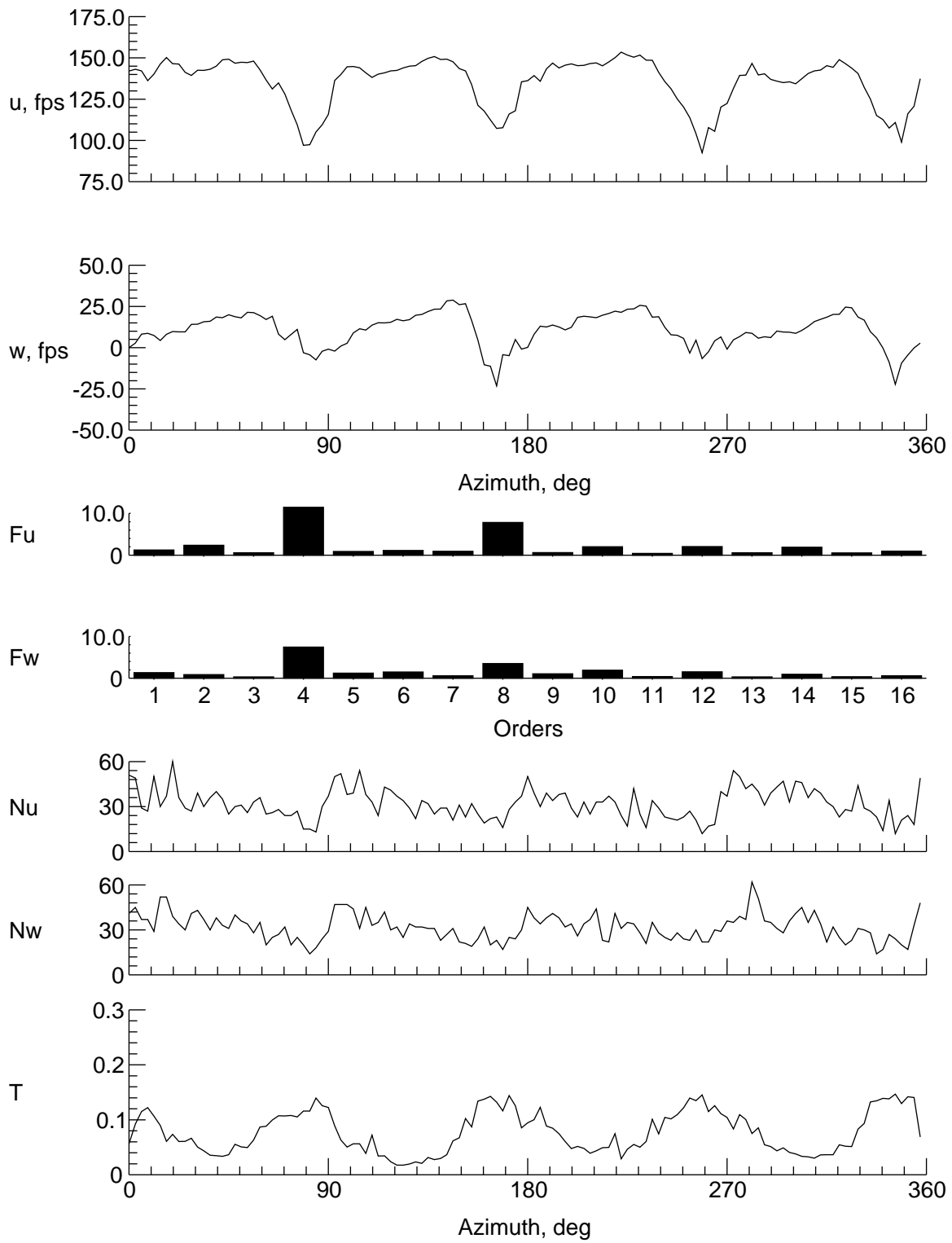
(h) $y = 8$ in., $z = -0.482$ in.

Figure 7. Continued.



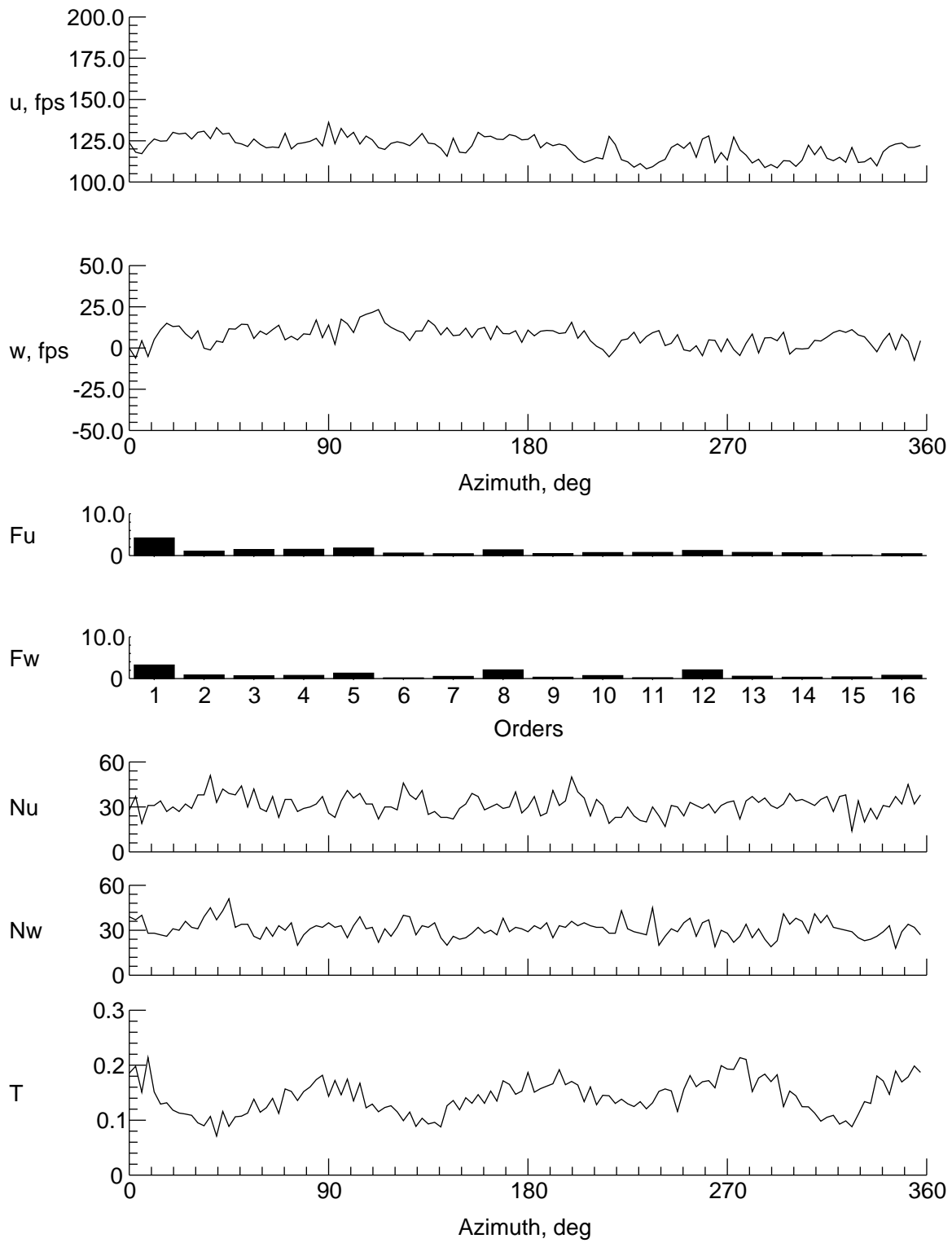
(i) $y = 6$ in., $z = -0.482$ in.

Figure 7. Continued.



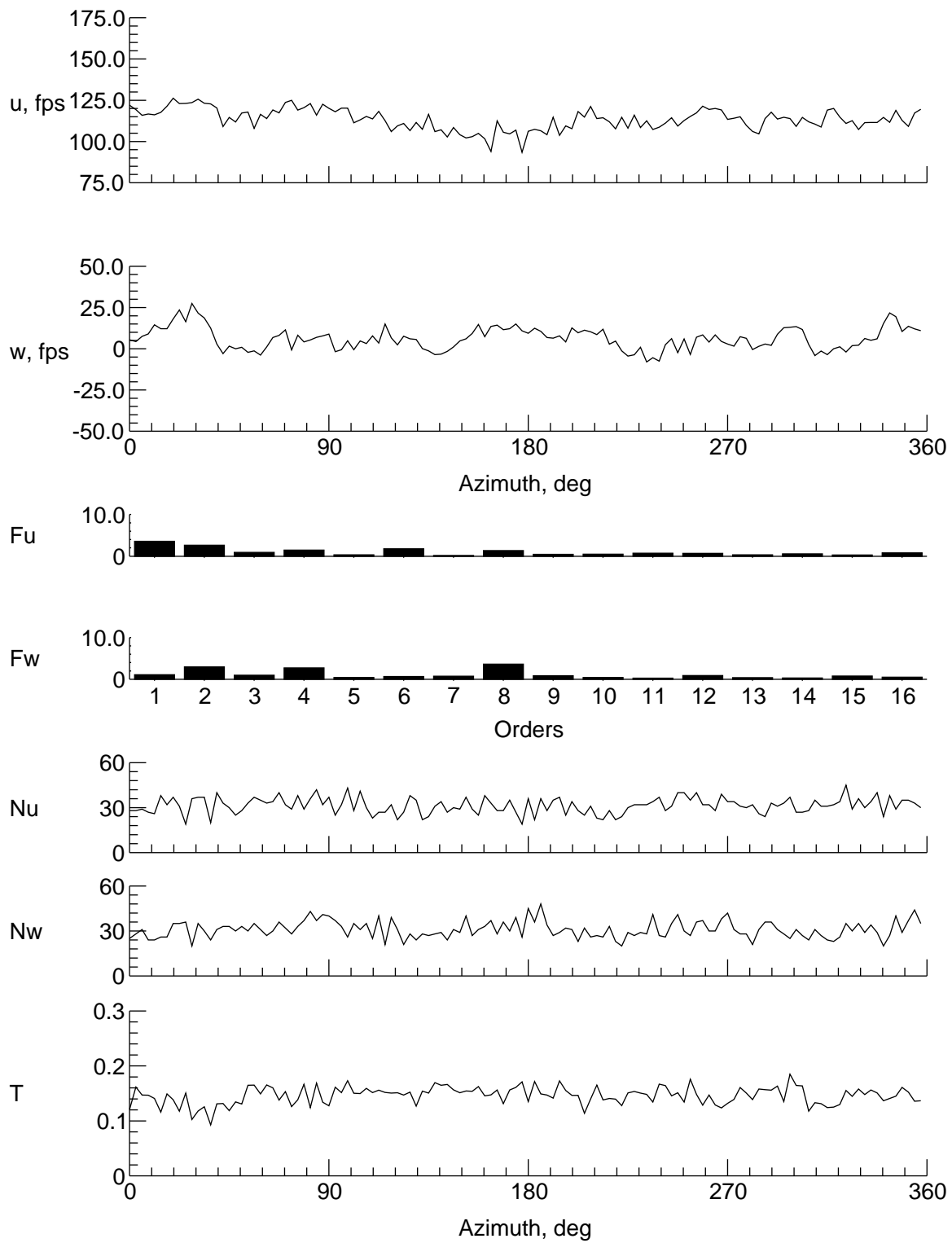
(j) $y = 4$ in., $z = -0.482$ in.

Figure 7. Continued.



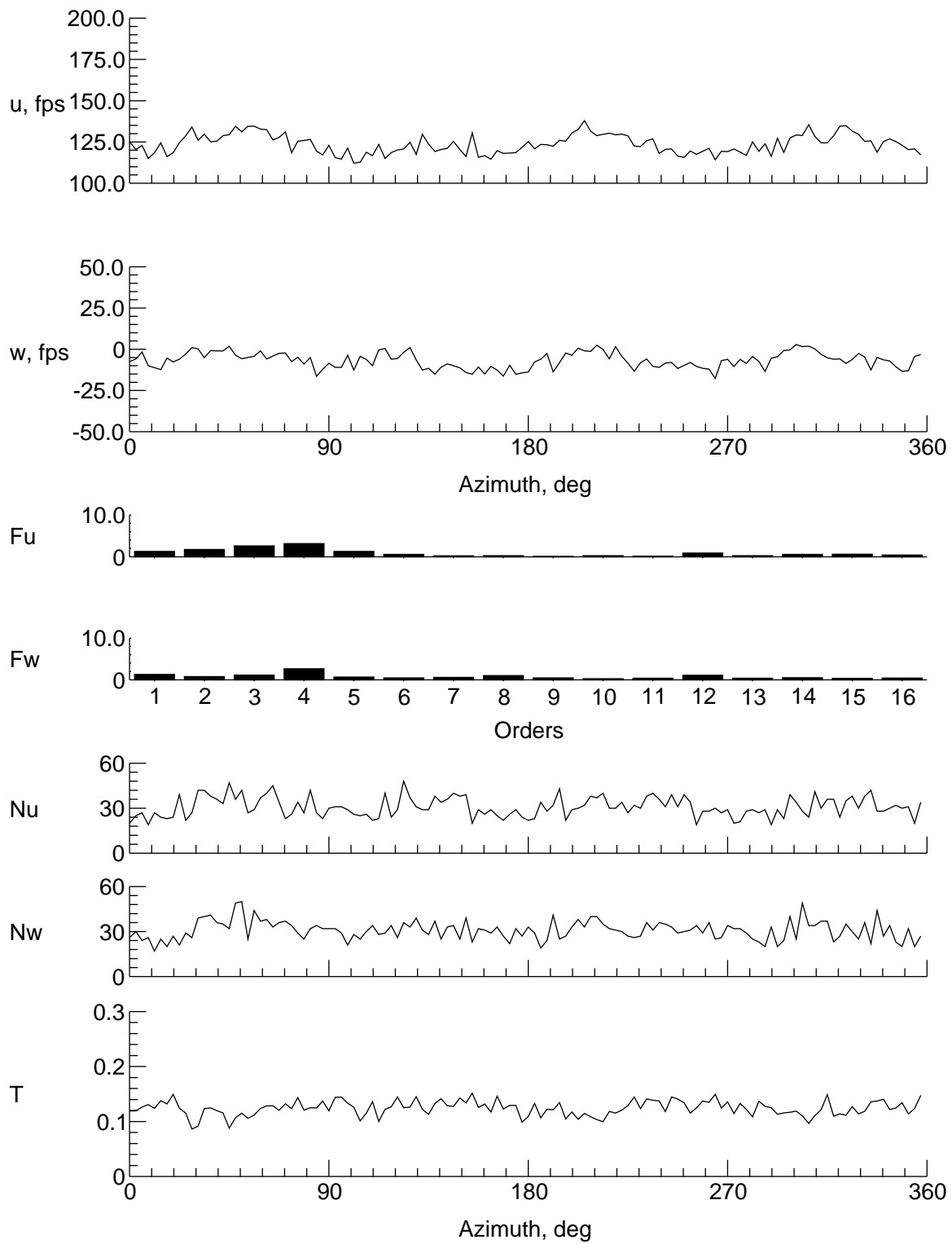
(k) $y = -4$ in., $z = -0.482$ in.

Figure 7. Continued.



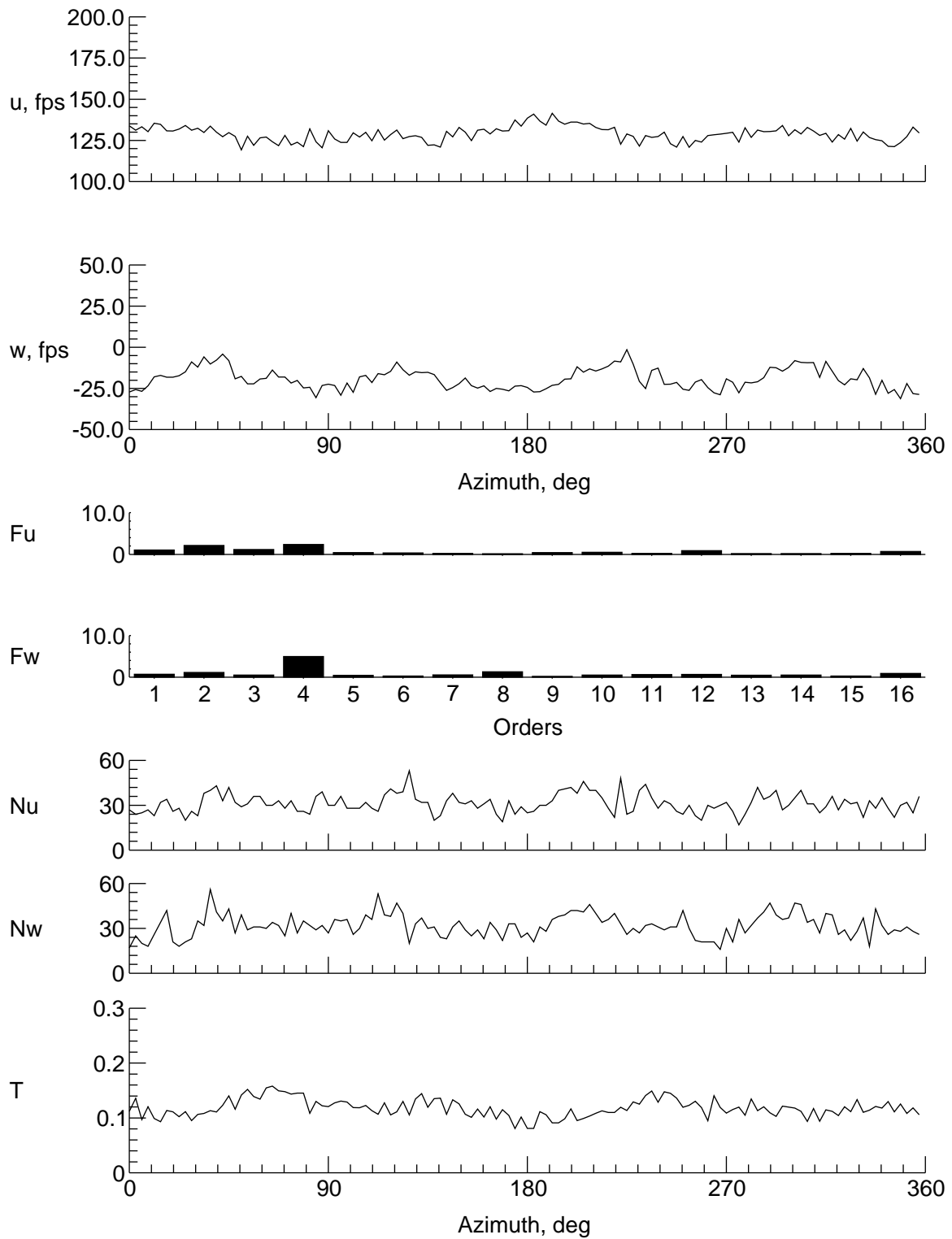
(l) $y = -6$ in., $z = -0.482$ in.

Figure 7. Continued.



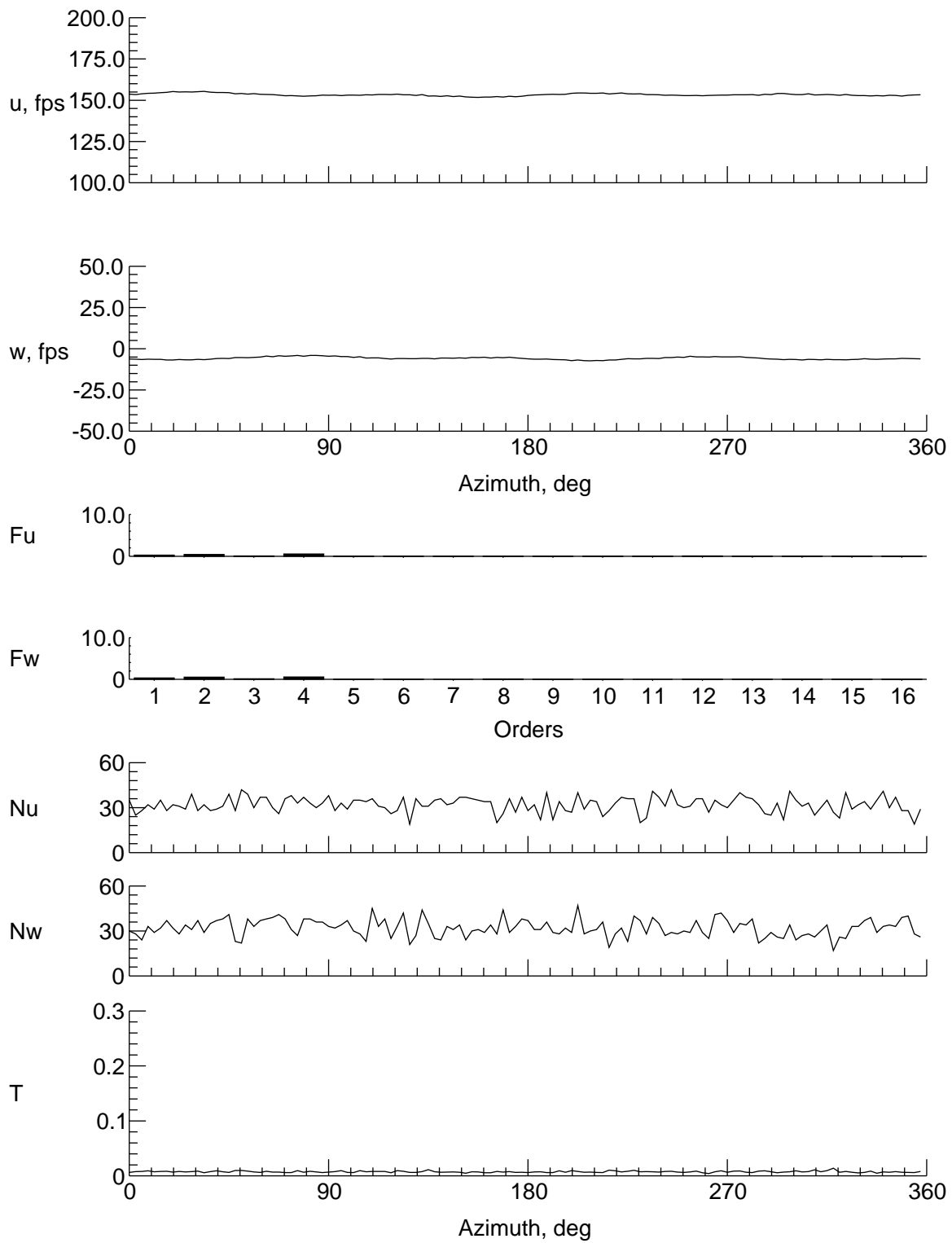
(m) $y = -8$ in., $z = -0.482$ in.

Figure 7. Continued.



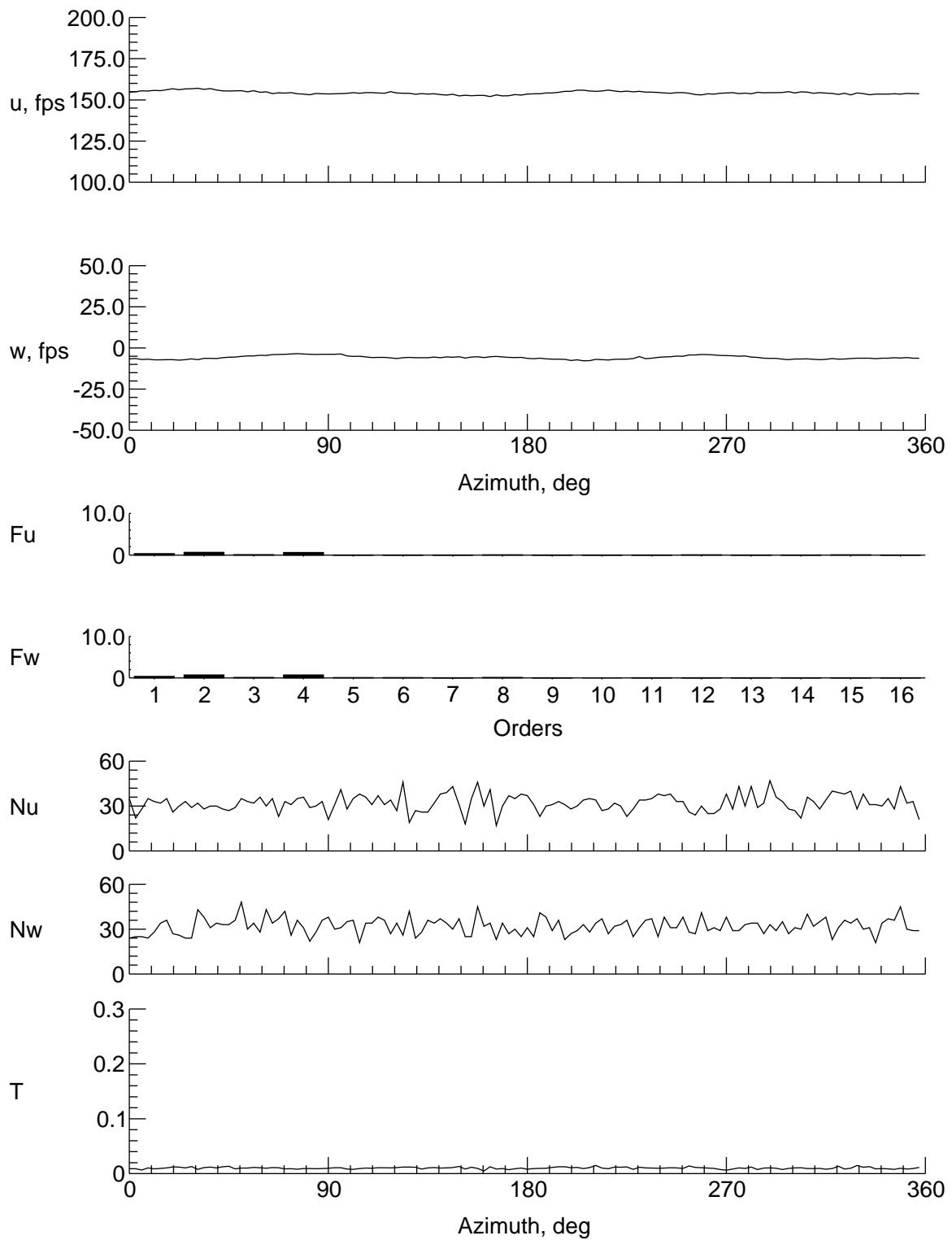
(n) $y = -9$ in., $z = -0.482$ in.

Figure 7. Concluded.



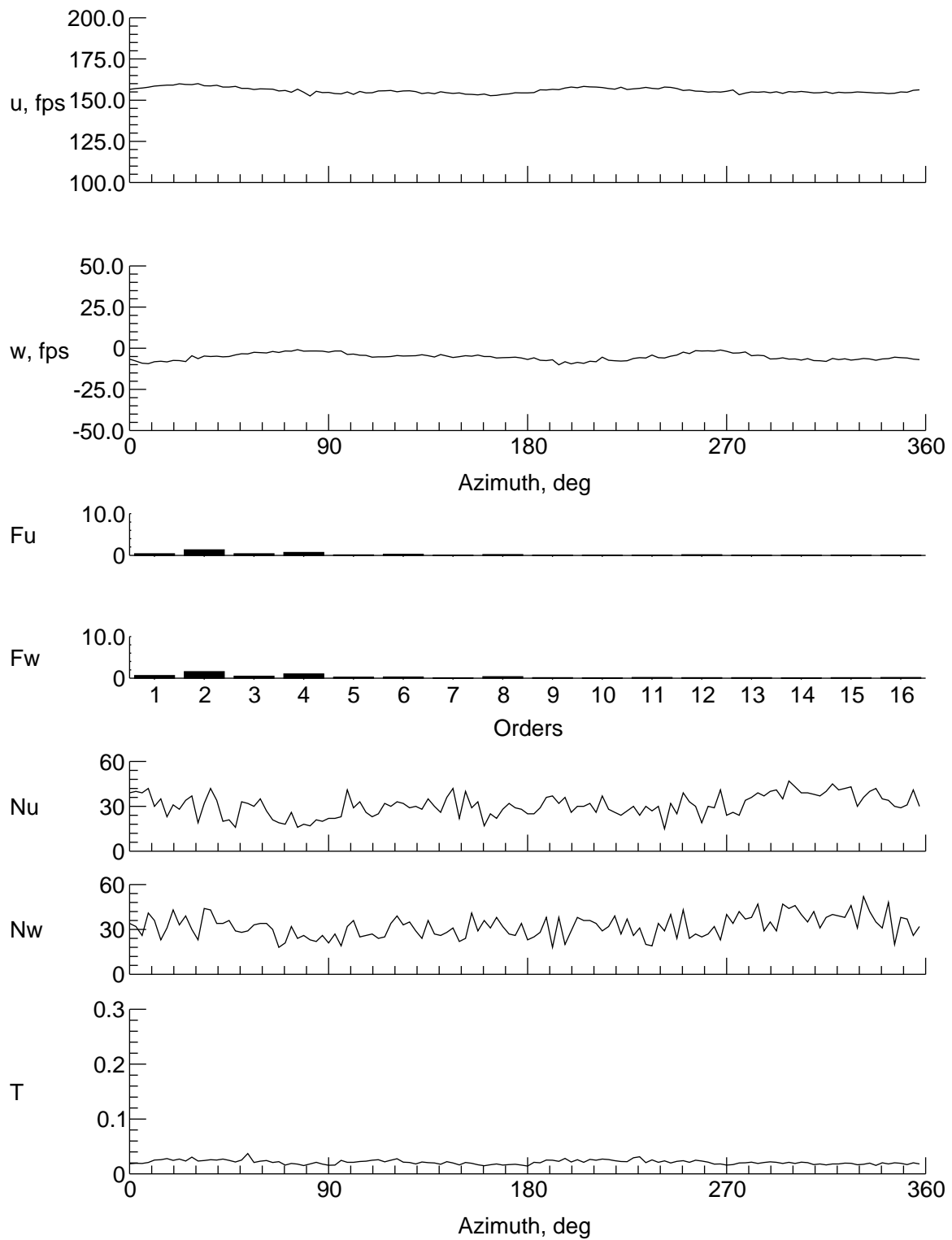
(a) $y = 0$ in., $z = 8.398$ in.

Figure 8. Velocity and turbulence at station 10 in.



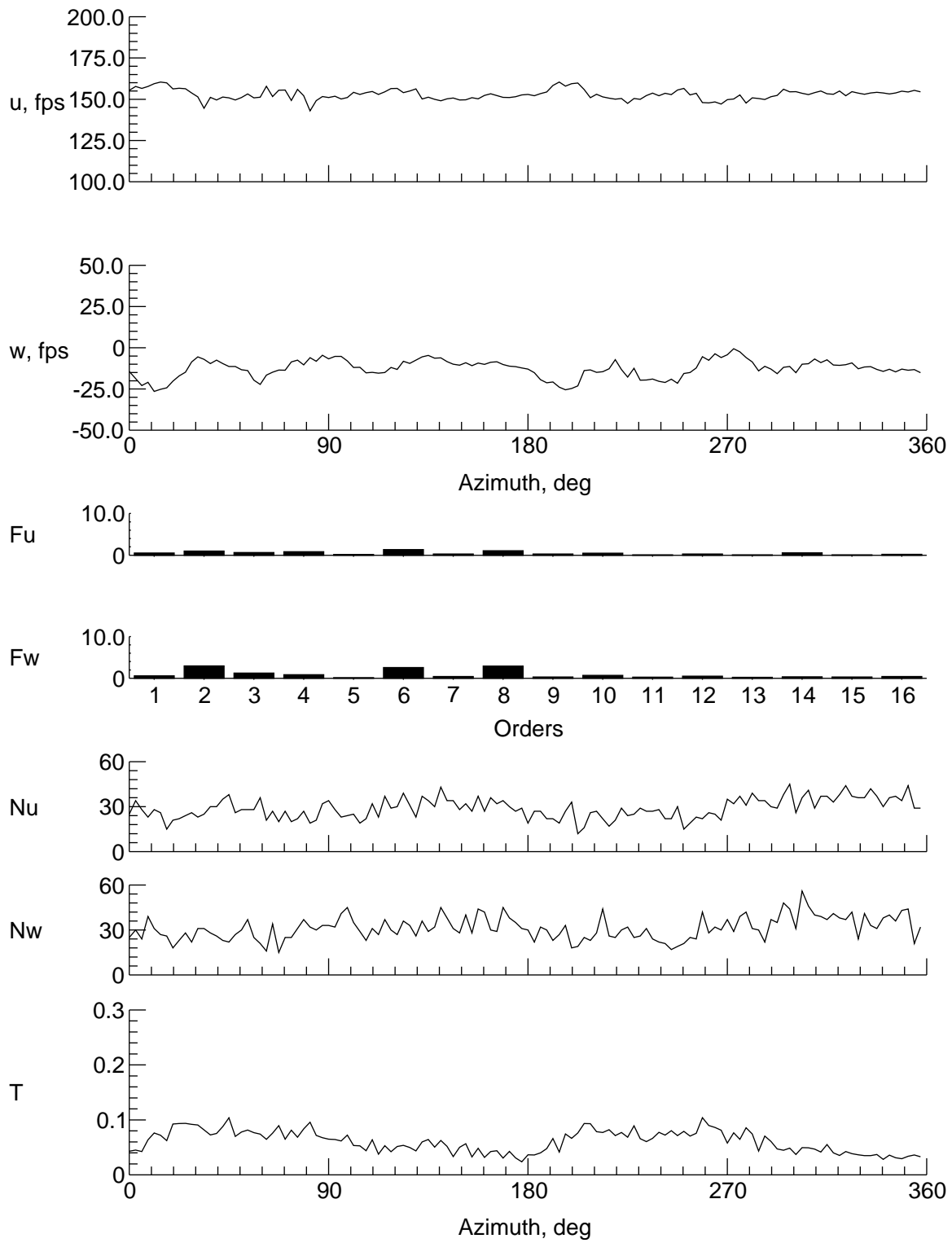
(b) $y = 0$ in., $z = 7.398$ in.

Figure 8. Continued.



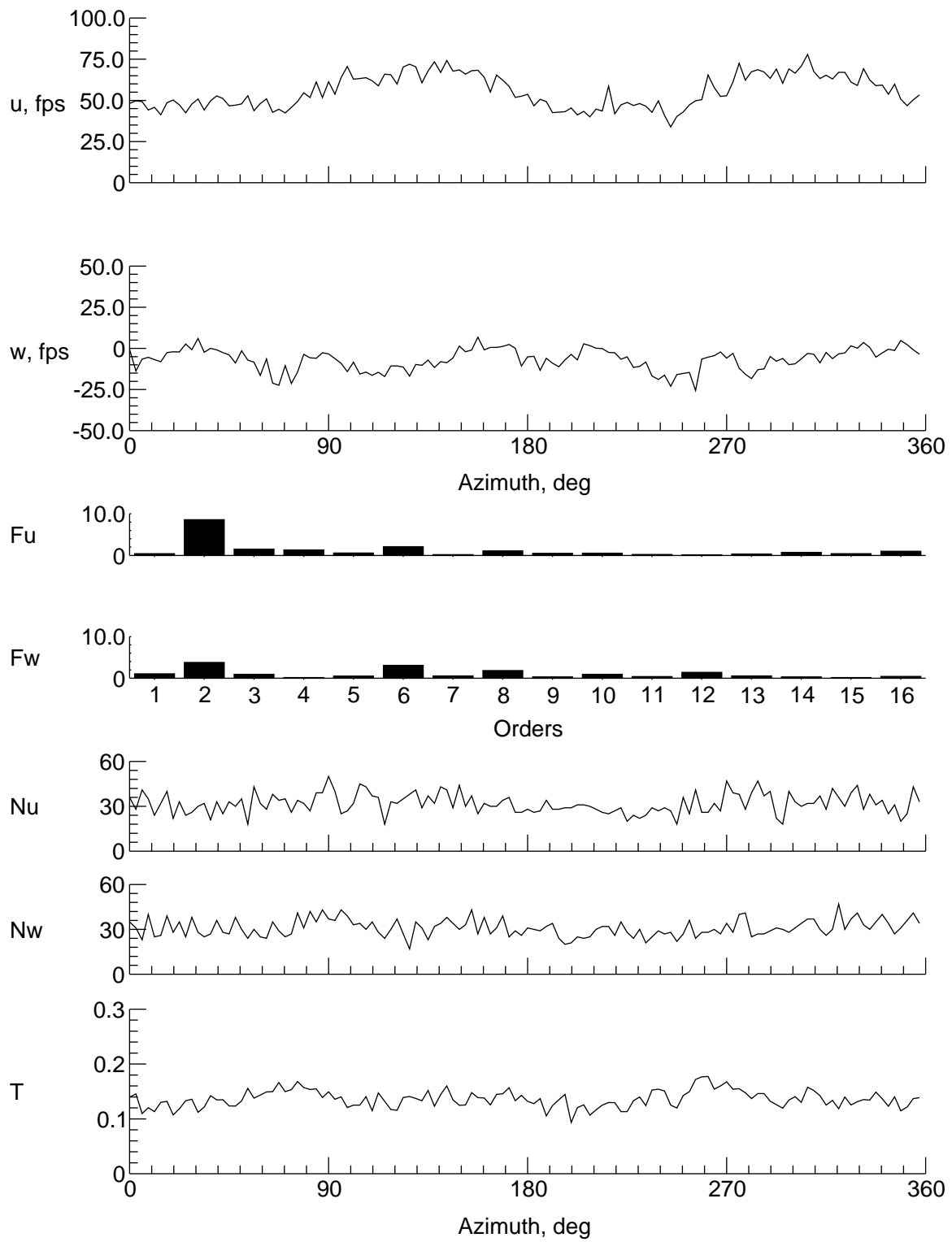
(c) $y = 0$ in., $z = 5.398$ in.

Figure 8. Continued.



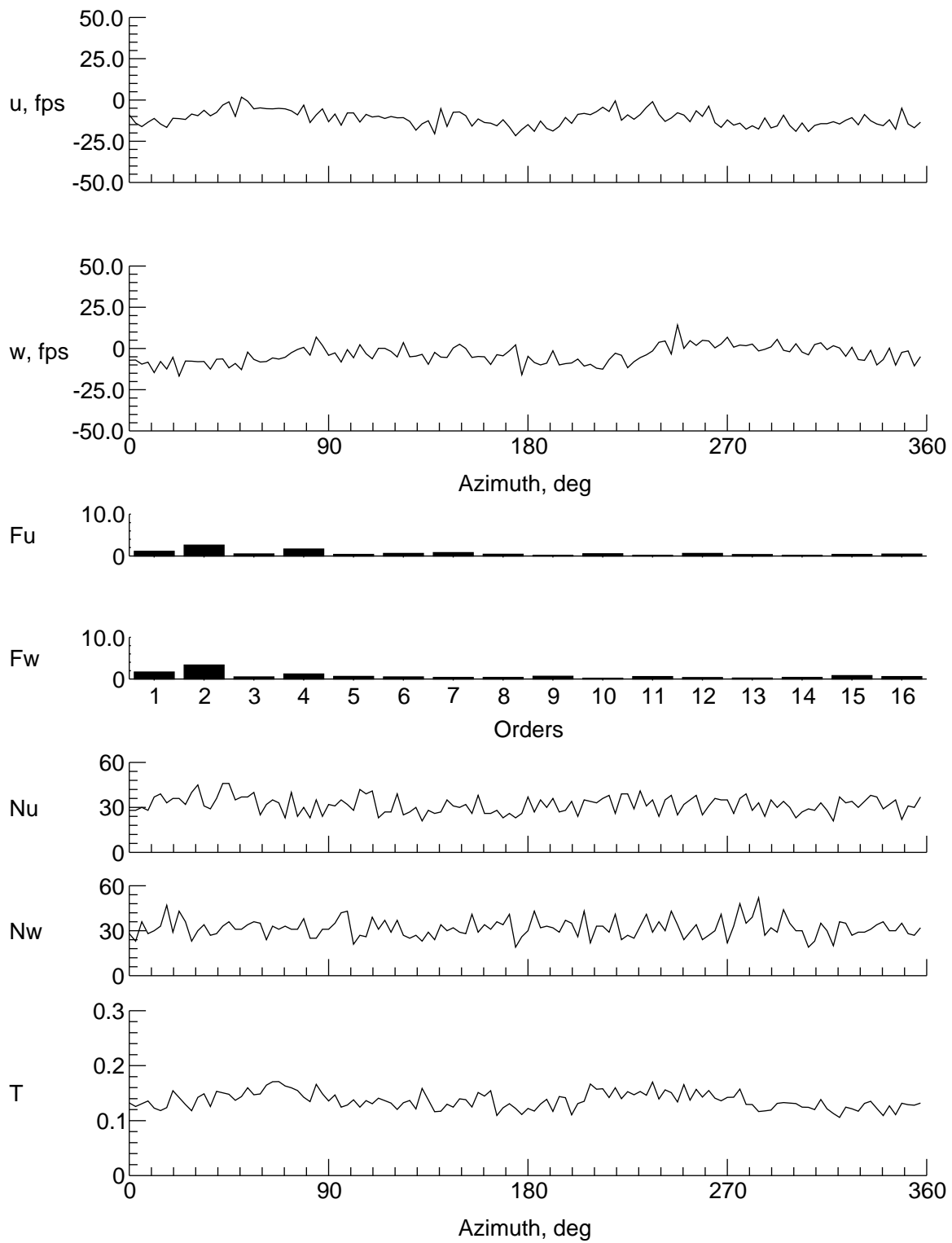
(d) $y = 0$ in., $z = 3.398$ in.

Figure 8. Continued.



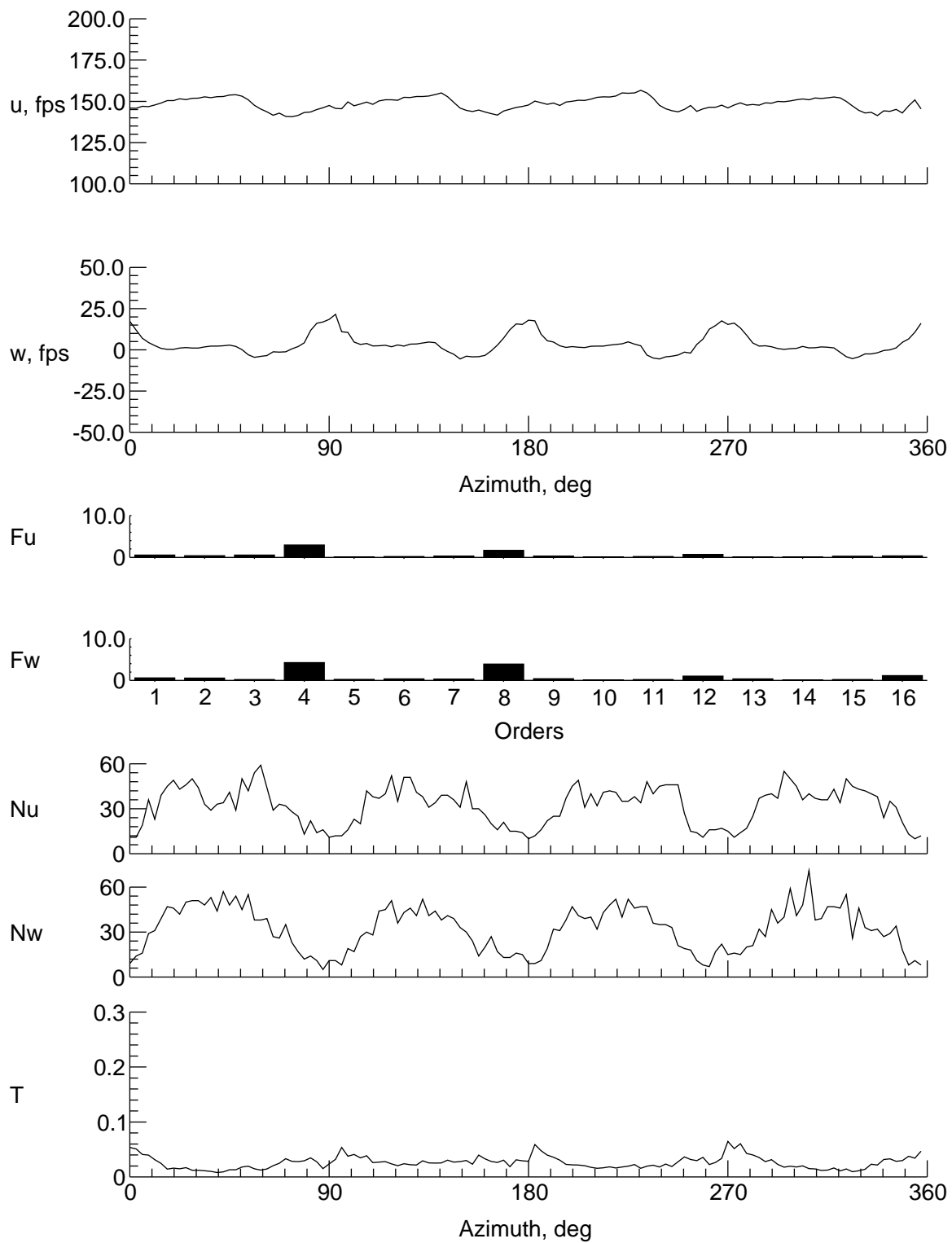
(e) $y = 0$ in., $z = -0.602$ in.

Figure 8. Continued.



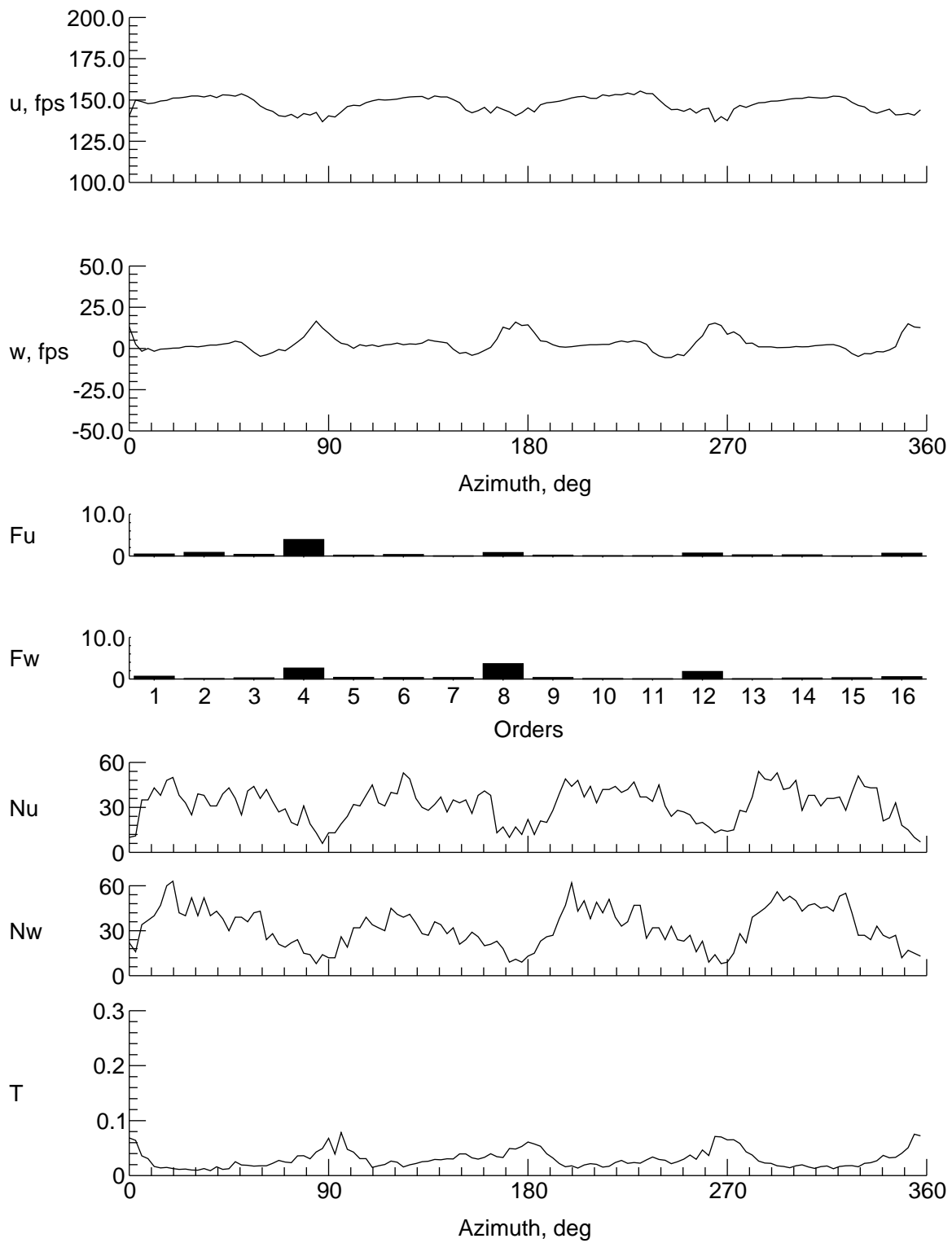
(f) $y = 0$ in., $z = -4.602$ in.

Figure 8. Continued.



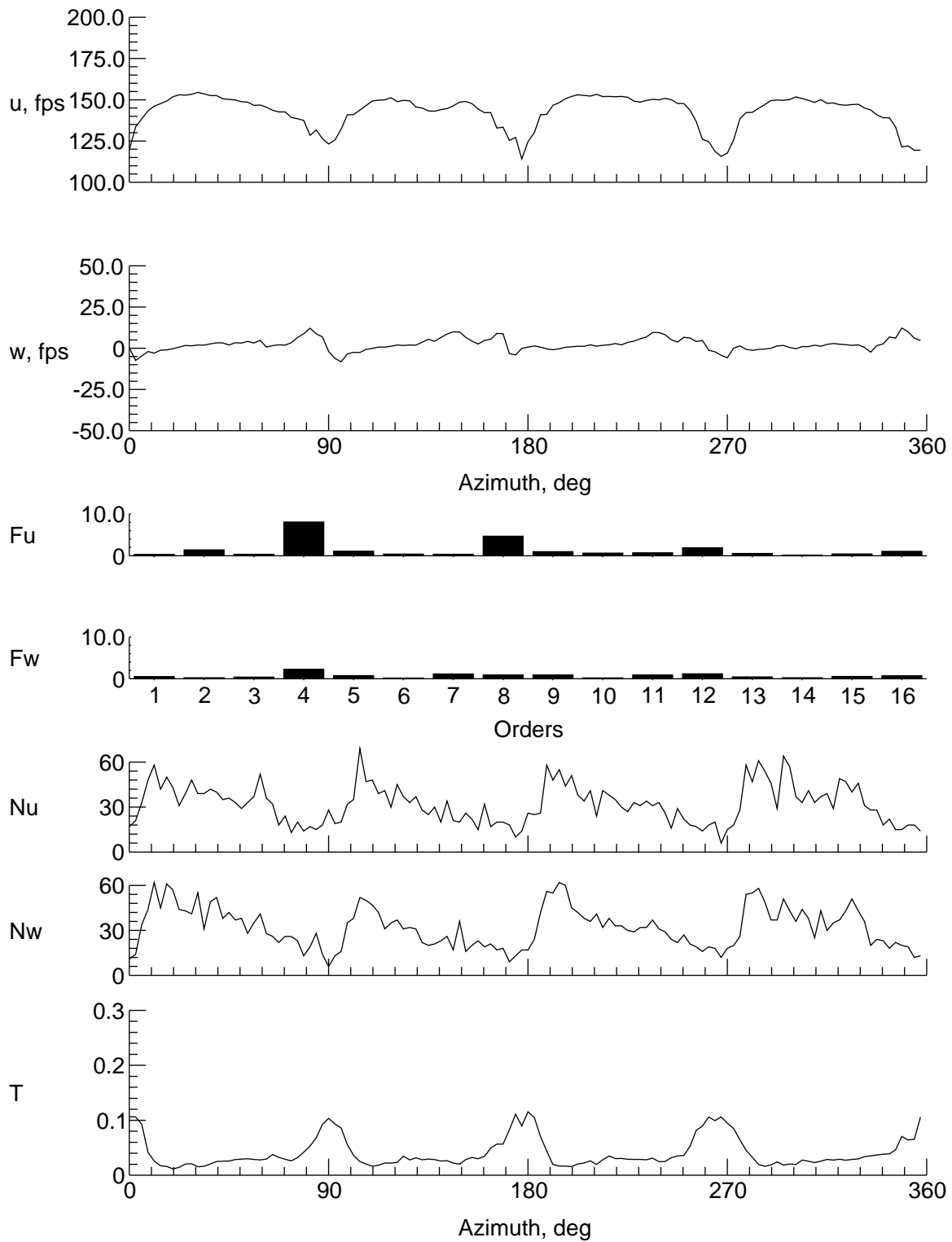
(g) $y = 9$ in., $z = -0.602$ in.

Figure 8. Continued.



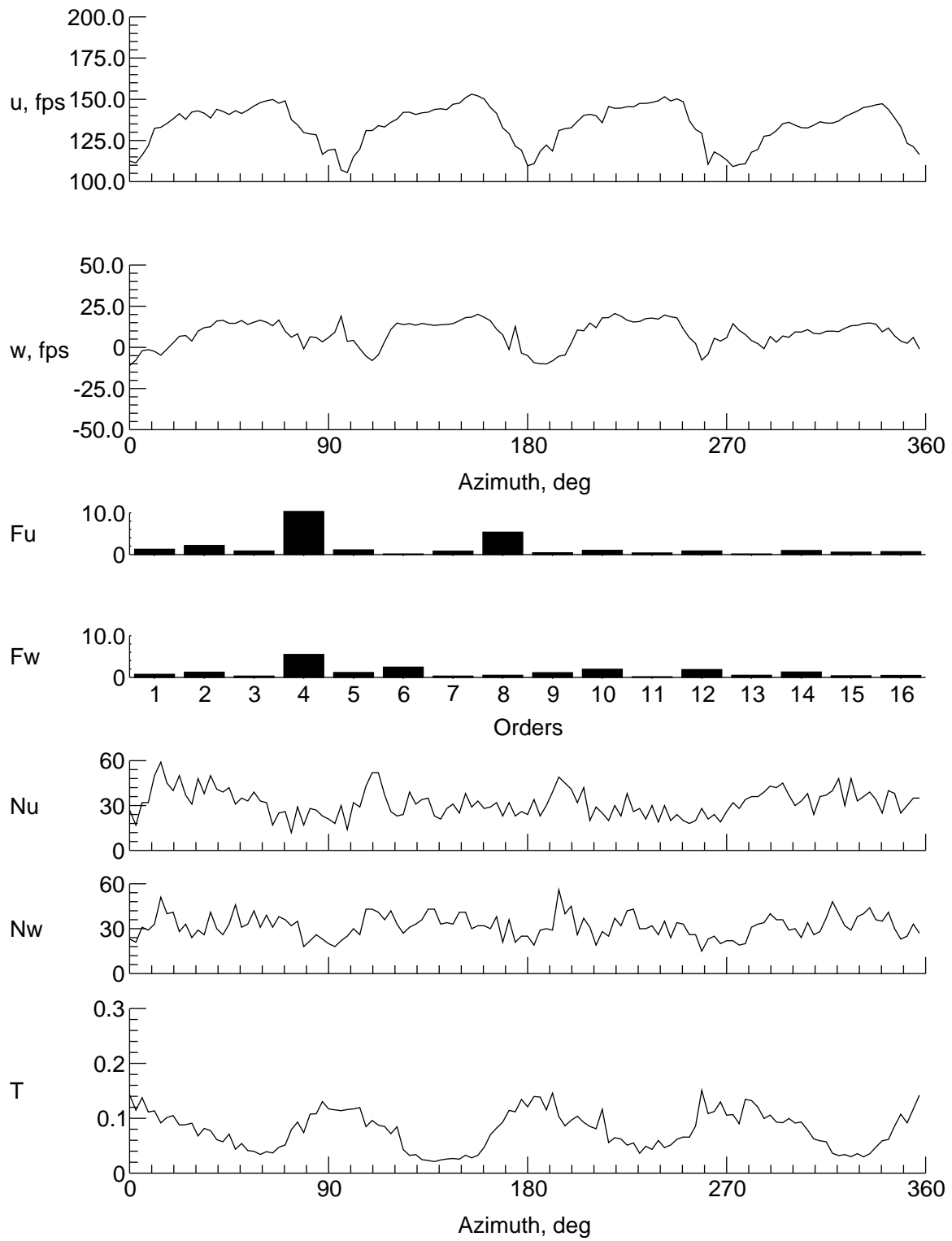
(h) $y = 8$ in., $z = -0.602$ in.

Figure 8. Continued.



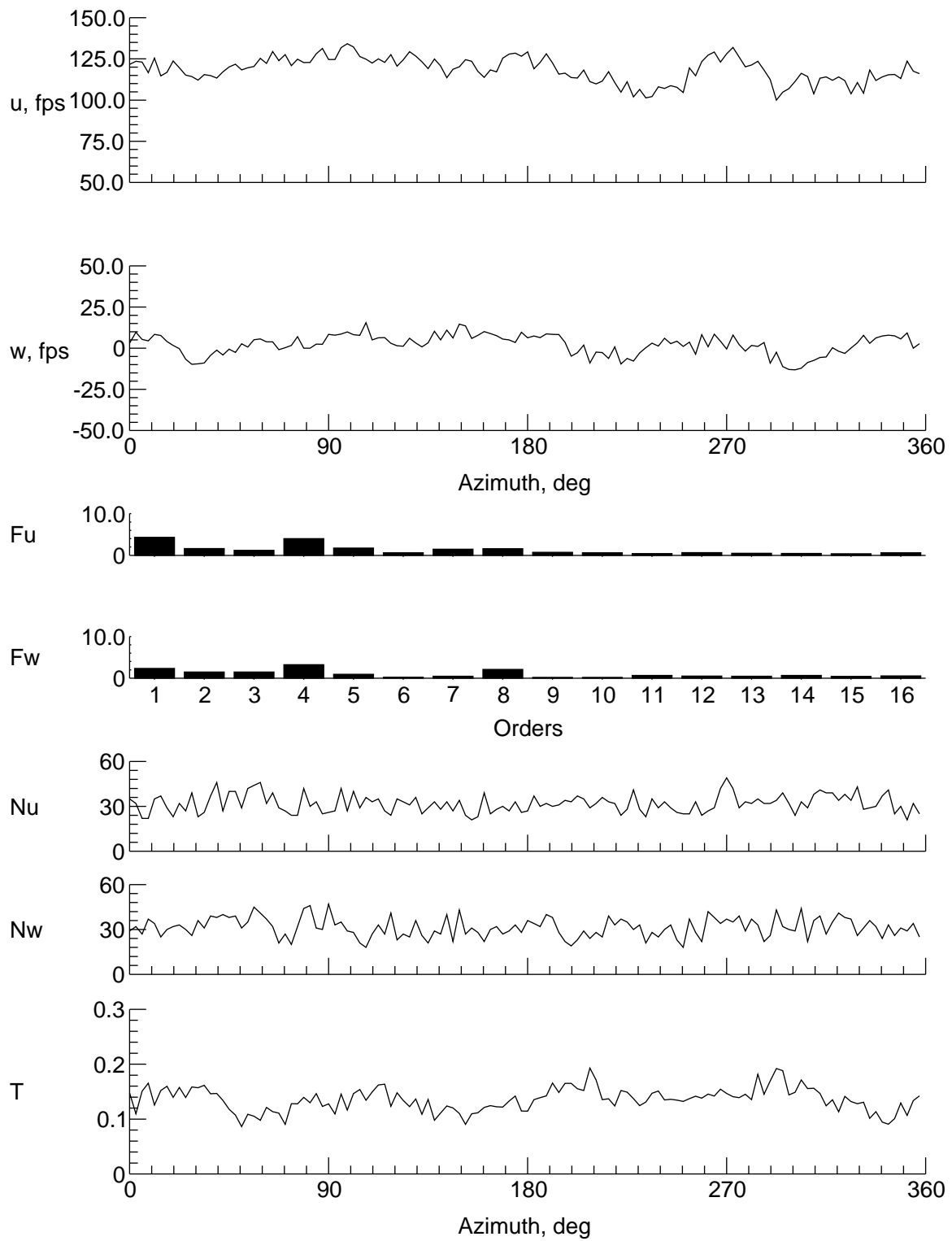
(i) $y = 6$ in., $z = -0.602$ in.

Figure 8. Continued.



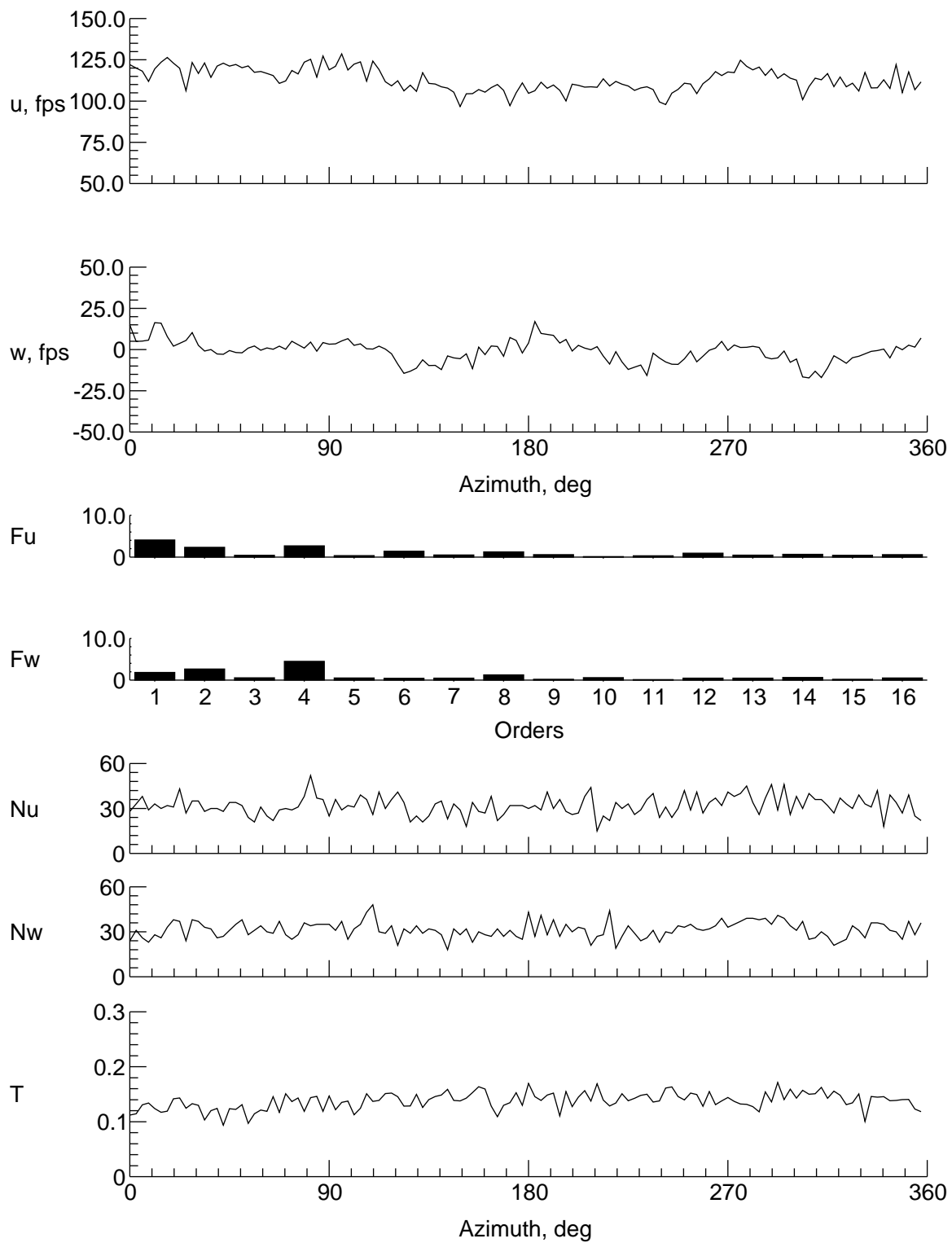
(j) $y = 4$ in., $z = -0.602$ in.

Figure 8. Continued.



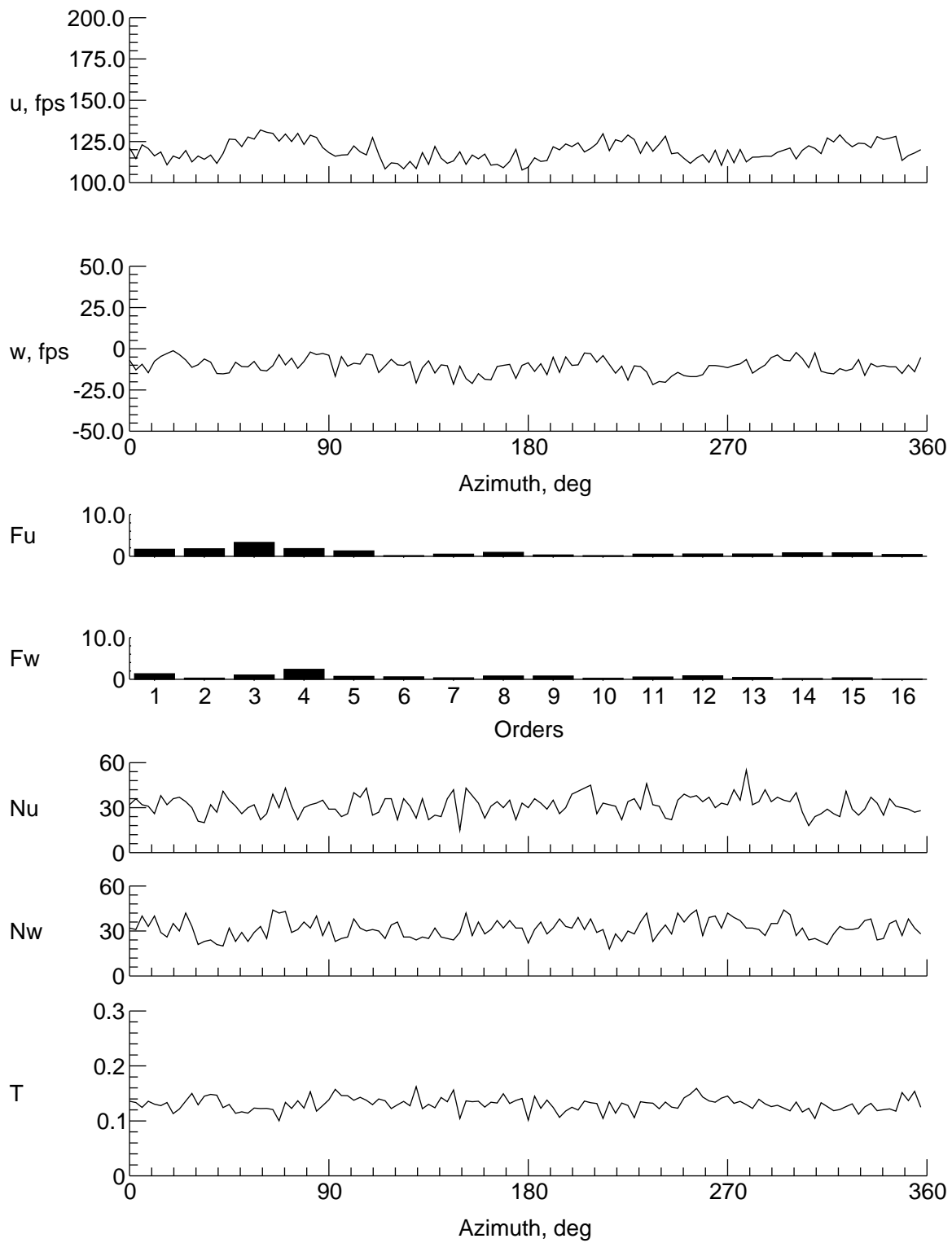
(k) $y = -4$ in., $z = -0.602$ in.

Figure 8. Continued.



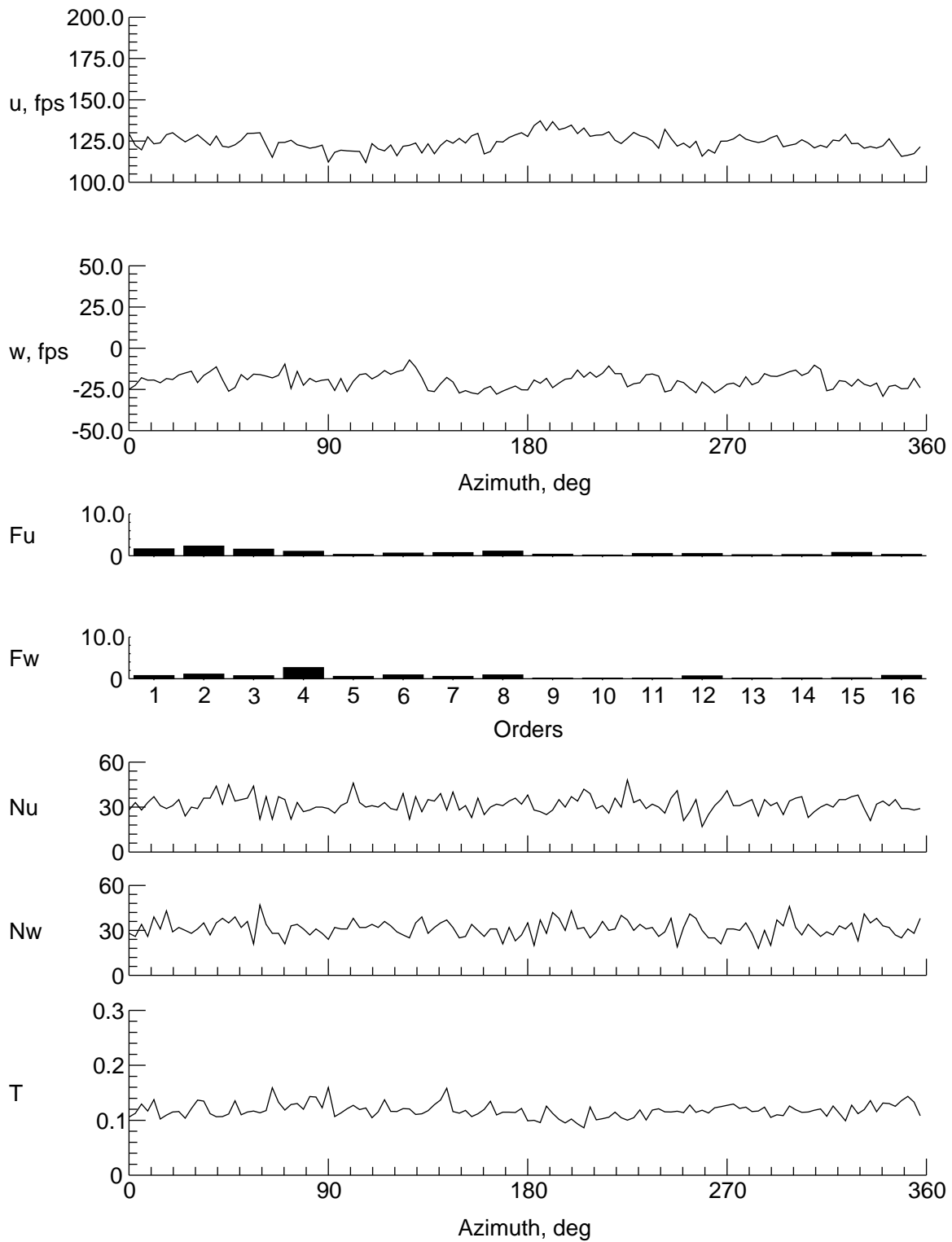
(l) $y = -6$ in., $z = -0.602$ in.

Figure 8. Continued.



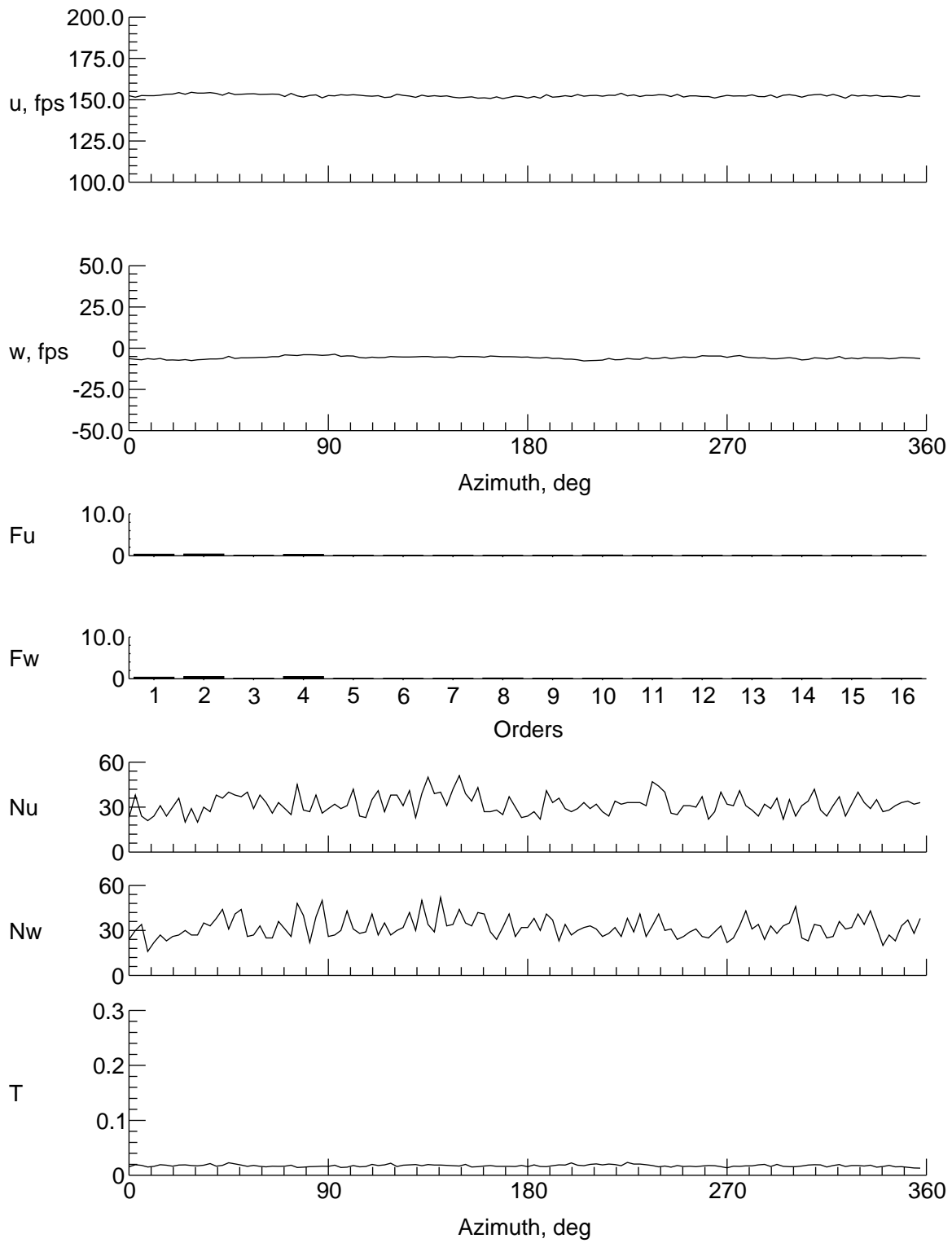
(m) $y = -8$ in., $z = -0.602$ in.

Figure 8. Continued.



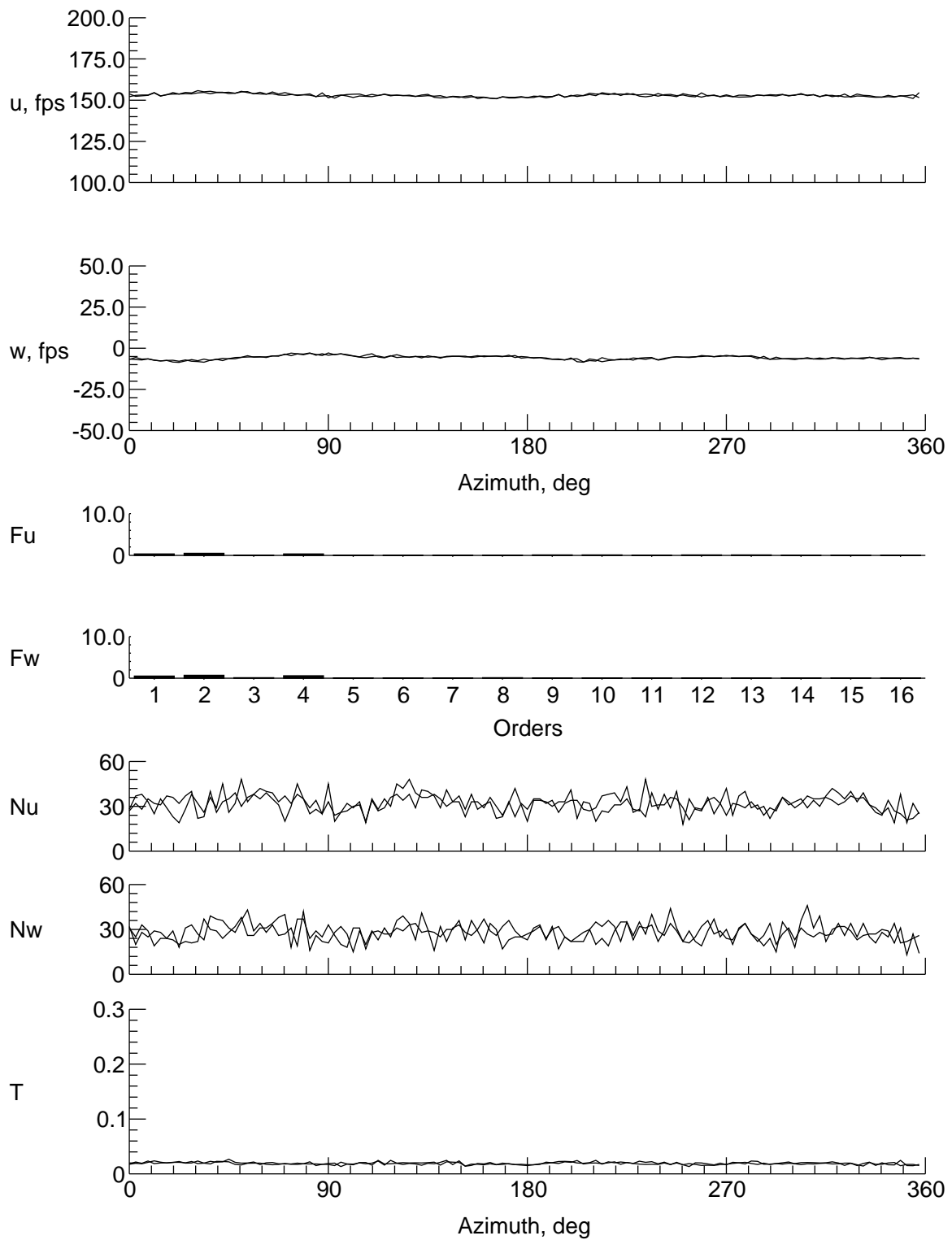
(n) $y = -9$ in., $z = -0.602$ in.

Figure 8. Concluded.



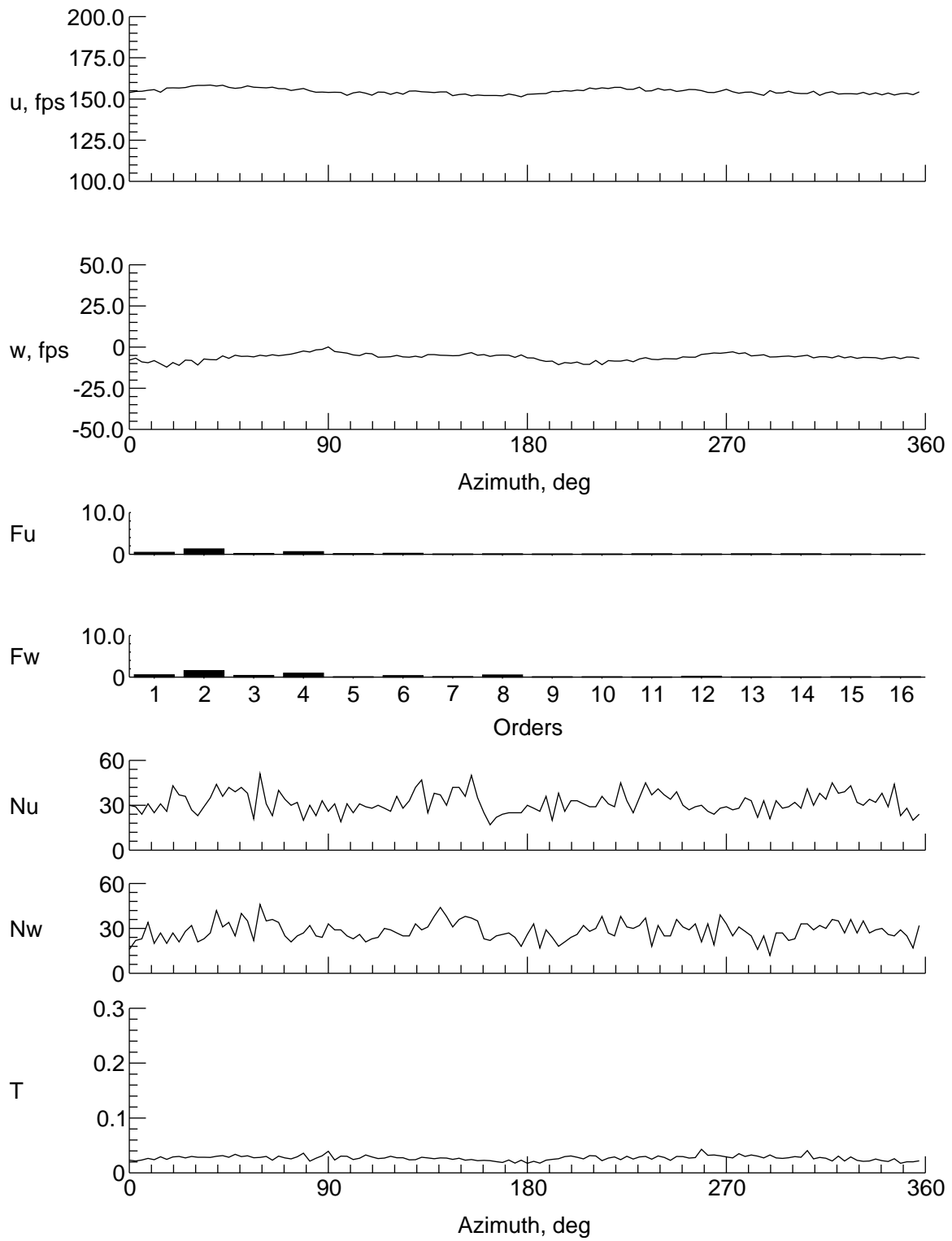
(a) $y = 0$ in., $z = 8.278$ in.

Figure 9. Velocity and turbulence at station 12 in.



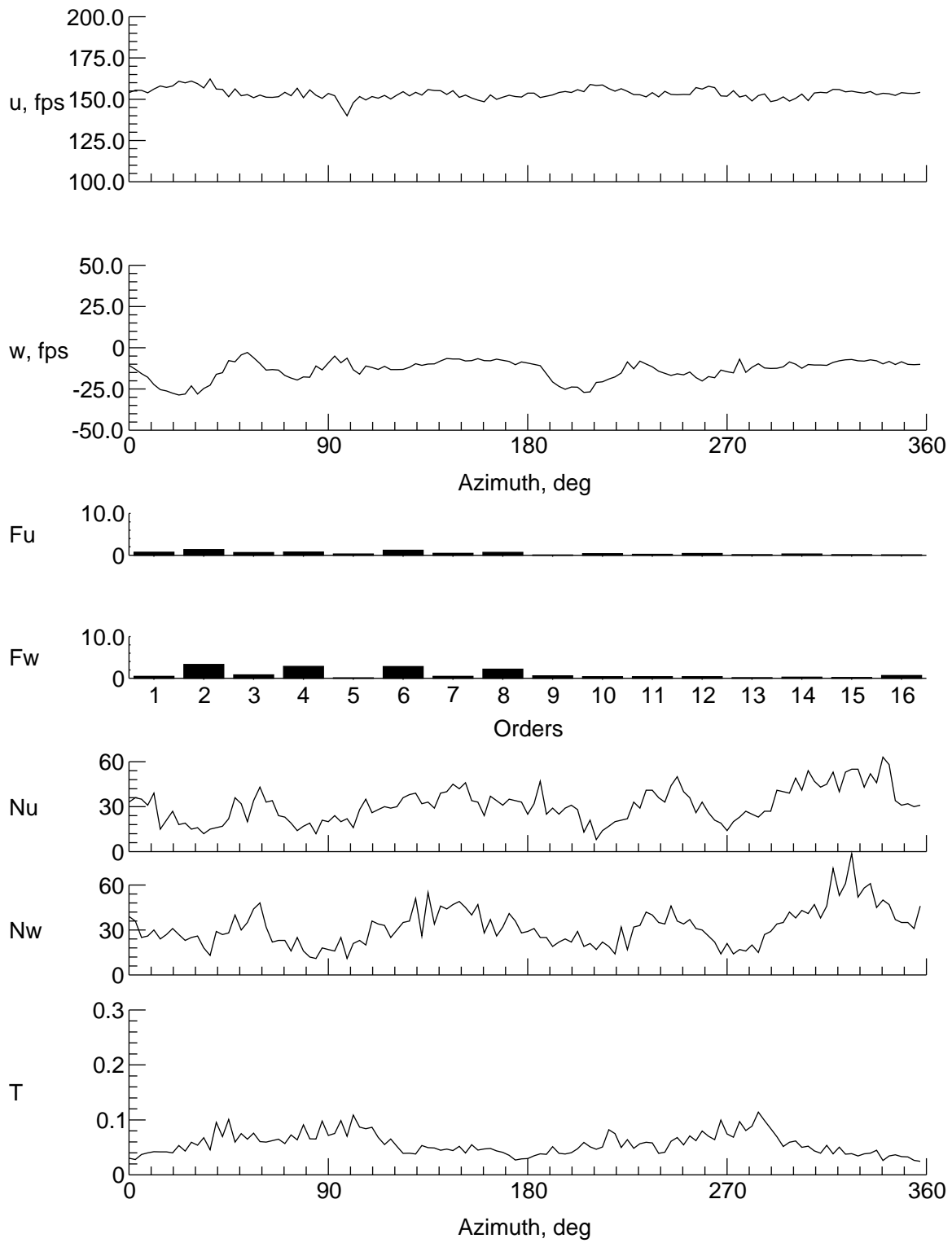
(b) $y = 0$ in., $z = 7.278$ in.

Figure 9. Continued.



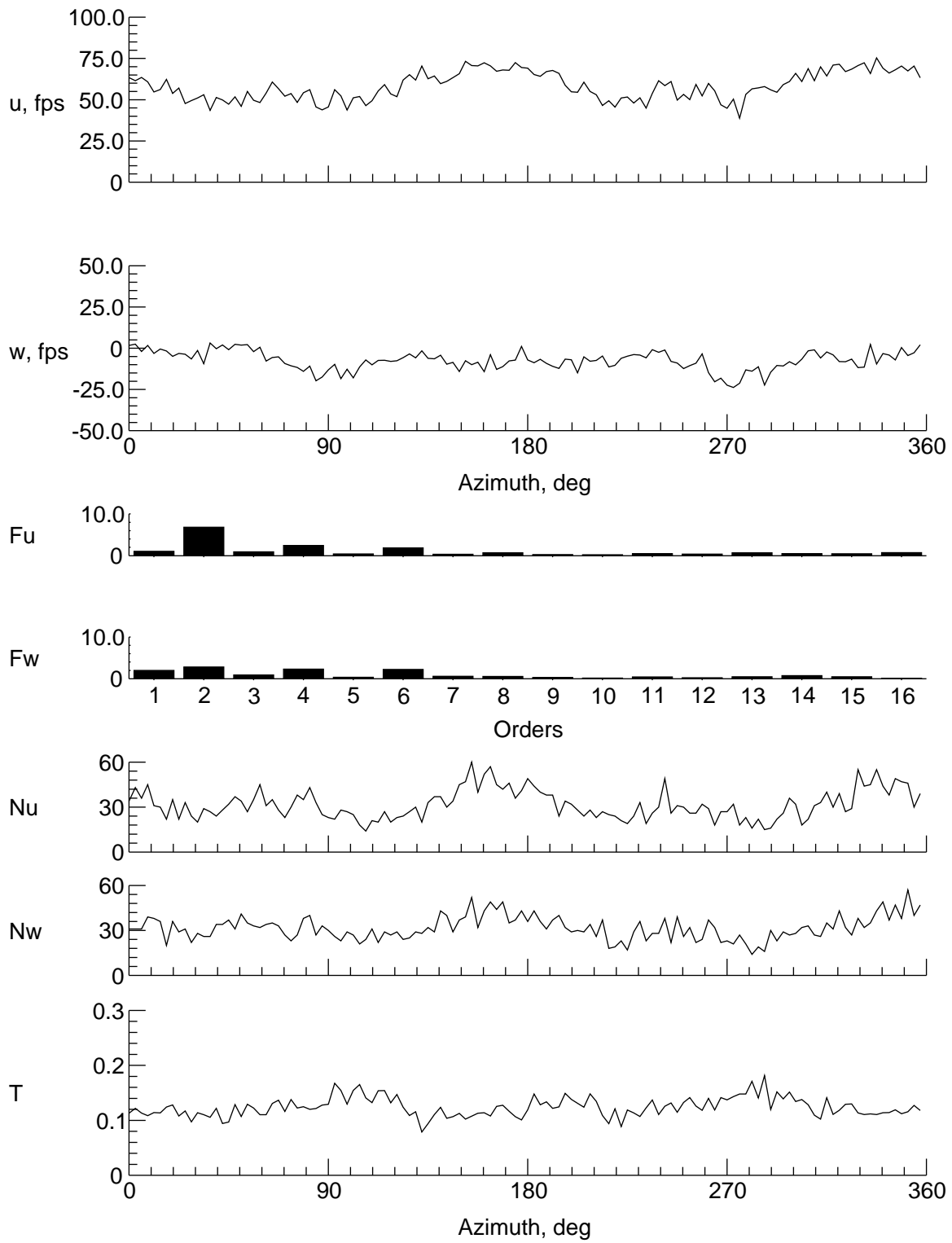
(c) $y = 0$ in., $z = 5.278$ in.

Figure 9. Continued.



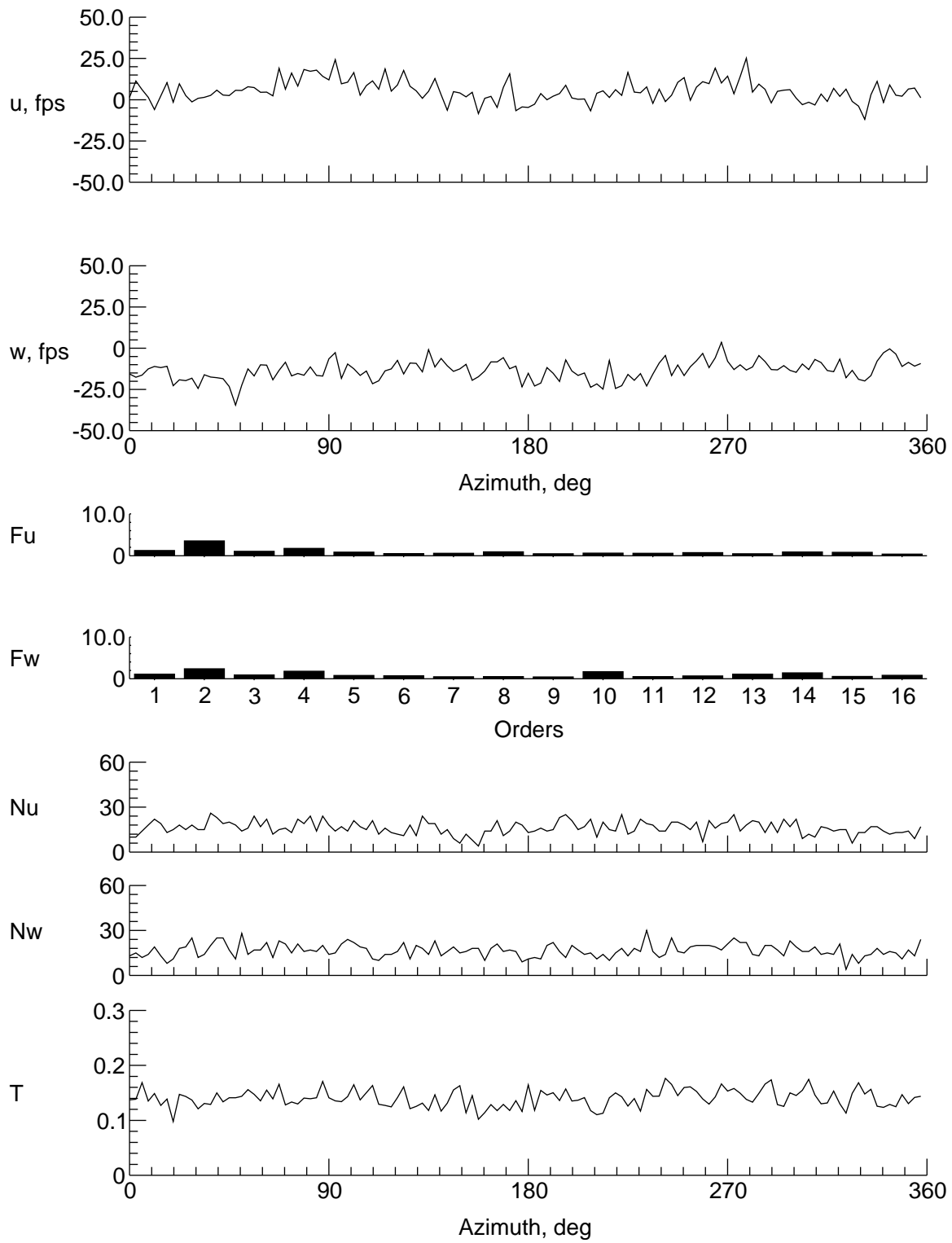
(d) $y = 0$ in., $z = 3.278$ in.

Figure 9. Continued.



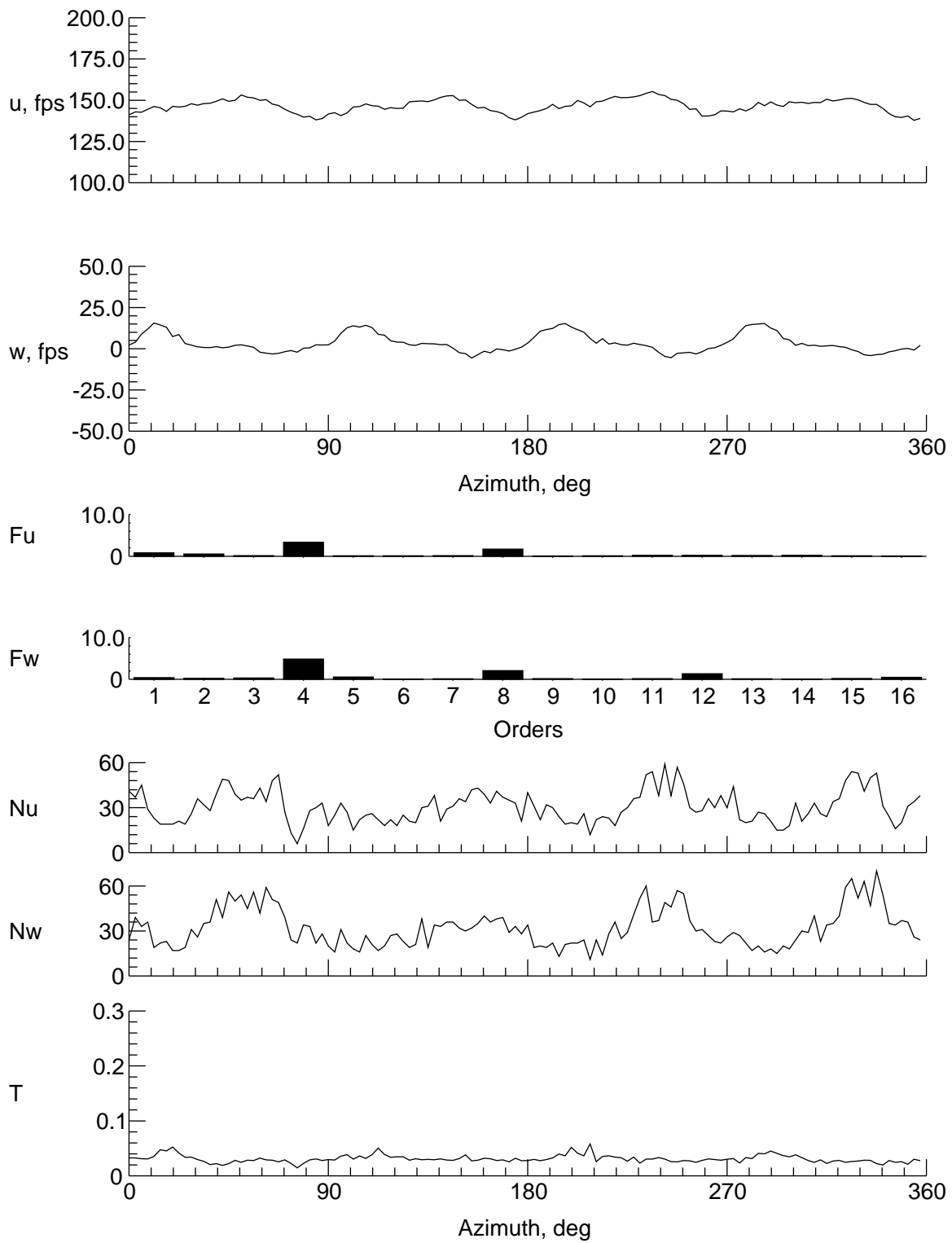
(e) $y = 0$ in., $z = -0.722$ in.

Figure 9. Continued.



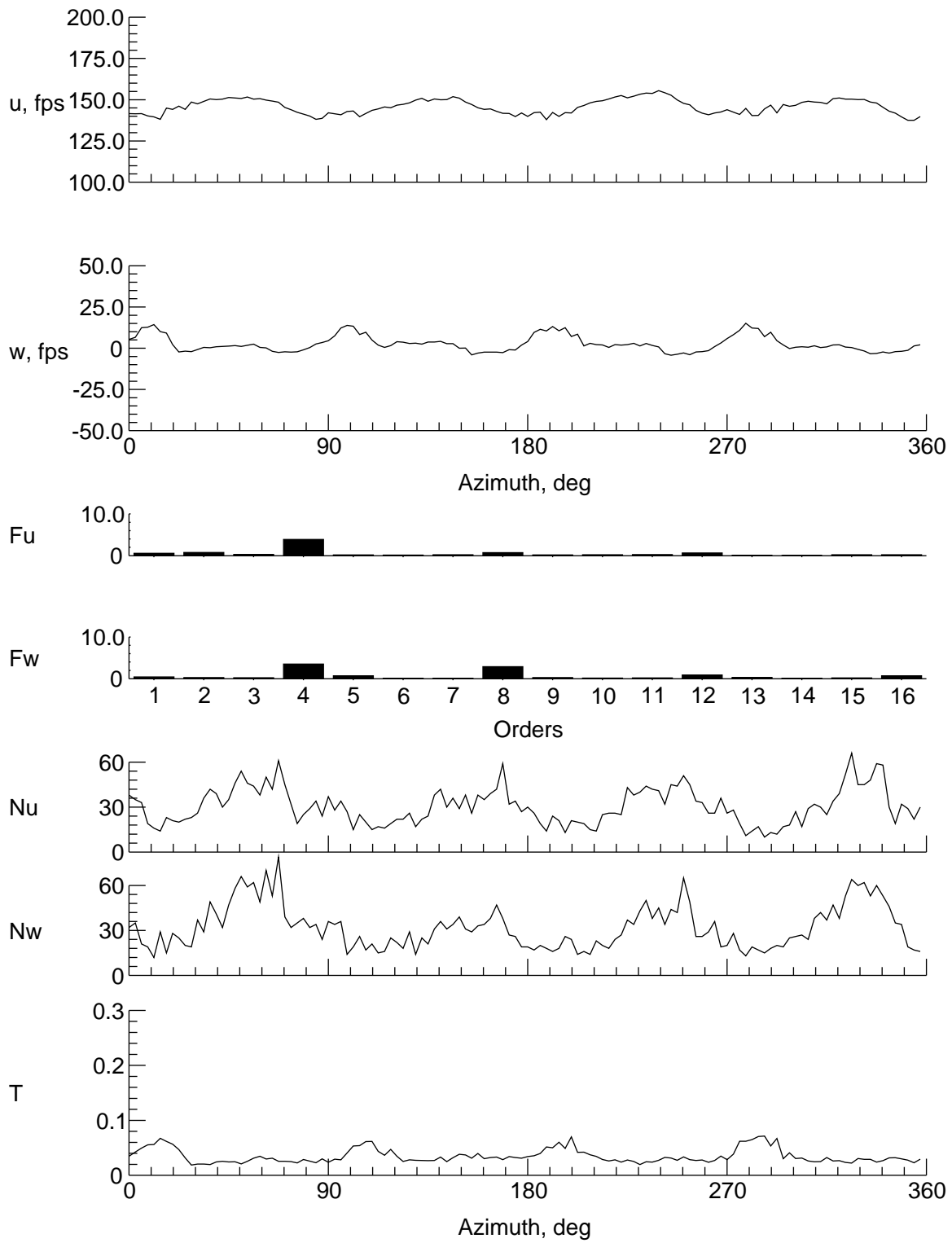
(f) $y = 0$ in., $z = -4.722$ in.

Figure 9. Continued.



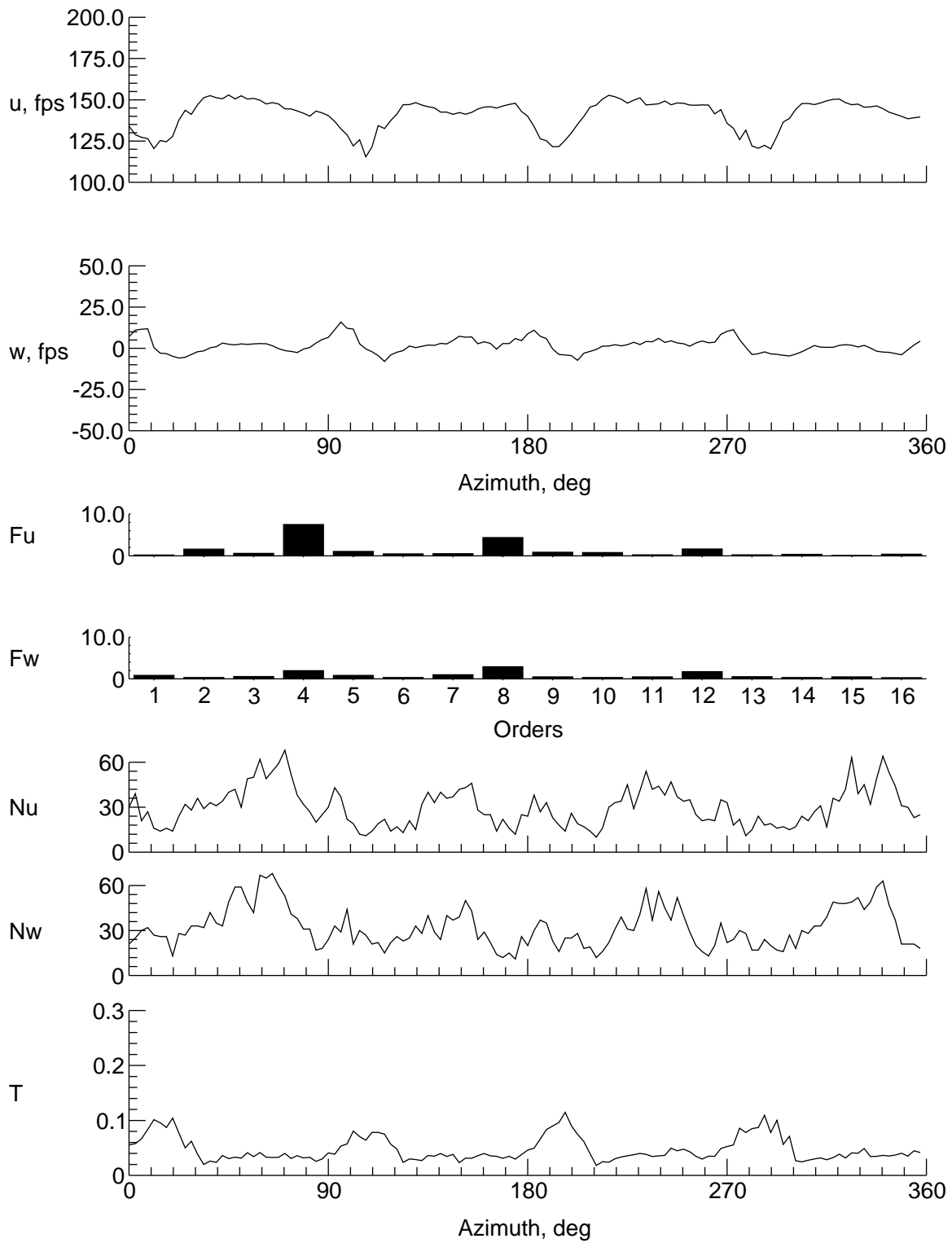
(g) $y = 9$ in., $z = -0.722$ in.

Figure 9. Continued.



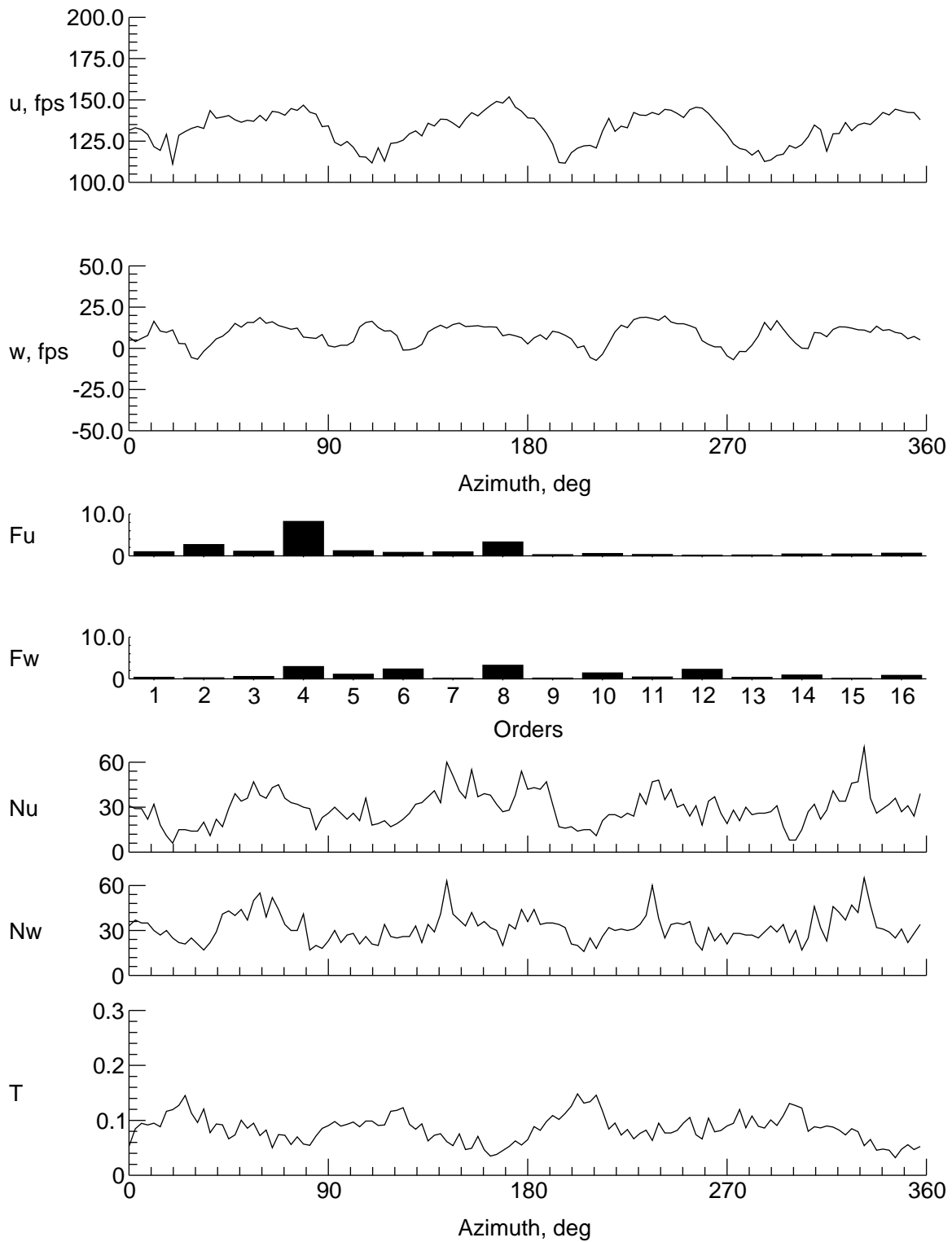
(h) $y = 8$ in., $z = -0.722$ in.

Figure 9. Continued.



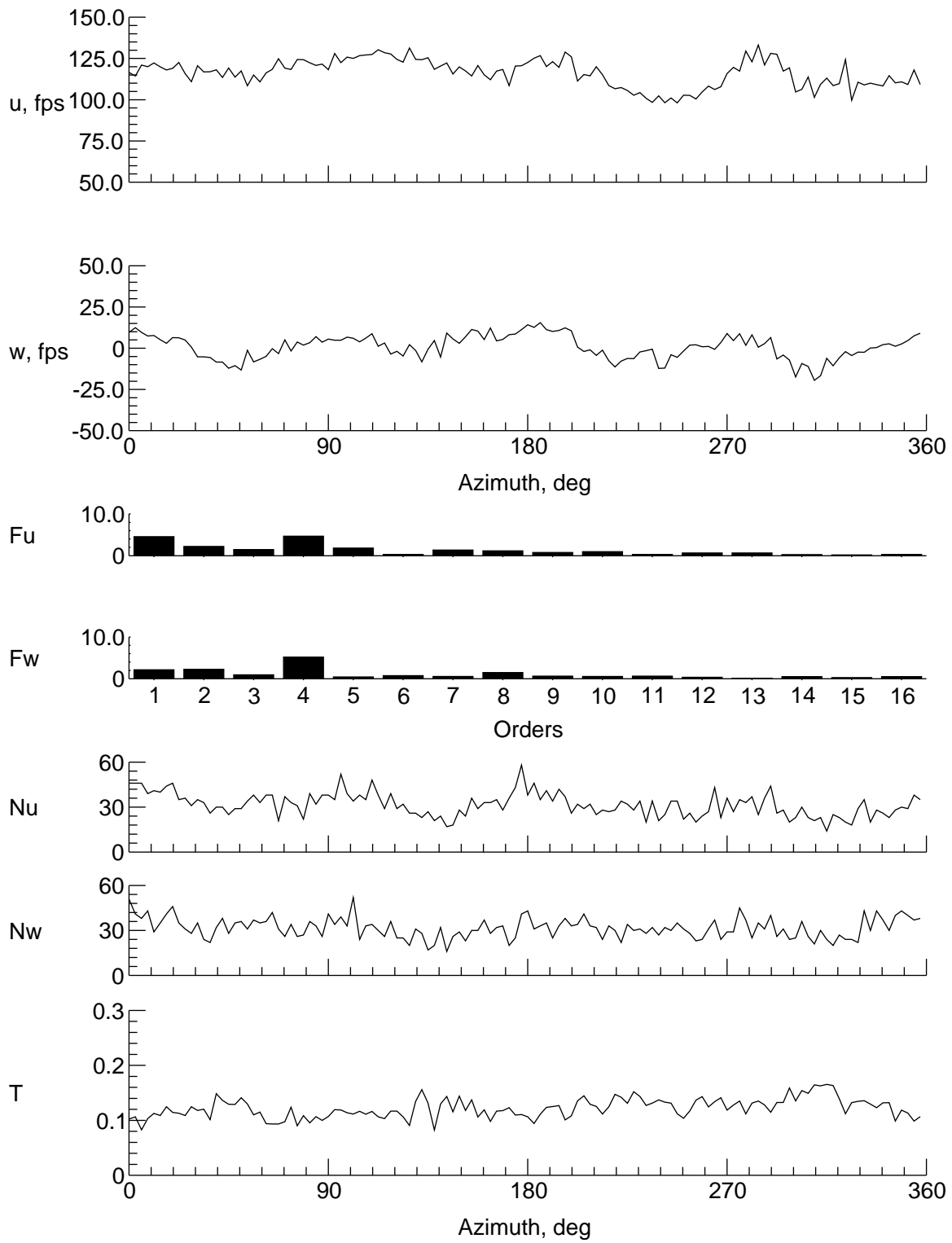
(i) $y = 6$ in., $z = -0.722$ in.

Figure 9. Continued.



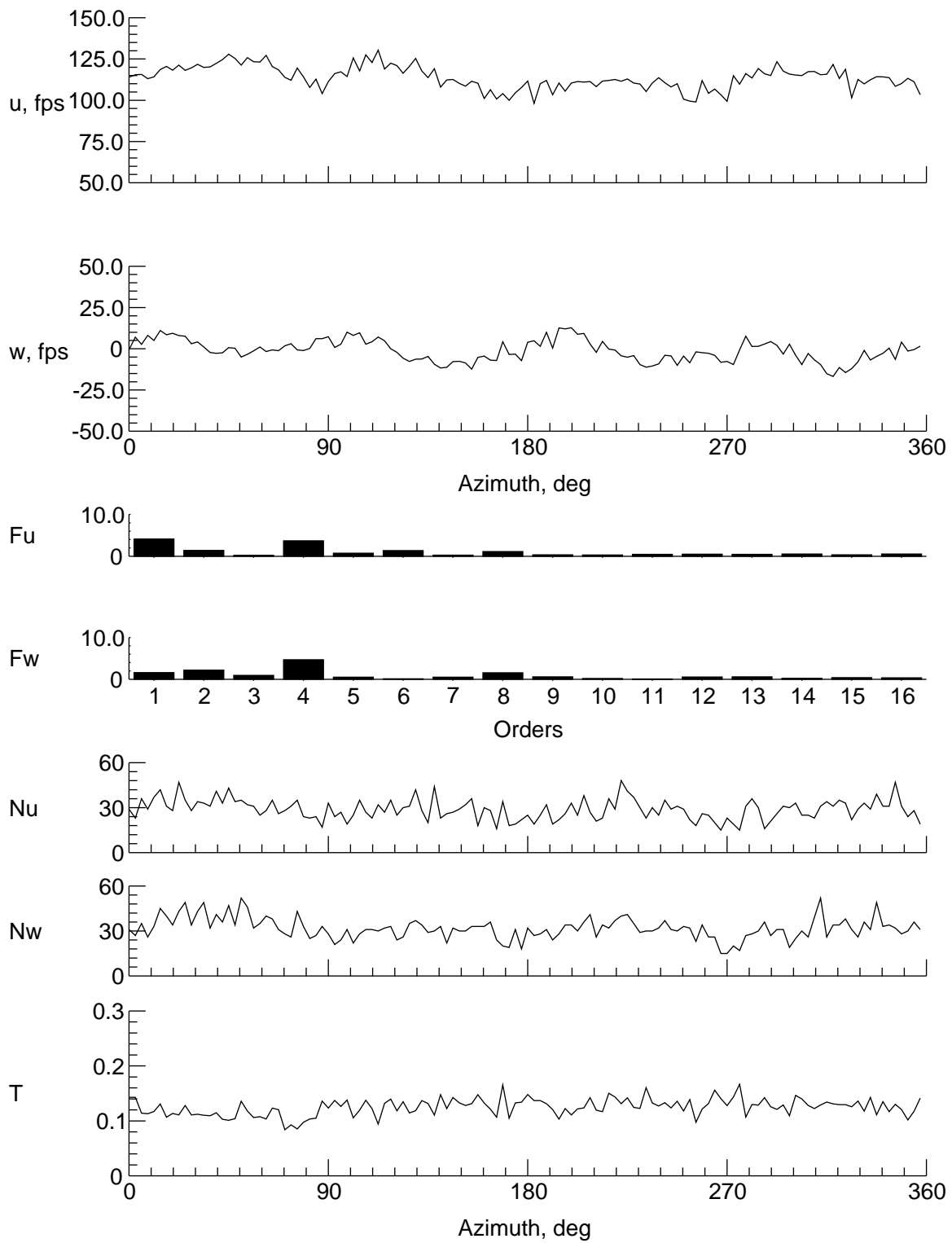
(j) $y = 4$ in., $z = -0.722$ in.

Figure 9. Continued.



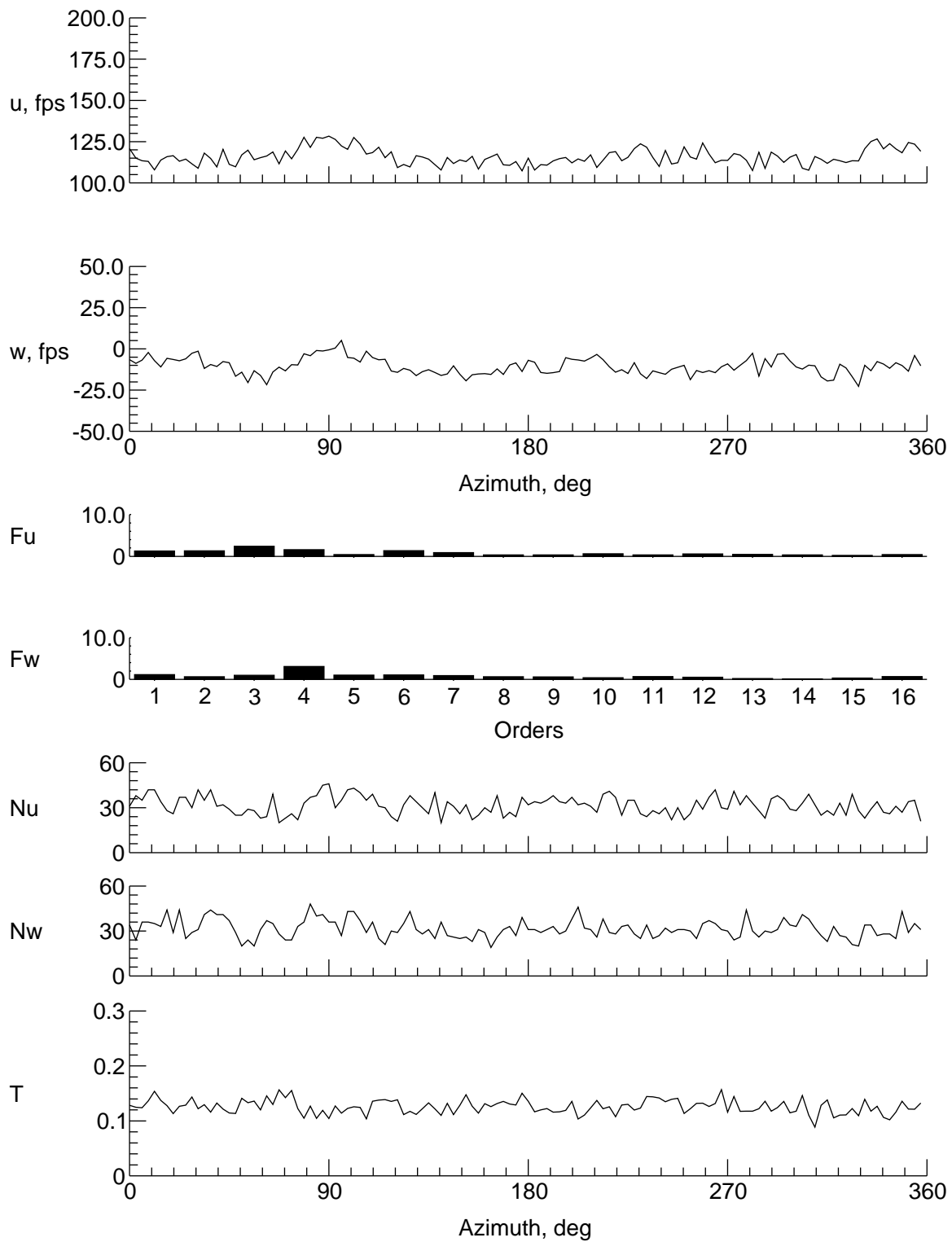
(k) $y = -4$ in., $z = -0.722$ in.

Figure 9. Continued.



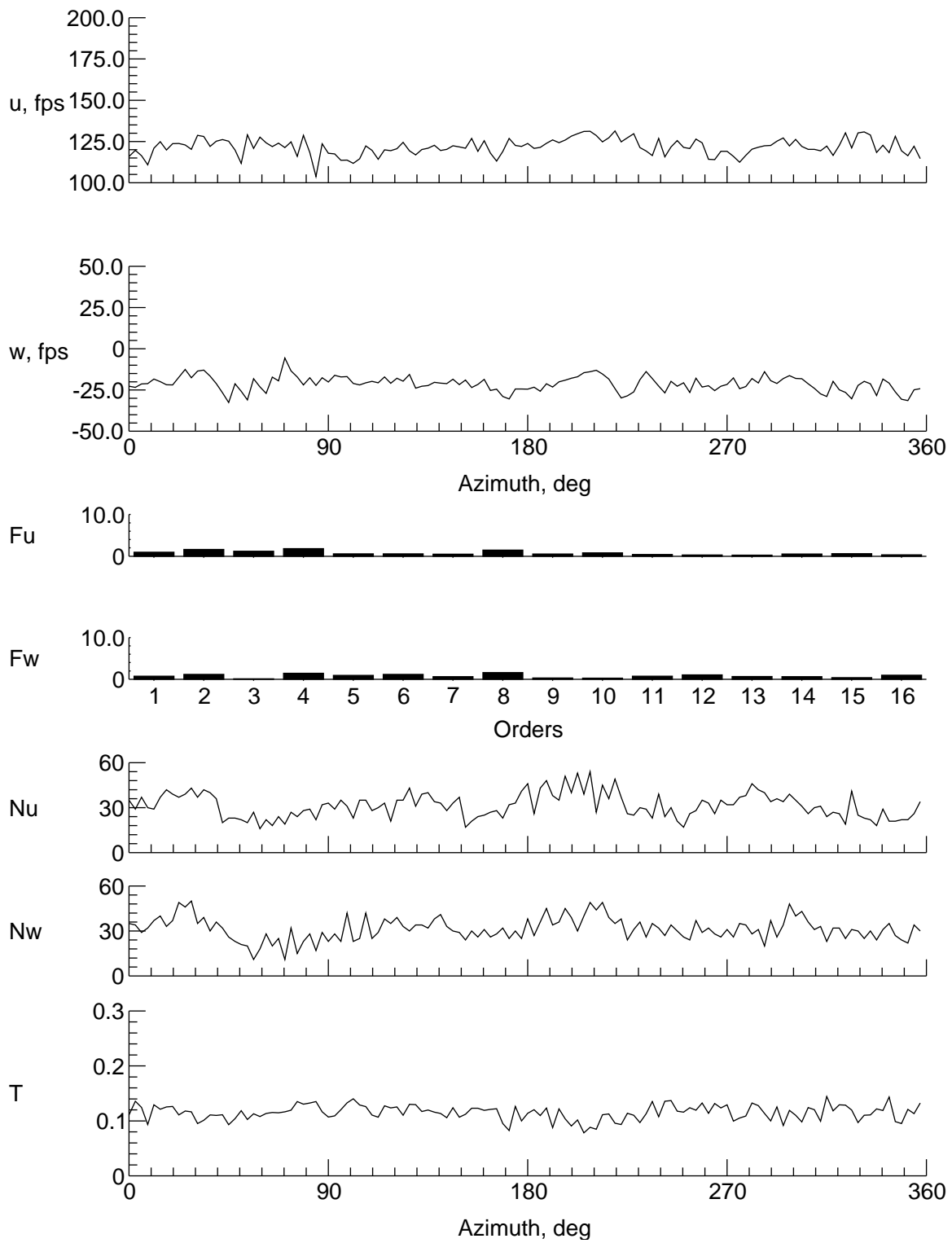
(l) $y = -6$ in., $z = -0.722$ in.

Figure 9. Continued.



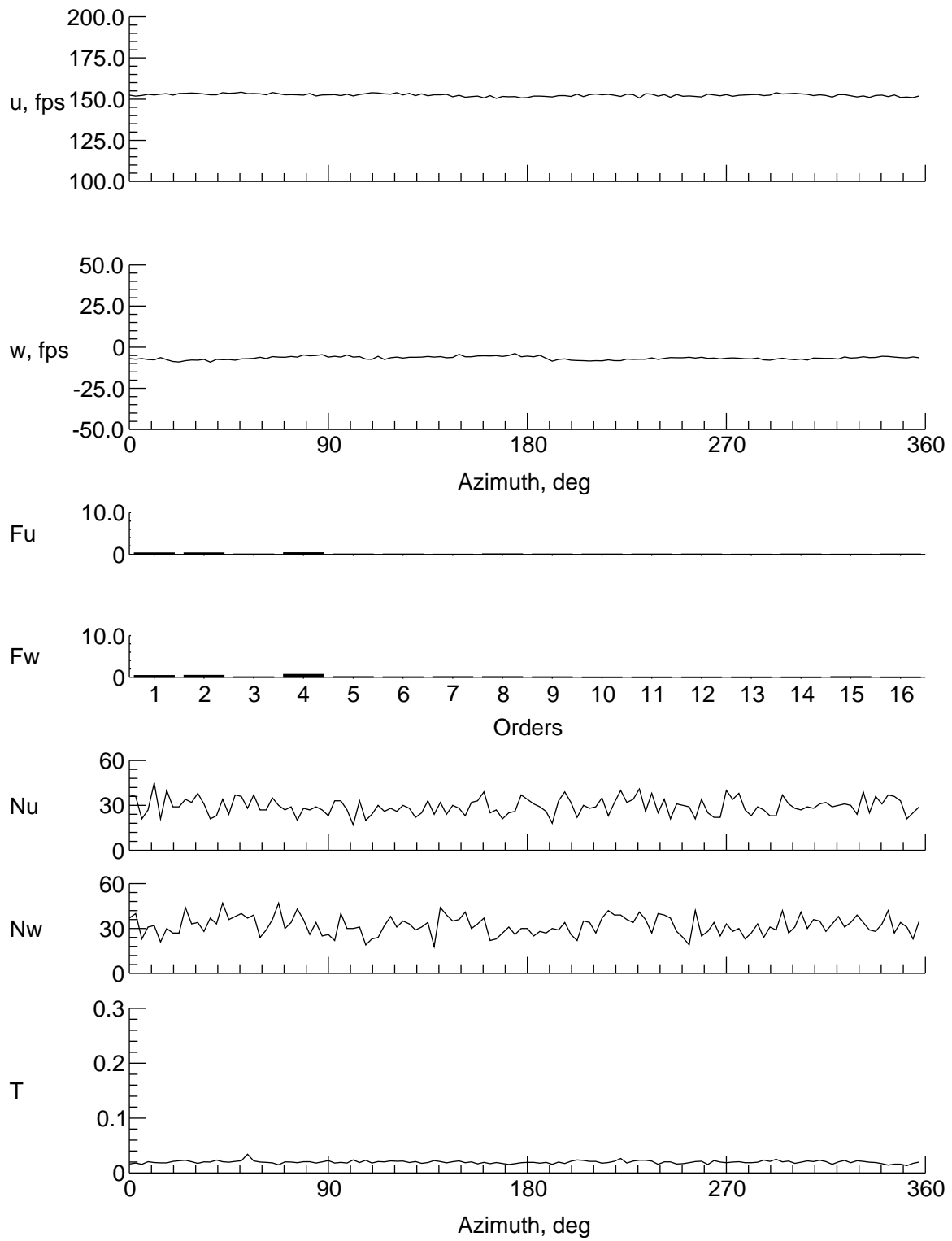
(m) $y = -8$ in., $z = -0.722$ in.

Figure 9. Continued.



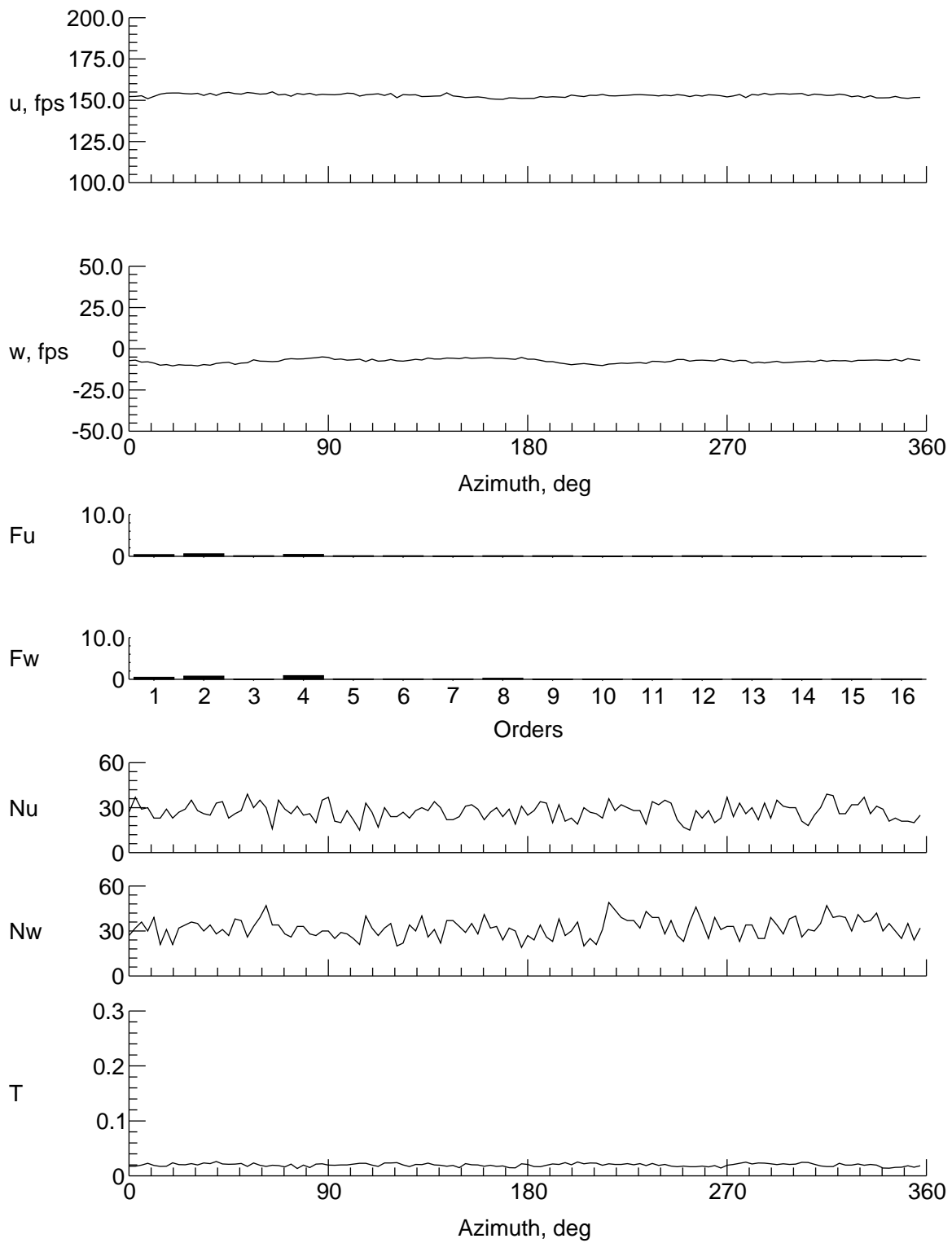
(n) $y = -9$ in., $z = -0.722$ in.

Figure 9. Concluded.



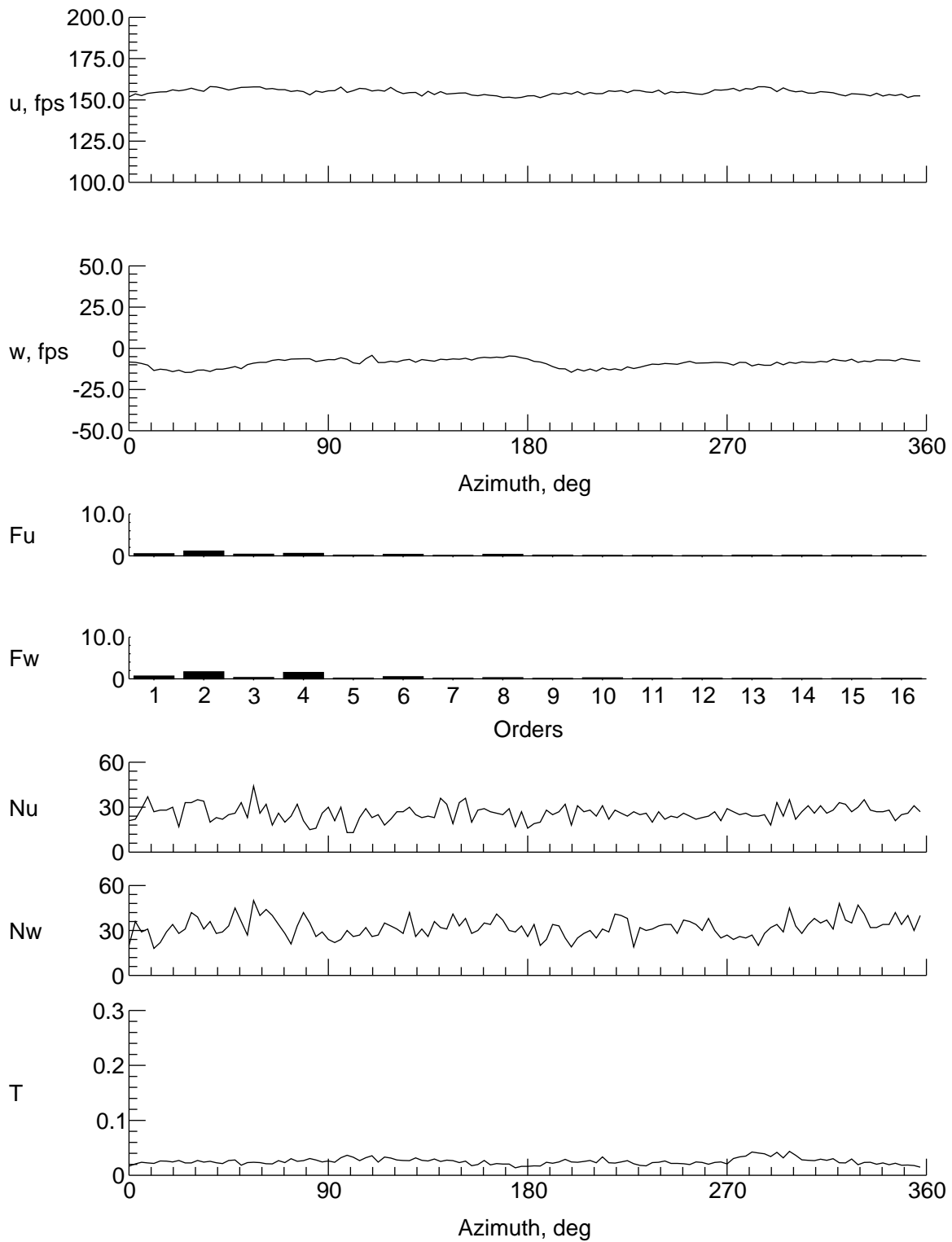
(a) $y = 0$ in., $z = 8.157$ in.

Figure 10. Velocity and turbulence at station 14 in.



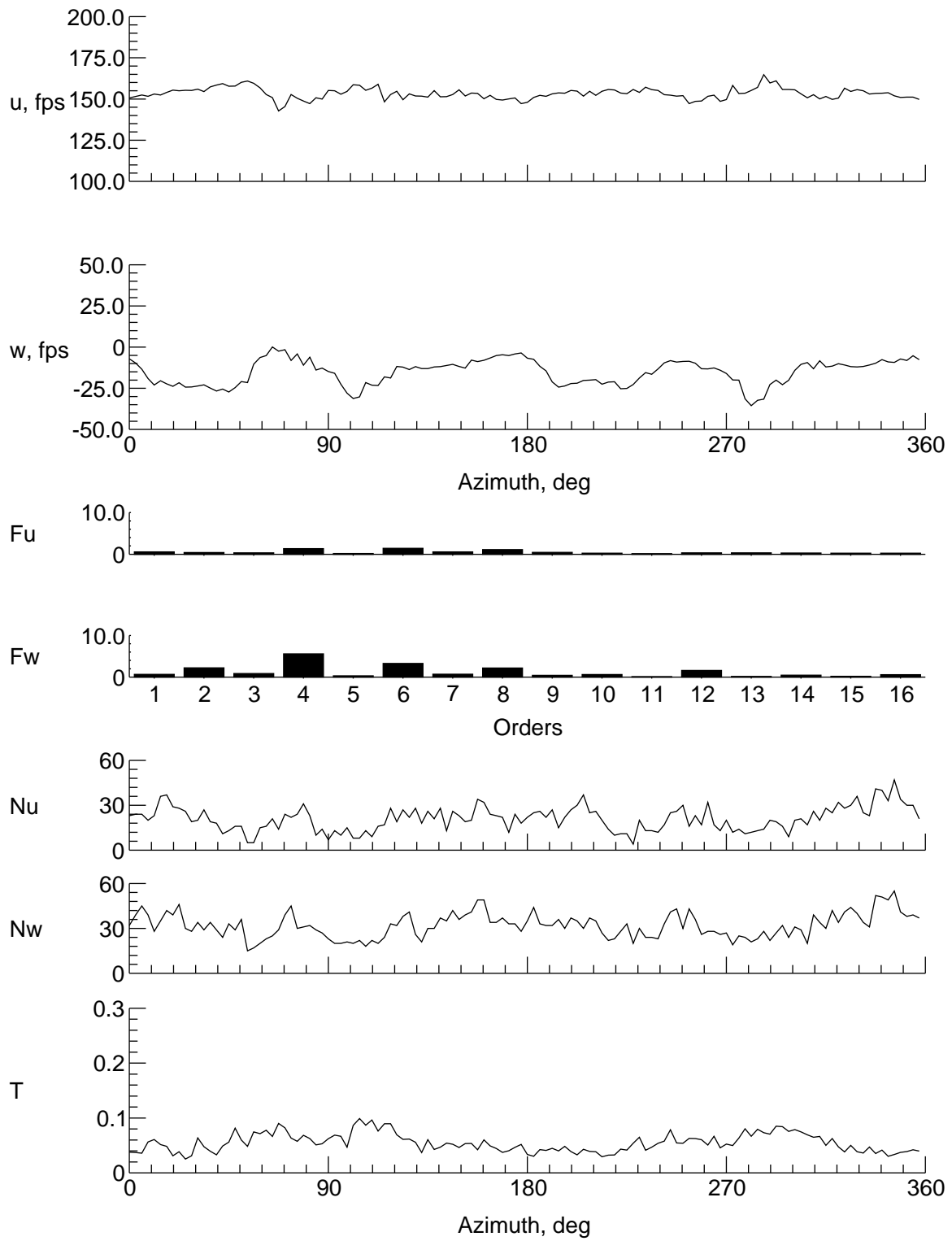
(b) $y = 0$ in., $z = 7.157$ in.

Figure 10. Continued.



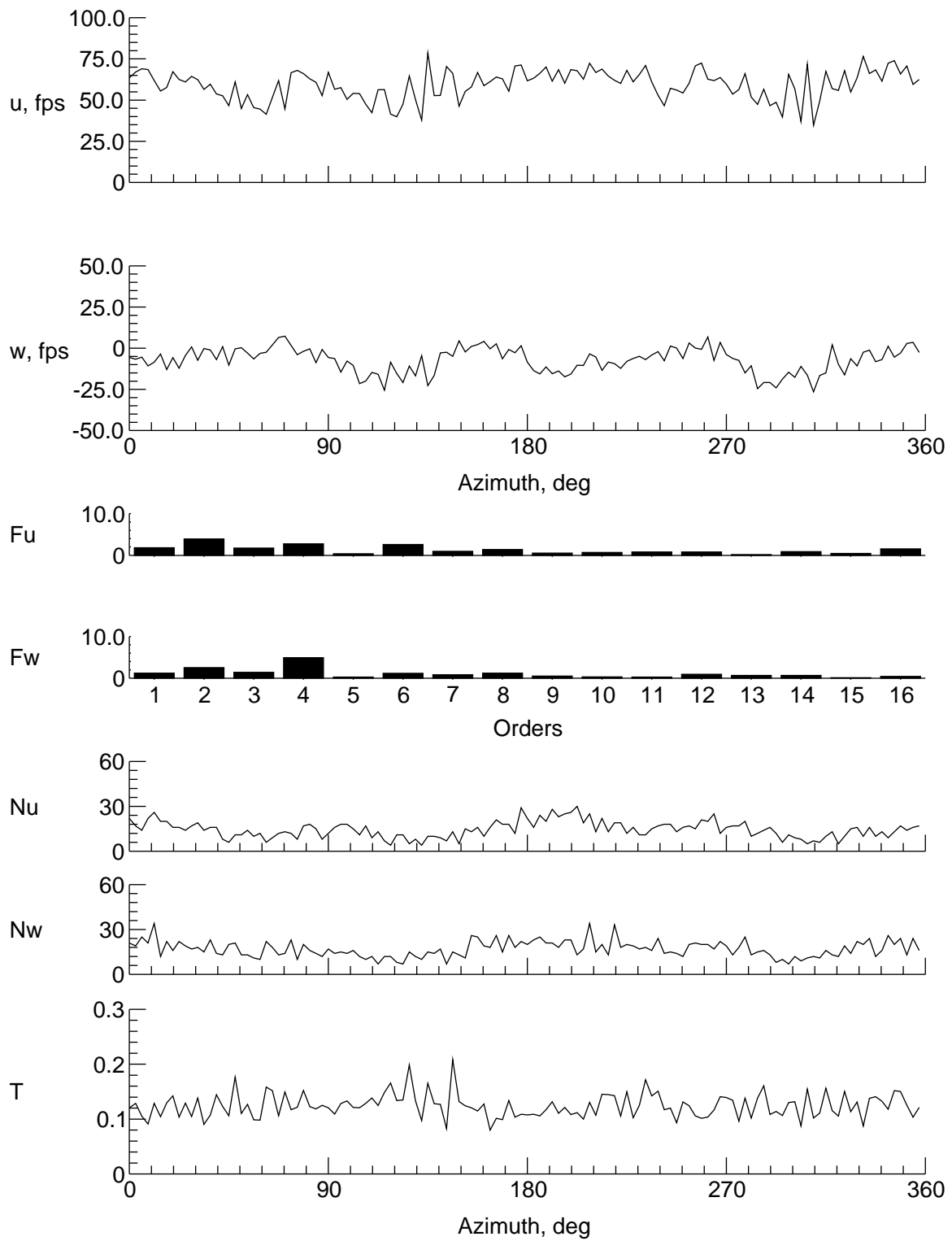
(c) $y = 0$ in., $z = 5.157$ in.

Figure 10. Continued.



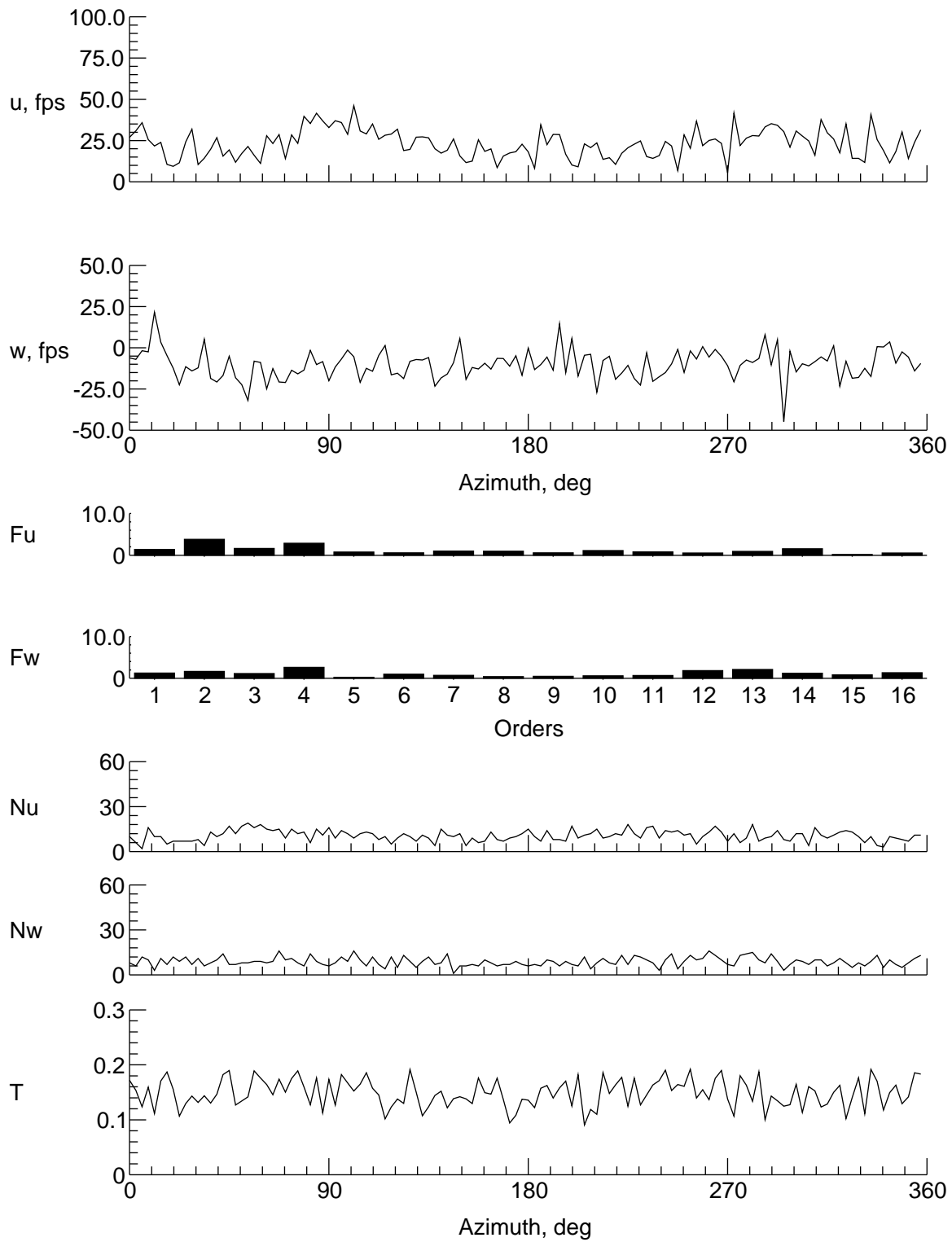
(d) $y = 0$ in., $z = 3.157$ in.

Figure 10. Continued.



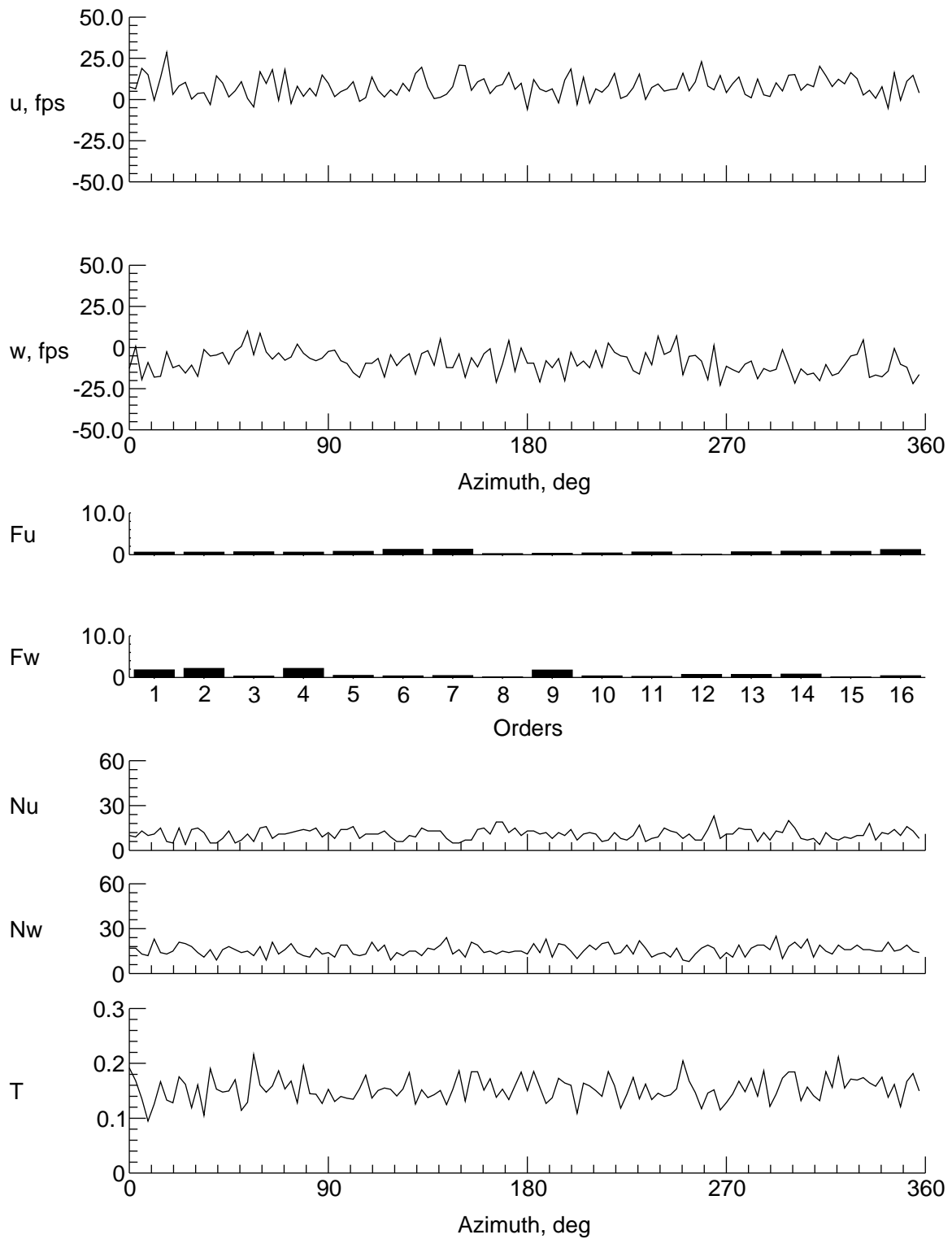
(e) $y = 0$ in., $z = -0.843$ in.

Figure 10. Continued.



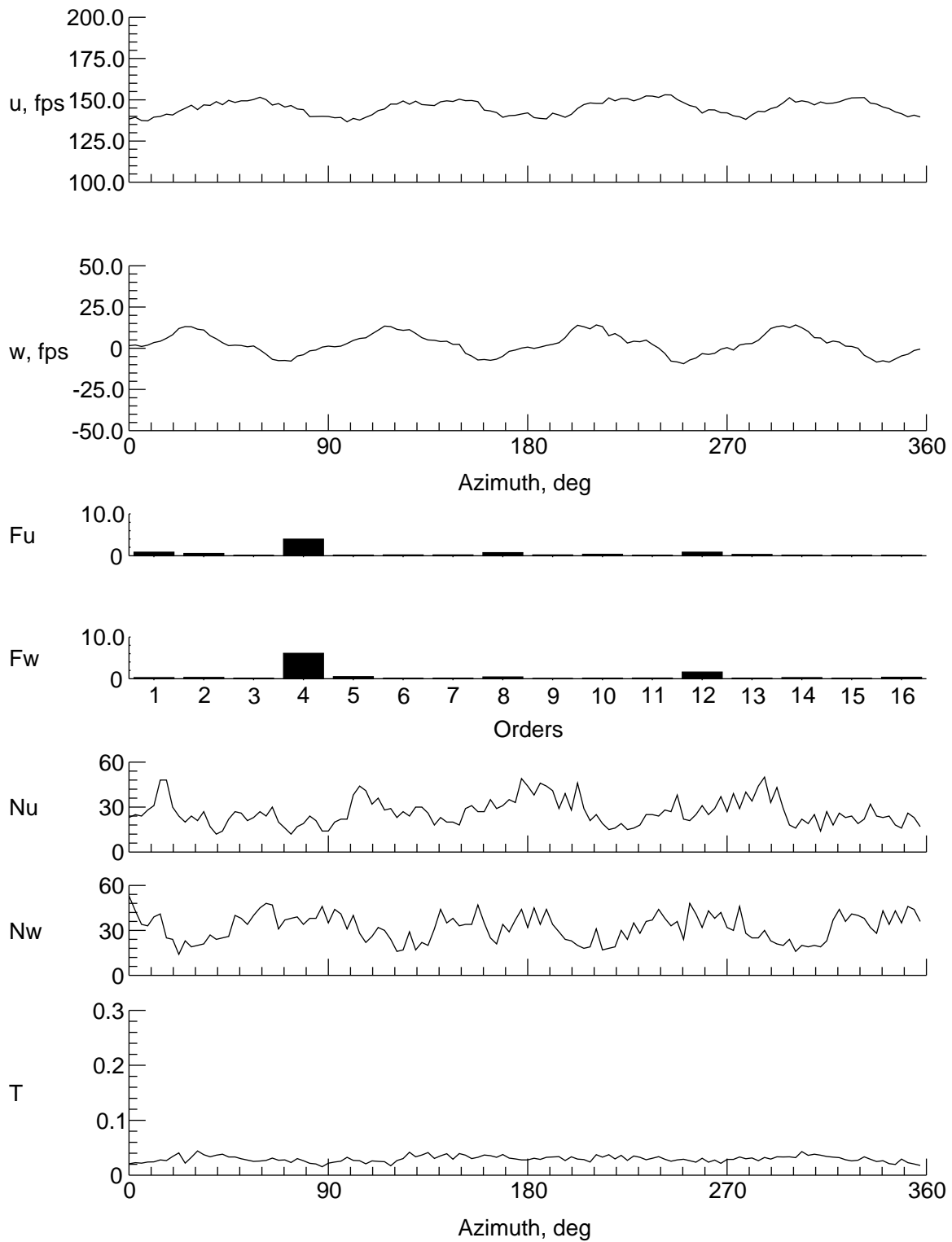
(f) $y = 0$ in., $z = -4.843$ in.

Figure 10. Continued.



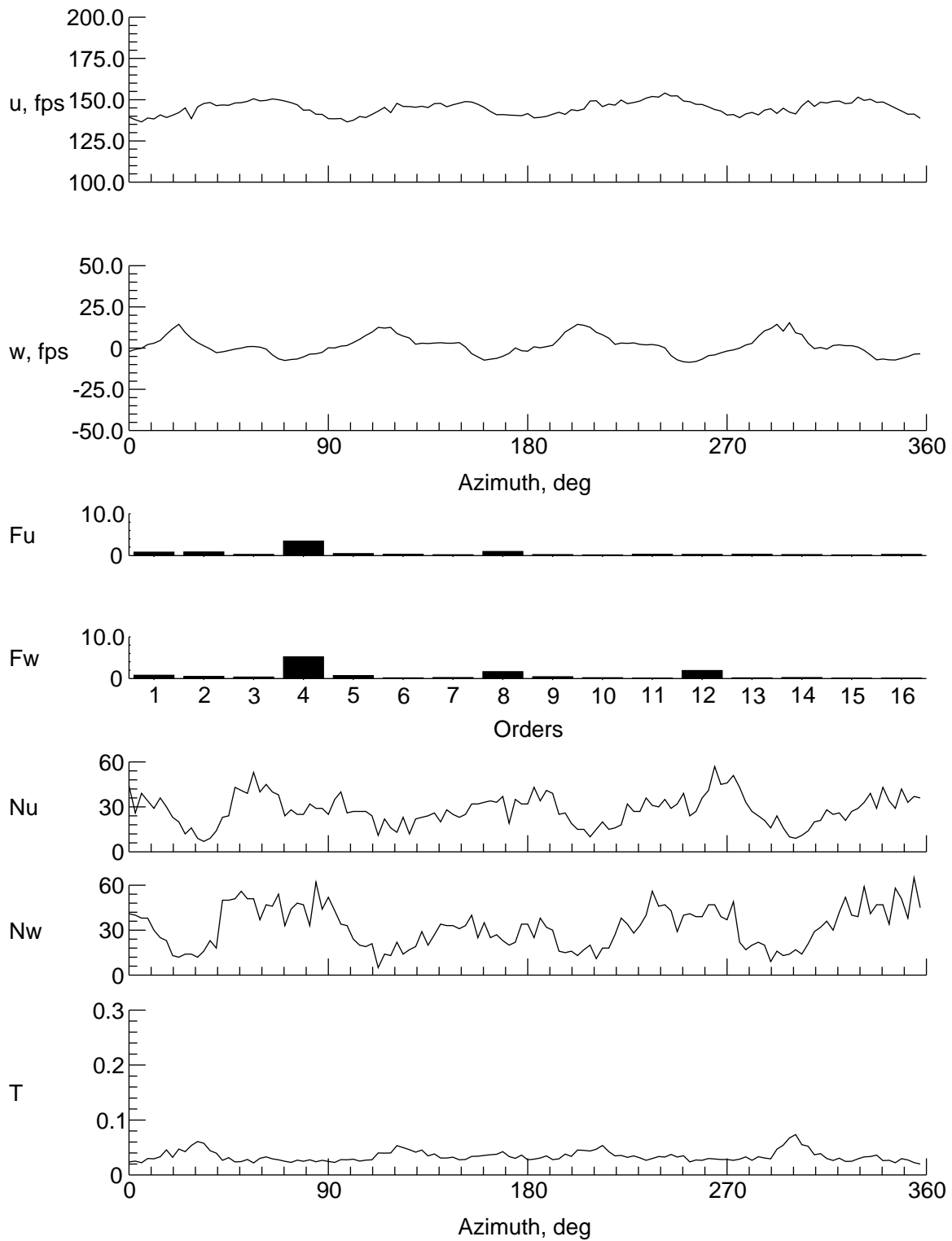
(g) $y = 0$ in., $z = -6.843$ in.

Figure 10. Continued.



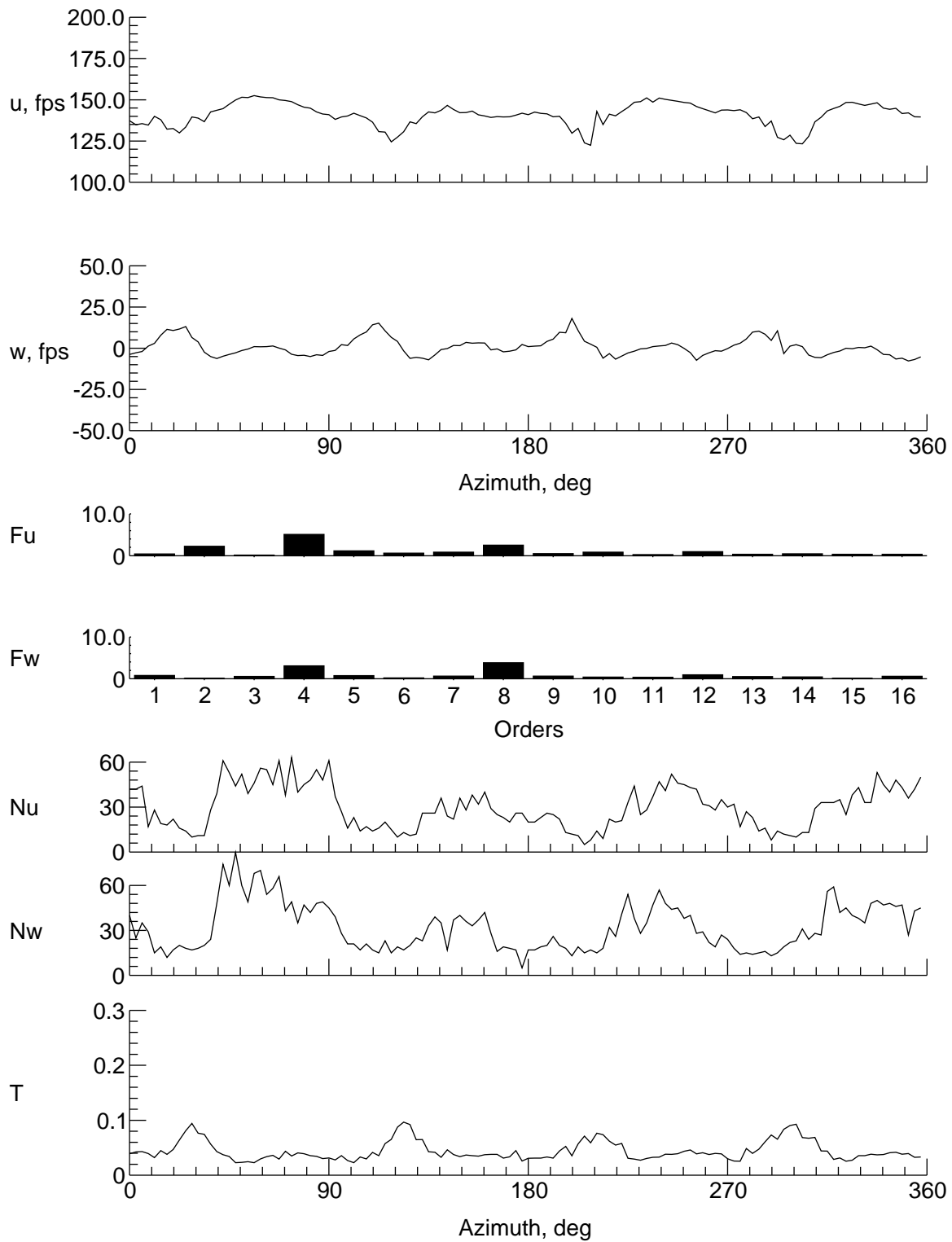
(h) $y = 9$ in., $z = -0.843$ in.

Figure 10. Continued.



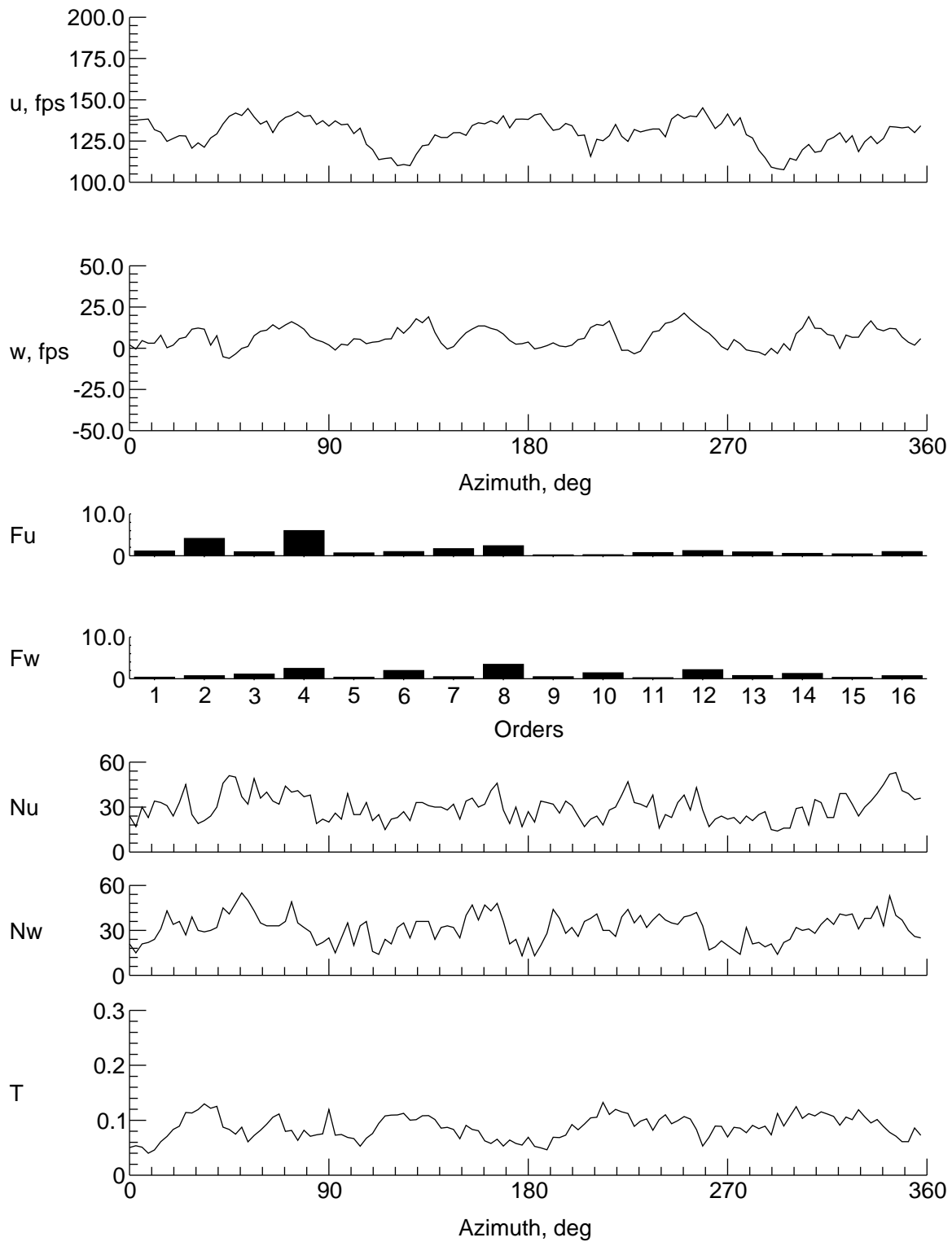
(i) $y = 8 \text{ in.}$, $z = -0.843 \text{ in.}$

Figure 10. Continued.



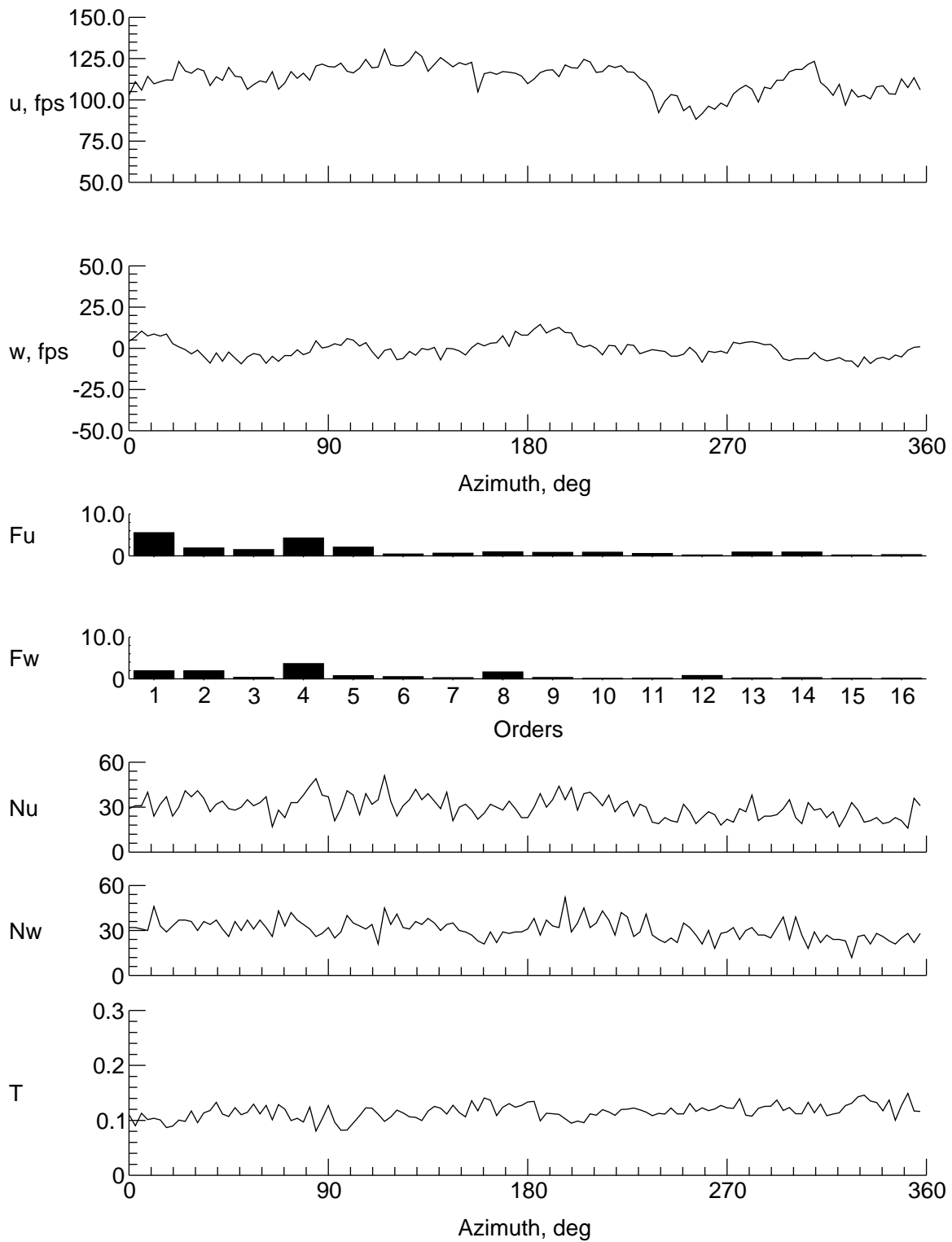
(j) $y = 6$ in., $z = -0.843$ in.

Figure 10. Continued.



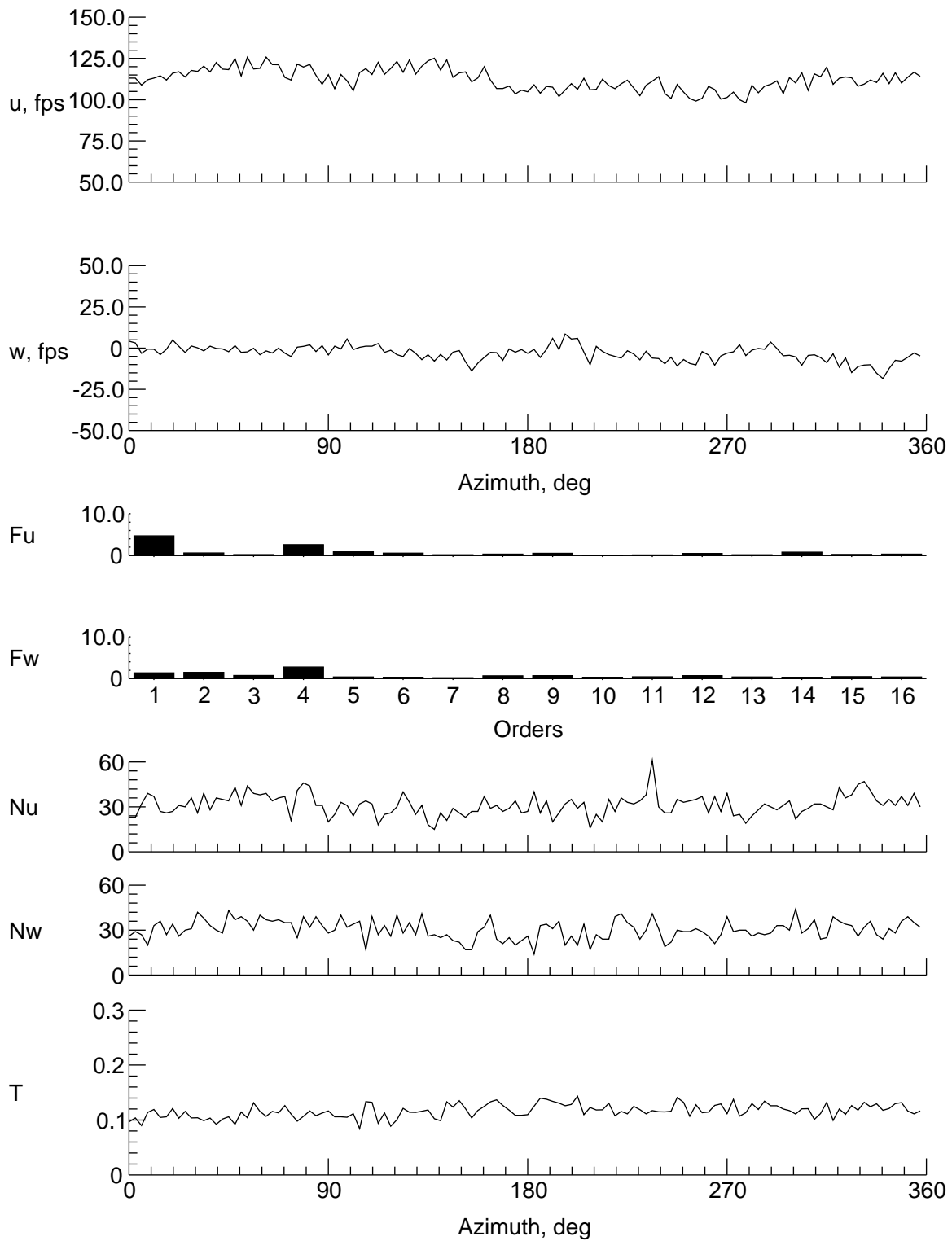
(k) $y = 4$ in., $z = -0.843$ in.

Figure 10. Continued.



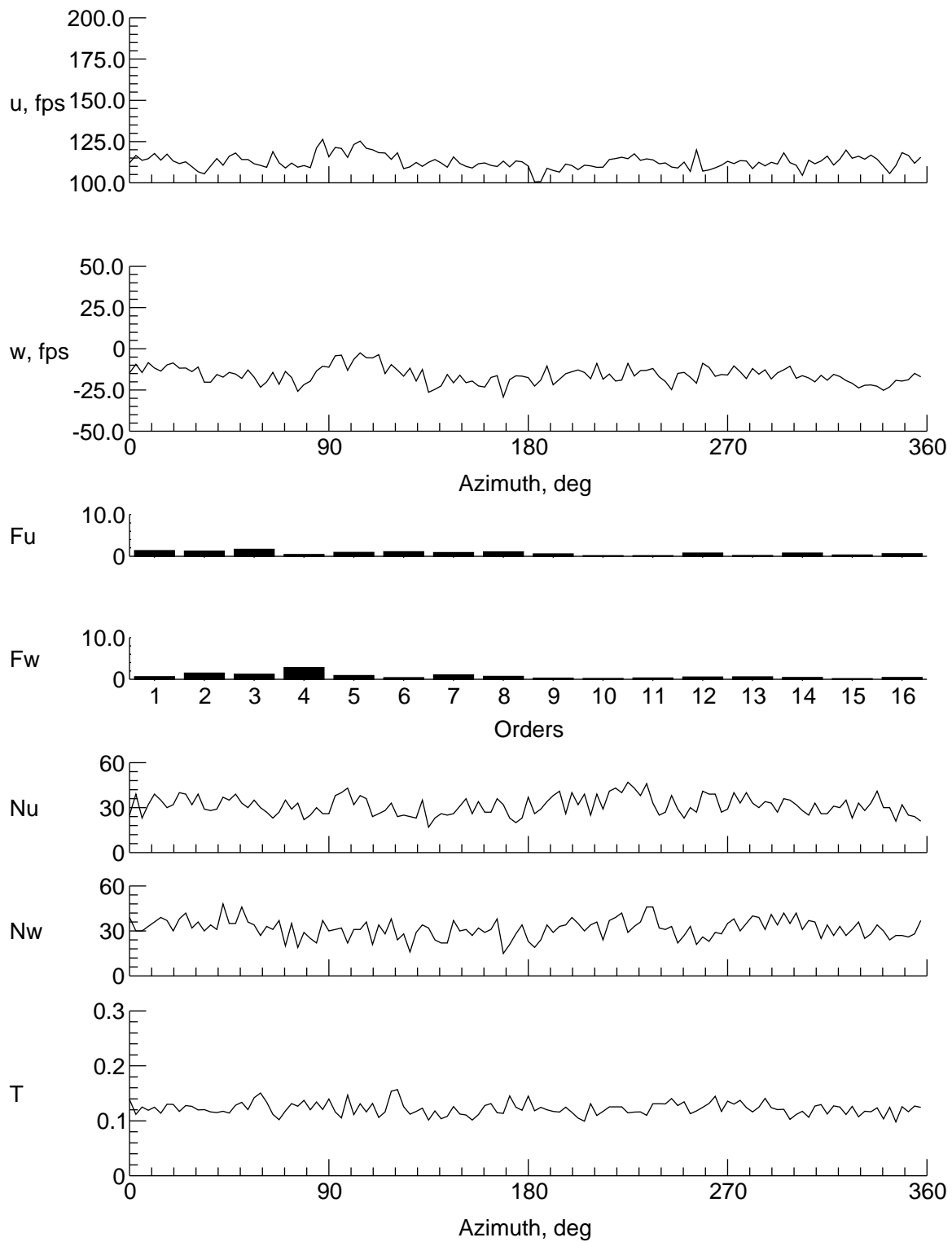
(l) $y = -4$ in., $z = -0.843$ in.

Figure 10. Continued.



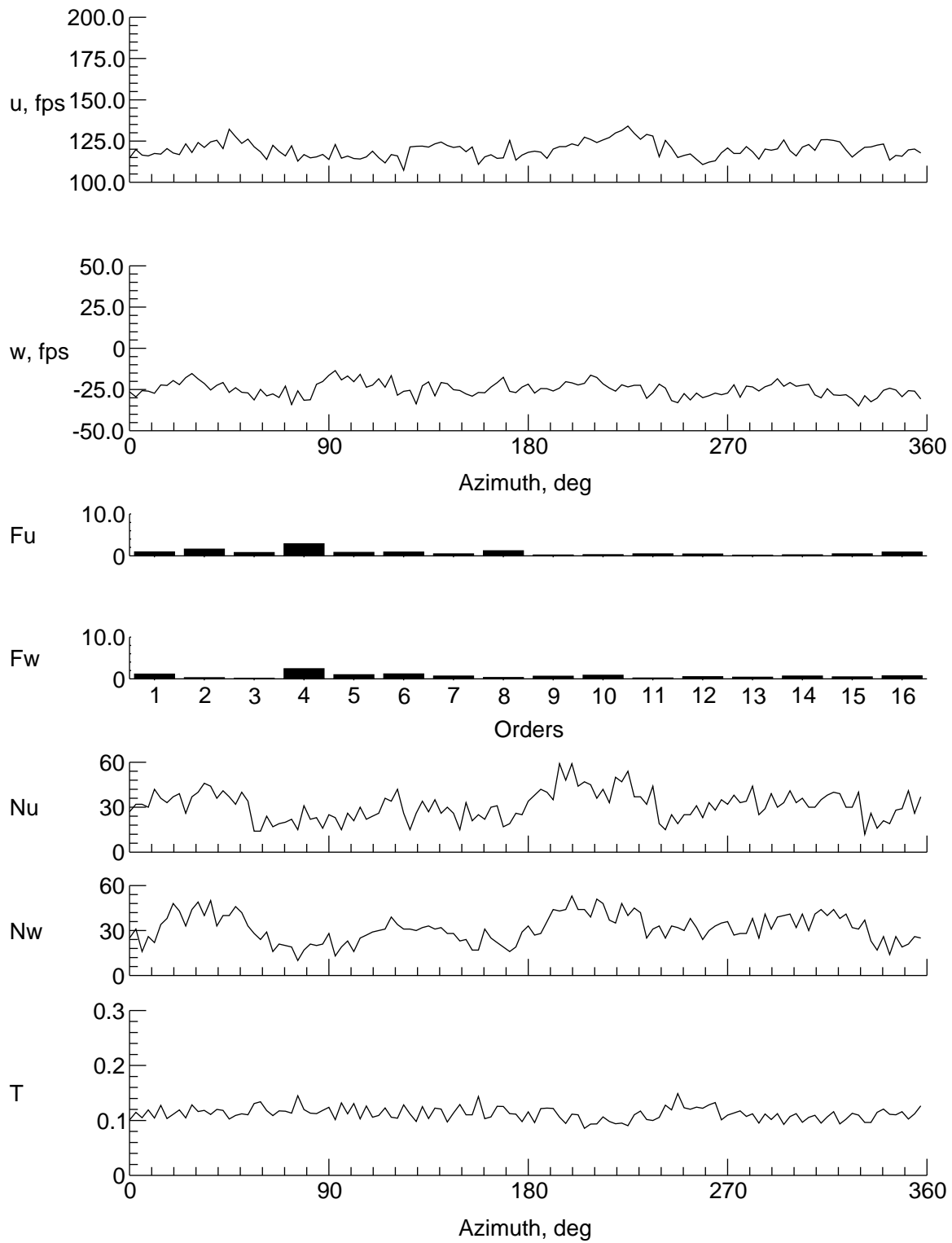
(m) $y = -6$ in., $z = -0.843$ in.

Figure 10. Continued.



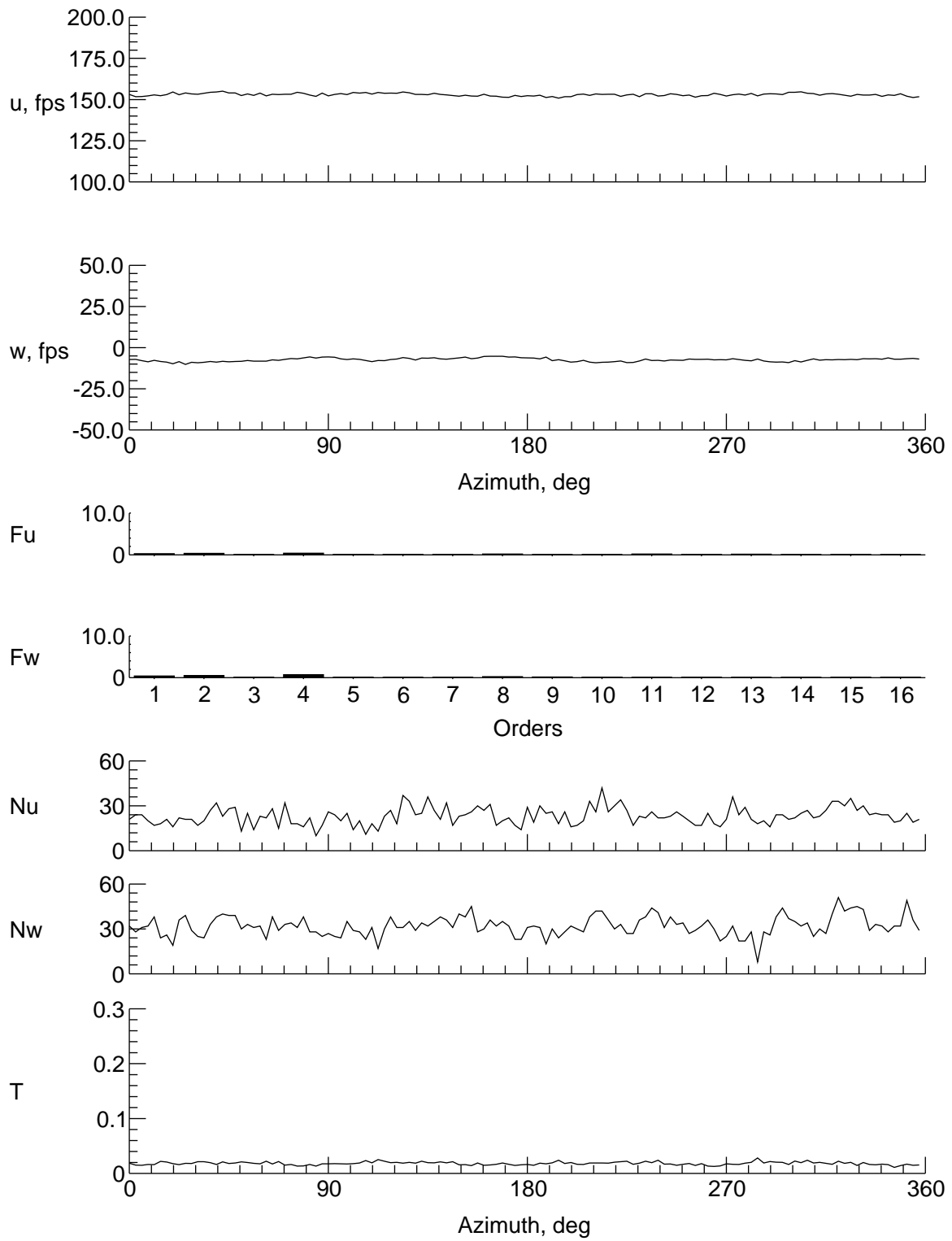
(n) $y = -8$ in., $z = -0.843$ in.

Figure 10. Continued.



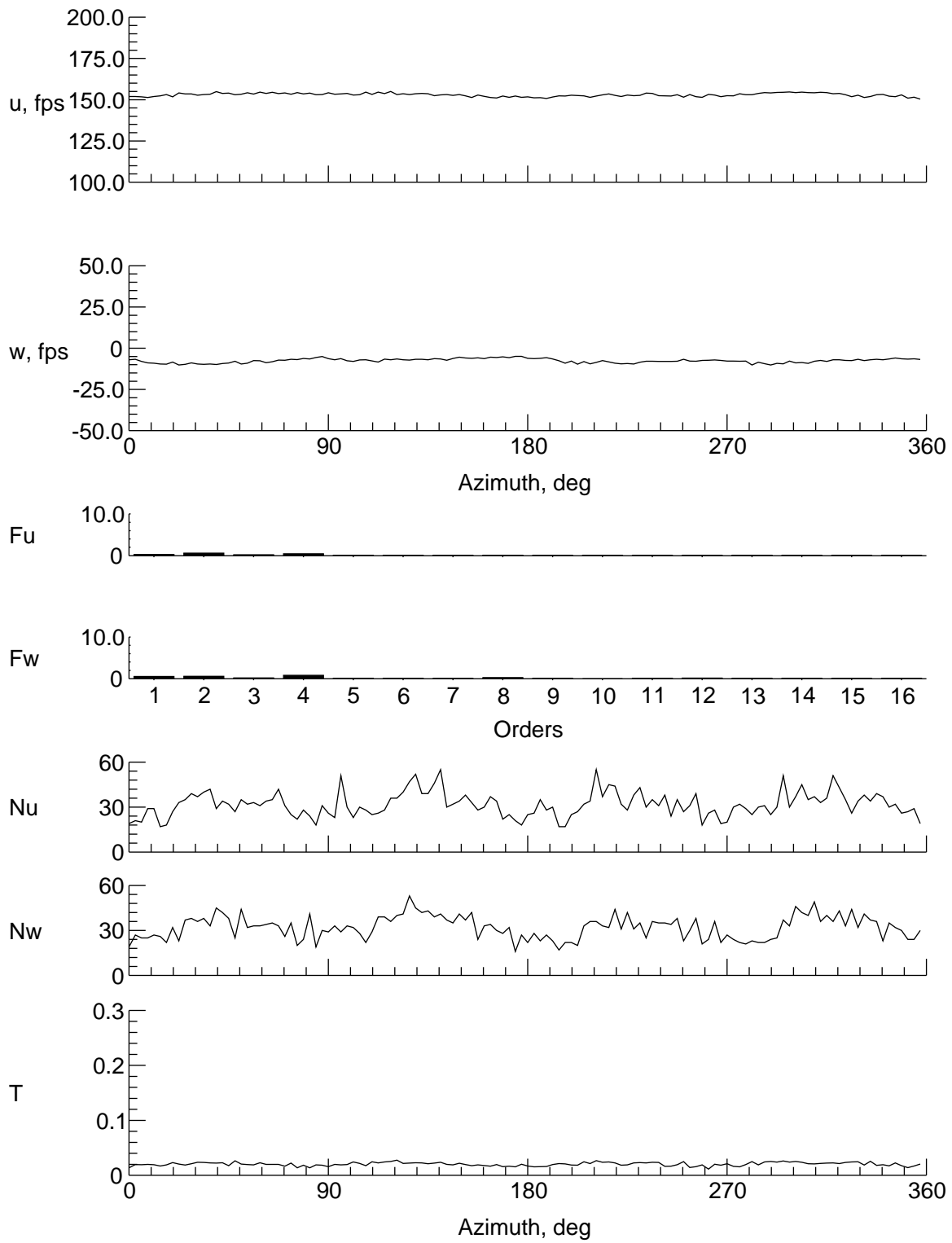
(o) $y = -9$ in., $z = -0.843$ in.

Figure 10. Concluded.



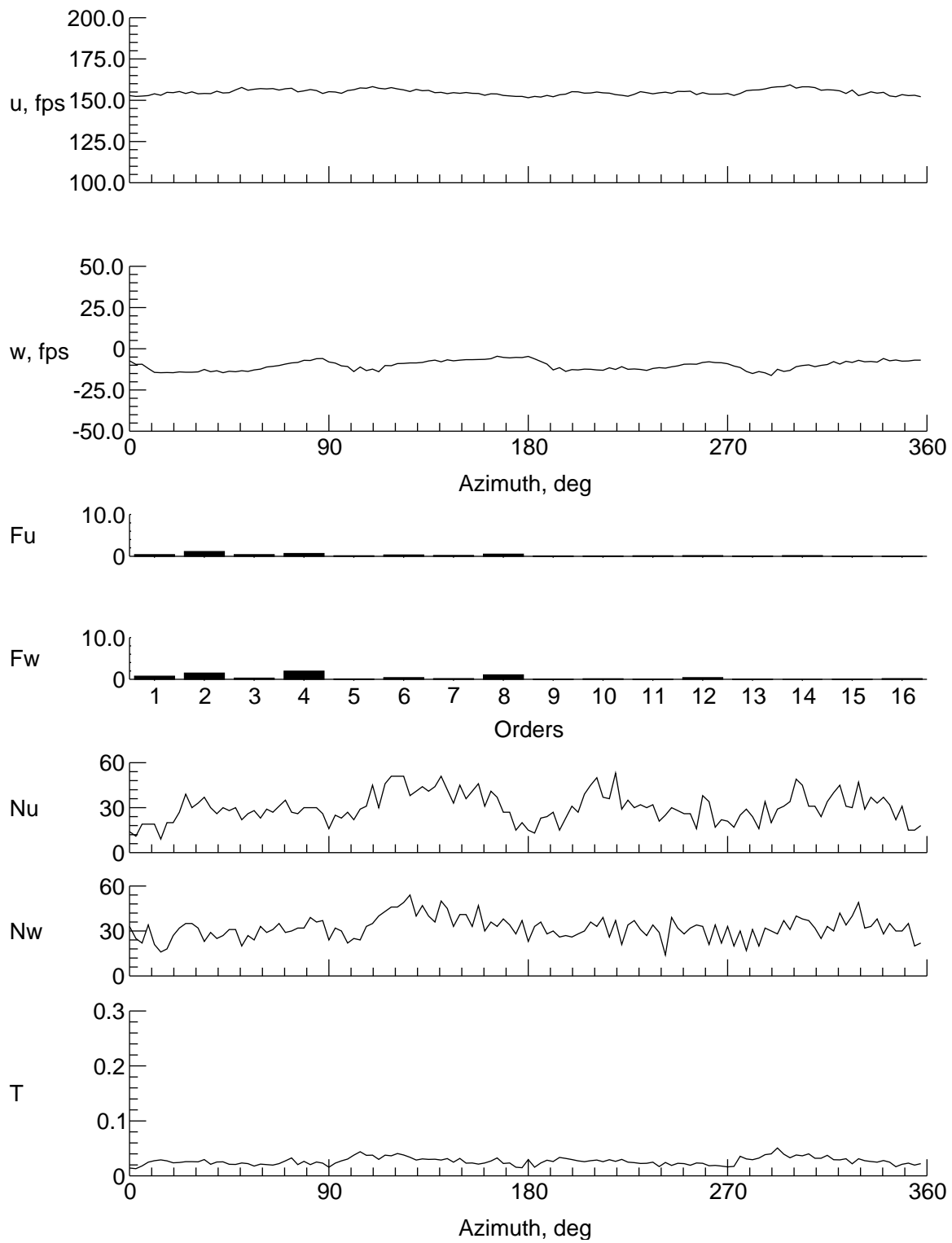
(a) $y = 0$ in., $z = 8.037$ in.

Figure 11. Velocity and turbulence at station 16 in.



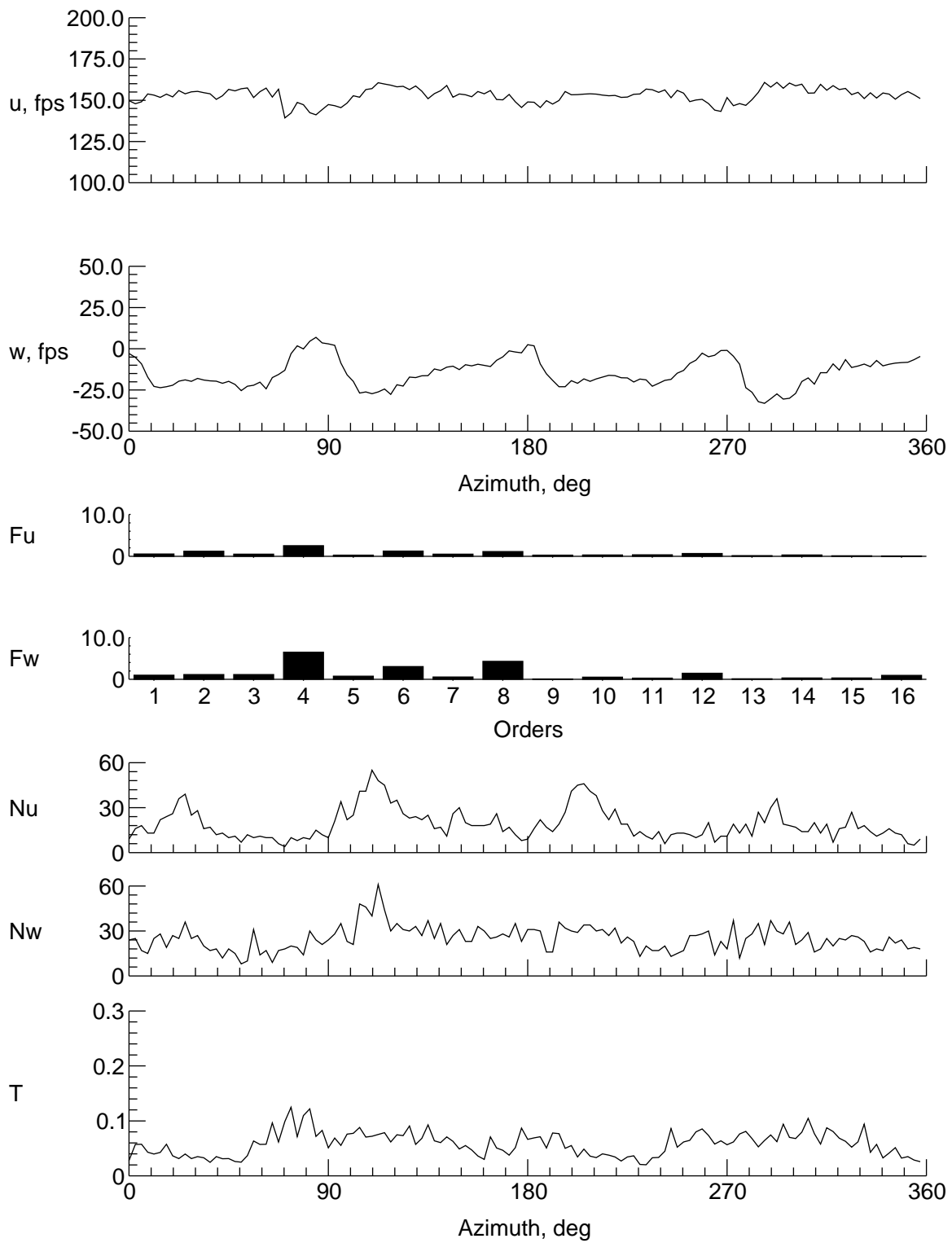
(b) $y = 0$ in., $z = 7.037$ in.

Figure 11. Continued.



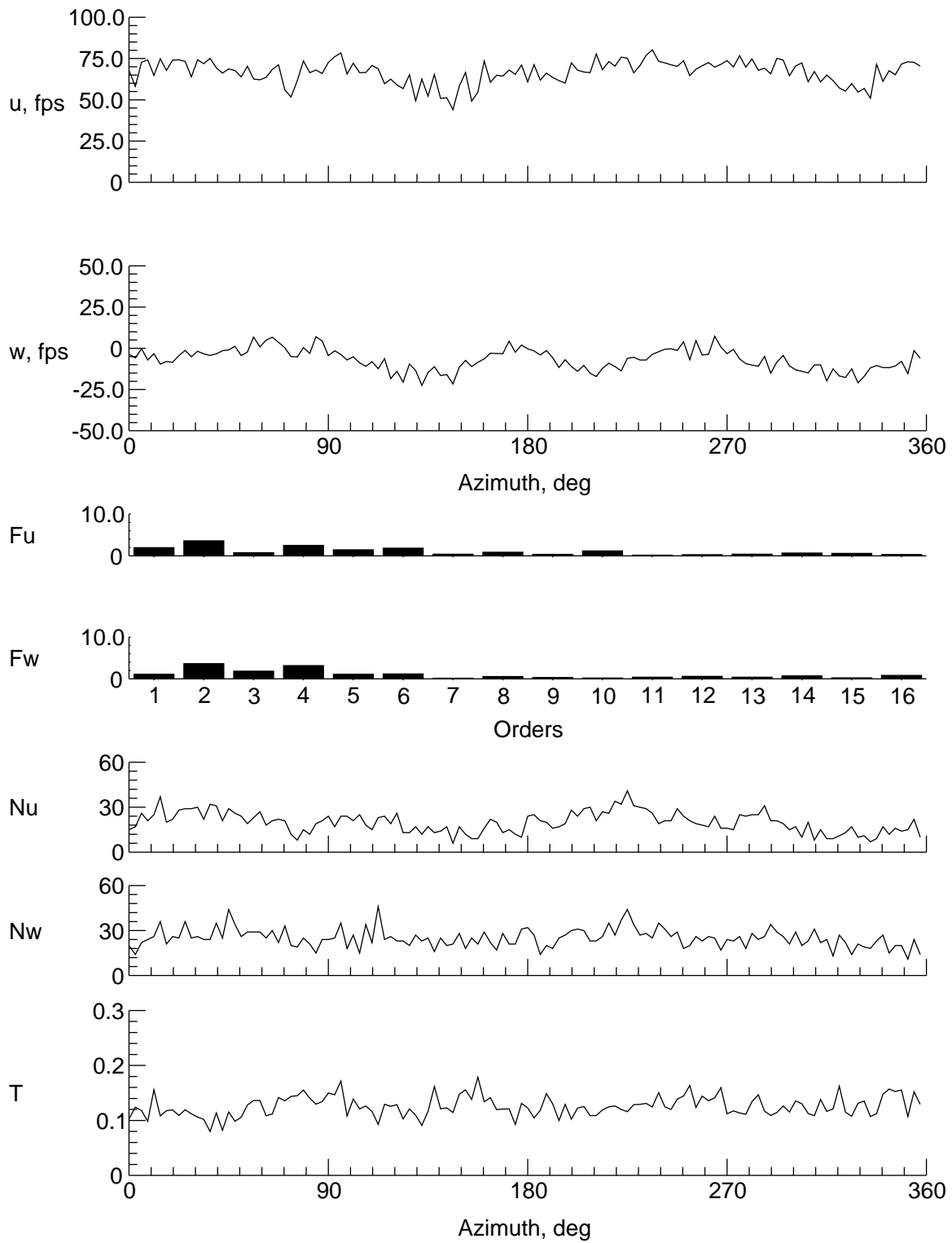
(c) $y = 0$ in., $z = 5.037$ in.

Figure 11. Continued.



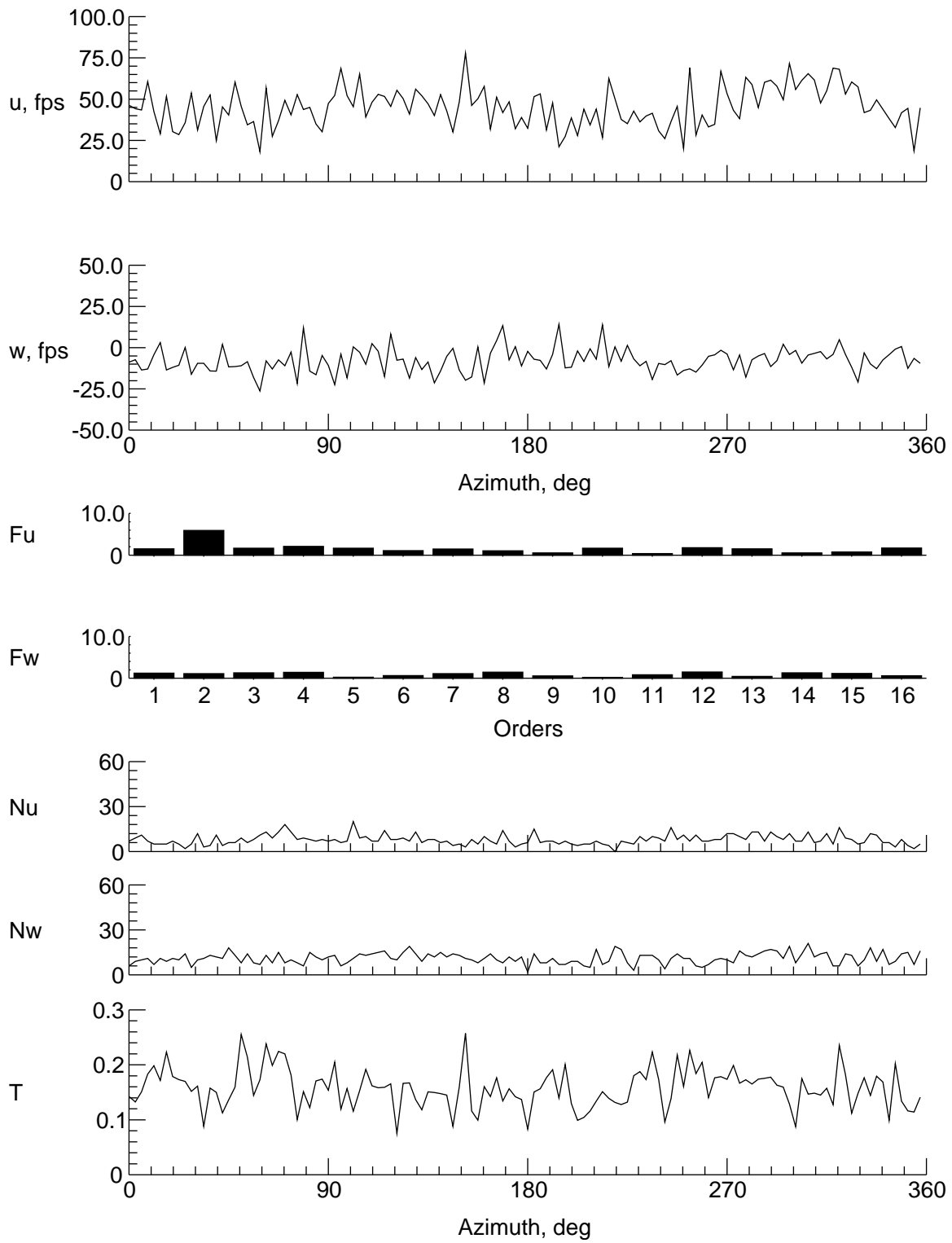
(d) $y = 0$ in., $z = 3.037$ in.

Figure 11. Continued.



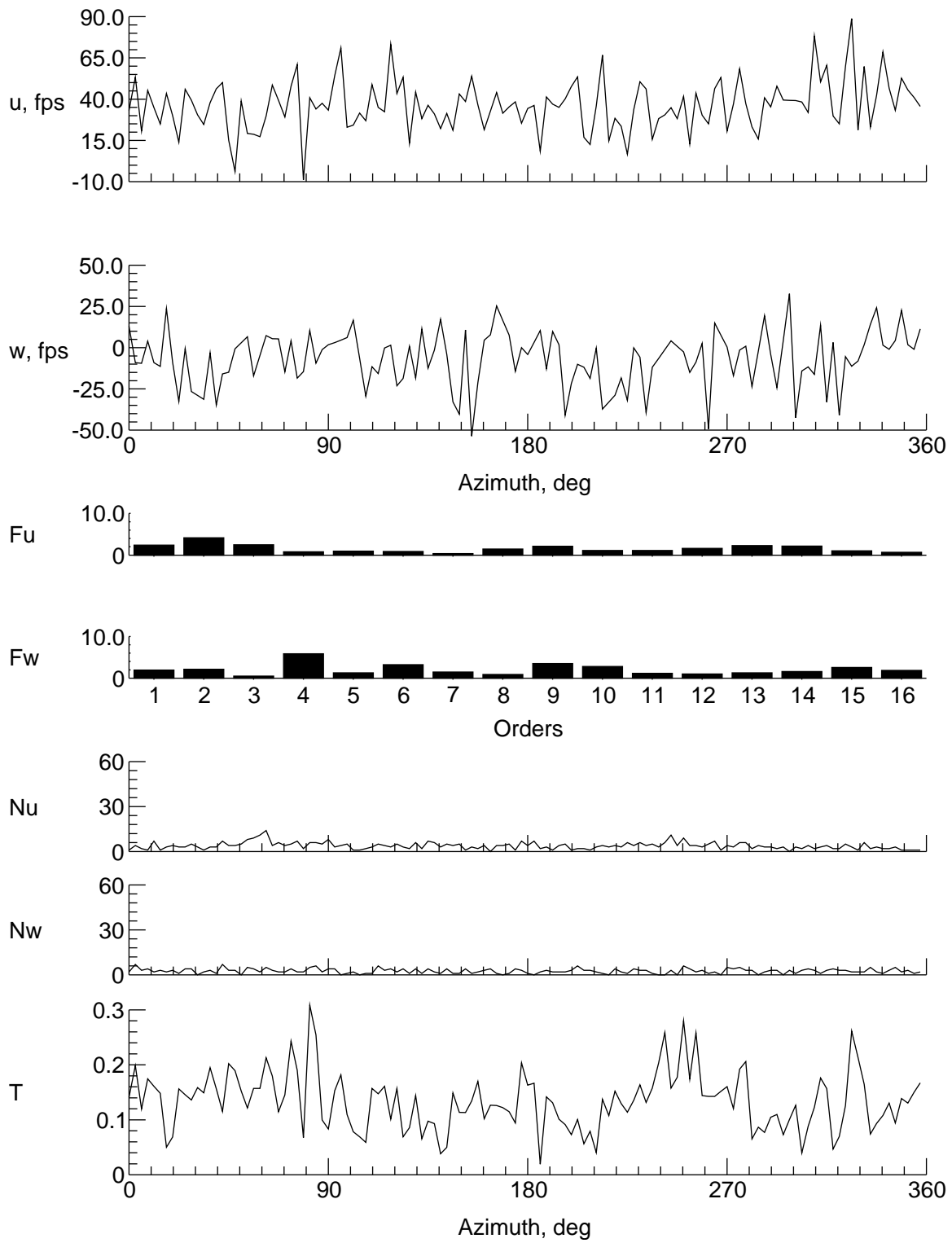
(e) $y = 0$ in., $z = -0.963$ in.

Figure 11. Continued.



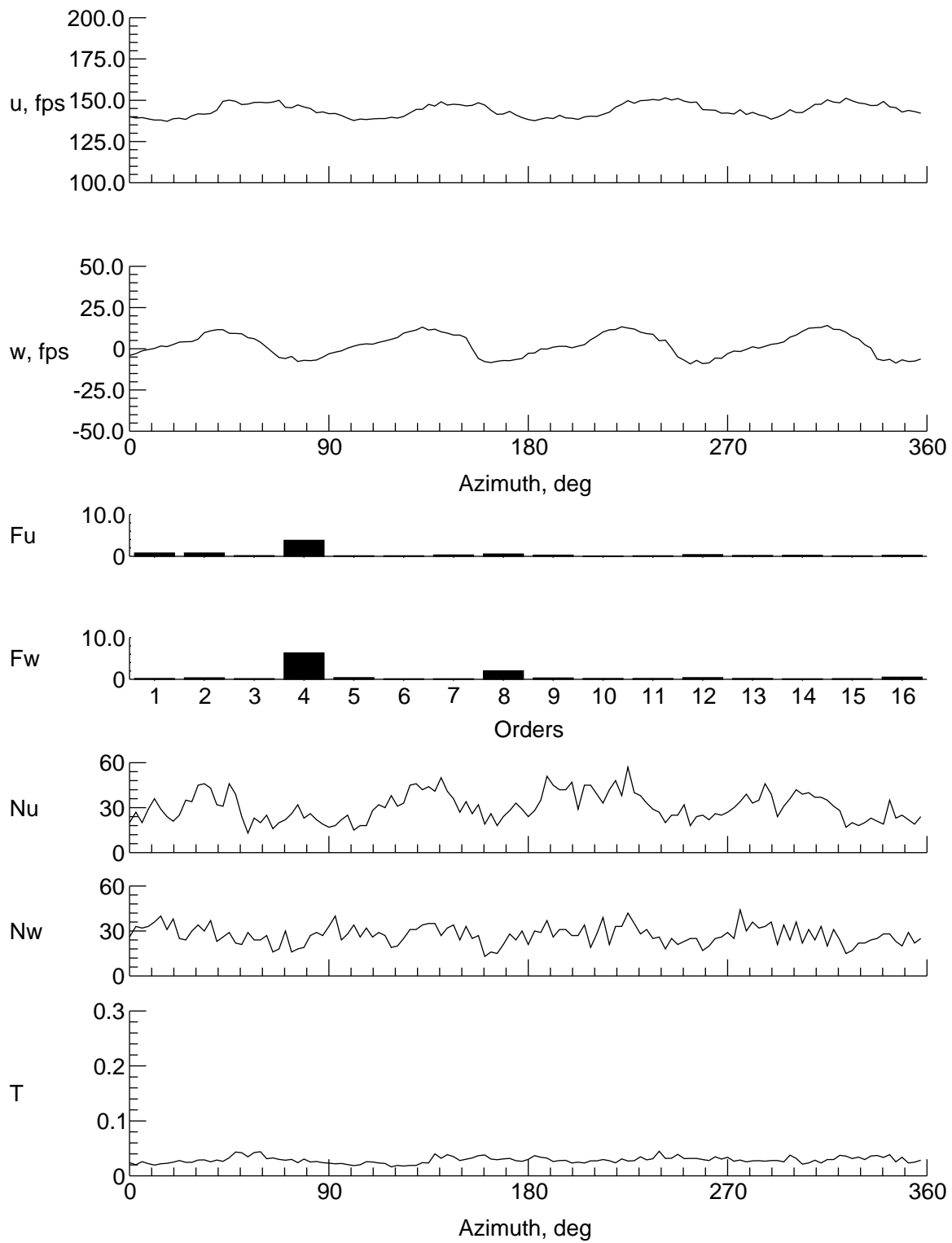
(f) $y = 0$ in., $z = -4.963$ in.

Figure 11. Continued.



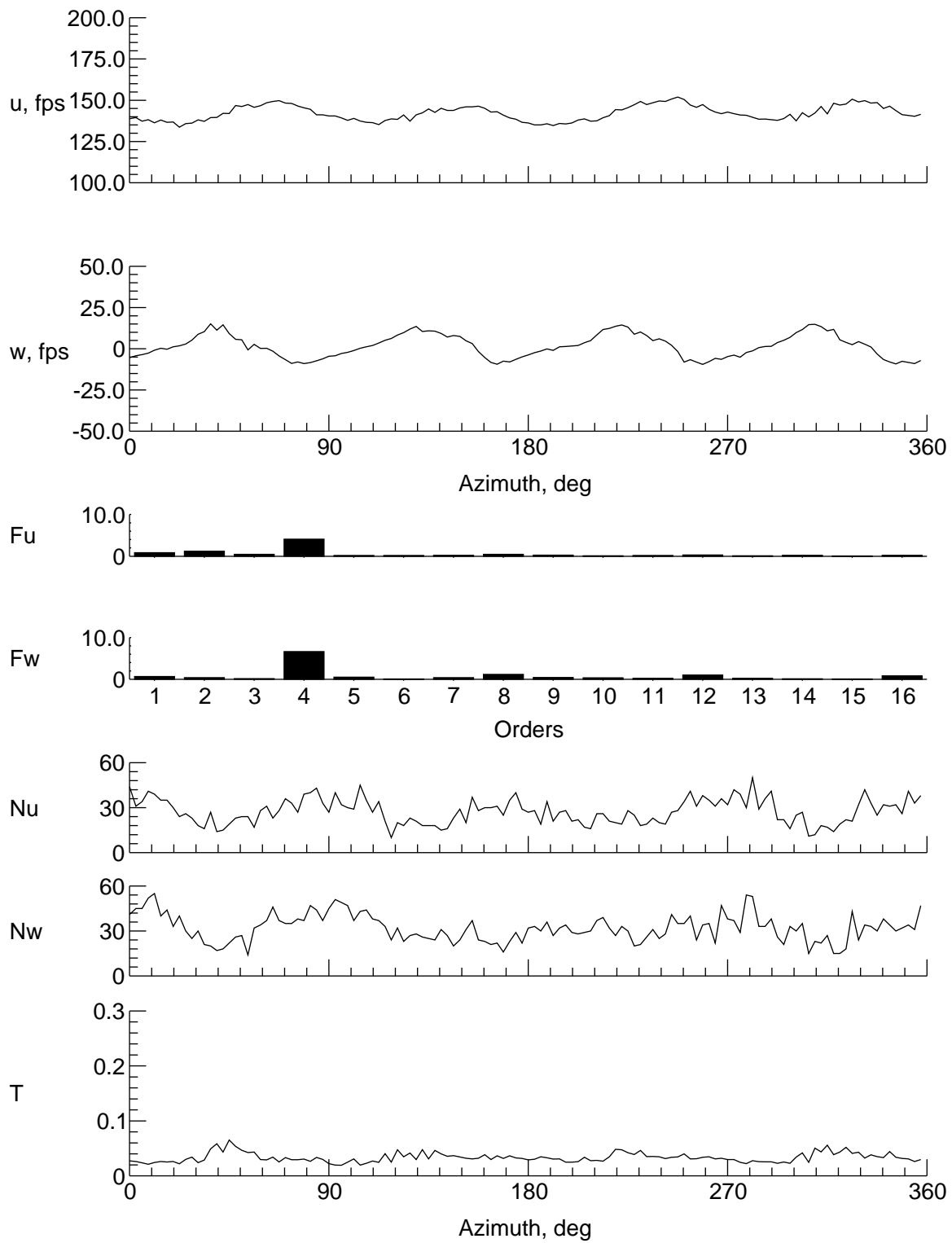
(g) $y = 0$ in., $z = -6.963$ in.

Figure 11. Continued.



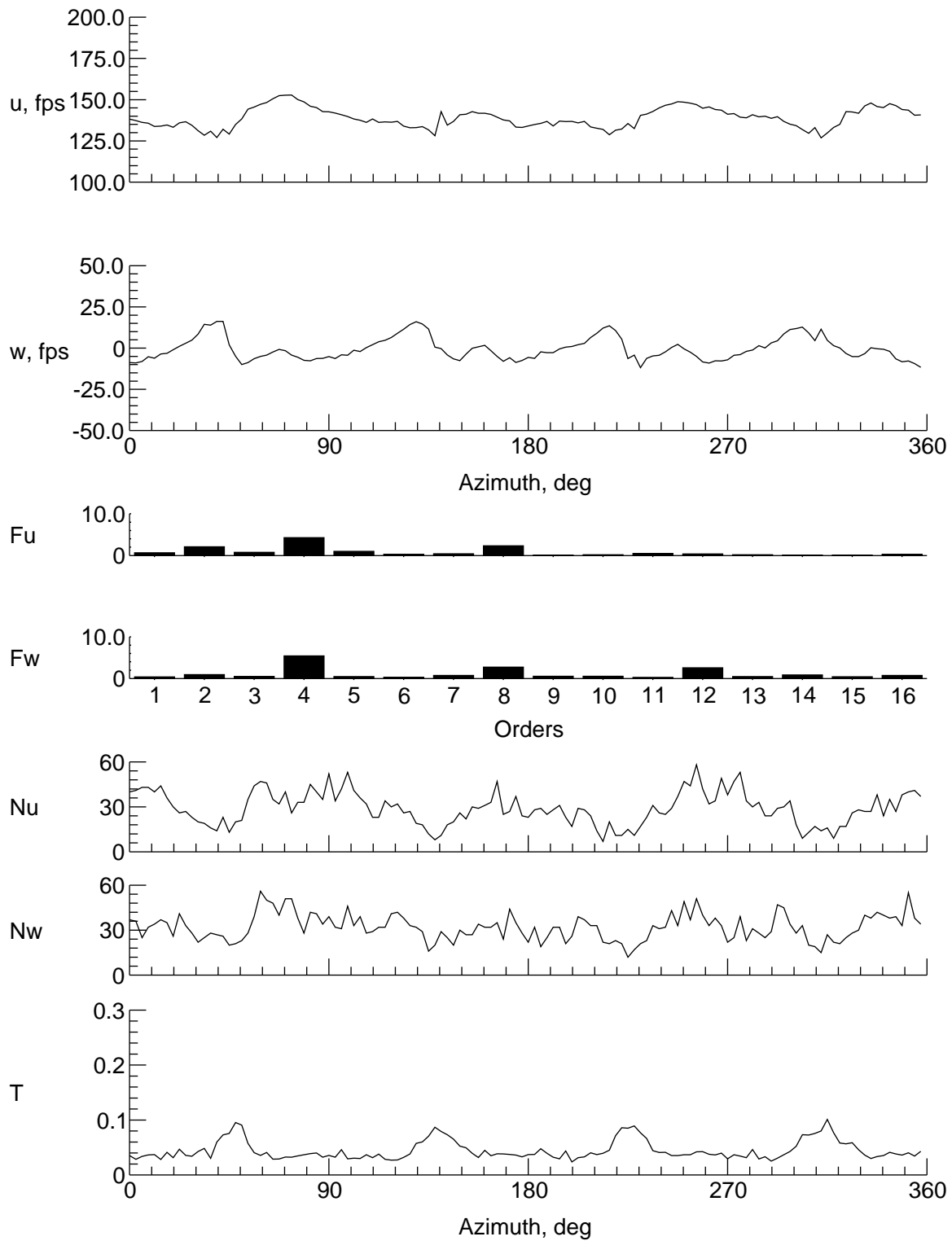
(h) $y = 9$ in., $z = -0.963$ in.

Figure 11. Continued.



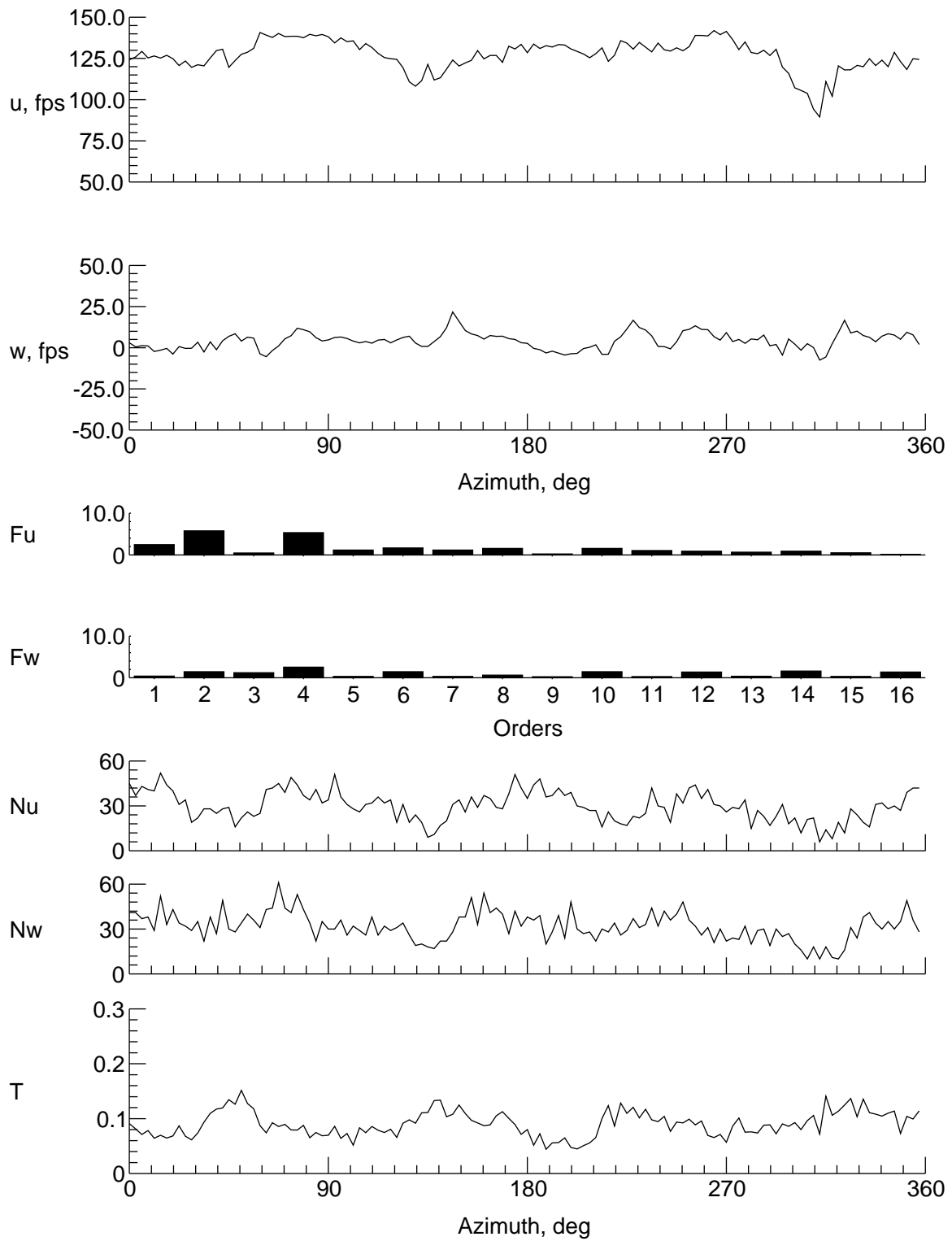
(i) $y = 8$ in., $z = -0.963$ in.

Figure 11. Continued.



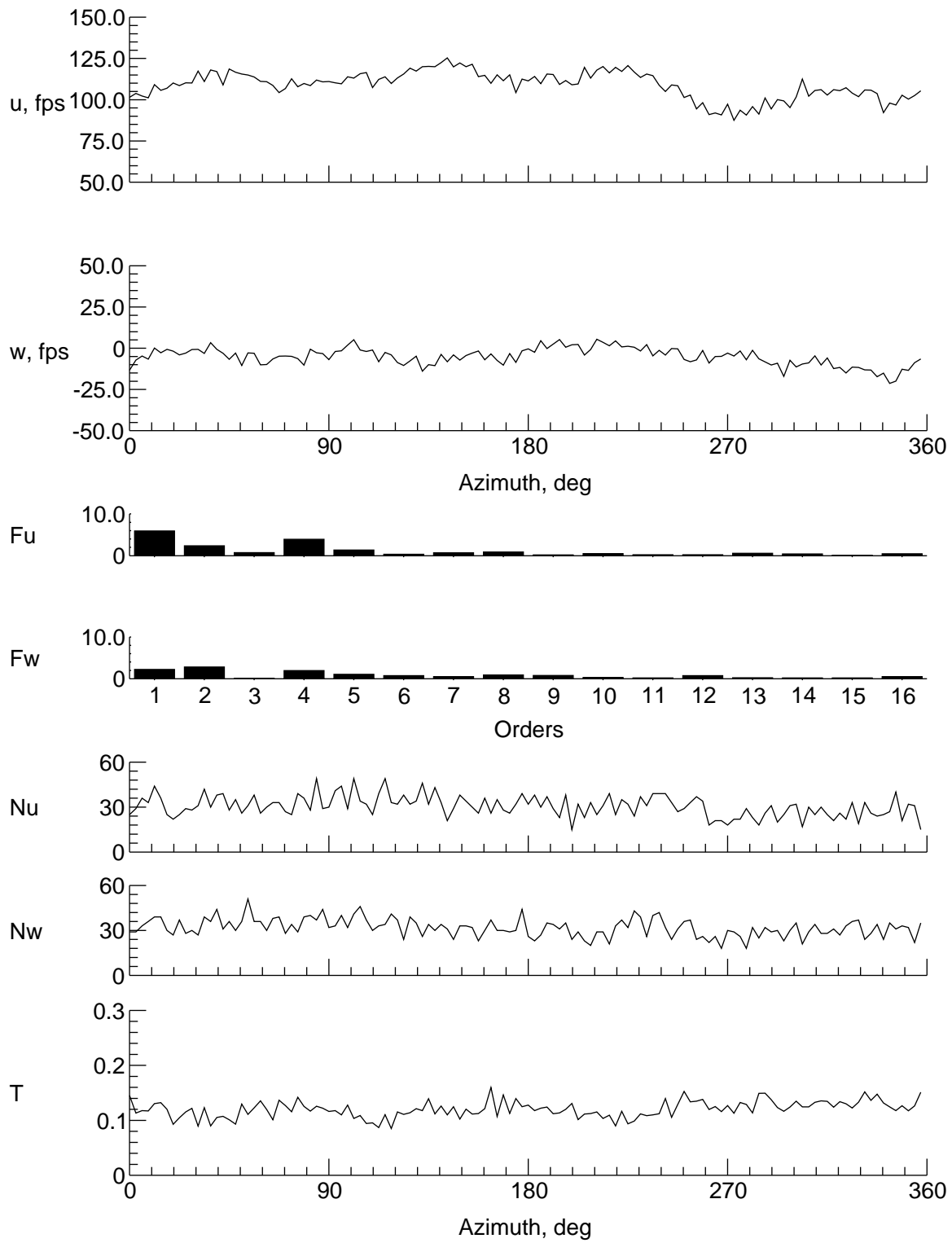
(j) $y = 6$ in., $z = -0.963$ in.

Figure 11. Continued.



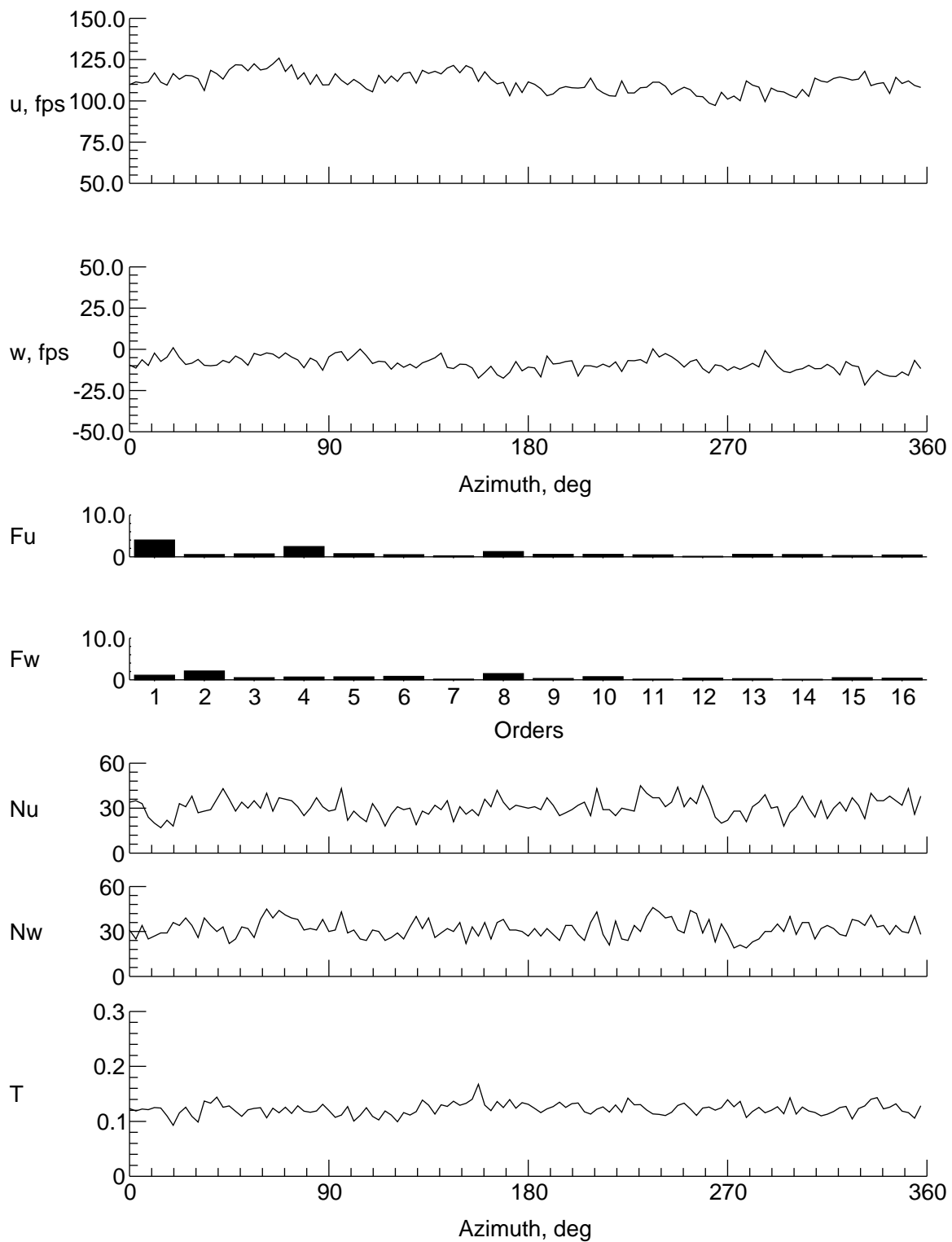
(k) $y = 4$ in., $z = -0.963$ in.

Figure 11. Continued.



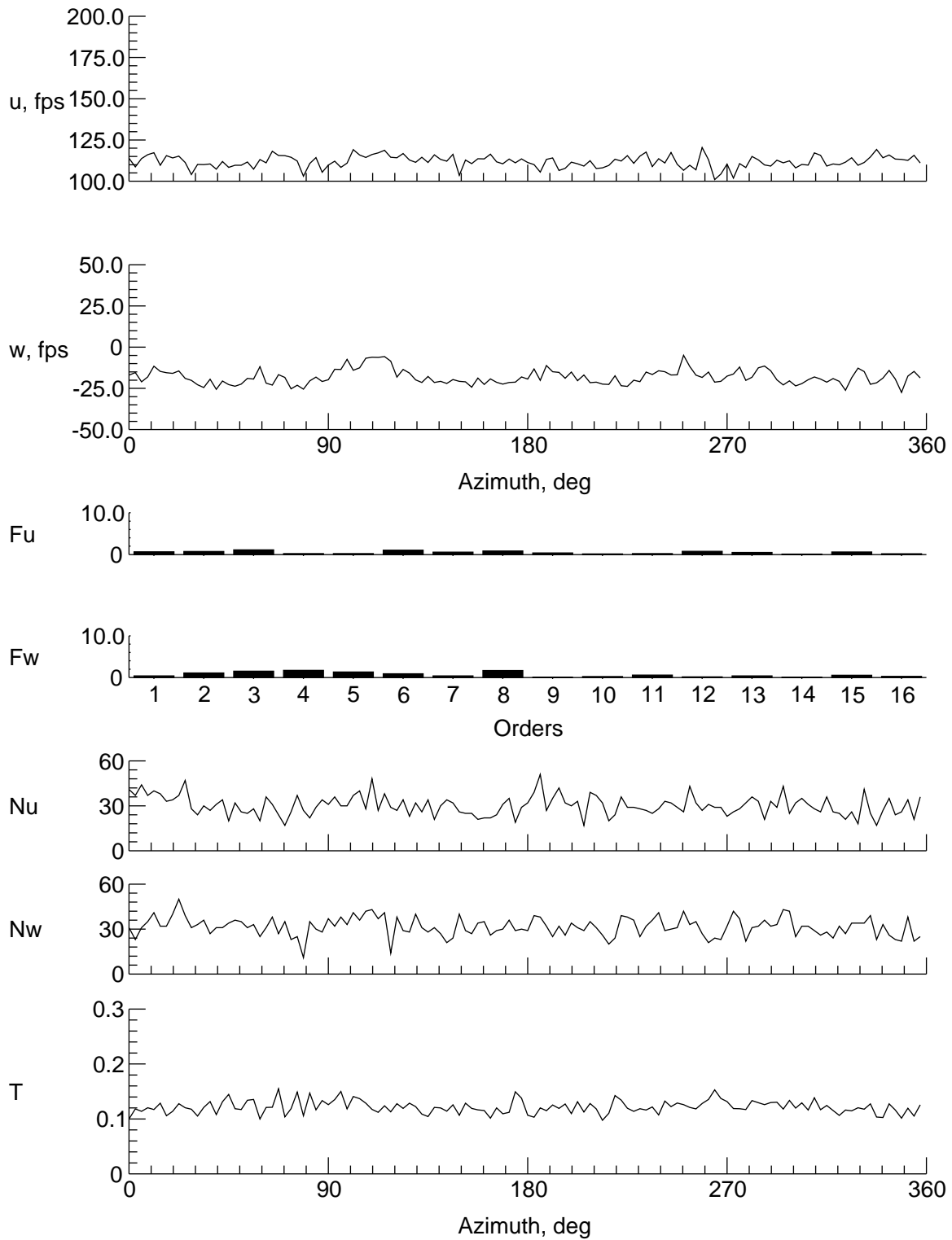
(l) $y = -4$ in., $z = -0.963$ in.

Figure 11. Continued.



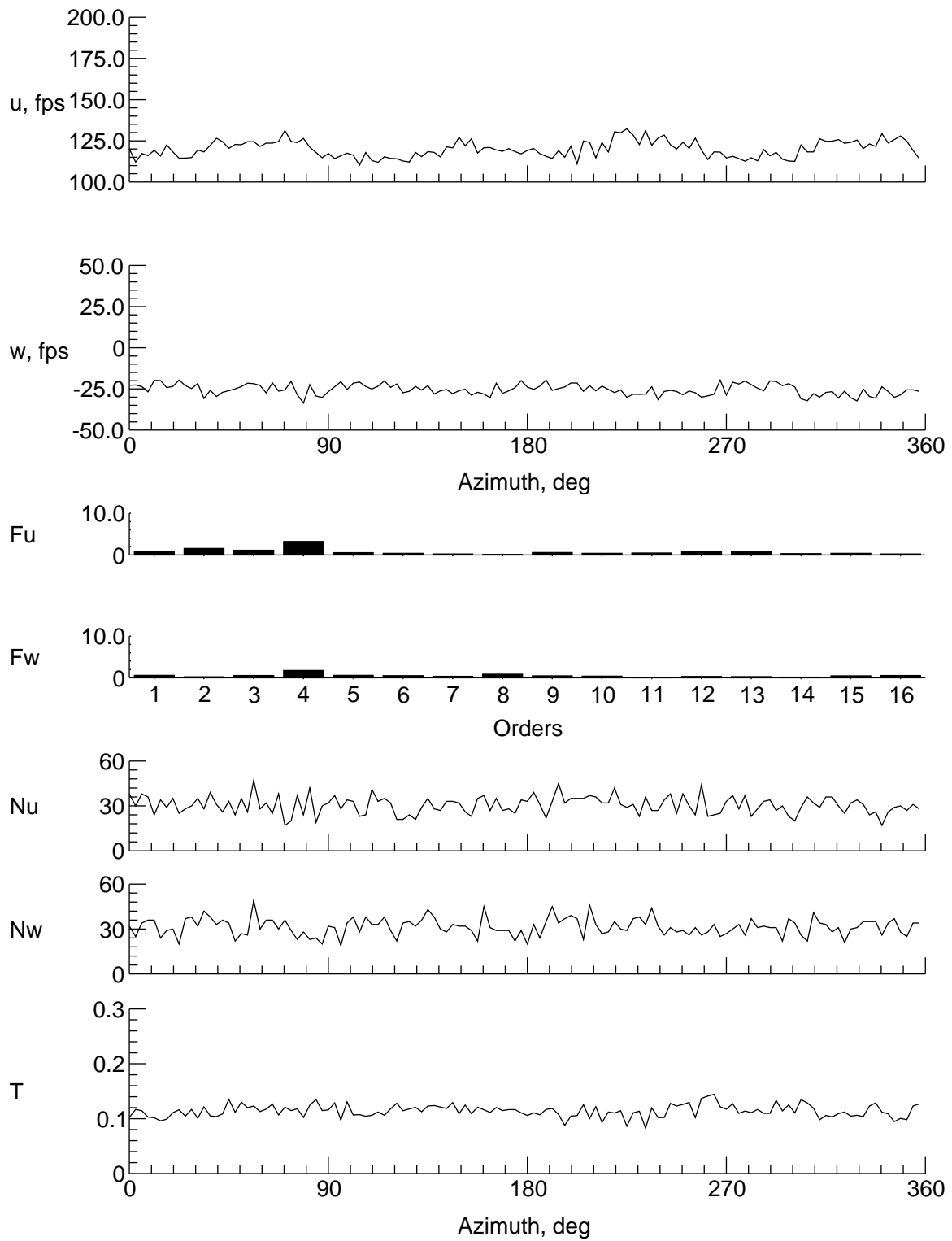
(m) $y = -6$ in., $z = -0.963$ in.

Figure 11. Continued.



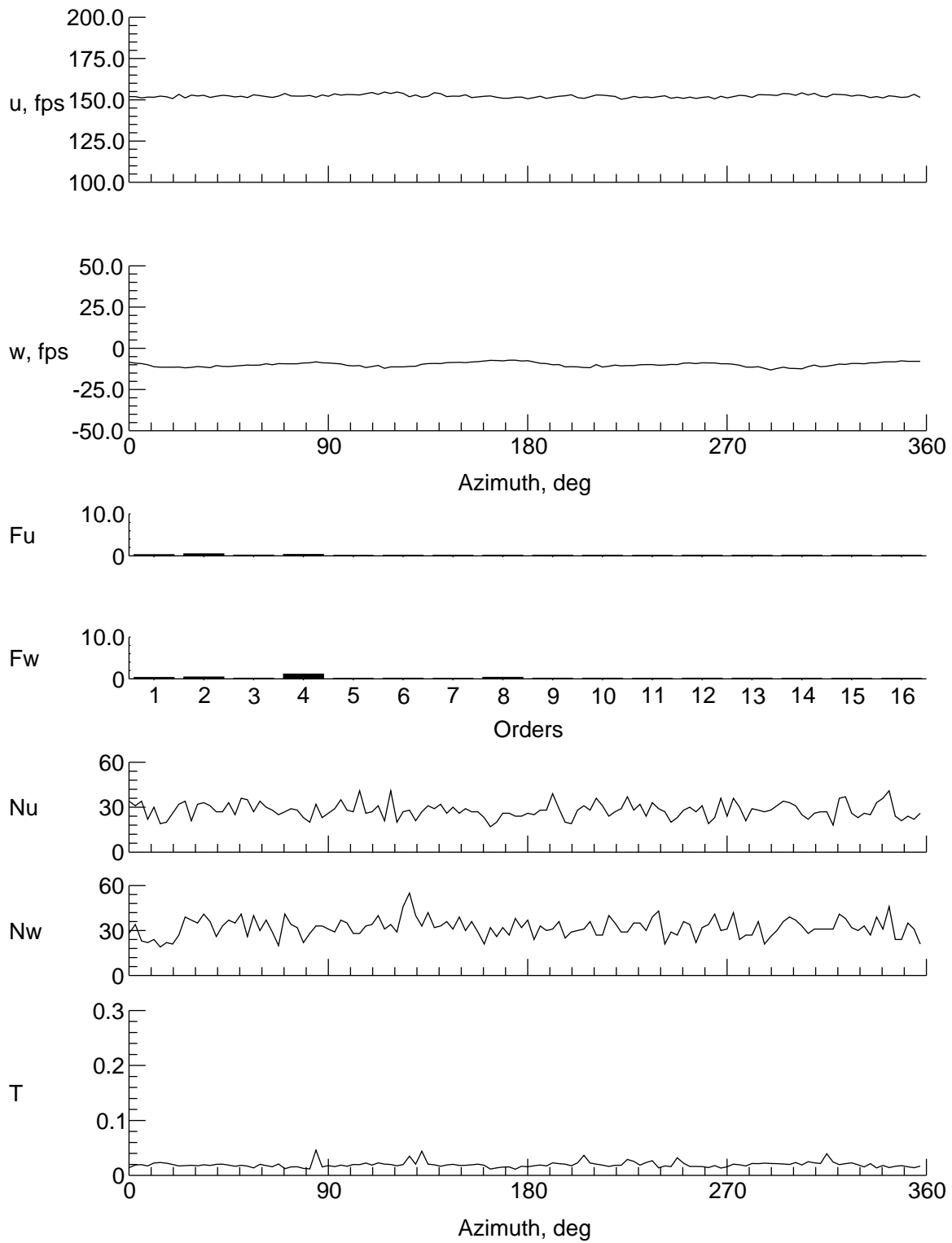
(n) $y = -8$ in., $z = -0.963$ in.

Figure 11. Continued.



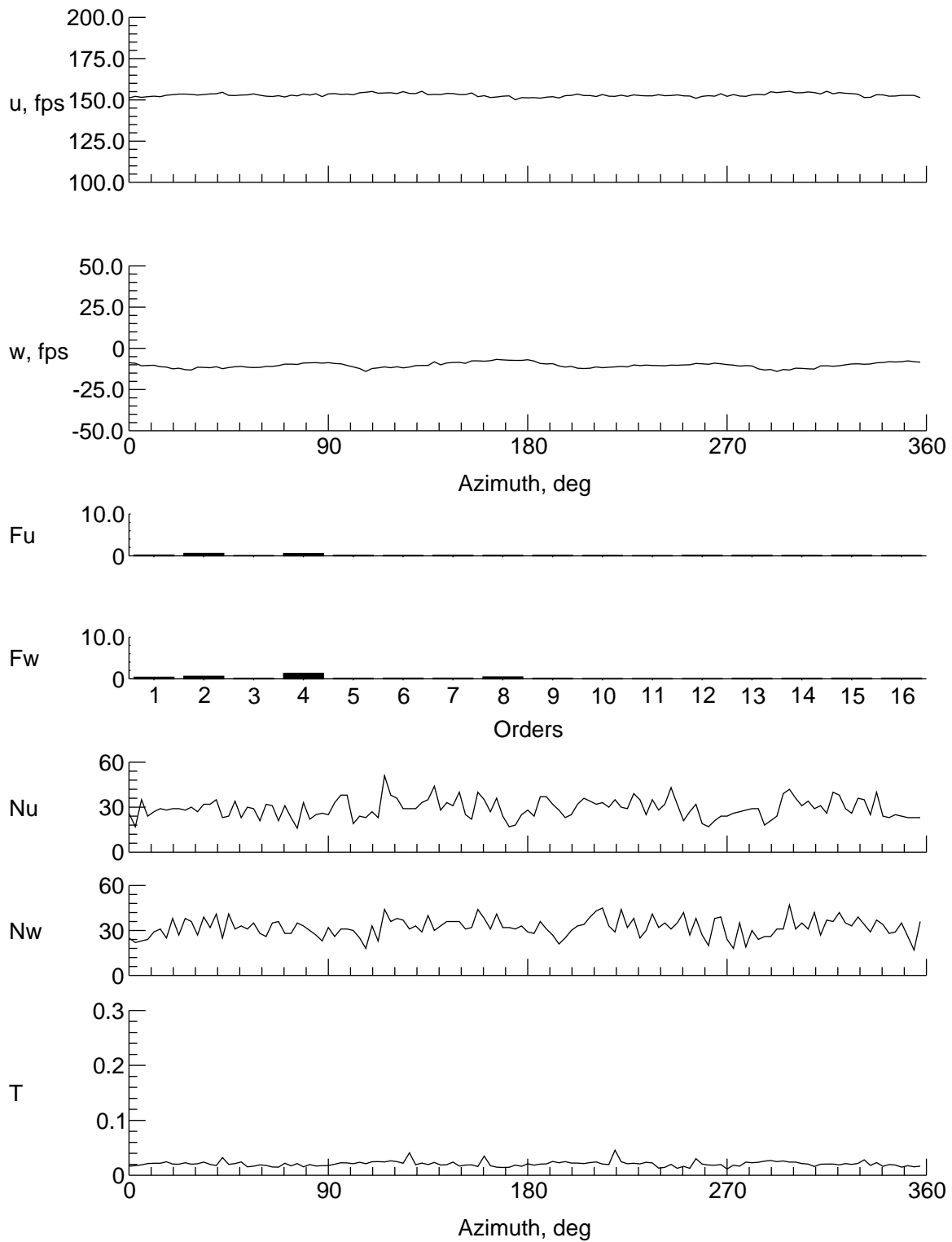
(o) $y = -9$ in., $z = -0.963$ in.

Figure 11. Concluded.



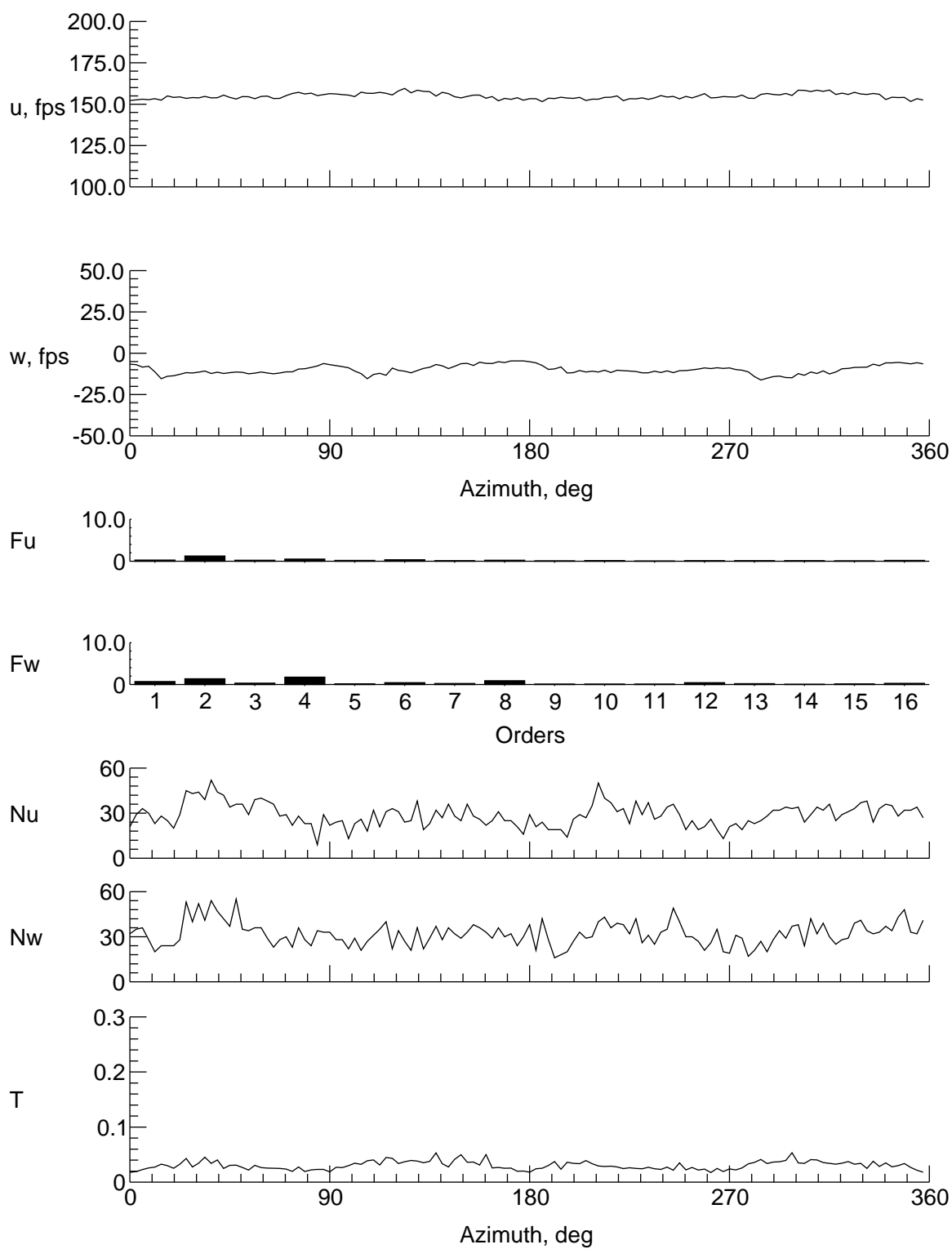
(a) $y = 0$ in., $z = 7.917$ in.

Figure 12. Velocity and turbulence at station 18 in.



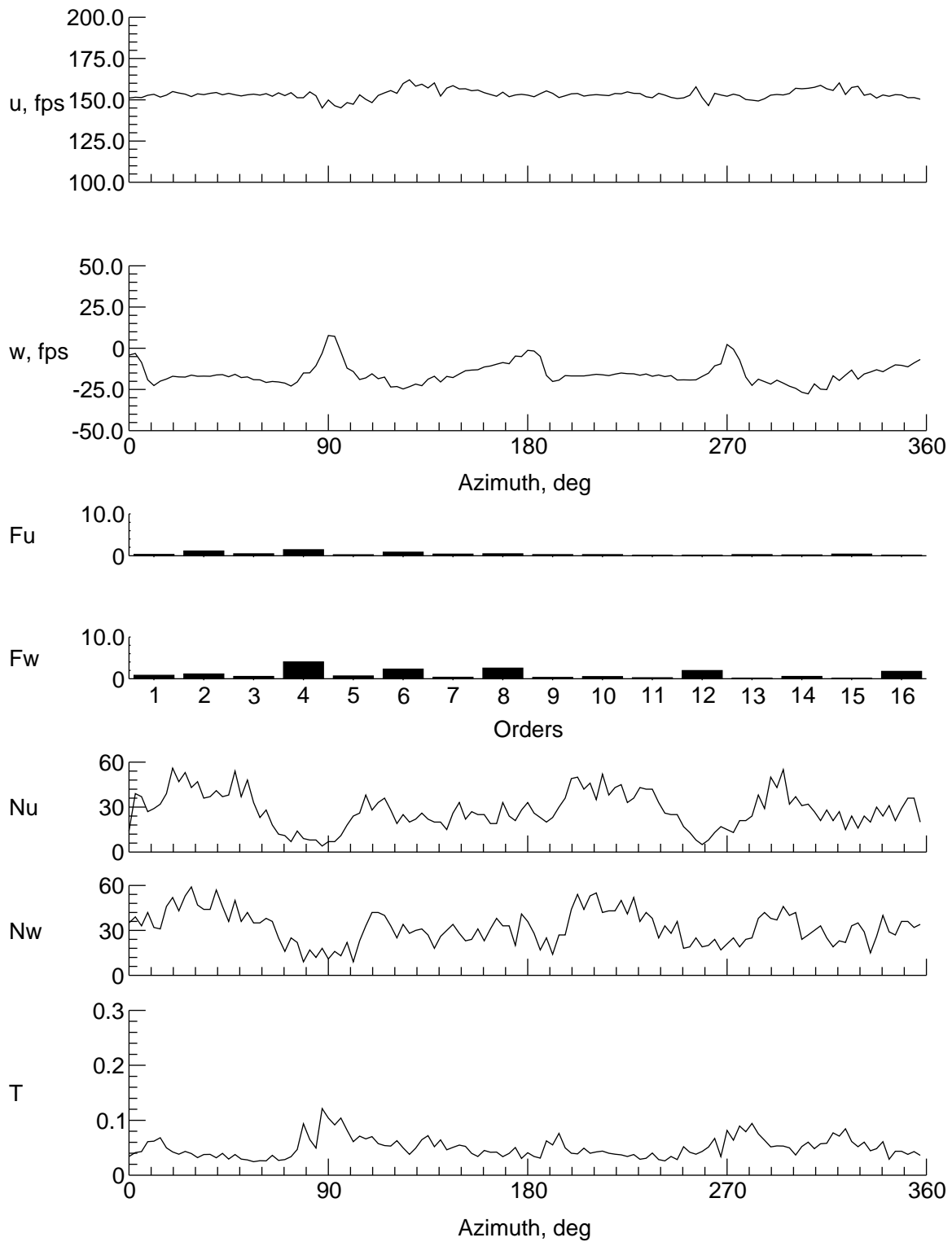
(b) $y = 0$ in., $z = 6.917$ in.

Figure 12. Continued.



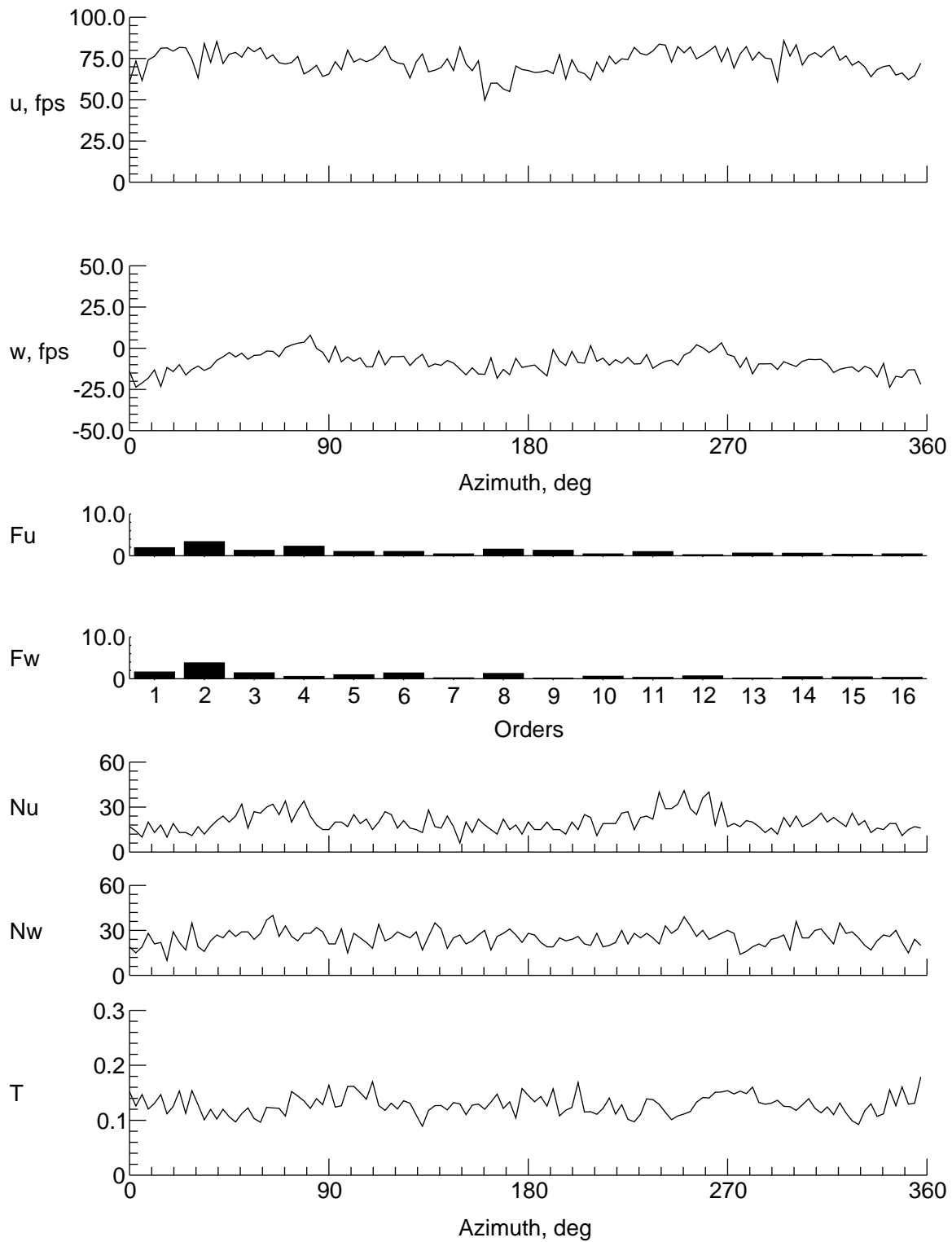
(c) $y = 0$ in., $z = 4.917$ in.

Figure 12. Continued.



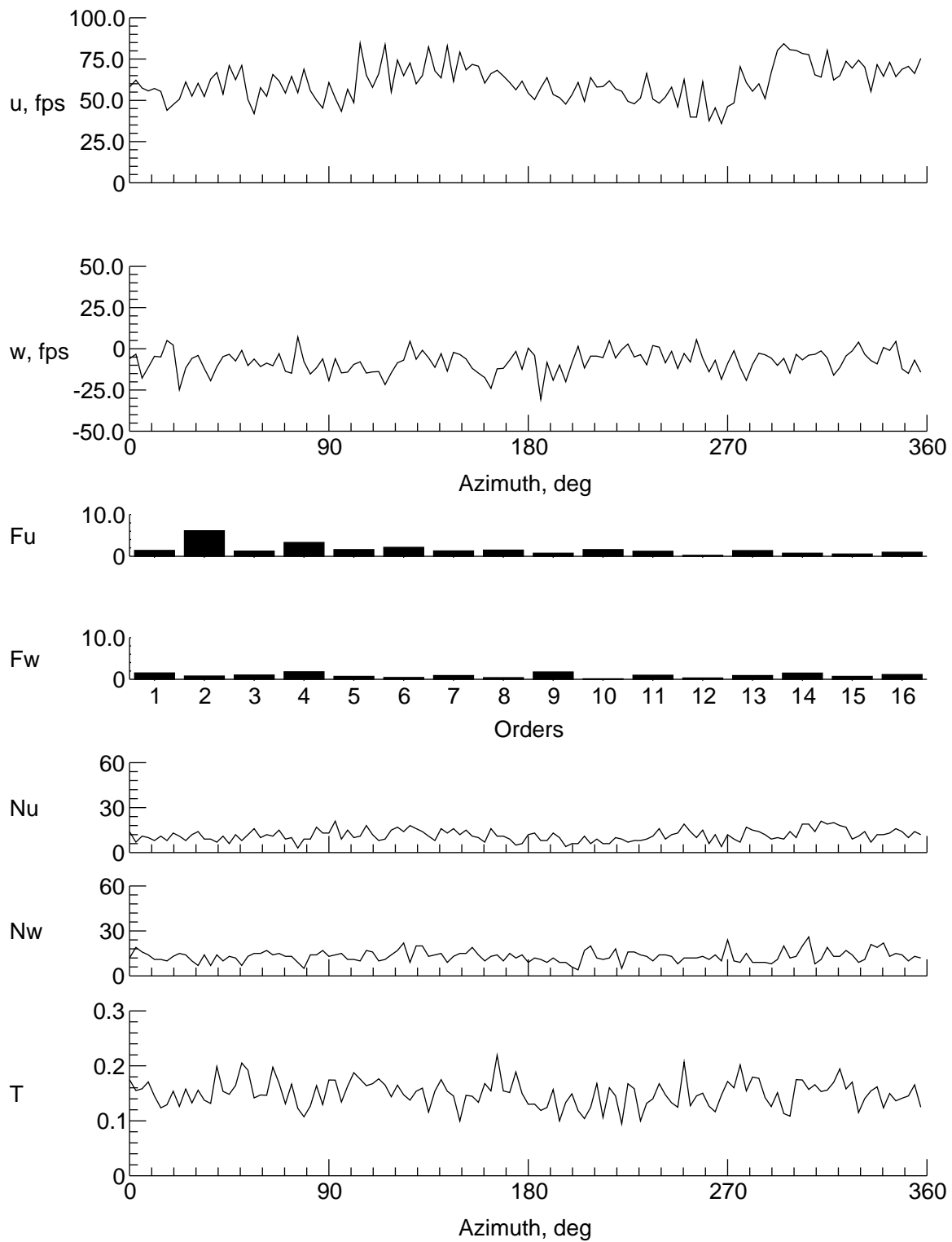
(d) $y = 0$ in., $z = 2.917$ in.

Figure 12. Continued.



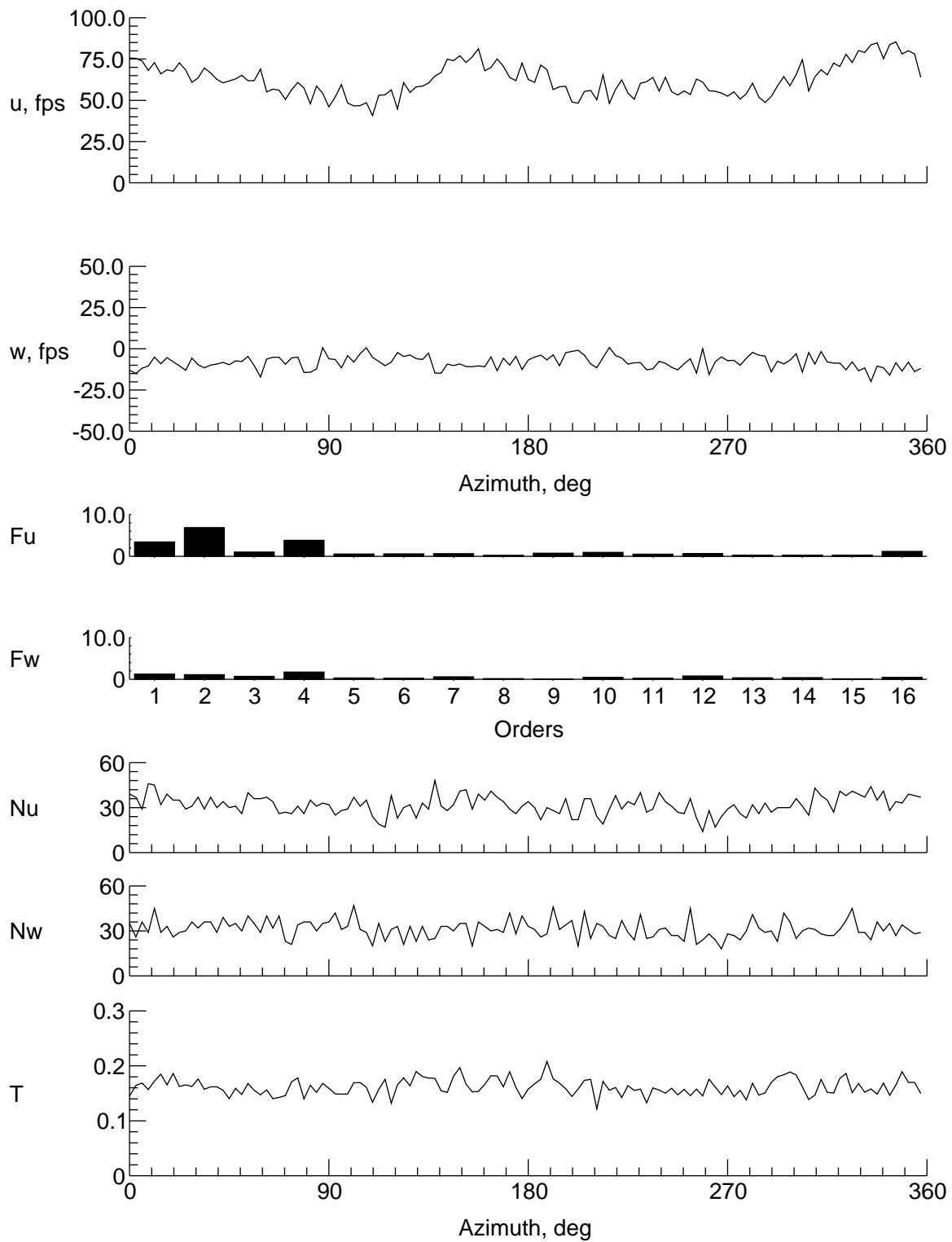
(e) $y = 0$ in., $z = -1.083$ in.

Figure 12. Continued.



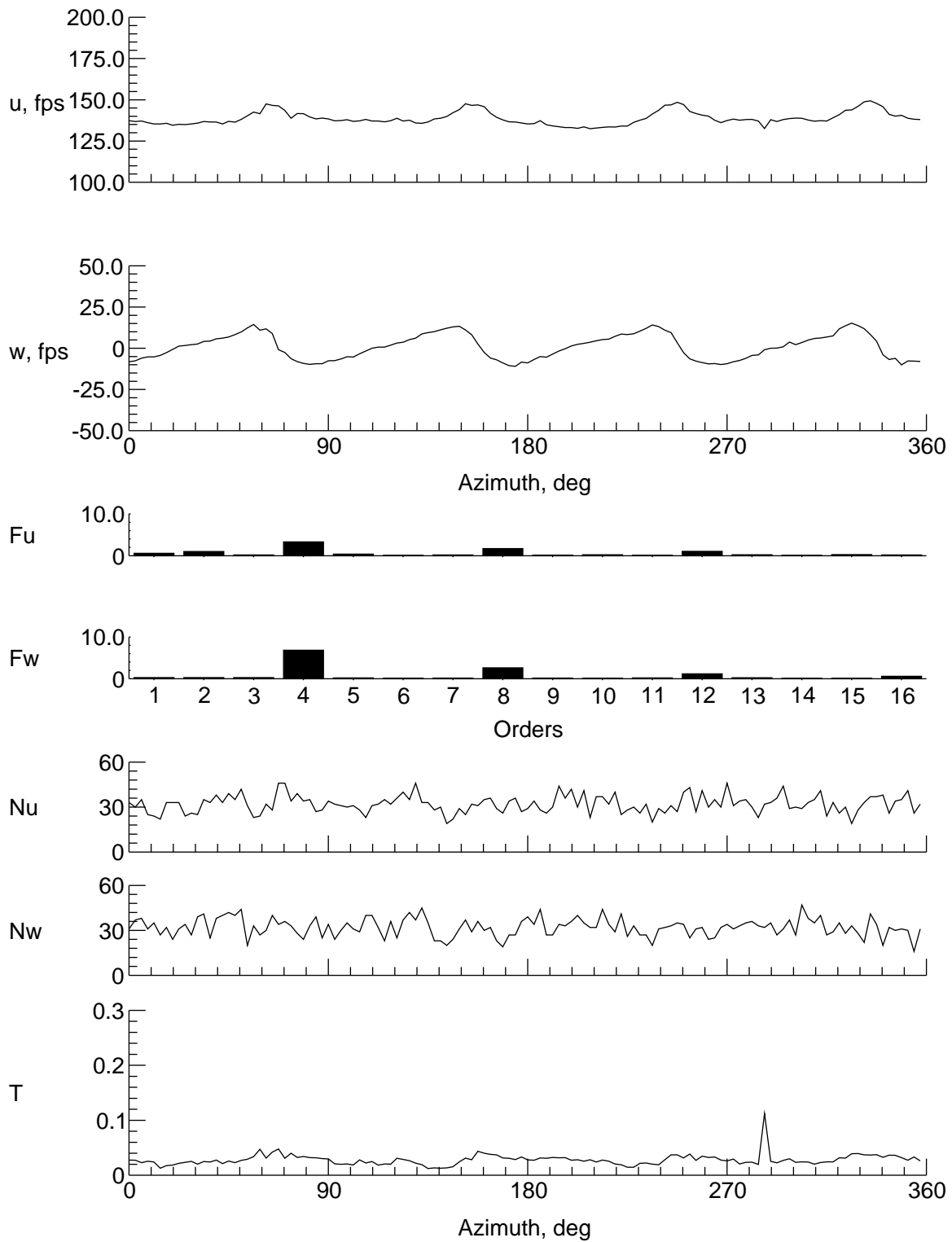
(f) $y = 0$ in., $z = -5.083$ in.

Figure 12. Continued.



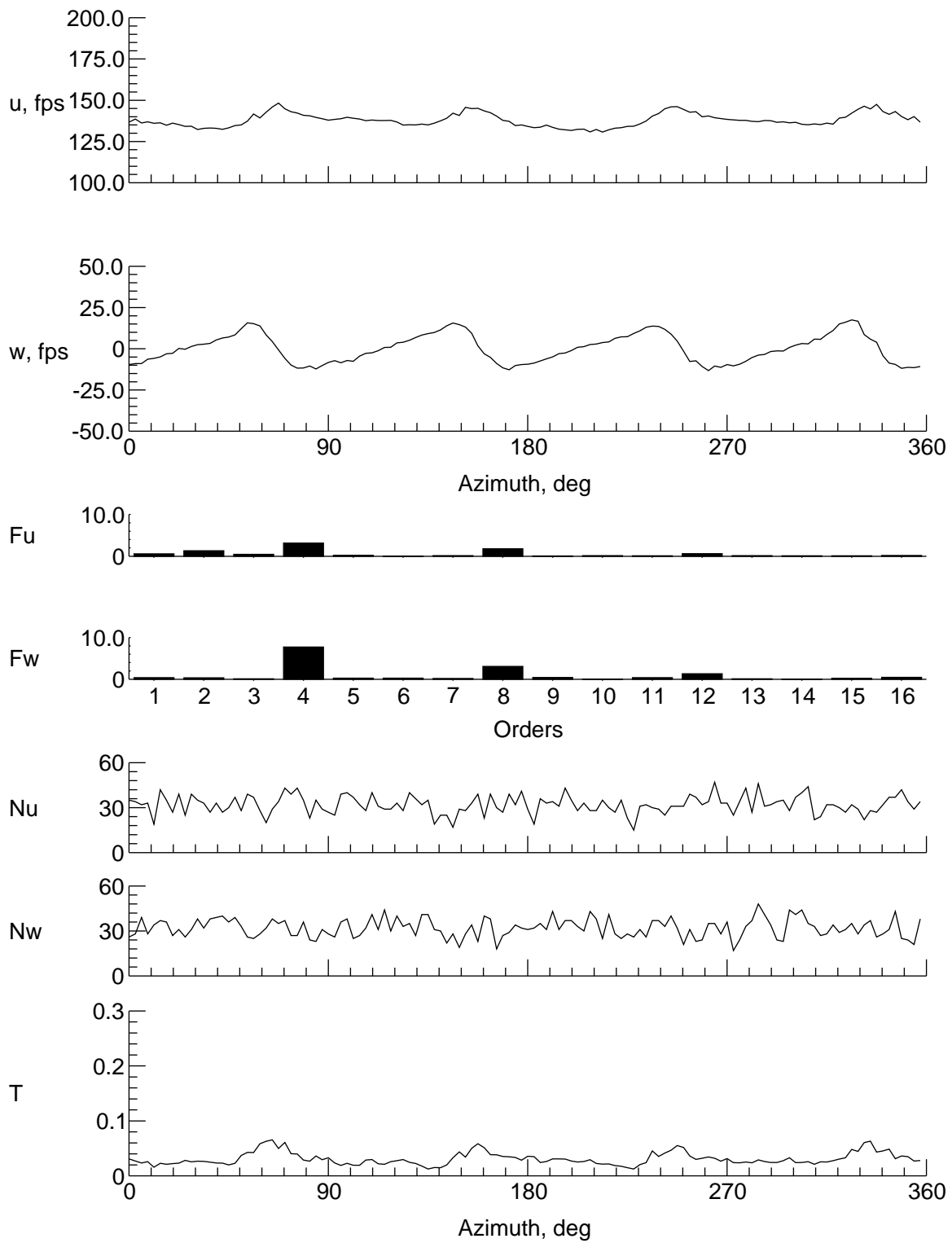
(g) $y = 0$ in., $z = -7.083$ in.

Figure 12. Continued.



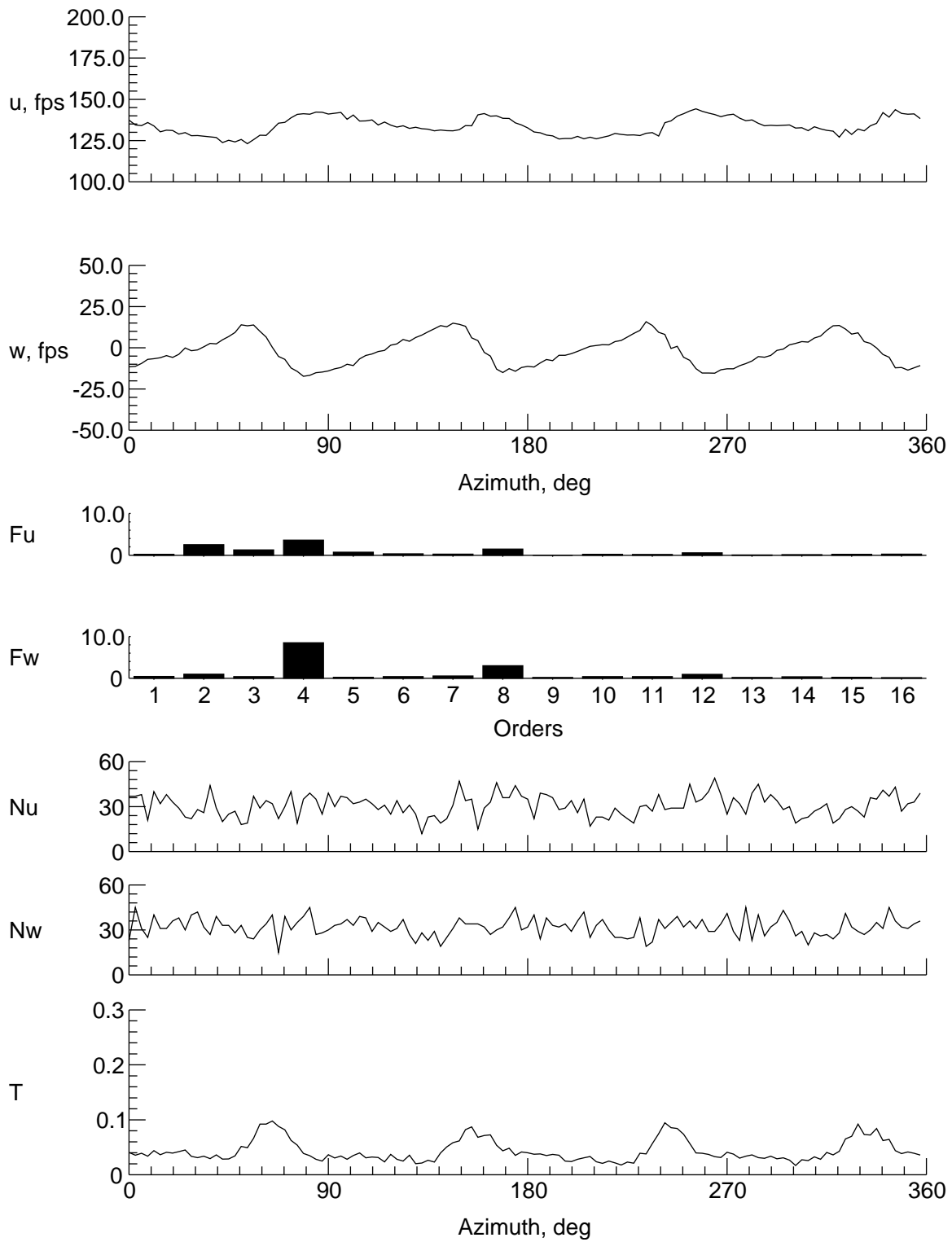
(h) $y = 9$ in., $z = -1.083$ in.

Figure 12. Continued.



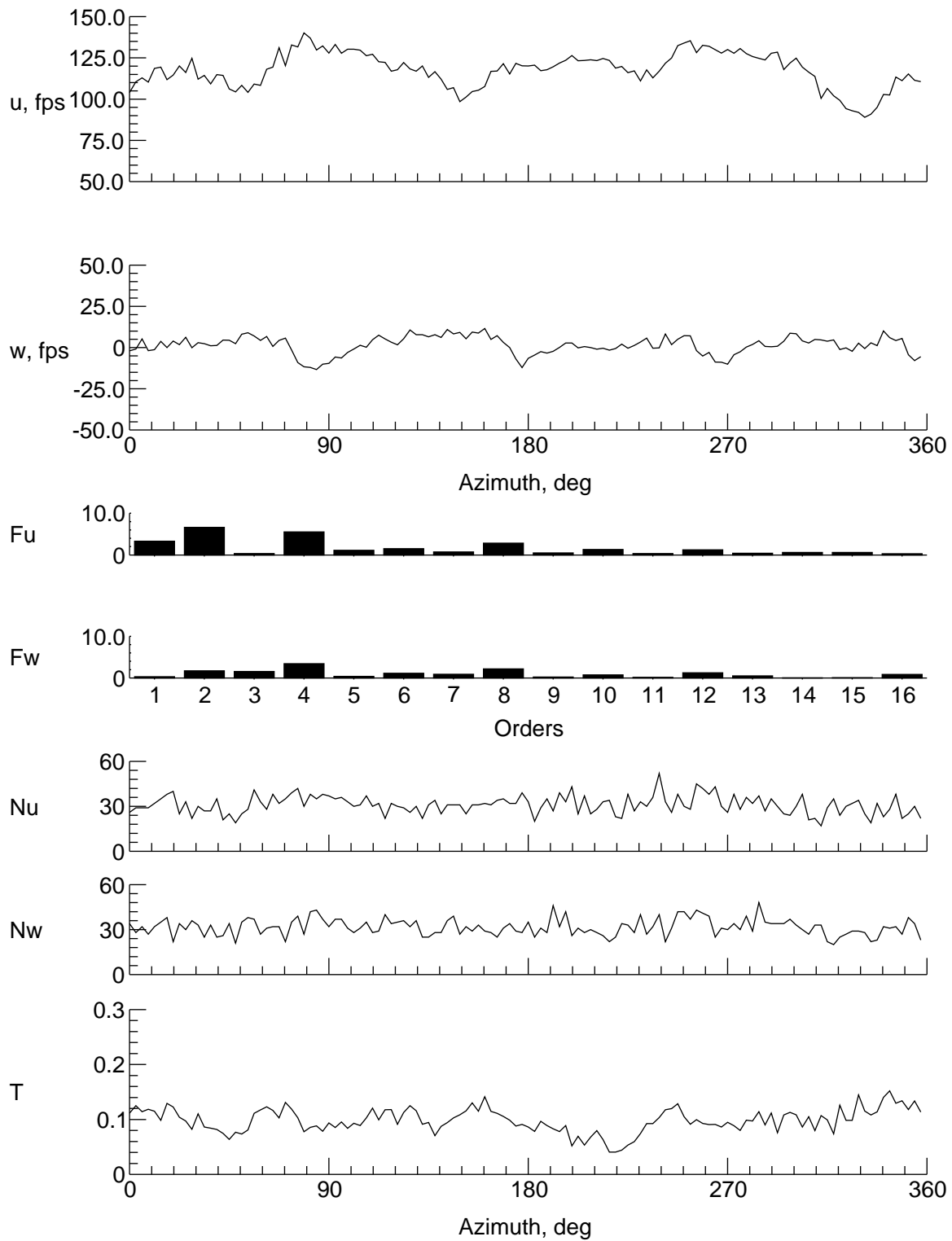
(i) $y = 8$ in., $z = -1.083$ in.

Figure 12. Continued.



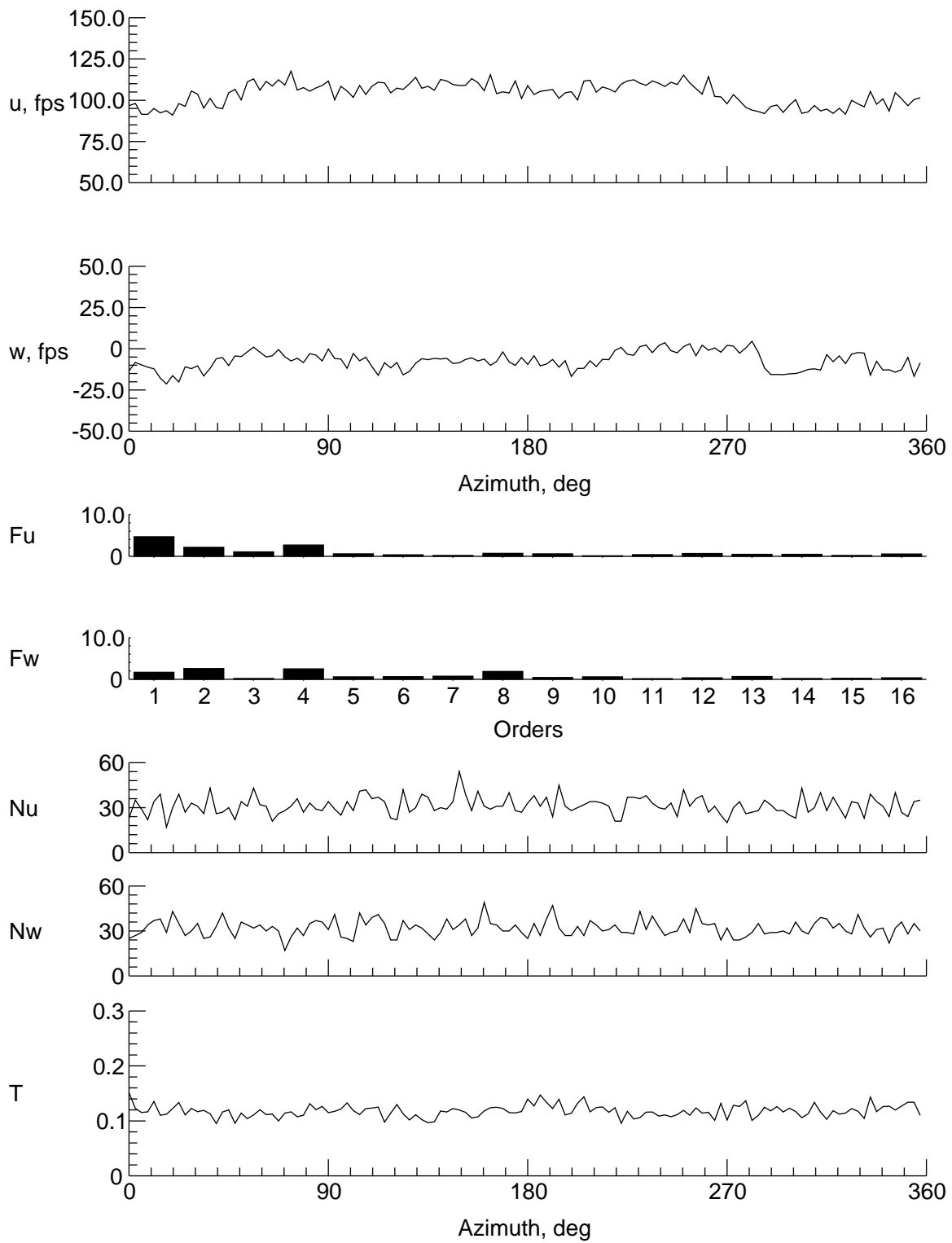
(j) $y = 6$ in., $z = -1.083$ in.

Figure 12. Continued.



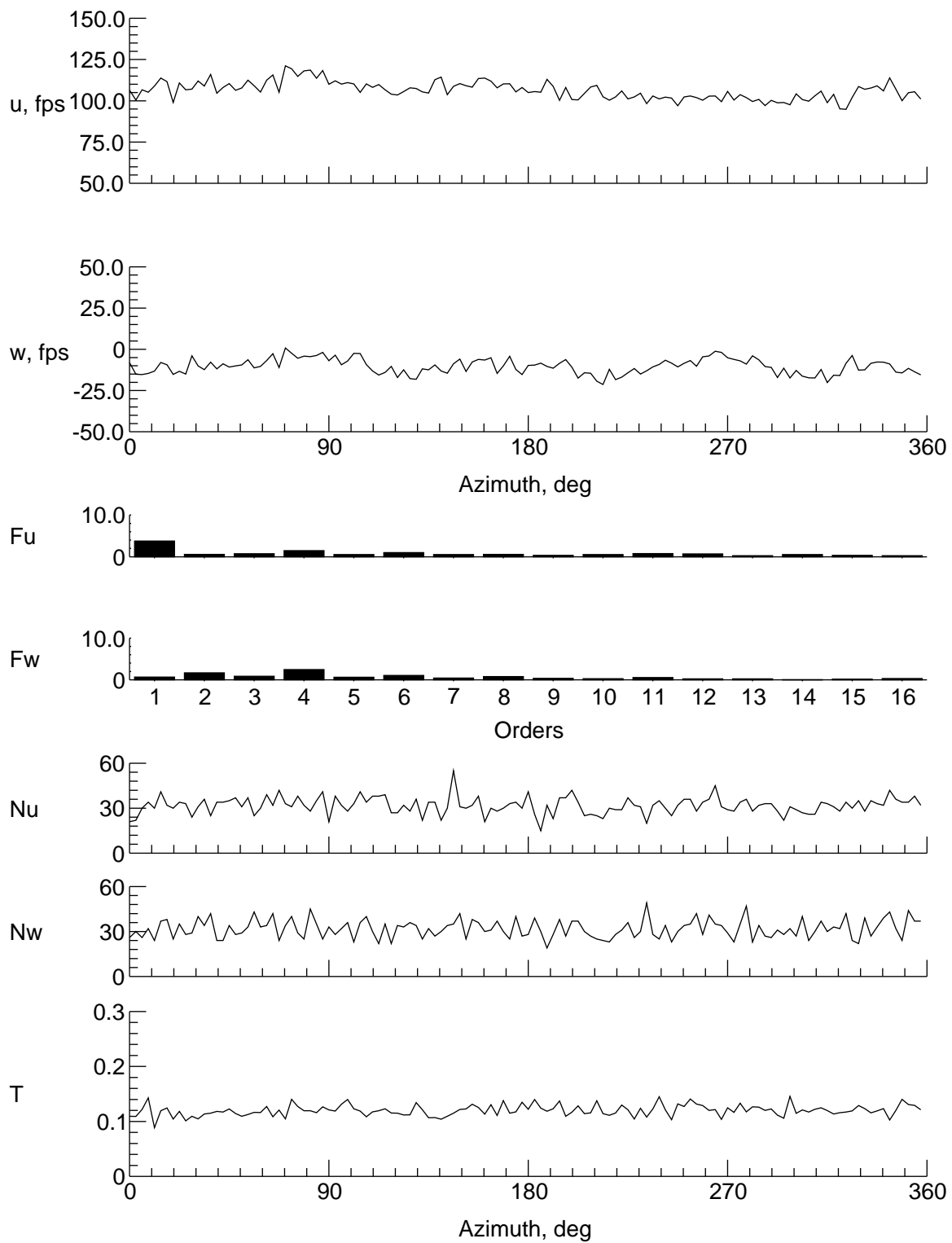
(k) $y = 4$ in., $z = -1.083$ in.

Figure 12. Continued.



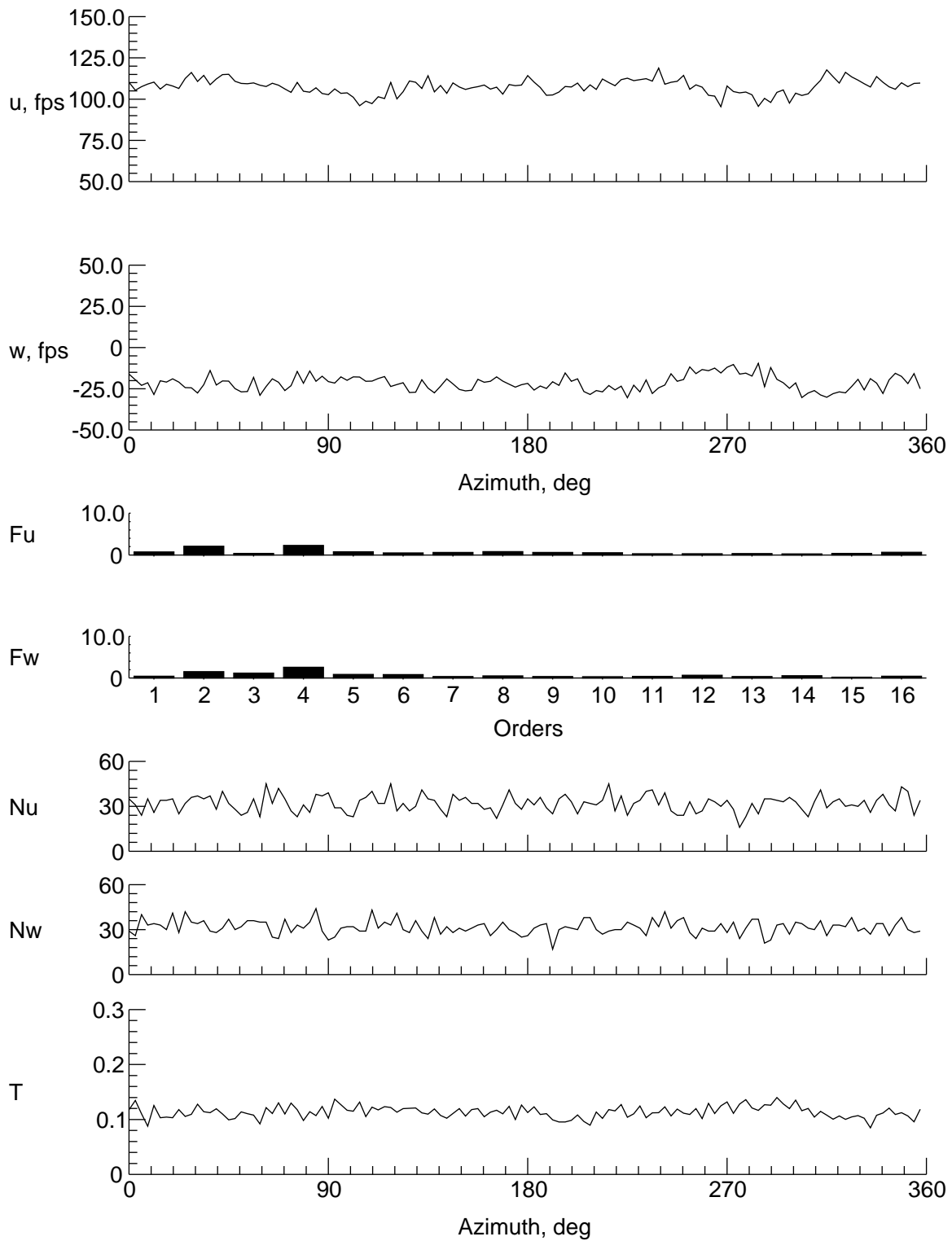
(l) $y = -4$ in., $z = -1.083$ in.

Figure 12. Continued.



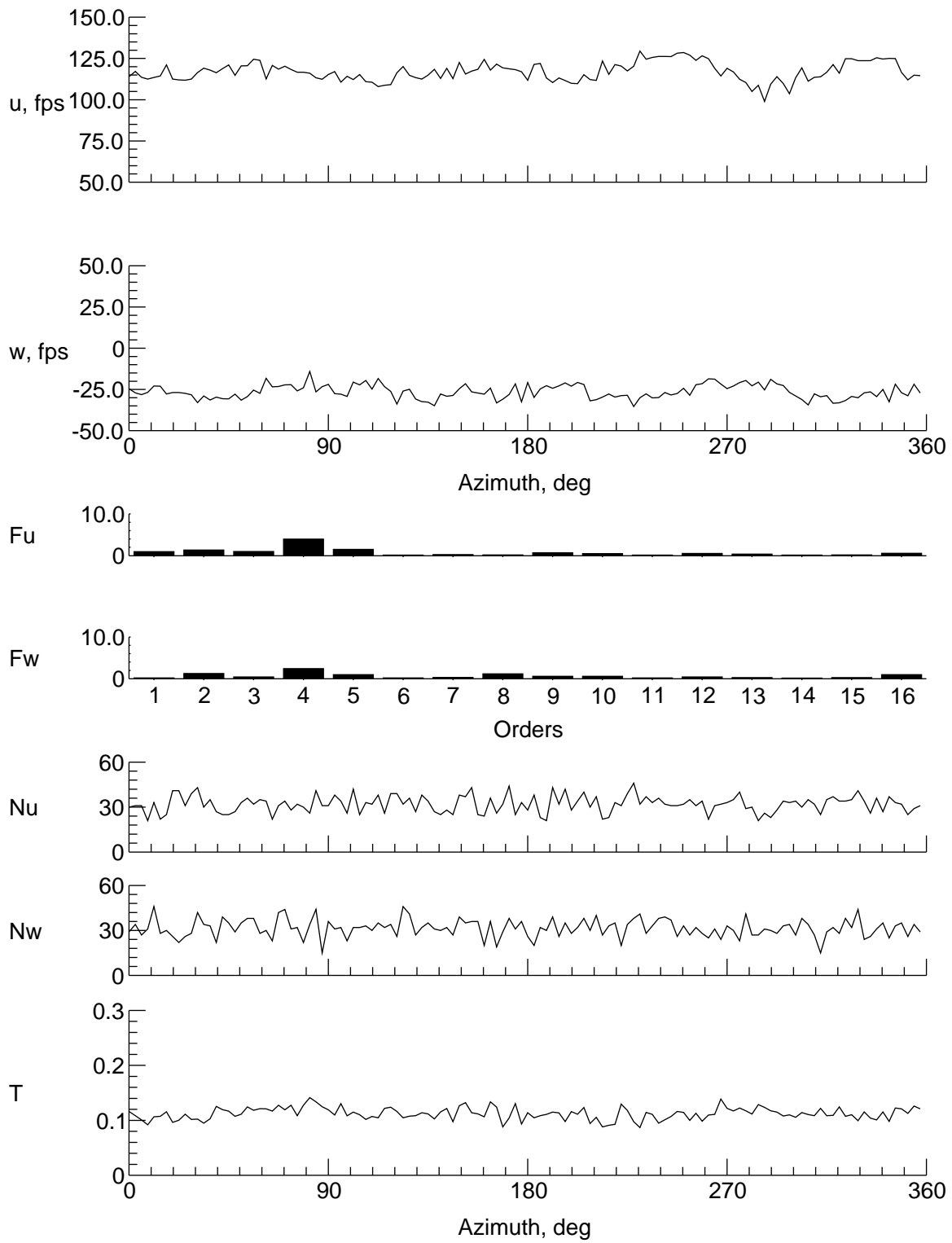
(m) $y = -6$ in., $z = -1.083$ in.

Figure 12. Continued.



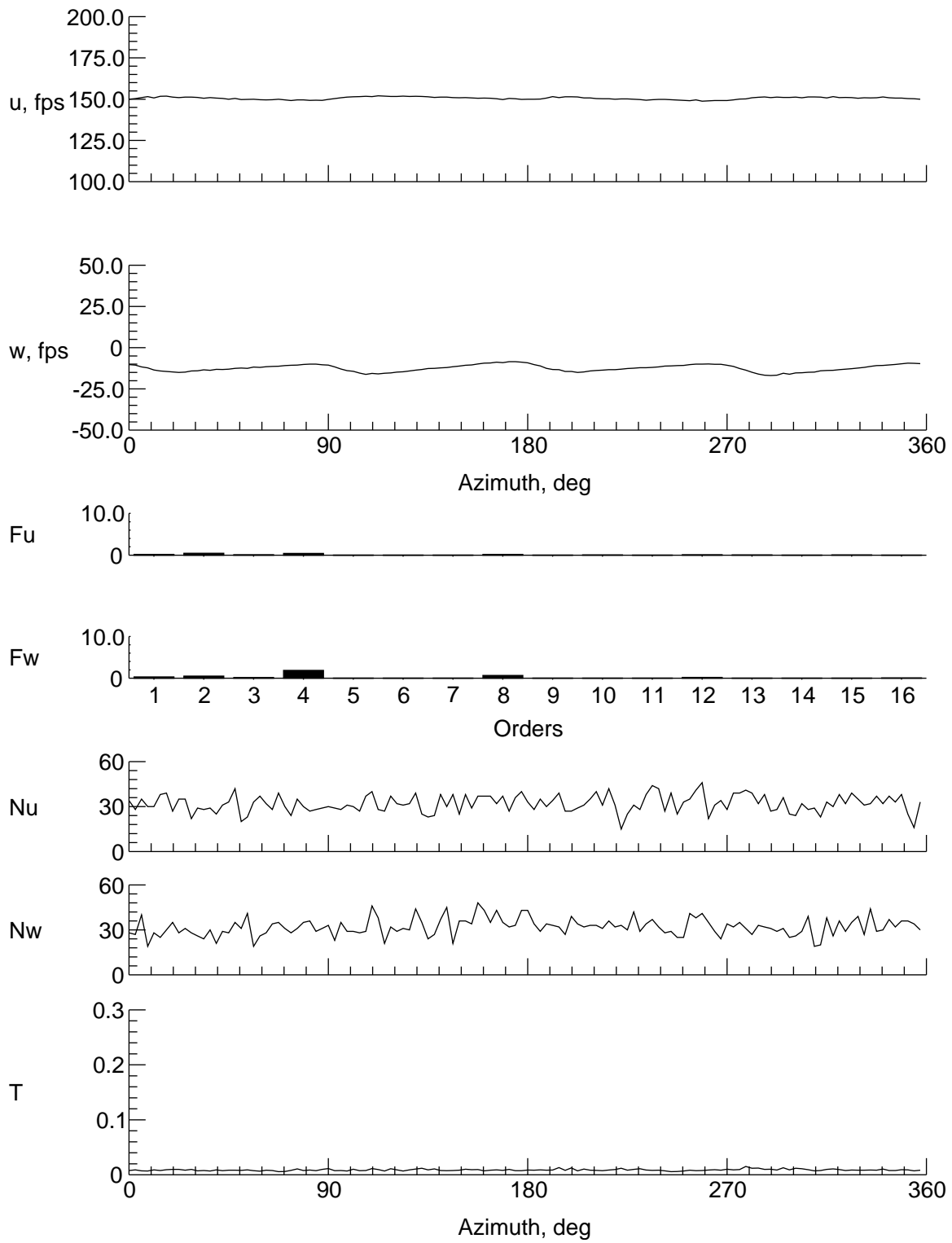
(n) $y = -8$ in., $z = -1.083$ in.

Figure 12. Continued.



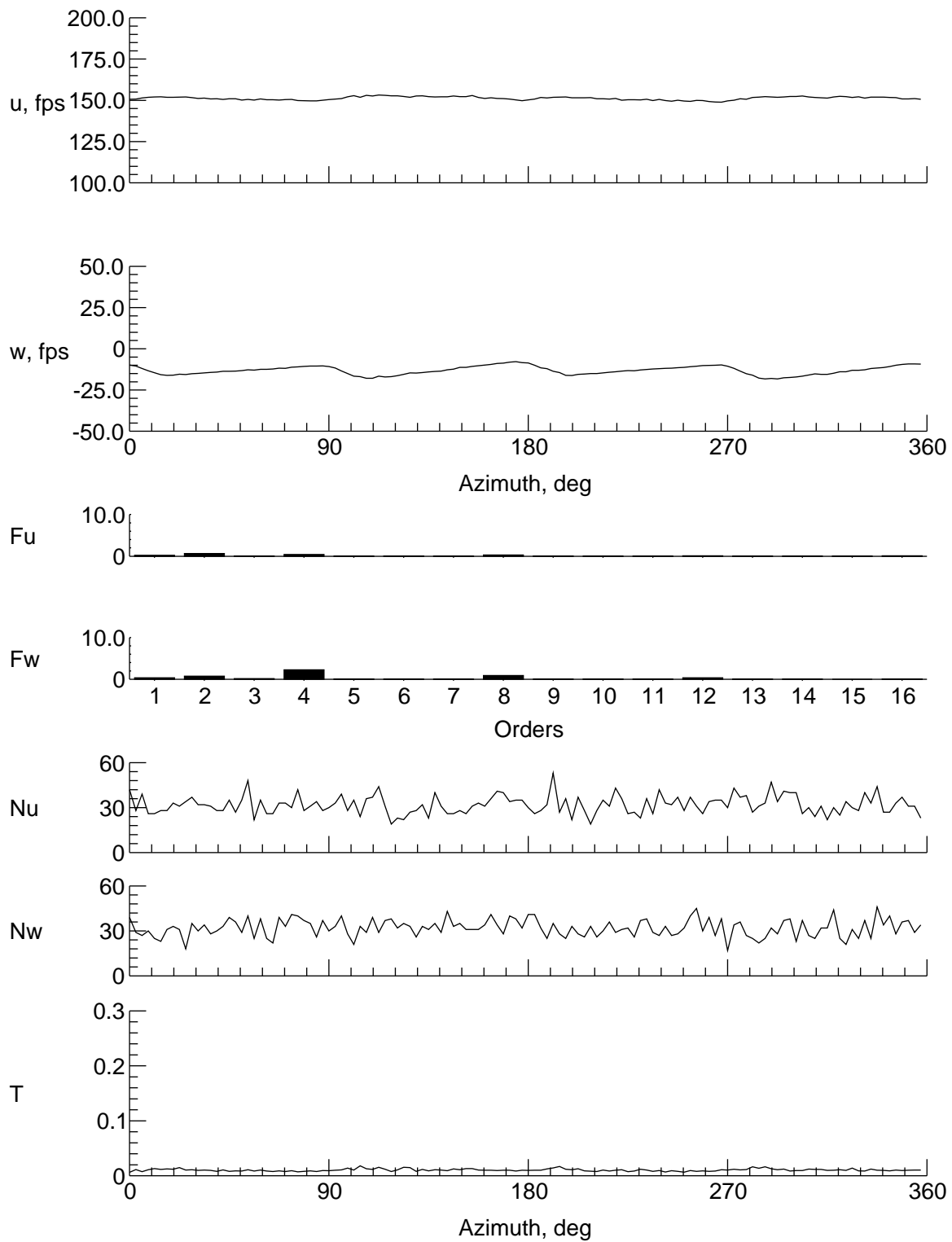
(o) $y = -9$ in., $z = -1.083$ in.

Figure 12. Concluded.



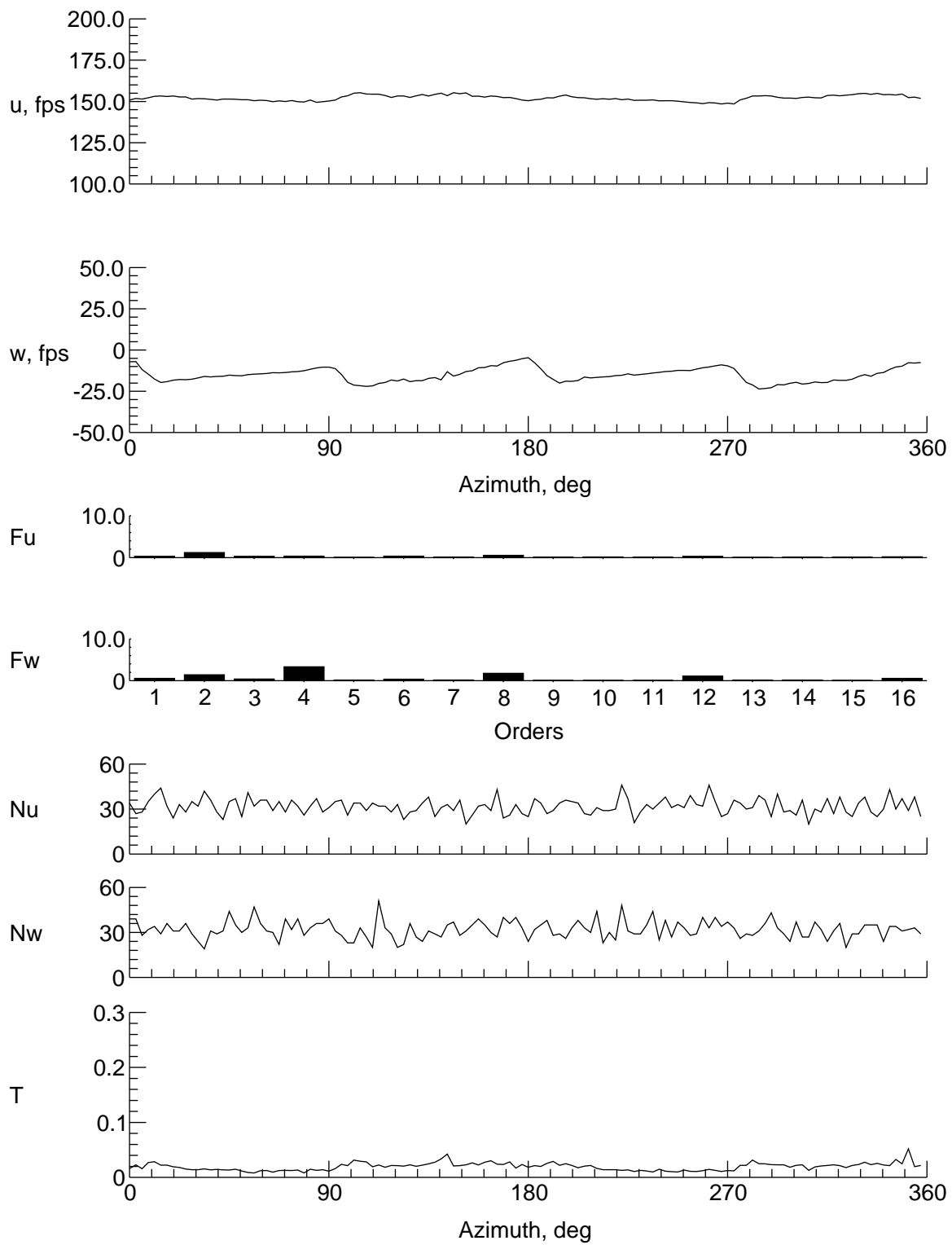
(a) $y = 0$ in., $z = 7.796$ in.

Figure 13. Velocity and turbulence at station 20 in.



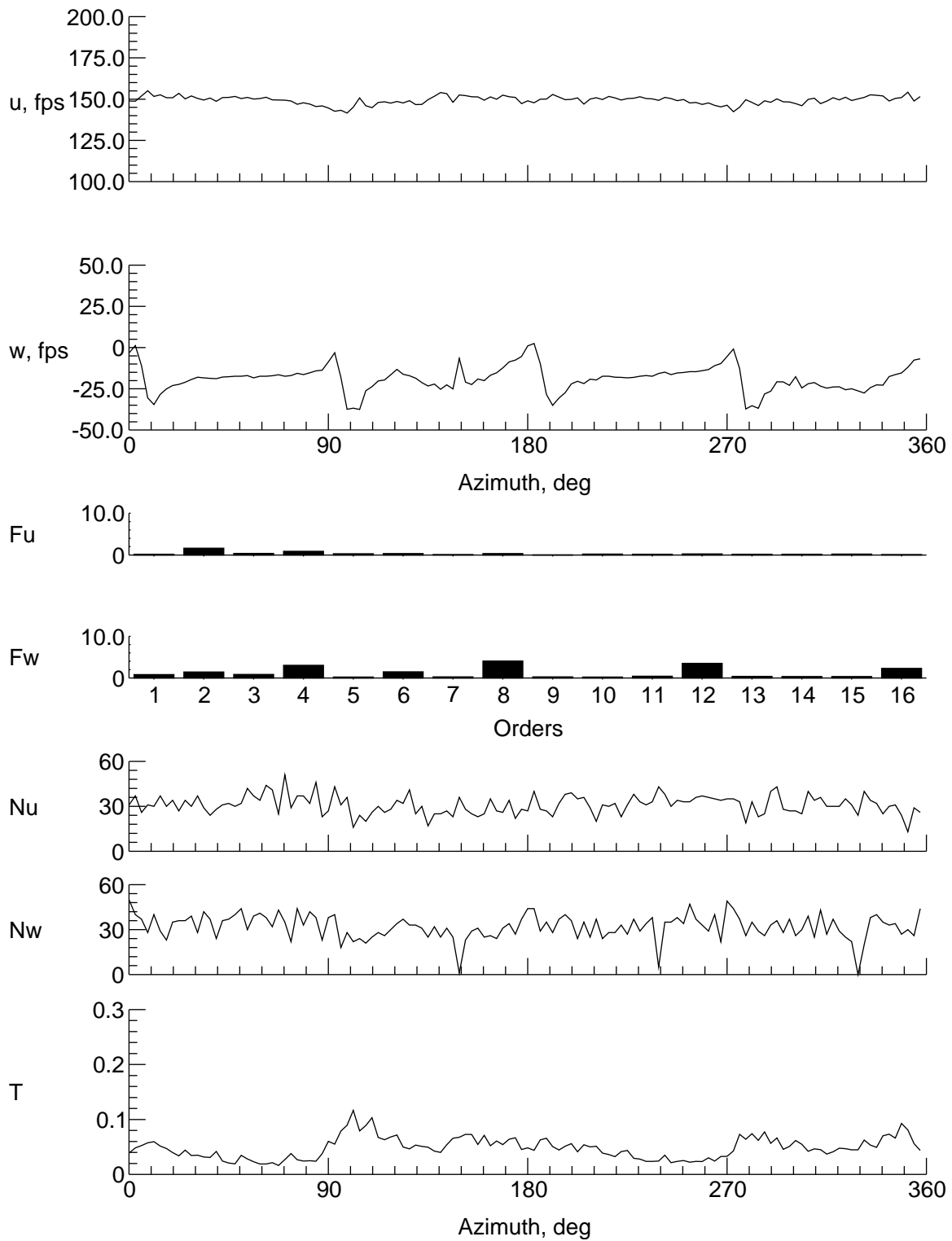
(b) $y = 0$ in., $z = 6.796$ in.

Figure 13. Continued.



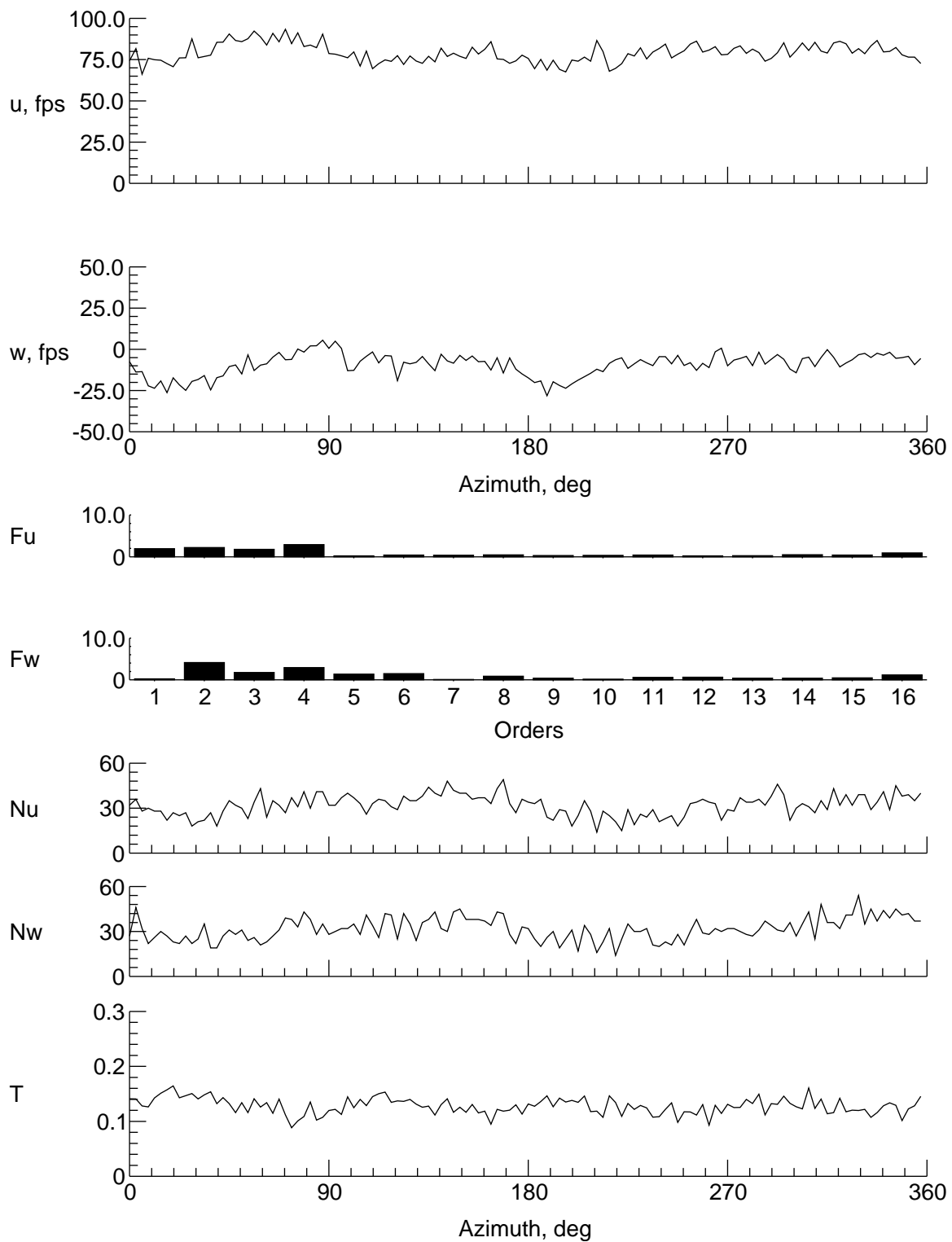
(c) $y = 0$ in., $z = 4.796$ in.

Figure 13. Continued.



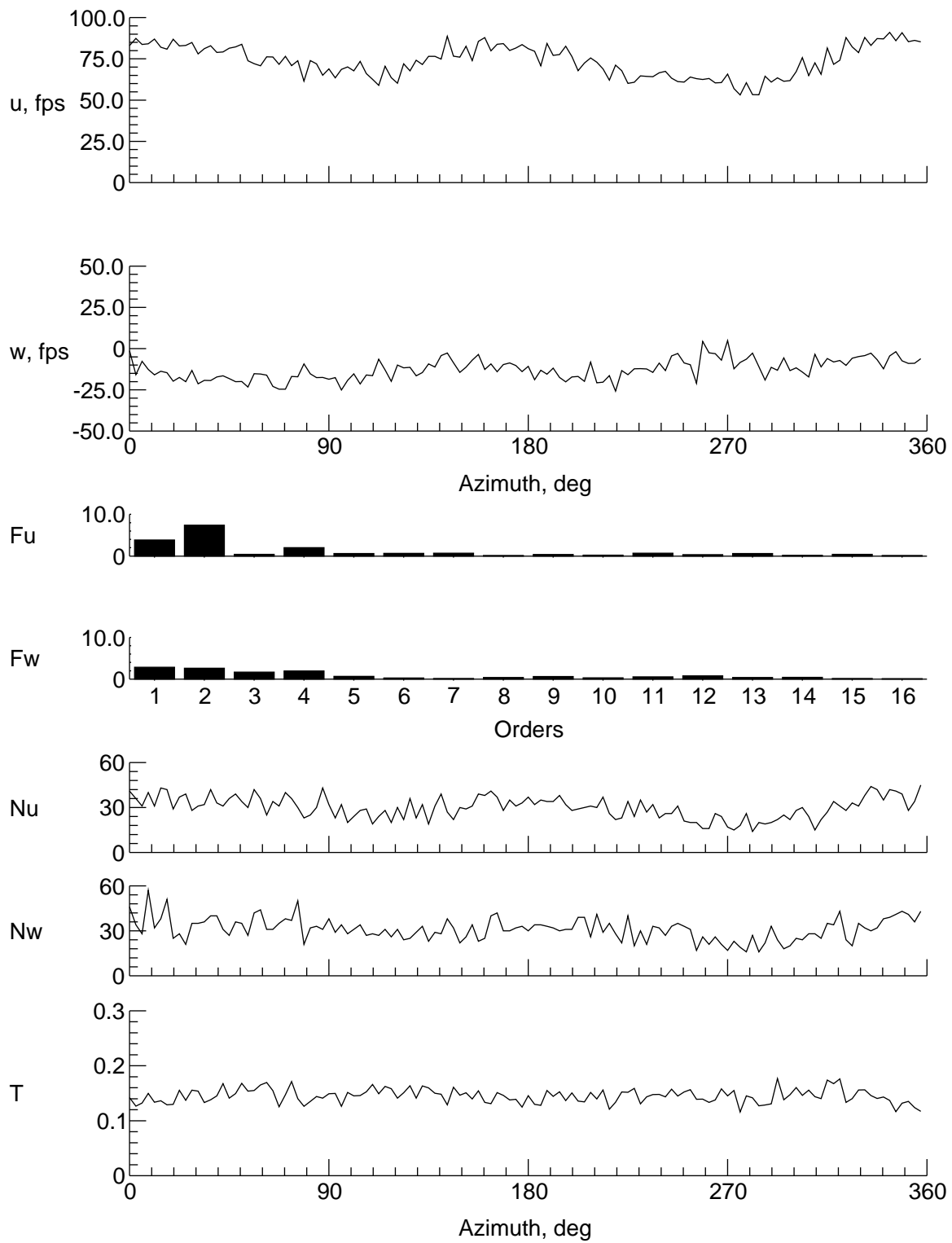
(d) $y = 0$ in., $z = 2.796$ in.

Figure 13. Continued.



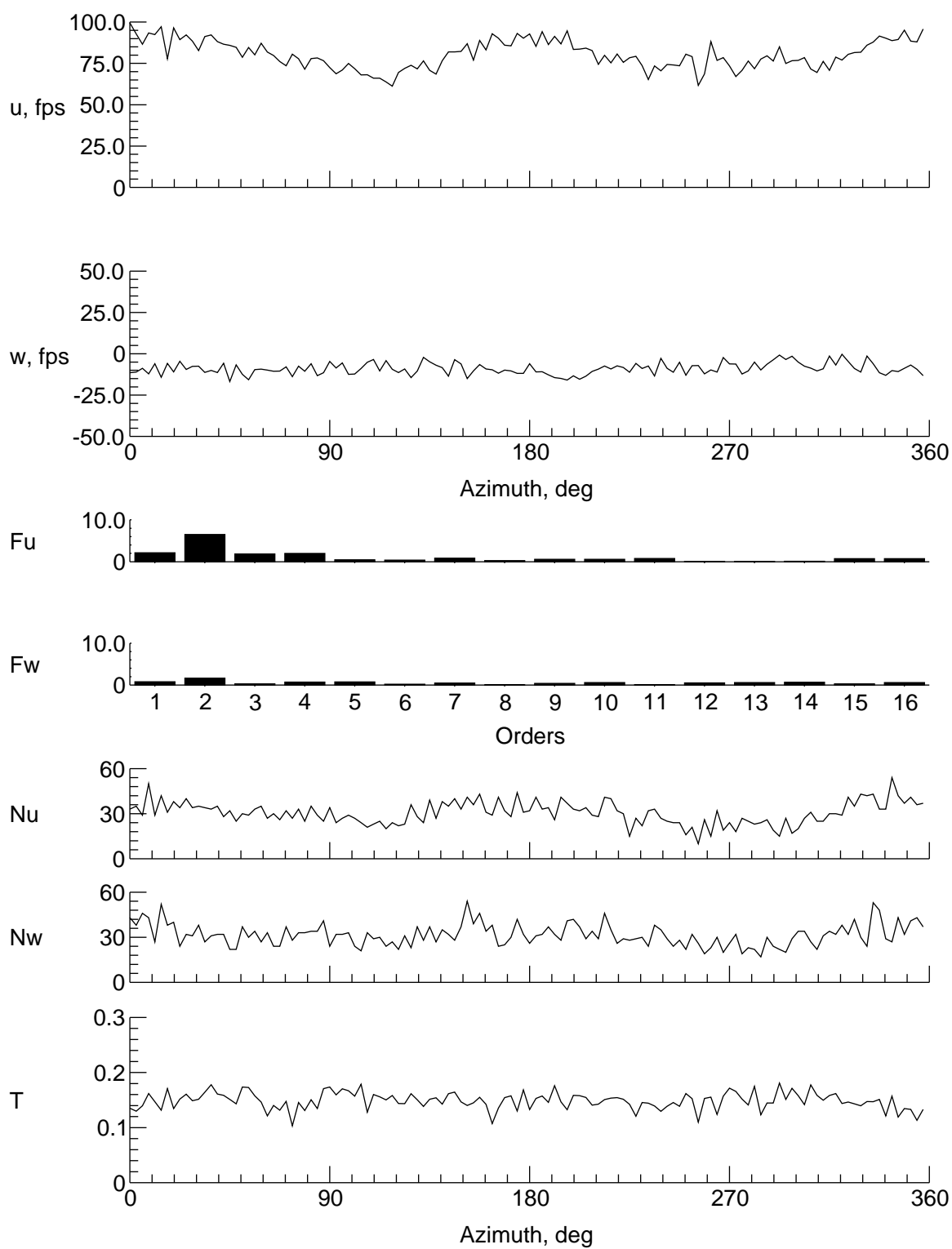
(e) $y = 0$ in., $z = -1.204$ in.

Figure 13. Continued.



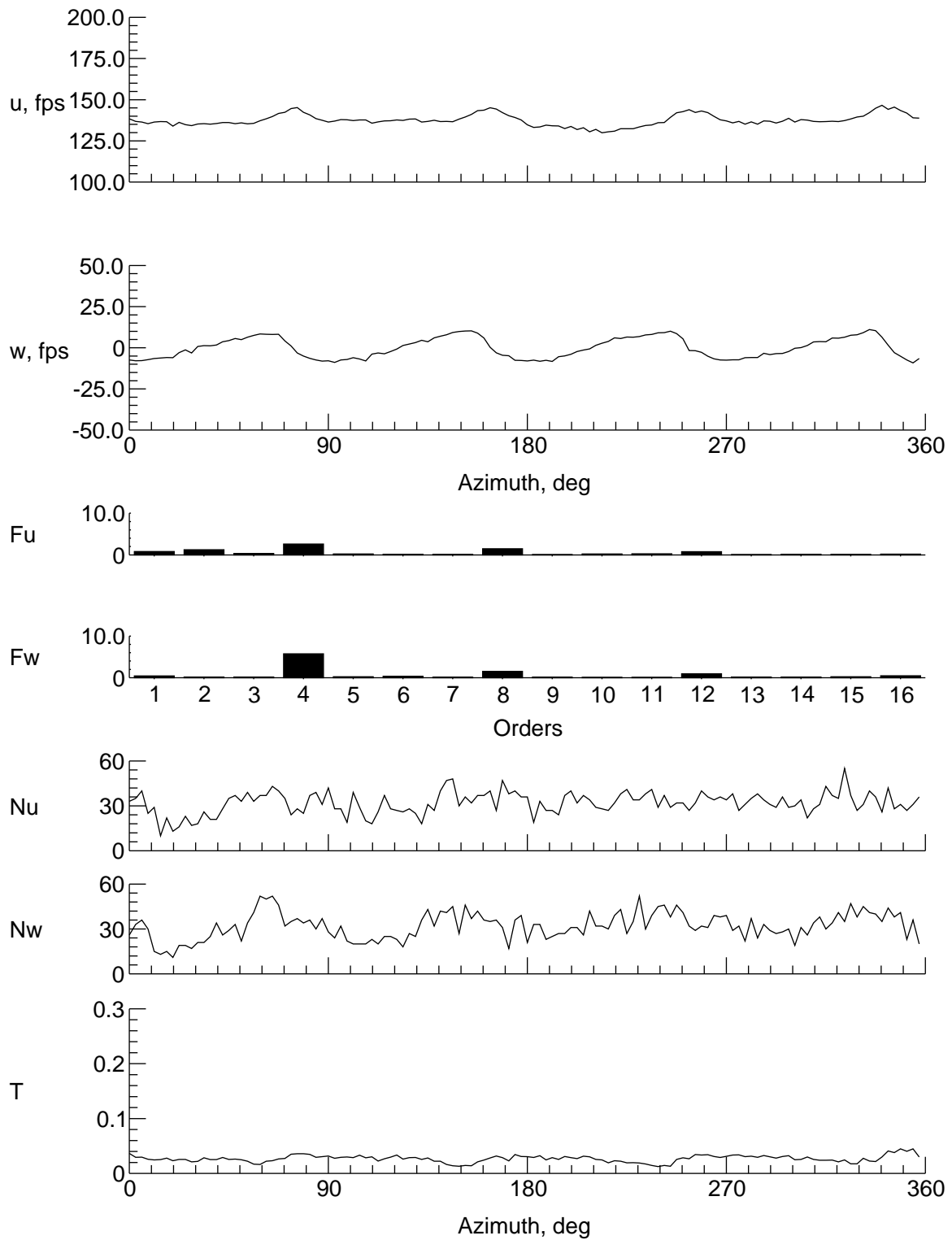
(f) $y = 0$ in., $z = -5.204$ in.

Figure 13. Continued.



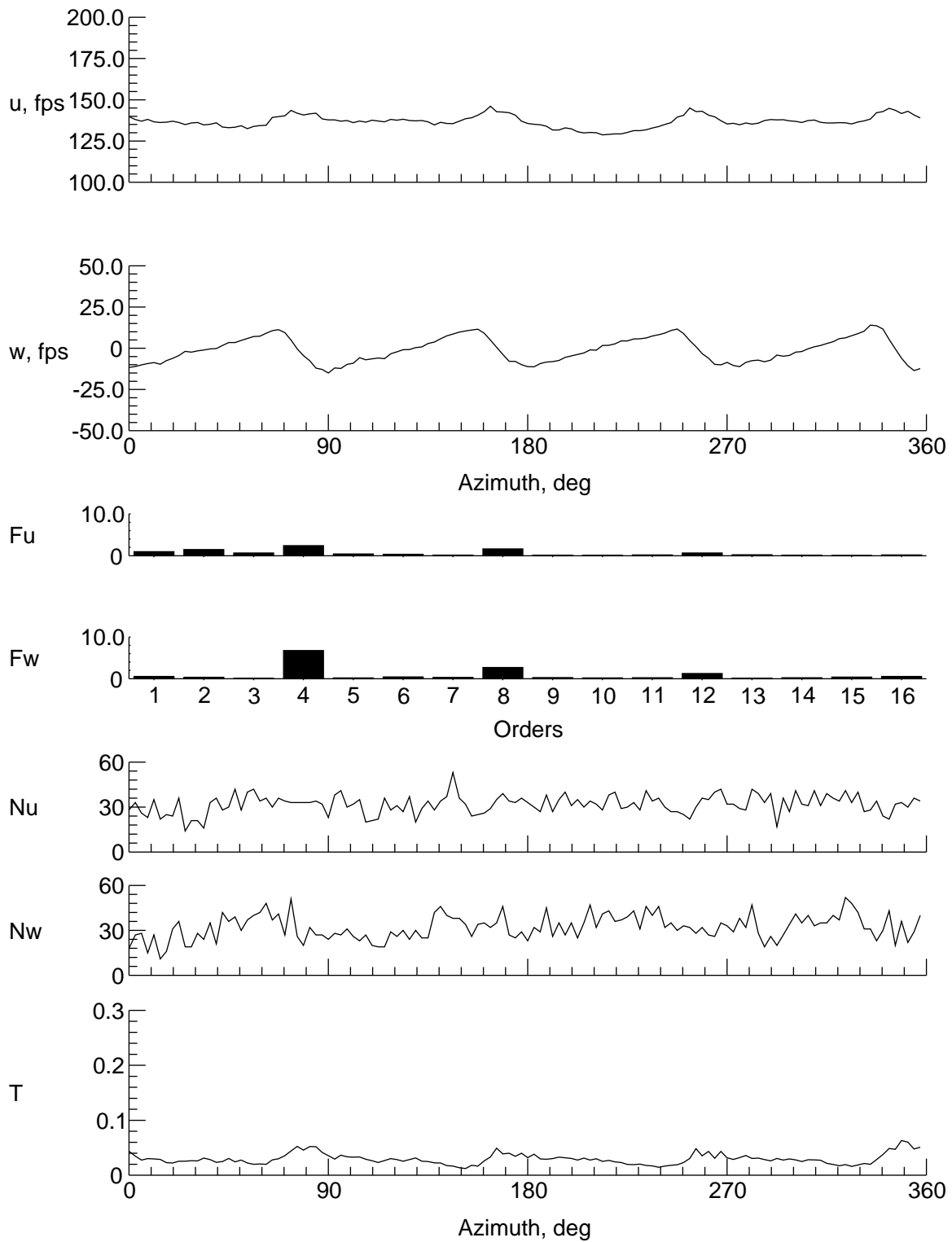
(g) $y = 0$ in., $z = -7.204$ in.

Figure 13. Continued.



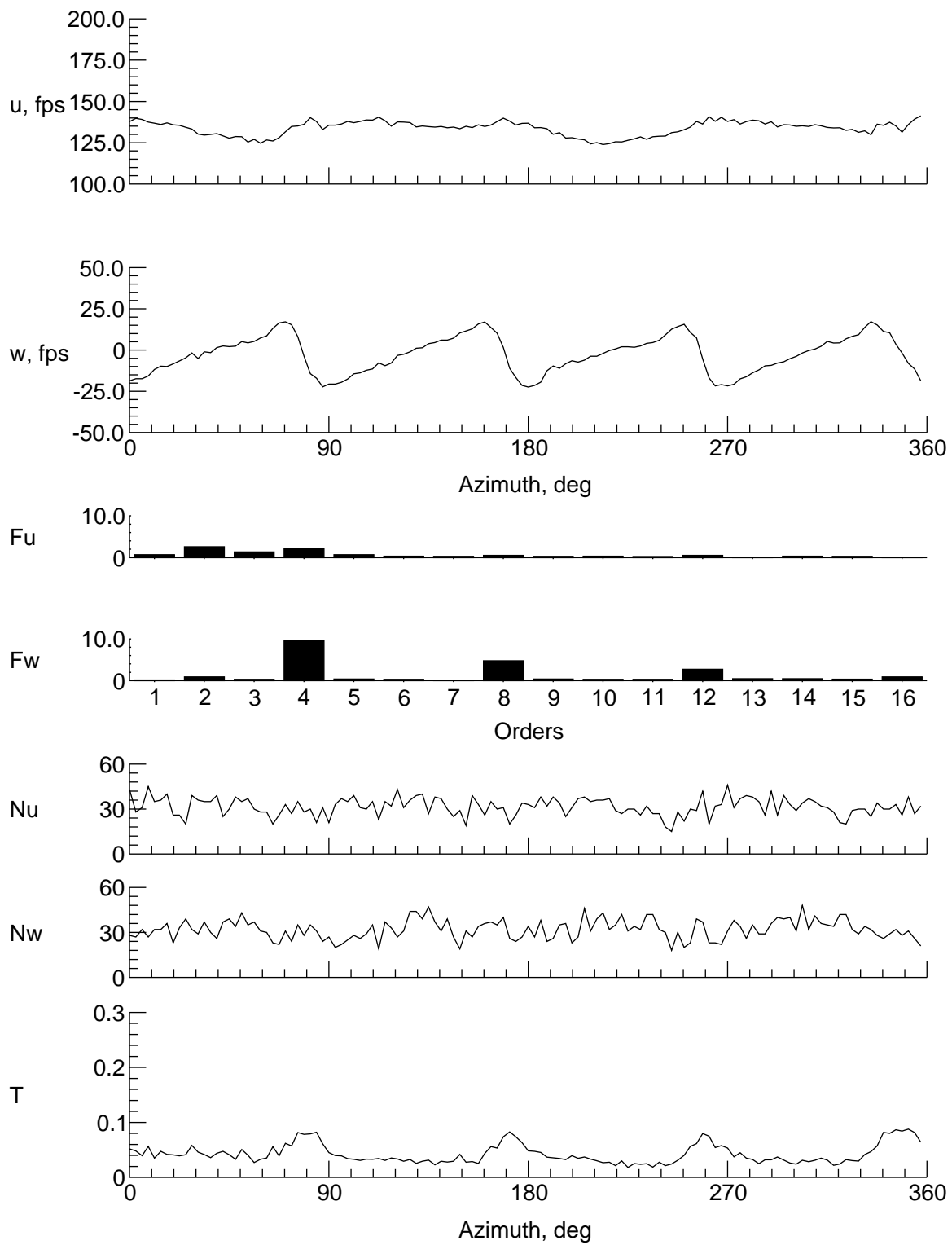
(h) $y = 9$ in., $z = -1.204$ in.

Figure 13. Continued.



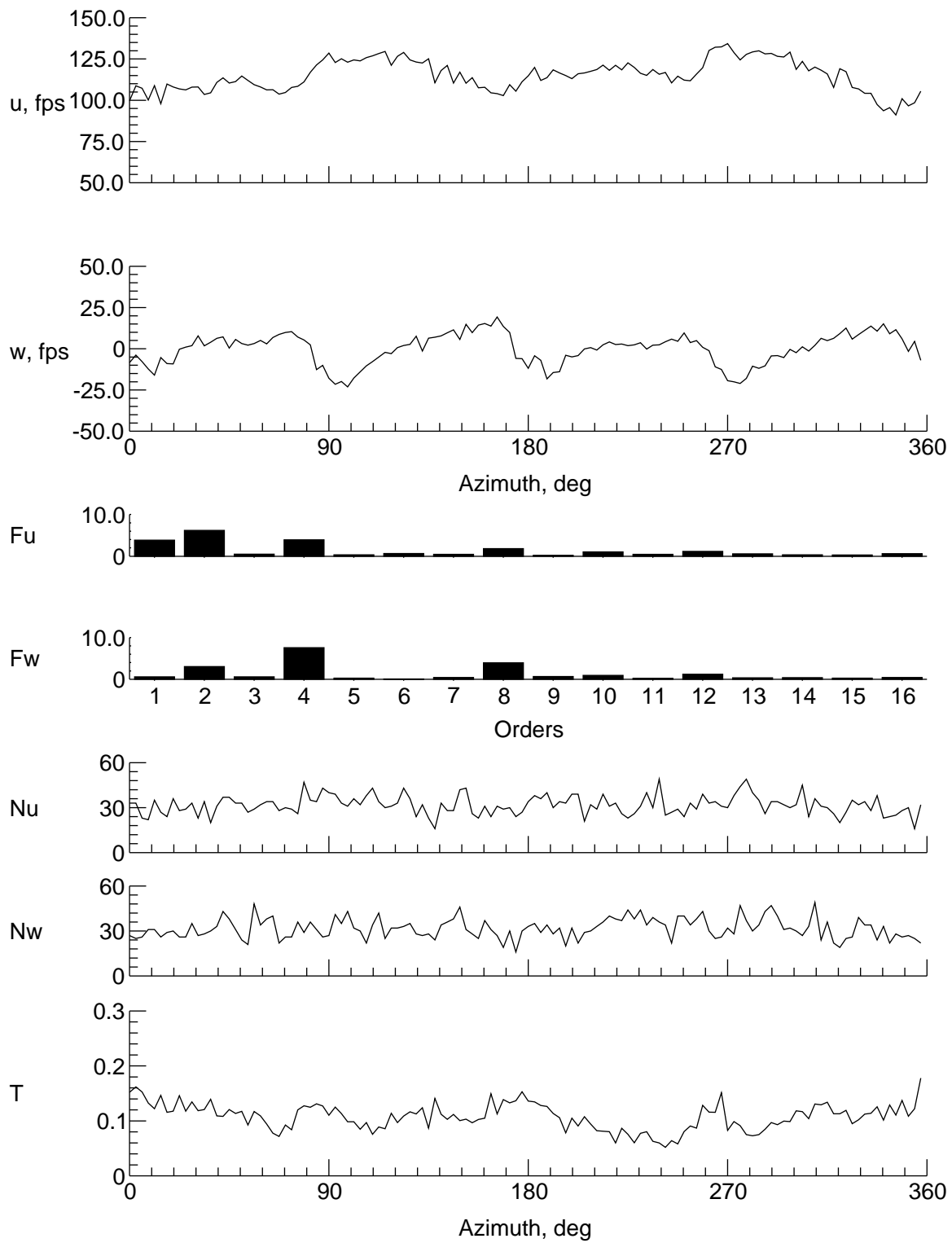
(i) $y = 8$ in., $z = -1.204$ in.

Figure 13. Continued.



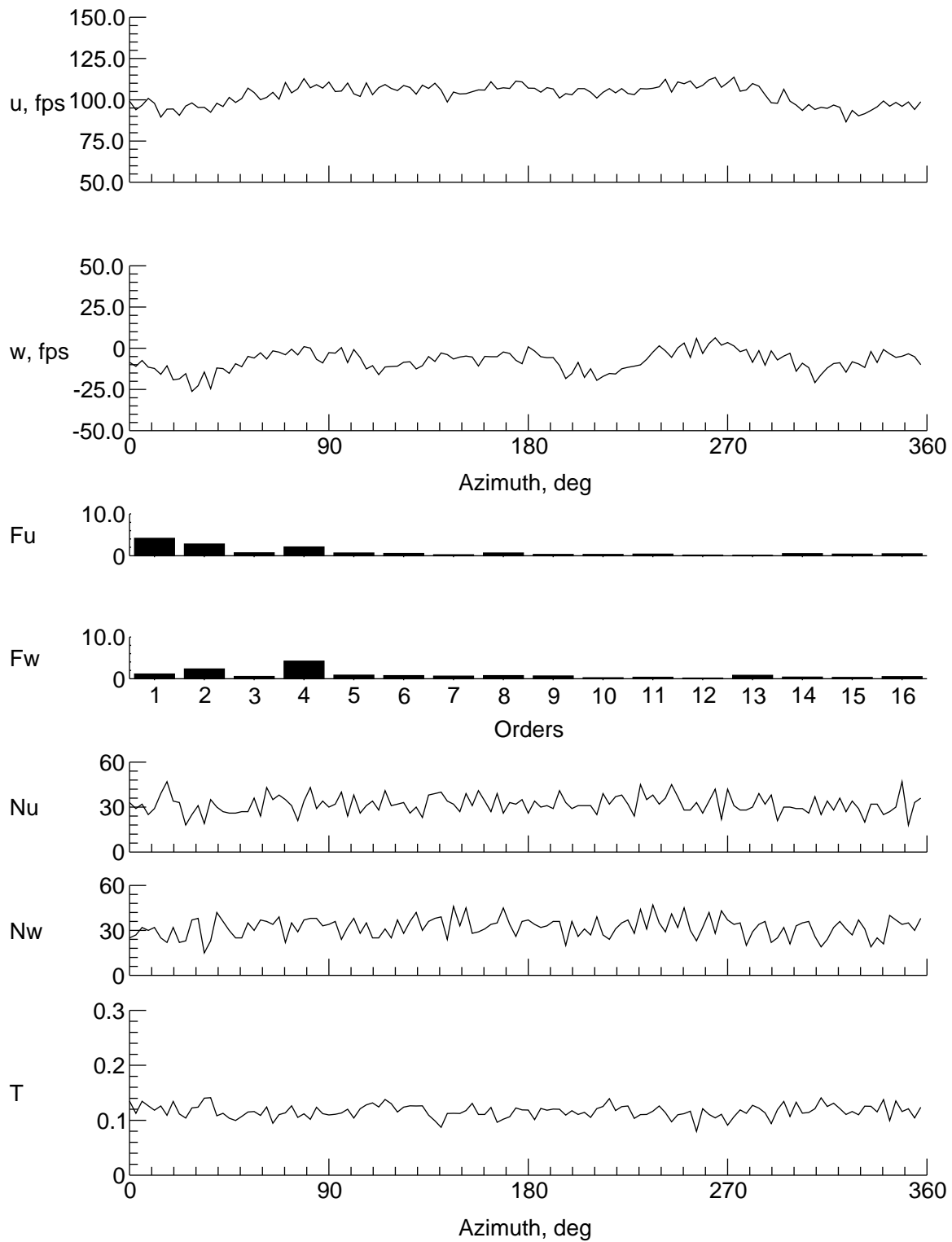
(j) $y = 6$ in., $z = -1.204$ in.

Figure 13. Continued.



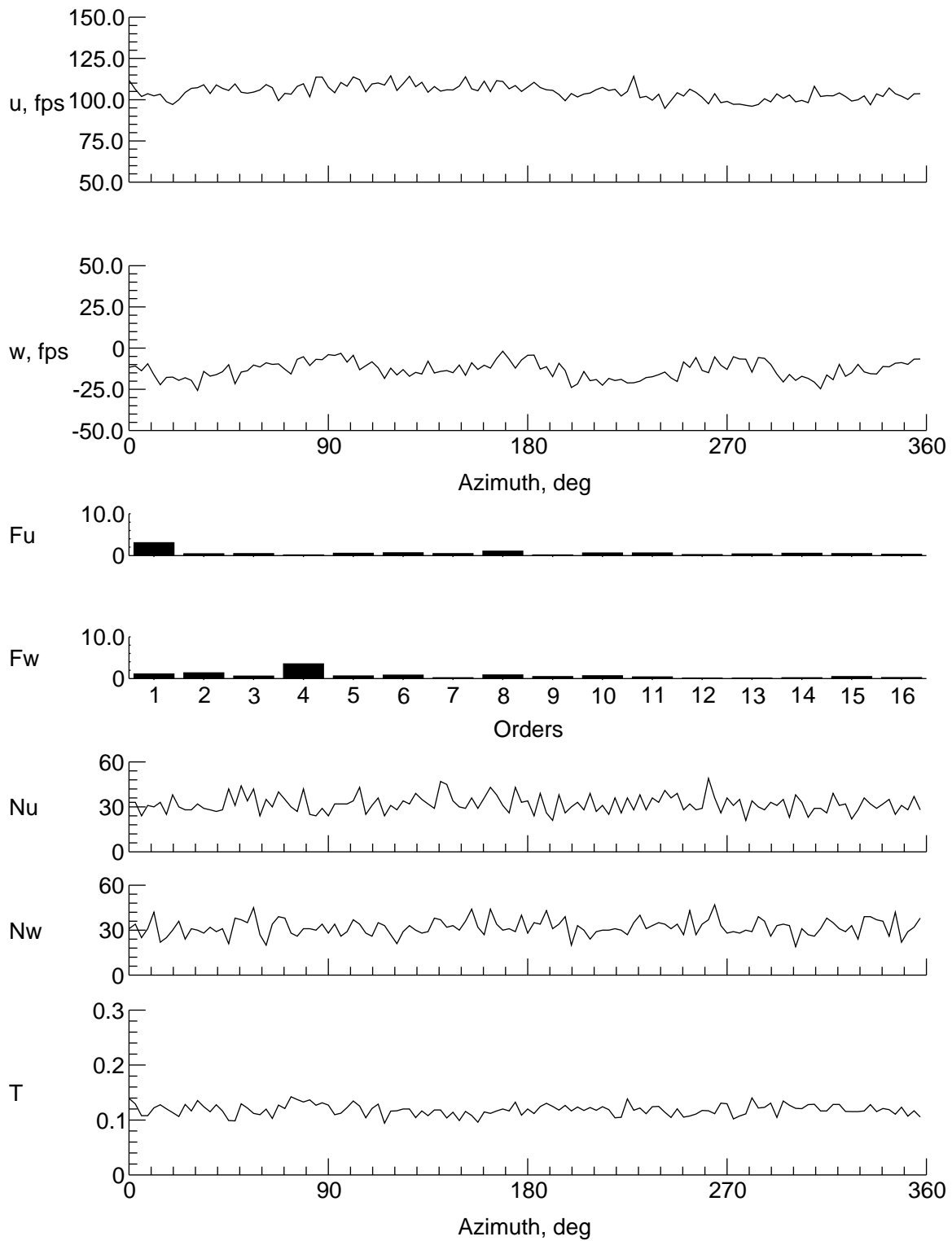
(k) $y = 4$ in., $z = -1.204$ in.

Figure 13. Continued.



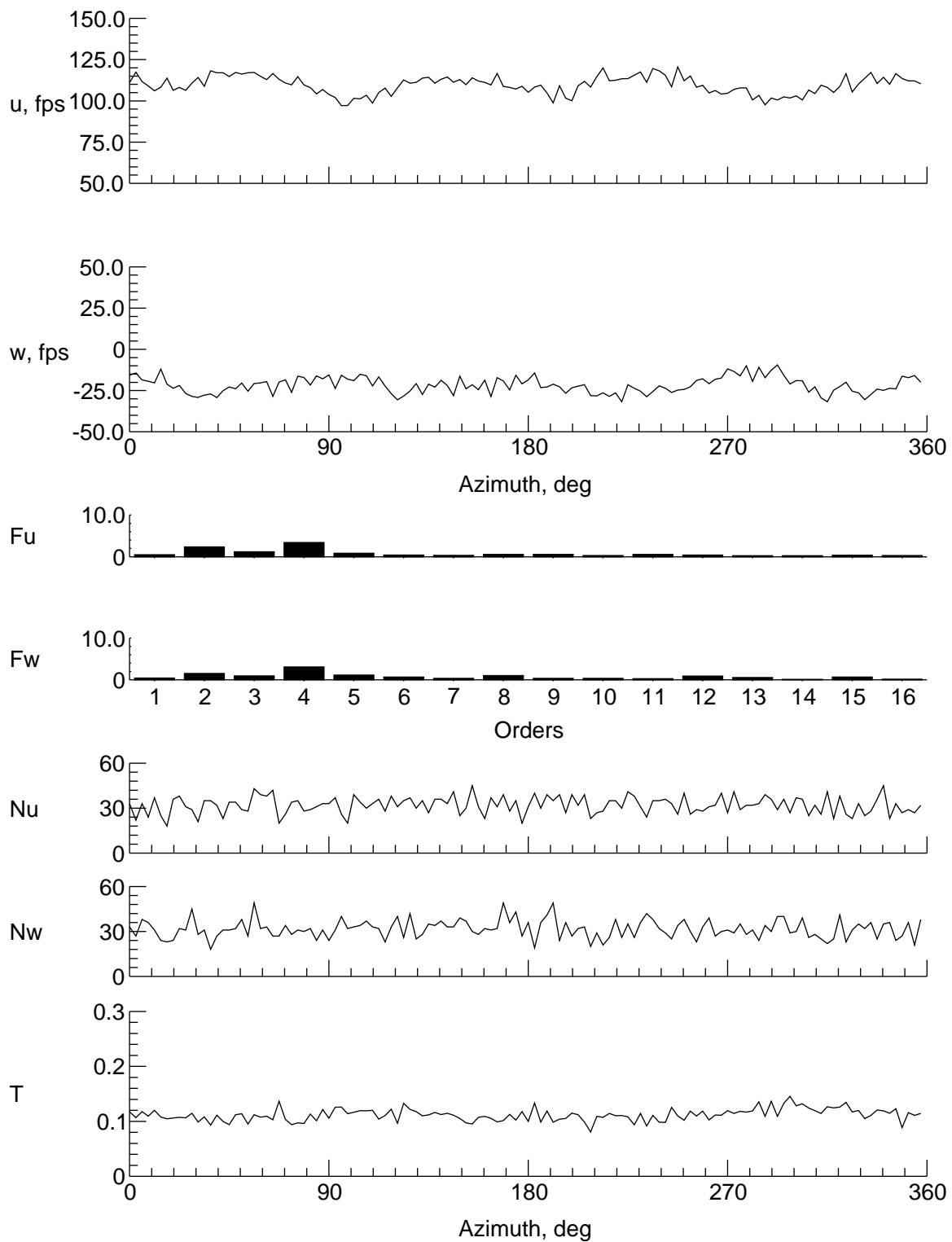
(l) $y = -4$ in., $z = -1.204$ in.

Figure 13. Continued.



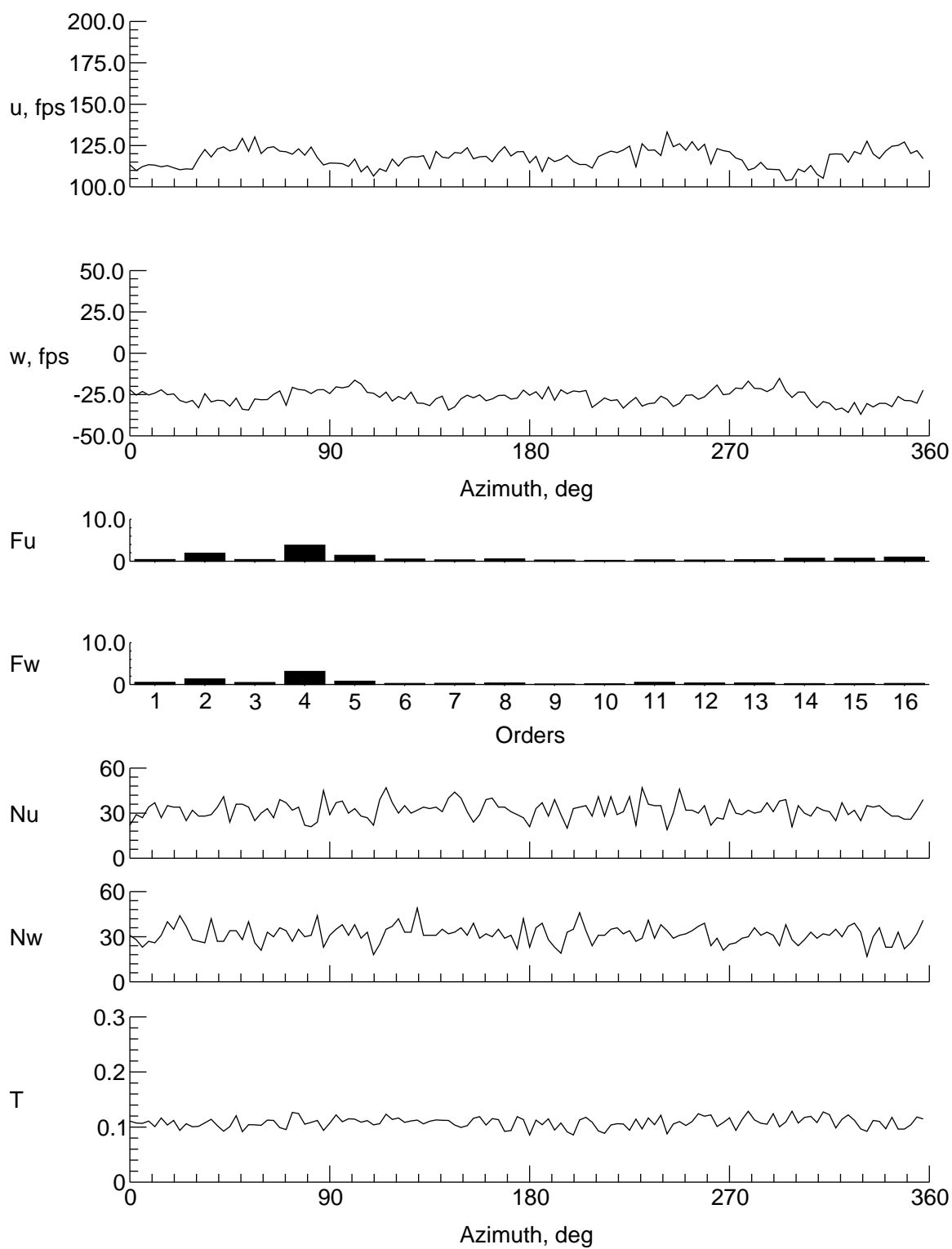
(m) $y = -6$ in., $z = -1.204$ in.

Figure 13. Continued.



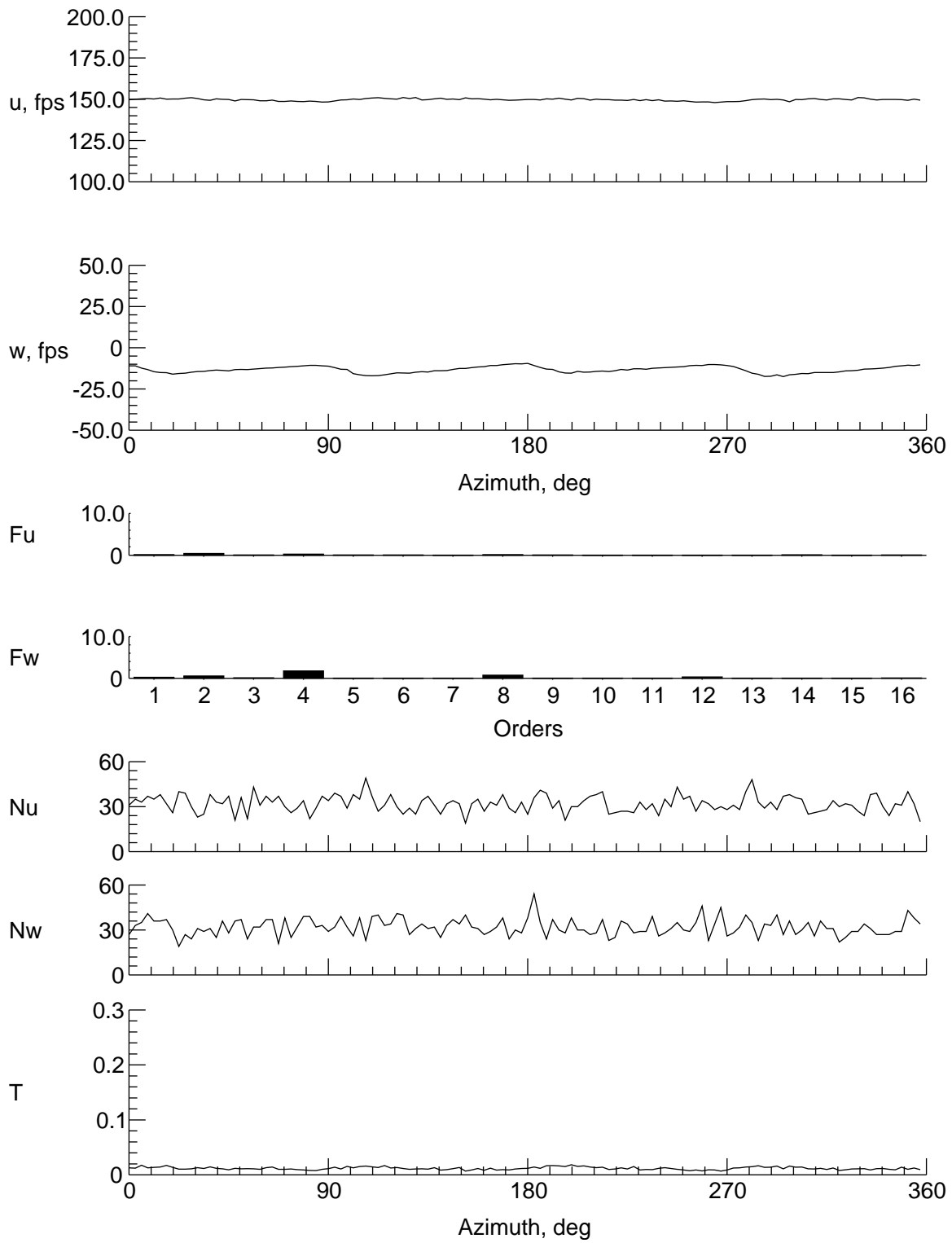
(n) $y = -8$ in., $z = -1.204$ in.

Figure 13. Continued.



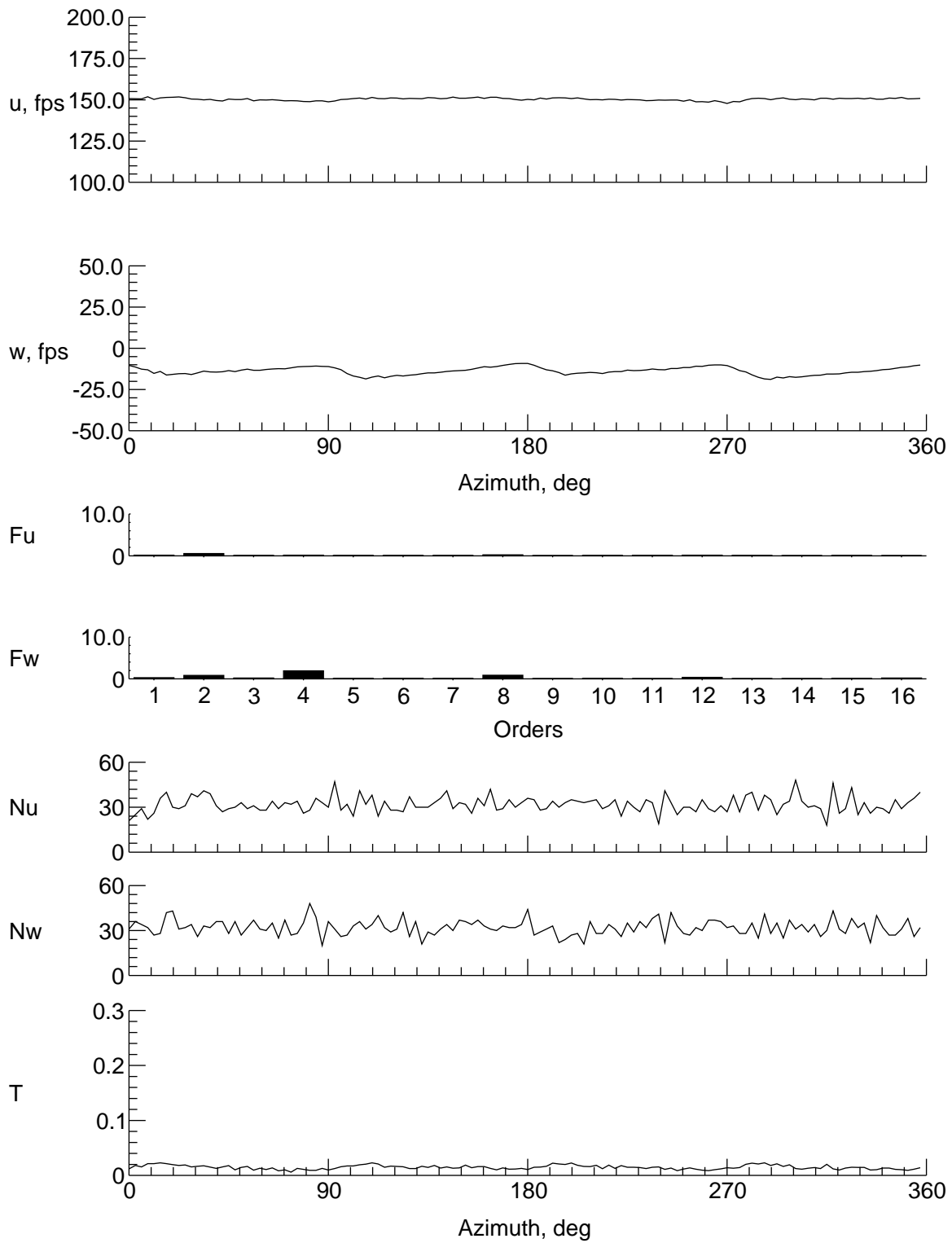
(o) $y = 9$ in., $z = -1.204$ in.

Figure 13. Concluded.



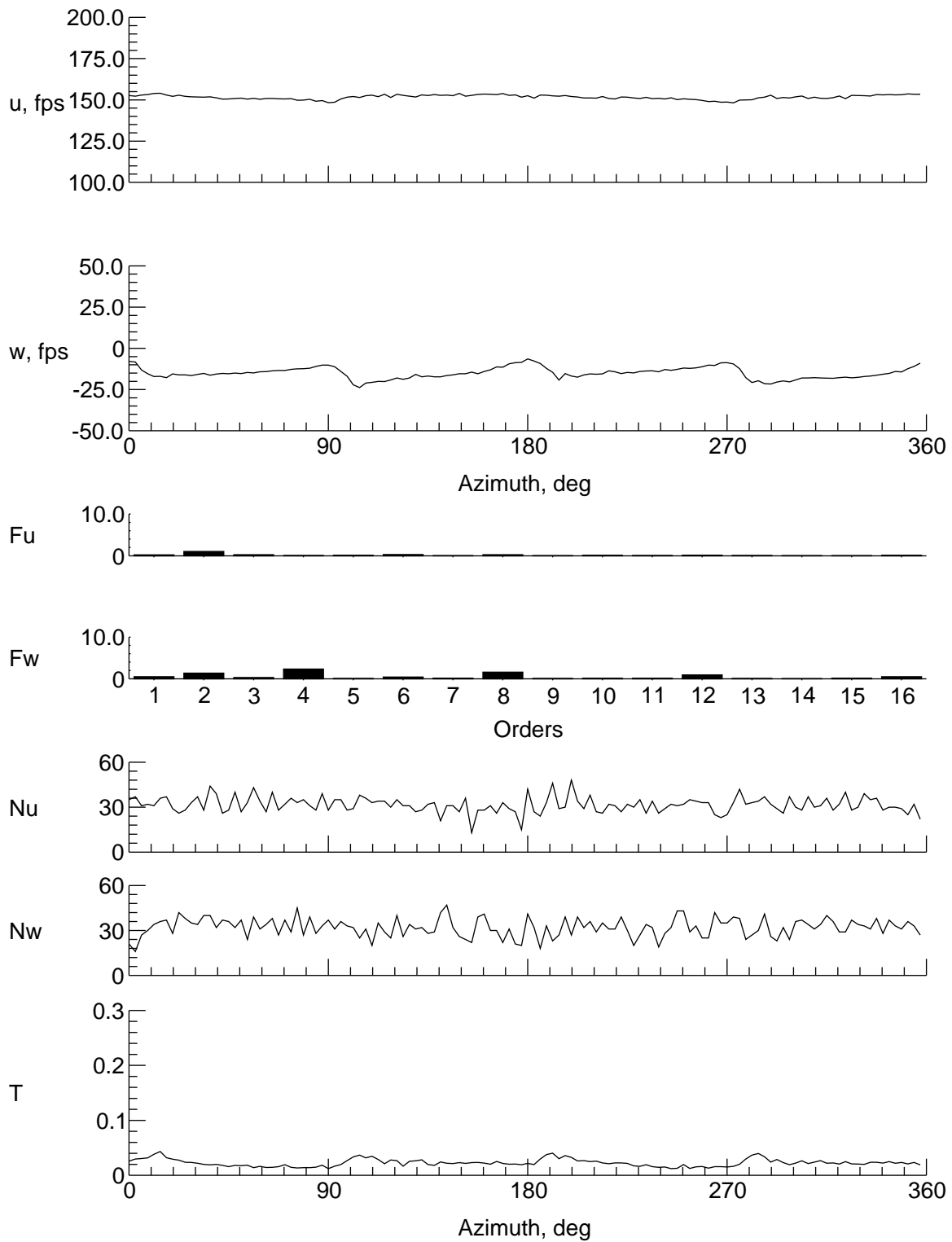
(a) $y = 0$ in., $z = 7.676$ in.

Figure 14. Velocity and turbulence at station 22 in.



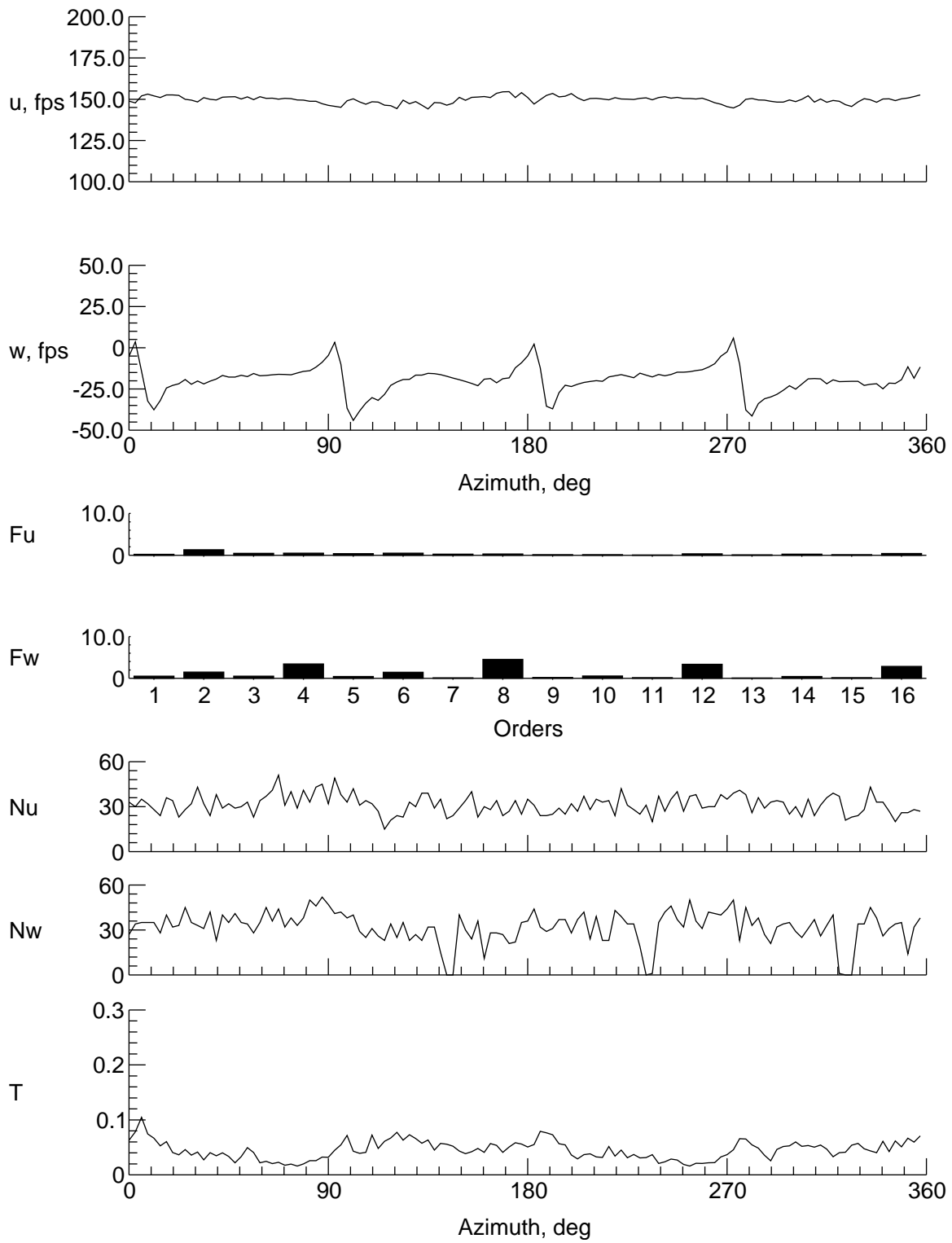
(b) $y = 0$ in., $z = 6.676$ in.

Figure 14. Continued.



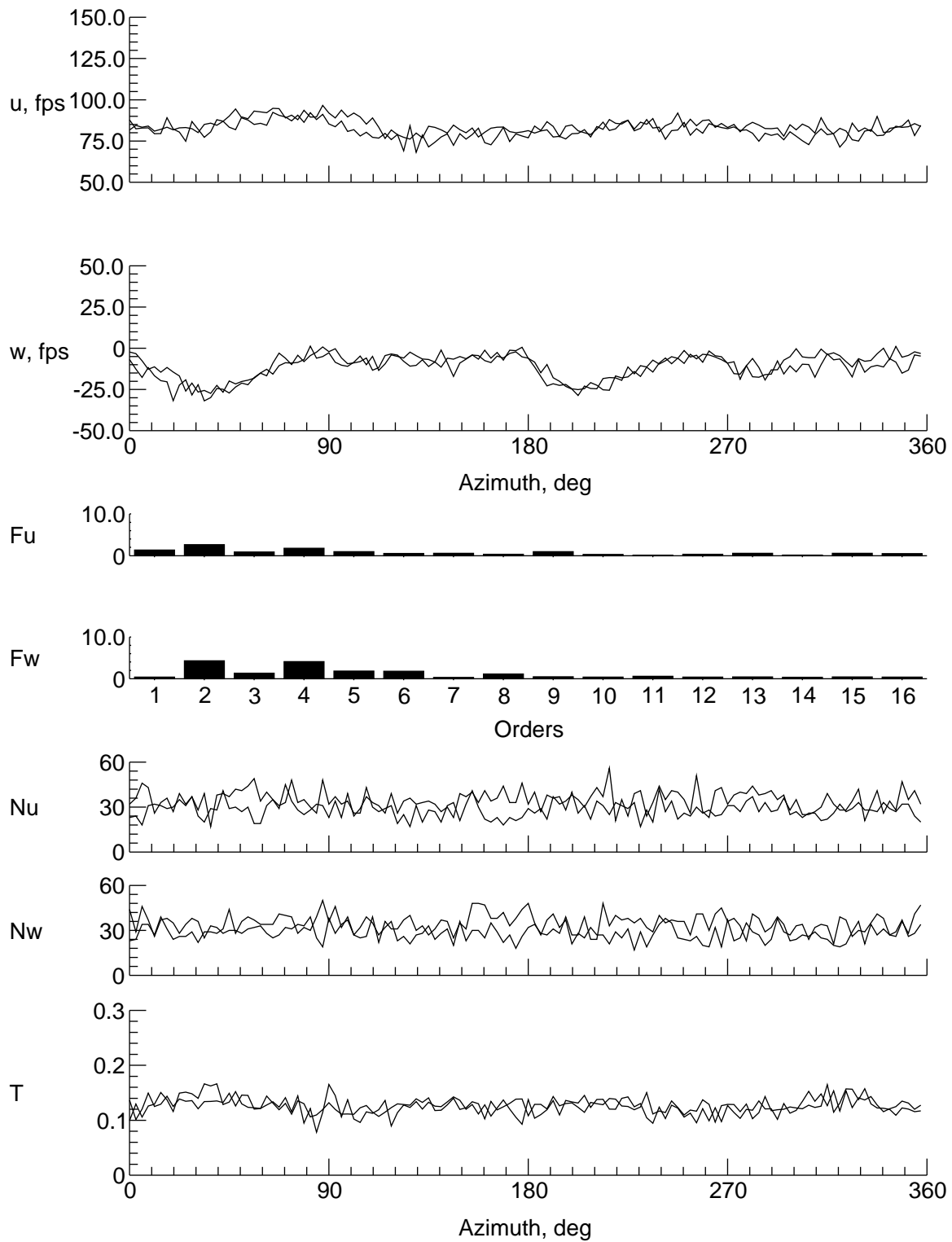
(c) $y = 0$ in., $z = 4.676$ in.

Figure 14. Continued.



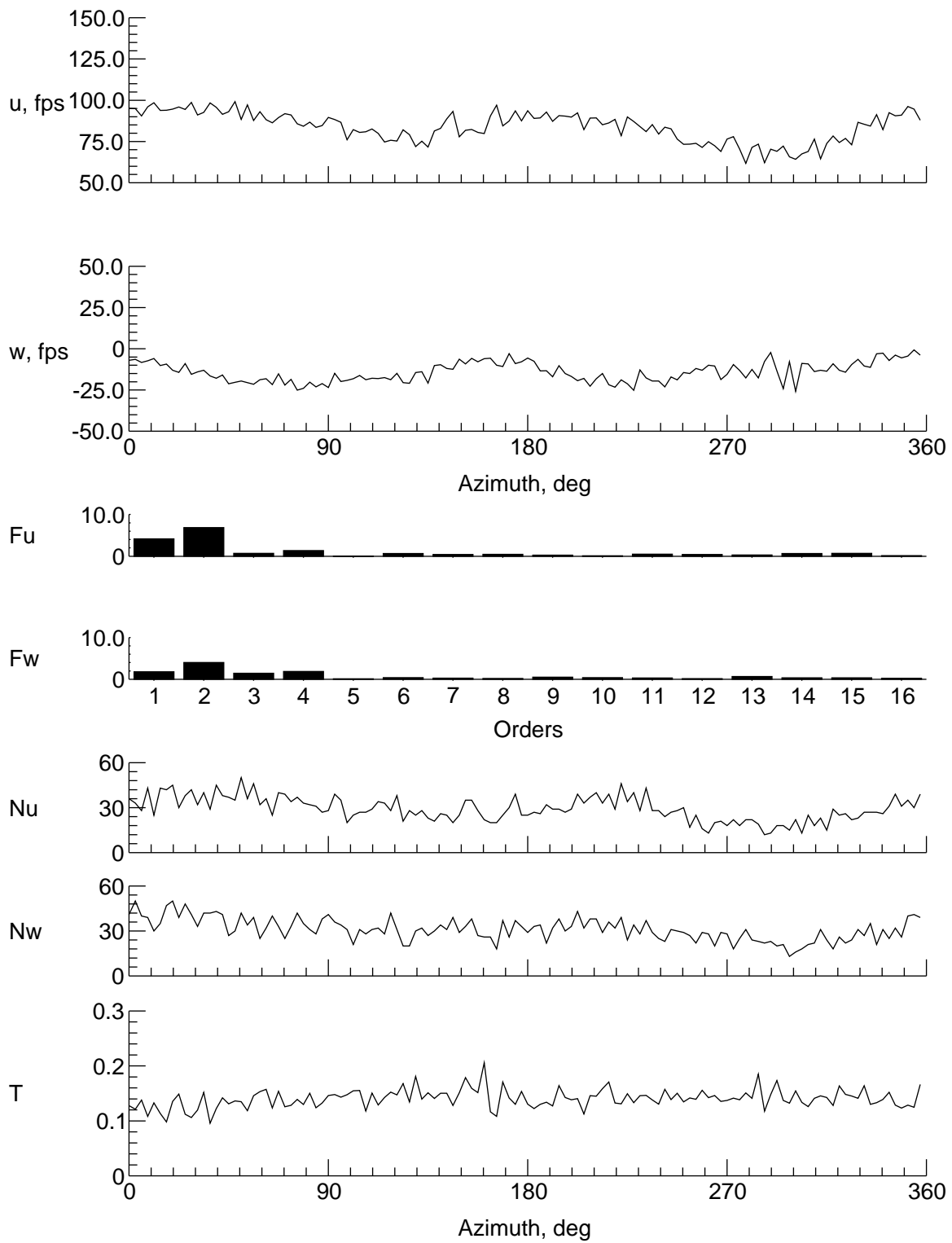
(d) $y = 0$ in., $z = 2.676$ in.

Figure 14. Continued.



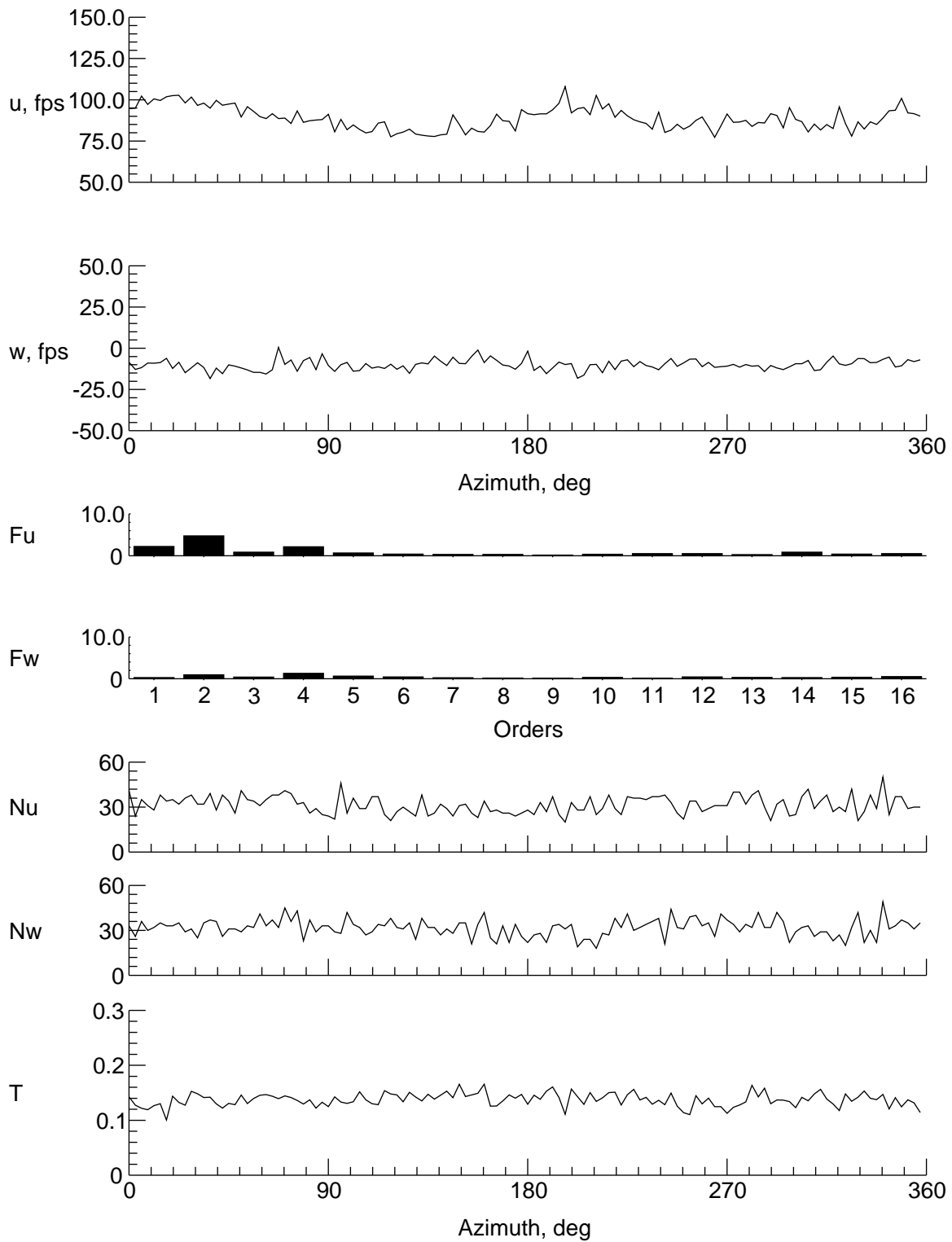
(e) $y = 0$ in., $z = -1.324$ in.

Figure 14. Continued.



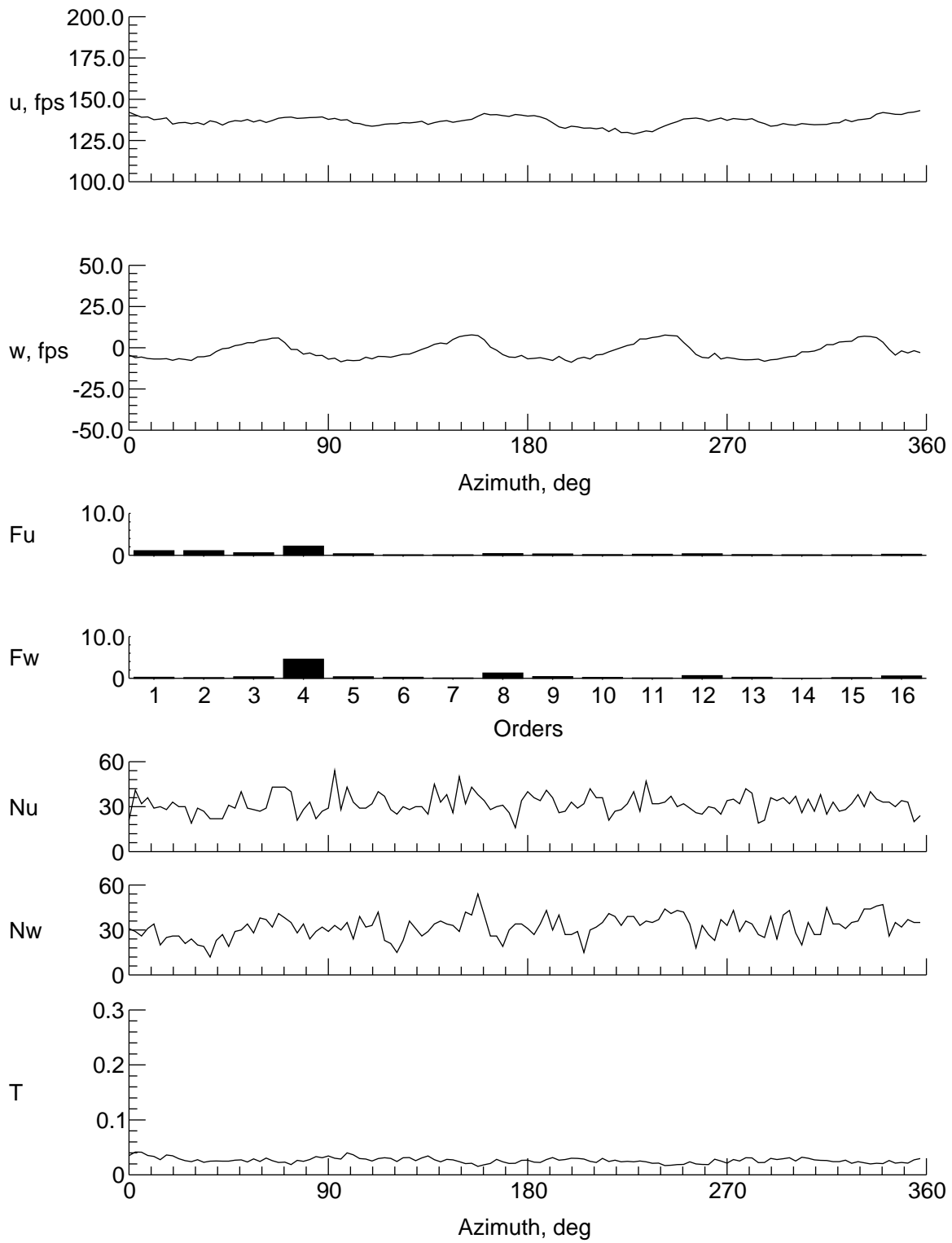
(f) $y = 0$ in., $z = -5.324$ in.

Figure 14. Continued.



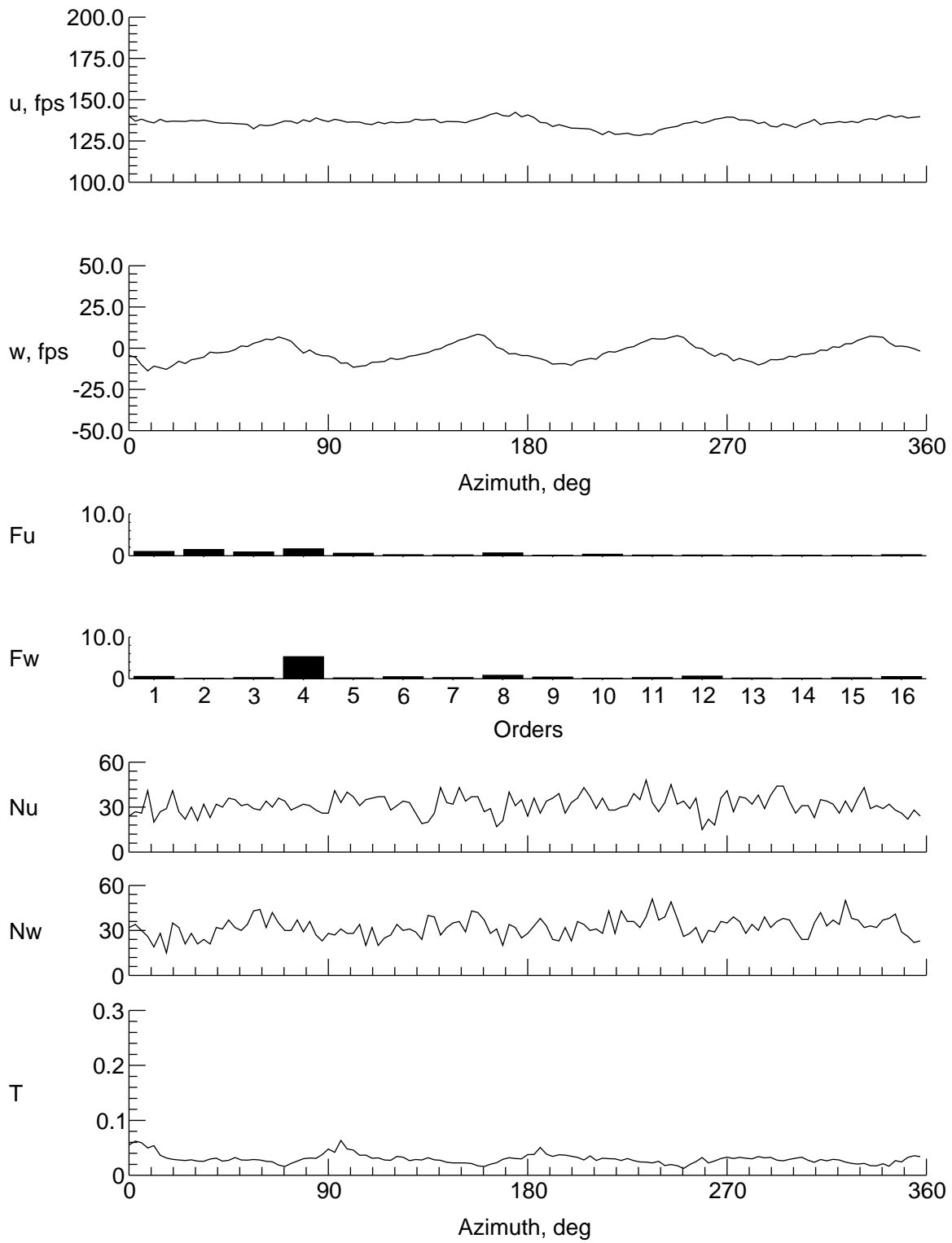
(g) $y = 0$ in., $z = -7.324$ in.

Figure 14. Continued.



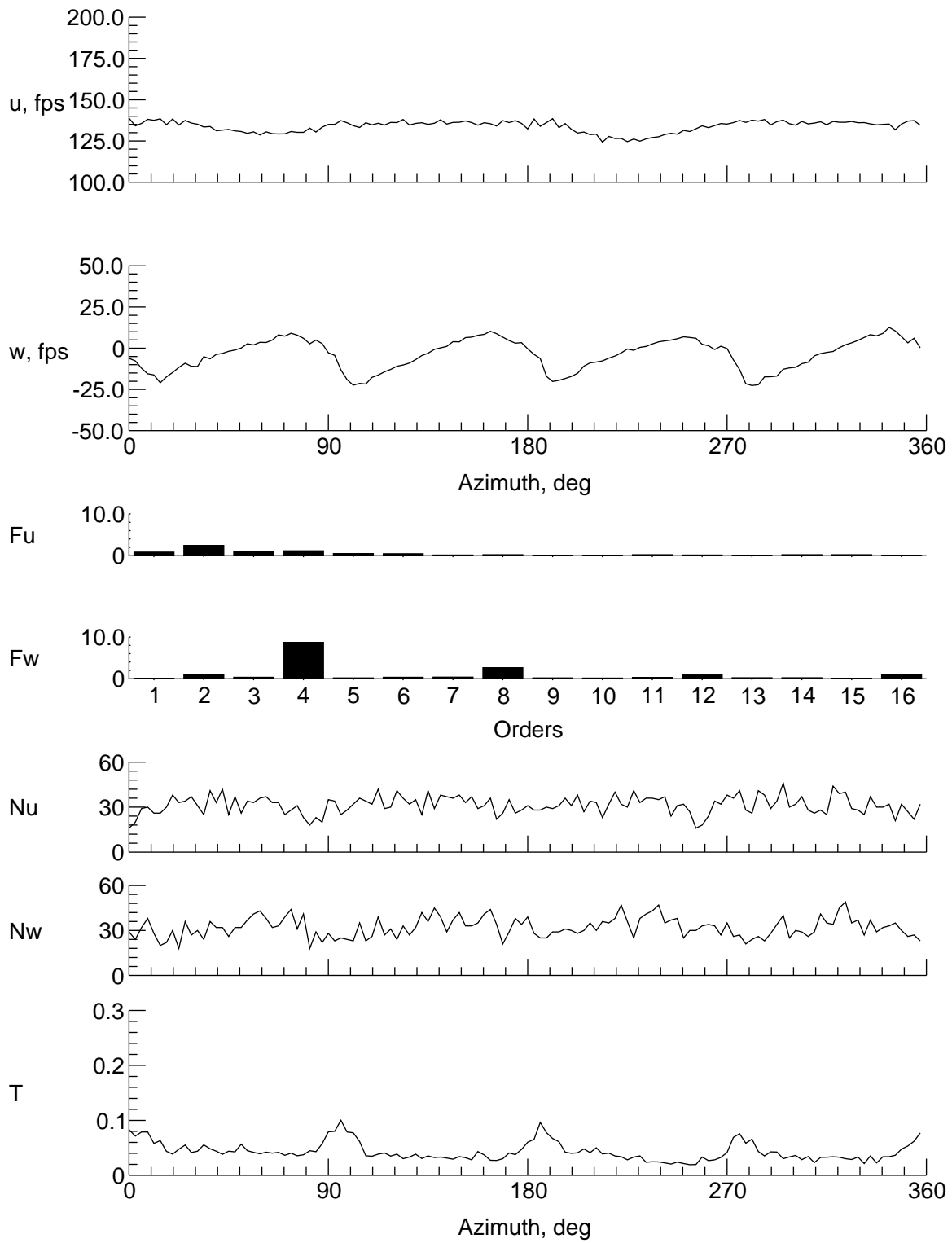
(h) $y = 9$ in., $z = -1.324$ in.

Figure 14. Continued.



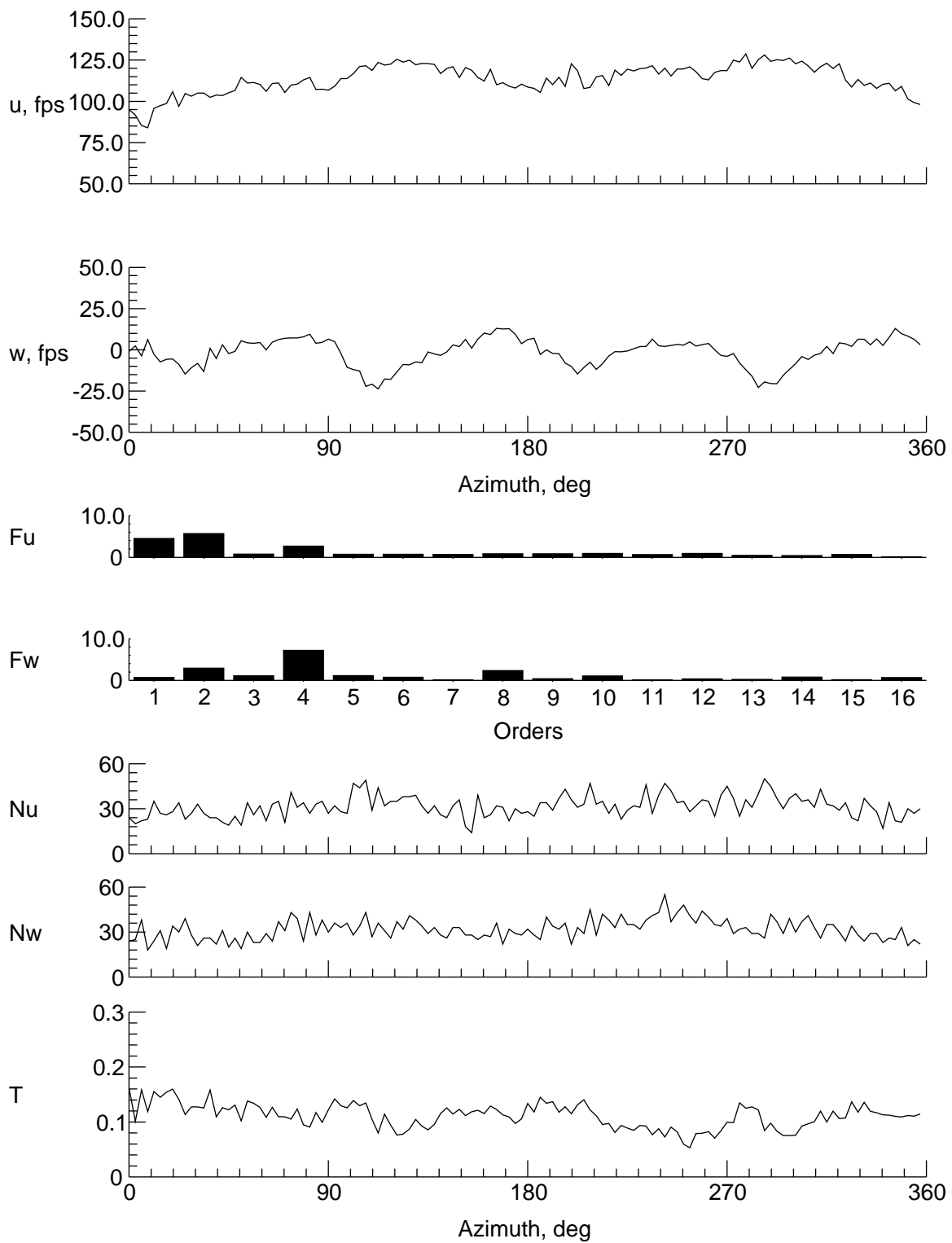
(i) $y = 8$ in., $z = -1.324$ in.

Figure 14. Continued.



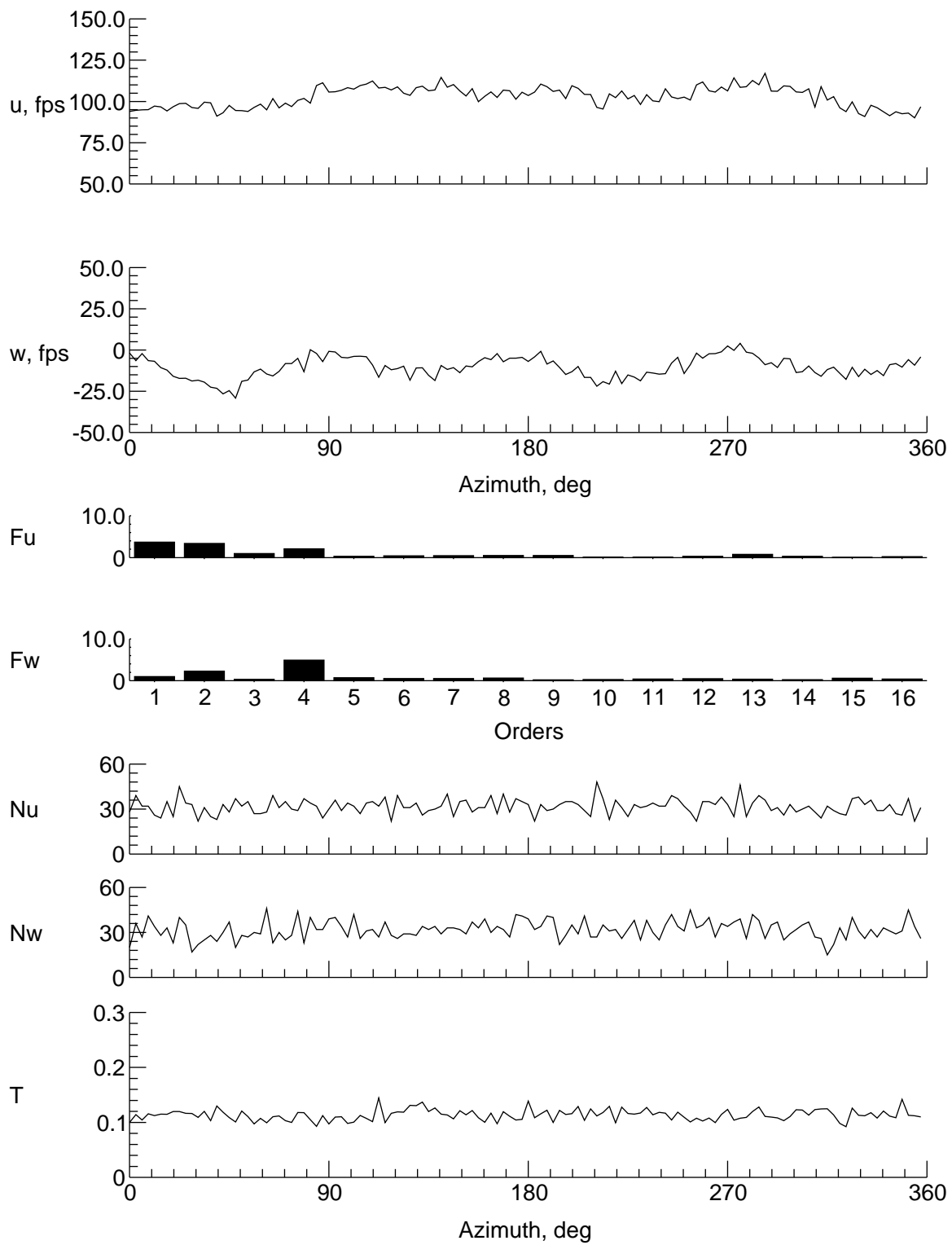
(j) $y = 6$ in., $z = -1.324$ in.

Figure 14. Continued.



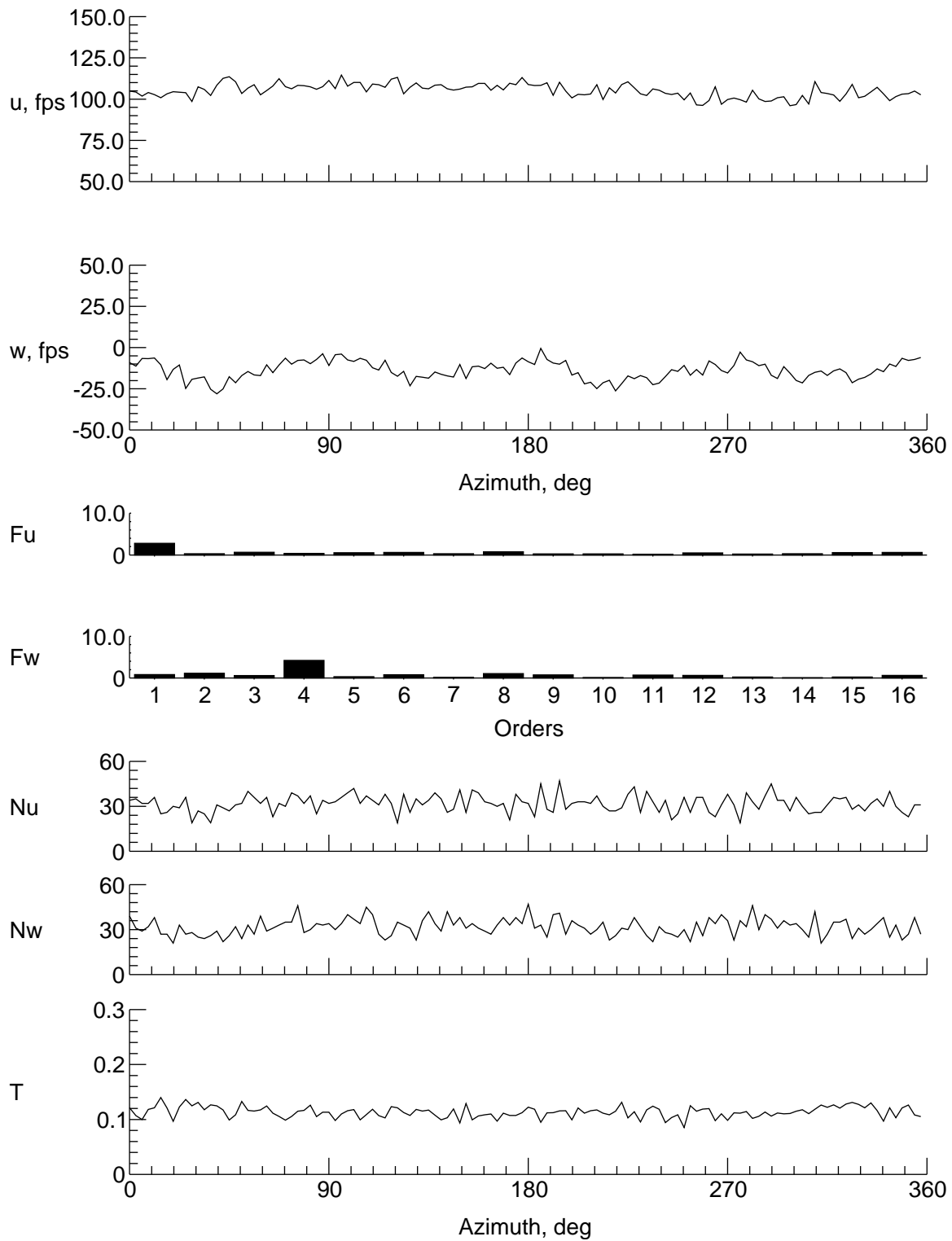
(k) $y = 4$ in., $z = -1.324$ in.

Figure 14. Continued.



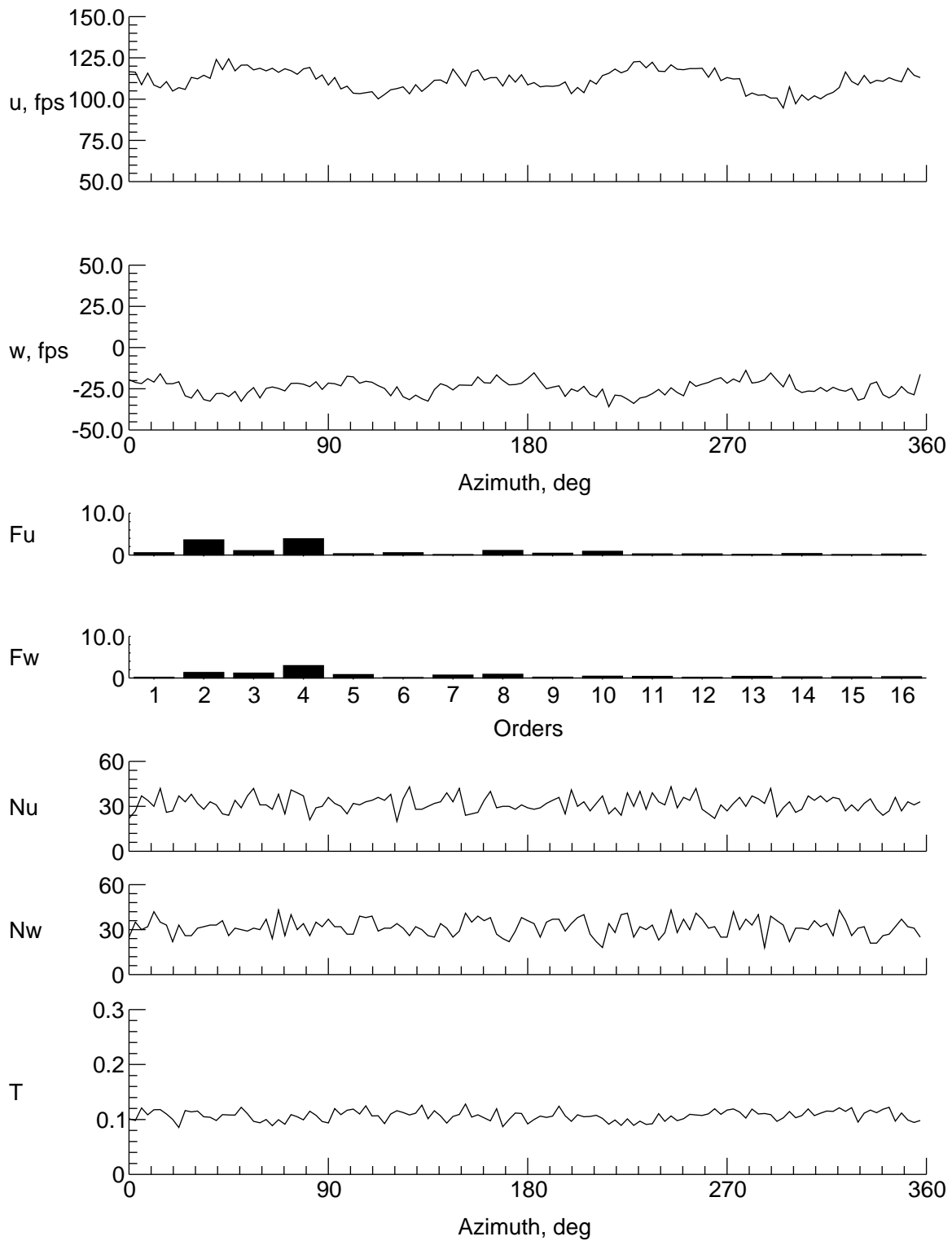
(I) $y = -4$ in., $z = -1.324$ in.

Figure 14. Continued.



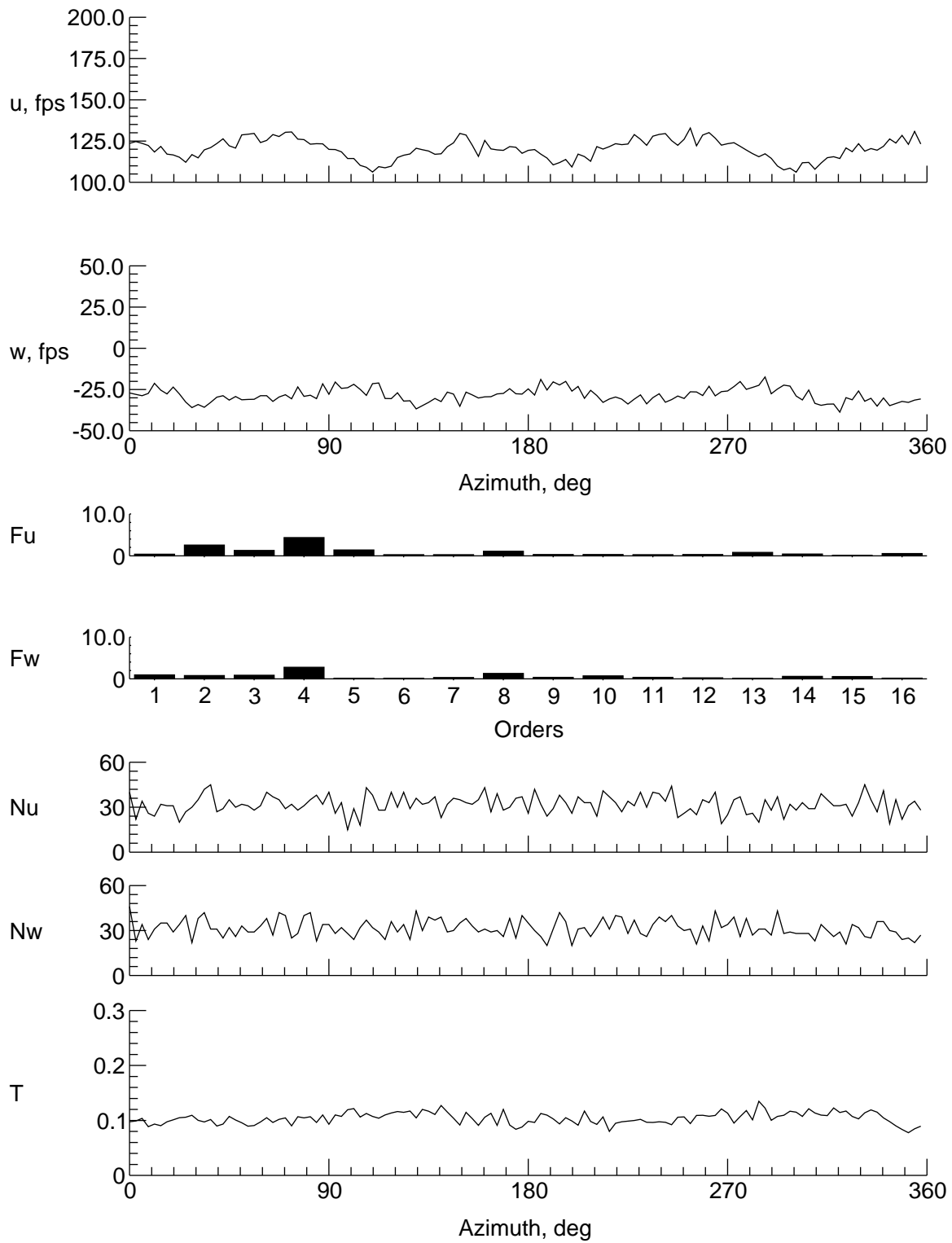
(m) $y = -6$ in., $z = -1.324$ in.

Figure 14. Continued.



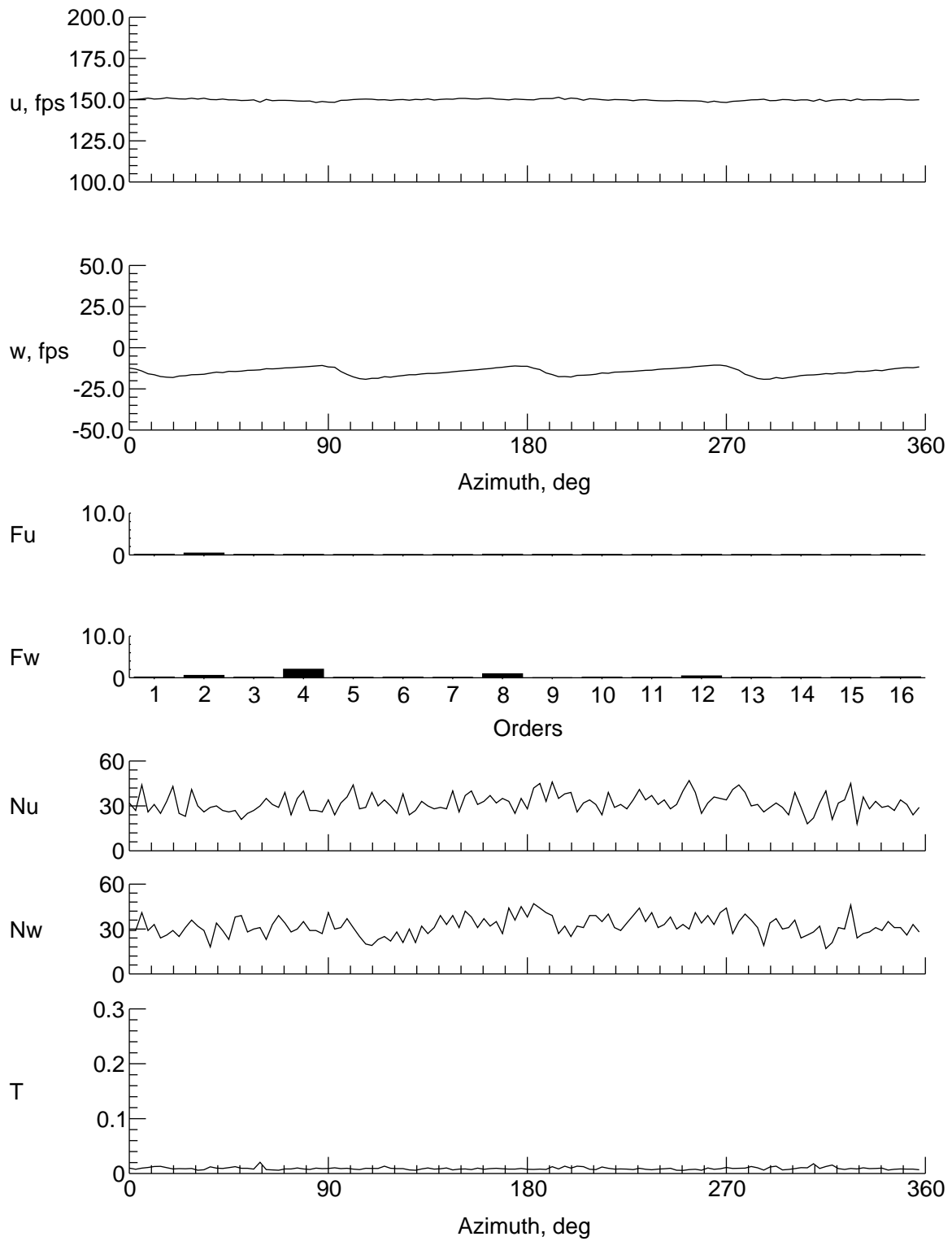
(n) $y = -8$ in., $z = -1.324$ in.

Figure 14. Continued.



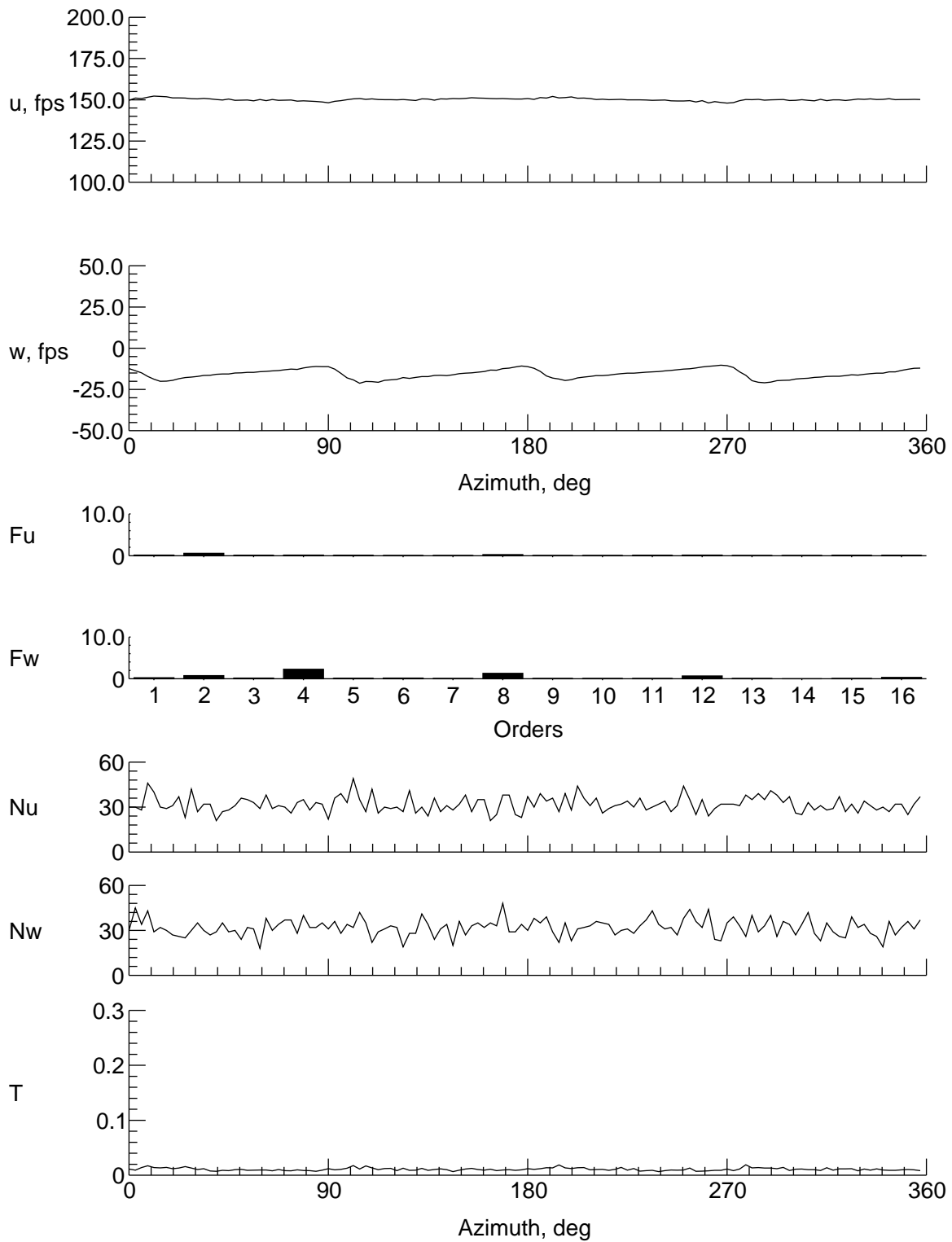
(o) $y = -9$ in., $z = -1.324$ in.

Figure 14. Concluded.



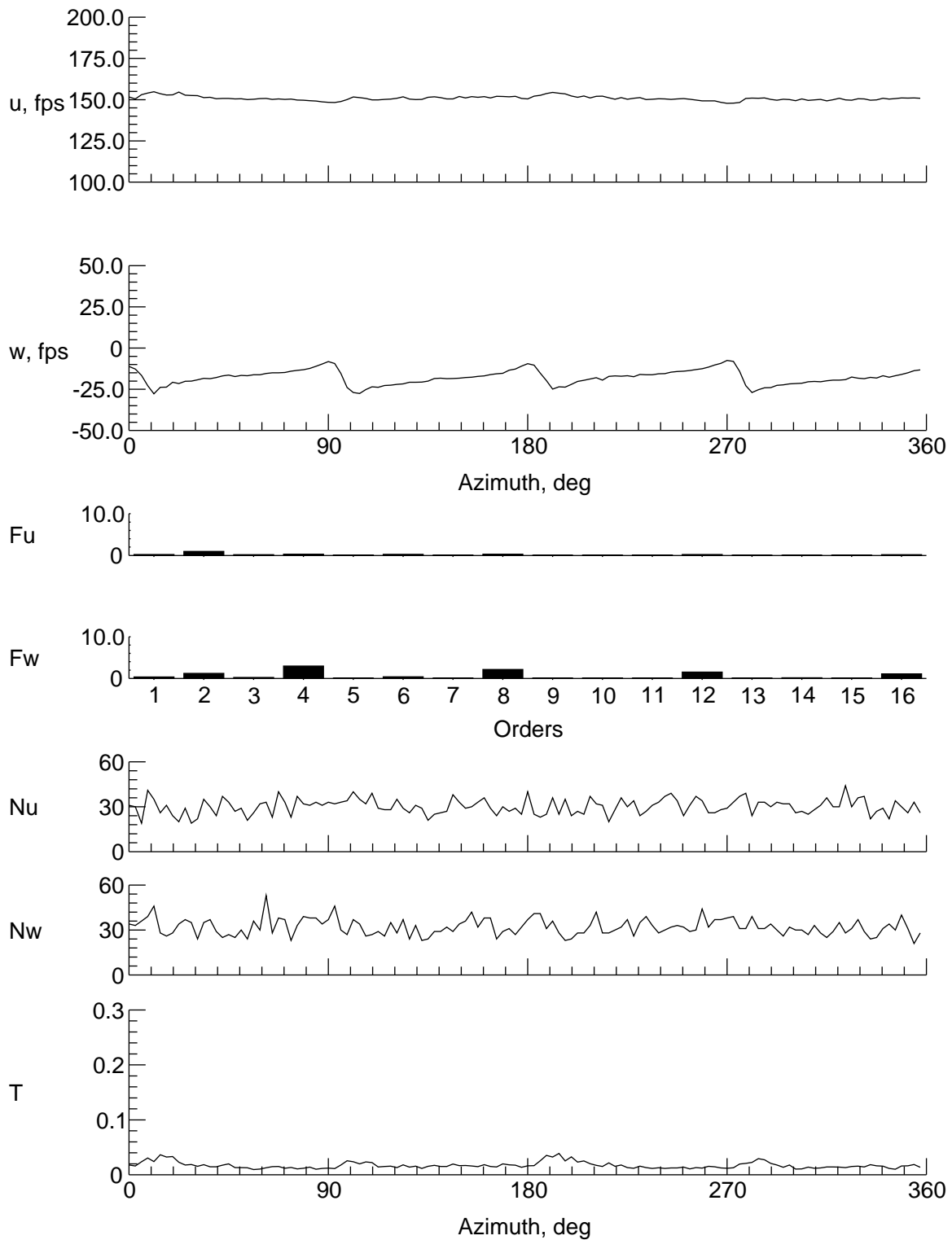
(a) $y = 0$ in., $z = 7.555$ in.

Figure 15. Velocity and turbulence at station 24 in.



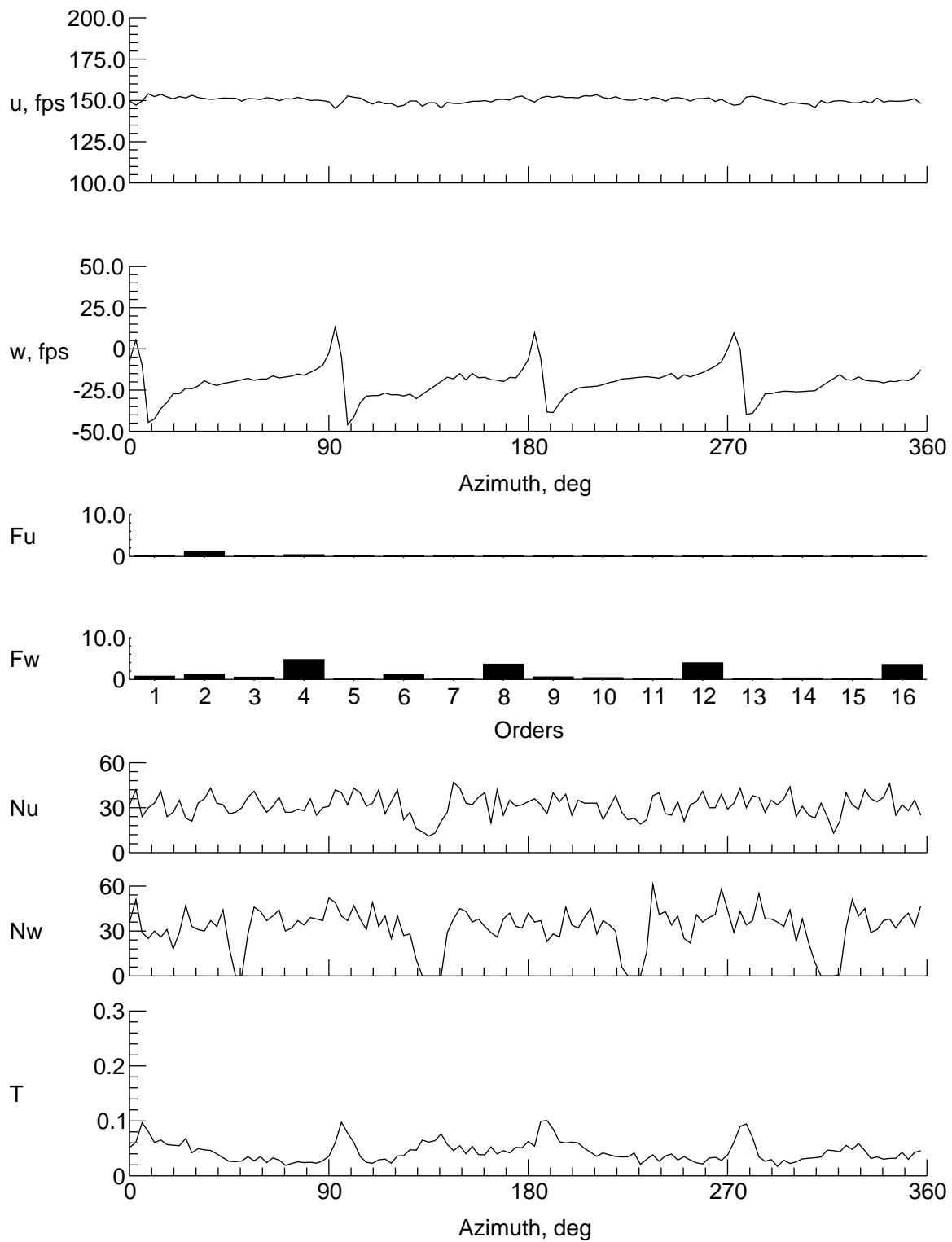
(b) $y = 0$ in., $z = 6.555$ in.

Figure 15. Continued.



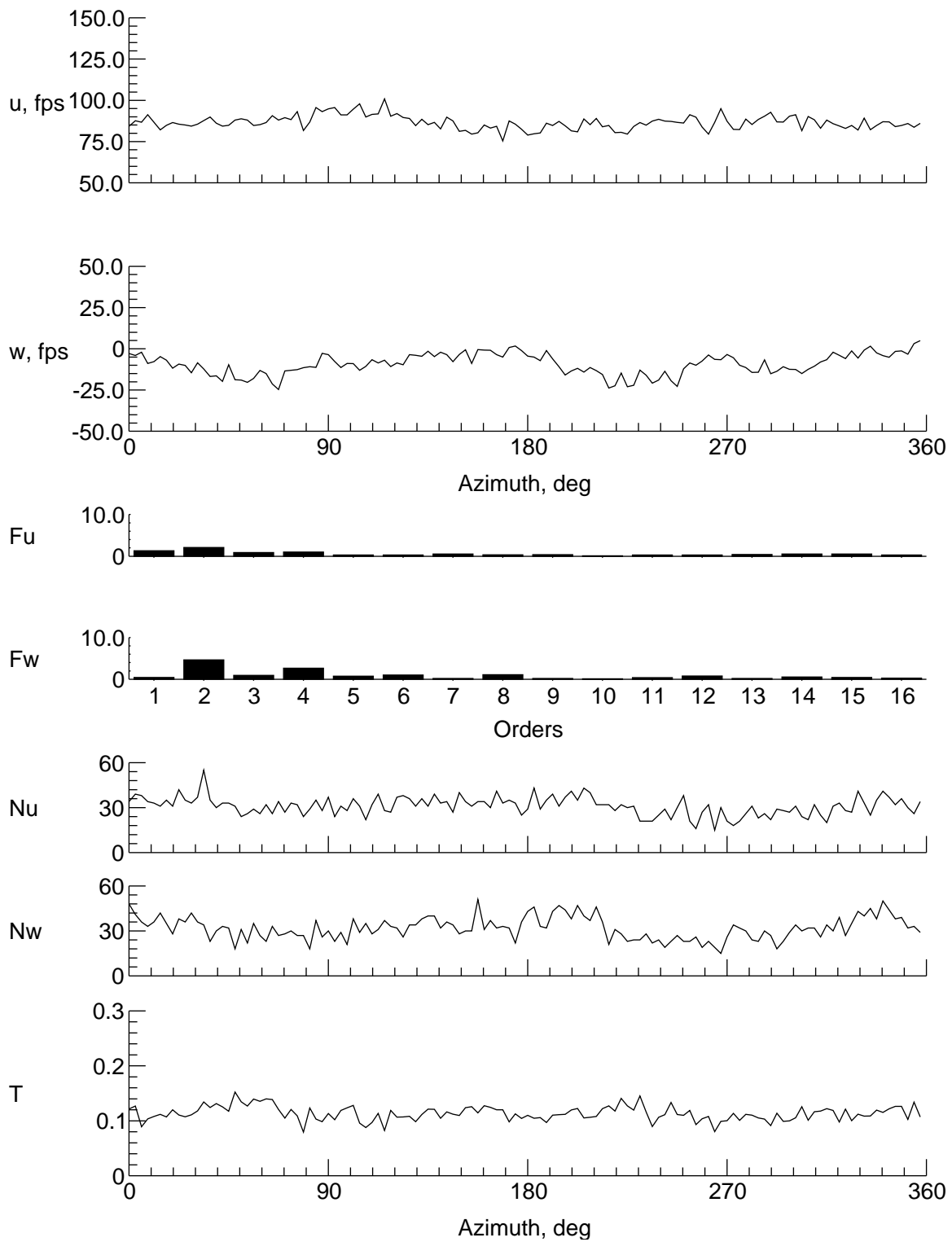
(c) $y = 0$ in., $z = 4.555$ in.

Figure 15. Continued.



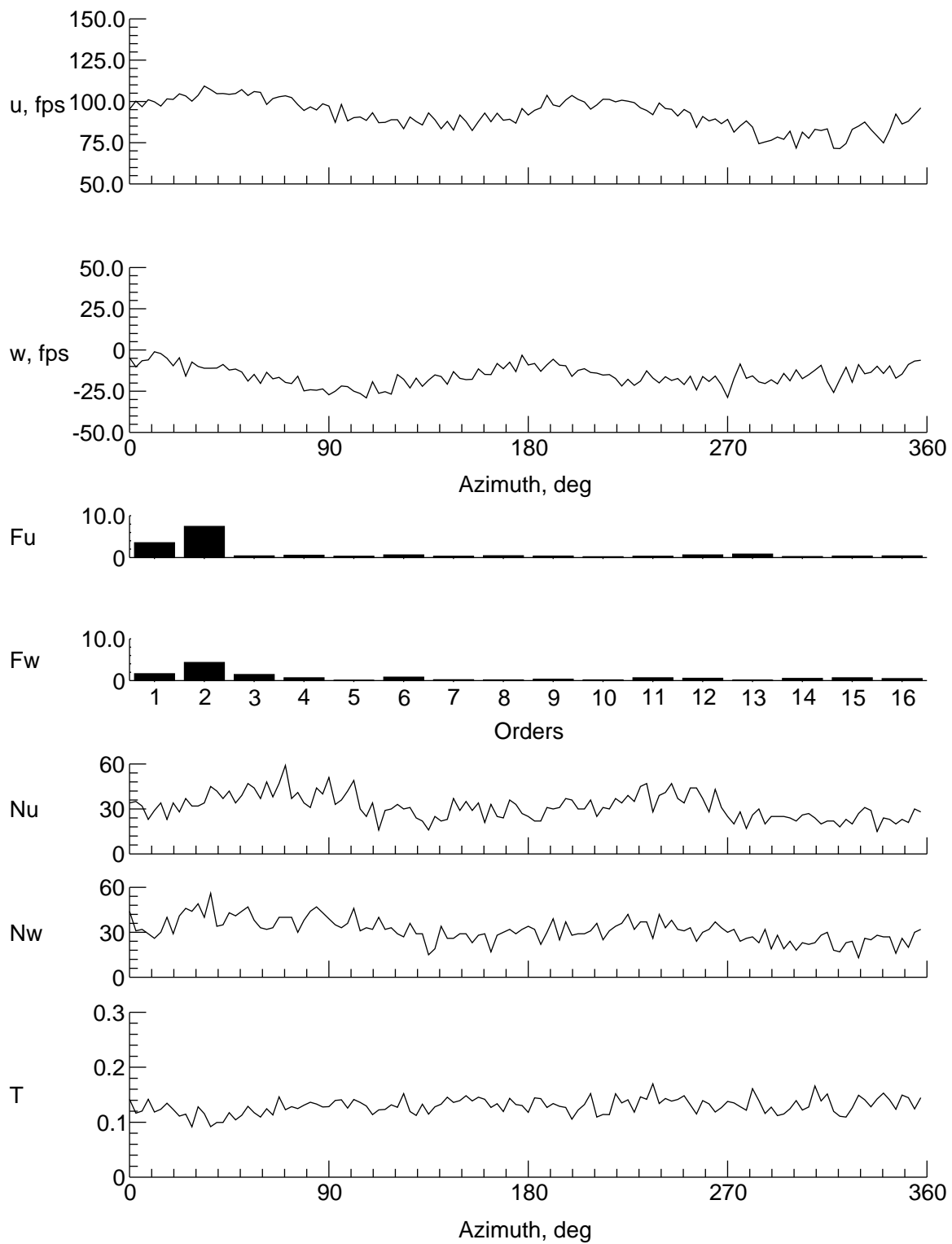
(d) $y = 0$ in., $z = 2.555$ in.

Figure 15. Continued.



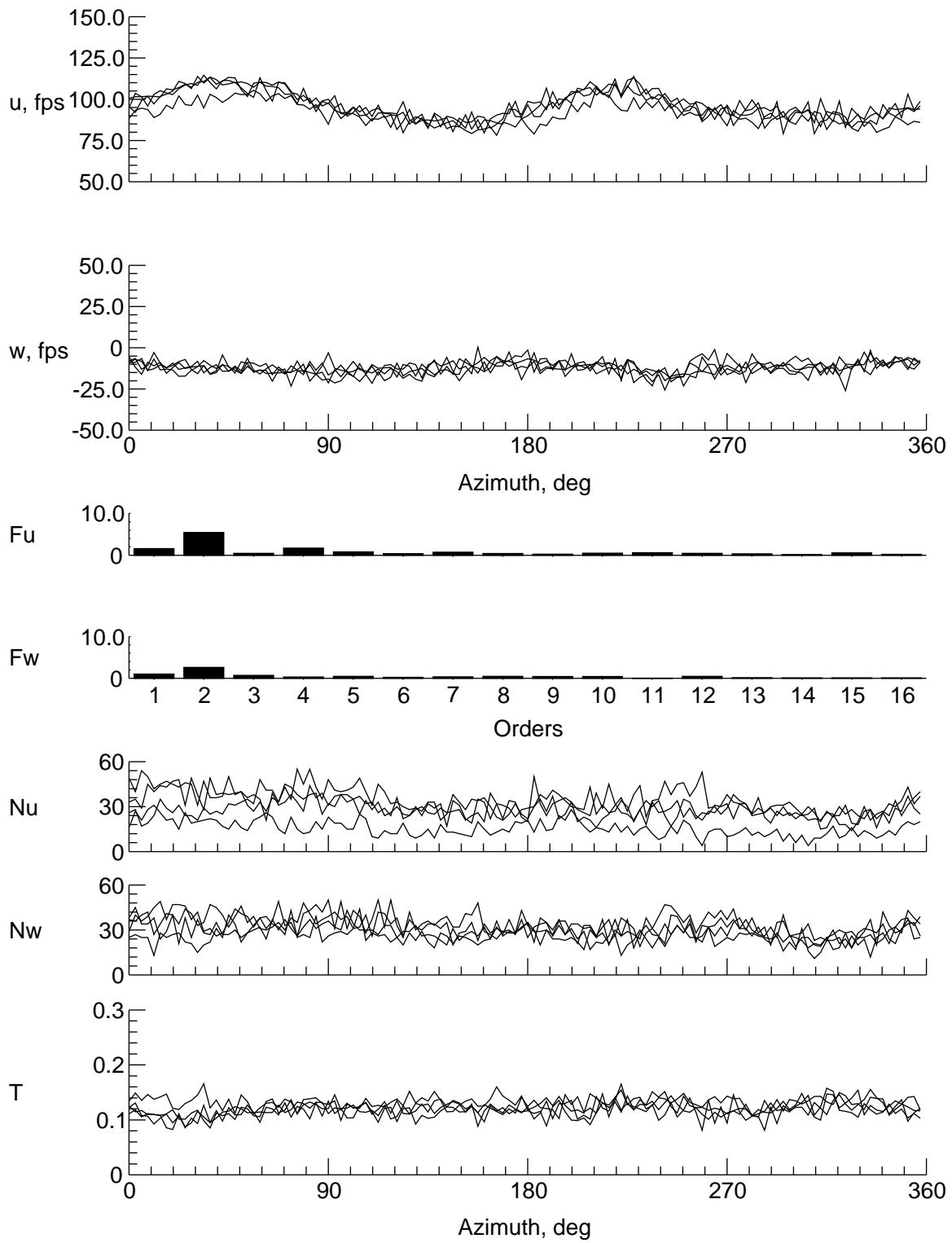
(e) $y = 0$ in., $z = -1.445$ in.

Figure 15. Continued.



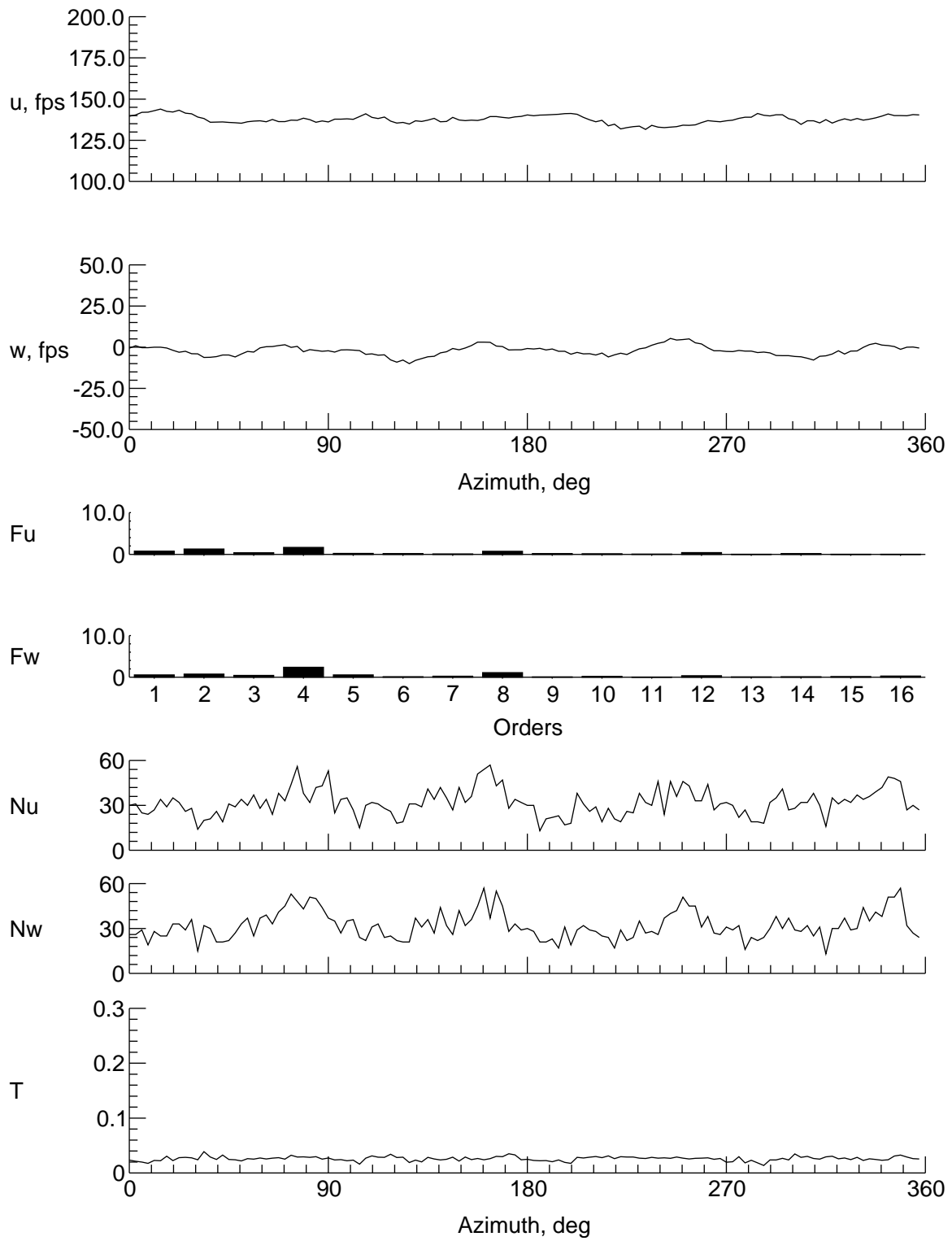
(f) $y = 0$ in., $z = -5.445$ in.

Figure 15. Continued.



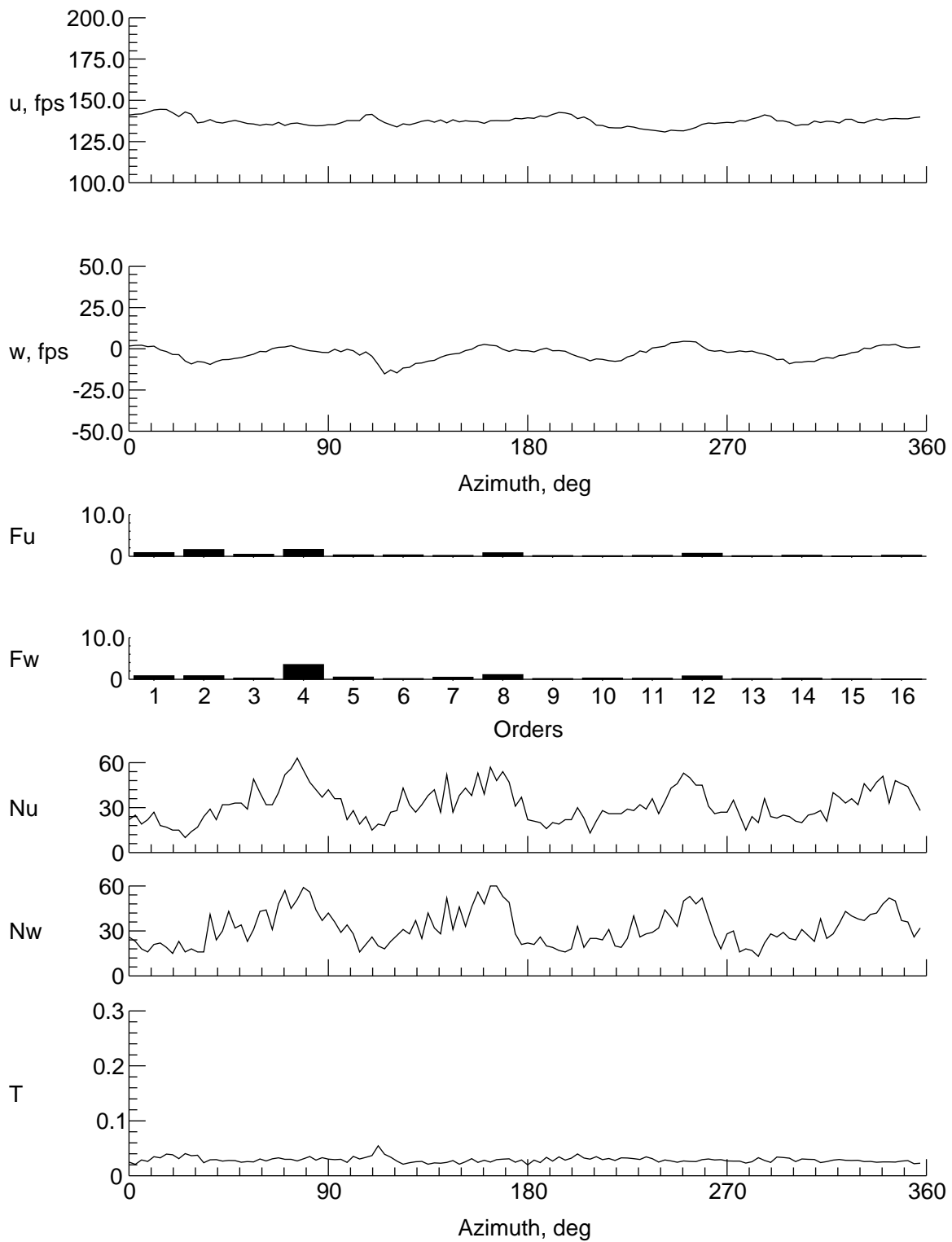
(g) $y = 0$ in., $z = -7.445$ in.

Figure 15. Continued.



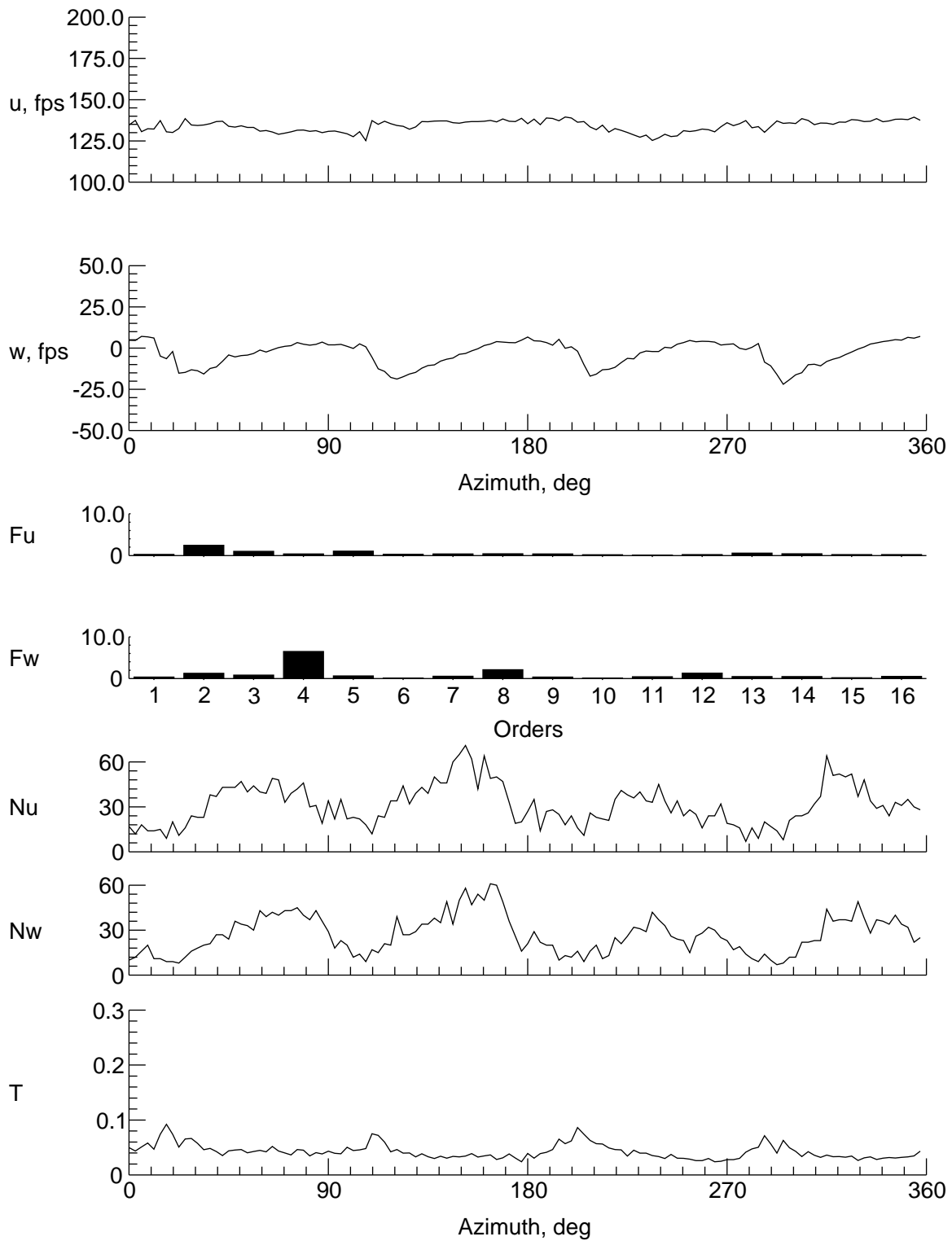
(h) $y = 9$ in., $z = -1.445$ in.

Figure 15. Continued.



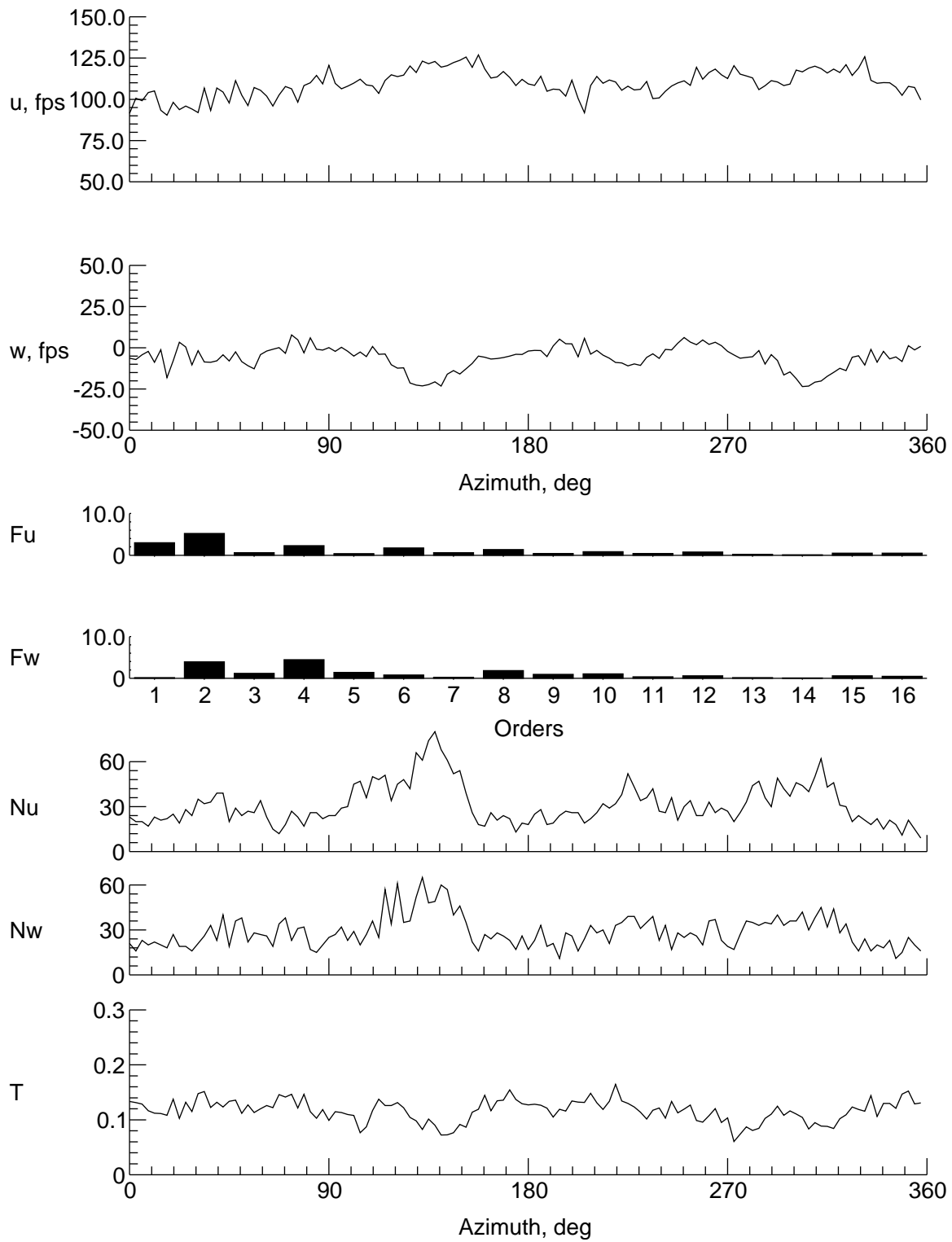
(i) $y = 8$ in., $z = -1.445$ in.

Figure 15. Continued.



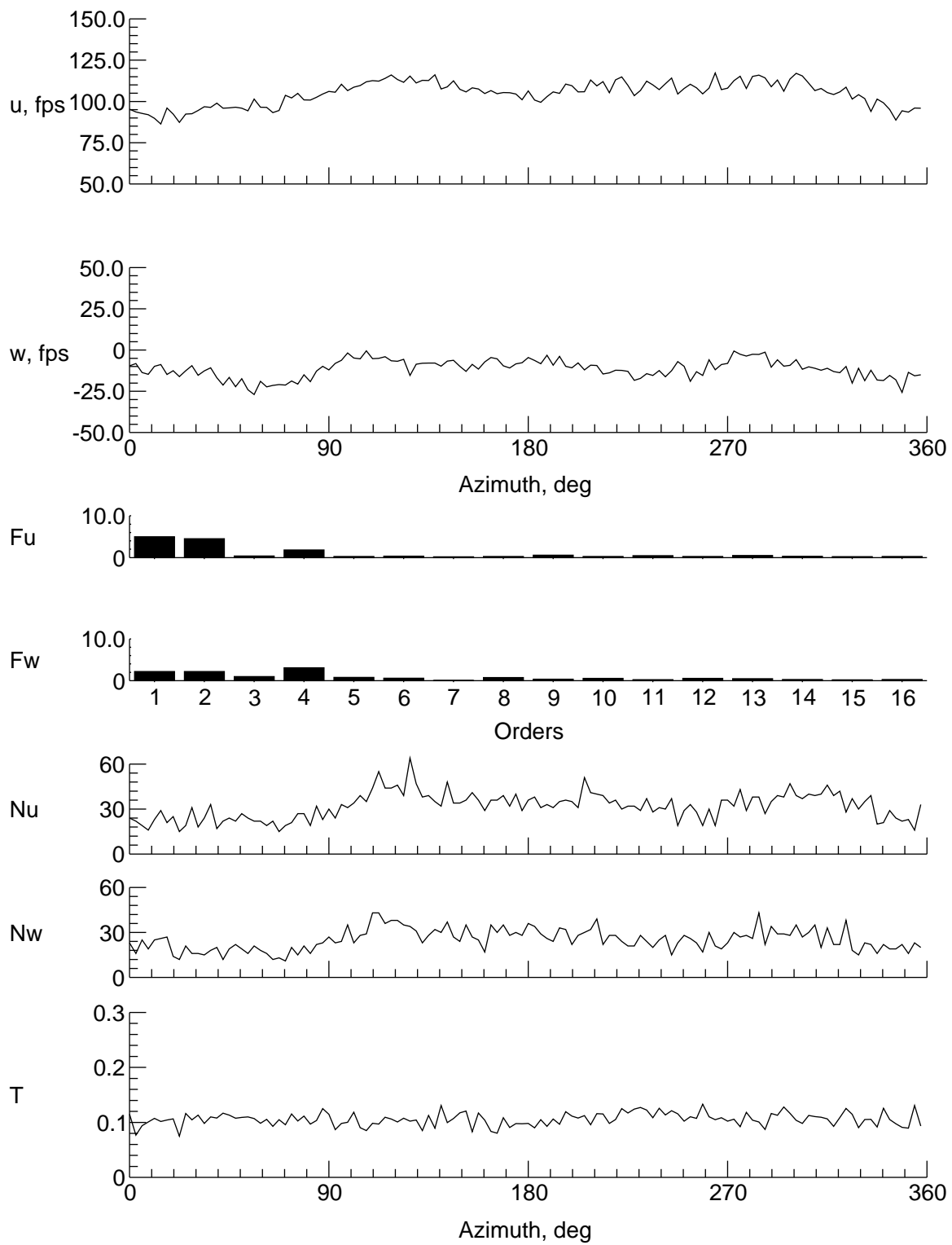
(j) $y = 6$ in., $z = -1.445$ in.

Figure 15. Continued.



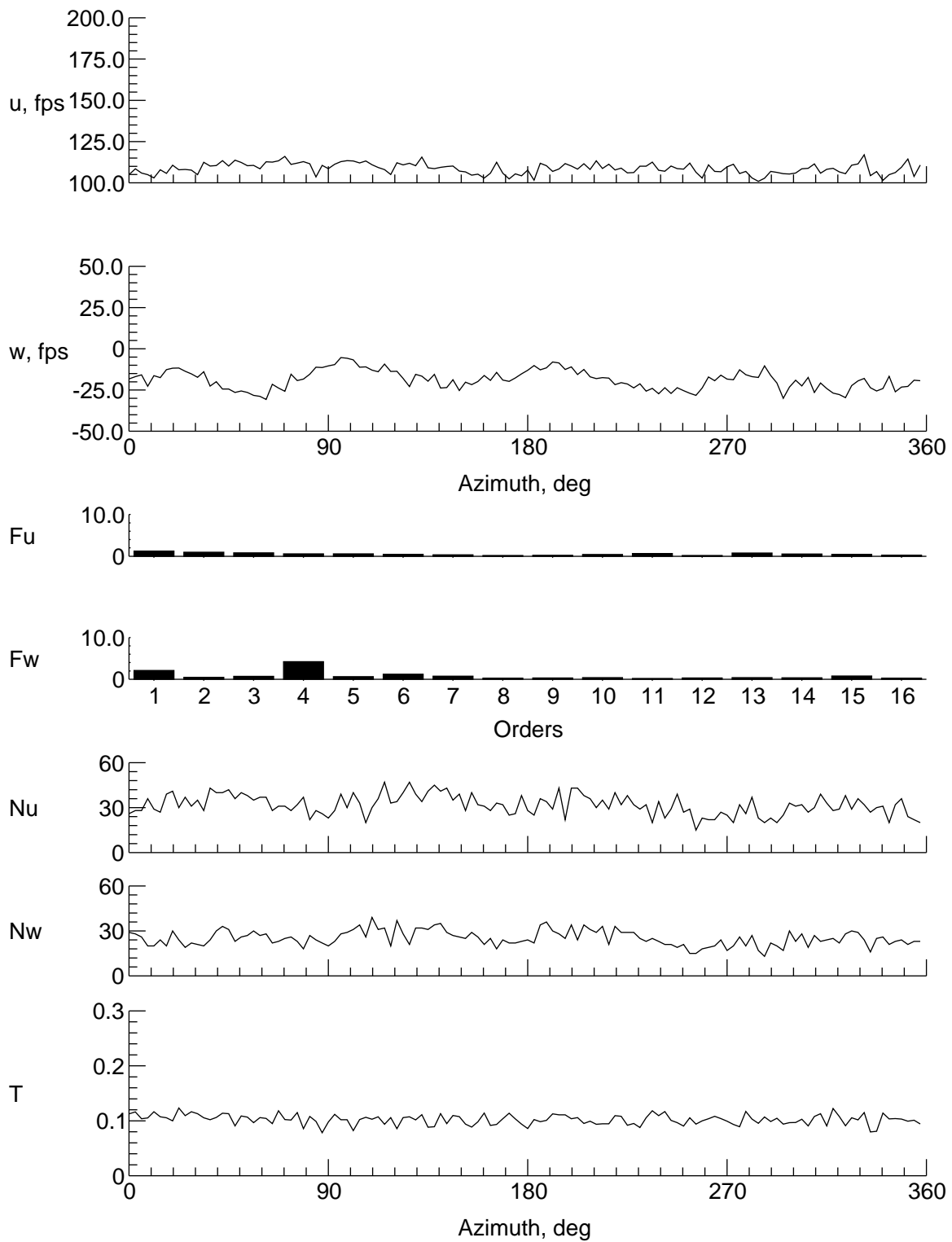
(k) $y = 4$ in., $z = -1.445$ in.

Figure 15. Continued.



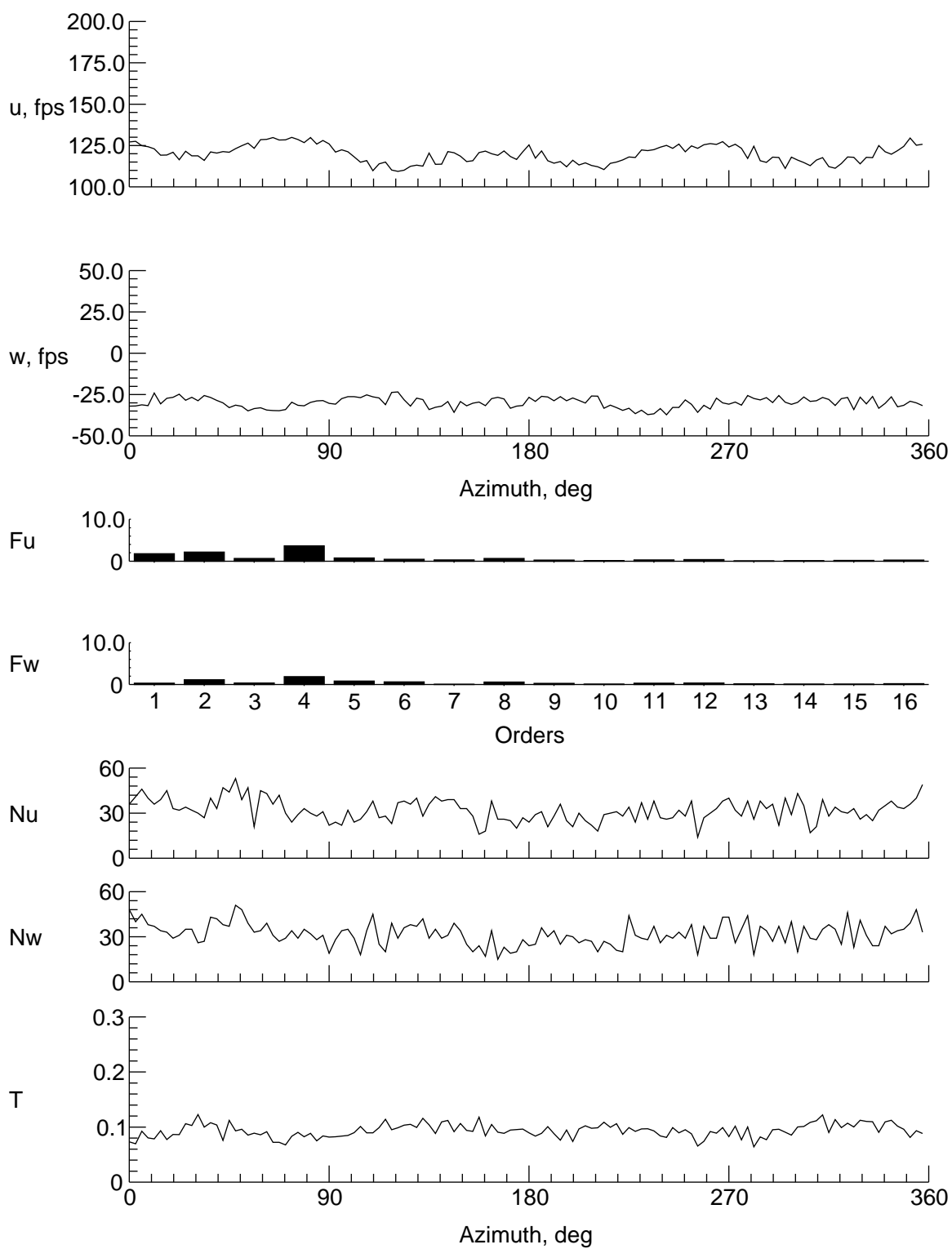
(l) $y = -4$ in., $z = -1.445$ in.

Figure 15. Continued.



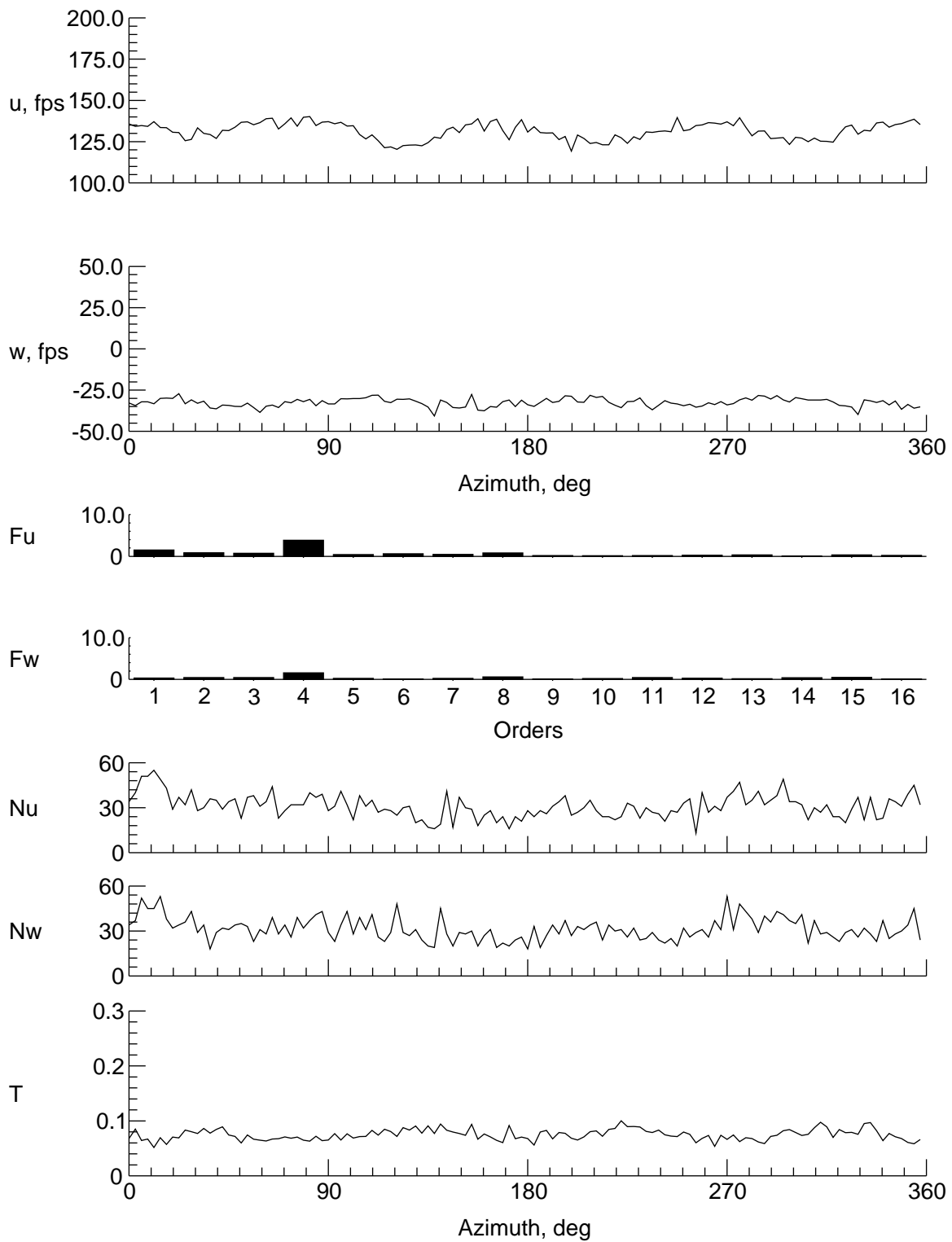
(m) $y = -6$ in., $z = -1.445$ in.

Figure 15. Continued.



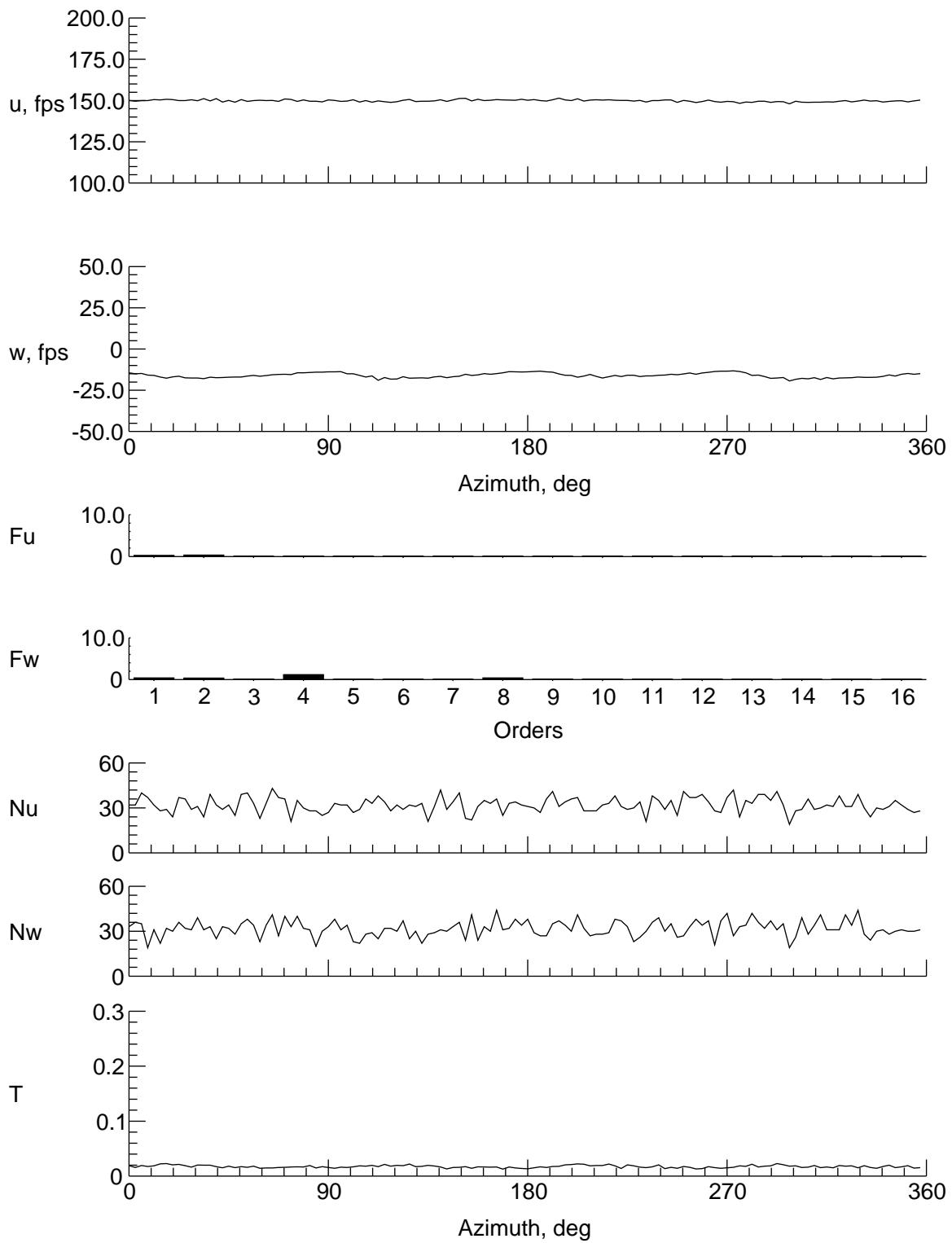
(n) $y = -8$ in., $z = -1.445$ in.

Figure 15. Continued.



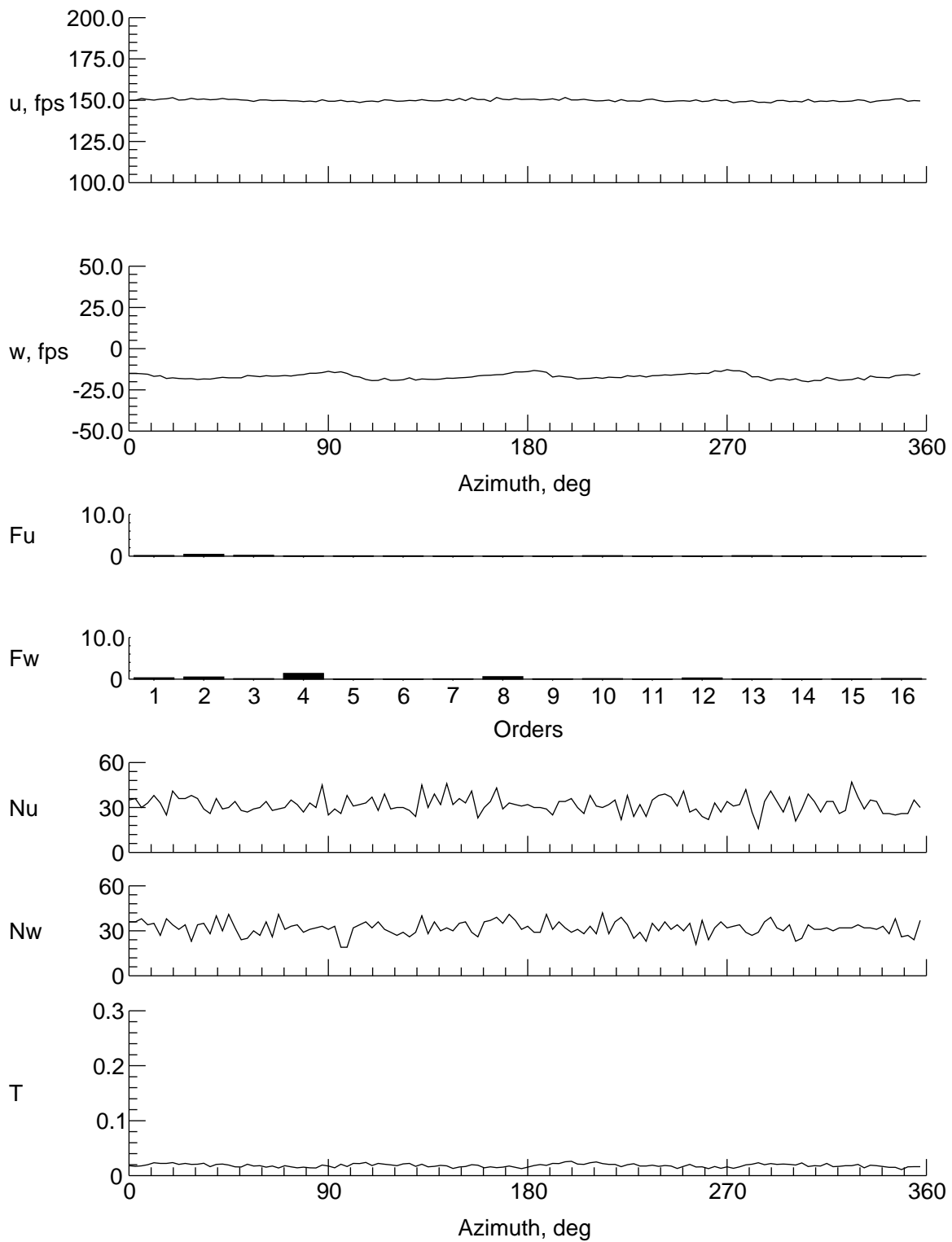
(o) $y = -9$ in., $z = -1.445$ in.

Figure 15. Concluded.



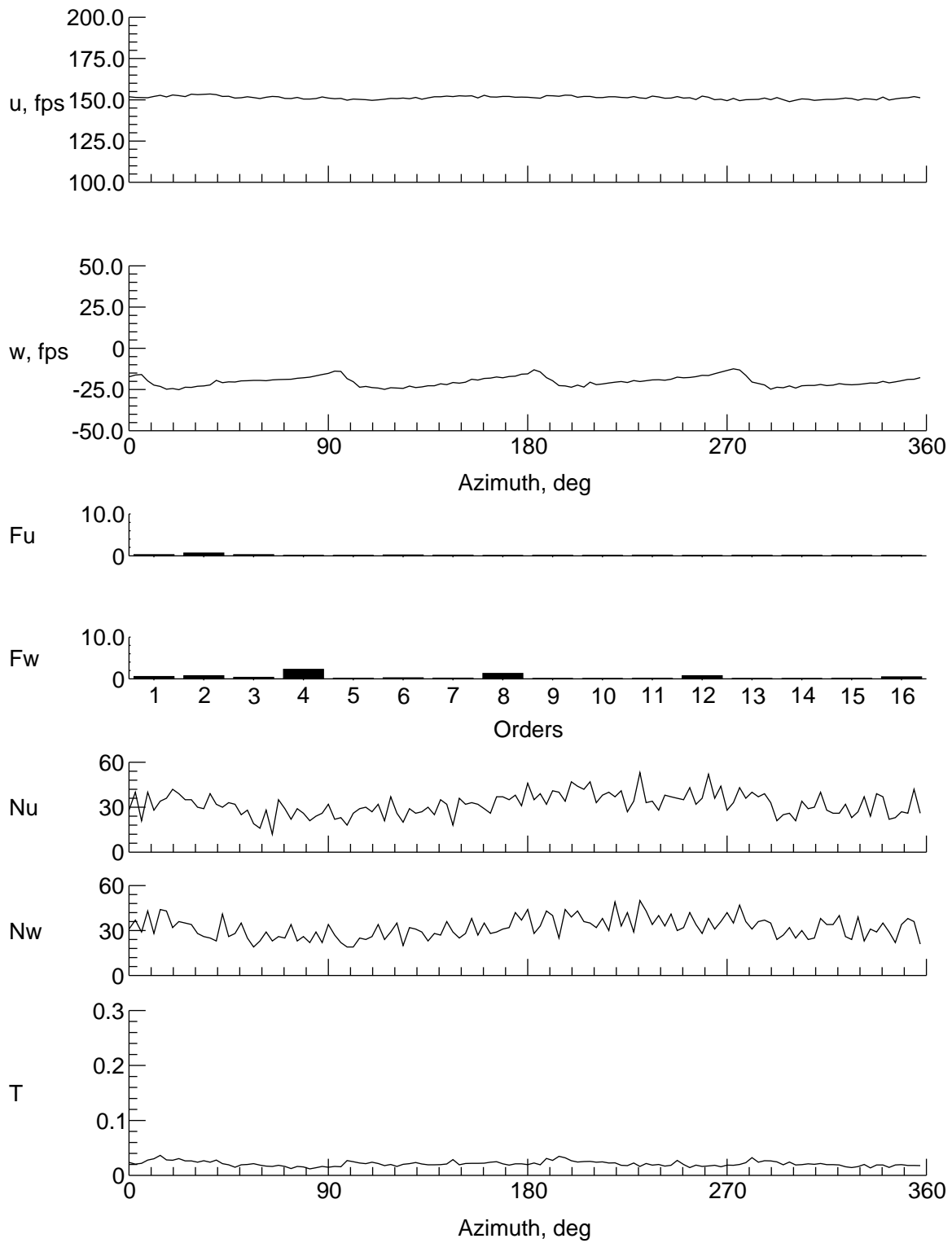
(a) $y = 0$ in., $z = 7.435$ in.

Figure 16. Velocity and turbulence at station 26 in.



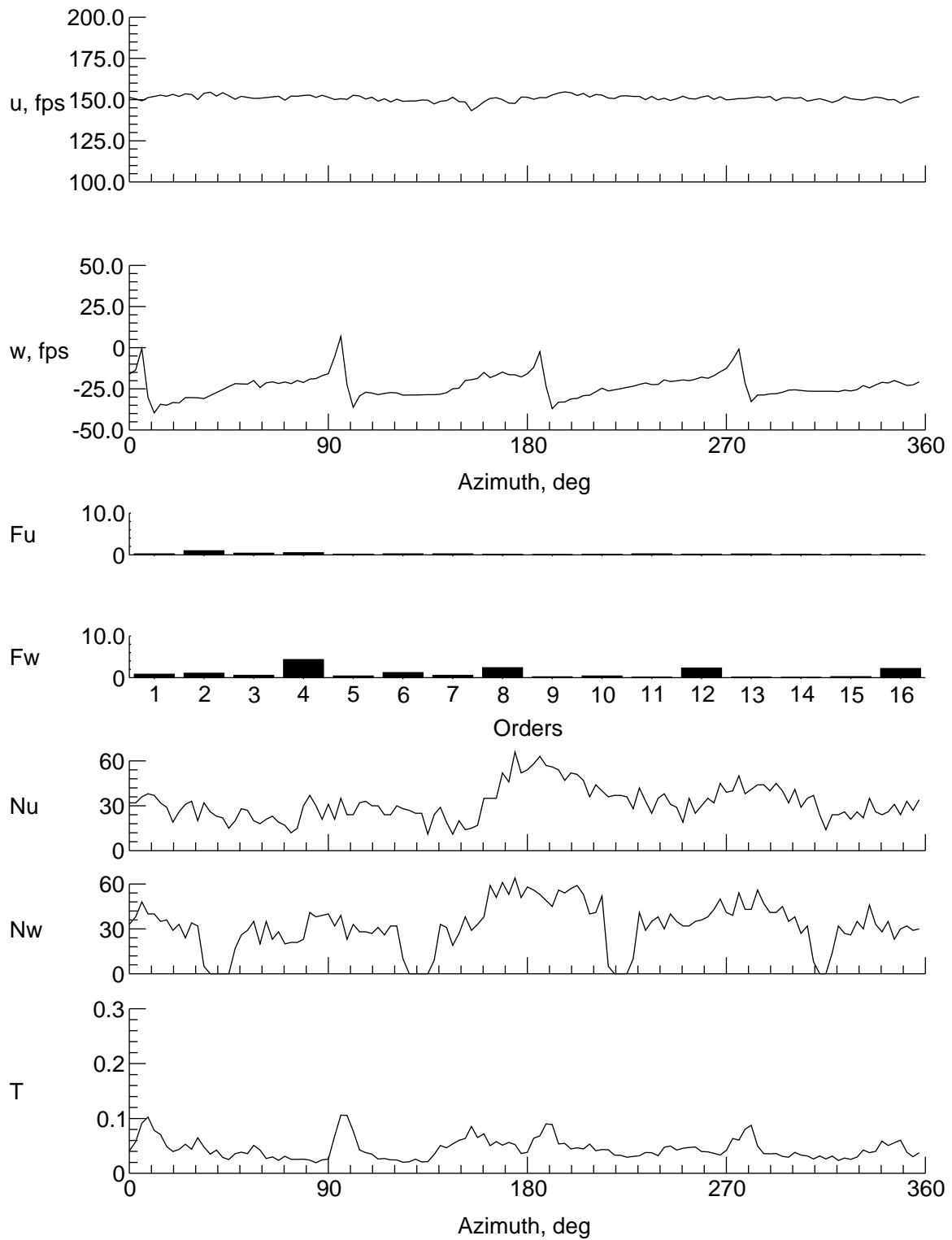
(b) $y = 0$ in., $z = 6.435$ in.

Figure 16. Continued.



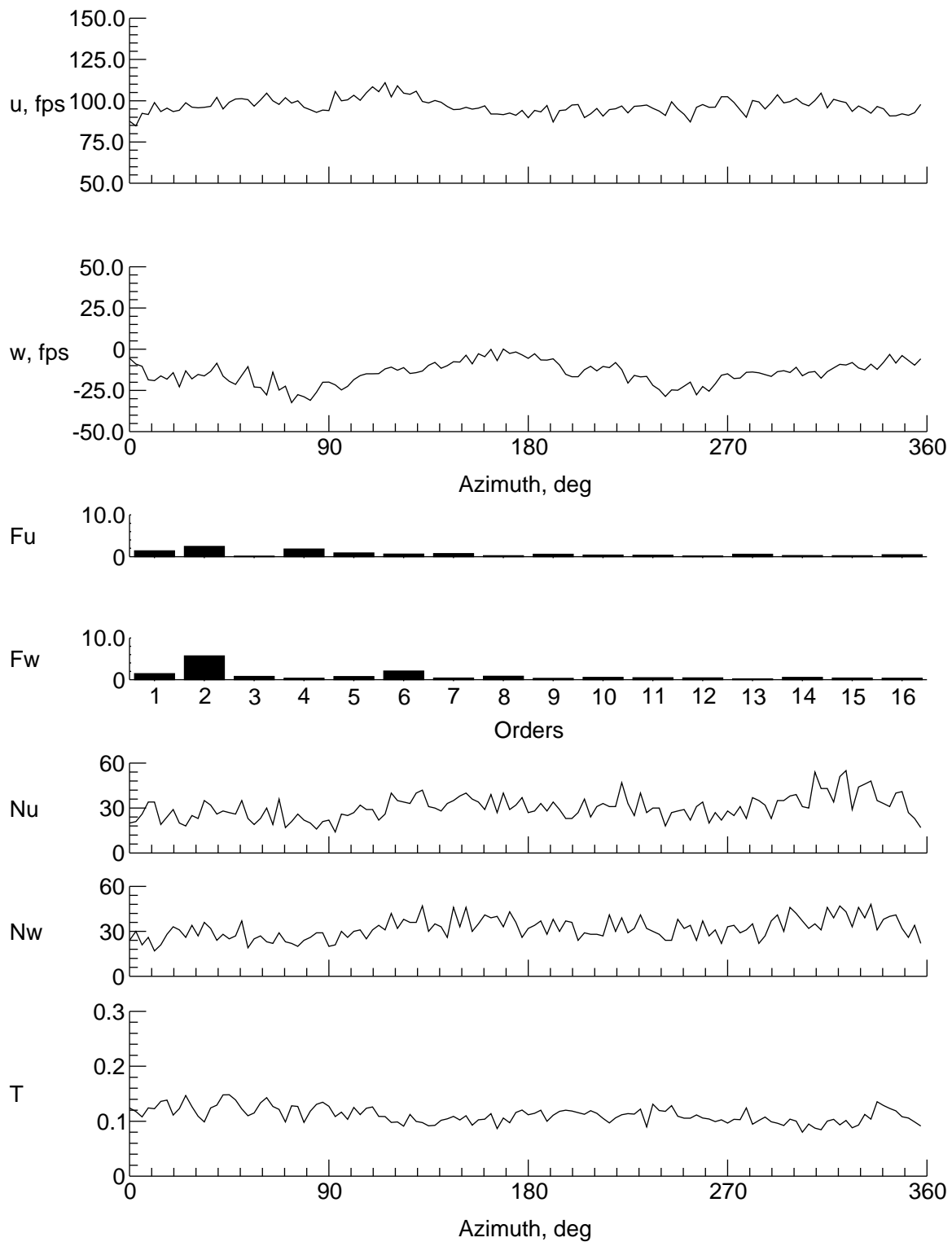
(c) $y = 0$ in., $z = 4.435$ in.

Figure 16. Continued.



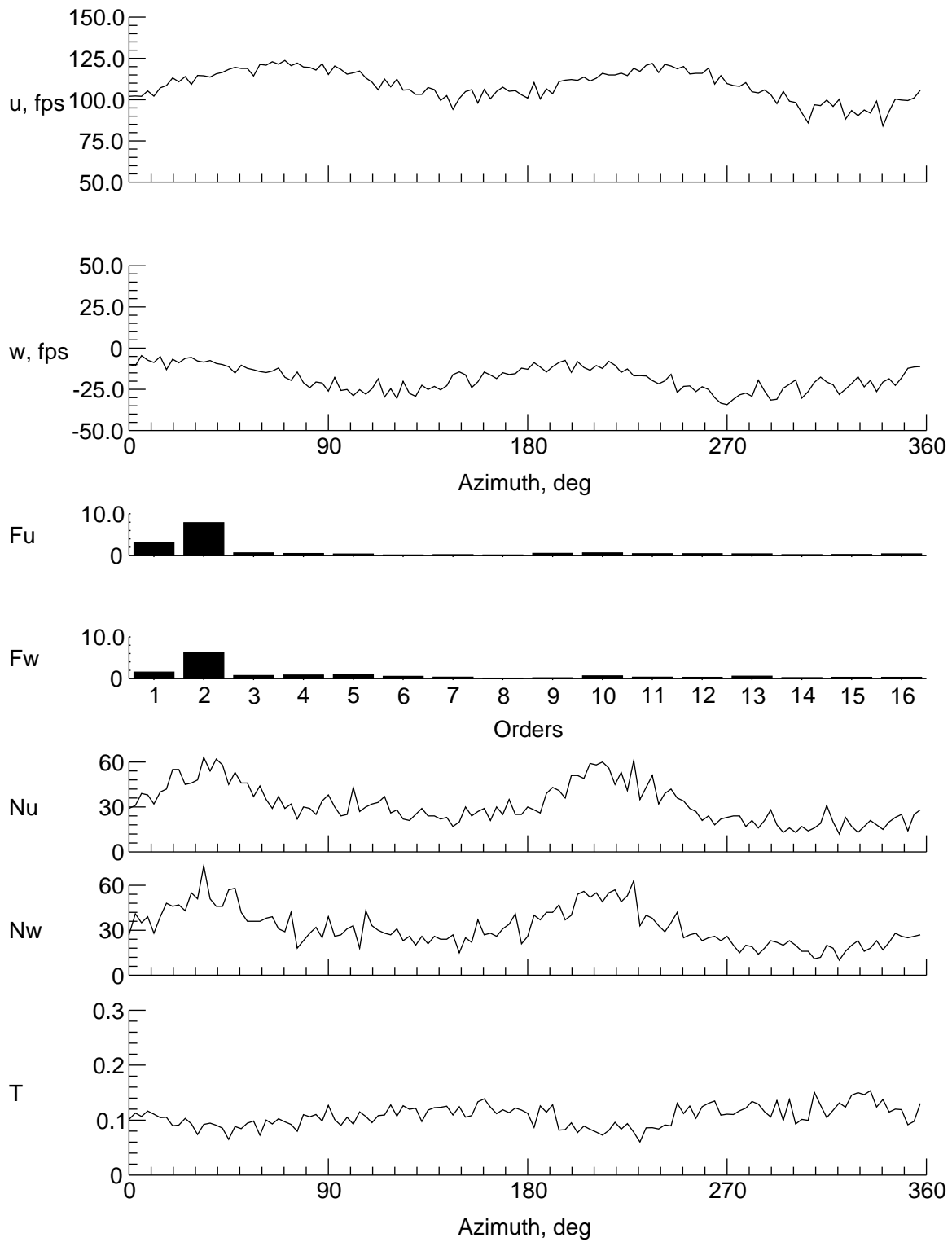
(d) $y = 0$ in., $z = 2.435$ in.

Figure 16. Continued.



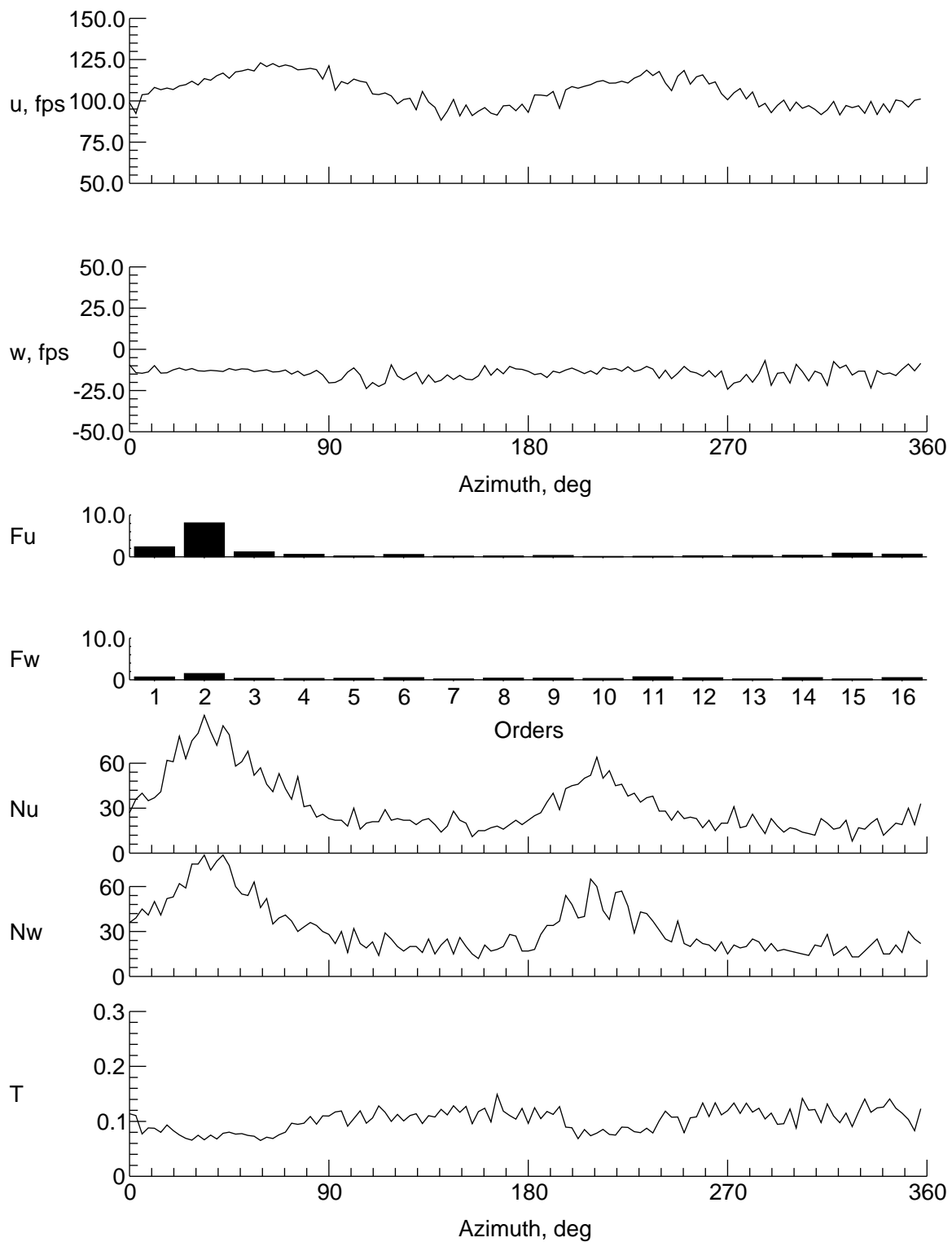
(e) $y = 0$ in., $z = -1.565$ in.

Figure 16. Continued.



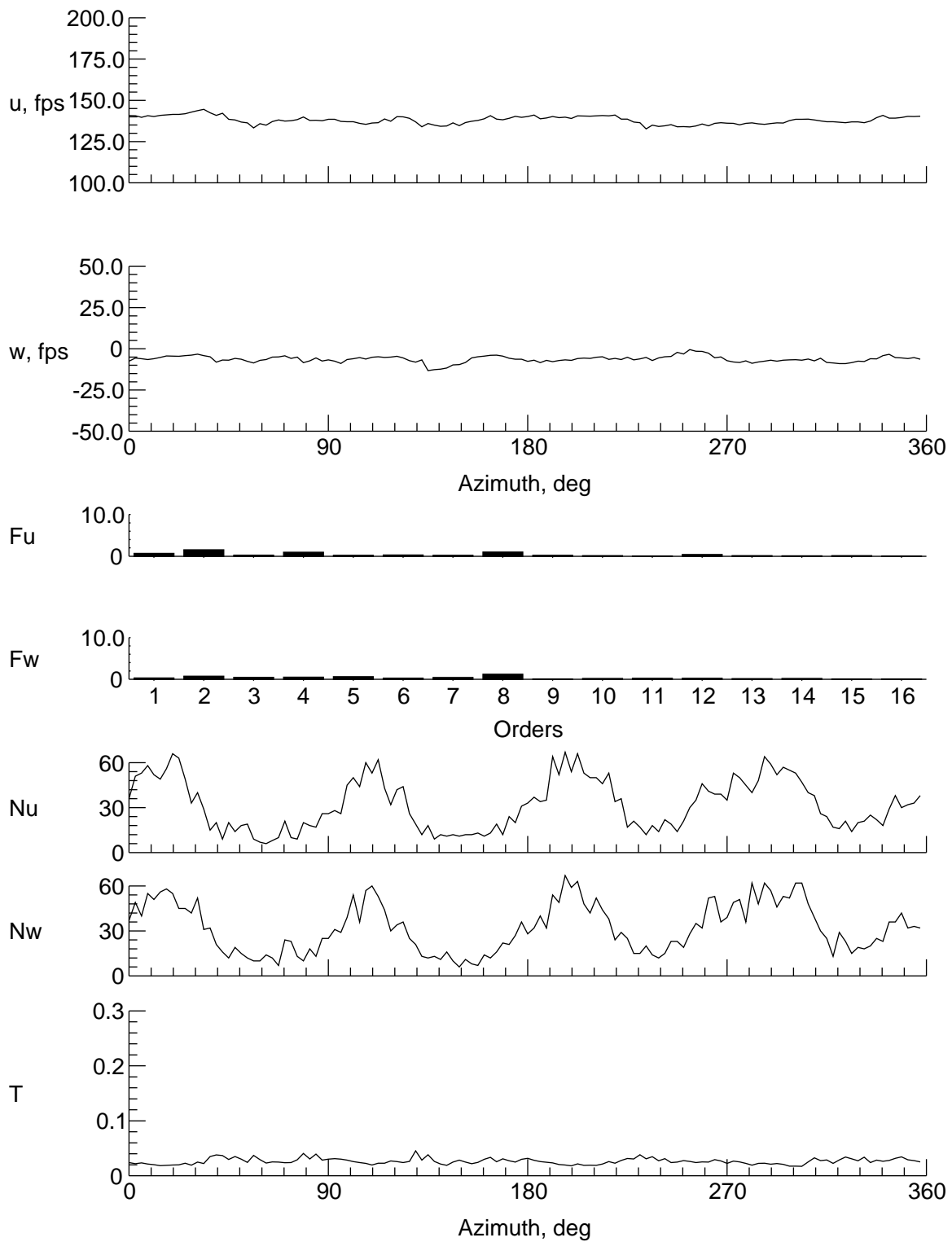
(f) $y = 0$ in., $z = -5.565$ in.

Figure 16. Continued.



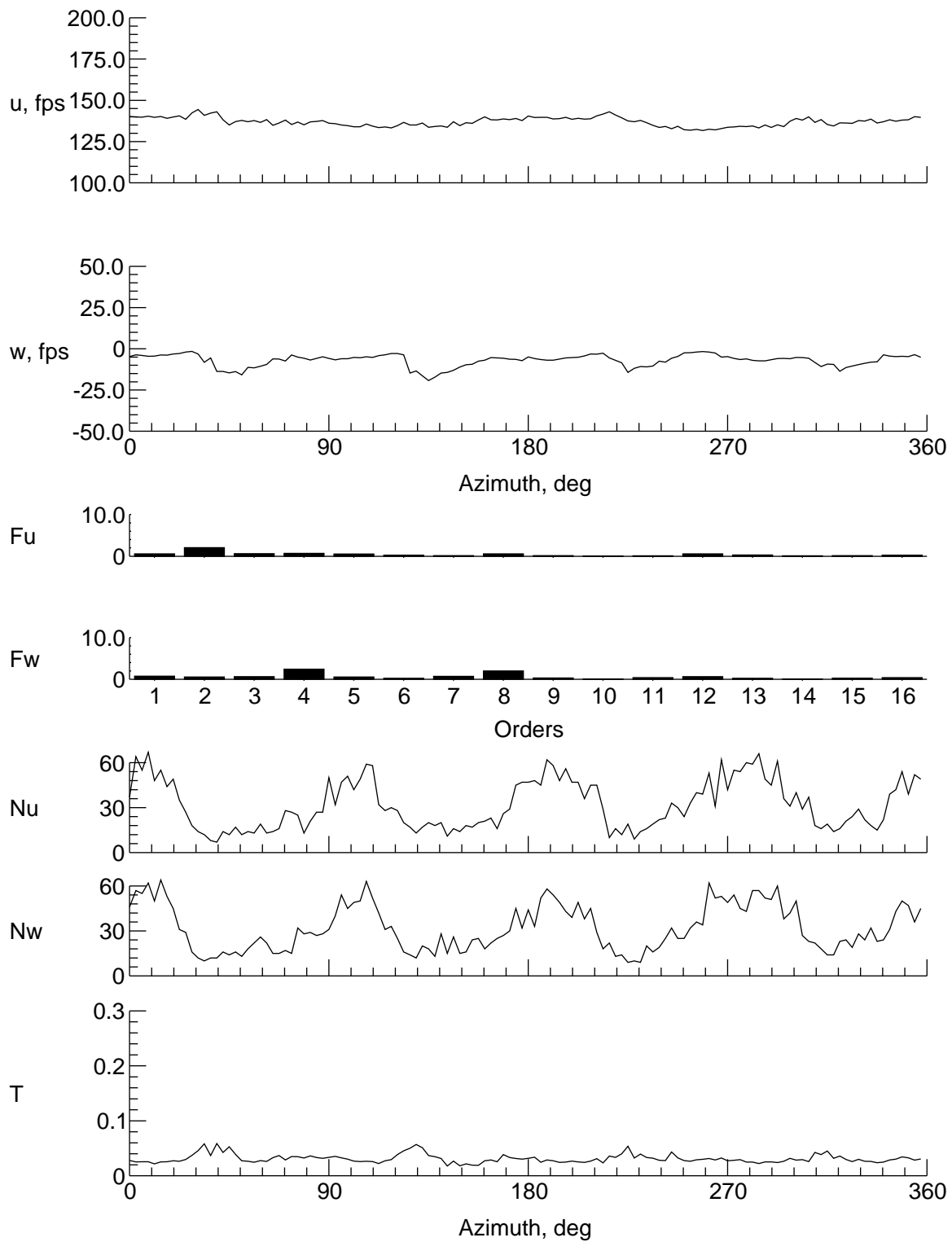
(g) $y = 0$ in., $z = -7.565$ in.

Figure 16. Continued.



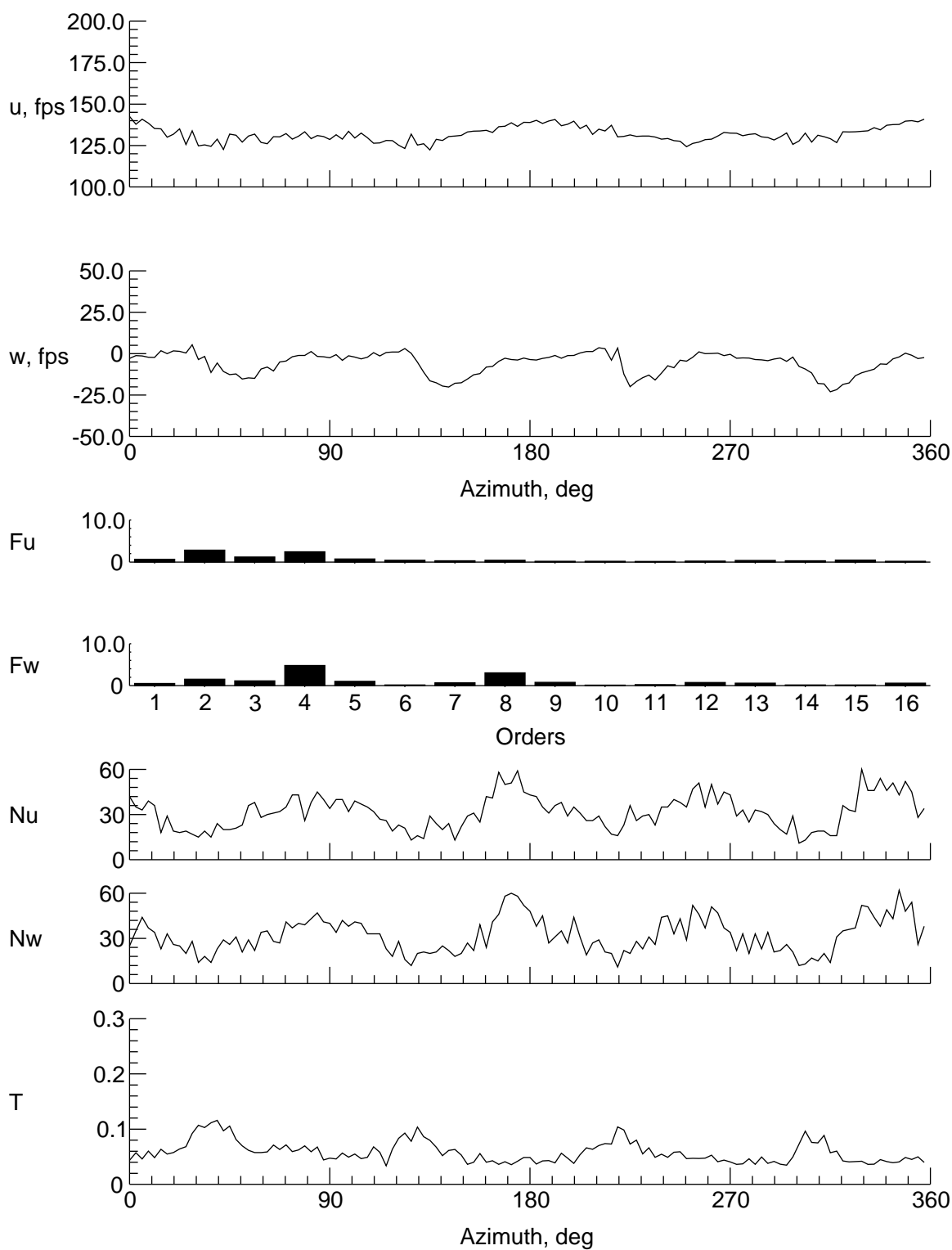
(h) $y = 9$ in., $z = -1.565$ in.

Figure 16. Continued.



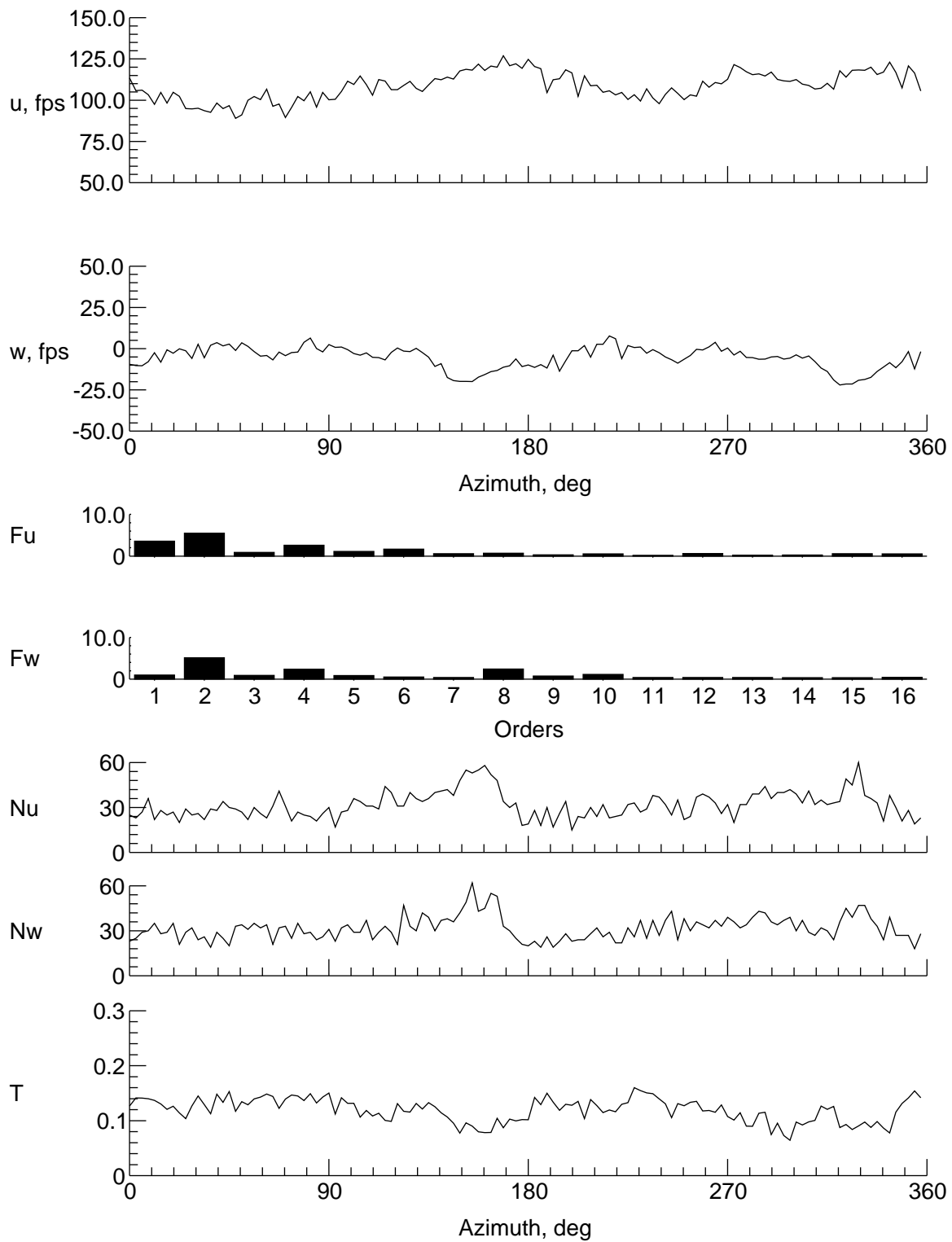
(i) $y = 8$ in., $z = -1.565$ in.

Figure 16. Continued.



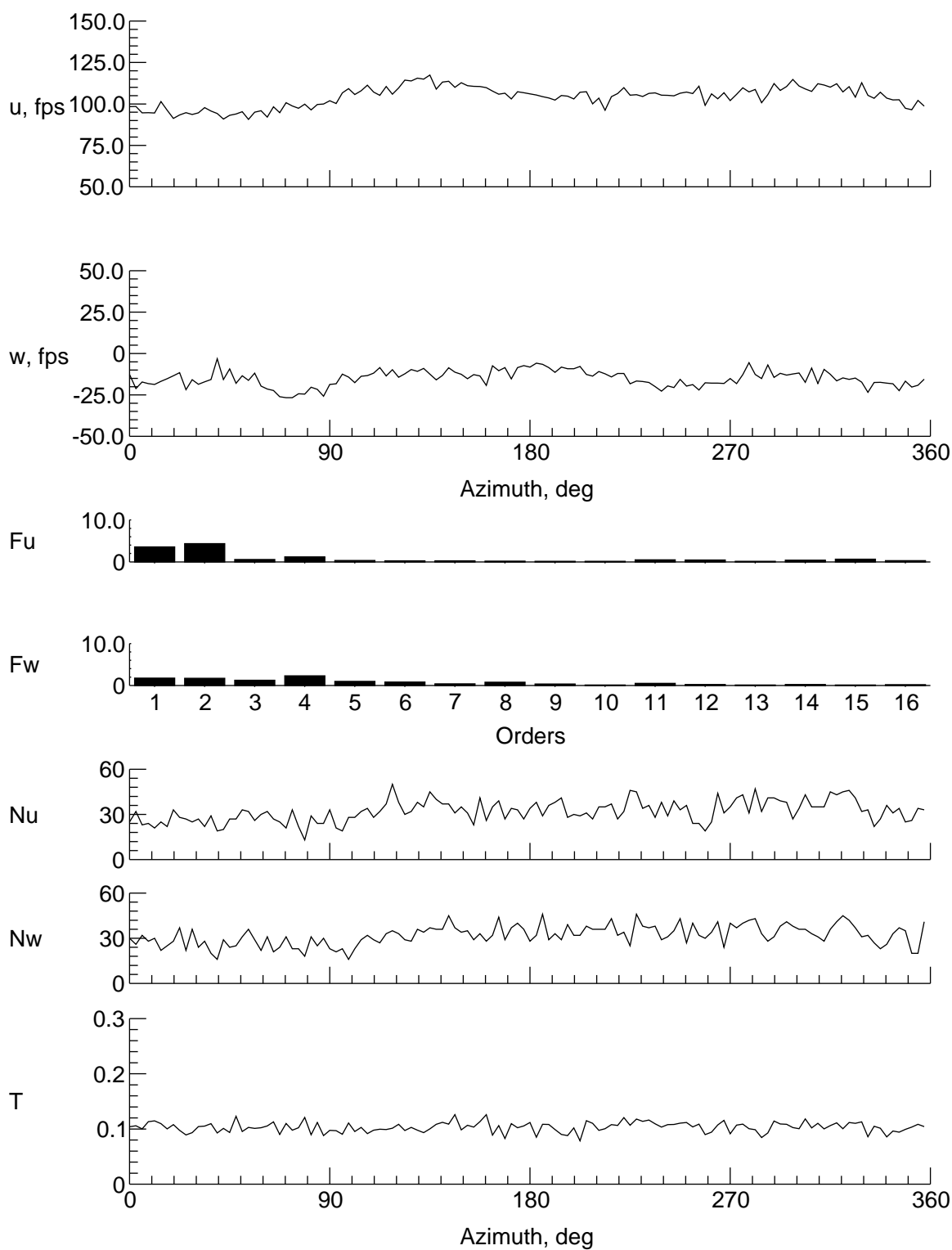
(j) $y = 6$ in., $z = -1.565$ in.

Figure 16. Continued.



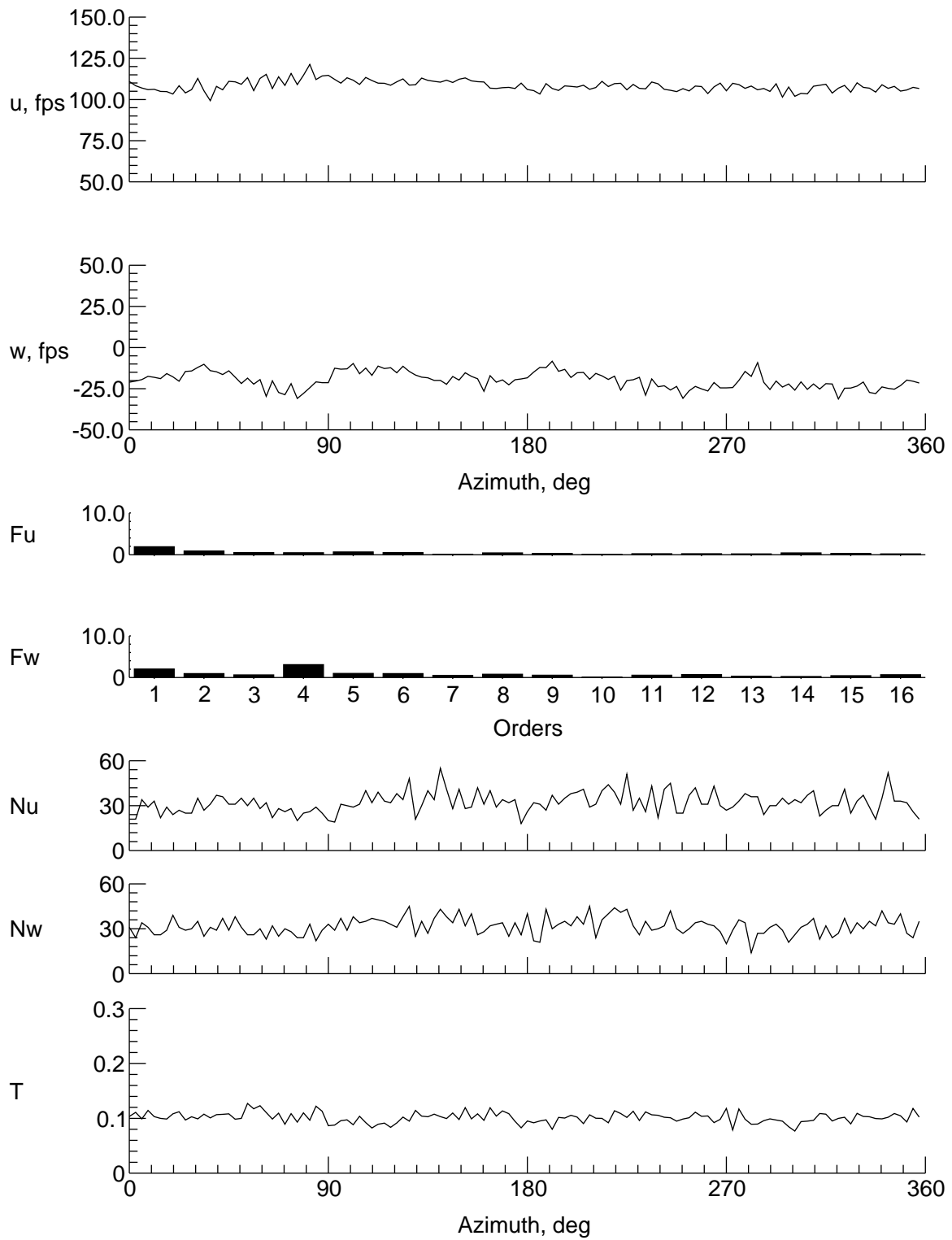
(k) $y = 4$ in., $z = -1.565$ in.

Figure 16. Continued.



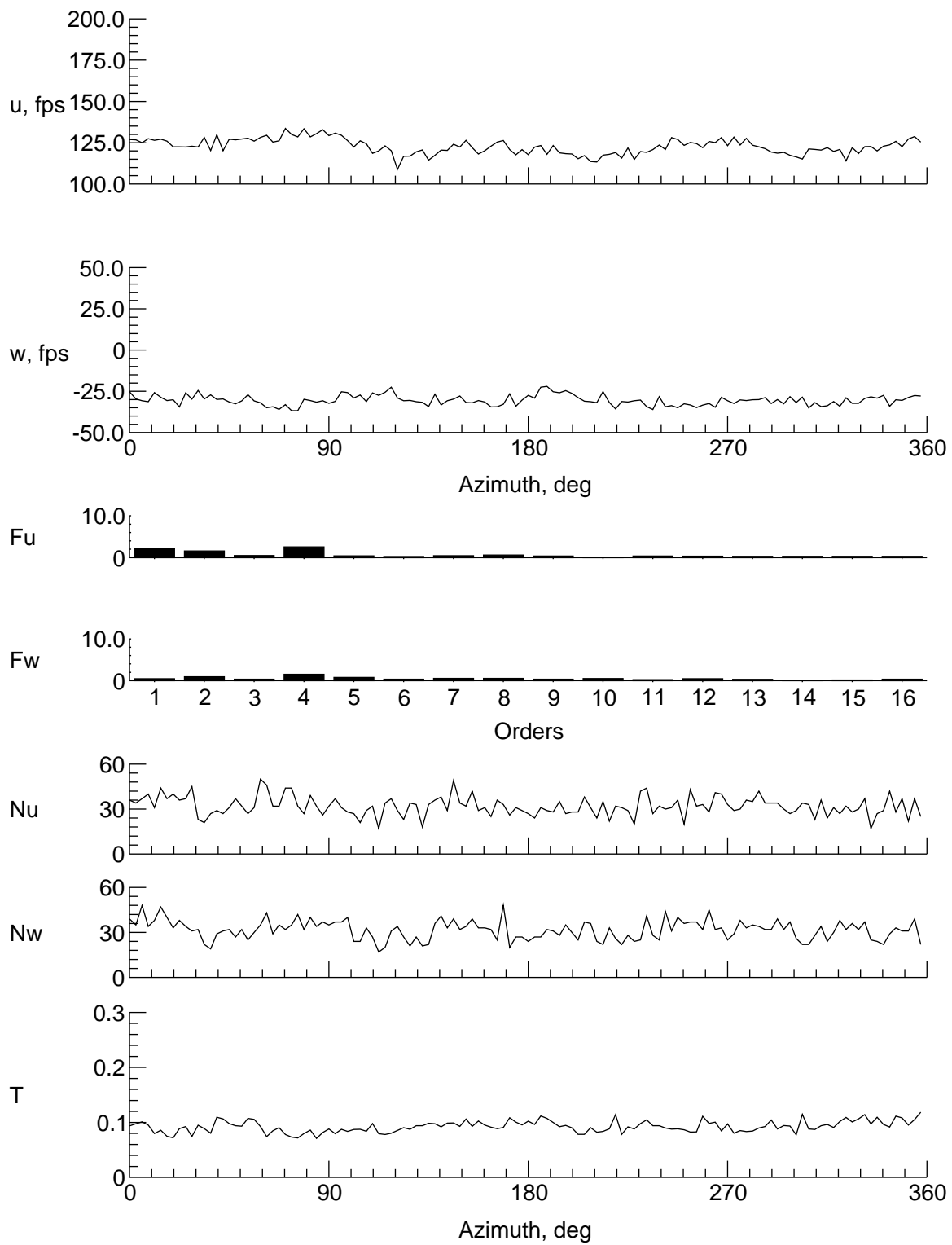
(l) $y = -4$ in., $z = -1.565$ in.

Figure 16. Continued.



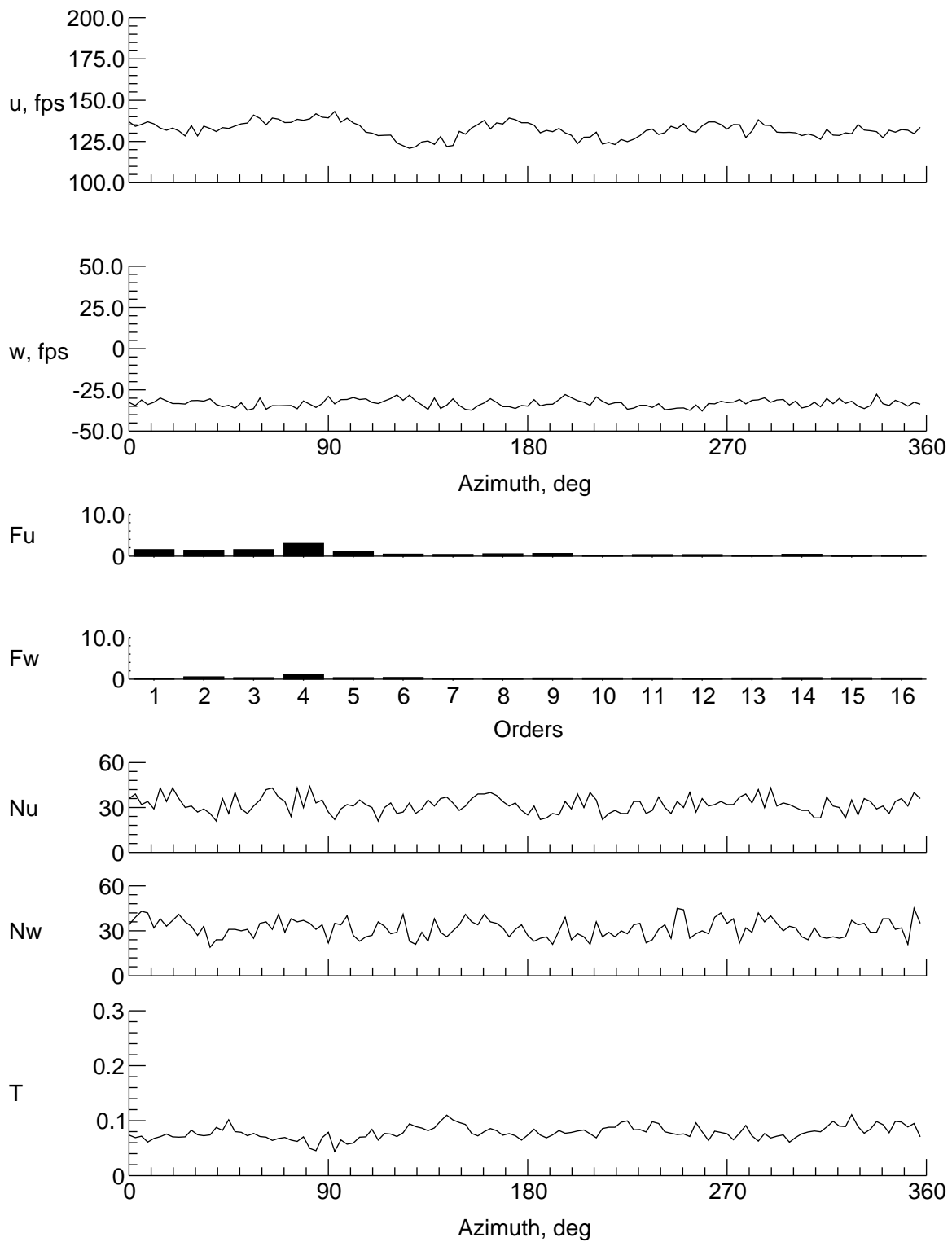
(m) $y = -6$ in., $z = -1.565$ in.

Figure 16. Continued.



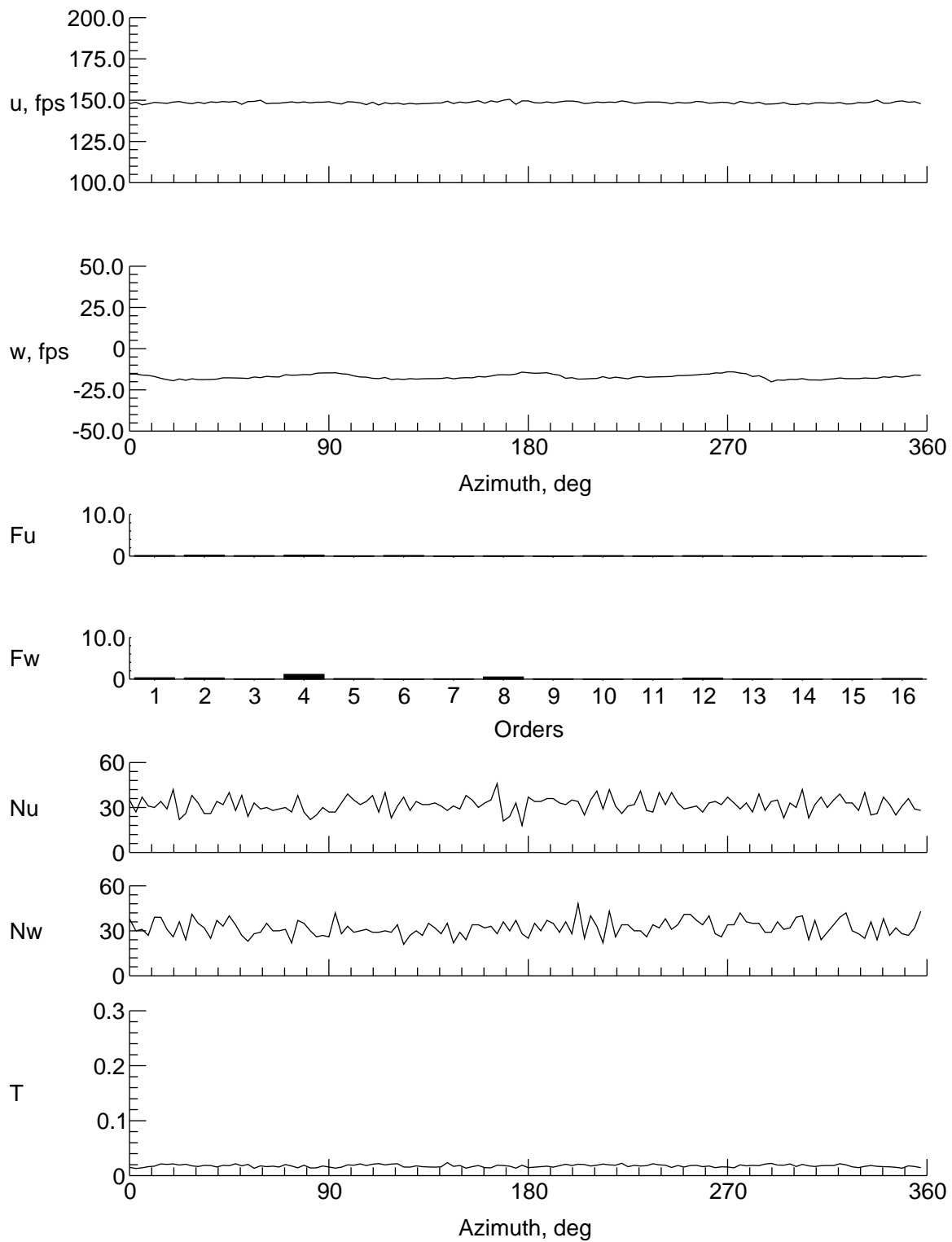
(n) $y = -8$ in., $z = -1.565$ in.

Figure 16. Continued.



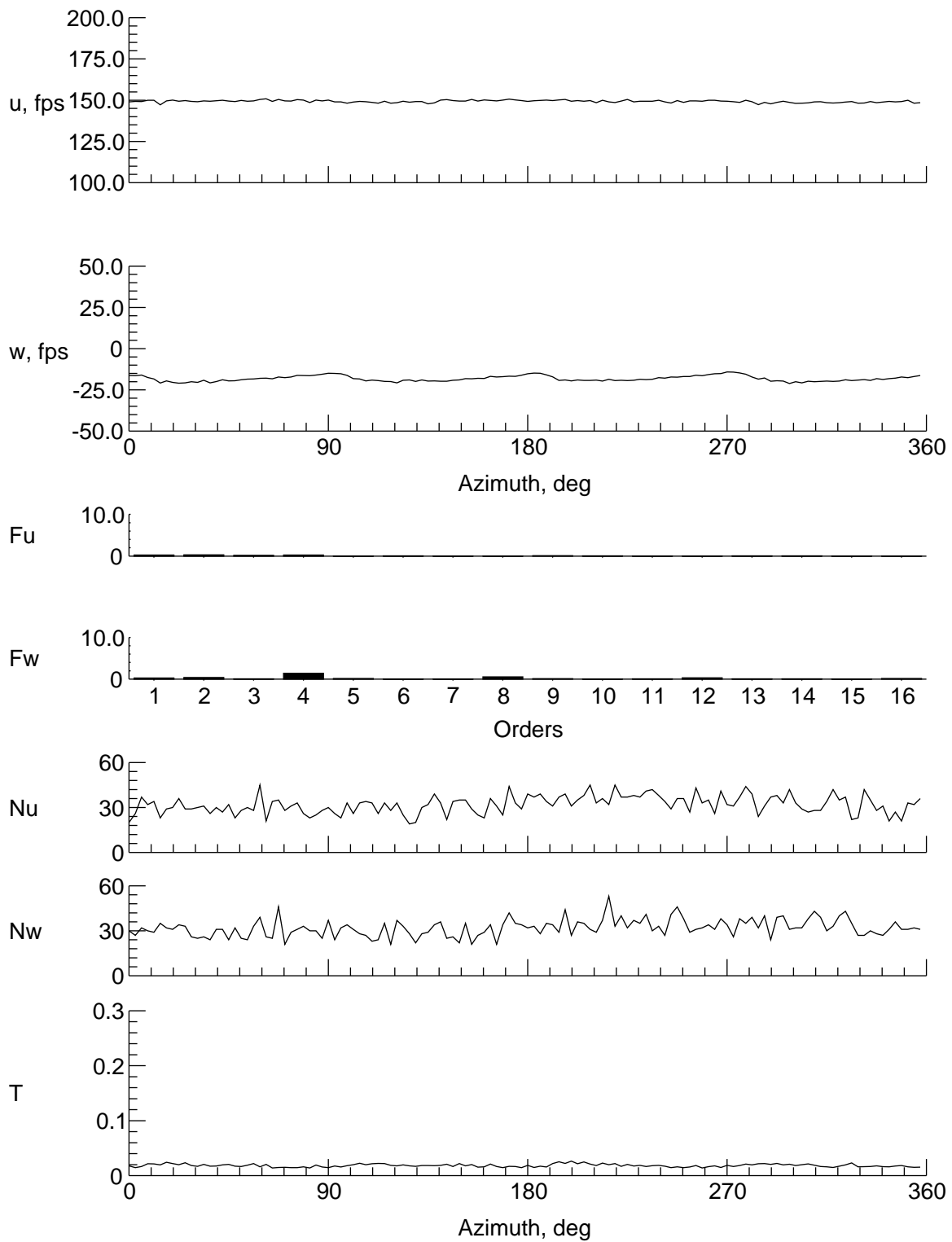
(o) $y = -9$ in., $z = -1.565$ in.

Figure 16. Concluded.



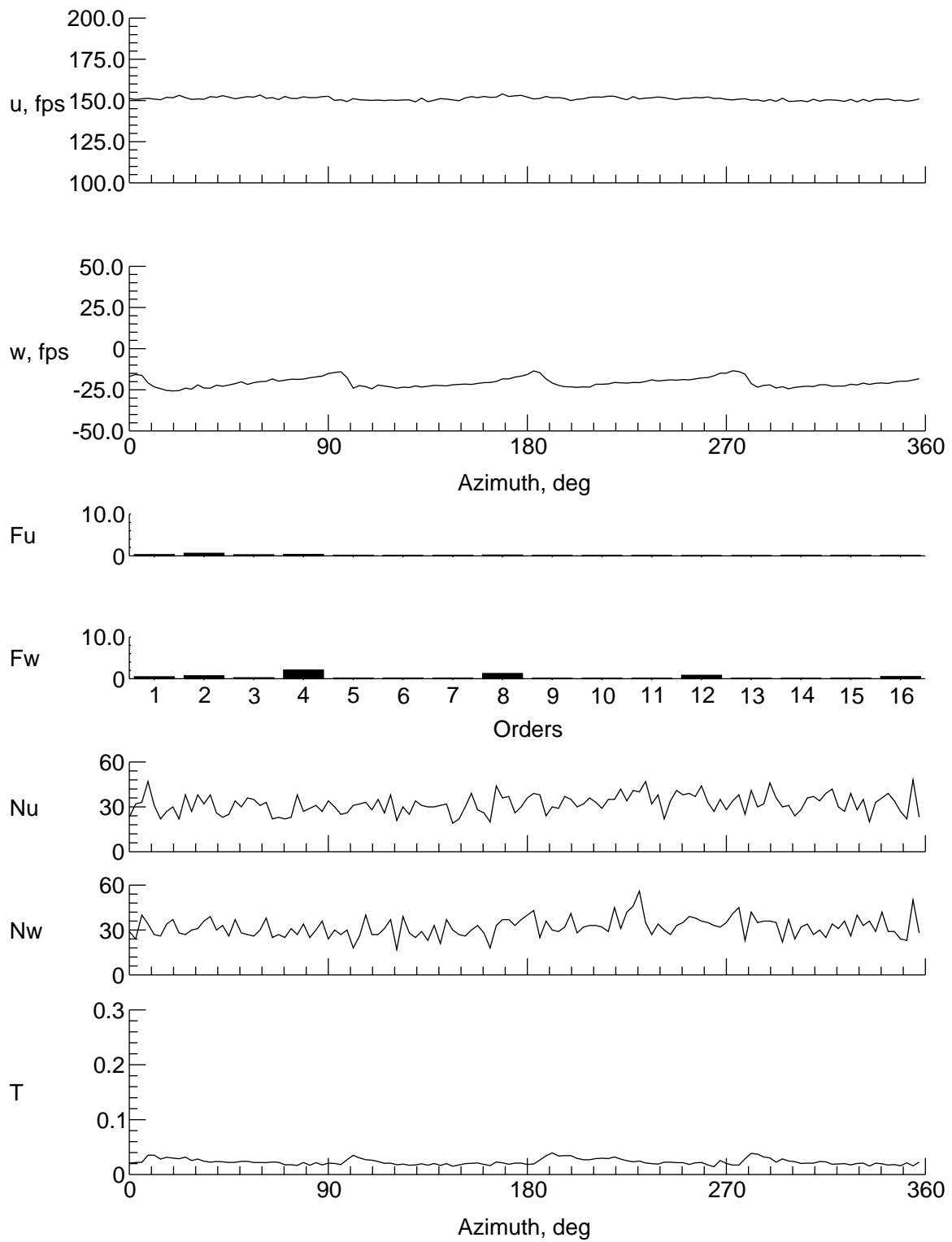
(a) $y = 0$ in., $z = 7.315$ in.

Figure 17. Velocity and turbulence at station 28 in.



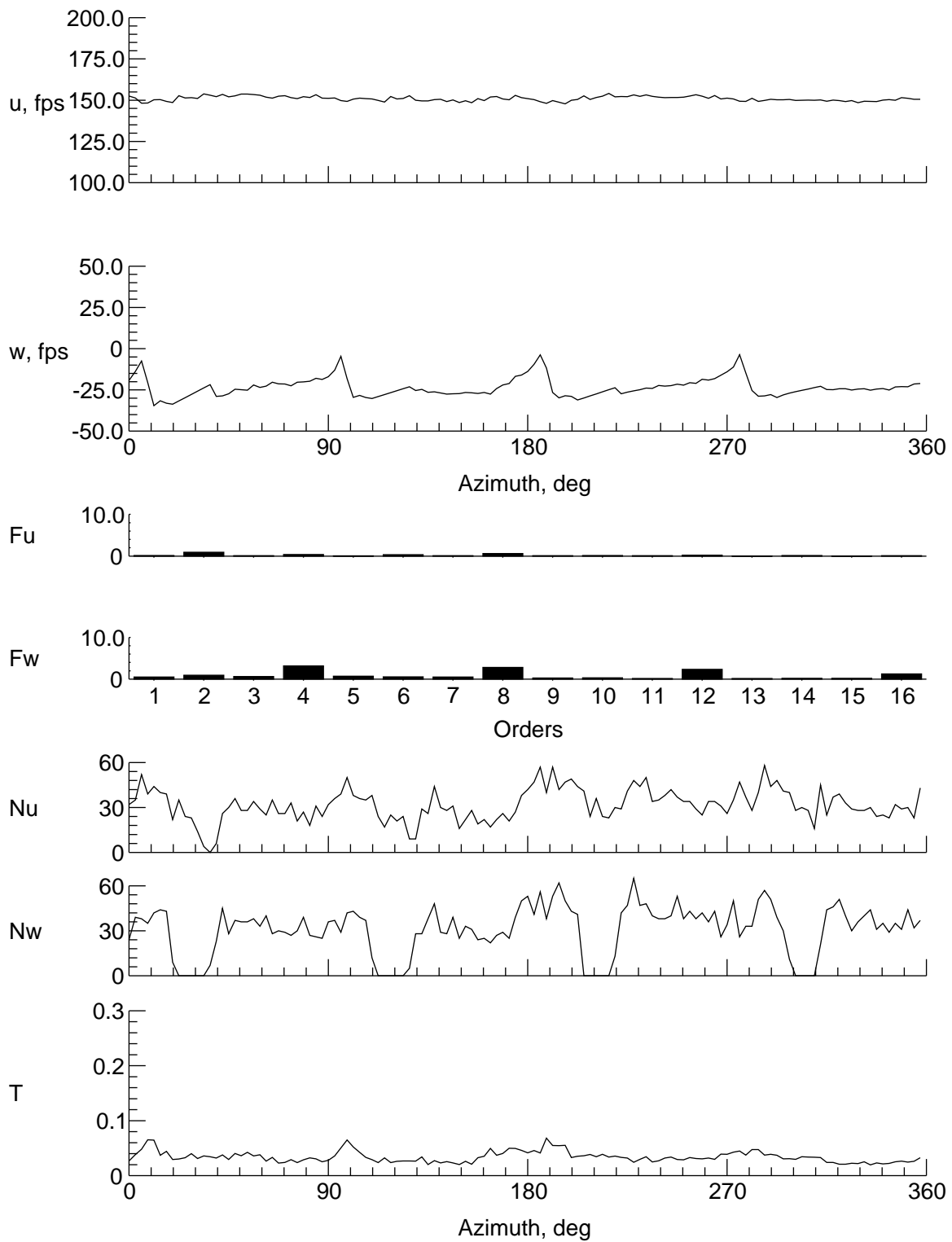
(b) $y = 0$ in., $z = 6.315$ in.

Figure 17. Continued.



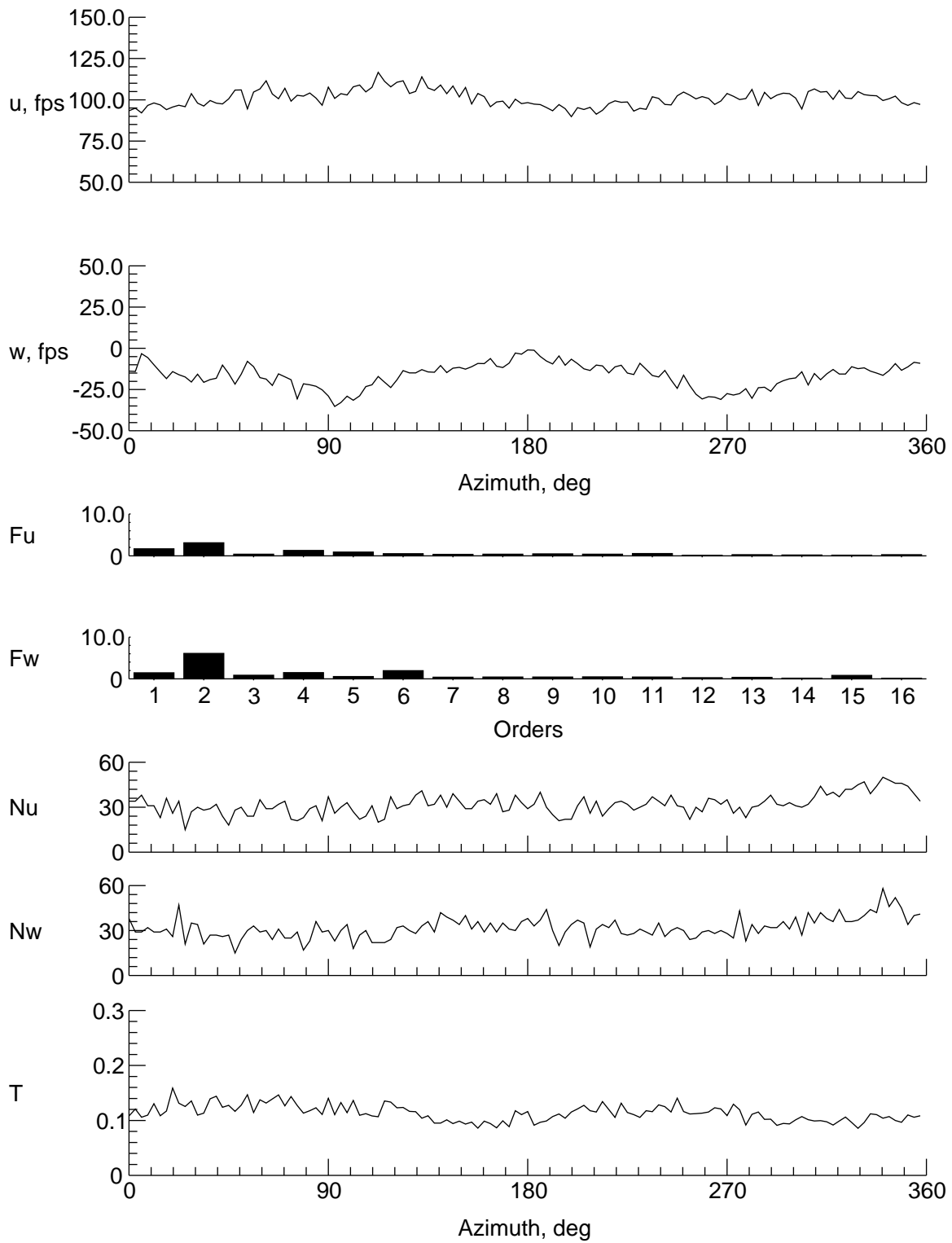
(c) $y = 0$ in., $z = 4.315$ in.

Figure 17. Continued.



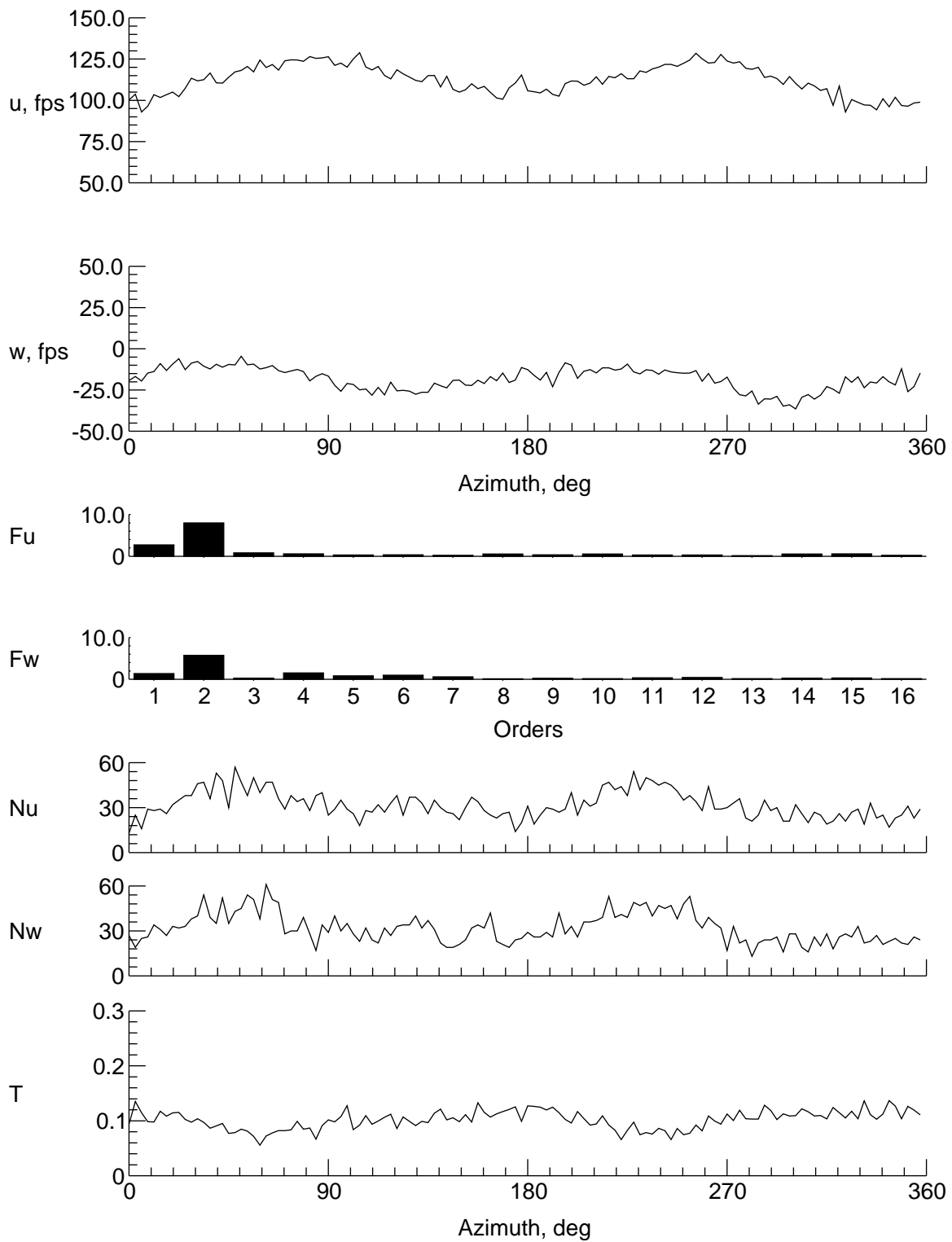
(d) $y = 0 \text{ in.}, z = 2.315 \text{ in.}$

Figure 17. Continued.



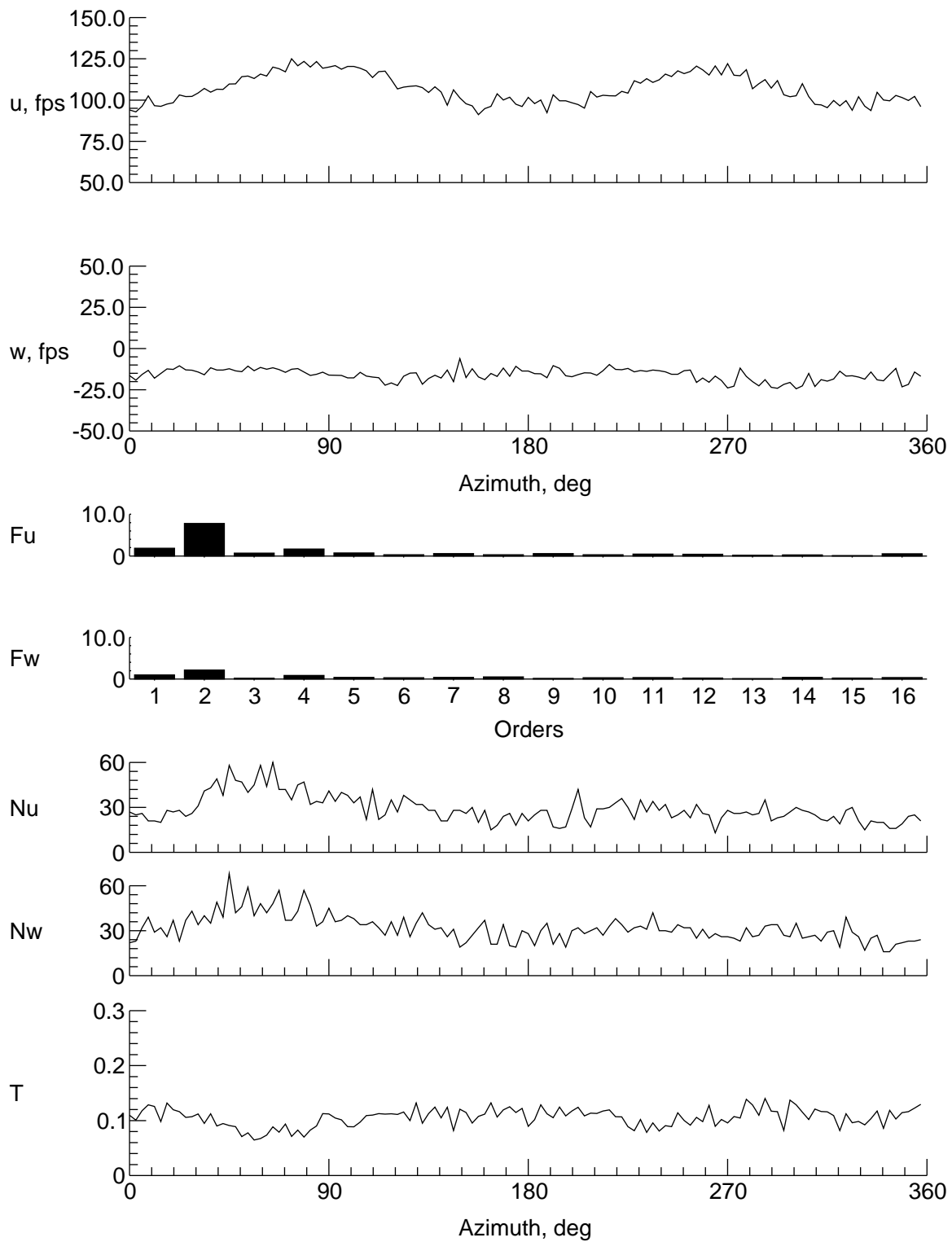
(e) $y = 0$ in., $z = -1.685$ in.

Figure 17. Continued.



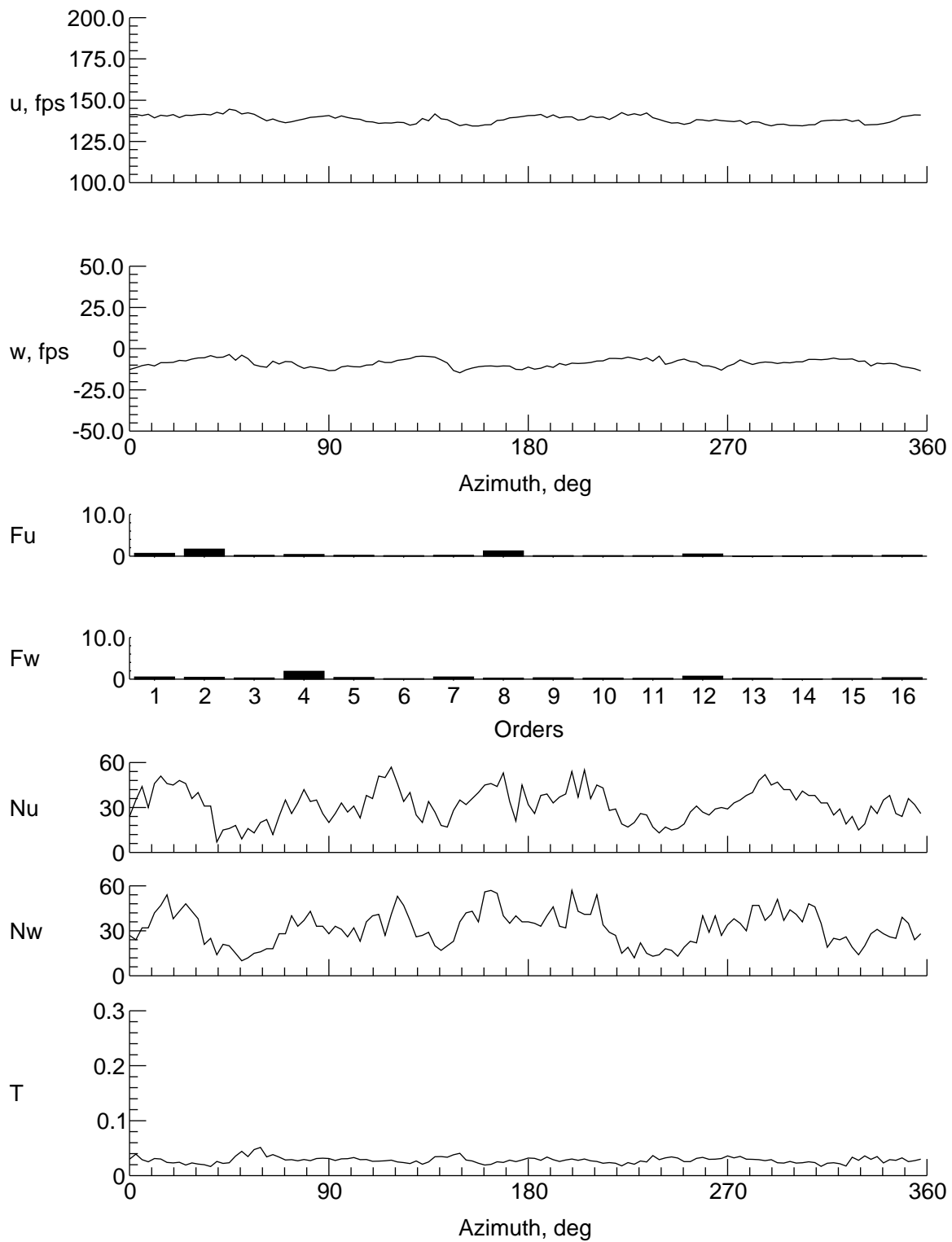
(f) $y = 0$ in., $z = -5.685$ in.

Figure 17. Continued.



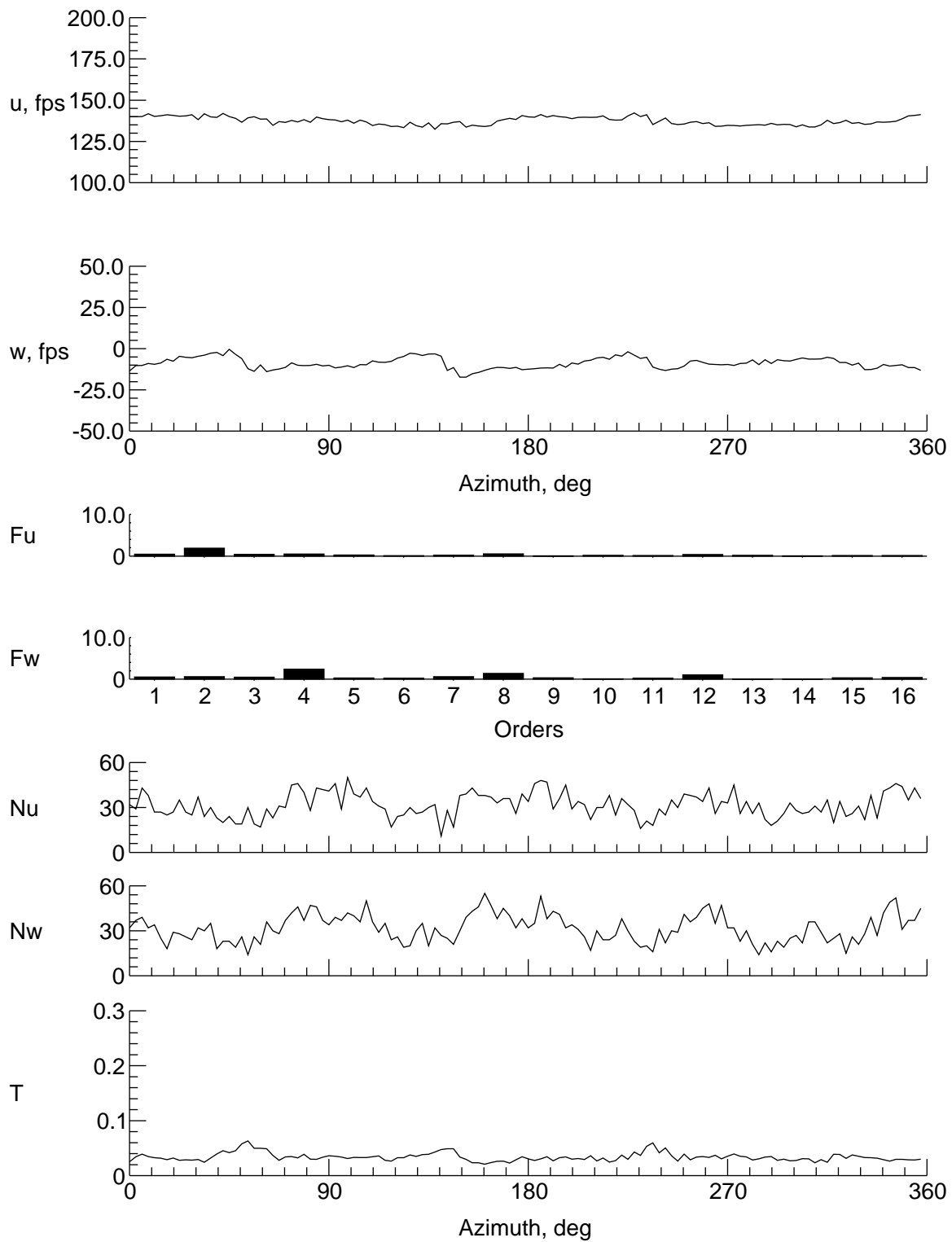
(g) $y = 0$ in., $z = -7.685$ in.

Figure 17. Continued.



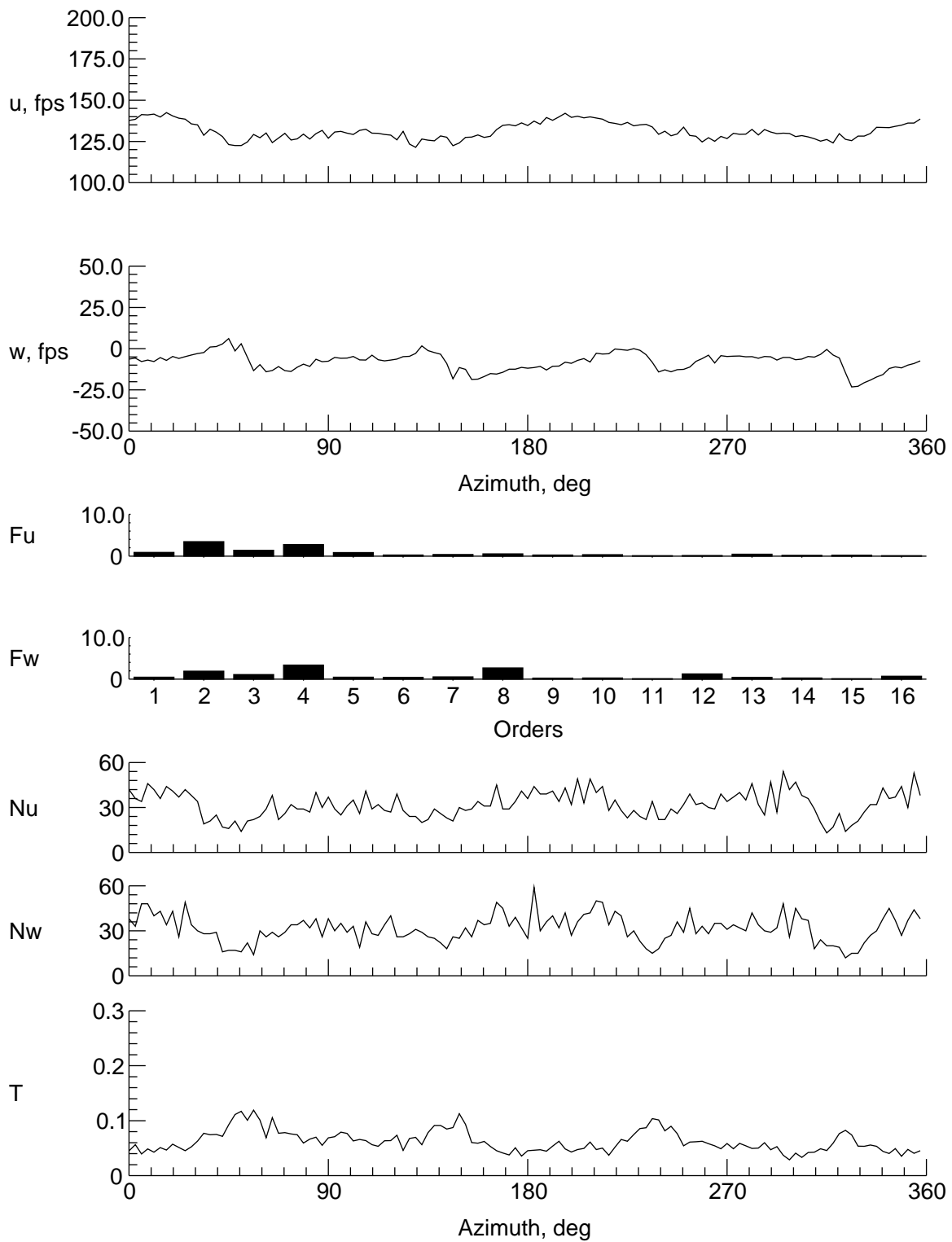
(h) $y = 9$ in., $z = -1.685$ in.

Figure 17. Continued.



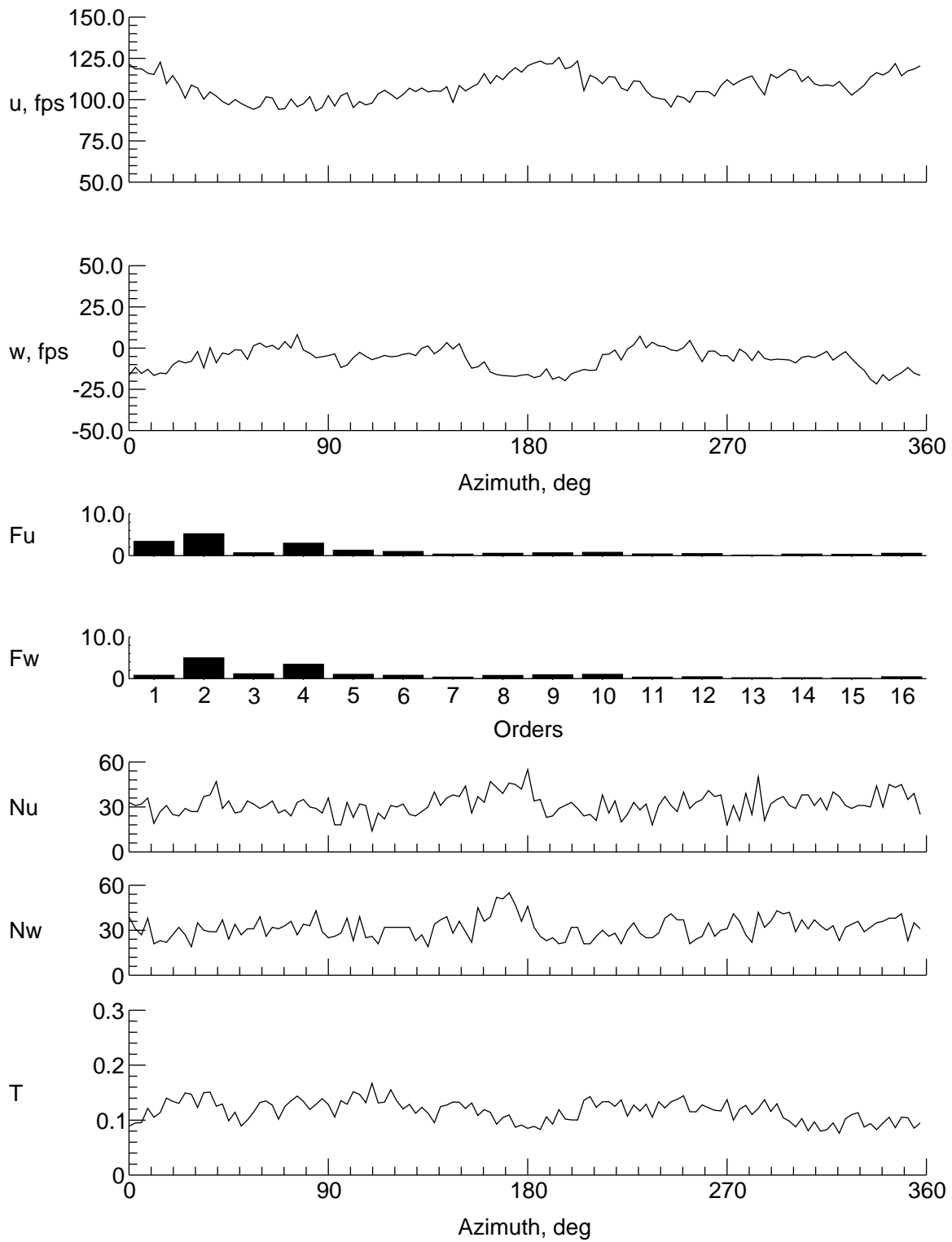
(i) $y = 8$ in., $z = -1.685$ in.

Figure 17. Continued.



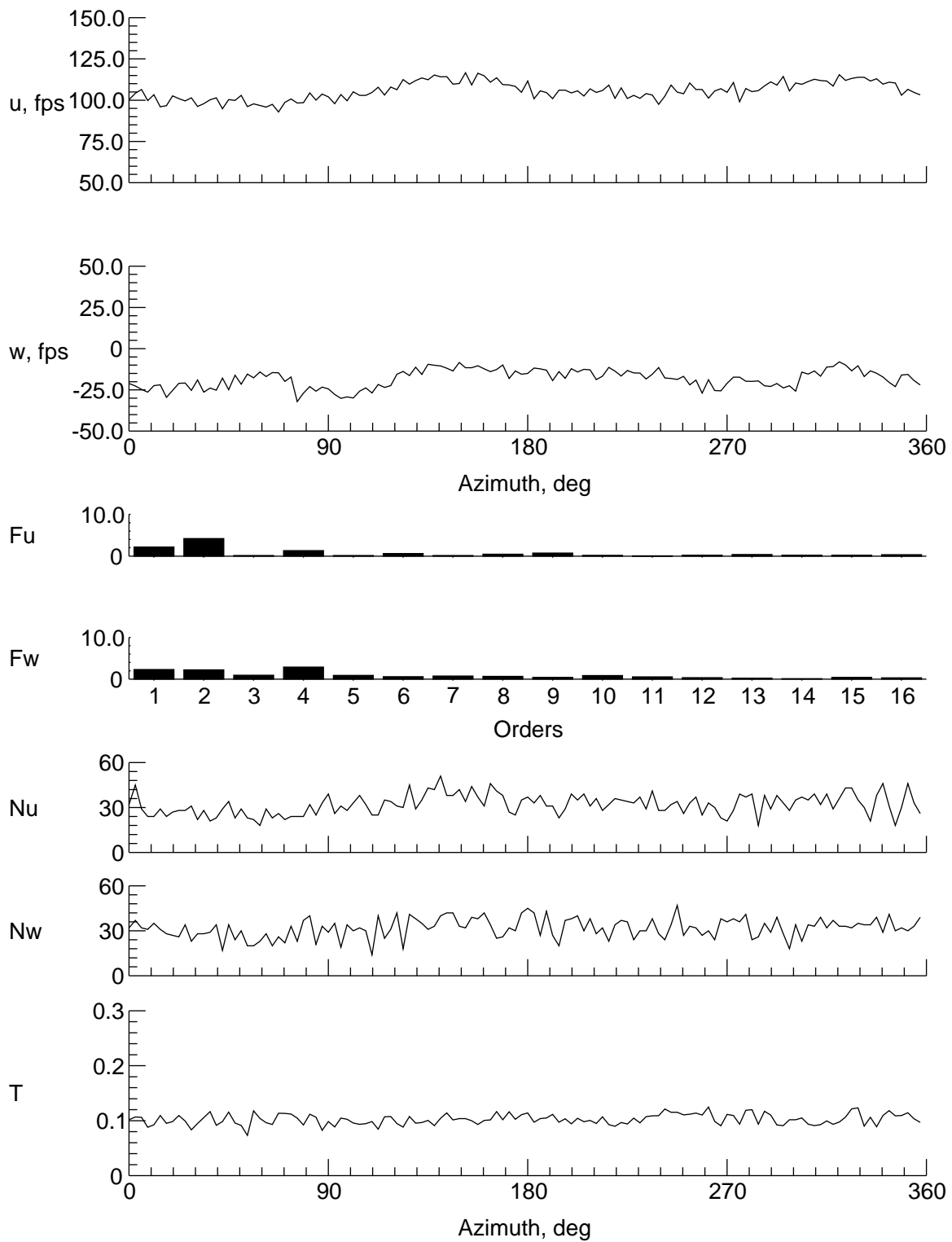
(j) $y = 6$ in., $z = -1.685$ in.

Figure 17. Continued.



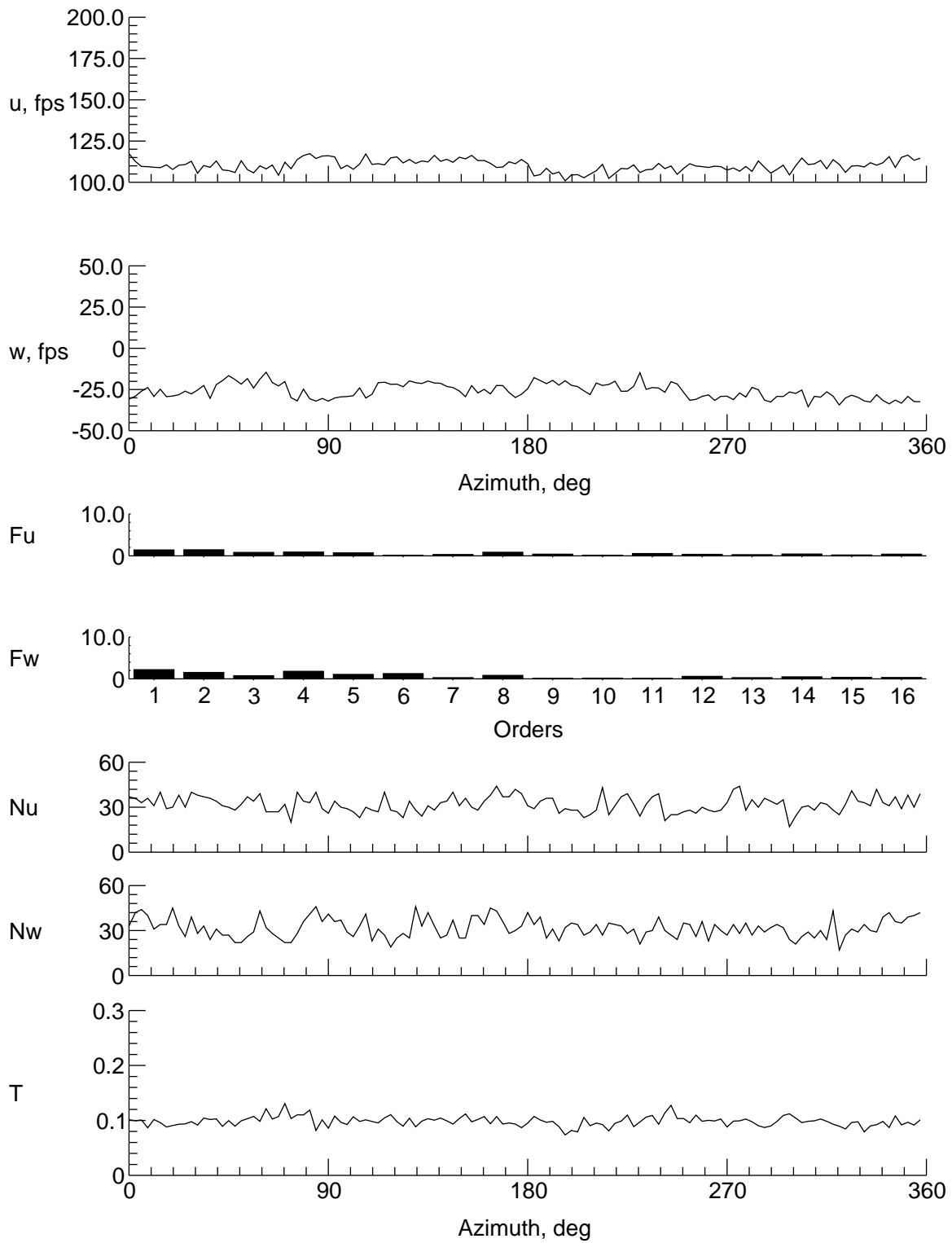
(k) $y = 4$ in., $z = -1.685$ in.

Figure 17. Continued.



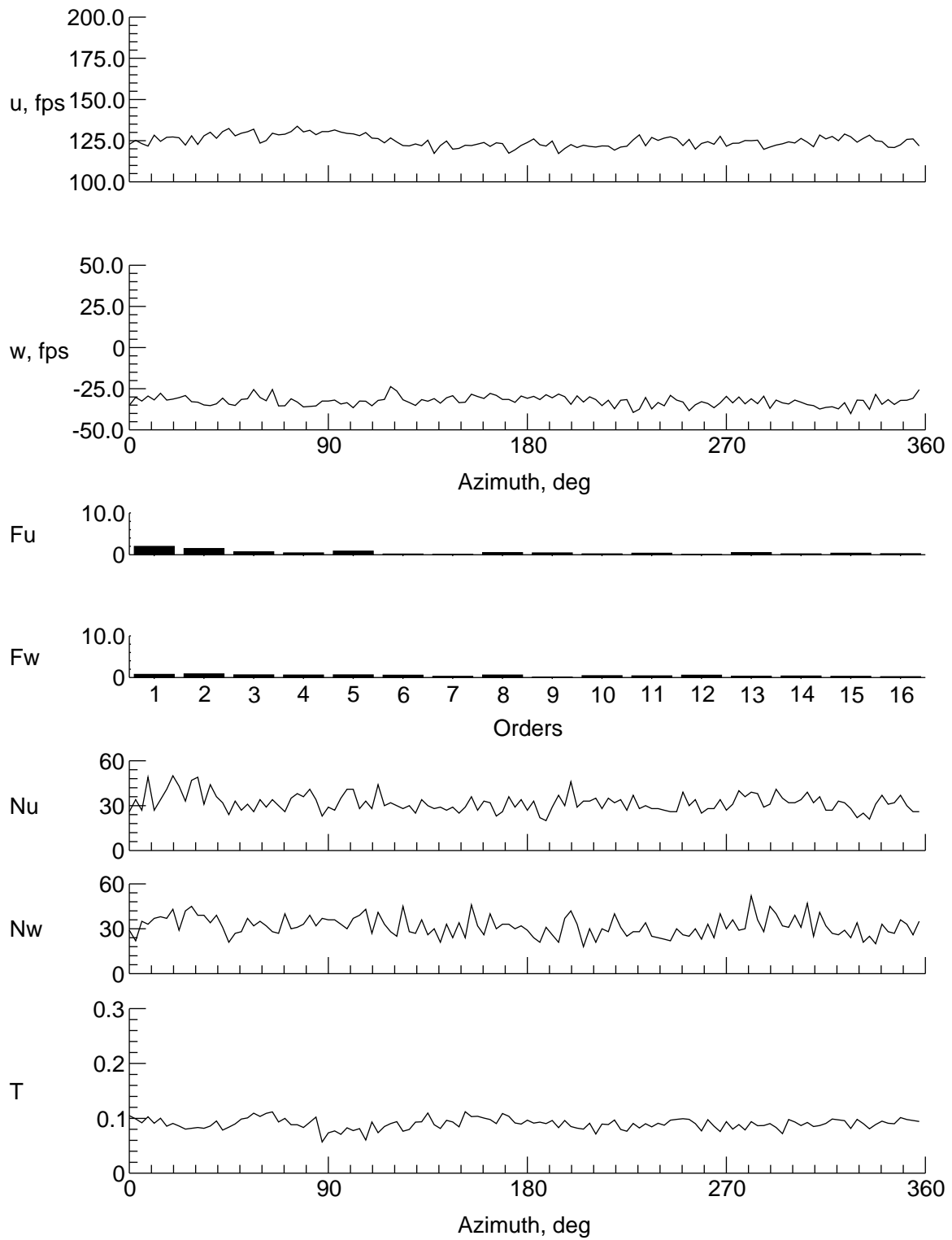
(l) $y = -4$ in., $z = -1.685$ in.

Figure 17. Continued.



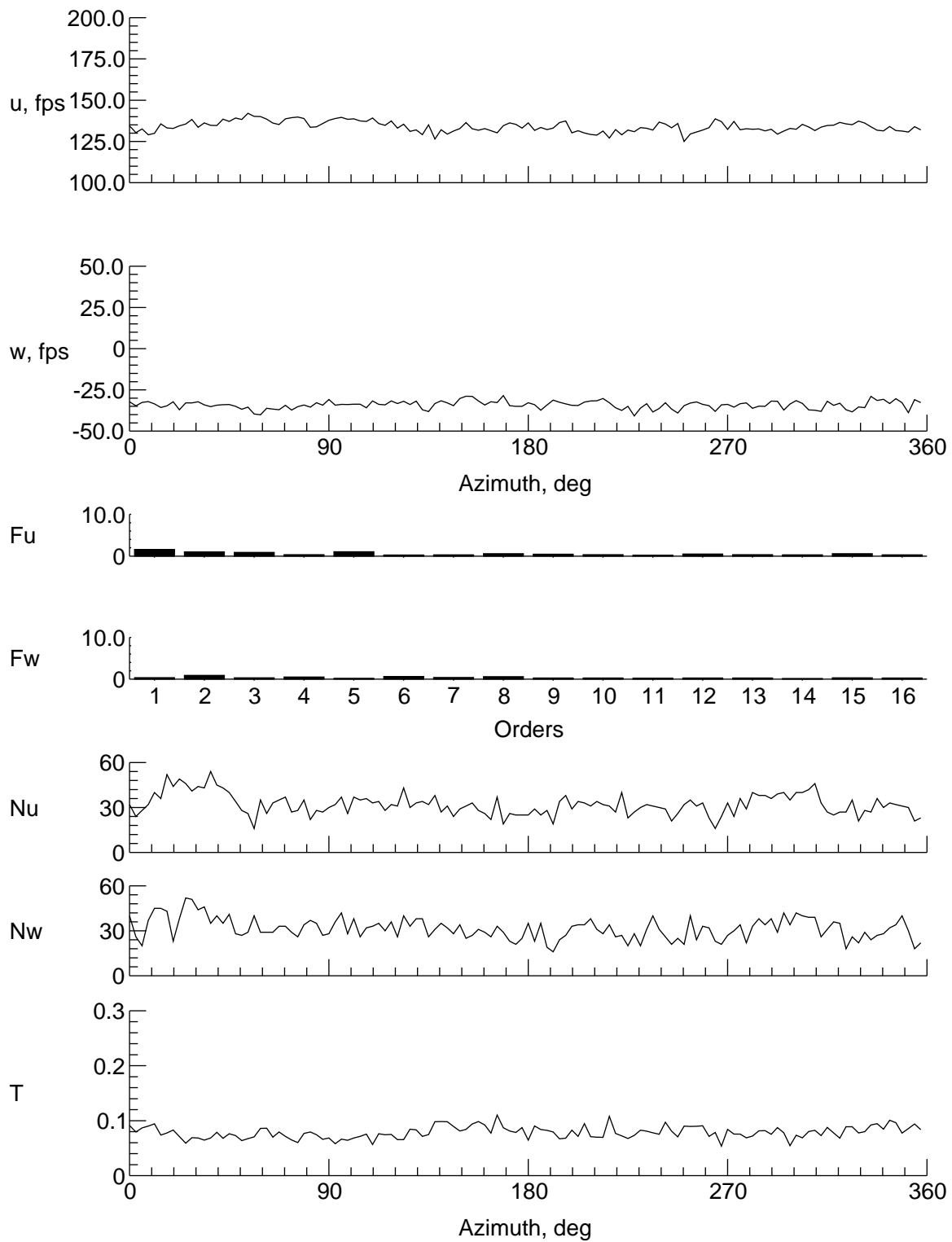
(m) $y = -6$ in., $z = -1.685$ in.

Figure 17. Continued.



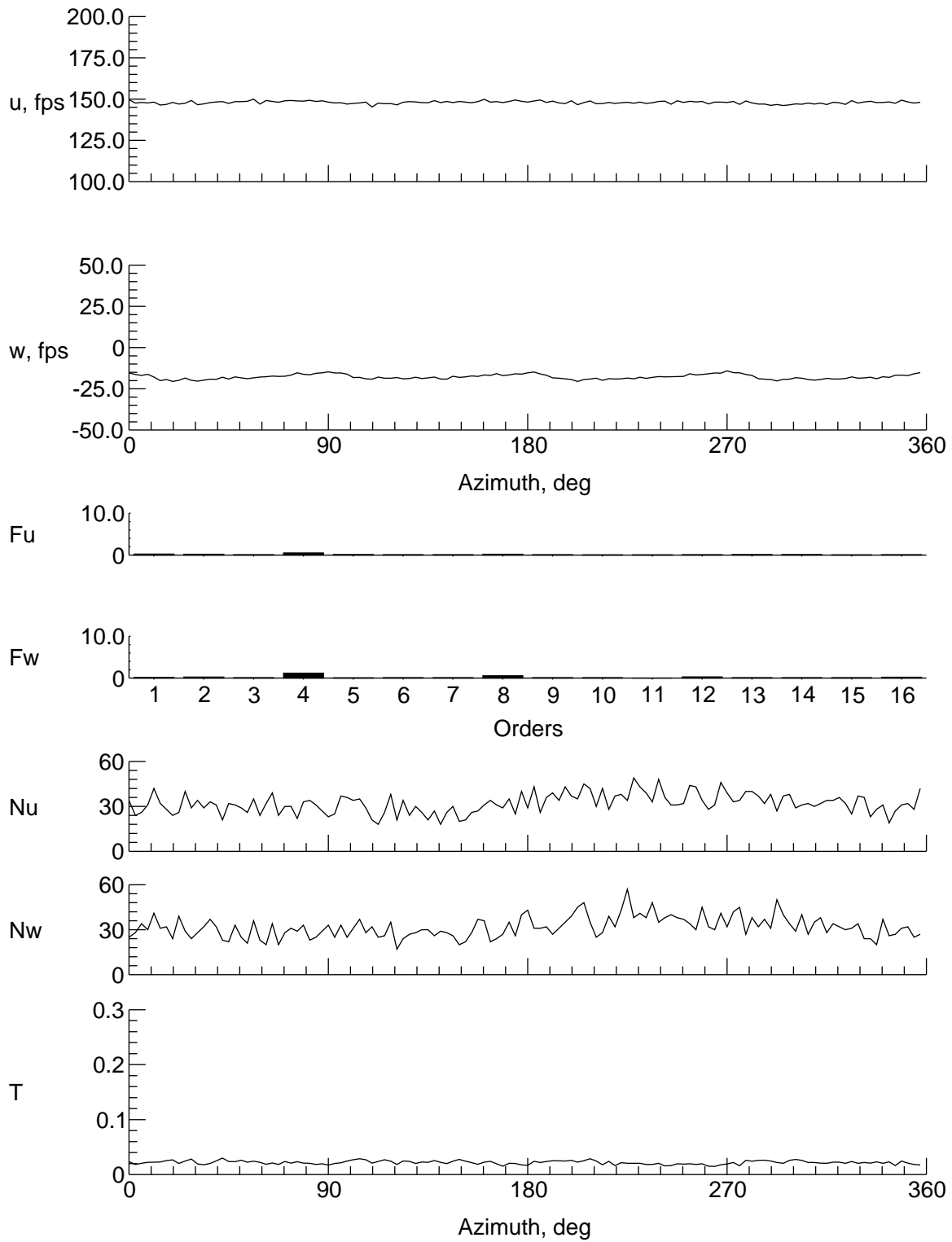
(n) $y = -8$ in., $z = -1.685$ in.

Figure 17. Continued.



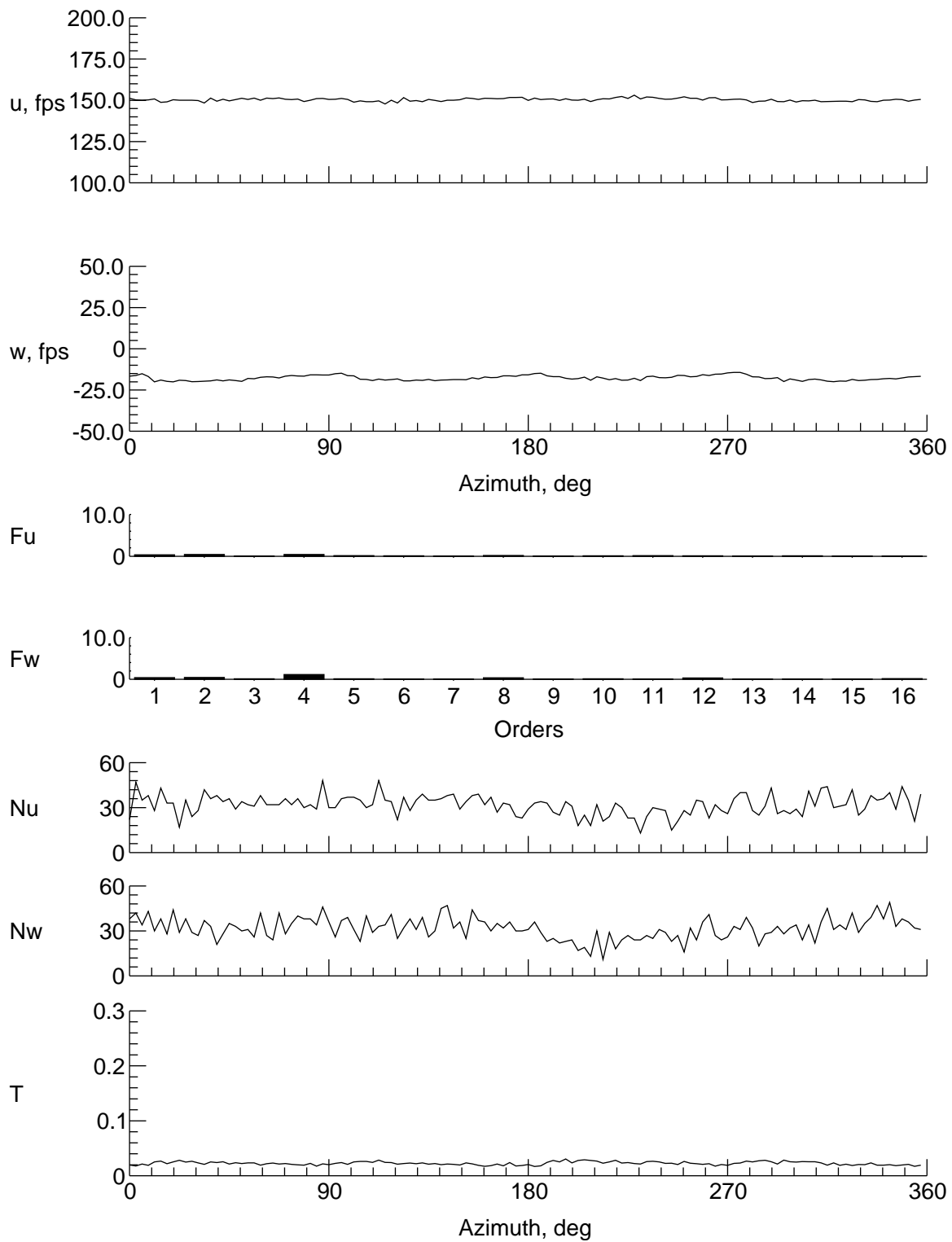
(o) $y = -9$ in., $z = -1.685$ in.

Figure 17. Continued.



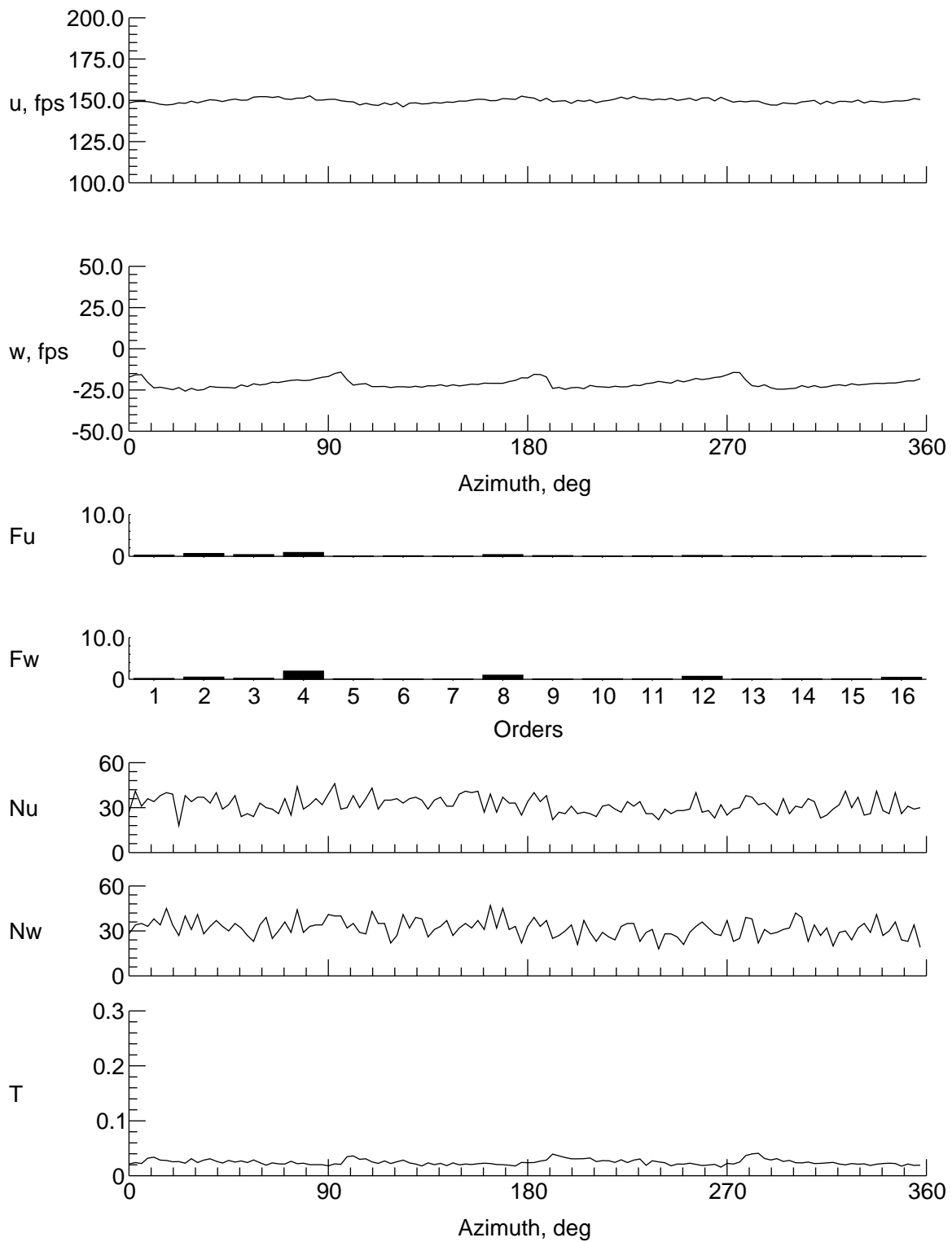
(a) $y = 0$ in., $z = 7.194$ in.

Figure 18. Velocity and turbulence at station 30 in.



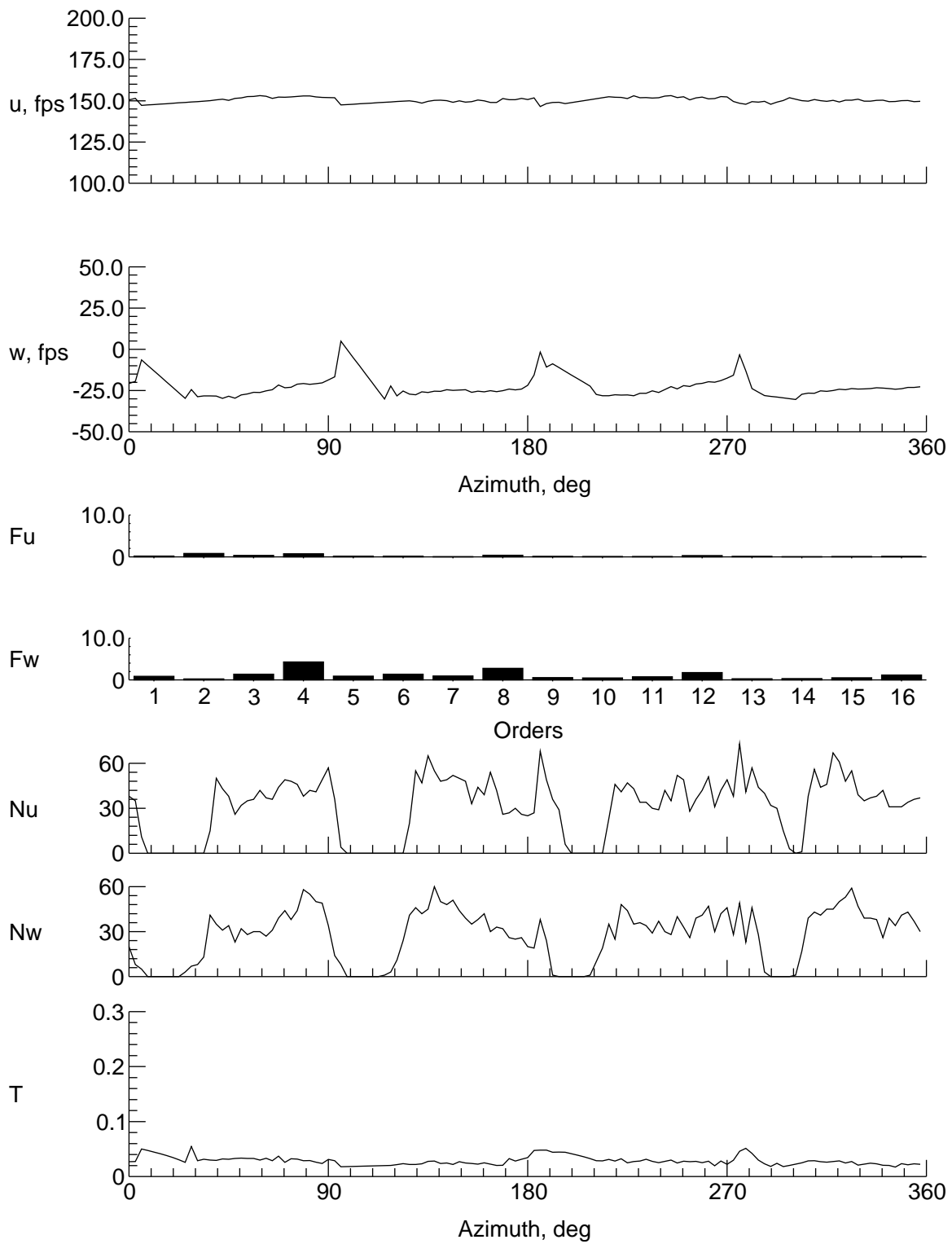
(b) $y = 0$ in., $z = 6.194$ in.

Figure 18. Continued.



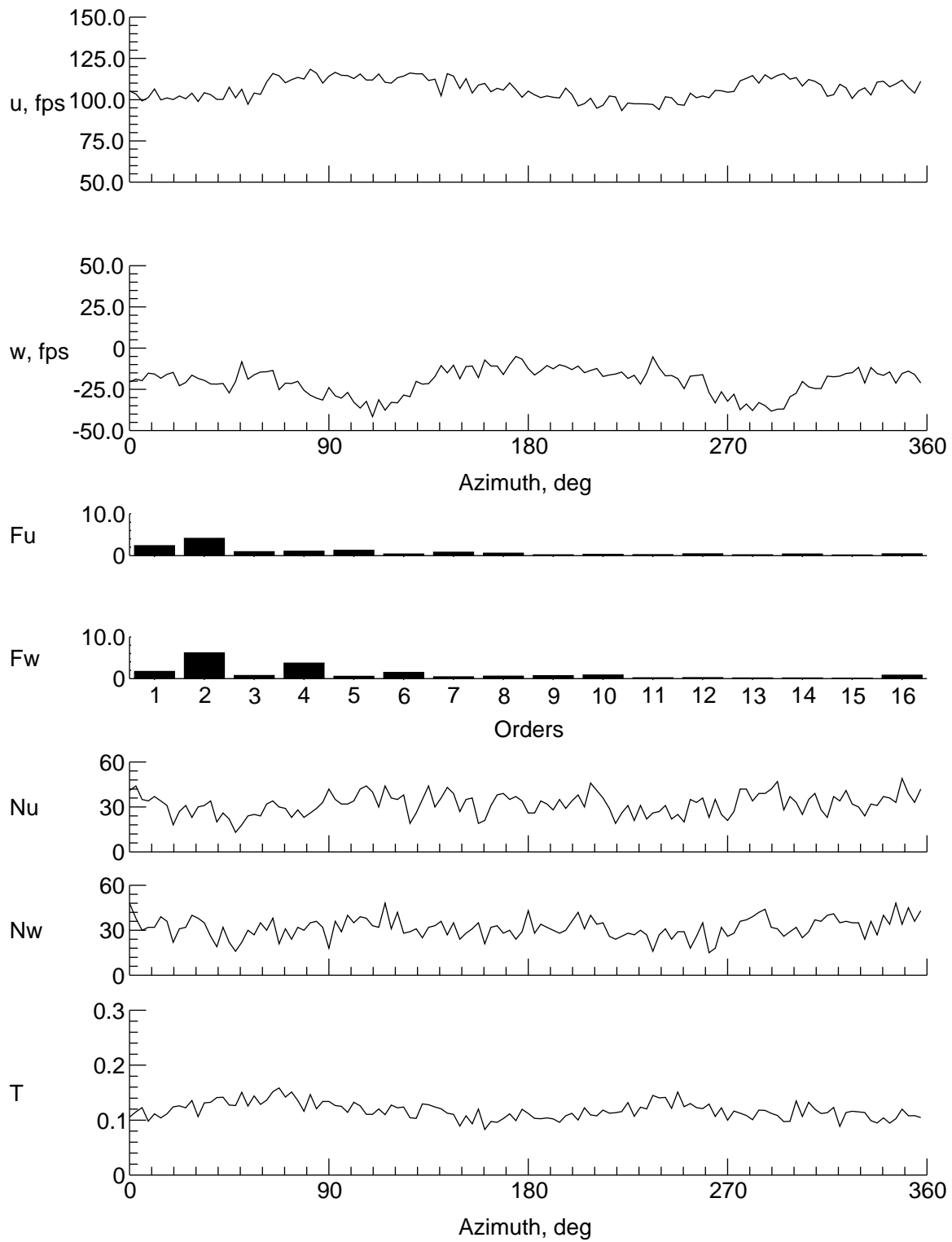
(c) $y = 0$ in., $z = 4.194$ in.

Figure 18. Continued.



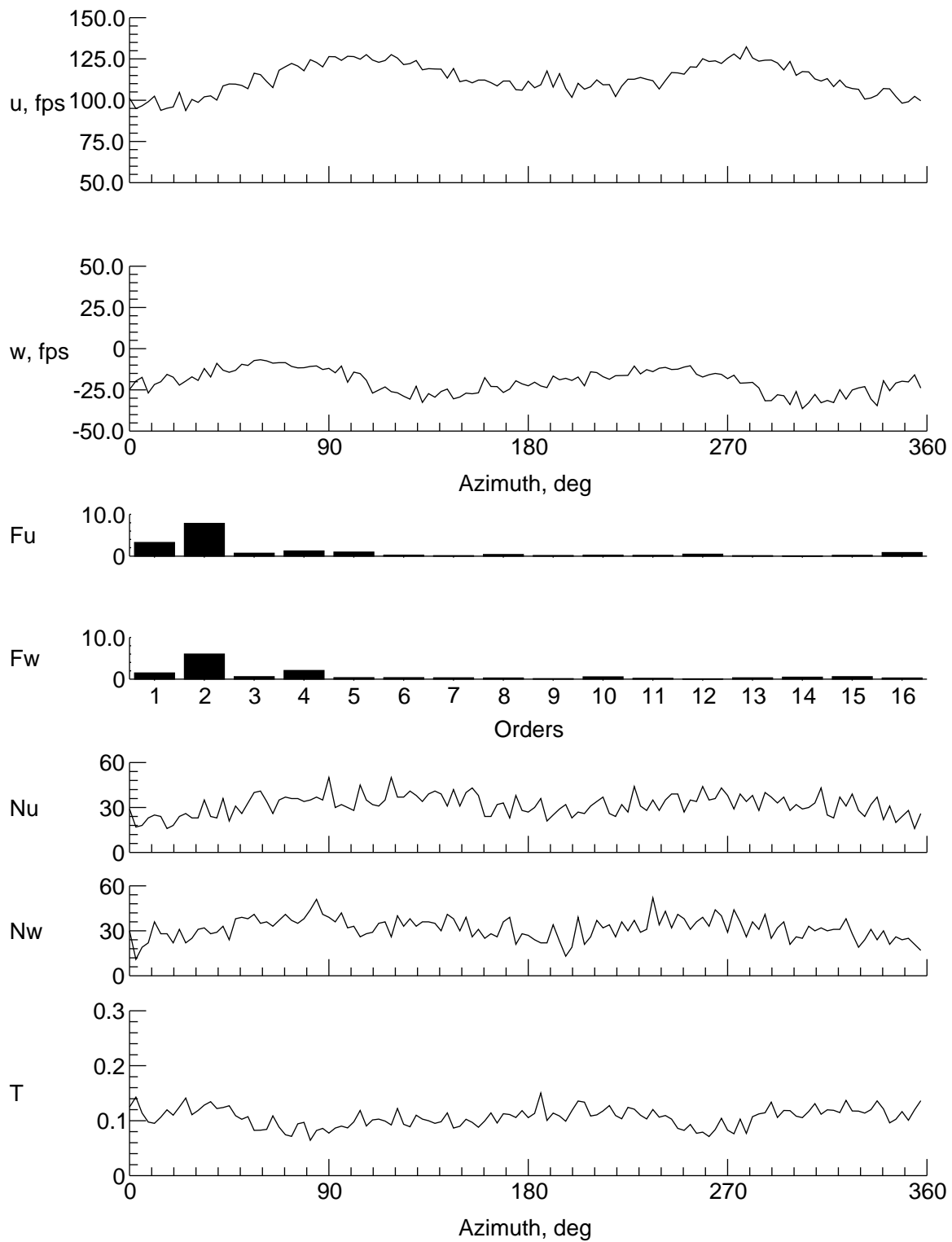
(d) $y = 0$ in., $z = 2.194$ in.

Figure 18. Continued.



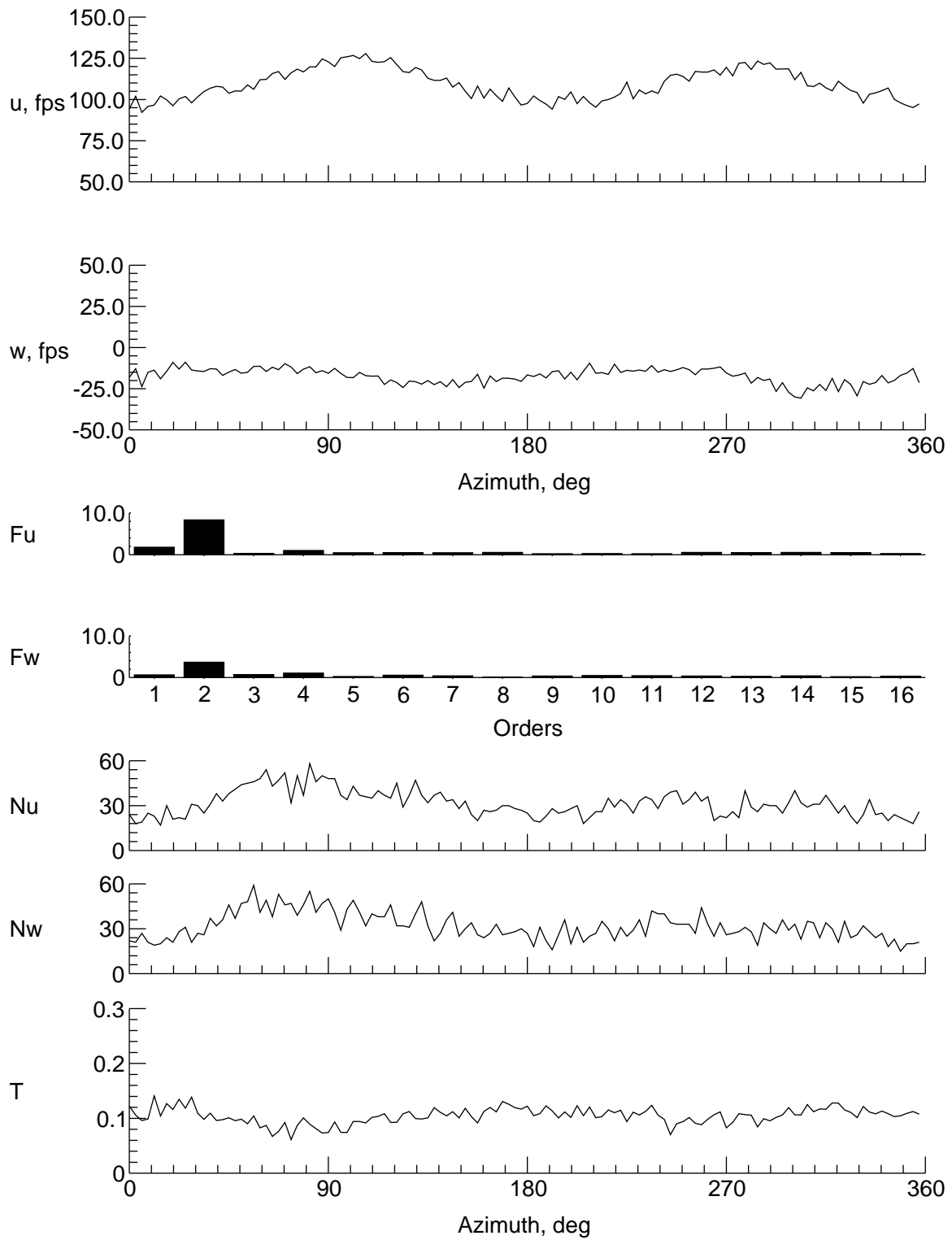
(e) $y = 0$ in., $z = -1.806$ in.

Figure 18. Continued.



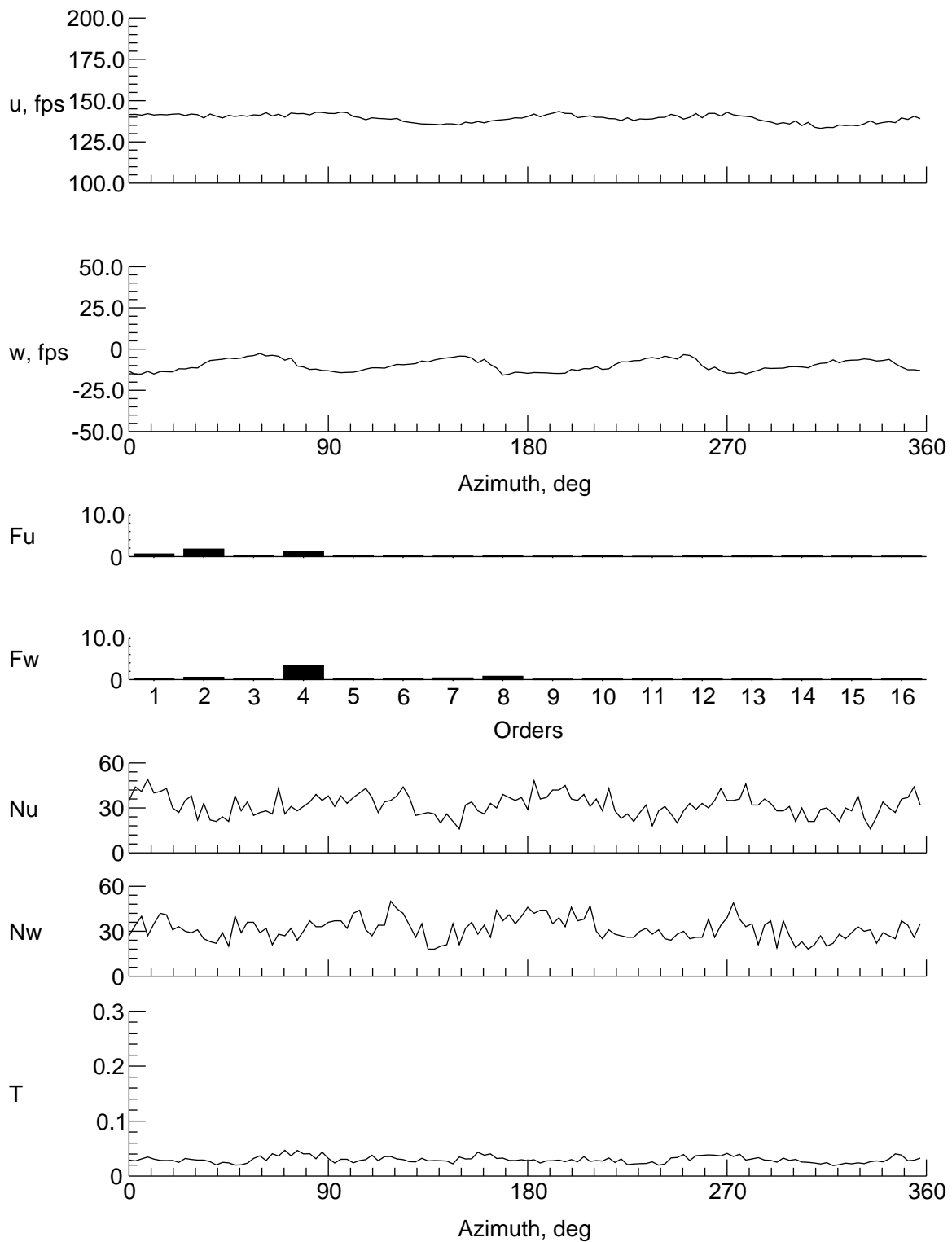
(f) $y = 0$ in., $z = -5.806$ in.

Figure 18. Continued.



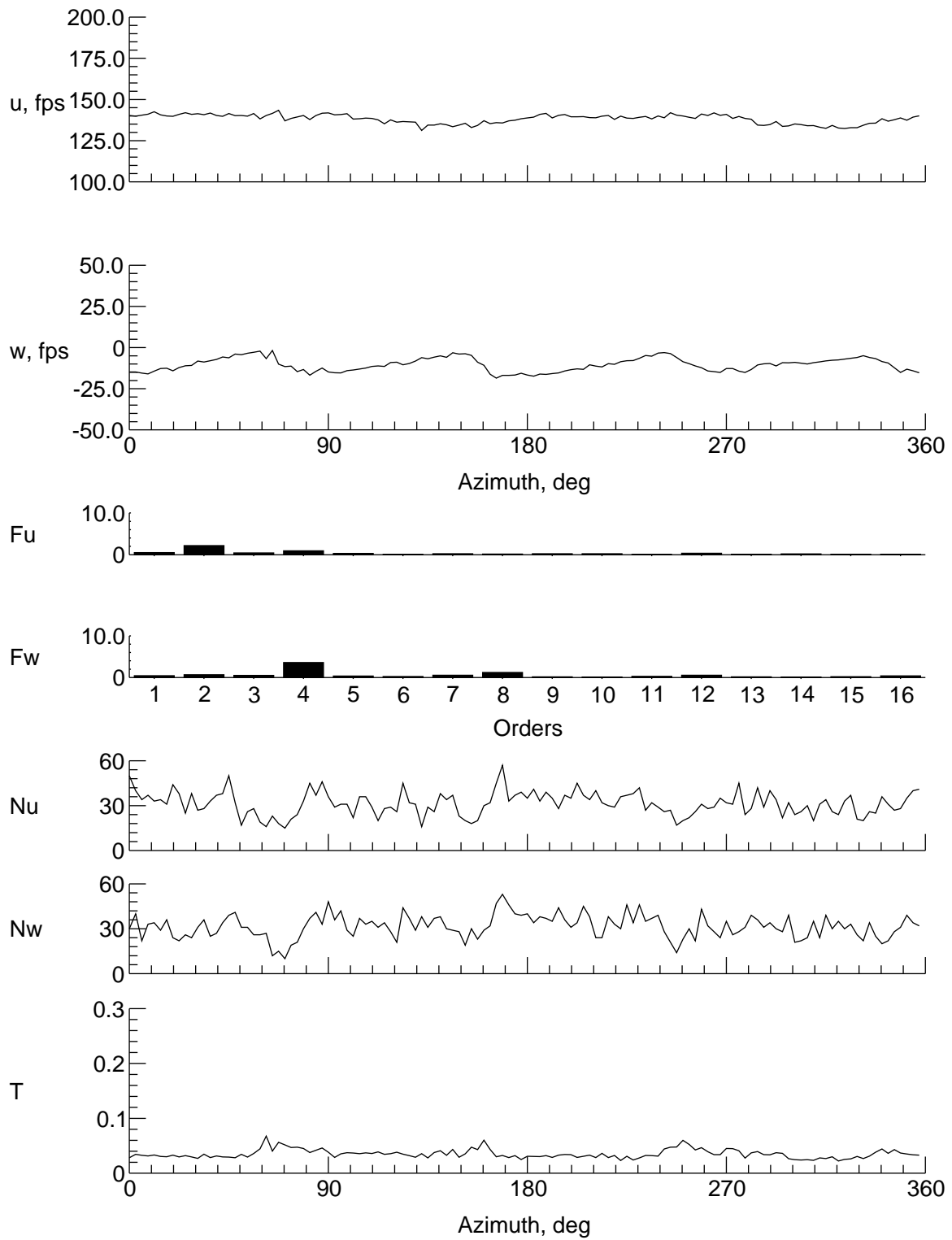
(g) $y = 0$ in., $z = -7.806$ in.

Figure 18. Continued.



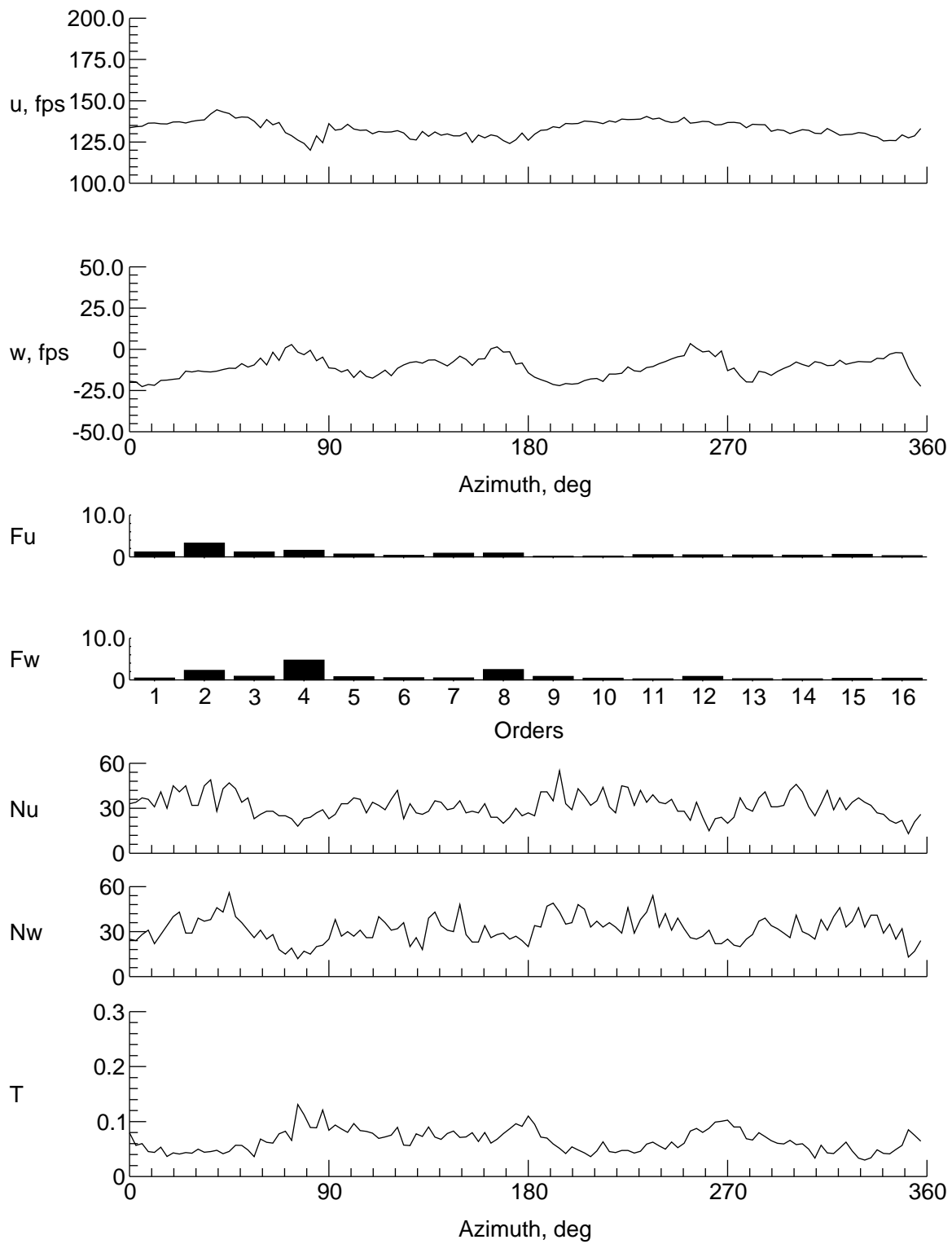
(h) $y = 9$ in., $z = -1.806$ in.

Figure 18. Continued.



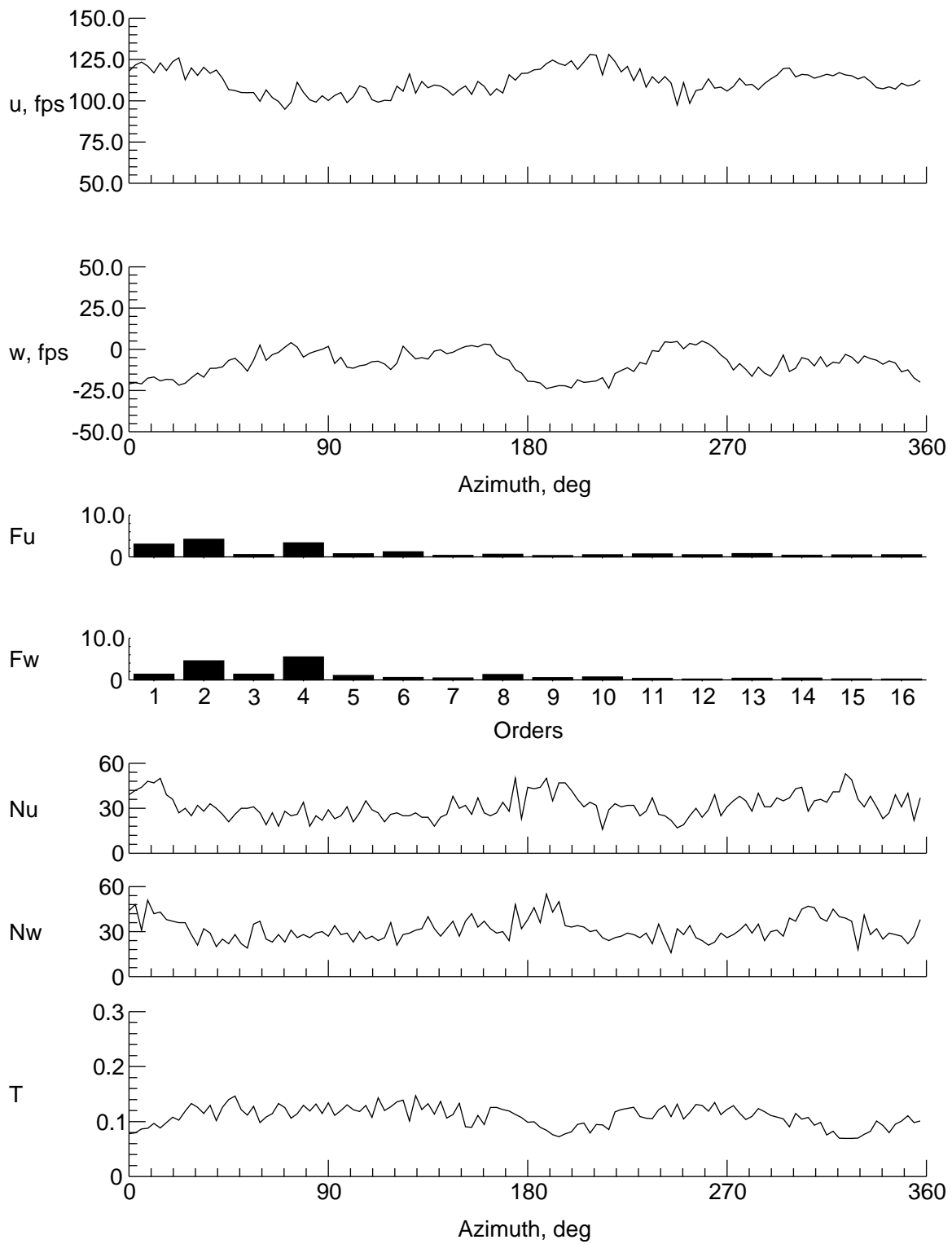
(i) $y = 8$ in., $z = -1.806$ in.

Figure 18. Continued.



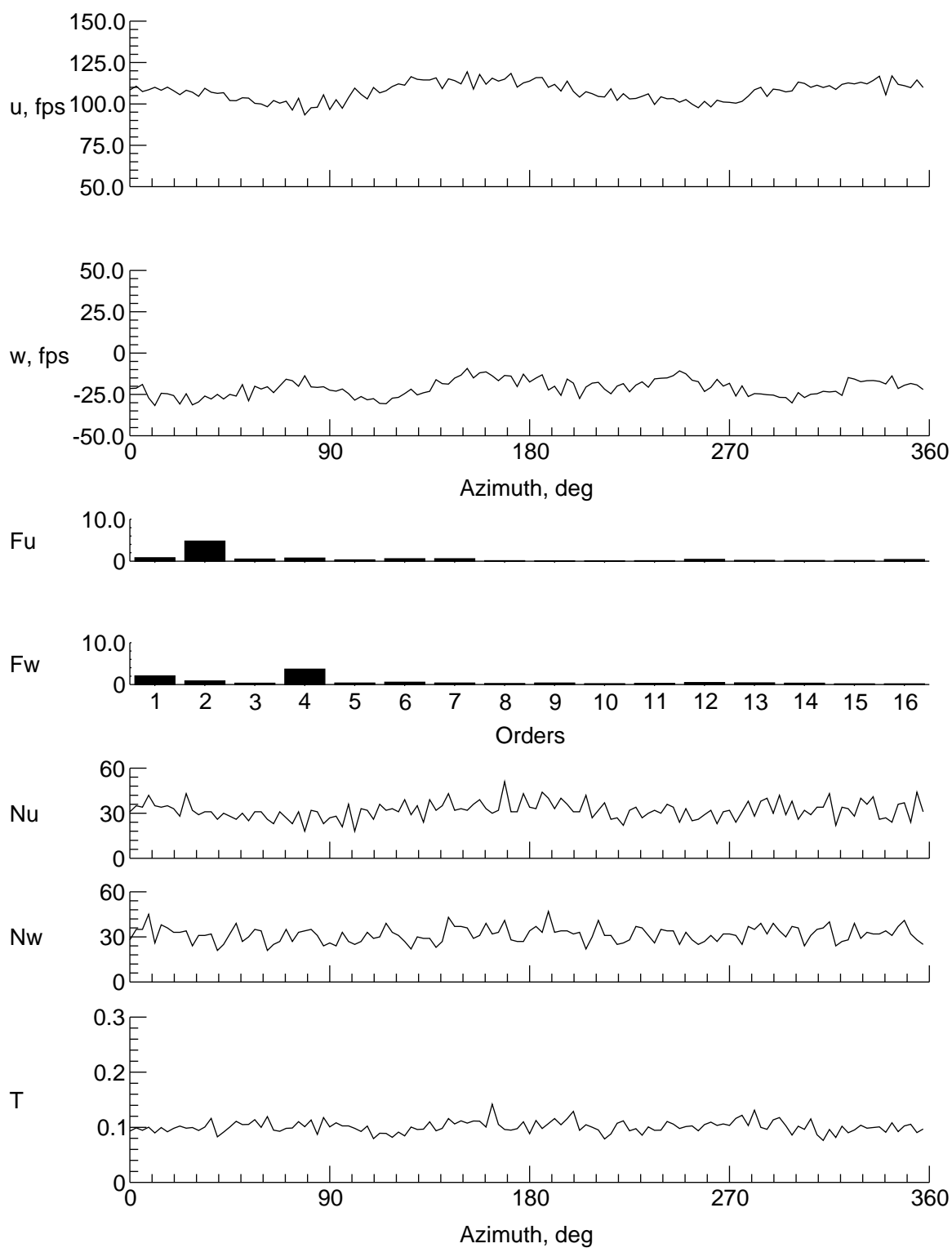
(j) $y = 6$ in., $z = -1.806$ in.

Figure 18. Continued.



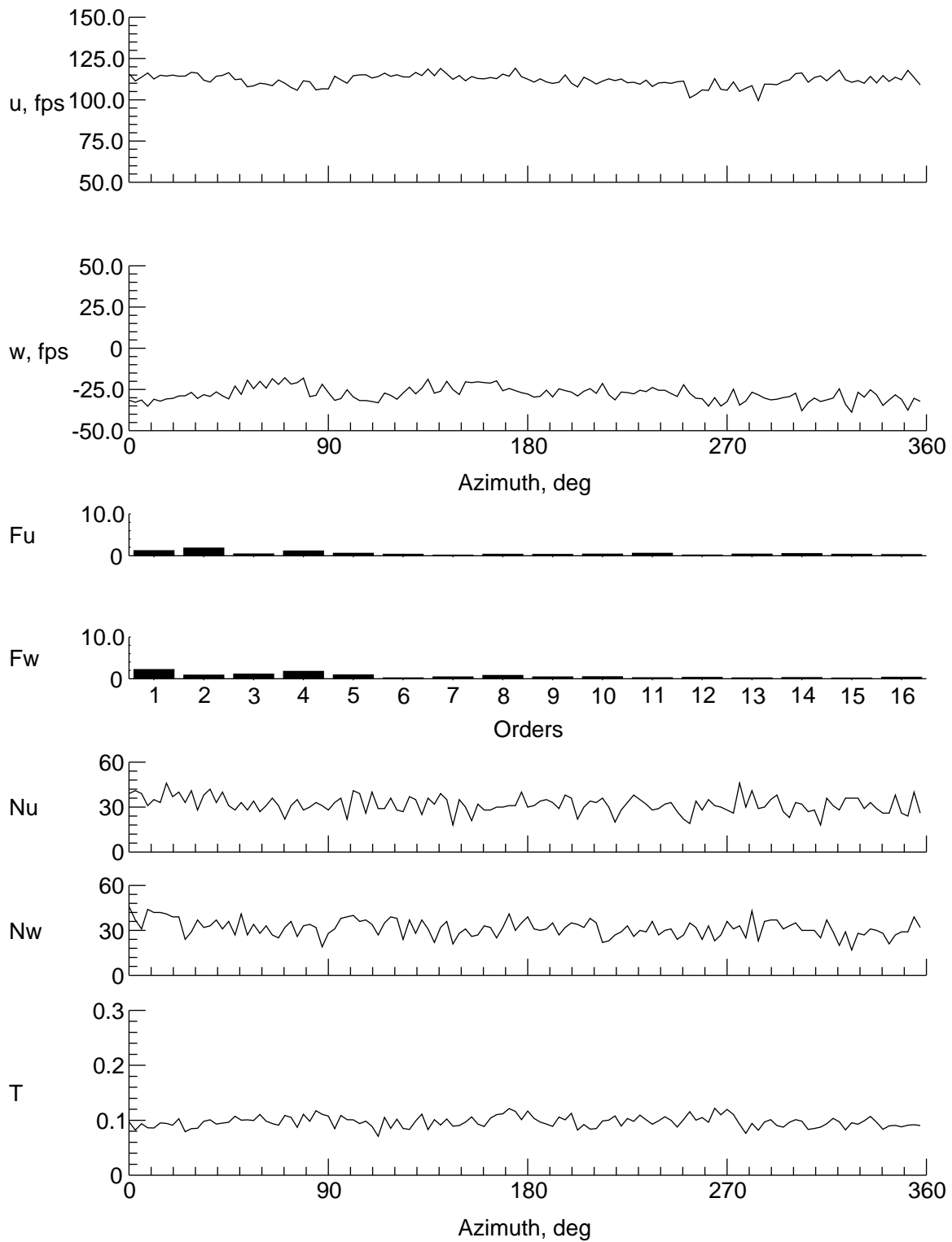
(k) $y = 6$ in., $z = -1.806$ in.

Figure 18. Continued.



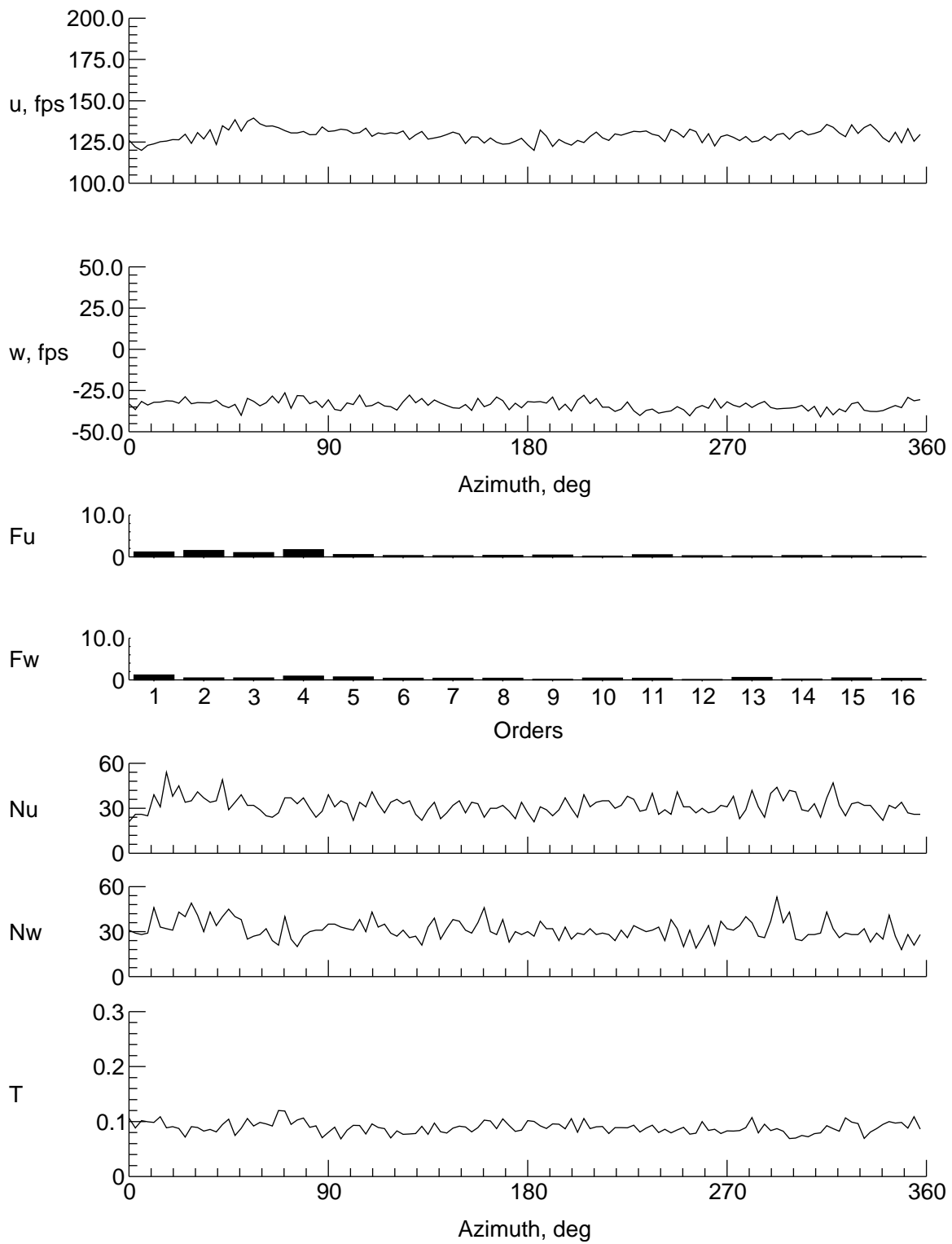
(l) $y = -4$ in., $z = -1.806$ in.

Figure 18. Continued.



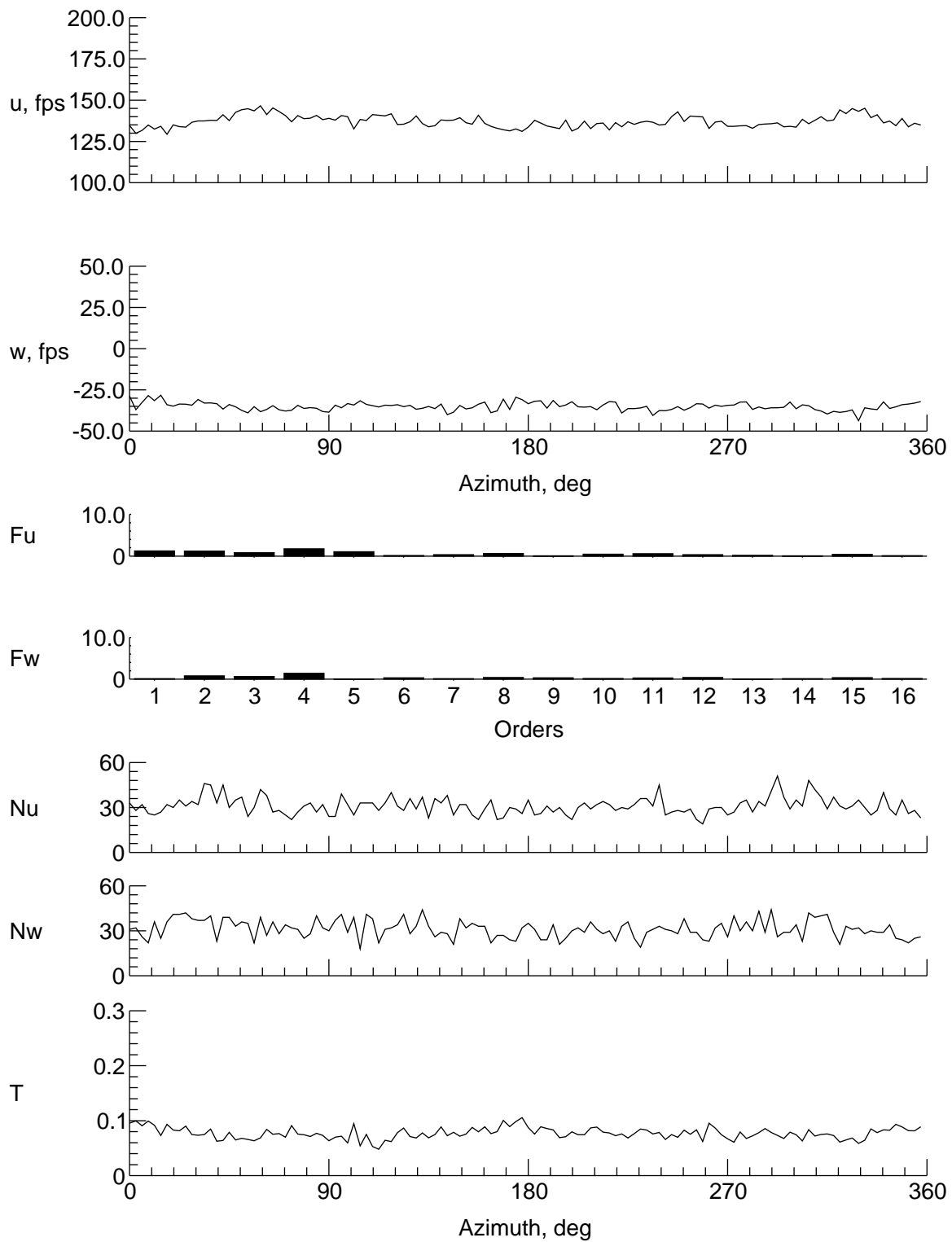
(m) $y = -6$ in., $z = -1.806$ in.

Figure 18. Continued.



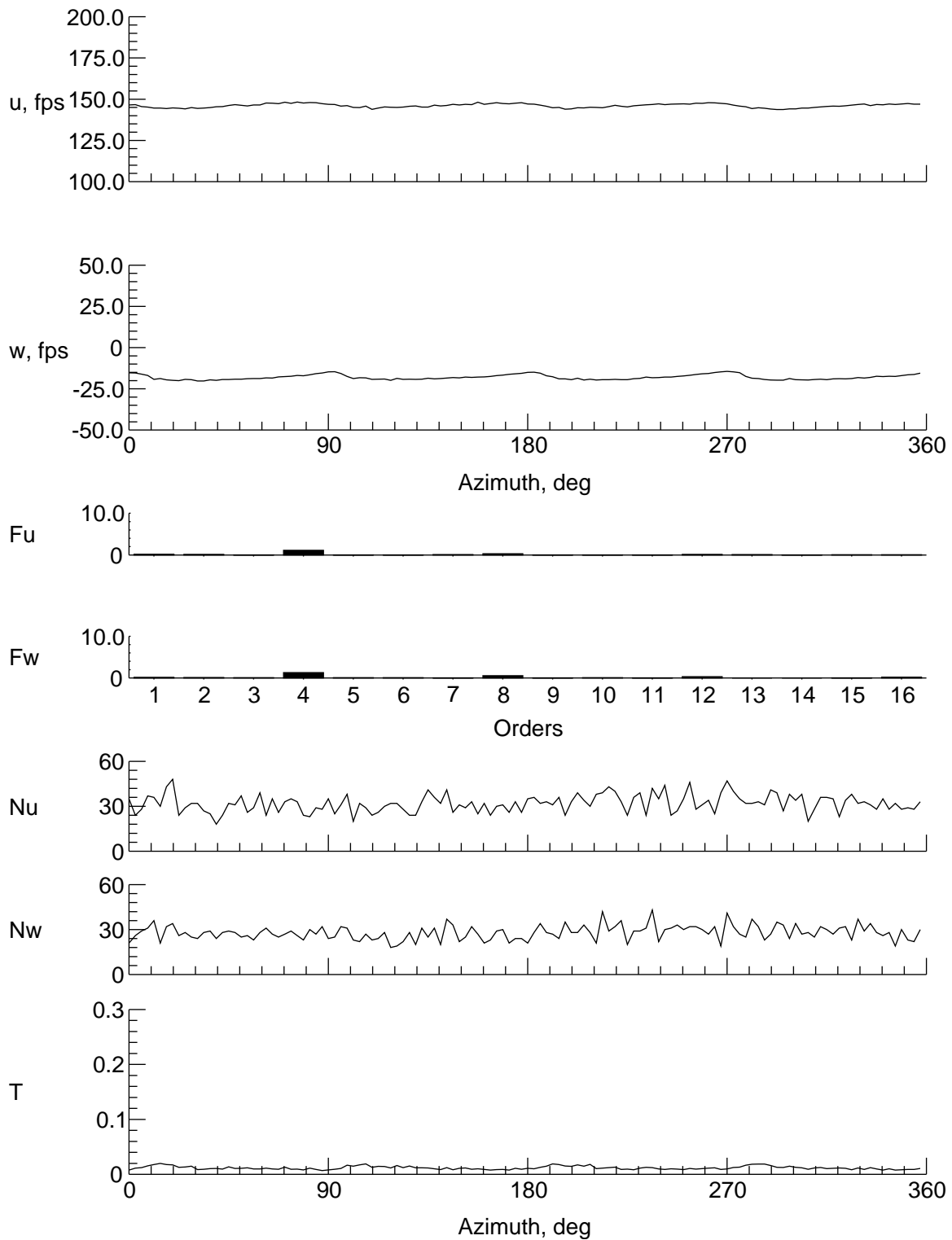
(n) $y = -8$ in., $z = -1.806$ in.

Figure 18. Continued.



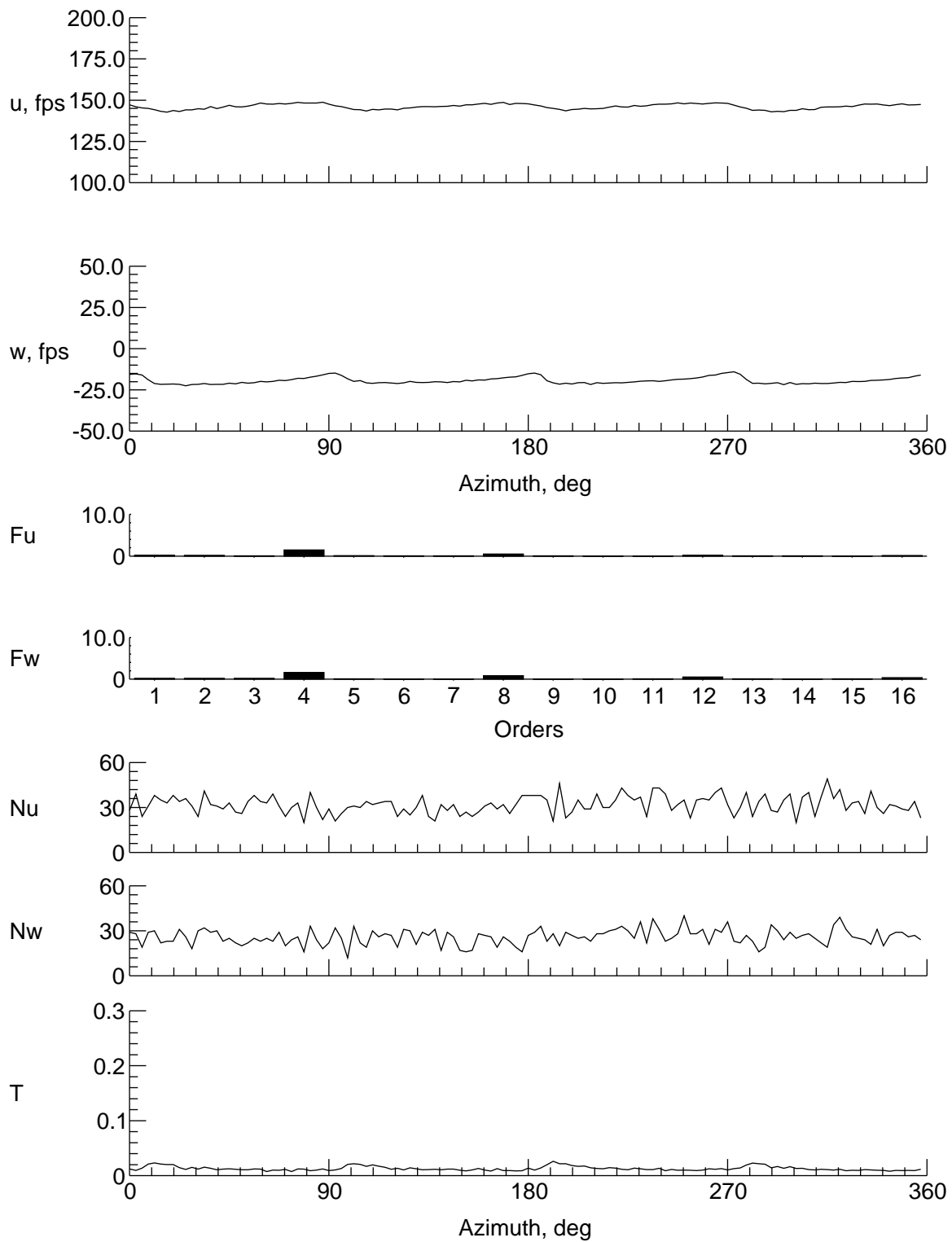
(o) $y = -9$ in., $z = -1.806$ in.

Figure 18. Concluded.



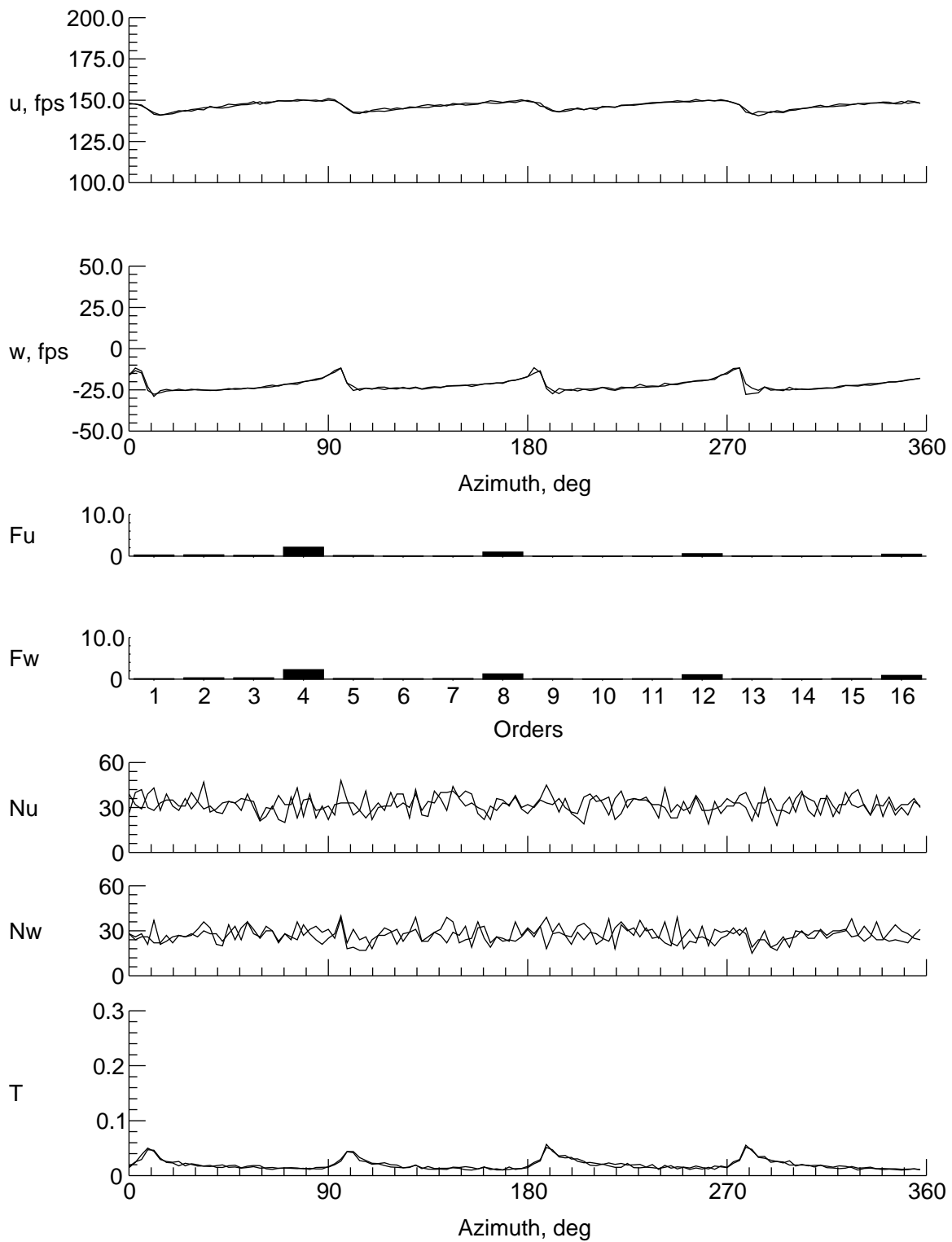
(a) $y = 0$ in., $z = -7.074$ in.

Figure 19. Velocity and turbulence at station 32 in.



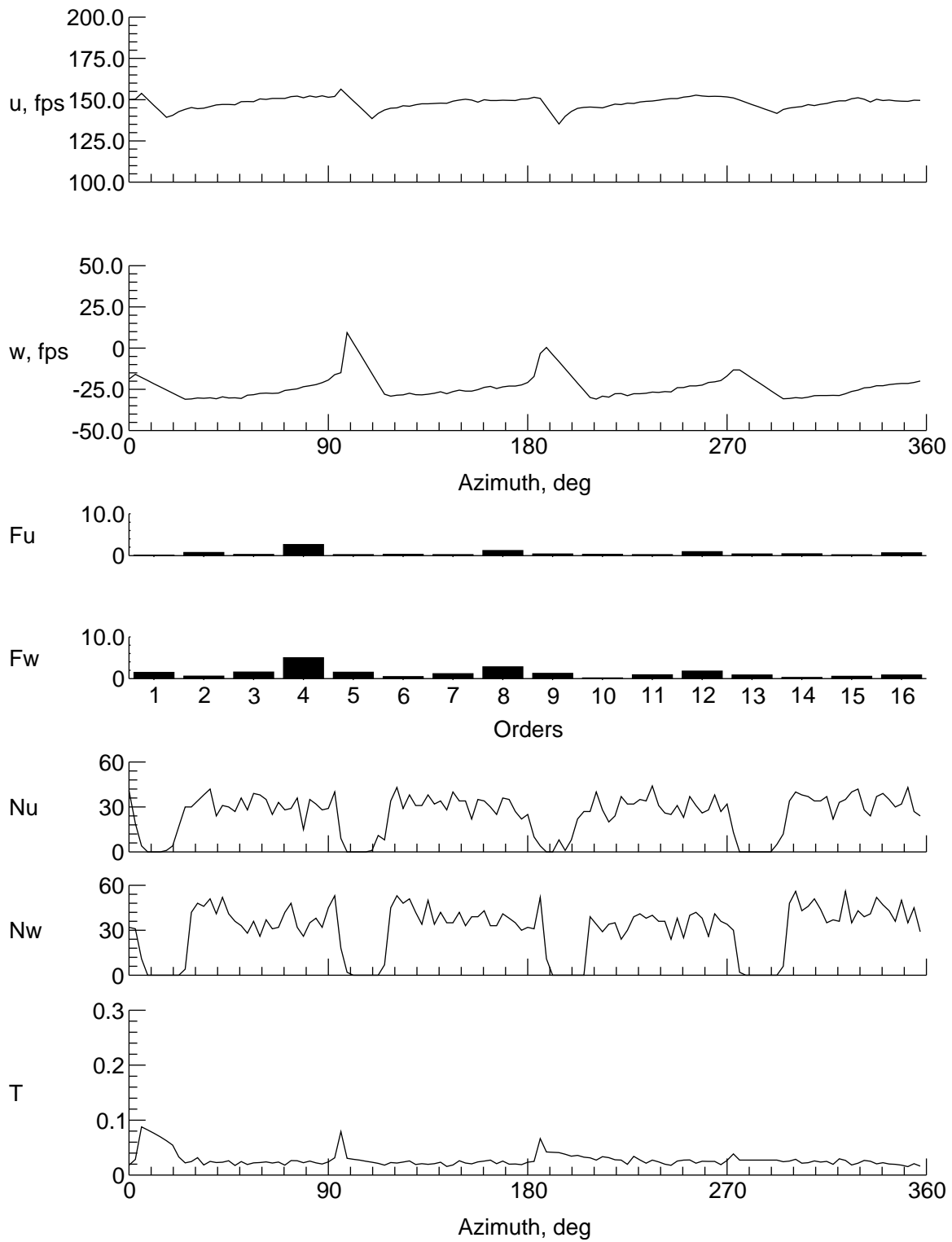
(b) $y = 0$ in., $z = 6.074$ in.

Figure 19. Continued.



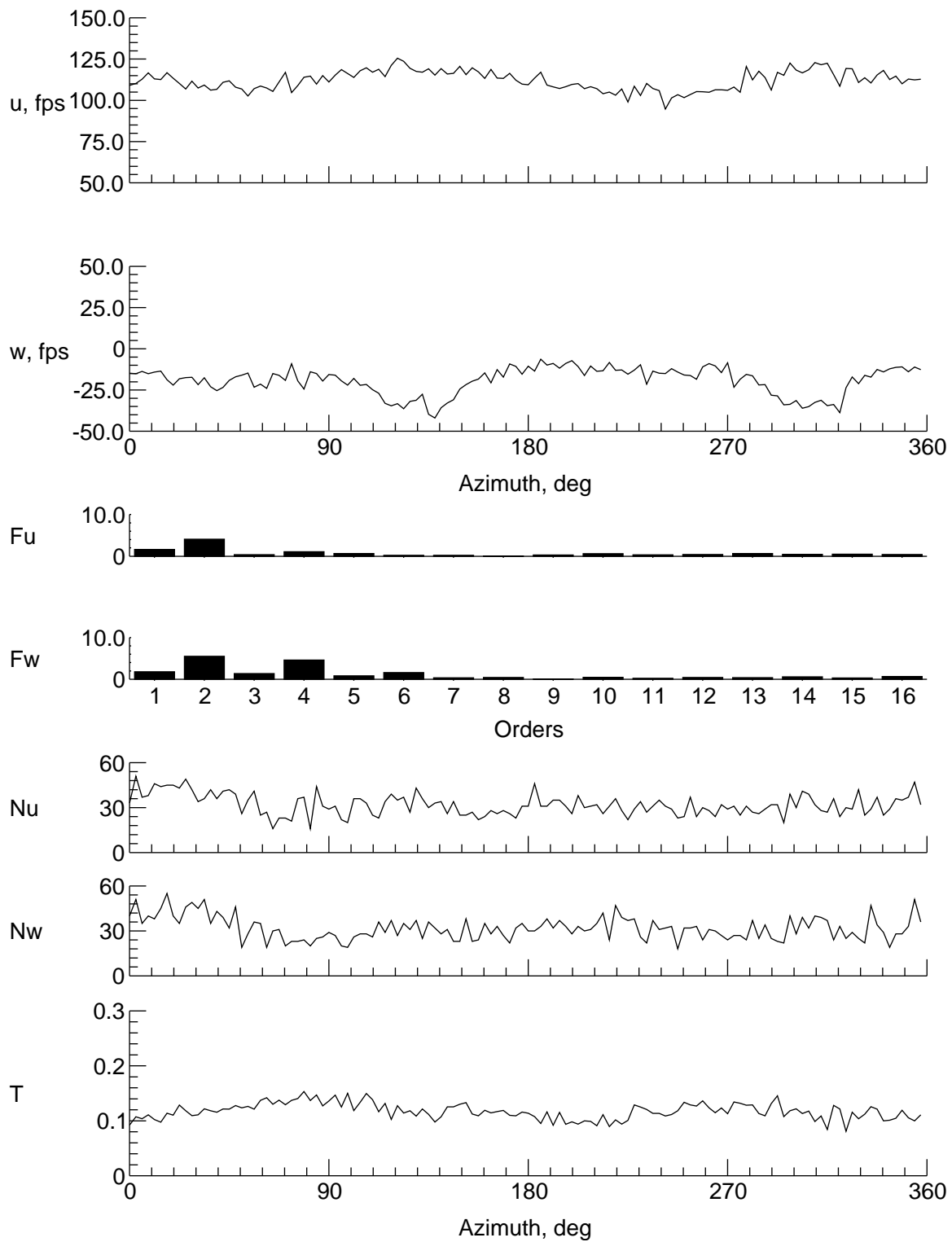
(c) $y = 0$ in., $z = 4.074$ in.

Figure 19. Continued.



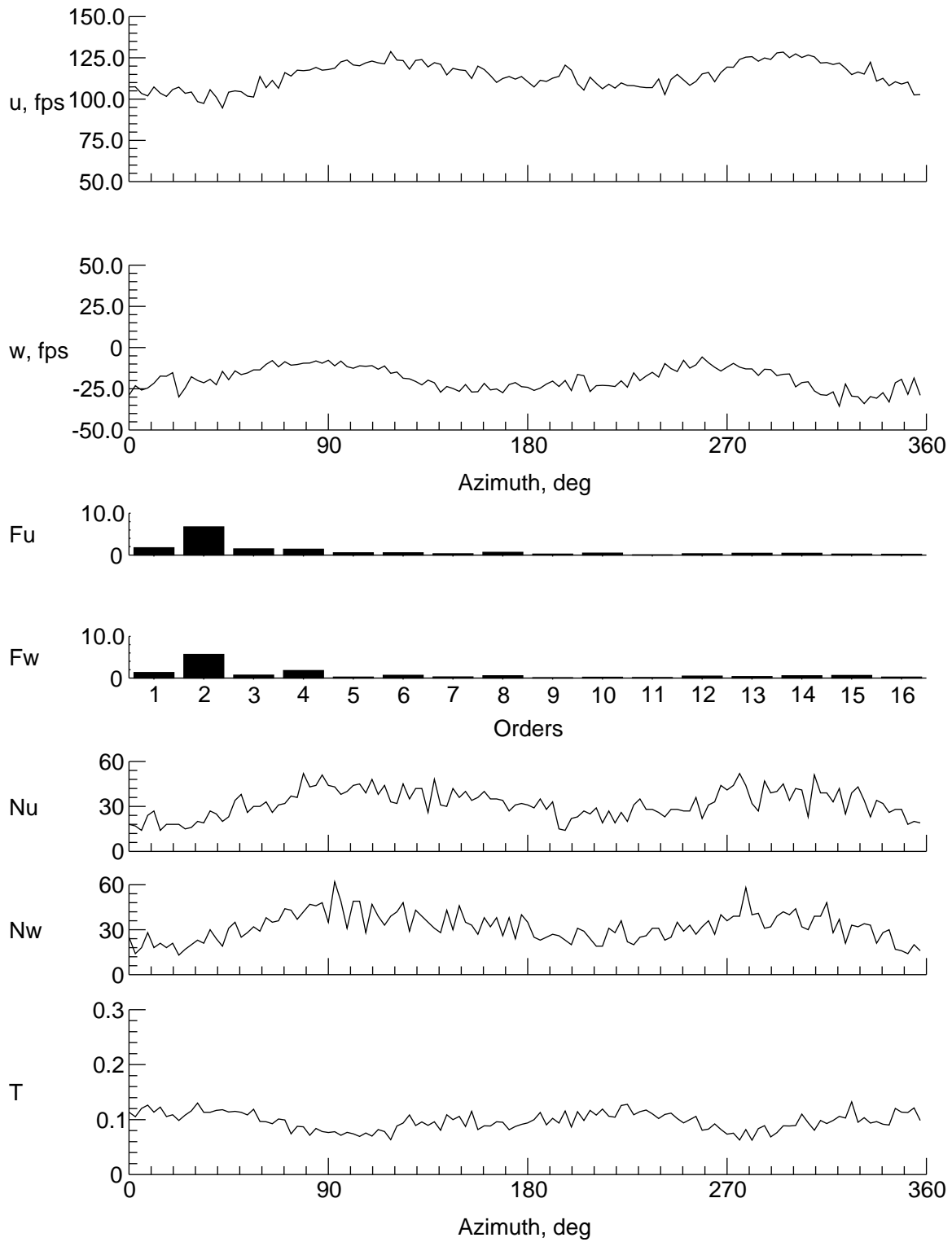
(d) $y = 0$ in., $z = 2.074$ in.

Figure 19. Continued.



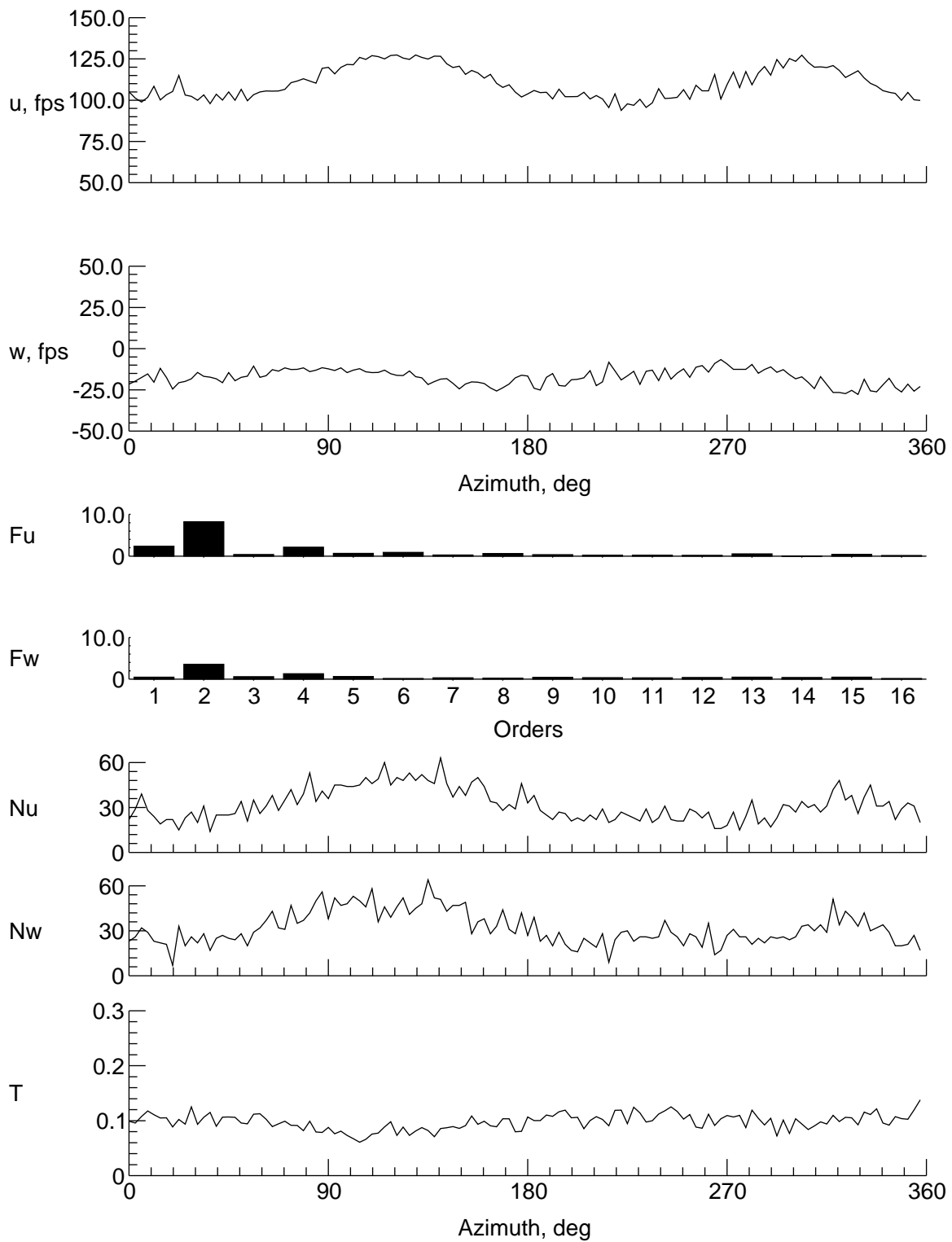
(e) $y = 0$ in., $z = -1.926$ in.

Figure 19. Continued.



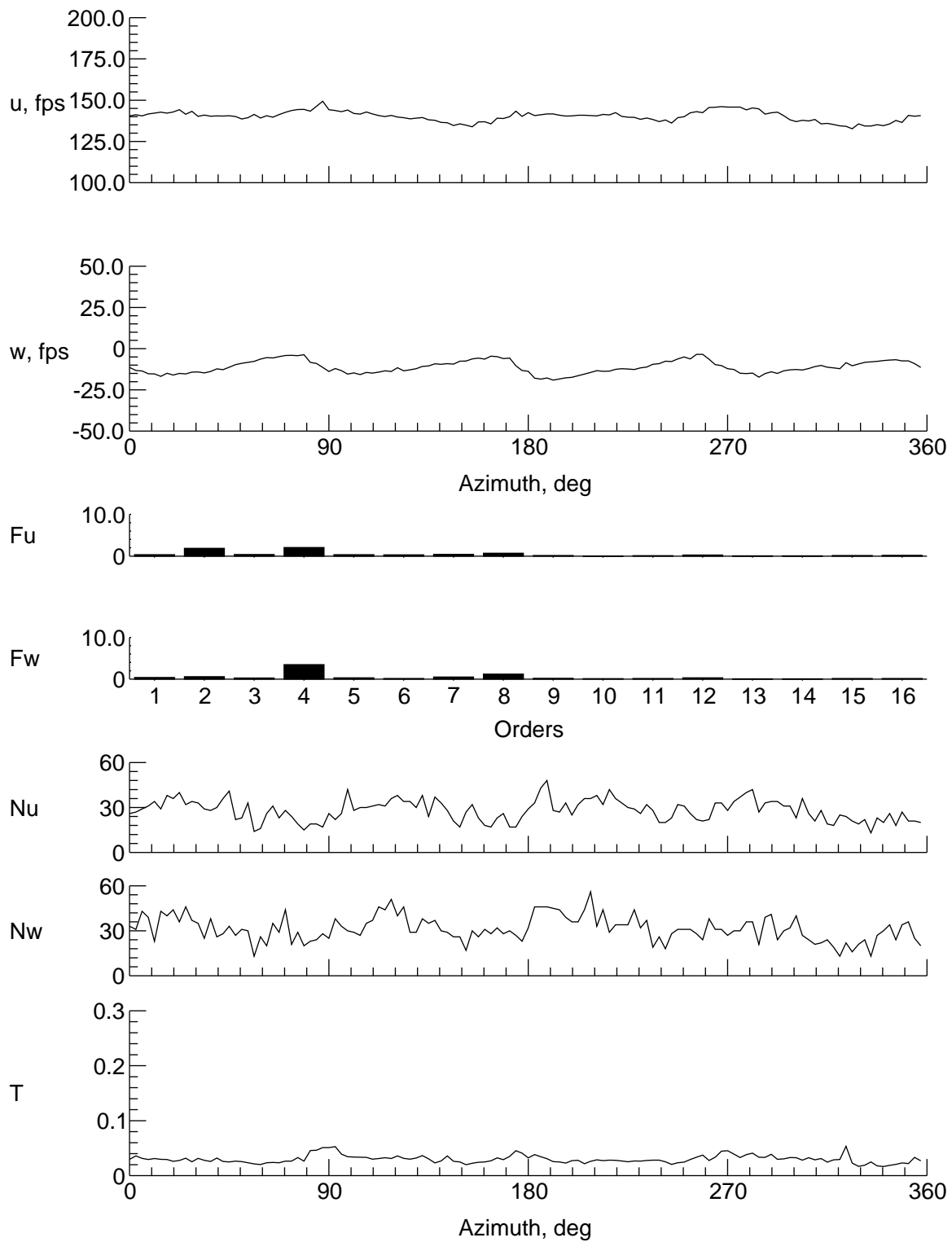
(f) $y = 0$ in., $z = -5.926$ in.

Figure 19. Continued.



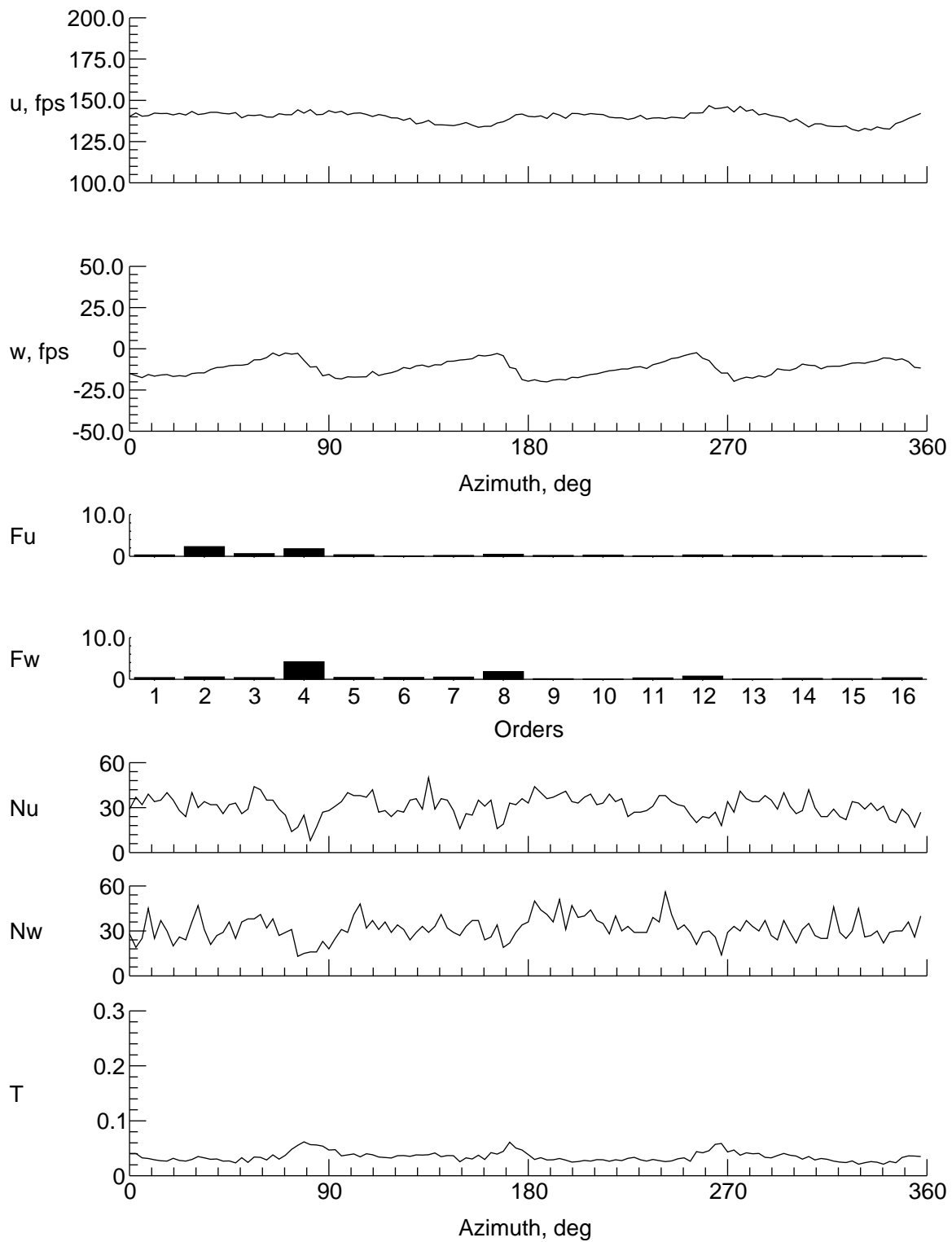
(g) $y = 0$ in., $z = -7.926$ in.

Figure 19. Continued.



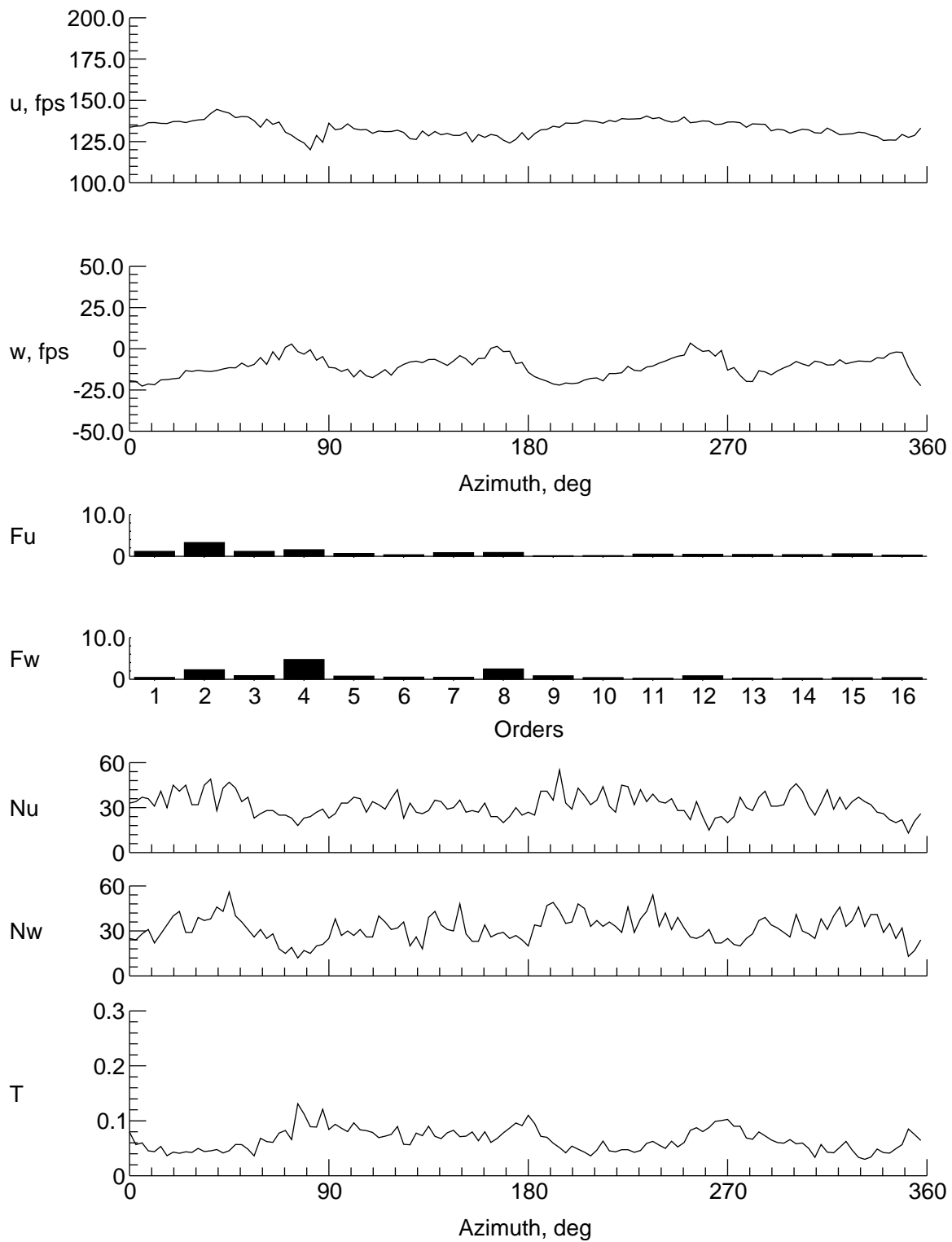
(h) $y = 9$ in., $z = -1.926$ in.

Figure 19. Continued.



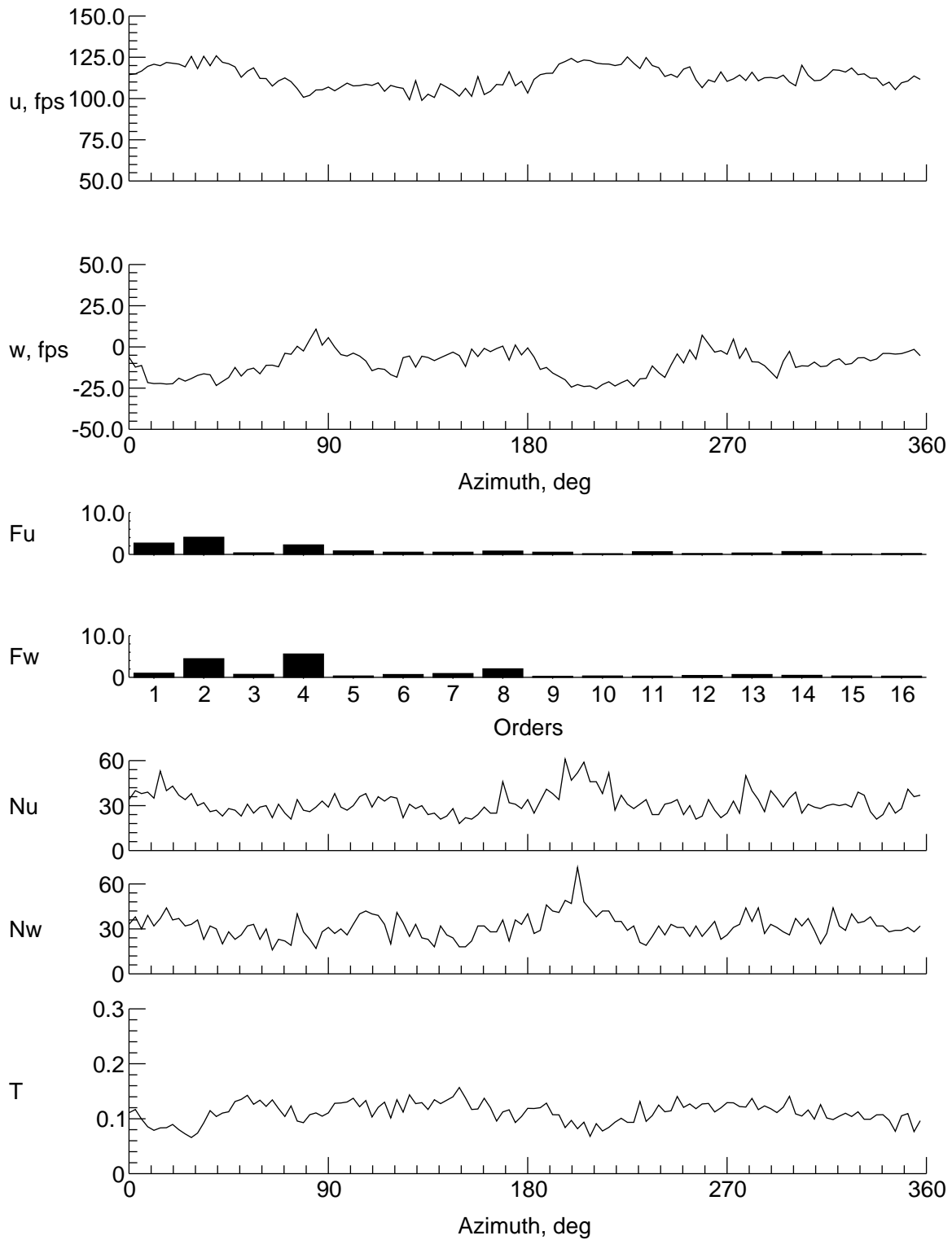
(i) $y = 8$ in., $z = -1.926$ in.

Figure 19. Continued.



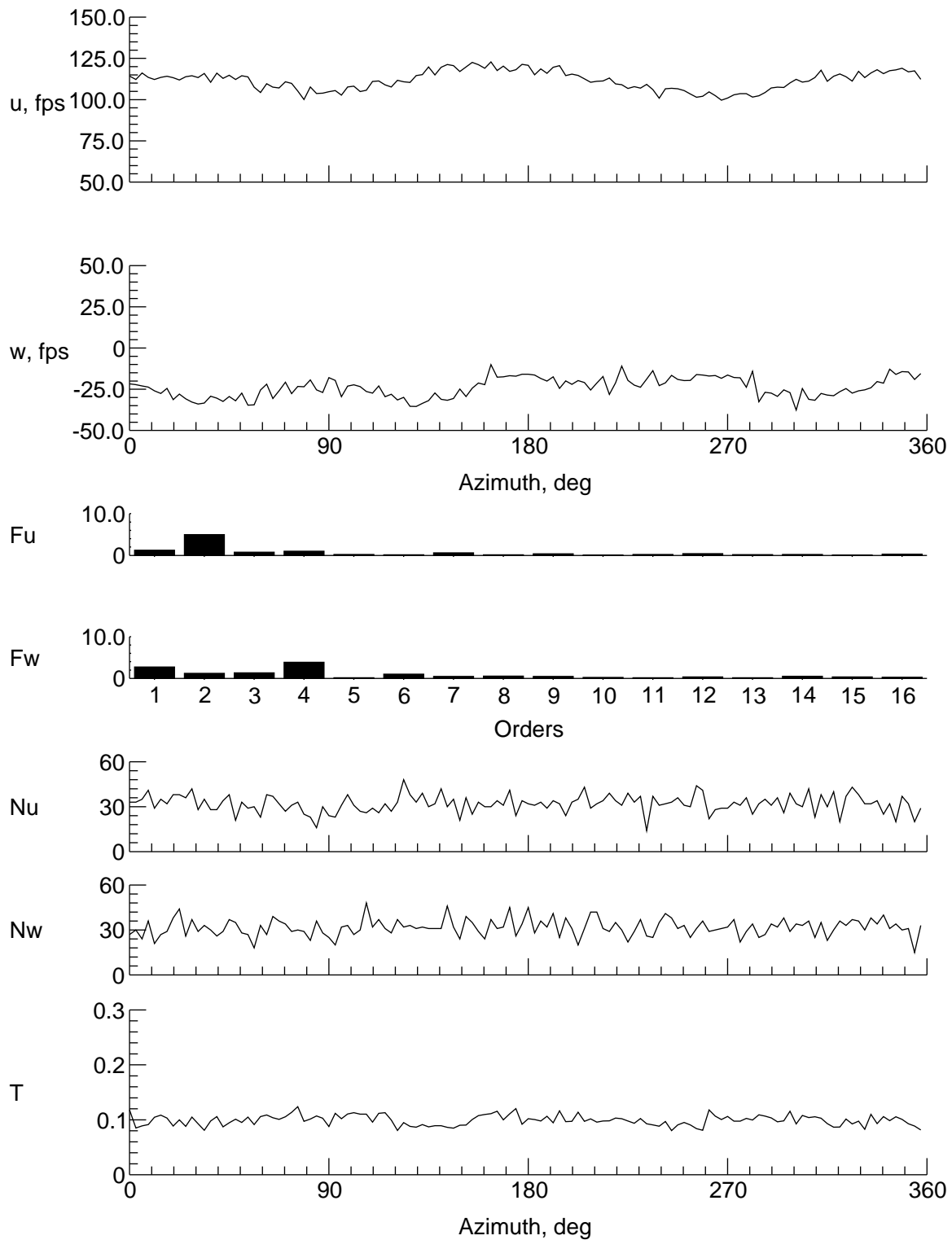
(j) $y = 6$ in., $z = -1.926$ in.

Figure 19. Continued.



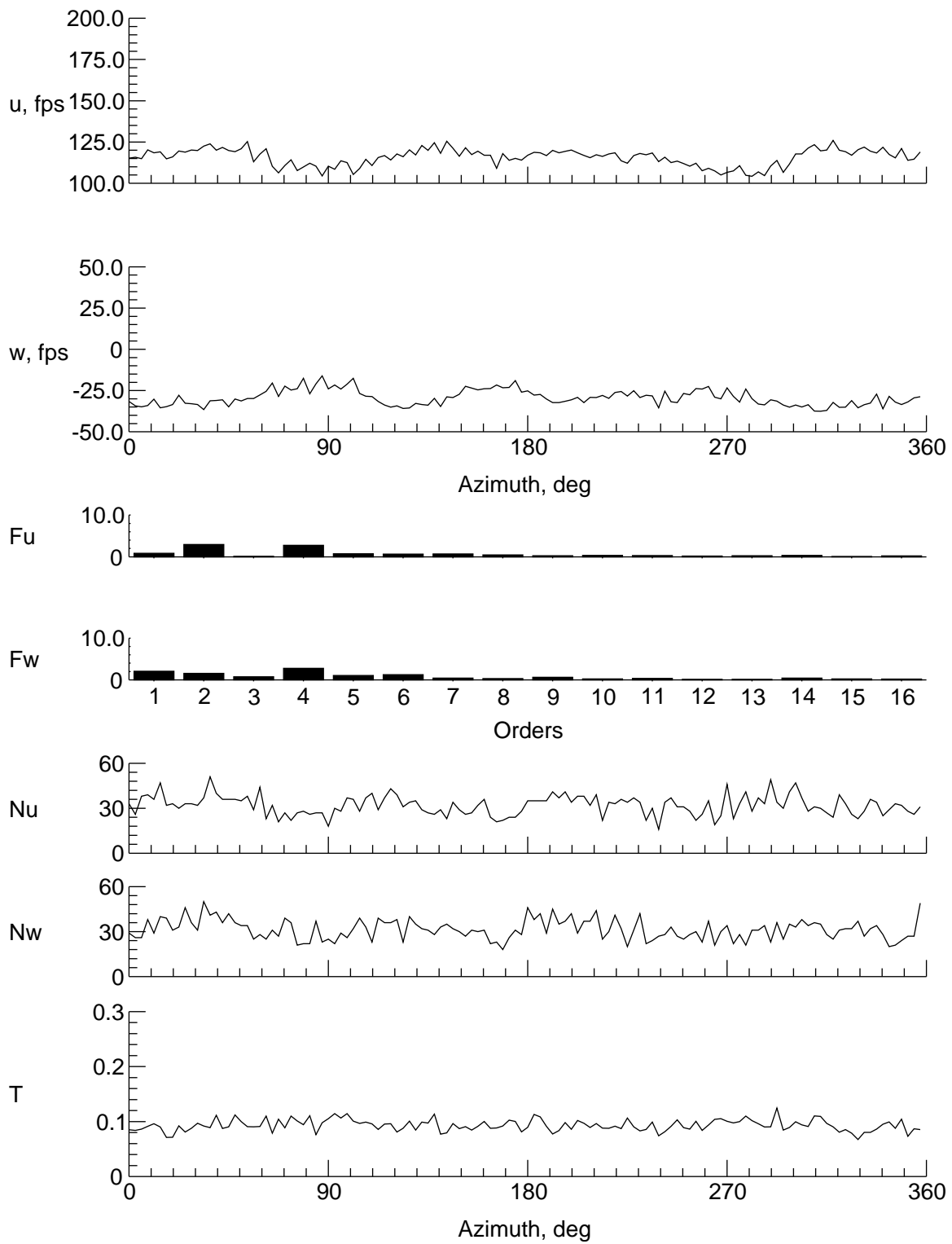
(k) $y = 4$ in., $z = -1.926$ in.

Figure 19. Continued.



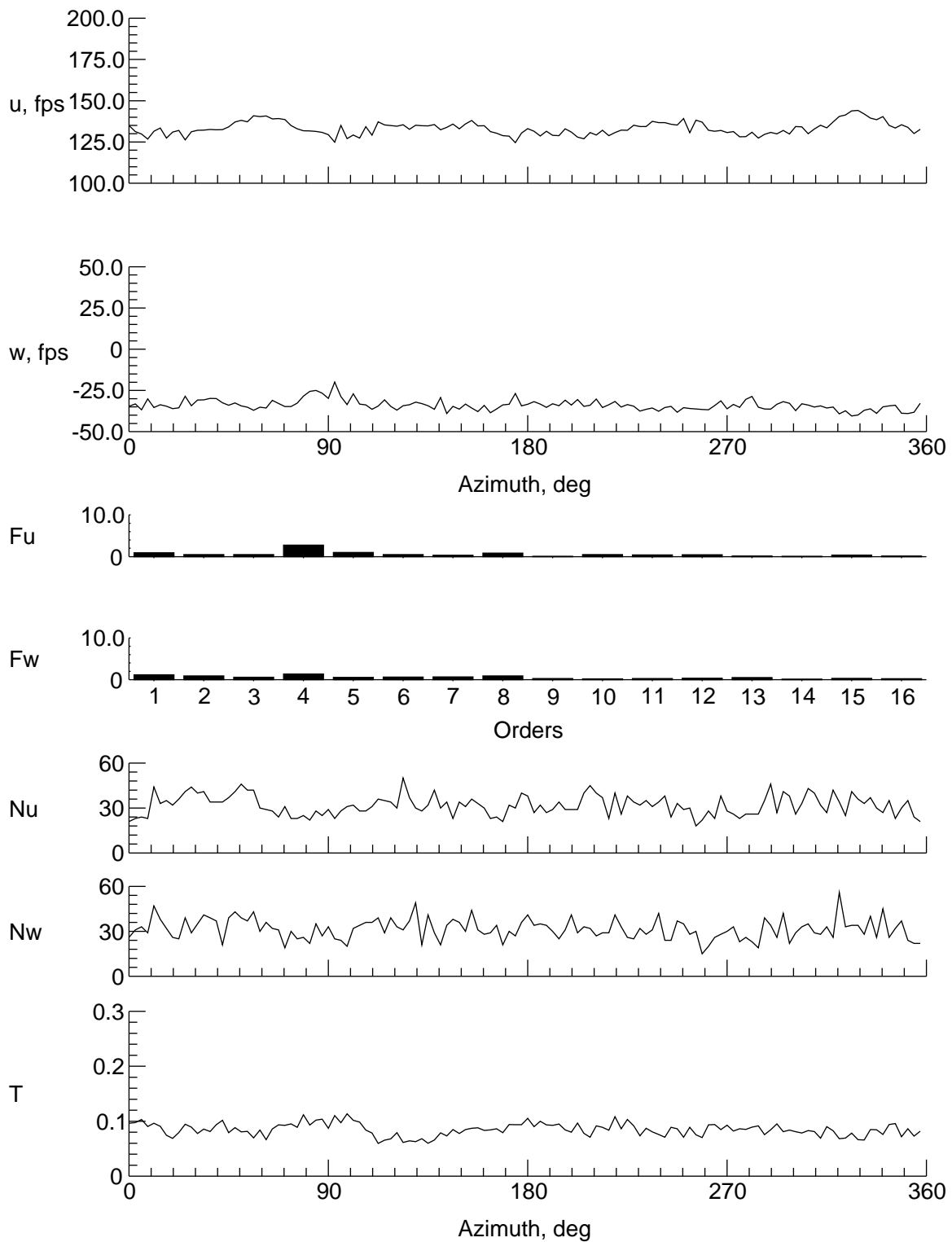
(l) $y = -4$ in., $z = -1.926$ in.

Figure 19. Continued.



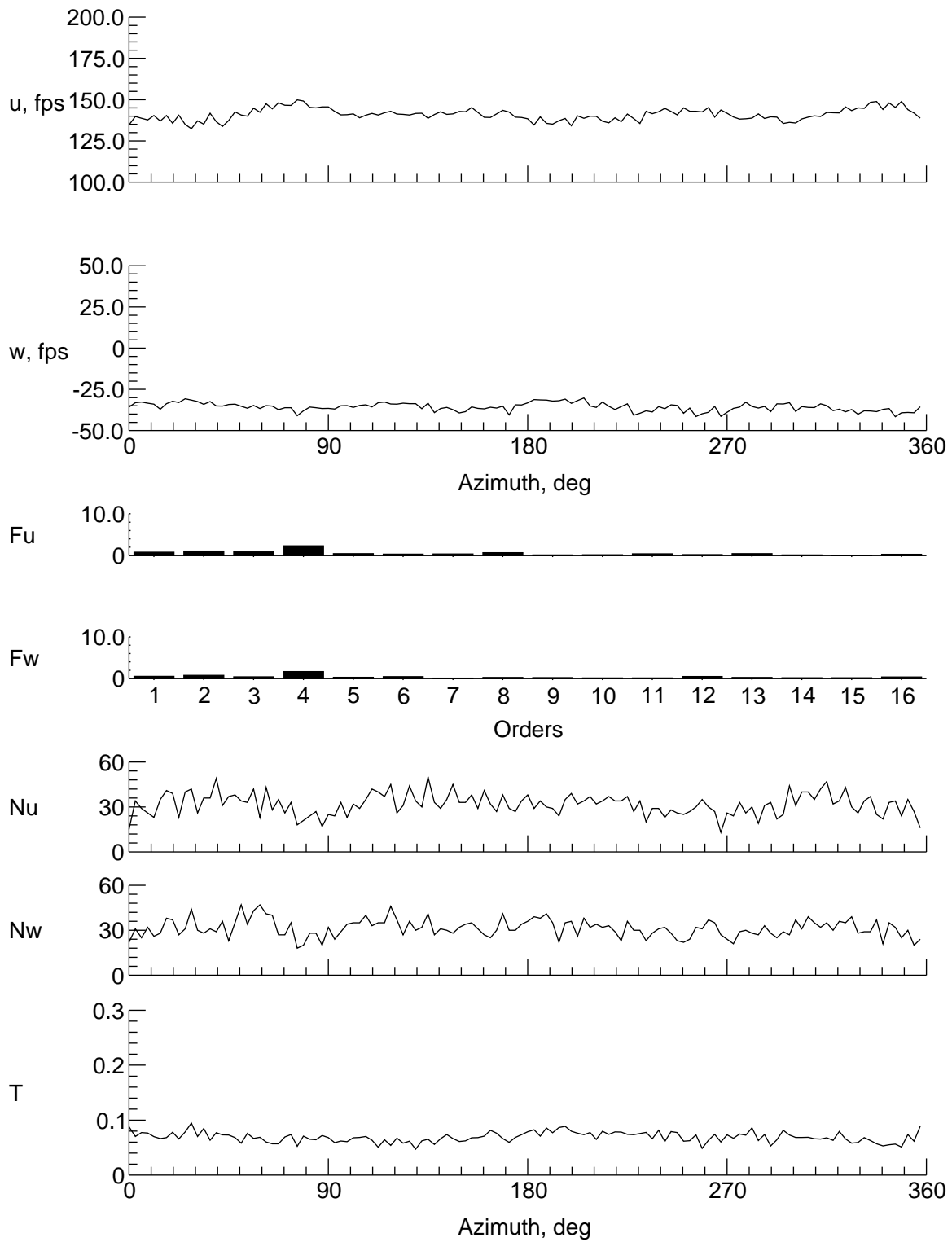
(m) $y = -6$ in., $z = -1.926$ in.

Figure 19. Continued.



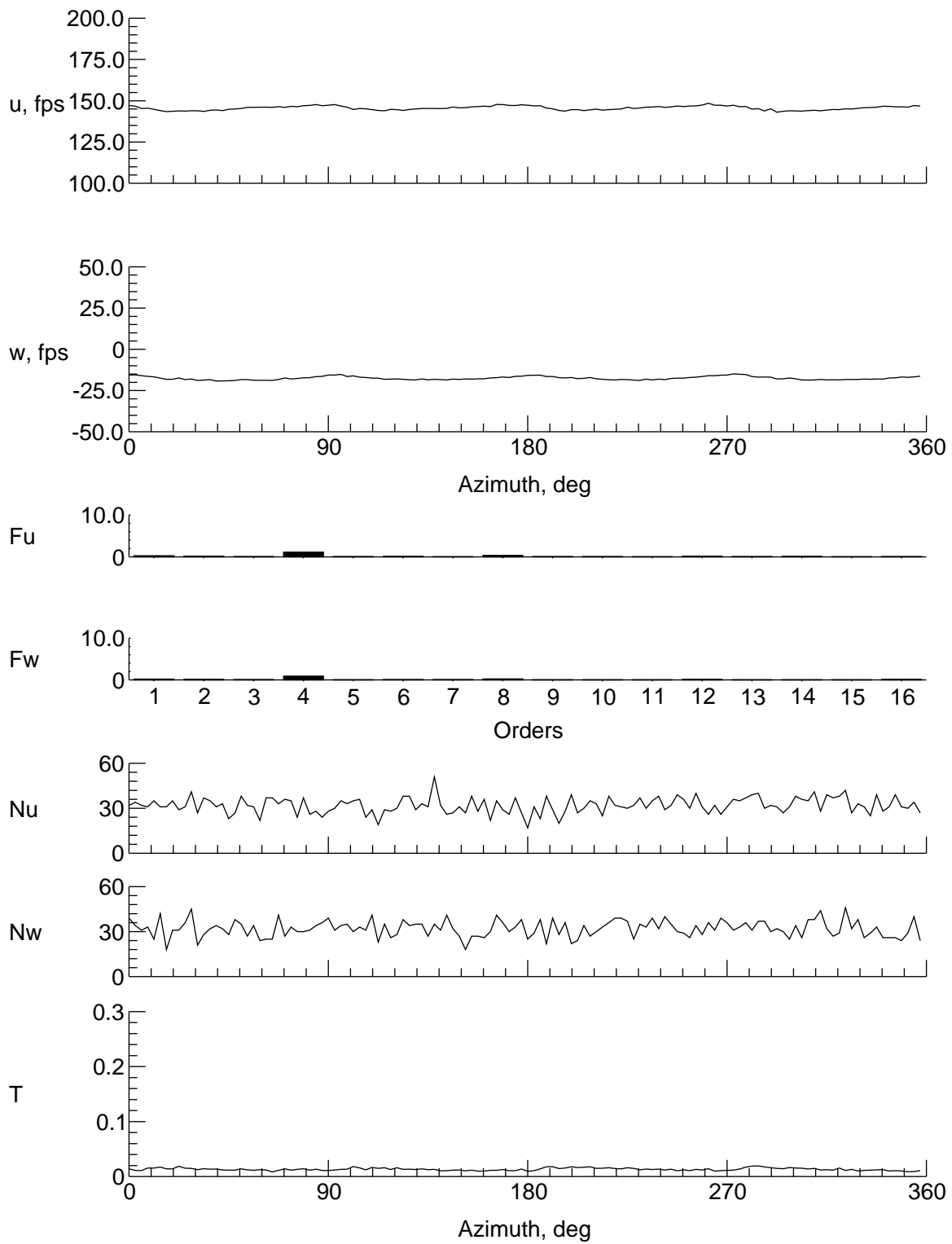
(n) $y = -8$ in., $z = -1.926$ in.

Figure 19. Continued.



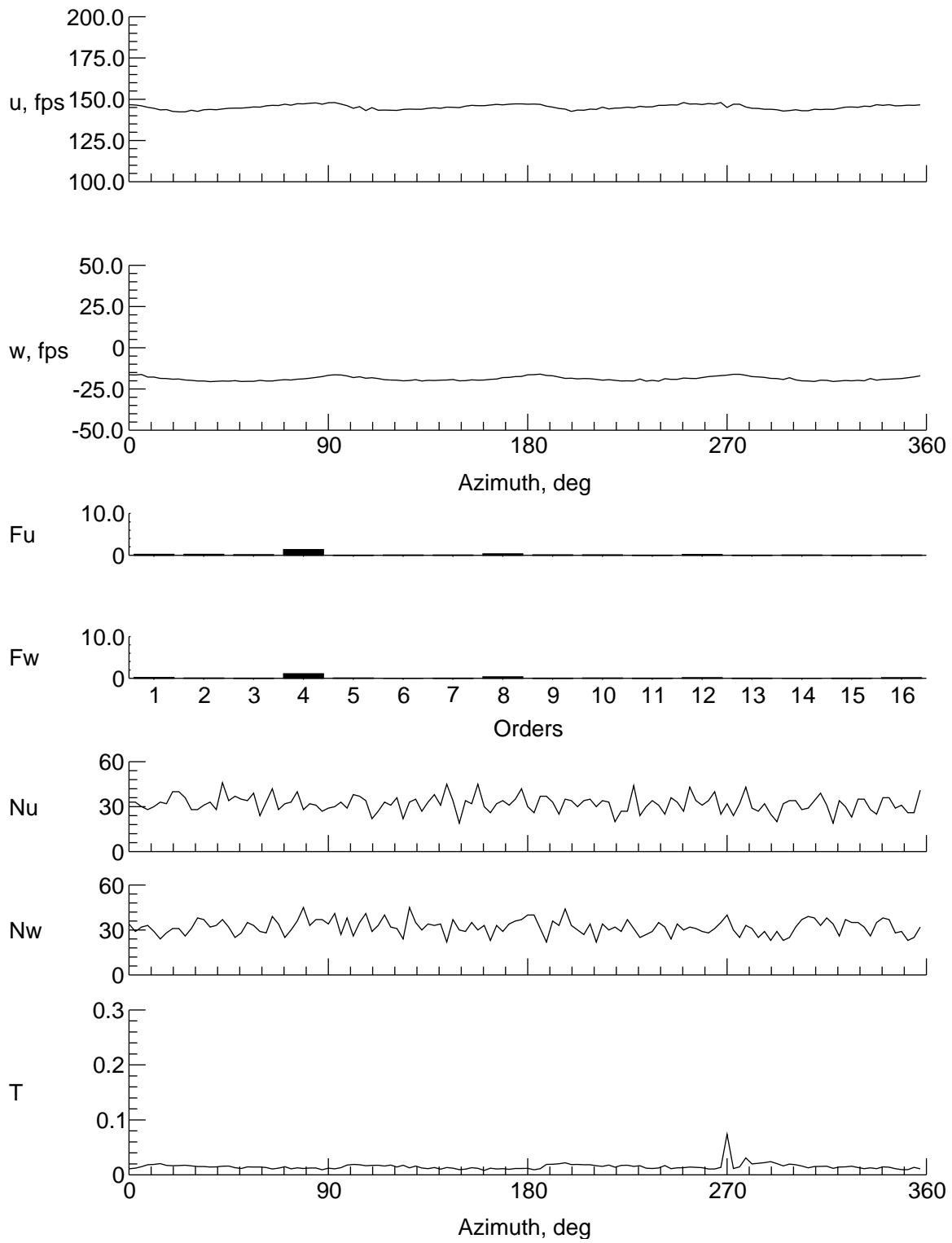
(o) $y = -9$ in., $z = -1.926$ in.

Figure 19. Concluded.



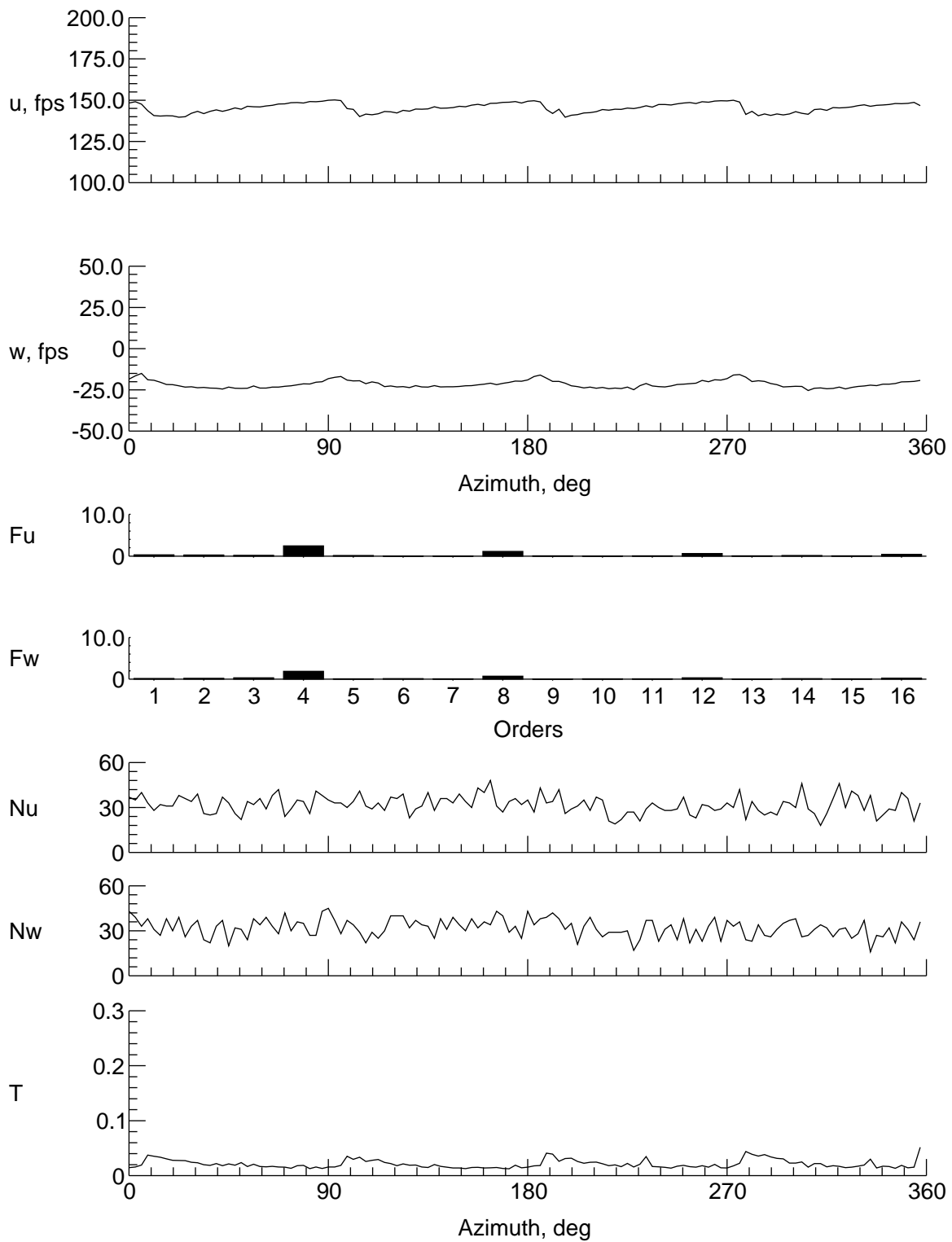
(a) $y = 0$ in., $z = 6.953$ in.

Figure 20. Velocity and turbulence at station 34 in.



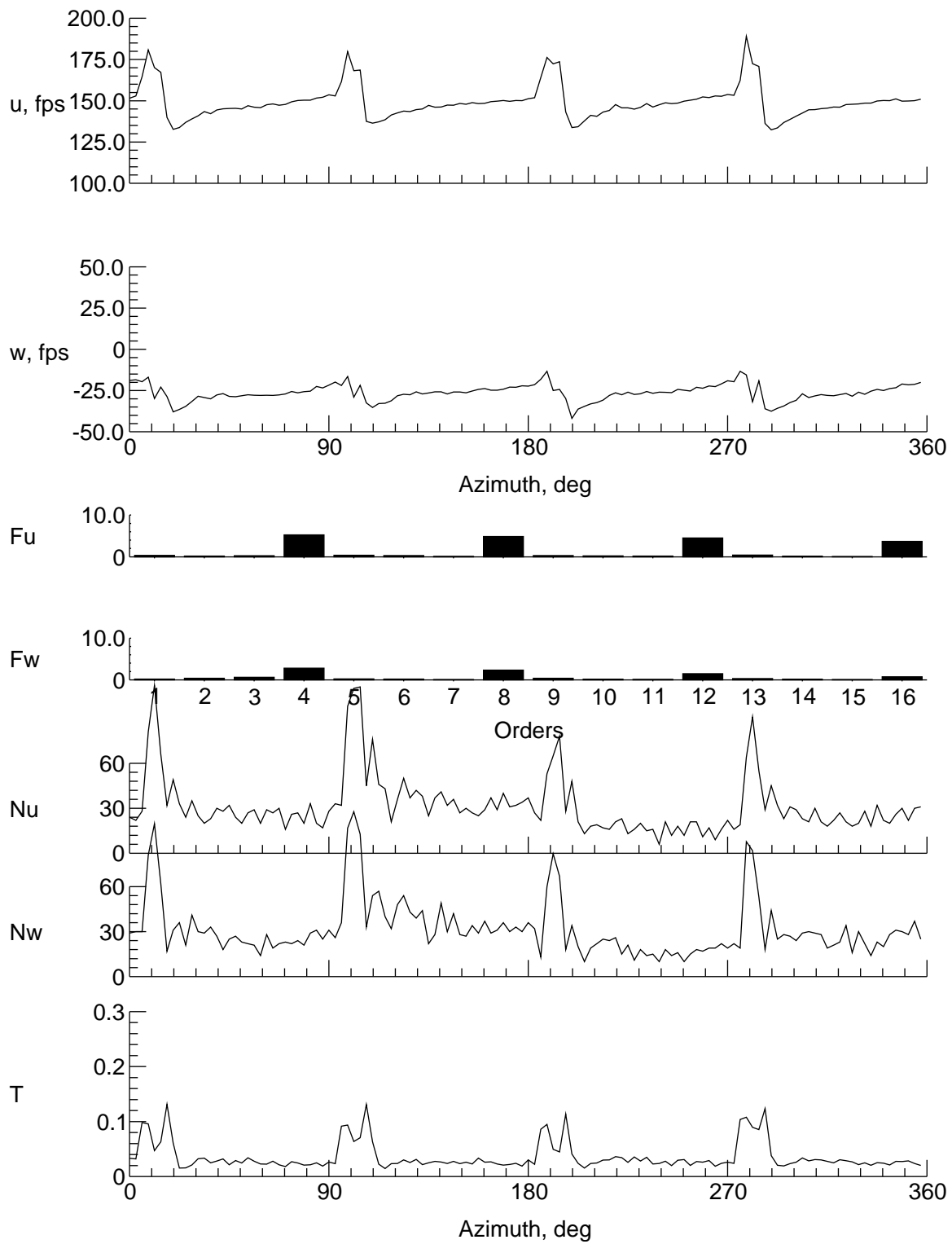
(b) $y = 0$ in., $z = 5.953$ in.

Figure 20. Continued.



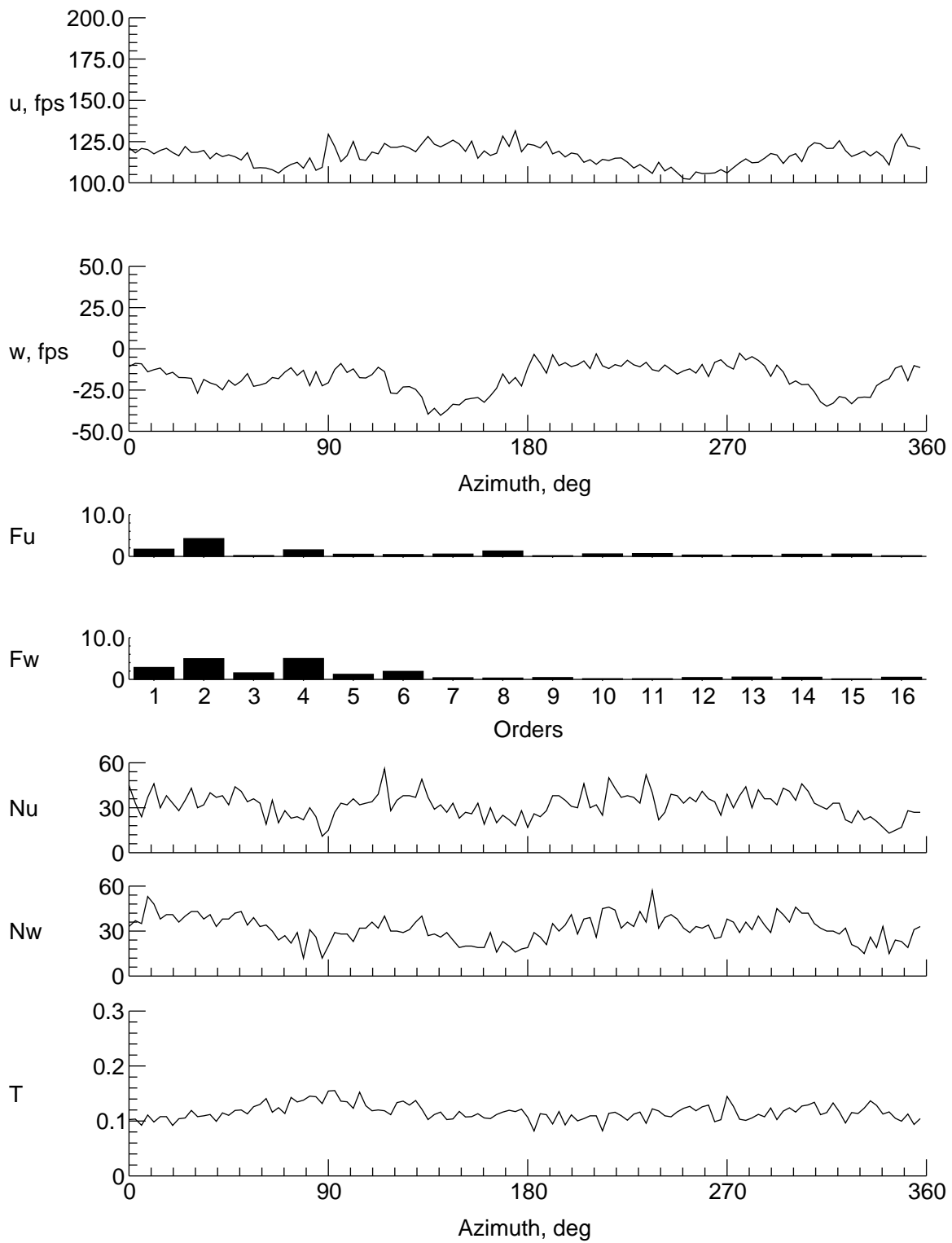
(c) $y = 0$ in., $z = 3.953$ in.

Figure 20. Continued.



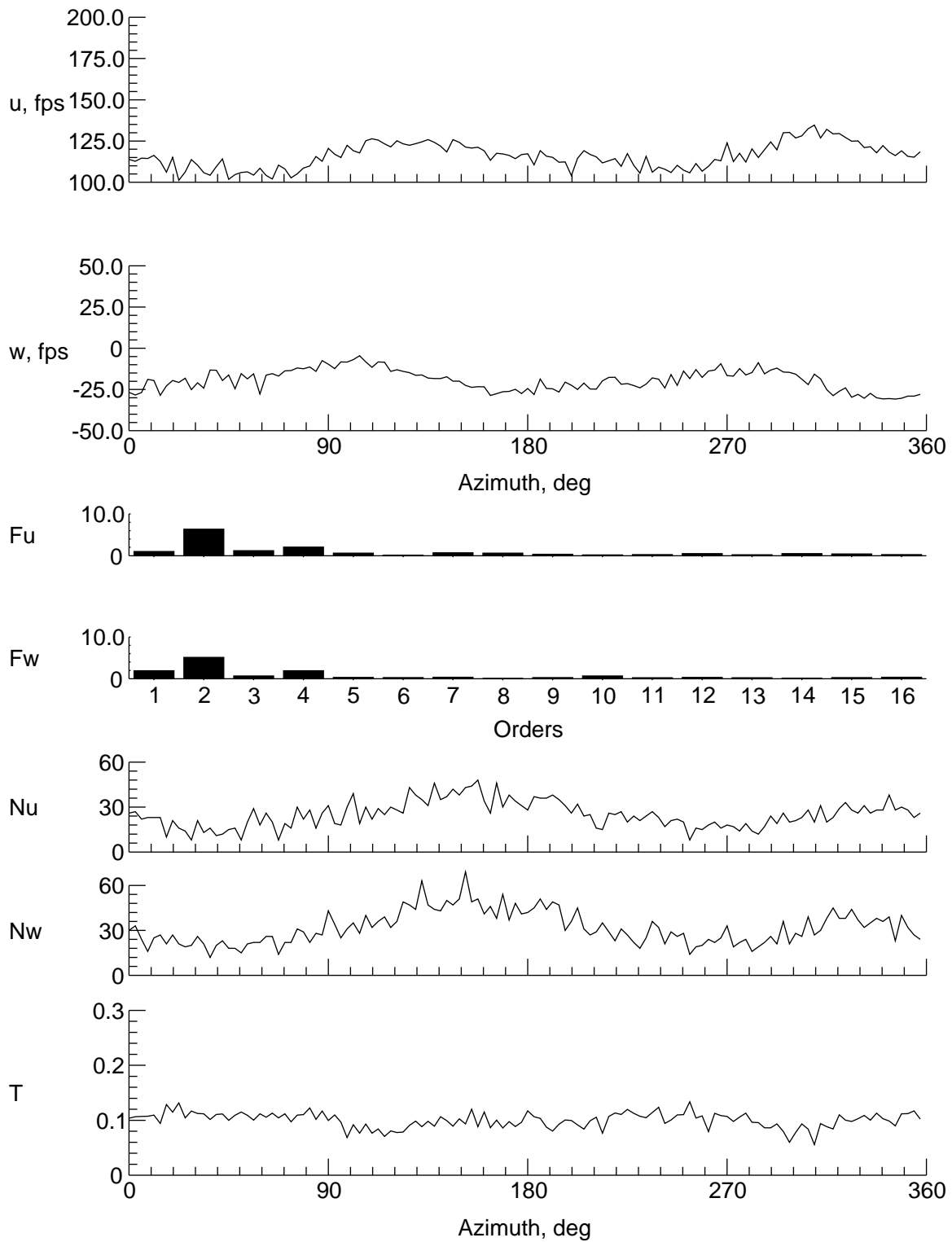
(d) $y = 0$ in., $z = 1.953$ in.

Figure 20. Continued.



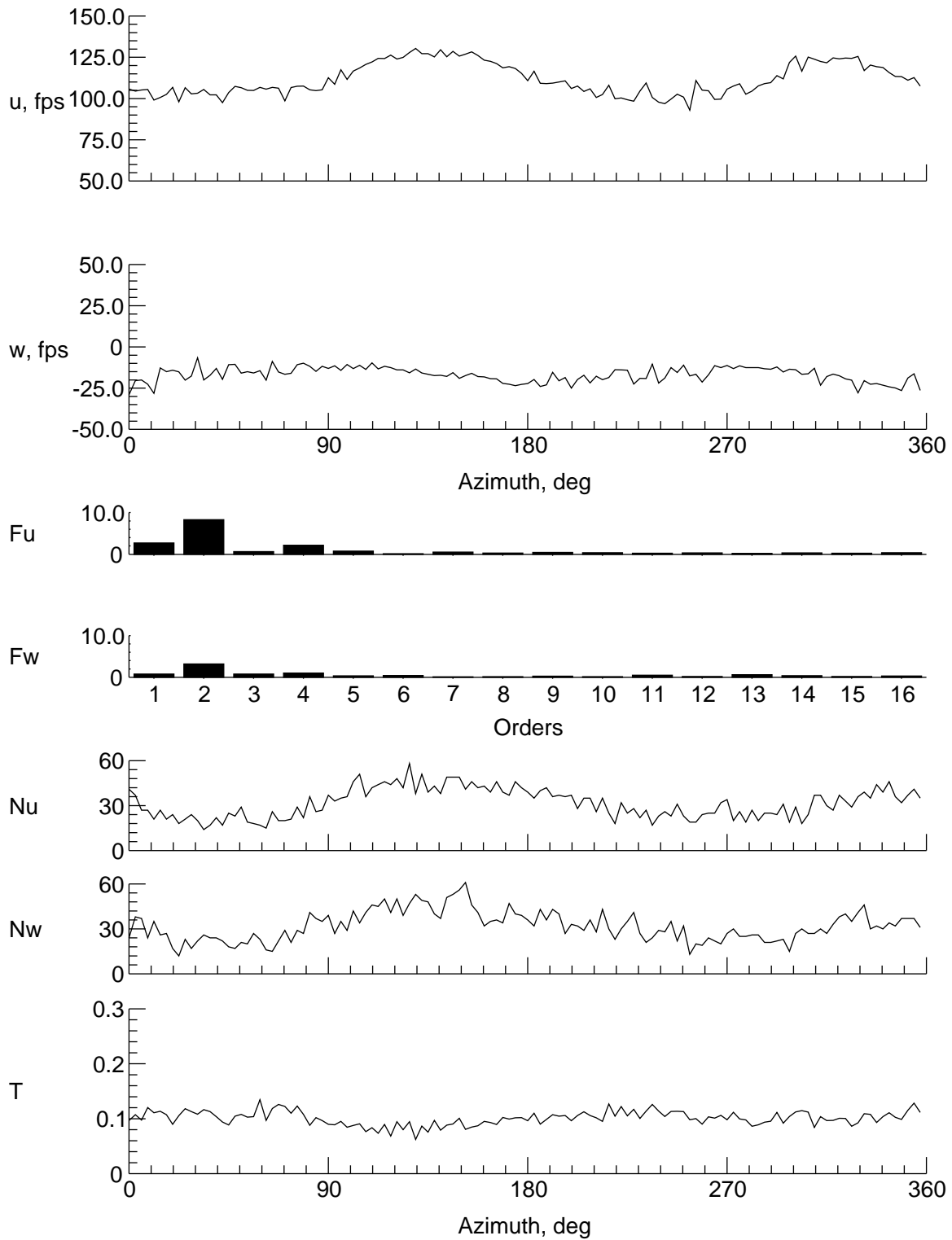
(e) $y = 0$ in., $z = -2.047$ in.

Figure 20. Continued.



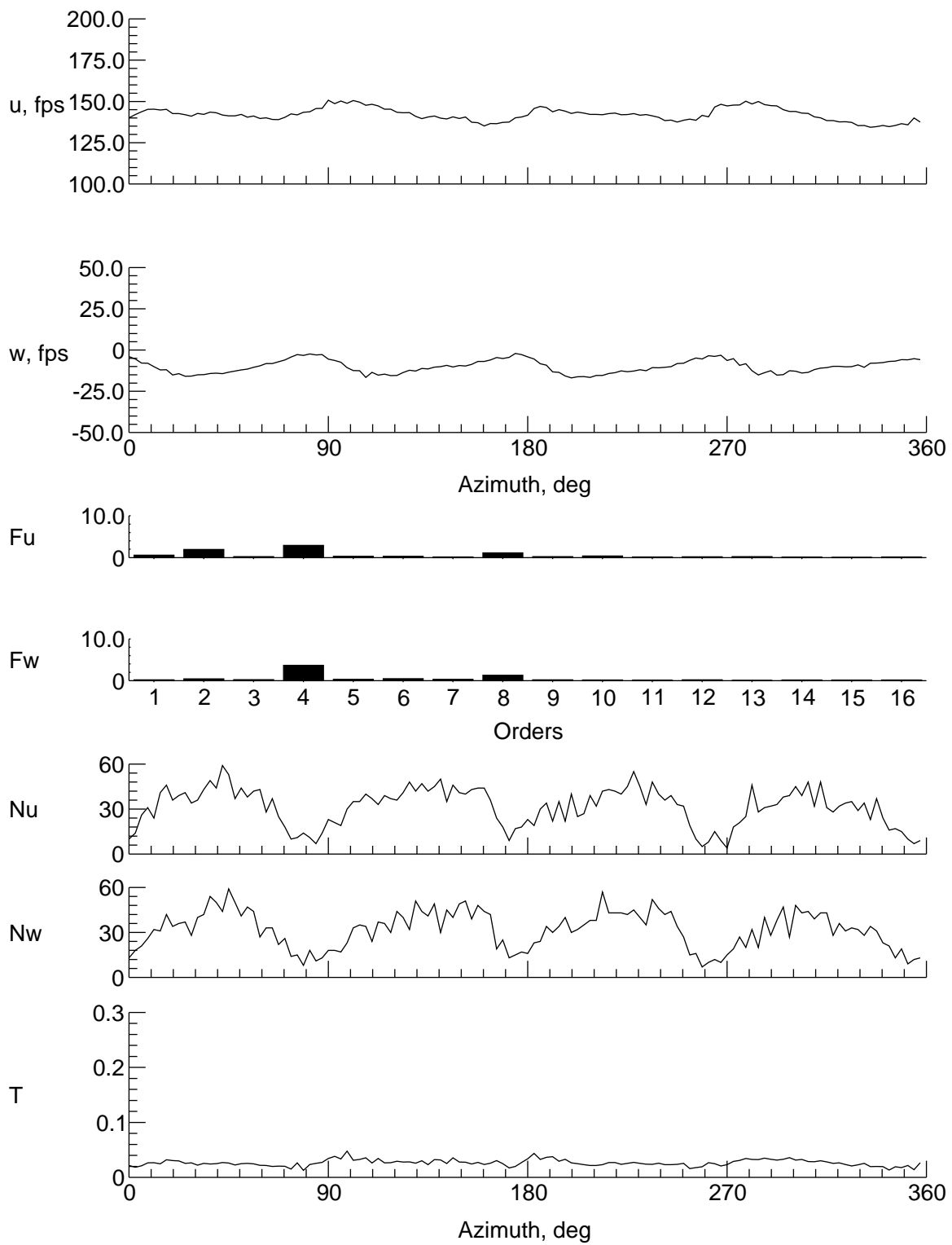
(f) $y = 0$ in., $z = -6.047$ in.

Figure 20. Continued.



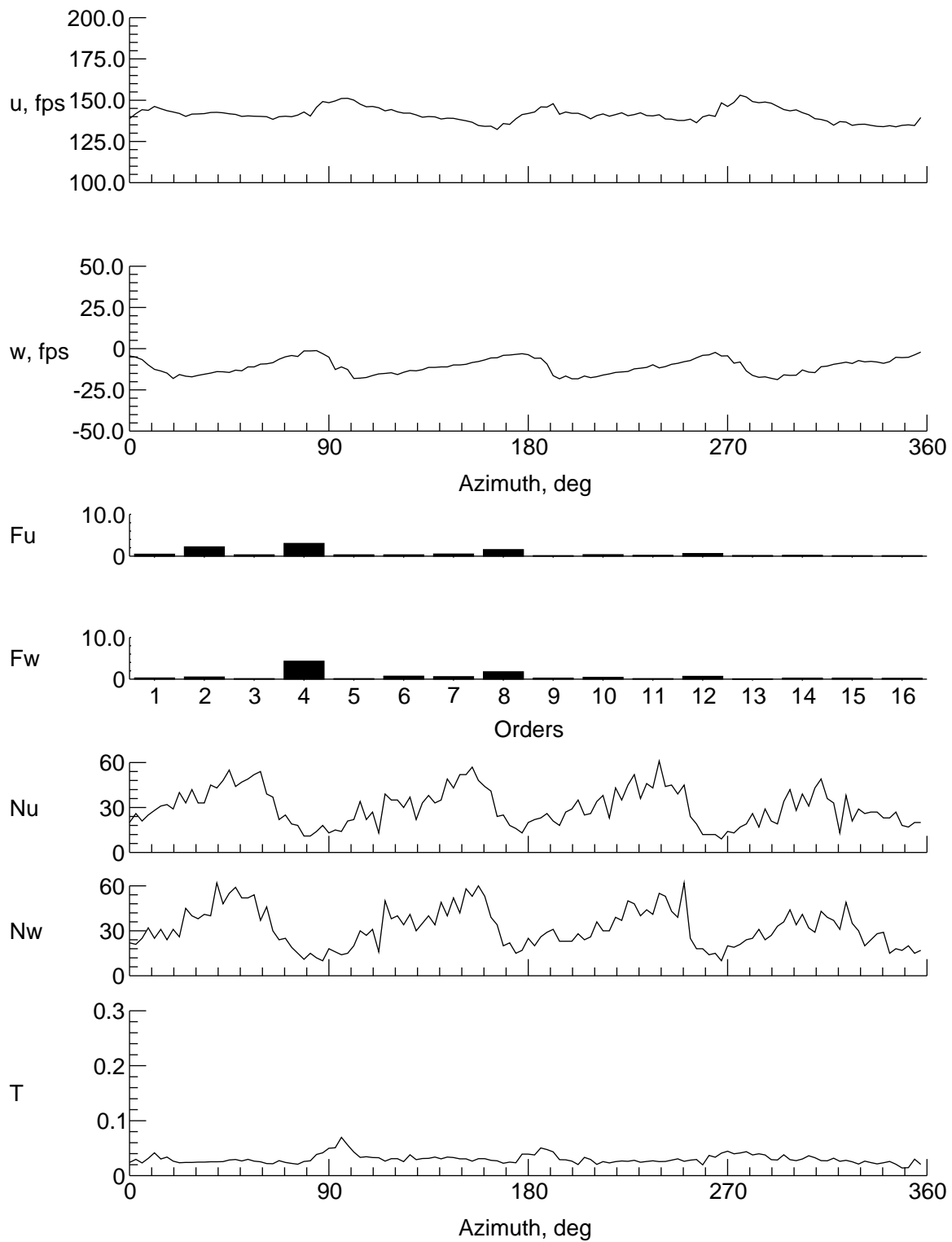
(g) $y = 0$ in., $z = -8.047$ in.

Figure 20. Continued.



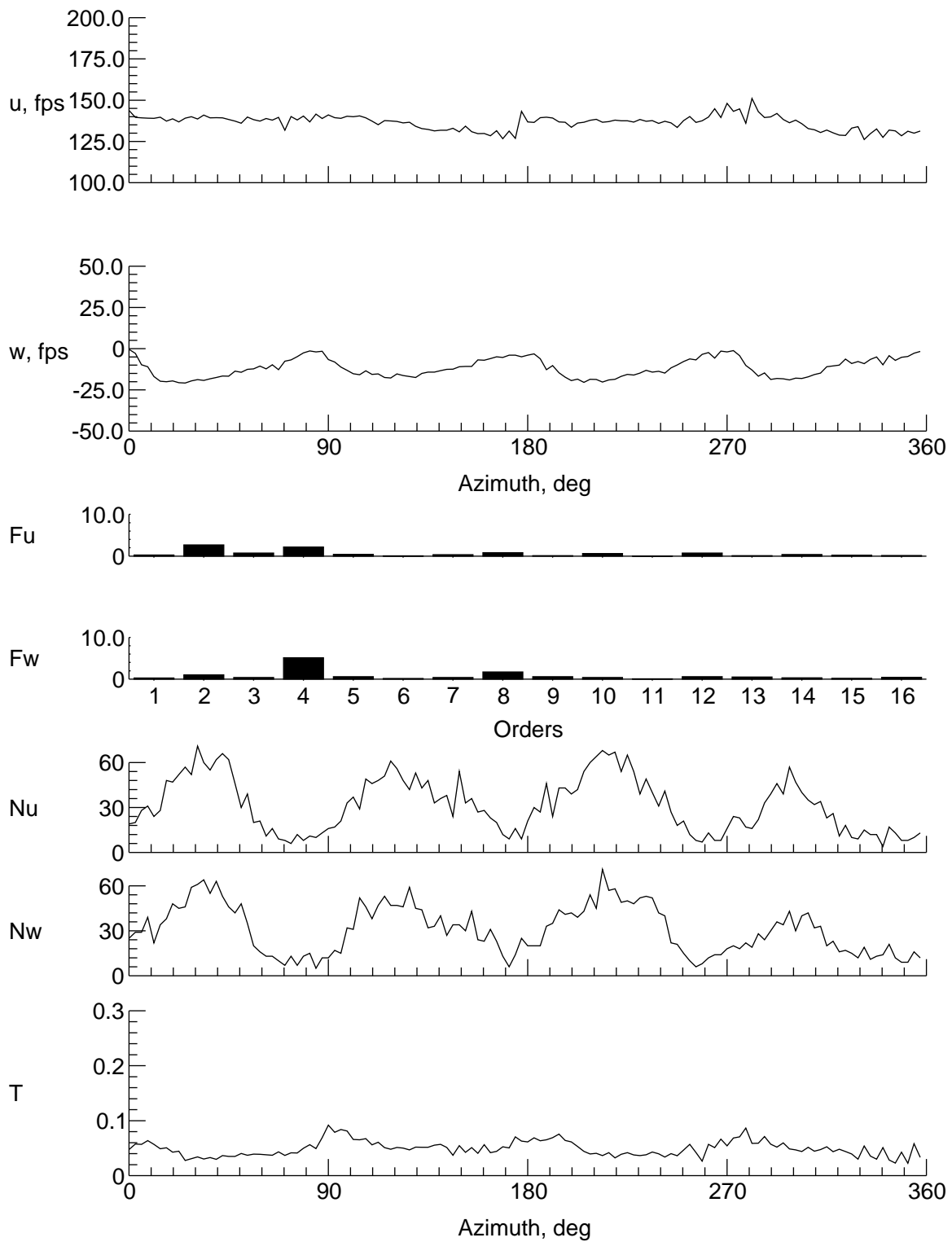
(h) $y = 9$ in., $z = -2.047$ in.

Figure 20. Continued.



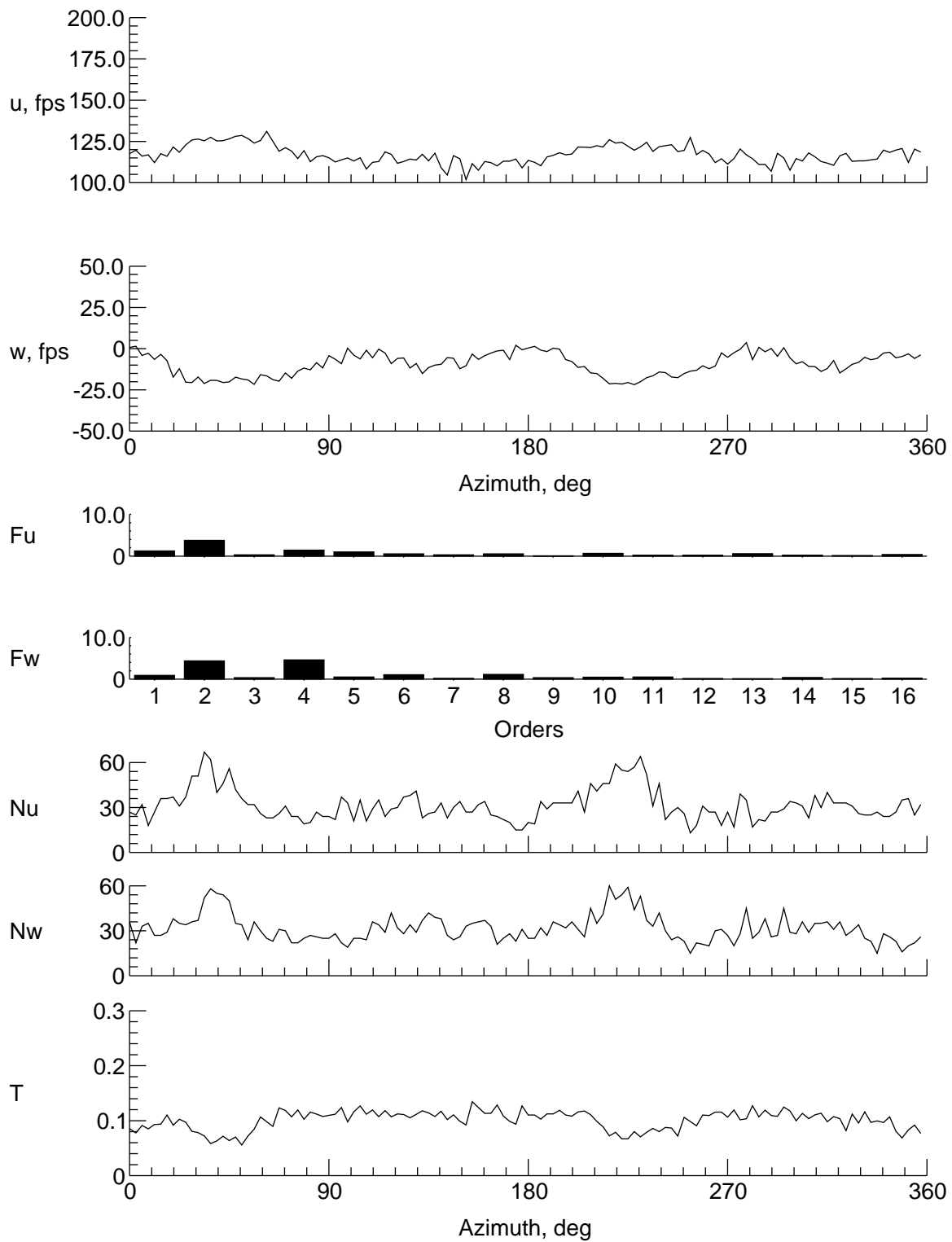
(i) $y = 8$ in., $z = -2.047$ in.

Figure 20. Continued.



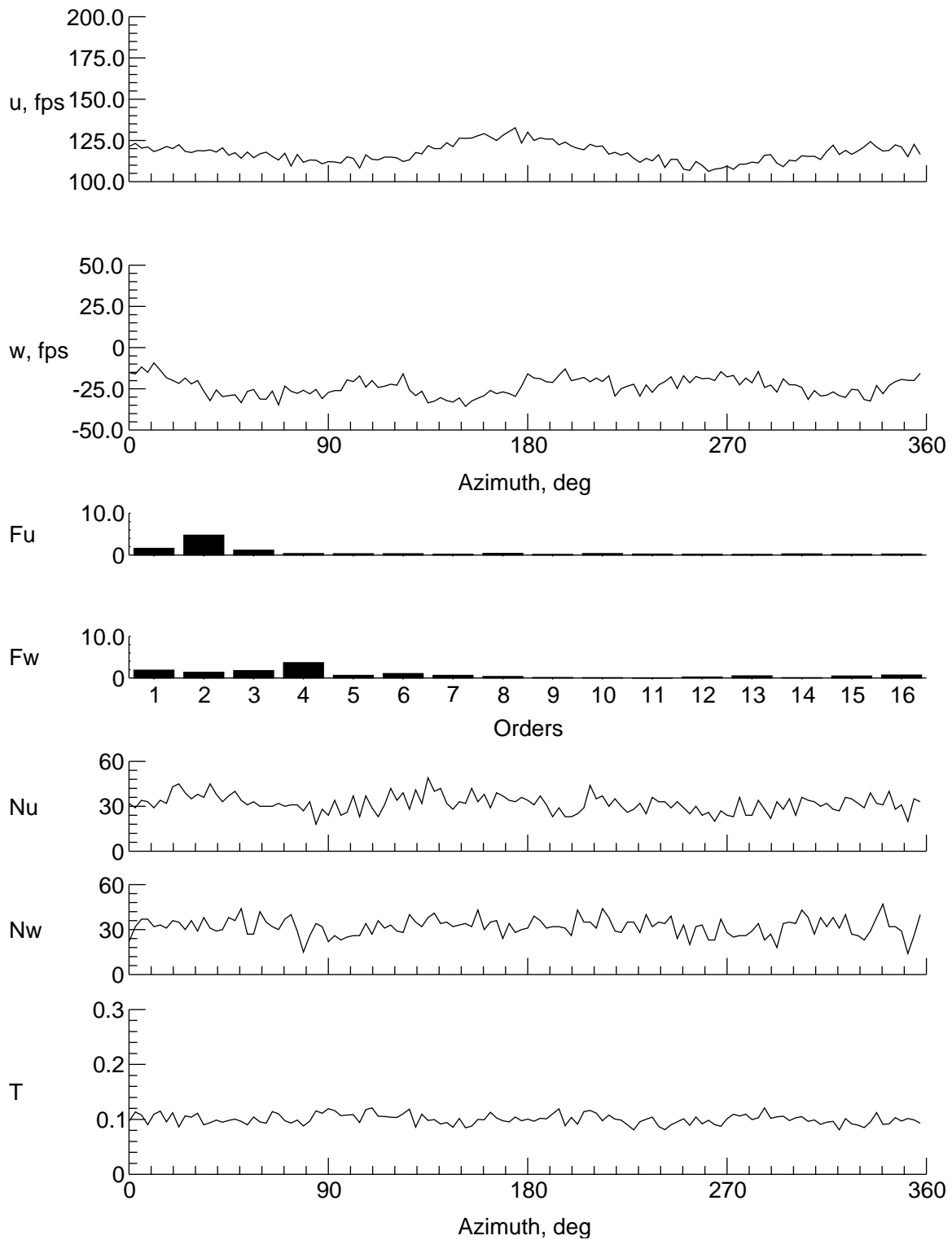
(j) $y = 6$ in., $z = -2.047$ in.

Figure 20. Continued.



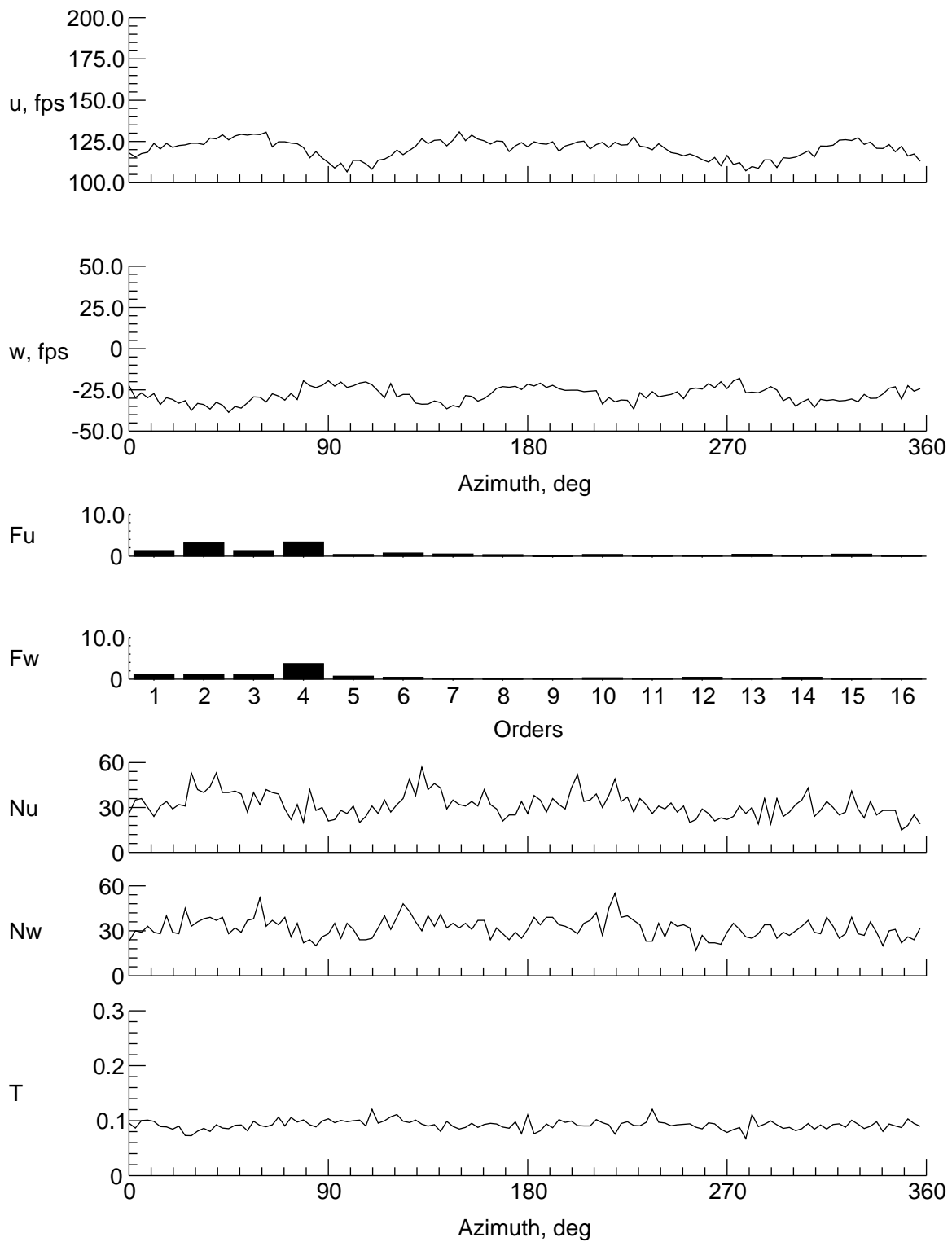
(k) $y = 4$ in., $z = -2.047$ in.

Figure 20. Continued.



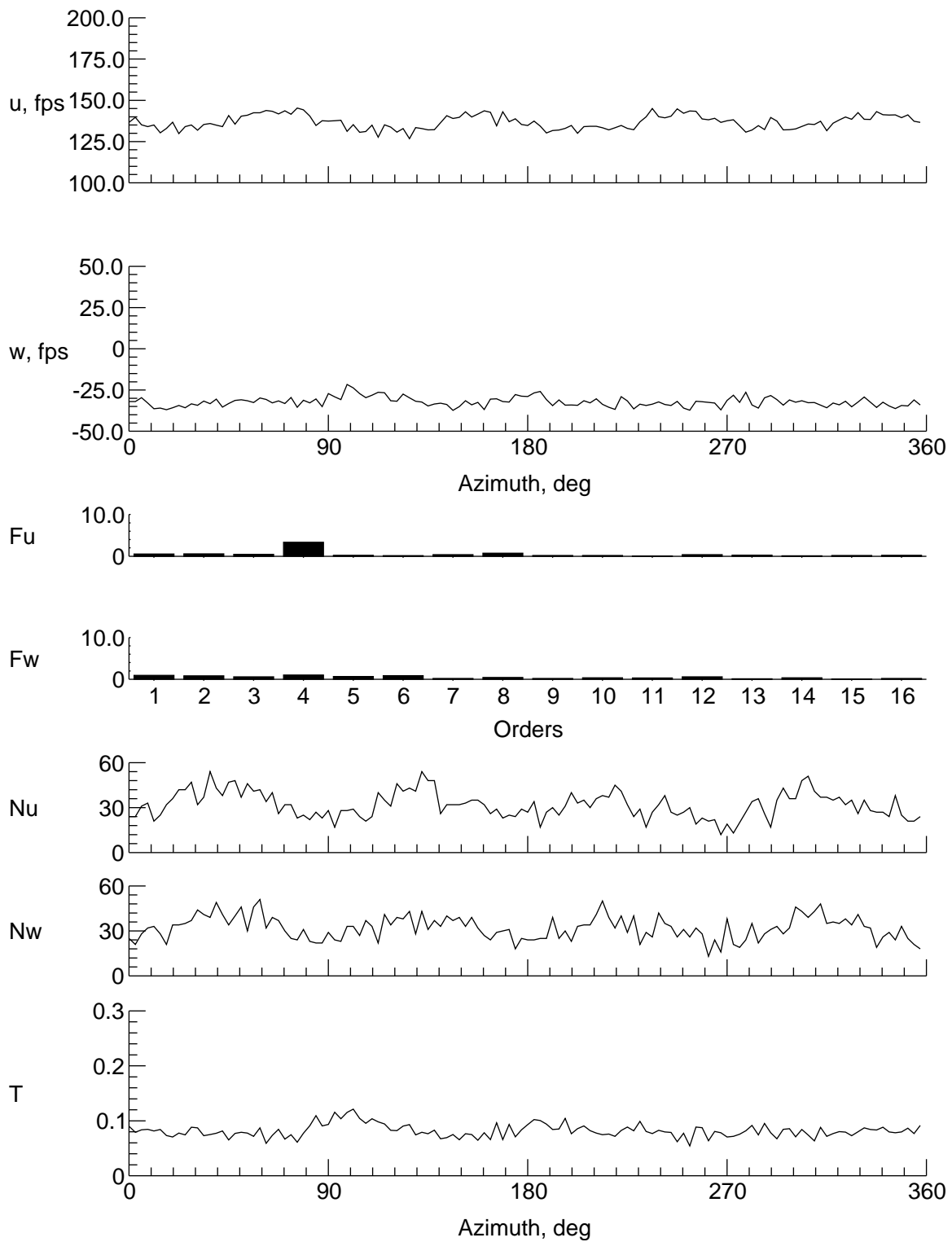
(l) $y = -4$ in., $z = -2.047$ in.

Figure 20. Continued.



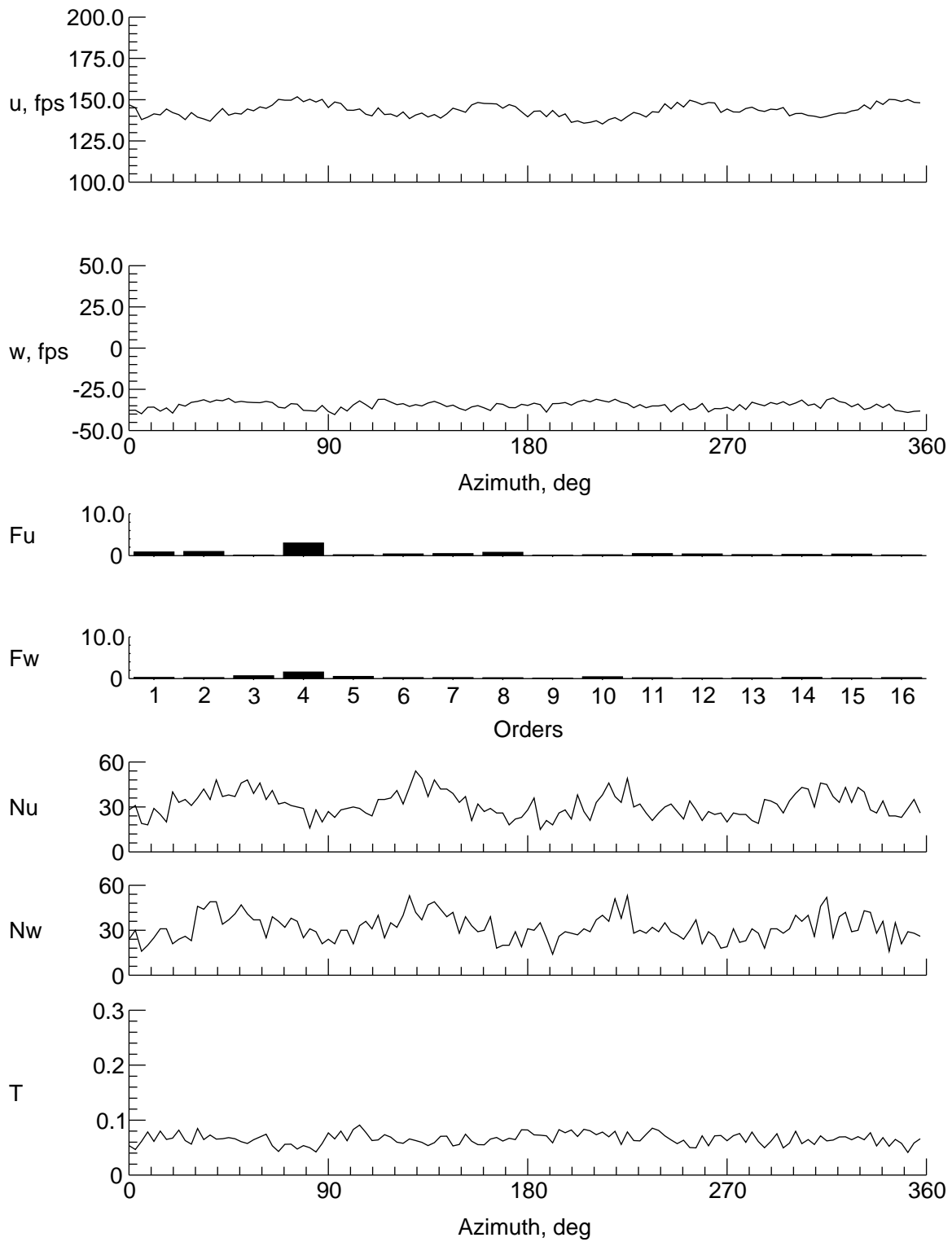
(m) $y = -6$ in., $z = -2.047$ in.

Figure 20. Continued.



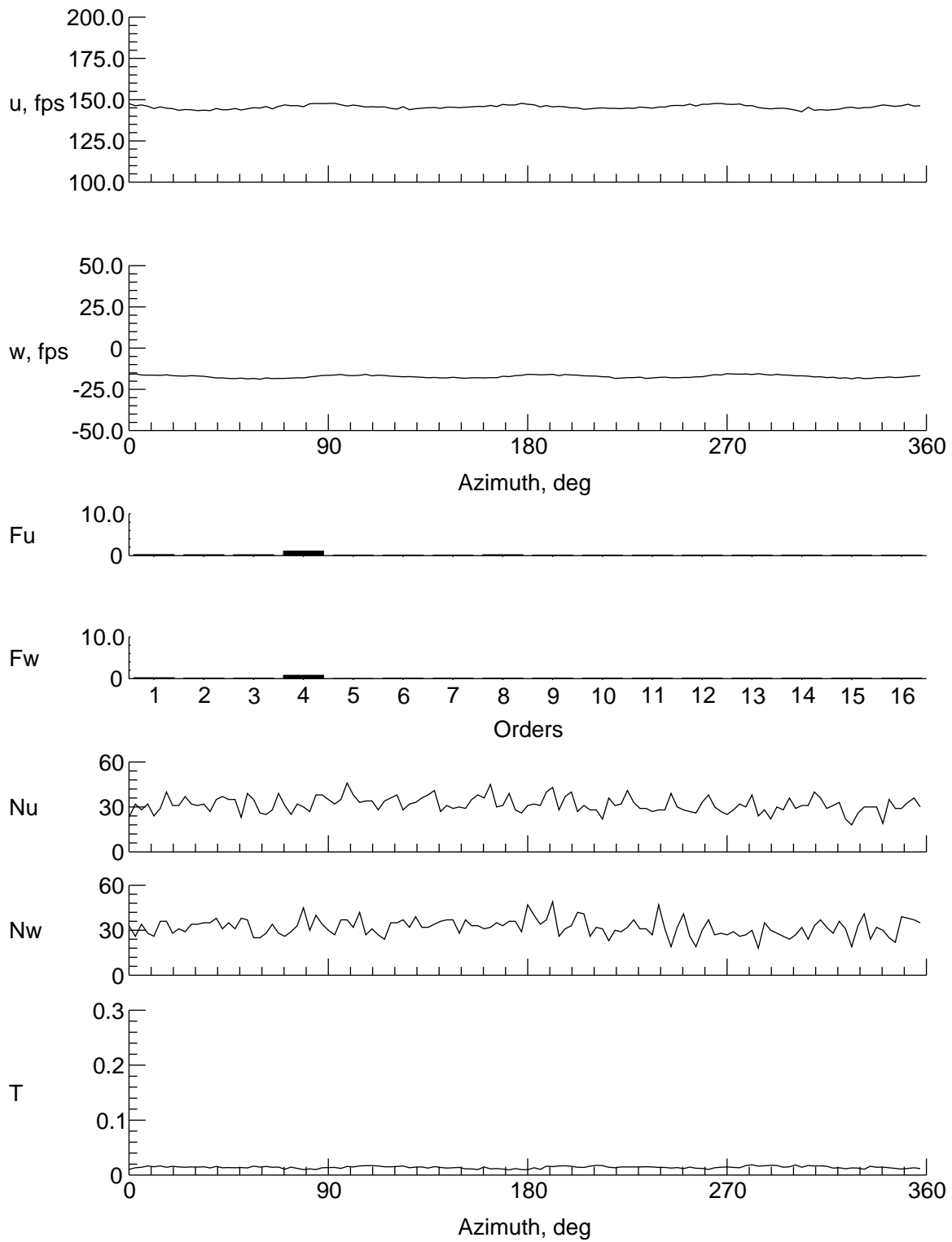
(n) $y = -8$ in., $z = -2.047$ in.

Figure 20. Continued.



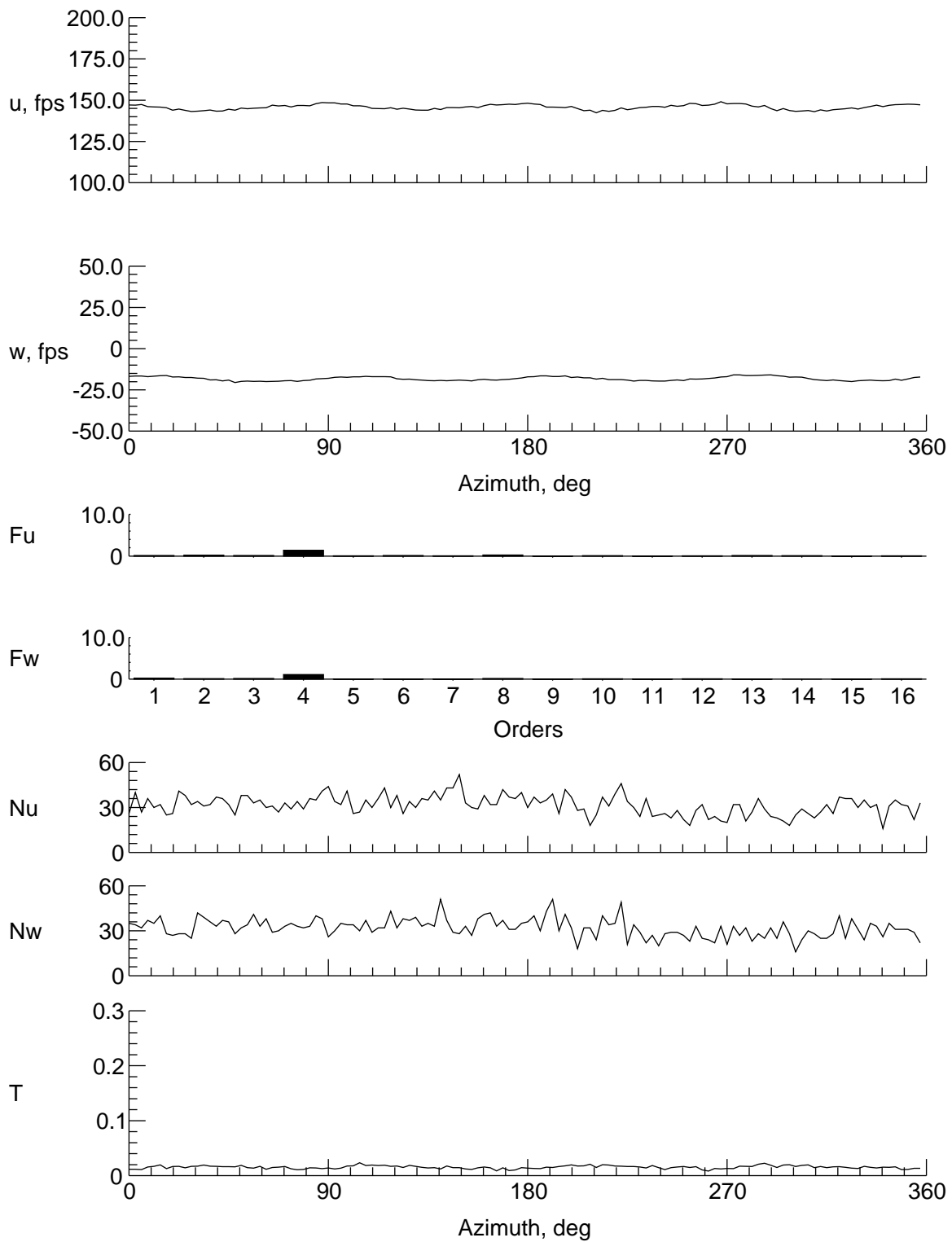
(o) $y = -9$ in., $z = -2.047$ in.

Figure 20. Concluded.



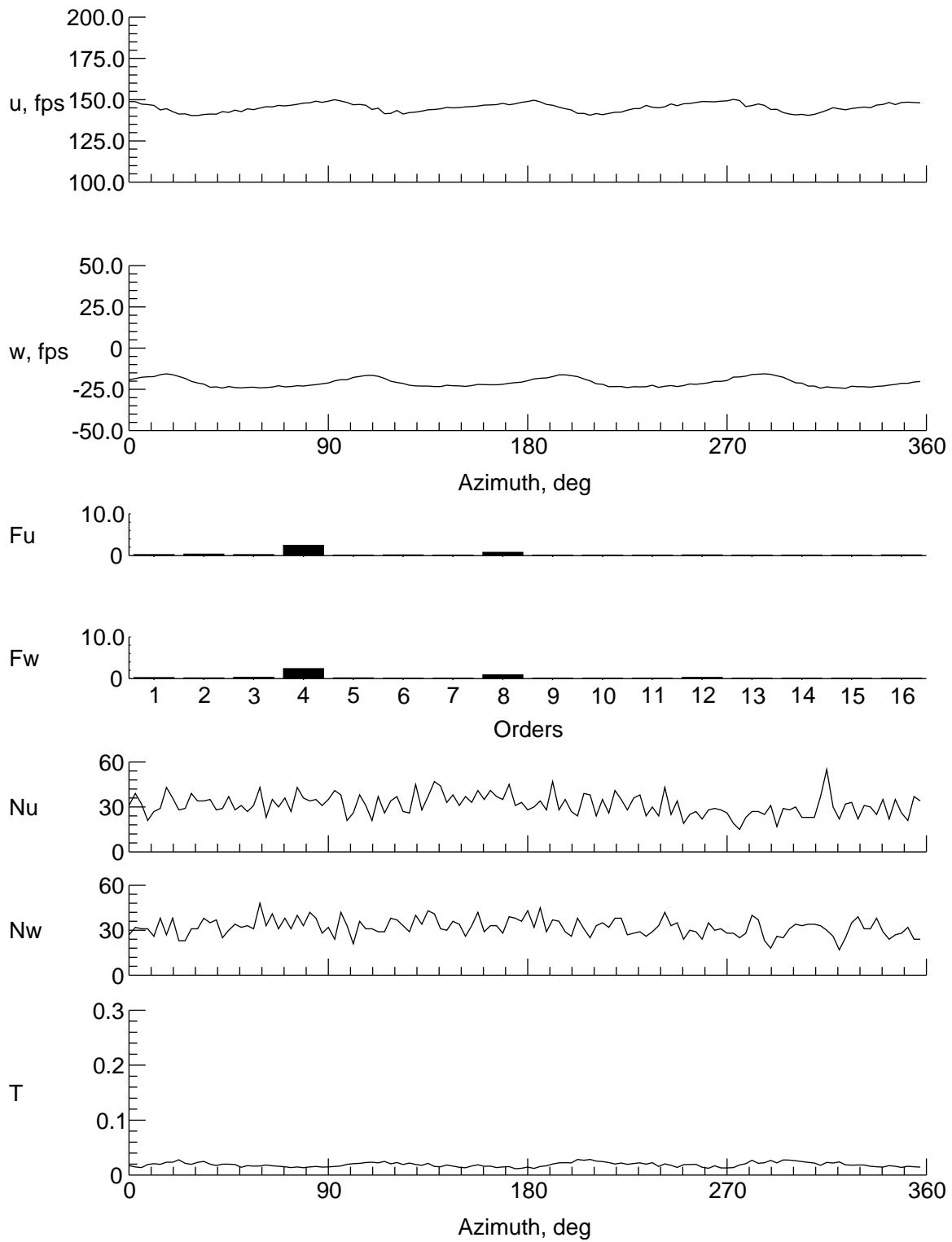
(a) $y = 0$ in., $z = 6.833$ in.

Figure 21. Velocity and turbulence at station 36 in.



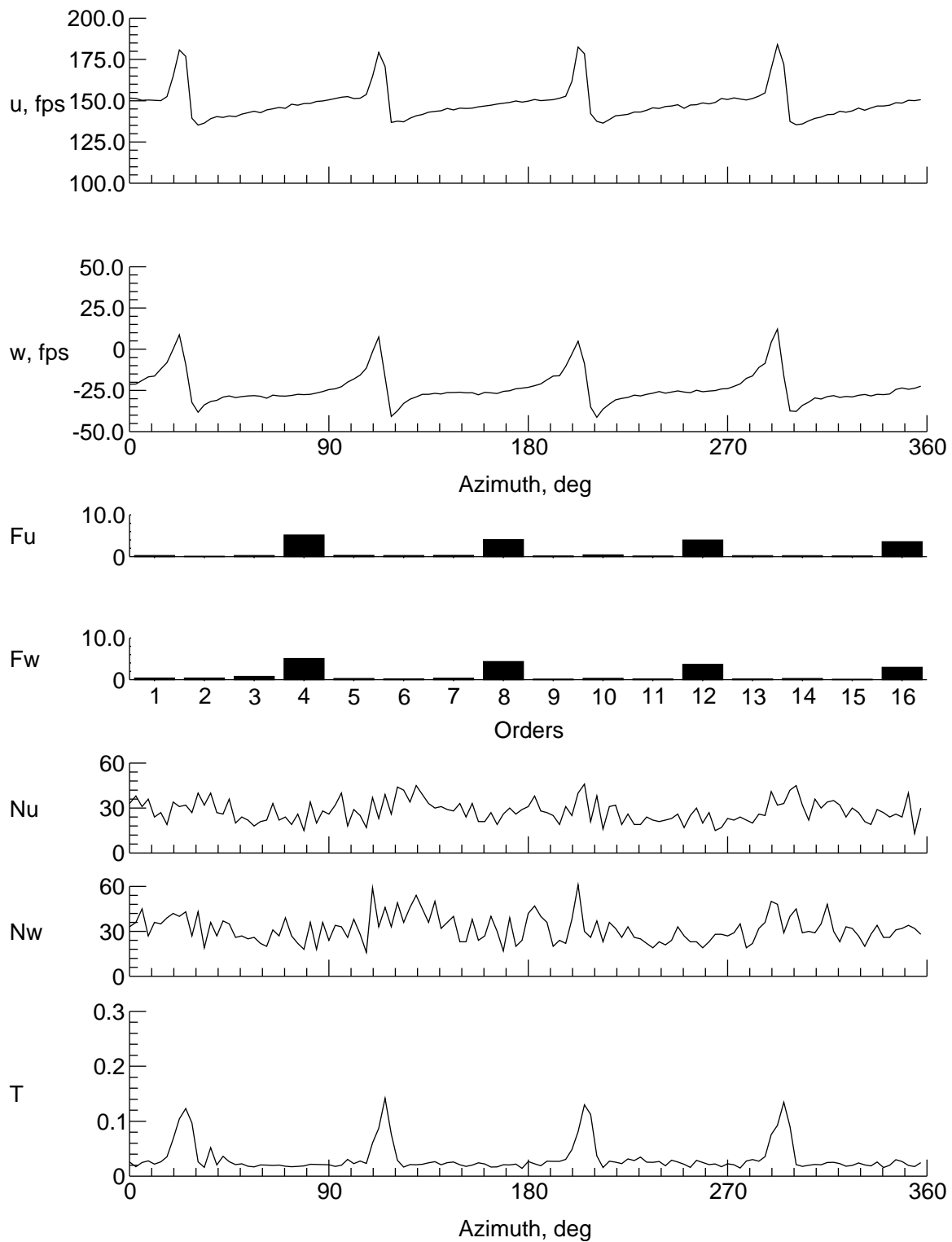
(b) $y = 0$ in., $z = 5.833$ in.

Figure 21. Continued.



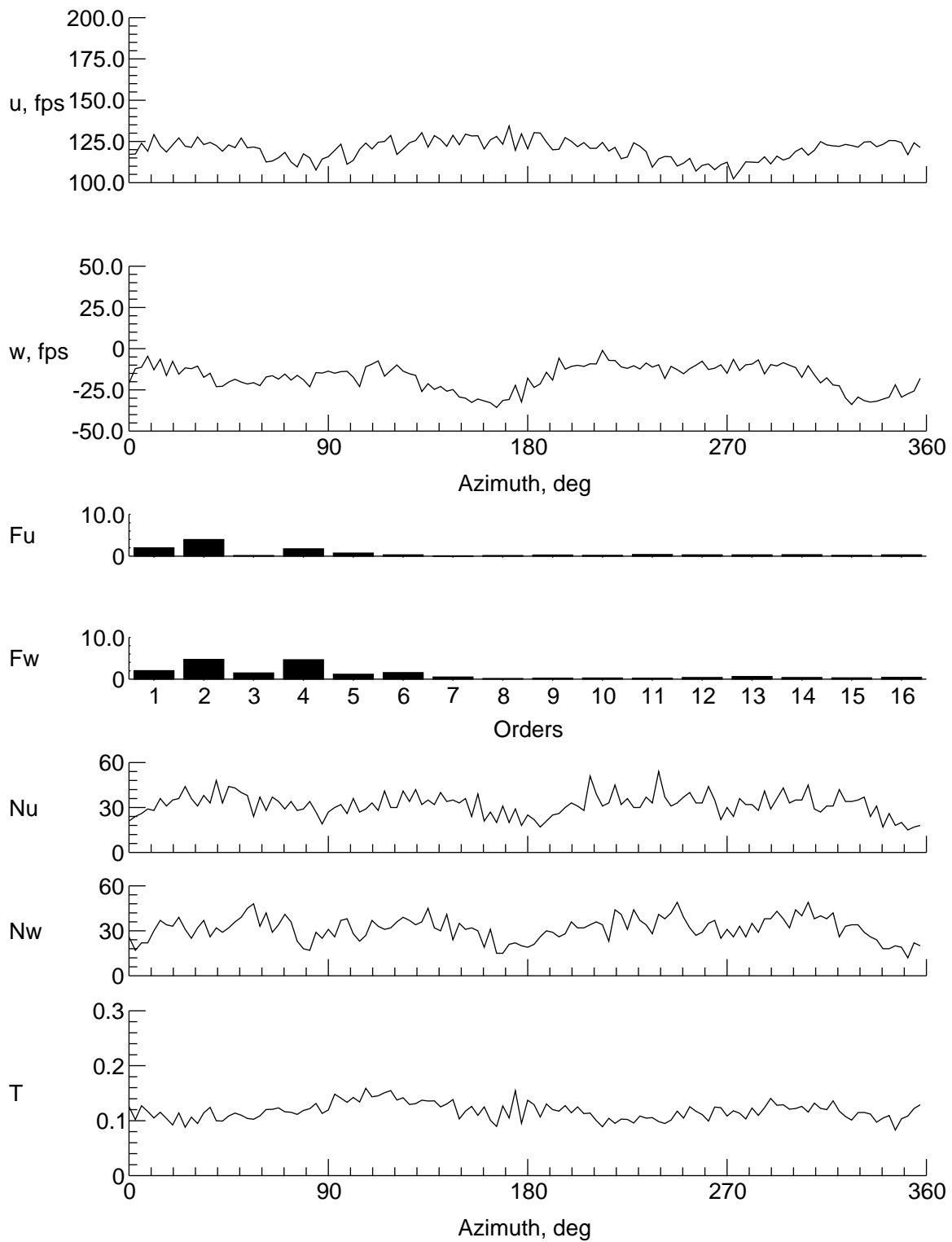
(c) $y = 0$ in., $z = 3.833$ in.

Figure 21. Continued.



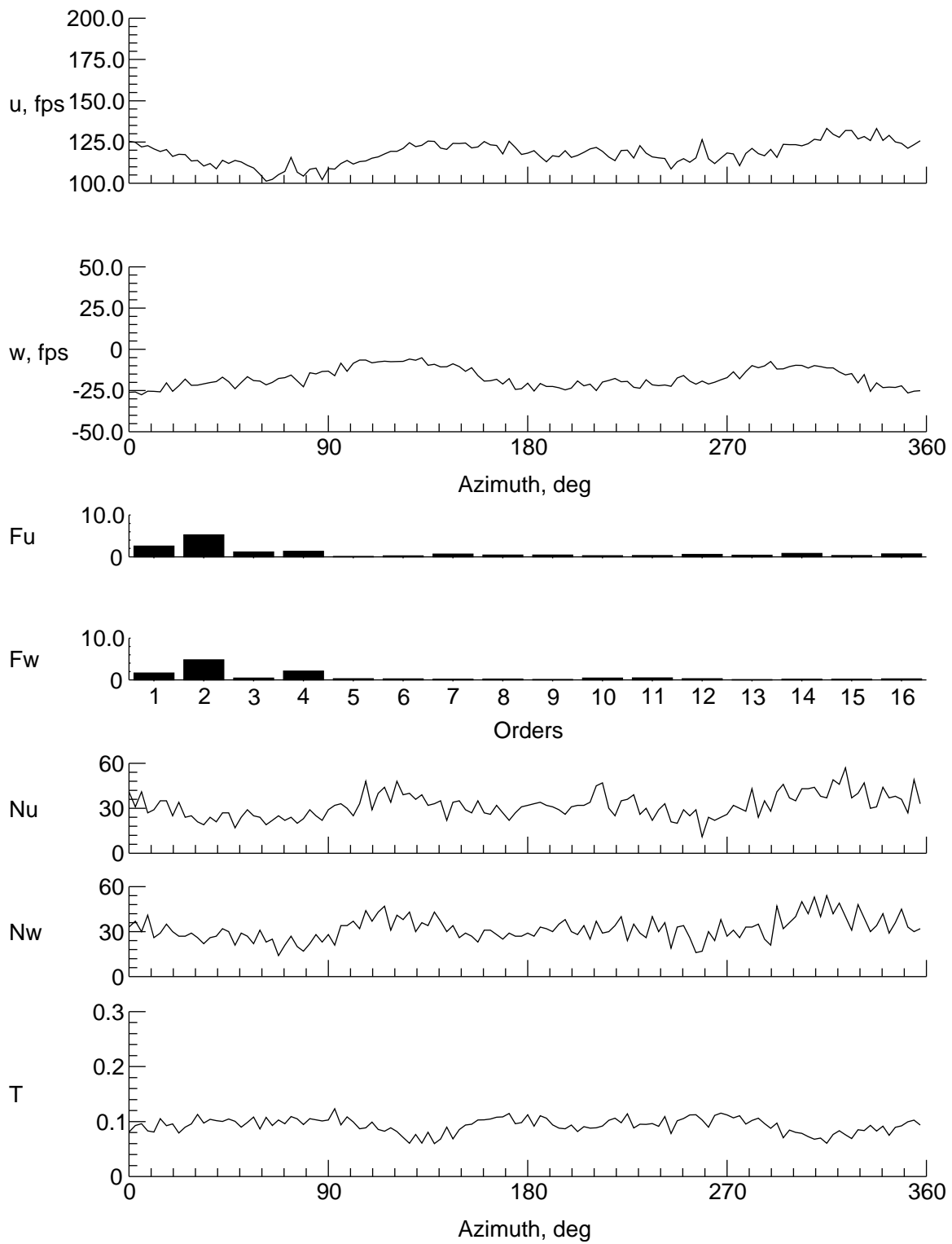
(d) $y = 0$ in., $z = 1.833$ in.

Figure 21. Continued.



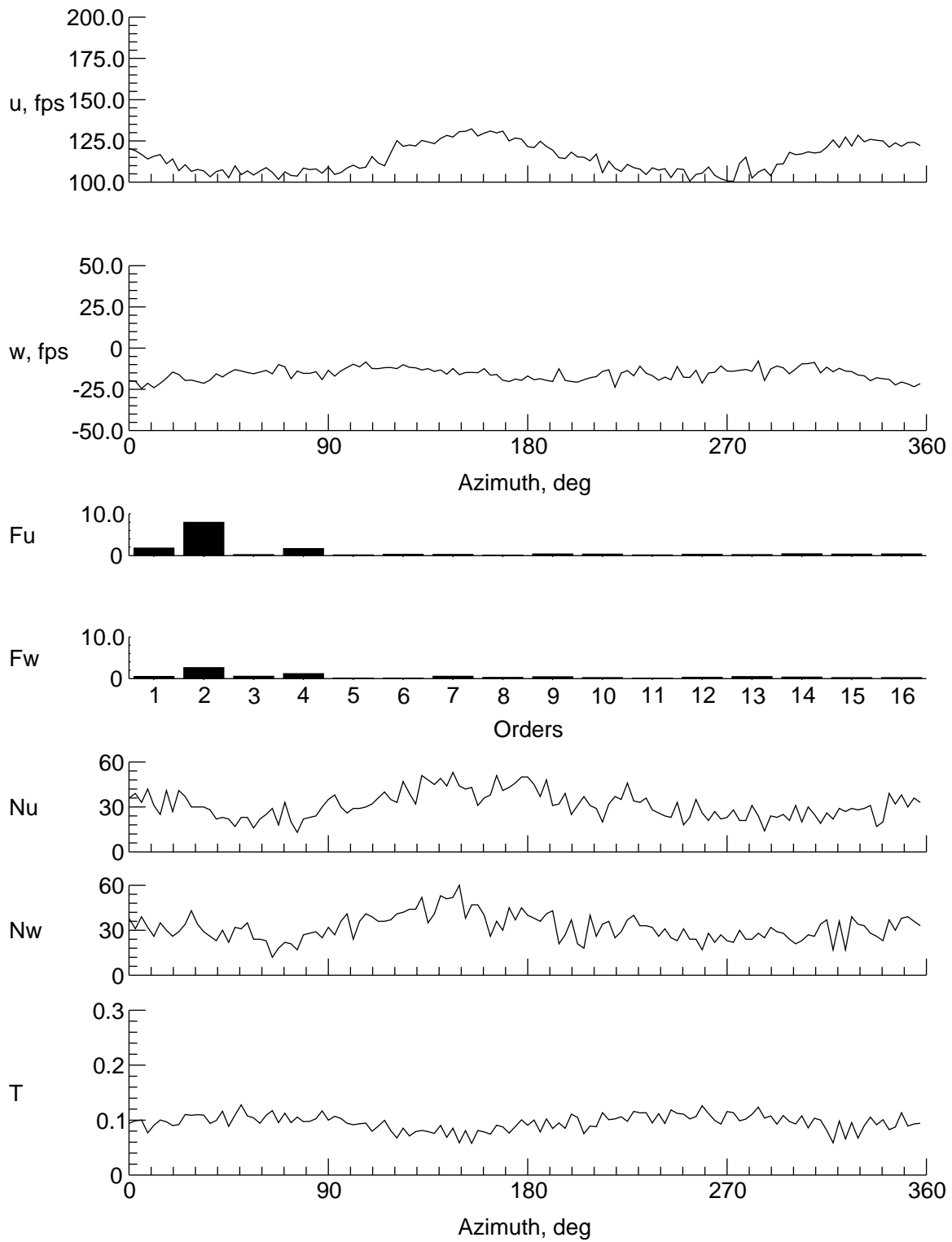
(e) $y = 0$ in., $z = -2.167$ in.

Figure 21. Continued.



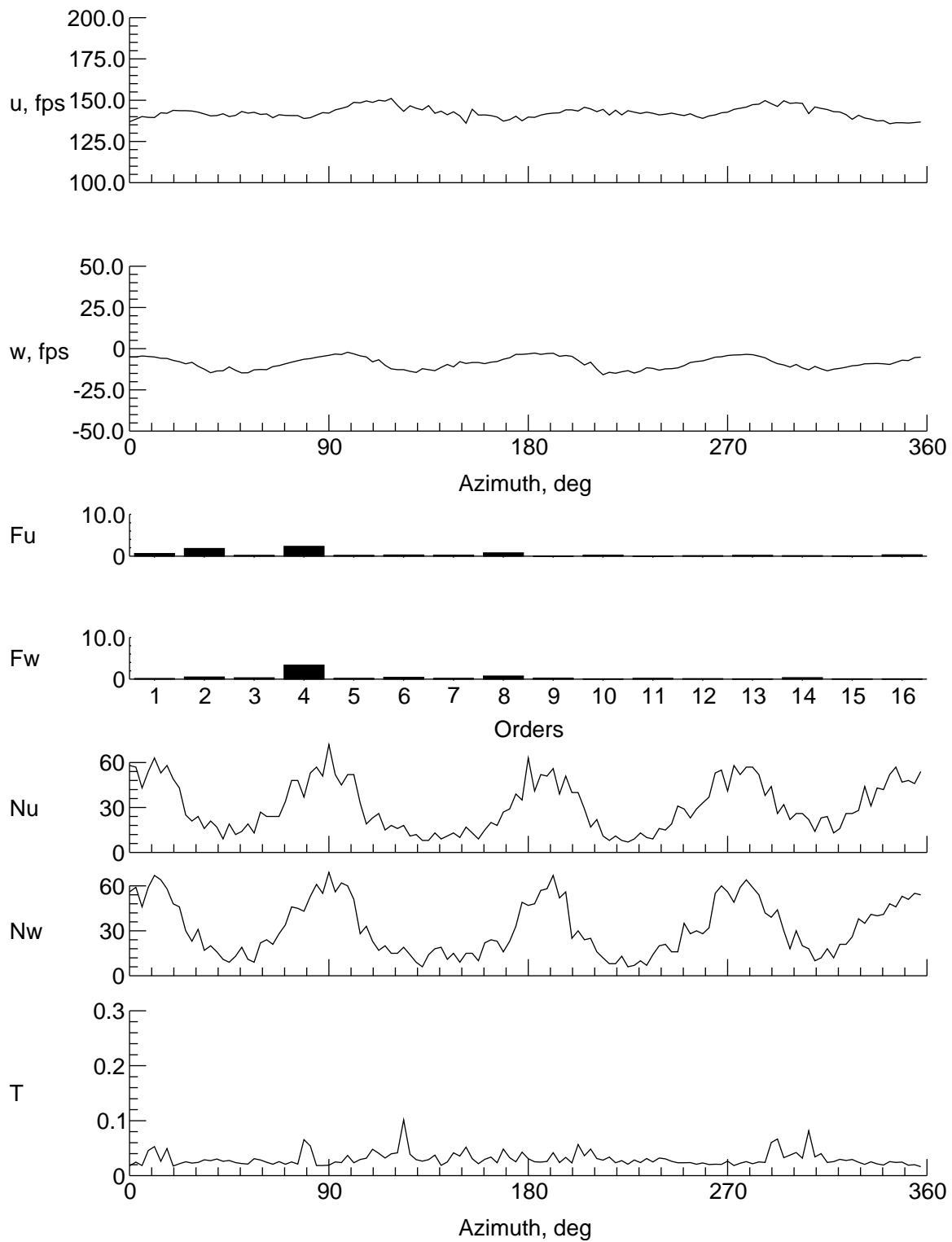
(f) $y = 0$ in., $z = -6.167$ in.

Figure 21. Continued.



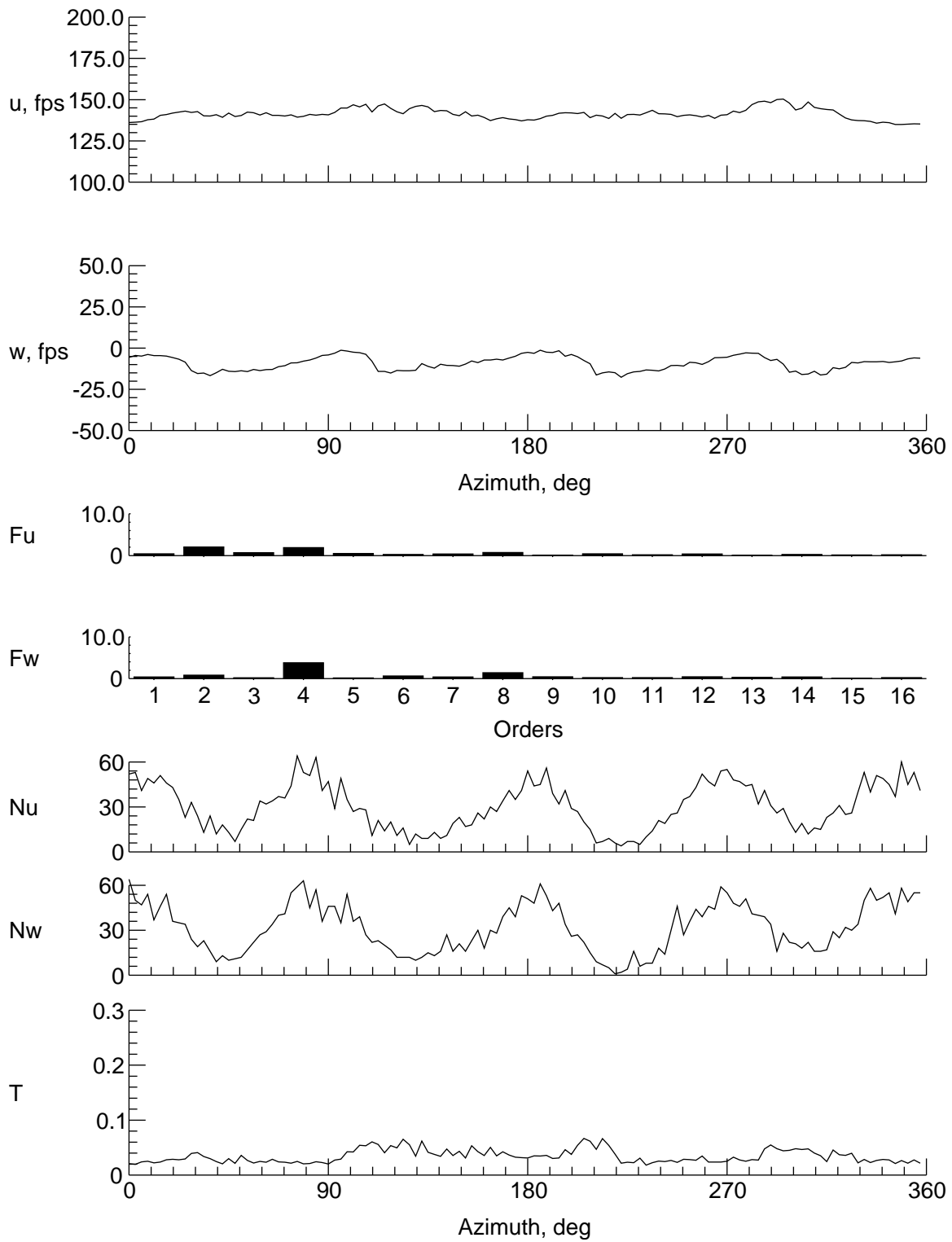
(g) $y = 0$ in., $z = -8.167$ in.

Figure 21. Continued.



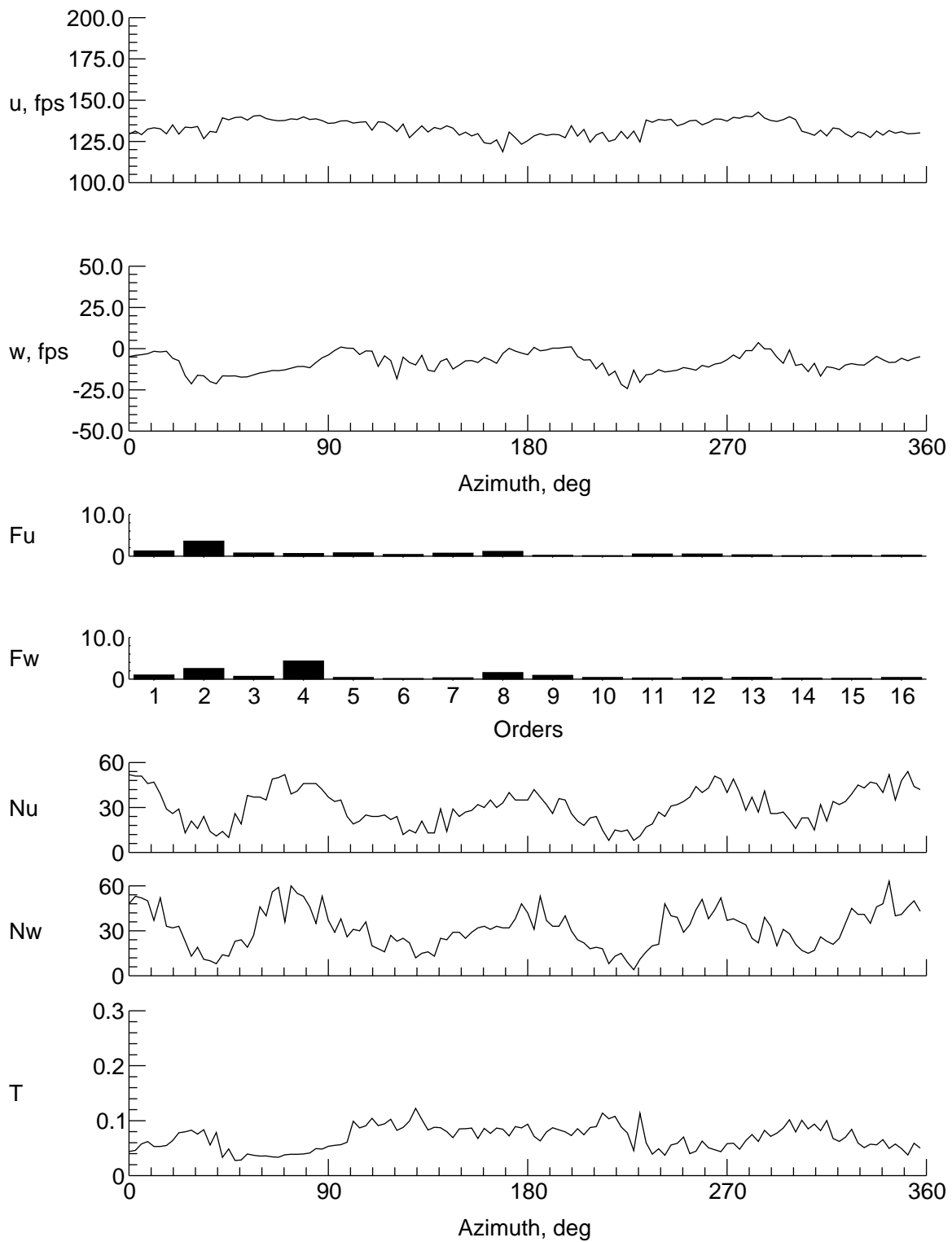
(h) $y = 9$ in., $z = -2.167$ in.

Figure 21. Continued.



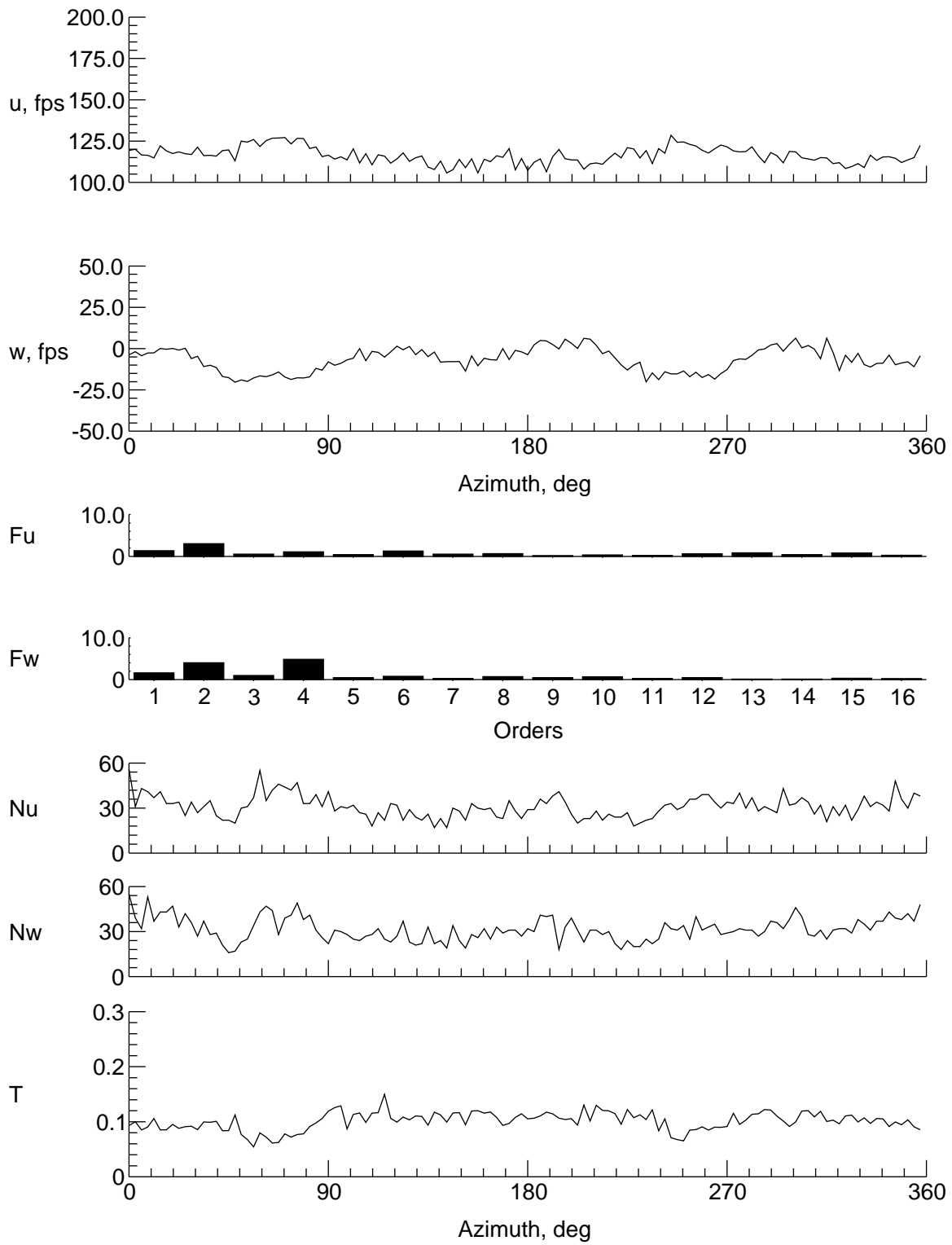
(i) $y = 8$ in., $z = -2.167$ in.

Figure 21. Continued.



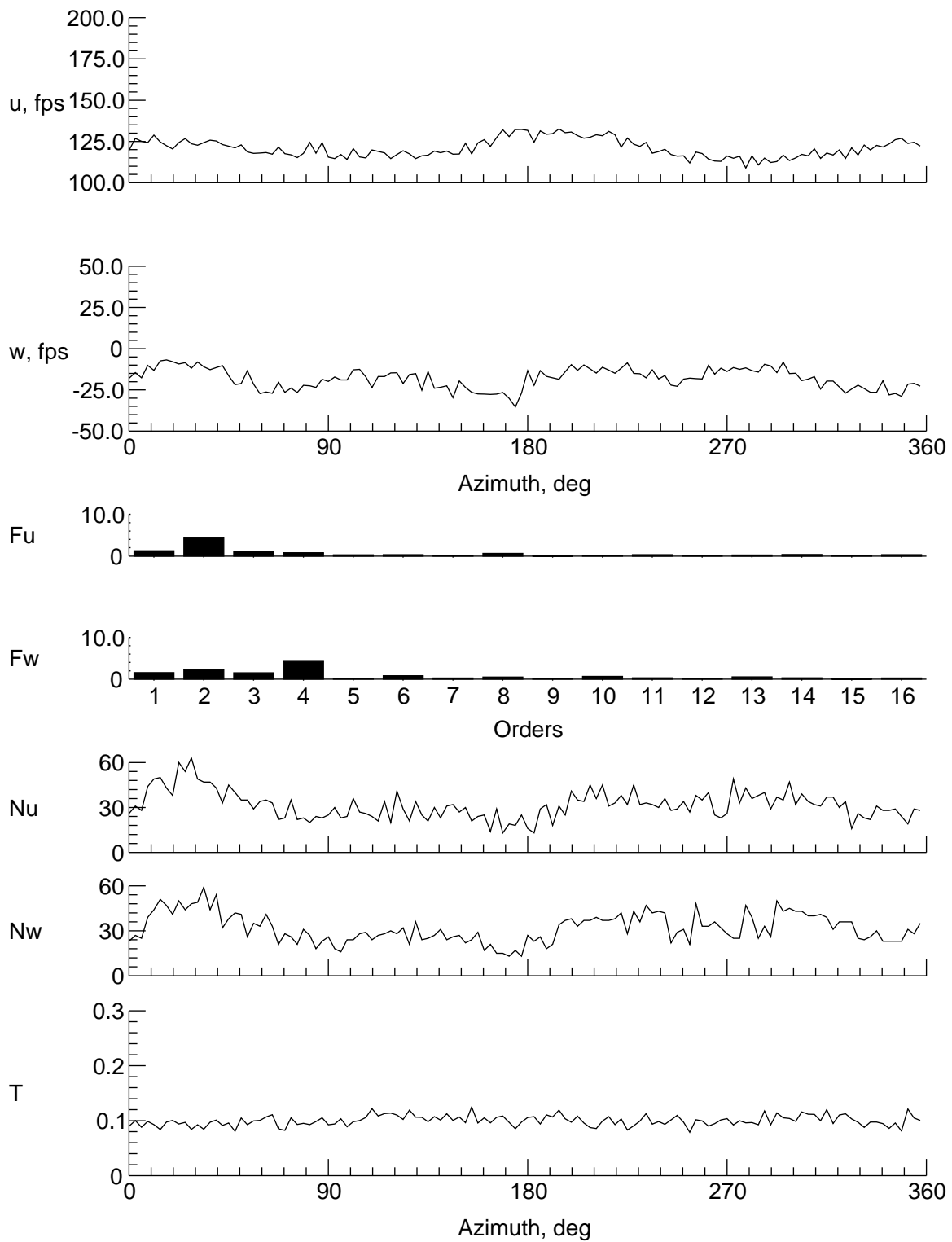
(j) $y = 6$ in., $z = -2.167$ in.

Figure 21. Continued.



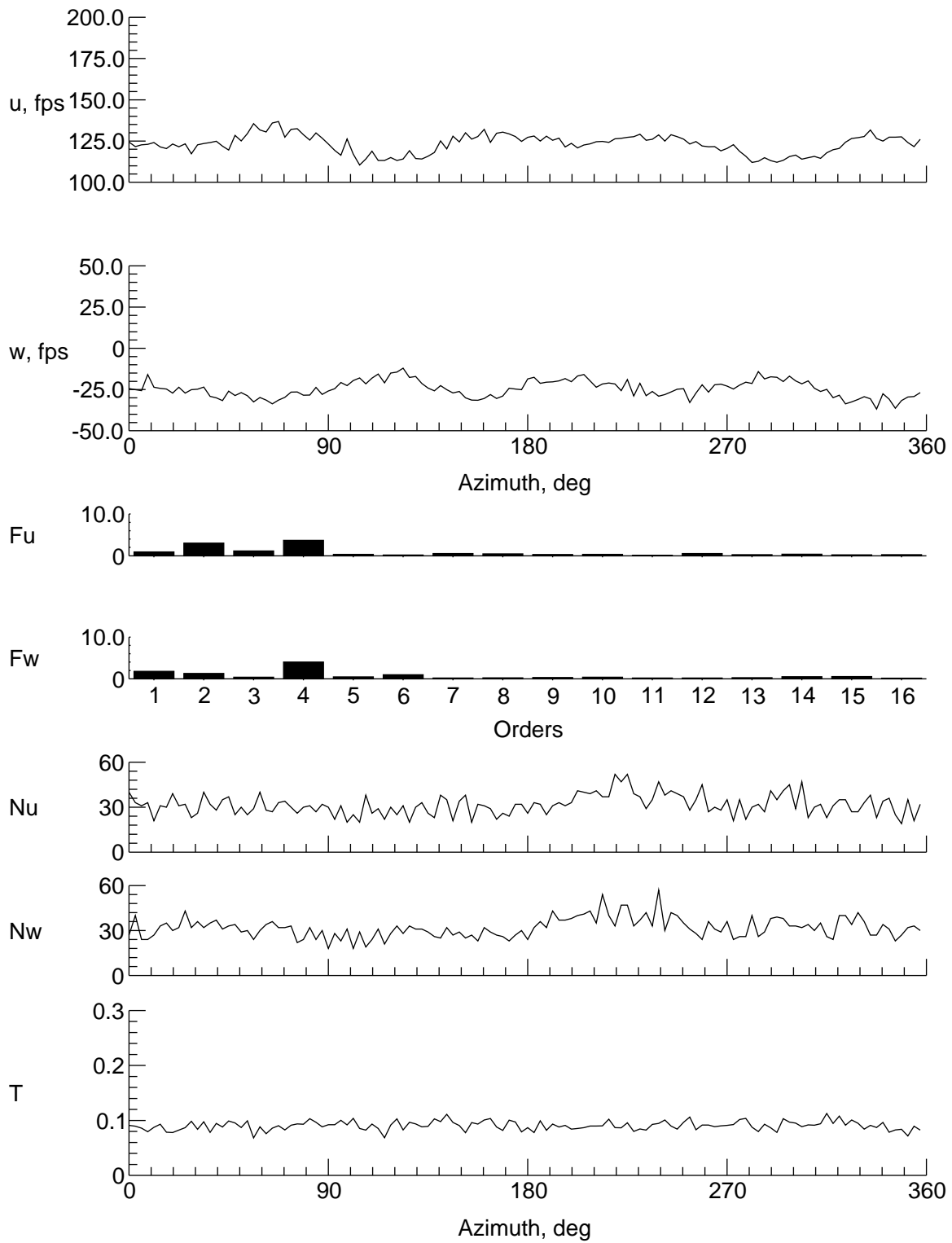
(k) $y = 4$ in., $z = -2.167$ in.

Figure 21. Continued.



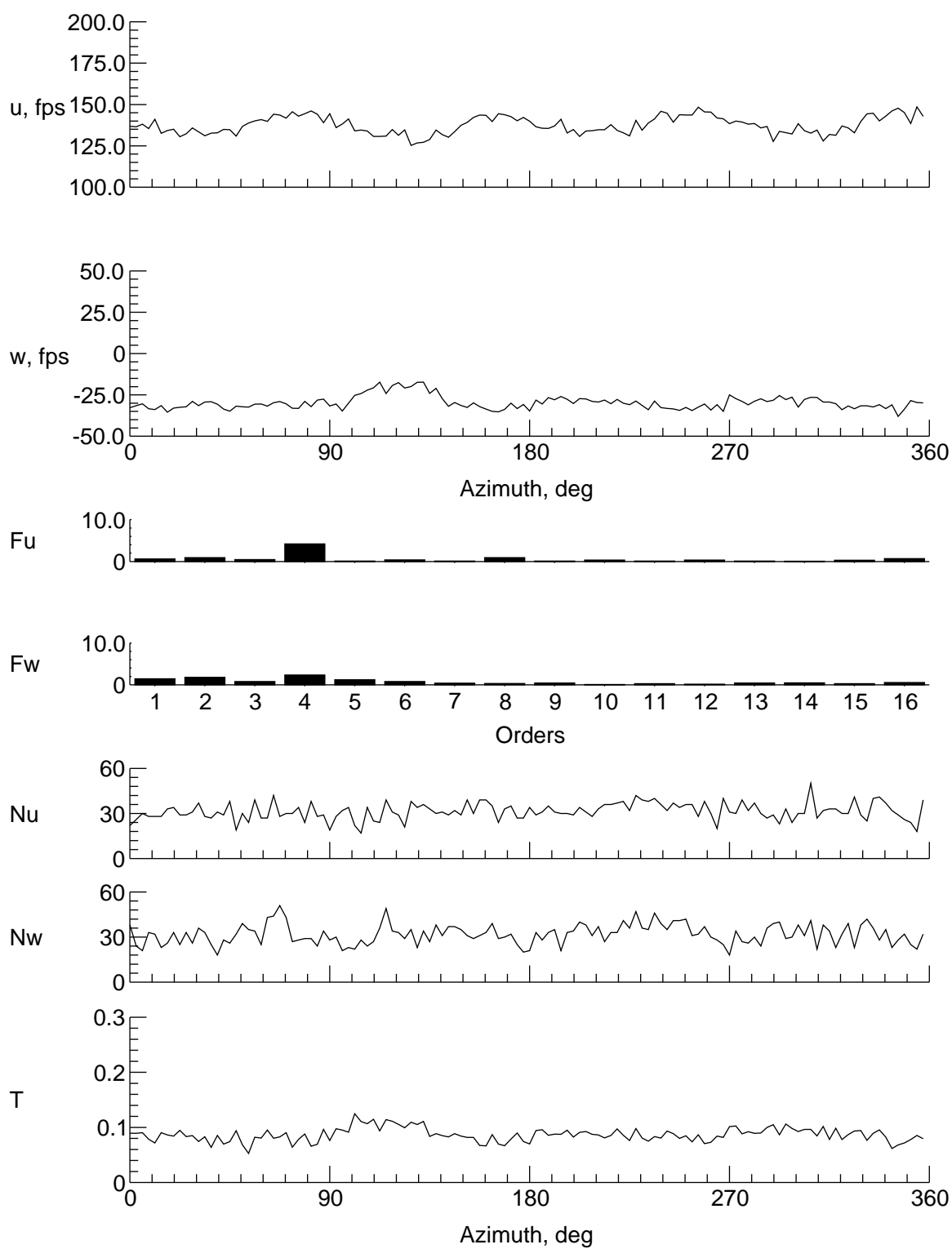
(l) $y = -4$ in., $z = -2.167$ in.

Figure 21. Continued.



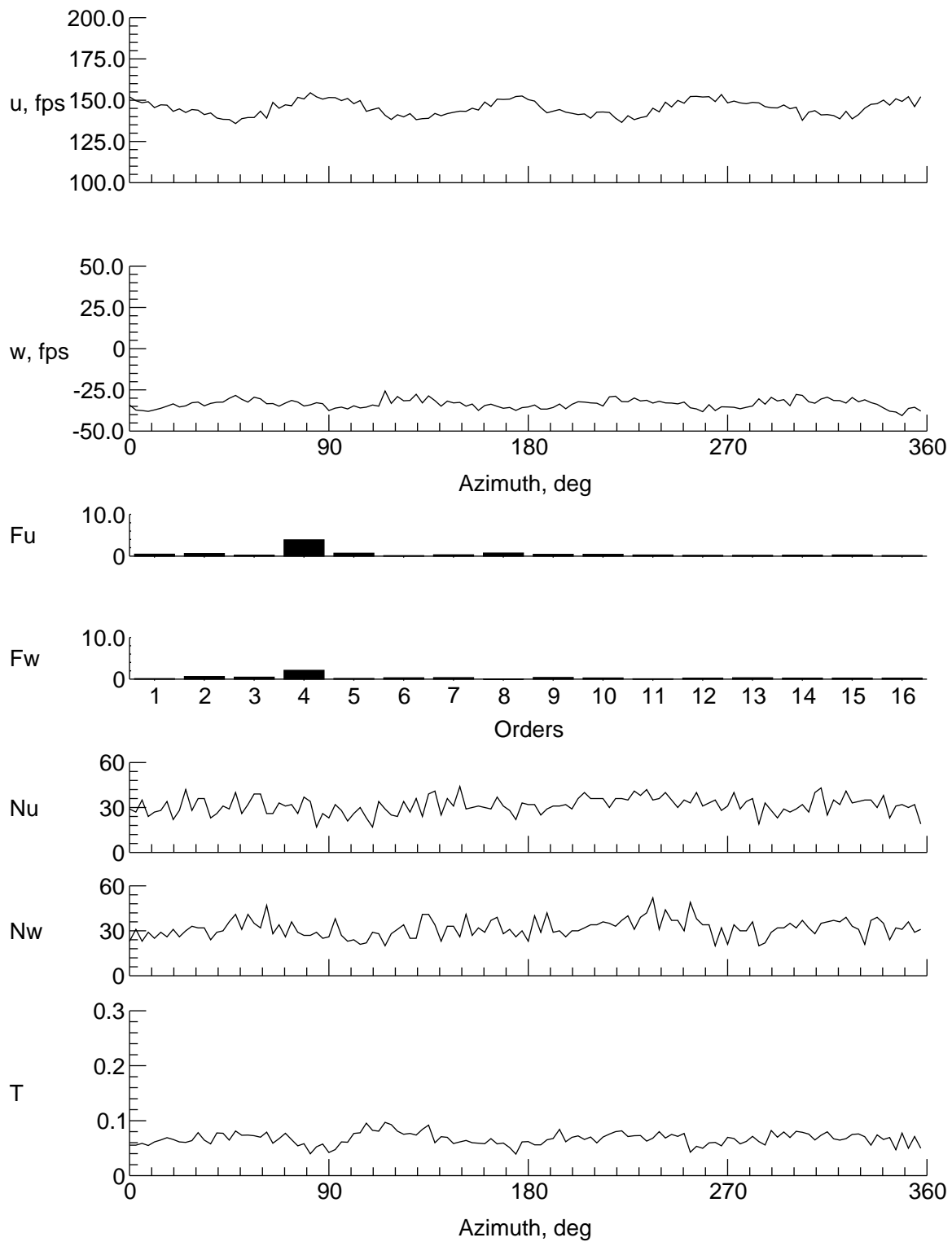
(m) $y = -6$ in., $z = -2.167$ in.

Figure 21. Continued.



(n) $y = -8$ in., $z = -2.167$ in.

Figure 21. Continued.



(o) $y = -9$ in., $z = -2.167$ in.

Figure 21. Concluded.

REPORT DOCUMENTATION PAGE			Form Approved OMB No. 0704-0188	
Public reporting burden for this collection of information is estimated to average 1 hour per response, including the time for reviewing instructions, searching existing data sources, gathering and maintaining the data needed, and completing and reviewing the collection of information. Send comments regarding this burden estimate or any other aspect of this collection of information, including suggestions for reducing this burden, to Washington Headquarters Services, Directorate for Information Operations and Reports, 1215 Jefferson Davis Highway, Suite 1204, Arlington, VA 22202-4302, and to the Office of Management and Budget, Paperwork Reduction Project (0704-0188), Washington, DC 20503.				
1. AGENCY USE ONLY (Leave blank)	2. REPORT DATE March 1997	3. REPORT TYPE AND DATES COVERED Technical Memorandum		
4. TITLE AND SUBTITLE Unsteady Velocity Measurement Taken Behind a Model Helicopter Rotor Hub in Foward Flight		5. FUNDING NUMBERS WU 505-59-36-01		
6. AUTHOR(S) John D. Berry				
7. PERFORMING ORGANIZATION NAME(S) AND ADDRESS(ES) NASA Langley Research Center Hampton, VA 23681-0001		8. PERFORMING ORGANIZATION REPORT NUMBER L-17524		
9. SPONSORING/MONITORING AGENCY NAME(S) AND ADDRESS(ES) National Aeronautics and Space Administration Washington, DC 20546-0001 and U.S. Army Aviation and Troop Command St. Louis, MO 63120-1798		10. SPONSORING/MONITORING AGENCY REPORT NUMBER NASA TM-4738 ATCOM TR-97-A-001		
11. SUPPLEMENTARY NOTES				
12a. DISTRIBUTION/AVAILABILITY STATEMENT Unclassified-Unlimited Subject Category 05 Availability: NASA CASI (301) 621-0390		12b. DISTRIBUTION CODE		
13. ABSTRACT (Maximum 200 words) Drag caused by separated flow behind the hub of a helicopter has an adverse effect on aerodynamic performance of the aircraft. To determine the effect of separated flow on a configuration used extensively for helicopter aerodynamic investigations, an experiment was conducted using a laser velocimeter to measure velocities in the wake of a model helicopter hub operating at Mach-scaled conditions in forward flight. Velocity measurements were taken using a laser velocimeter with components in the vertical and downstream directions. Measurements were taken at 13 stations downstream from the rotor hub. At each station, measurements were taken in both a horizontal and vertical row of locations. These measurements were analyzed for harmonic content based on the rotor period of revolution. After accounting for these periodic velocities, the remaining unsteady velocities were treated as turbulence. Turbulence intensity distributions are presented. Average turbulent intensities ranged from approximately 2 percent of free stream to over 15 percent of free stream at specific locations and azimuths. The maximum average value of turbulence was located near the rear-facing region of the fuselage.				
14. SUBJECT TERMS Helicopter; Wind tunnel model; Turbulence; Rotorcraft; Unsteady velocities; Rotor hub; Laser velocimeter			15. NUMBER OF PAGES 246	
			16. PRICE CODE A11	
17. SECURITY CLASSIFICATION OF REPORT Unclassified	18. SECURITY CLASSIFICATION OF THIS PAGE Unclassified	19. SECURITY CLASSIFICATION OF ABSTRACT Unclassified	20. LIMITATION OF ABSTRACT Unlimited	